Spectroscopic Investigation, Kinetic Analysis, and Ligand Field Theory Rationalization of Catalytic Reactivity for Data-Driven Methodology Development

Thesis by

Zhengjia Jaron Tong

In Partial Fulfillment of the Requirements

for the Degree of

Doctor of Philosophy

CALIFORNIA INSTITUTE OF TECHNOLOGY

Pasadena, California

2025

Defended December 7th, 2023

Zhengjia Jaron Tong

ORCID: 0000-0002-8476-6032

To friends, mentors, and women in my life that have lifted me up.

"In the dream where I am an island,

I grow green with hope. I'd like to end there."

—Jericho Brown

ACKNOWLEDGEMENTS

No one could have ever imagined that I would reach this milestone, and for a long time, I was among those naysayers. But even in days when there was no hope, against everyone else, my mother believed in me. And that was enough to give me the strength to move forward. Ms. Volcensek was among the first to believe in my ability, and the day she opened her college chemistry book and said, "Figure it out yourself," planted the seeds of curiosity. At Purdue, Dr. Beatrize Cisneros was the one who cultivated that seed, overriding each and every requirement so that I could do undergraduate research and take a second major in ways that I was not supposed to. Prof. Suzanne Bart was instrumental in shaping me into a researcher, so much so that she treated me like a graduate student in my senior year and allowed me to carry out exploratory experiments to synthesize uranium alkylidene. Without her, I would not have pursued graduate school, let alone studied at Caltech. Everyone's Ph.D. study is challenging in its way; at Caltech, I'm fortunate to have Prof. Sarah Reisman's brilliant one-liner comments at subgroups that forced me to think about chemistry differently, but more importantly, I'm fortunate to have Sarah's support, even in moments when it was the more difficult thing for her to do. Women have uplifted my career, and I will always be grateful.

At Caltech, I was fortunate to have great collaborators, and their intelligence, experience, and perspective have played a central role in shaping my scientific thinking regarding transition-metal catalysis. I owe a great deal of thanks to Dr. Carina Jette, who was my first project partner in the mechanistic elucidation of Cu-catalyzed alkyl alkylation reaction. She patiently helped me appreciate the nuance behind developing a good catalytic reaction while encouragingly inviting my contribution to design mechanistic experiments

with her. The brief six months of working with her lay much of the foundations for my approach of "staying close to the catalytic condition" for mechanistic interrogation. Although our collaboration was unfortunately cut short by the COVID-19 pandemic, I'm extremely proud of what we were able to produce, both the published and the unfinished work.

Regarding the Ni projects, I have an unending gratitude for Dr. Raymond Turro. I distinctly remember, after my first presentation in front of Sarah, in a joint-group meeting, Sarah commented on how well we worked together. True to Sarah's foresight, working with Ray was fun and fulfilling *because* we would disagree at every stage of our mechanistic interpretation and then help each other to design the next sets of experiments. I truly believe that our moments of bouncing off each other's findings and ideas helped us to reach a new height that neither of us anticipated. Aside from being an excellent collaborator, Ray was a true friend who provided me with unwavering support, even in difficult moments full of frustration. He always offered me help in the lab and life, and he was willing to listen. I'd always cherish the time Ray, his partner Larrisa, and I hung out. I only hope that our friendship will only grow and continue in the years to come.

It'd be remiss not to mention other members of the Reisman Lab that I have worked with and shared space with. Dr. Alex Shimozono and Ángel Hernández-Mejías, whom I worked with for the anhydride alkylation project, were truly inspiring experimental chemists. The extensive experimental data were truly humbling to me. They served as a continued reminder that I needed to strive to identify possible underlying design paradigms underpinning these complex data. I'm glad to be a part of a talented team, and other members of Team Nickel—Emily Chen, Travis DeLano, Golsa Gheibi, Will Chen, and

Julie Wahlman (even though we never overlapped)—have, in one way or another, helped me by sharing data with me, providing valuable discussions, or troubleshooting experiments with me. I'm also eternally grateful for my bench mates Dr. Caitlin Clacker, Dr. Simon Cooper, Cedric Lozano, along with Dr. Ray Turro, who helped me catch up on my synthetic skills. Outside of the lab, I'm thankful for the staff scientists at Caltech, particularly Dr. Paul Oyala, Dr. Mona Shahgholi, and Dr. Scott Virgil, who had always been available to help me brainstorm, learn and, use various instruments.

It is no hidden knowledge that my time at Caltech was filled with difficult moments of relapse, grief, and sociopolitical challenges, but friends and mentors carried me through. From helping me move to new apartments to getting me home safely from the hospital, they are always there for me. My friendships with Linh Le, Christian Johansen, Andrea Stegner, Dr. Ray Turro, Dr. Michael Zott, Dr. Sarah Zott, Dr. Gautam Stroscio, Dr. Ryan Ribson, Dr. Alex Barth, and Dr. Alex Folmer are invaluable to me. While I might have run out of opportunities to host dinners for them, I look forward to our future encounters.

Outside of Caltech, Los Angeles Aikido Center anchored me. Even though I did not get to go there often, I will take the lessons I learned training to heart. I appreciate my dance friends, particularly Philip M., Holly J., and Andrew B., for lending me an ear on the dance floor. Also, much gratitude to Dr. Nita Little and Nancy Stark Smith, my dance mentors, as well as Prof. Francis Robicheaux, Dr. Caleb Tatebe, Prof. Suzanne Part, and Dr. Beatriz Cisneros, my scientific mentors, my longtime friends Dr. Sadie Piatt, Adam Kline, Megan Harwell, and Devika Pradhan, all of whom I know carry me in their thoughts. Last but not least, my friends from the LGBTQ community, Travis L., Kinsley R., Seth, and Aiden D., thank you for being my beaconing light in storms.

ABSTRACT

First-row transition metal catalysis can leverage one or two-electron redox chemistry to catalyze selective C–C bond formation between two stereoelectronically differentiated substrates. Owing to this redox flexibility, many competing reaction pathways could occur, leading to the formation of both desired and undesired products. The electronic structure of the catalytic intermediates and reaction conditions are empirically recognized to modulate product distributions, but identifying the underlying design principle is often challenging. Mechanistic elucidation of the catalytic cycle and spectroscopic elucidation of important factors that influence catalytic reactivity could be beneficial to this endeavor. With the aid of ligand field theory and molecular orbital theory, a direct relationship may be established between the electronic structures of the metal catalysts and the thermodynamic or kinetic parameters of the elementary transformation they catalyze. To this end, this thesis describes the effort of combining spectroscopy, reactivity interpretation, and reaction kinetics to understand Ni-catalyzed reductive alkenylation and acylation of benzylic electrophiles and Cu-catalyzed allylic alkylation of γ-butyric lactone. The research approach and the results described herein are anticipated to aid the emergent effort of data-driven reaction development.

PUBLISHED CONTENT AND CONTRIBUTIONS

Portions of the work described herein were disclosed in the following publications:

1. Jette, C.I.; Tong, Z.J.; Hadt, R.G..; Stoltz, B.M.; Copper-Catalyzed Enantioselective Allylic Alkylation with a γ-Butyrolactone-Derived Silyl Ketene Acetal. *Angew. Chem. Int. Ed.*, **2019**, *59* (5), 2033. DOI: 10.1002/anie.201912618.

Z.J.T. conducted the spectroscopic and computational investigations.

2. McNicholas, B.*; Tong, Z.J.*; Bím, D.; Turro, R.F.; Kazmierczak, N.; Chalupský, J.; Chen. E.P.; Reisman, S.E.; Hadt, R.G. Electronic structures of nickel(II)-bis(indanyloxazoline)-dihalide catalysts: Understanding ligand field contributions that promote C(sp2)–C(sp3) cross-coupling. *Inorg. Chem.*, **2023**. *62* (34), 14010. DOI: 10.1021/acs.inorgchem.3c02048.

Z.J.T. collected seminal optical spectra, located the energies of optical transition, and provided initial optical assignments. Z.J.T. established the appropriate level of theory for DFT calculations and identified the appropriate active space for multi-configuration CASSCF calculations. Z.J.T. provided the initial draft of the manuscript.

3. Turro, R.F.; Wahlman, J.L.H.; Tong, Z.J.; Chen, X.; Yang, M.; Chen. E.P.; Hong, X.; Hadt, R.G.; Houk, K.N.; Yang, Y.; Reisman, S.E. Mechanistic Investigation of Ni-

Catalyzed Reductive Cross-Coupliong of Alkenyl and Benzyl Electrophiles. *J. Am. Chem. Soc.*, **2023**, *145* (27), 14705. DOI: 10.1021/jacs.3c02649

Z.J.T. contributed to the spectroscopic elucidation of the catalytic cycle. Z.J.T. facilitated the preparation of the manuscript and the mechanistic discussion therein.

4. Hernández-Mejías, A.; Shimozono, A. M.; Hazra, A.; Richter, S.; Tong, Z.J.; Langille, N.F.; Quasdorf, K.; Parsons, A. T.; Sigman, M.S.; Reisman, S.E.; Ni-Catalyzed Enantioselective Desymmetrization: Development of Divergent Acyl and Decarbonylative Cross-Coupling Reactions. *J . Am. Chem. Soc.* **2025**, *147* (4), 3468. DOI: 10.1021/jacs.4c14767

Z.J.T. contributed to the mechanistic elucidation and conducted preliminary electrochemical studies.

TABLE OF CONTENTS

LIST OF ABBREVIATIONS

$[a]_D$	angle of optical rotation of plane-polarized light
A	ampere(s)
Å	angstrom(s)
Ac	acetyl
Alk	generic alkyl group
anti-	from opposite sides
Ar, (het)Ar	generic aryl, heteroaryl group
Bn	benzyl
Box	Bis(oxazoline)
bpy	2,2′-bipyridine
CASSCF	complete active space self-consistent field
CASPT2	complete active space second-order perturbation theory
CD	circular dichroism
cm^{-1}	wavenumber(s)
COD	1,5-cyclooctadiene
$C(sp^2)$	sp^2 hybridized carbon center
$C(sp^3)$	sp^3 hybridized carbon center
Cu	copper
CPCM	conductor like polarizable continuum
CV	cyclic voltammetry/cyclic voltammogram
δ	chemical shift in ppm

DCM	dichloromethane
DFT	density functional theory
DFTB	density functional tight binding
DMA	dimethylacetamide
dme	1,2-dimethoxyethane
DMSO	dimethyl sulfoxide
dr	diastereomeric ratio
ee	enantiomeric excess
E	reduction potential
EPR	electron paramagnetic resonance
equiv	equivalent(s)
ESI	electrospray ionization
Et_2O	Diethyl ether
EtOAc	ethyl acetate
Fc	ferrocene
Fc^+	ferrocenium
FID	flame ionization director
fwhm	full width half max
HOMO	highest occupied molecular orbital
G	gauss or Gibs free energy
GC	gas chromatography
h	hour(s)
IB	IndaBox

IndaBox	(3aR,3a′R,8aS,8a′S)-2,2′-(cyclopropane-1,1-diyl)bis(3a,8a-dihydro-8H-indeno[1,2-d]-oxazole) and its enantiomer
in situ	in the reaction mixture
IR	infrared
LUMO	lowest unoccupied molecular orbital
M	molar
MCD	magnetic circular dichroism
MeCN	acetonitrile
mg	milligram(s)
min	minute(s)
mL	milliliter(s)
m/z	mass-to-charge ratio
nm	nanometer(s)
NHE	normal hydrogen electrode
NHP	N-hydroxylphthalimide
Ni	nickel
NIR	near infrared
NMR	nuclear magnetic resonance
Ph	phenyl
PhH	benzene
PF_6	hexafluorophosphate
Py	pyridine
RAMO	redox active molecular orbital

rpm	rotation per minute
SCE	standard calomel electrode
SMD	universal solvation model
sp^2	sp^2 hybidized
sp^3	sp^3 hybirdized
syn-	from the same side
TBA	tetra-n-butylammonium
TDAE	tetrakis(dimethylamino)ethene
TES	triethylsilyl
THF	tetrahydrofuran
THP	tetrahydropyran
TMS	trimethylsilyl
TS	transition state
UV	ultraviolet
V	volt(s)
vide infra	see below
vide supra	see above
Vis	visible spectrum
Vn	vinyl, specifically *trans*-1-(2-aryl)vinyl (styrenyl)
VT	variable temperature
XAT	halogen atom abstraction
XRD	X-ray diffraction

ABOUT THE AUTHOR

Jaron Tong was born in Xinxiang, a small city in central China. He moved to Beijing in 2003 and then to the United States in 2012, where he attended Dominican High School in Milwaukee, WI. At Dominican, Jaron independently studied AP chemistry by watching recorded lectures on MIT OpenCourseWare and discovered his love for science.

Jaron attended Purdue University to study chemistry and physics. Encouraged by his academic advisor, Dr. Beatriz Ciscnero, Jaron conducted honors freshman research with Prof. Suzanne Bart, and he ended up staying in her group for four years. He first studied the formation of uranium imido with Dr. Nicholas Anderson. In 2016, he turned his attention to the formation of the uranium oxo and uranium alkylidene complexes under the tutelage of Dr. John Kiernicki and Dr. Caleb Tatebe, culminating in his first scientific publication. Concurrently, his interest in quantum mechanics was furthered by Prof. Francis Robicheaux, with whom he studied atomic physics. Jaron conducted one year of theoretical physics research in Prof. Chris Greene's group. Working with Dr. Mathew Eiles, Jaron played an instrumental role in identifying the perturbation conditions to generate long-range polarized Rydberg atoms by showing the limitations of random trials. Jaron graduated from Purdue with the highest distinction, obtaining degrees in chemistry (B.S.Ch) and applied physics honors (B.S.) with minors in mathematics and gender studies.

Seeking to unify his training, Jaron joined Prof Ryan Hadt's group to use optical spectroscopy to study first-row transition metal catalysis. Upon realizing his passion lies in synthetic chemistry, he joined Prof. Sarah Reisman to gain a deeper appreciation for method development. Jaron looks forward to furthering his skills in synthesis and using his interdisciplinary training to tackle complex societal challenges in his future career.

Chapter 1

Cu-Catalyzed Enantioselective Allylic Alkylation with a γ-Butyrolactone-Derived Silyl Ketene Acetal.[†]

1.1 Introduction

γ-Butyrolactones are important structural motifs present in numerous natural products and pharmaceutically relevant compounds, and are also useful synthetic building blocks that serve as precursors for other highly functionalized molecules.[1] Although there are a number of reports on the α-functionalization of γ-butyrolactones to form chiral quaternary centers, only a limited number of examples have demonstrated the construction of chiral α-*tertiary* γ-butyrolactones.[1b] Some previously disclosed strategies include chiral auxiliary-directed alkylation and subsequent cyclization,[1b] Claisen-type rearrangements[1c], and catalytic hydrogenation approaches.[1d] However, reports on the construction of these molecules via enantioselective α-functionalization remain limited, as the potential for

[†] This chapter was reproduced from a published manuscript.

racemization of the product necessitates the development of exceptionally mild reaction conditions.[2]

Since the seminal report by Tsuji,[3] transition-metal catalyzed allylic alkylation of enolate-derived nucleophiles continues to be an attractive approach for α-functionalization of carbonyl-containing compounds, as the alkene may be easily converted to a diverse array of functional groups. Nonetheless, the use of γ-butyrolactones in this transformation remains underdeveloped.[4]

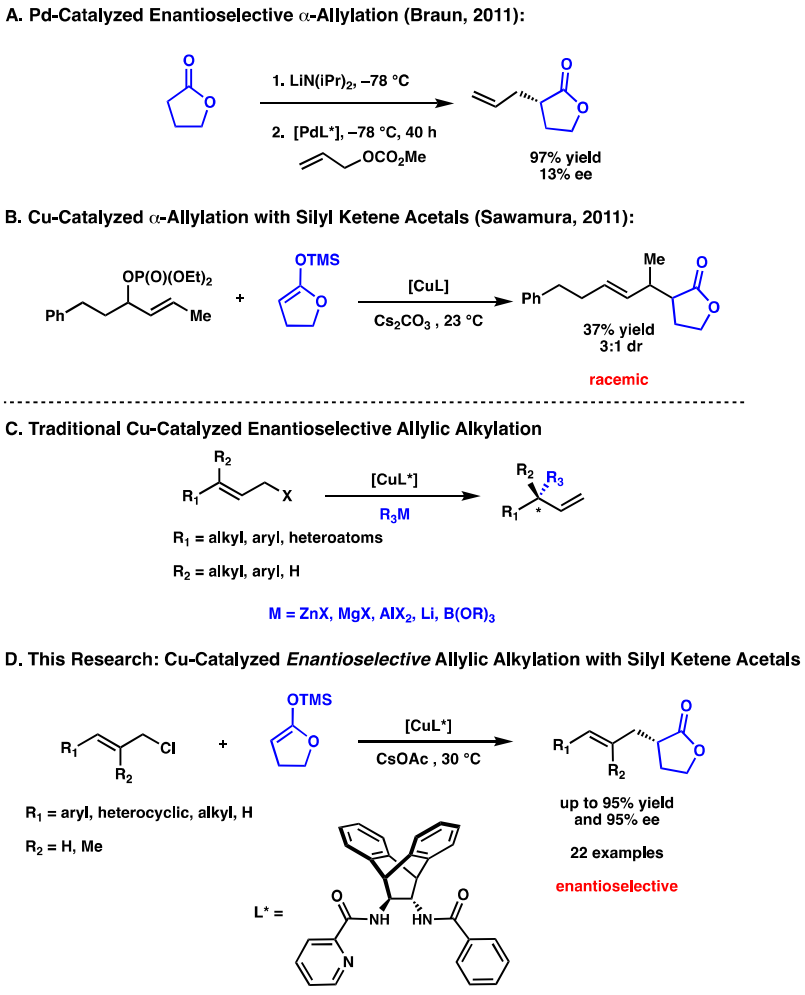

Figure 1. *Transition-metal catalyzed α-allylation of γ-butyrolactones.*

More specifically, there is only one example on the use of this transformation to

produce enantioenriched α-*tertiary* lactones.[4c] Although the desired product is obtained in moderate diastereoselectivity and good *ee* when an electrophile possessing terminal substitution is used, the *ee* is extremely low when simple allyl carbonate is employed (**Figure 1A**). As part of our ongoing interest in exploring first row transition metals in enantioselective catalysis,[5] we became interested in a system previously reported by Sawamura, wherein a Cu catalyst was used to obtain the desired α-allyl γ-butyrolactone in a racemic fashion by reaction of silyl ketene acetals with allylic phosphates (**Figure 1B**).[6] It should be noted that Cu as a catalyst in allylic substitutions with hard, organometallic nucleophiles (p*K*a > 40) has been extensively studied, and the desired branched products can be accessed in high yields and enantioselectivities (**Figure 1C**).[7] However, the use of Cu with softer, enolate derived nucleophiles (p*K*a < 30), remains underdeveloped.[8,9]

One challenge associated with the development of the enantioselective variant of this transformation is that it involves a prochiral nucleophile, which, to our knowledge, is unprecedented in Cu-allylic alkylations. For this reason, we believe that we would not be able to rely on chiral ligand scaffolds previously used in this type of transformation. Herein, we report a Cu-catalyzed asymmetric allylic alkylation with a γ-butyrolactone-derived enolate.

1.2 Results and Discussion

1.2.1 Reaction Optimization

Table 1. *Evaluation of Ligands for Enantioselective Cu-Catalyzed Allylic Alkylation*[a]

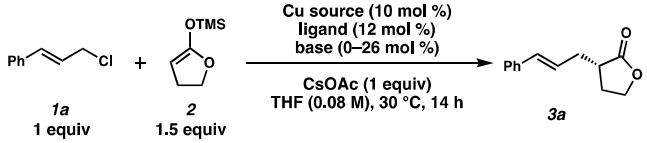

entry	Cu source	base	ligand	yield (%)[b]	ee (%)[c]
1	$[Cu(MeCN)_4]PF_6$	none	***L1***	74	22
2	$CuCl_2$	*n*-BuLi (24 mol %)	***L2***	44	62
3	$CuCl_2$	*n*-BuLi (12 mol %)	***L3***	60	11
4	$CuCl_2$	*n*-BuLi (12 mol %)	***L4***	64	14
5	$CuCl_2$	*n*-BuLi (24 mol %)	***L5***	44	40
6	$CuCl_2$	*n*-BuLi (24 mol %)	***L6***	54	62
7	$CuCl_2$	*n*-BuLi (24 mol %)	***L7***	33	62
8	$CuCl_2$	LiHMDS (26 mol %)	***L8***	90	92
9	$CuCl_2$	LiHMDS (26 mol %)	***L9***	73	91
10	$CuCl_2$	LiHMDS (26 mol %)	***L10***	83	89
11	$CuCl_2$	LiHMDS (26 mol %)	***L11***	80	87
12[d]	**$CuCl_2$**	**LiHMDS (13 mol %)**	***L8***	**90**	**94**
13[d,e]	$CuCl_2$	NaHMDS (13 mol %)	***L8***	94	87
14[d,e]	$CuCl_2$	KHMDS (13 mol %)	***L8***	95	85

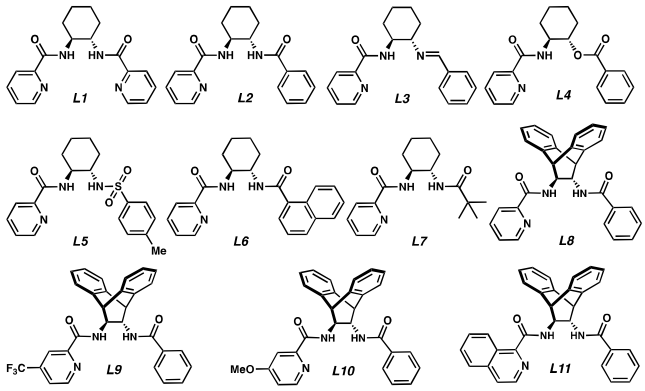

(a*) Conditions: 0.1 mmol scale. See SI for details about the reaction setup. (b) Determined by [1]HNMR analysis of the crude reaction mixture using 1,3,5–trimethoxybenzene as a standard. (c) Determined by chiral SFC analysis of isolated product. (d) 5 mol% $CuCl_2$, 6 mol% ligand, 0.042 M, 6 h. (e) 3 h reaction time instead.*

Upon examination of more than 20 commercially available ligands, we found chiral cyclohexyl bis-picolinamide ligand **L1** (**Table 1**, entry 1) was the only ligand to impart any degree of stereocontrol.[10] Although encouraged by these preliminary results, we found that the reaction outcome was highly variable, and after careful examination of all the reaction

parameters, we concluded that the source of variability was the ligand itself. As a consequence of the large number of coordinating atoms present and its flexibility, we believed **L1** could bind to Cu in a variety of conformations. As a result, small changes in the reaction set-up could alter the distributions of different Cu complexes in solution. We found that by employing mono-picolinamide **L2** as the ligand, $CuCl_2$ as the Cu source, and by deprotonation of both amide hydrogens on the ligand with *n*-BuLi, we were able to consistently obtain our product in moderate yields and *ee* (entry 2).

To determine whether the benzamide moiety was critical for reactivity and selectivity, we synthesized and tested ligands bearing a mono-imine (**L3**), an ester moiety (**L4**) and a sulfonamide (**L5**). The anionic benzamide appears to be especially important for stereocontrol, as removing this moiety led to a drastic decrease in *ee* (**L3** and **L4**, entries 3 and 4). In comparison, anionic sulfonamide-containing **L5** performed most similarly to **L2** (entry 5). Interestingly, we found the *ee* was not very sensitive to the identity of the organic substituent on the amide; although the use of naphthylamide **L6** and pivalamide **L7** resulted in very different yields, the *ee*'s were identical (entries 6 and 7).

After synthesizing and testing a number of chiral mono-picolinamide ligands, we found that a bulkier backbone (**L8**, entry 8) was crucial for consistently high levels of reactivity and selectivity. We also noted that altering the electronics at the position *para* to the nitrogen (**L9** and **L10**, entries 9 and 10) or increasing the steric bulk of the pyridine moiety (**L11**, entry 11) led to no improvement in yield or *ee*.

Upon more extensive optimization we found that lowering the reaction concentration from [0.08 M] to [0.042 M] led to a slight increase in ee, and with 5 mol % Cu, the reaction was complete in 6 h (entry 12).[15] Furthermore, we noted that the counterion on the catalytic

base did have an effect on the overall outcome of the reaction: when NaHMDS (entry 13) or KHMDS (entry 14) is used instead of LiHMDS, the ee is slightly reduced but the reaction is complete in only 3 hours.

1.2.2 Substrate Scope

Table 2. *Scope of Allylic Chloride*[a]

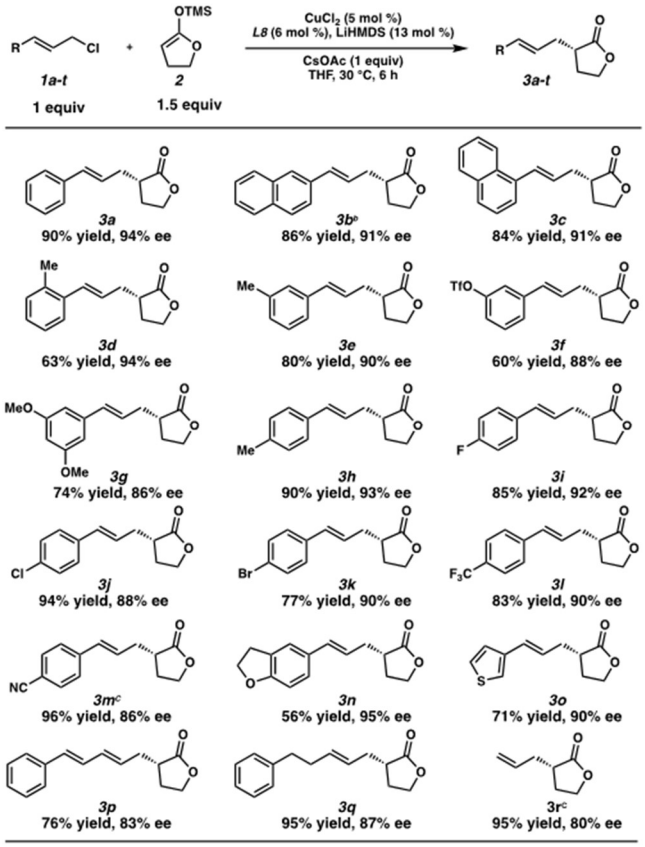

*(a) Isolated yields on 0.2 mmol scale. Enantiomeric excess was determined by SFC analysis. (b) Absolute stereochemistry was determined by X-ray diffraction. (c) With 10 mol % $CuCl_2$, 12 mol % **L8**, and 26 mol % LiHMDS.*

With optimized conditions in hand, we examined the scope of the electrophile (**Table 2**). We were pleased to find 2-napthyl **3c** and *ortho*- methylphenyl (**3d**) substituents were well tolerated. *Meta*-phenyl substituted electrophiles (**3b**, **3e**) also fared well, and even a sensitive triflate (**3f**) and a bulky 3,5-dimethoxy phenyl group (**3g**) led to products

in good yield and *ee*. Furthermore, substituents at the *para*-phenyl position such as halogens (**3i**, **3j**, **3k**), a trifluoromethyl (**3l**), and a nitrile (**3m**) were also well-tolerated. Even heterocyclic compounds (**3n** and **3o**), a diene substrate (**3p**), an aliphatic allylic chloride (**3q**) and unsubstituted allyl chloride (**3r**) led to product formation in good yields and *ee*'s.

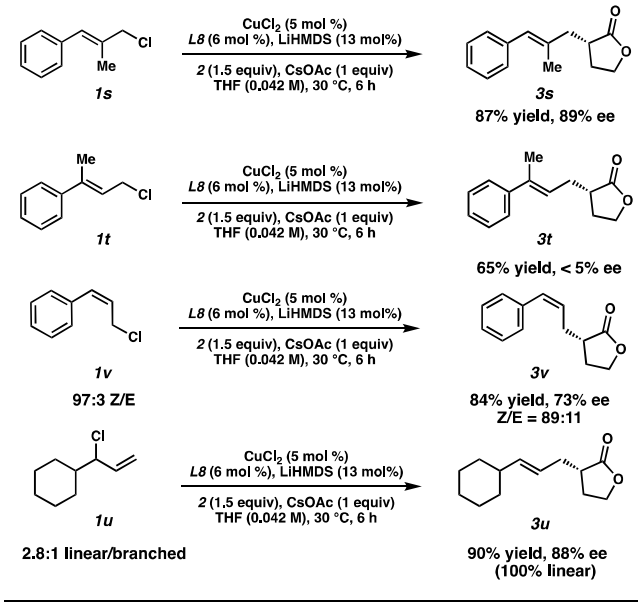

Scheme 1. *Importance of Olefine Substitution Pattern. (a) Isolated yields on 0.2 mmol scale. Enantiomeric excess was determined by supercritical fluid chromatography.*

Although trisubstituted olefin **1s** (**Scheme 1**) led to the desired product **3s** in good selectivity and yield, the product formed from α-,α- disubstituted olefin **1t** was obtained in significantly lower yield and *ee*. Intrigued by this result, we exposed *Z*-olefin substrate **1v** to our reaction conditions. Interestingly, we obtained the corresponding *Z*-olefin product **3v** in good yield, but in only moderate ee. Furthermore, we also noted that even when a mixture of linear and branched electrophiles is used, only the linear product is obtained (**3u**).[16] Taking these results into account, and also considering that other electrophiles such as benzyl chloride and phenethyl chloride result in no product formation, we believe the

reaction is proceeding through a $Cu^{III}[\sigma+\pi]$ allyl species (see **Scheme 3**, **D**).[17]

1.2.3 Spectroscopic and Computational Characterization of Precatalyst

Given the novelty of the Cu/**L8** complex, we chose to examine it using continuous wave (CW) X-band electron paramagnetic resonance (EPR), UV-vis spectroscopies, and density functional theory (DFT) calculations. Although the crystal structure of a planar Cu^{II} complex with a tetradentate, deprotonated **L1** has been reported,[13] it was unclear how exclusion of one of the pyridine moieties would affect the binding mode of the ligand. For this reason, we aimed to determine whether our best performing ligand **L8** coordinates through the two amide nitrogens, or if it adopts an alternative binding mode through the benzamide oxygen, similarly to the previously disclosed Mo/**L2** complex.[14]

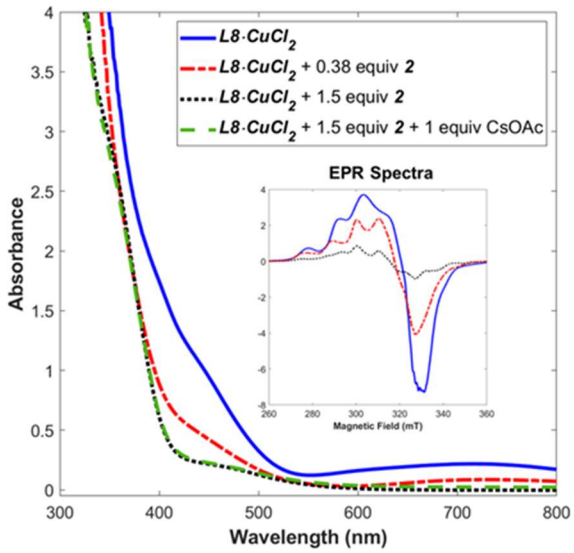

***Figure 2**. Room temperature UV-vis and 77 K X-band EPR (inset) spectroscopic monitoring of the reaction of 5 mol% of L8•$CuCl_2$ with silyl ketene acetal 2. (Additional details in Supporting Information.)*

Preparing the pre-catalyst in THF afforded a green solution with low intensity d-d transitions ranging from 560 to 1400 nm (Figure 2 and S4). Spin quantification of the 77

K X-band EPR spectra revealed a monomeric Cu^{II} center was the major species at the reaction concentration.[15] Negative ion mode ESI-MS generated product ions and isotope patterns consistent with the ionization of the fully deprotonated $[\mathbf{L8{\bullet}CuCl_2}]^{2-}$ species, indicating the Cl^- counter-ions may be playing a role in the generation of a consistent complex.

***Table 3**. DFT Calculations on L8 and L8•$CuCl_2$[a].*

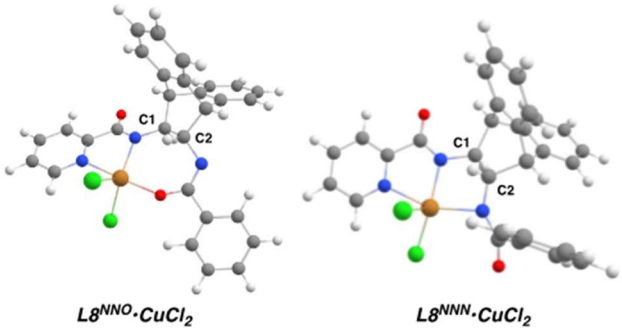

$L8^{NNO}{\cdot}CuCl_2$ $L8^{NNN}{\cdot}CuCl_2$

entry	ligand binding mode	$E_{gas\ phase}$ (kcal/mol)	$E_{solvent\ corrected}$ (kcal/mol)[c]	τ_4' C1	τ_4' C2
with $CuCl_2$					
1	$L8^{NNO}{\cdot}CuCl_2$	0	0	0.93	0.95
2	$L8^{NNN}{\cdot}CuCl_2$	22.5	19.5	0.86	0.85
without $CuCl_2$[b]					
3	relaxed $L8^{2-}$	0	0	0.96	0.97
4	$L8^{NNO}$	18.7	13.6	0.93	0.95
5	$L8^{NNN}$	39.5	30.0	0.86	0.85

(a) Obtained using B3LYP density functional with 38% Hartree-Fock exchange. (b) Ligand coordination geometry was obtained by removing $CuCl_2$ from the optimized geometry of the corresponding complex.

DFT calculations indicate **L8** preferentially binds to Cu in a tridentate fashion, via $N_{pyridine}$, $N_{picolinamide}$, and $O_{benzamide}$ atoms ($\mathbf{L8^{NNO}{\bullet}CuCl_2}$, **Table 3**, entry 1). Regardless of the level of theory employed, the alternative tridentate binding mode via the benzamide nitrogen ($\mathbf{L8^{NNN}{\bullet}CuCl_2}$) is disfavored by 14-23 kcal/mol (entry 2 and **Table S2**). This large energy difference renders the thermal interconversion between the two binding modes

unlikely; for this reason, we postulate only one conformer of the pre-catalyst accounts for the observed asymmetric catalytic activity.

To further probe the origin for this binding preference, we performed single-point calculations on **L8** (entries 3-5). In the absence of $CuCl_2$, the energy gap between the two conformations $\mathbf{L8^{NNO}}$ and $\mathbf{L8^{NNN}}$ is still retained (entry 4 and 5), implying ligand sterics affect the binding preference and tune the metal coordination geometry. As demonstrated by the geometry index τ_4',[16] the two sp^3 ring carbons **C1** and **C2** exhibit a stronger deviation from the ideal tetrahedral geometry (τ_4' = 1) in $\mathbf{L8^{NNN}}$ relative to $\mathbf{L8^{NNO}}$. By comparison, the more flexible **L2** shows a lesser degree of distortion as well as a reduced energetic preference for $\mathbf{L2^{NNO}}$.[17] Thus, in addition to providing steric bulk to assist in stereocontrol, the rigid backbone of **L8** likely plays an important role in enforcing NNO binding.

1.2.4 Activation of Precatalyst and Proposed Mechanism

The characteristic d-d transitions and 77 K X-band EPR signal of the starting **L8•CuCl₂** complex disappear at the start of the reaction, signifying the Cu^{II} precatalyst is reduced to an active Cu^{I} complex (**Figure 2**). We found reduction occurs even in the absence of CsOAc, indicating the silyl ketene acetal **2** is the reductant.[19] Consequently, we propose the reaction follows a Cu^{I}-Cu^{III} catalytic cycle as shown in Scheme 2.[20]

We believe the catalytic cycle commences with coordination of the electron-rich olefin of the silyl ketene acetal to Cu^{I} bis-amidate complex **A**, forming **B**. The Si–O bond is then cleaved via outer sphere attack by the acetate anion to afford the desired C-bound Cu enolate **C**.[21] We envision this could be the enantiodetermining step, during which the lithium counter-ion may assist through electrostatic interactions, preventing rotation of the silyl ketene acetal. Dissociation of the benzamide then allows for the coordination and

subsequent oxidative addition of the allyl chloride, generating $Cu^{III}[\sigma+\pi]$ species **D**.[12, 22] The sterically encumbered Cu^{III} species can undergo reductive elimination to generate the desired α-allyl γ-butyrolactone and the starting Cu^{I} species **A**.

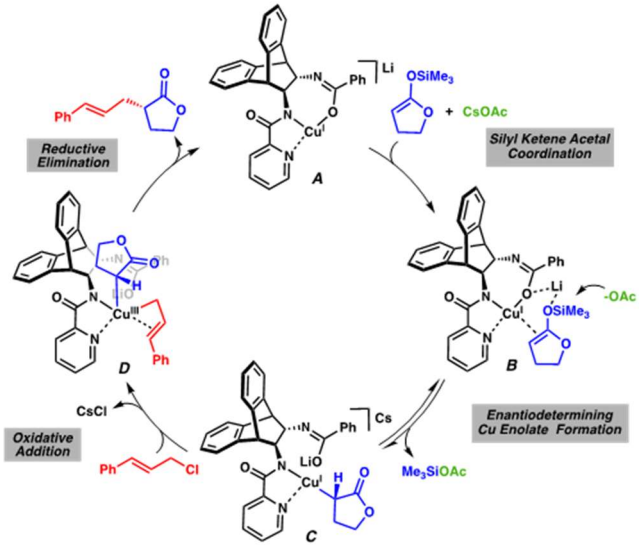

Scheme 2. *Proposed Mechanism*

1.2.5 Product Derivatization

In order to demonstrate the synthetic utility of these products, we subjected α-allyl γ-butyrolactone **3a** and **3r** to a number of transformations (**Scheme 3**)[23]. Lactone **3a** was reduced to the corresponding lactol **4** using DIBAL-H. Lactol **4** was then converted to the unsaturated ester, which spontaneously cyclized to the corresponding furan **5** in high yields using lithium aluminum hydride. We also found **3r** could be swiftly converted to the corresponding methyl acrylate species via cross metathesis.

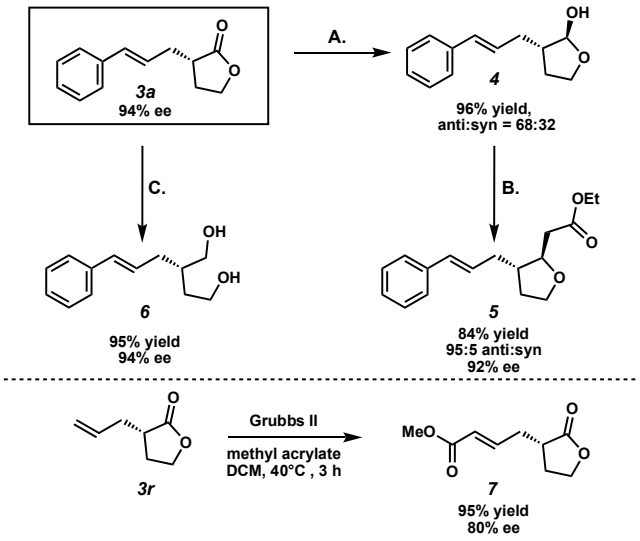

Scheme 3. Derivatization of Allyl γ-Butyrolactone Products[a] *(a) Conditions: A. DIBAL-H, CH_2Cl_2, –78 °C, 30 min. B. NaH, triethylphosphonoacetate, THF, 0 °C to 23 °C, 3 h. C. $LiAlH_4$, Et_2O, reflux, 3 h.*

1.3 Concluding Remarks

In conclusion, we have developed a Cu-catalyzed enantioselective allylic alkylation with a non-stabilized enolate-derived nucleophile. Critical to the development of this reaction was the identification of a novel mono-picolinamide ligand that led to product formation in high yields (up to 96%) and enantiomeric excess (up to 95%). A number of electrophiles with a broad range of functionality were well-tolerated in this reaction, including aryl, heteroaryl, and aliphatic allylic chlorides. DFT calculations suggest ligand sterics play an important role in determining metal coordination geometry, leading to tri-dentate NNO Cu coordination by the ligand. Preliminary mechanistic investigations indicate that a Cu^{I} species is likely the active catalyst, and that the reaction may proceed through a $Cu^{III}[\sigma+\pi]$ intermediate. Future work will focus on understanding ligand contributions to reactivity and expanding the scope of this reaction to include other enolate derived nucleophiles[24].

1.4 Experimental Sections

IR spectra were obtained using a Perkin Elmer Spectrum BXII spectrometer or Nicolet 6700 FTIR spectrometer using thin films deposited on NaCl plates and reported in frequency of absorption (cm^{-1}). X-Band (9.4 GHz) Continuous-wave(CW) EPR spectra were obtained using a Bruker EMX spectrometer with its Bruker Win-EPR software (version 3.0). A vacuum-insulated quartz liquid nitrogen dewar was inserted into the EPR resonator to obtain all spectra at 77 K. For optimal sensitivity, all spectra were collected with 0.5 mW microwave power and averaged over four scans. UV-Vis-NIR spectra were acquired using Varian Cary 500 Scan spectrophotometer with Varian Cary WinUV software(version 4.10(464)). Samples were loaded into 1 cm Starna Cell borosilicate cuvettes enclosed with screw caps. The spectra were collected from 300 nm to 1650 nm at a 600 nm/min scan rate and corrected for THF background. IR spectra were collected using a Bruker Alpha Platinum ATR spectrometer with OPUS software (version 7.0.129) stored in a glovebox under N_2. An aliquot of sample solution was deposited onto the spectrometer to form a thin film, and the spectra were collected over 32 scans

All calculations were performed using the ORCA 4.1.2 package.[25] Unless otherwise specified, the spectroscopically calibrated Becke3-Lee-Yang-Parr density functional with 38% exact Hartree-Fock exchange (B3(38HF)LYP was employed, similar to that reported by Solomon and coworkers.[26] All atoms were described with the def2-TZVP basis set. Calculations were performed with the finest available grid (Grid7) and the chain of sphere approximation (RIJCOSX) for two-electron integrals on the corresponding finest auxiliary integration grid (GRIDX9) for the RI/J auxiliary basis set. Gas-phase geometries were optimized with tight convergence criteria ($\Delta E \leq 1*10^{-8}$ Hartree).

Frequency calculations were used to confirm optimized structures represented local minima on the potential energy surfaces. To approximate solvent effects, single point energy calculations were performed on gas-phase optimized geometries using a conductor-like polarizable continuum model for THF. In all cases, counter ions were excluded from calculations.

Supporting Computational Results

To understand how variations in the optimized geometry affected single point energy calculations, we re-optimized the B3(38HF)LYP-optimized geometry (**geometry B**) with the B3(0HF)LYP density functional. The resulting structures (**geometry A**) show increased deviation from a trigonal bipyramidal geometry (τ_5 = 1) towards square pyramidal geometry (τ_5 = 0) (Figure S1 and Table S1).

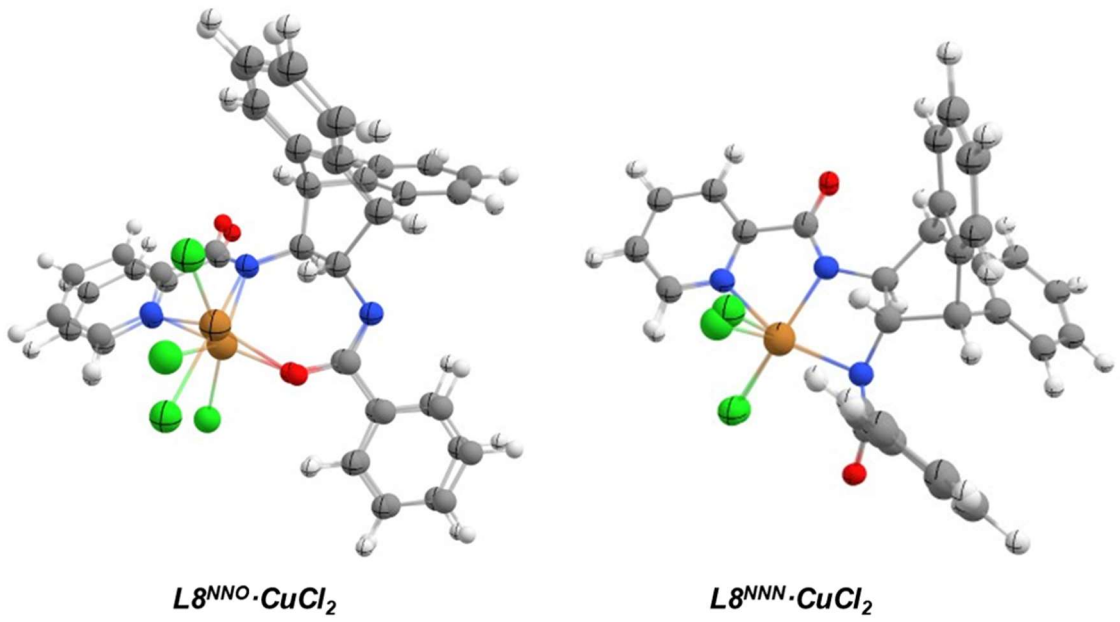

Figure S1. *Hartree-Fock dependence on* ***L8^{NNO}•CuCl$_2$*** *(left) versus* ***L8^{NNN}•CuCl$_2$*** *(right) geometry. Geometry A (grid): B3(0HF)LYP optimized geometry; Geometry B (filled): B3(38HF)LYP optimized geometry.*

Table S1. *Effects of Levels of Theory on the Optimized Geometry of* ***L8•CuCl₂.***

$L8^{NNO}$·$CuCl_2$	geometry A	geometry B	$L8^{NNN}$·$CuCl_2$	geometry A	geometry B
bond lengths (Å)			bond lengths (Å)		
Cu-N1	2.16	2.07	Cu-N1	2.10	2.20
Cu-N2	2.06	2.16	Cu-N2	2.03	2.05
Cu-O	2.10	1.95	Cu-N3	2.17	2.15
Cu-Cl1	2.39	2.48	Cu-Cl1	2.62	2.62
Cu-Cl2	2.37	2.54	Cu-Cl2	2.31	2.36
bond angles (°)			bond angles (°)		
N1-Cu-N2	78	77	N1-Cu-N2	77	75
N1-Cu-O	125	174	N1-Cu-N3	160	158
N1-Cu-Cl1	108	89	N1-Cu-Cl1	88	87
N1-Cu-Cl2	90	86	N1-Cu-Cl2	92	89
N2-Cu-O	90	99	N2-Cu-N3	83	83
N2-Cu-Cl1	96	122	N2-Cu-Cl1	99	103
N2-Cu-Cl2	165	120	N2-Cu-Cl2	151	143
O-Cu-Cl1	127	97	N3-Cu-Cl1	96	98
O-Cu-Cl2	89	92	N3-Cu-Cl2	105	108
Cl1-Cu-Cl2	97	114	Cl1-Cu-Cl2	108	109
τ_5	0.64	0.86	τ_5	0.15	0.24

Table S2. *Effects of Levels of Theory on the Energy Barrier.*

Entry	Density Functional	Geometry	Solvent Correction	E_{NNO} (Hartree)	E_{NNN} (Hartree)	ΔE (Hartree)	ΔE (kcal/mol)
1	B3(0HF)LYP	Geometry A	none	-3987.8133	-3987.7866	0.0267	16.8
2	B3(38HF)LYP	Geometry A	none	-3997.8498	-3997.8189	0.0309	19.4
3	BP86	Geometry B	none	-3994.4699	-3994.4422	0.0277	17.4
4	THSSh	Geometry B	none	-3994.2266	-3994.1974	0.0292	18.3
5	B3LYP	Geometry B	none	-3993.0735	-3993.0411	0.0324	20.3
6	B3(0HF)LYP	Geometry B	none	-3987.8063	-3987.7774	0.0289	18.1
7	B3(10HF)LYP	Geometry B	none	-3990.4324	-3990.4018	0.0306	19.2
8	**B3(38HF)LYP**	**Geometry B**	**none**	**-3997.8647**	**-3997.8289**	**0.0358**	**22.5**
9	BP86	Geometry B	CPCM	-3994.6932	-3994.6685	0.0247	15.5
10	THSSh	Geometry B	CPCM	-3994.4522	-3994.4265	0.0257	16.1
11	B3LYP	Geometry B	CPCM	-3993.2977	-3993.2728	0.0249	15.6
12	B3(0HF)LYP	Geometry B	CPCM	-3988.0281	-3988.0059	0.0222	13.9
13	B3(10HF)LYP	Geometry B	CPCM	-3990.6555	-3990.6321	0.0234	14.7
14	**B3(38HF)LYP**	**Geometry B**	**CPCM**	**-3998.0902**	**-3998.0591**	**0.0311**	**19.5**

Using the two optimized structures, we examined the Hartree-Fock dependence on the energy difference between $\mathbf{L8^{NNO}{\bullet}CuCl_2}$ and $\mathbf{L8^{NNN}{\bullet}CuCl_2}$ ($\Delta E \equiv E_{NNN} - E_{NNO}$) (Table S2). Despite $\mathbf{L8^{NNO}{\bullet}CuCl_2}$ exhibiting a modest structural variation between different functionals, the energy difference between NNO vs. NNN coordination between the different geometries remains relatively small (entries 1 and 6, or entries 2 and 8). Additionally, within the same geometry, increasing the amount of Hartree-Fock exchange

increases the energy gap between NNO/NNN coordination (entries 1 and 2; entries 3-5, or entries 5-8); this observation is maintained for calculations with solvent correction (entries 9-11, or entries 11-14). Solvent correction also reduces the energy separation between the two coordination modes. As discussed in the manuscript, similar energy differences between **L8^{NNO}** and **L8^{NNN}** are observed upon removal of $Cu^{II}Cl_2$, suggesting electronic differences between Cu-O and Cu-N bonding do not play a major role in determining the ligand binding and are likely secondary to steric contributions. Indeed, by comparing both electronic energy and Gibbs free energy, we found steric contributions enforce **L8^{NNO}** coordination mode for a series of possible copper intermediates (Table S3).

Table S3. *Steric Preference for **L8^{NNO}** Coordination Across Different Possible Intermediates.*

entry	geometry	E_{NNO} (Hartree)	E_{NNN} (Hartree)	ΔE (Hartree)	ΔE (kcal/mol)	G_{NNO} (Hartree)	G_{NNN} (Hartree)	ΔG (Hartree)	ΔG (kcal/mol)
without solvent correction									
1	***L8·Cu^{II}Cl$_2$***	**-3997.8647**	**-3997.8289**	**0.0358**	**22.5**	**-3997.4815**	**-3997.4457**	**0.0357**	**22.5**
2	***L8·Cu^{II}Cl***	-3537.3202	-3537.2842	0.0360	22.7	-3536.9324	-3536.8956	0.0368	23.2
3	***L8·Cu^{II}***	-3076.6231	-3076.6029	0.0202	12.7	-3076.2324	-3076.2123	0.0201	12.7
4	***L8·Cu^{I}Cl$_2$***[a]	n.a	n.a	n.a	n.a	n.a	n.a	n.a	n.a
5	***L8·Cu^{I}Cl***	-3537.2750	n.a[b]	n.a	n.a	-3536.8937	n.a	n.a	n.a
6	***L8·Cu^{I}***	**-3076.7185**	**-3076.6810**	**0.0375**	**23.6**	**-3076.3314**	**-3076.2943**	**0.0370**	**23.3**
with solvent correction									
8	***L8·Cu^{II}Cl$_2$***	**-3998.0902**	**-3998.0591**	**0.0311**	**19.5**	**-3997.7070**	**-3997.6759**	**0.0310**	**19.5**
9	***L8·Cu^{II}Cl***	-3537.3972	-3537.3682	0.0290	18.3	-3537.0094	-3536.9796	0.0298	18.8
10	***L8·Cu^{II}***	-3076.6523	-3076.6288	0.0235	14.8	-3076.2616	-3076.2382	0.0234	14.8
11	***L8·Cu^{I}Cl$_2$***[a]	n.a	n.a	n.a	n.a	n.a	n.a	n.a	n.a
12	***L8·Cu^{I}Cl***	-3537.4968	n.a[b]	n.a	n.a	-3537.1155	n.a	n.a	n.a
13	***L8·Cu^{I}***	**-3076.7939**	**-3076.7650**	**0.0289**	**18.2**	**-3076.4068**	**-3076.3783**	**0.0284**	**17.9**

*(a) This structure failed to converge; dissociation of chloride was energetically favorable during the optimization cycles (b) The benzamide moiety dissociated in the optimized structure, resulting a T-shaped copper complex with a bidentate **L8** ligand.*

The electronic effect of Cu-O vs. Cu-N coordination is hinted at, however, by comparing **L2** and **L8**. Removing $Cu^{II}Cl_2$ from **L8•CuCl$_2$** leads to a reduced energy gap (NNO vs. NNN) in both gas phase and solvent corrected calculations. In contrast, removing $Cu^{II}Cl_2$ from **L2•CuCl$_2$** increases the energy barrier (Table S4). The C-O bond appears to

be favored over the C-N bond for **L8•CuCl₂** in THF, but the opposite holds true for **L2•CuCl₂**.

Table S4. *DFT Calculation of* ***L2•CuCl₂*** *complex[a].*

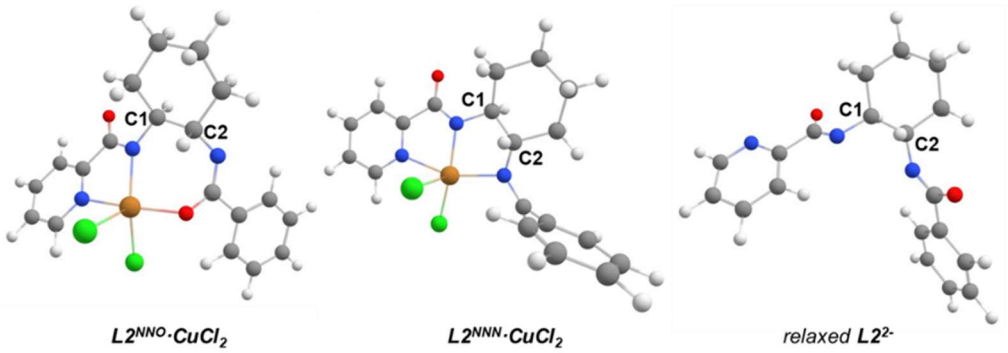

$L2^{NNO}$·$CuCl_2$ $L2^{NNN}$·$CuCl_2$ relaxed $L2^{2-}$

entry	ligand binding mode	$E_{gas\ phase}$ (kcal/mol)	$E_{solvent\ corrected}$ (kcal/mol)	τ_4' C1	τ_4' C2
with $CuCl_2$					
1	$L2^{NNO}$·$CuCl_2$	0	0	0.95	0.97
2	$L2^{NNN}$·$CuCl_2$	12.9	7.6	0.94	0.94
without $CuCl_2$[b]					
3	relaxed $L2^{2-}$	0	0	0.97	0.97
4	$L2^{NNO}$	20.9	12.7	0.97	0.95
5	$L2^{NNN}$	35.8	24.6	0.94	0.93

(a) Obtained using a B3LYP density functional with 38% Hartree-Fock exchange. (b) Ligand coordination geometry was obtained by removing $CuCl_2$ from the optimized geometry of the corresponding complex.

Absorption Spectrum and Spin Quantification Experiment

50.0(2) mg of $CuSO_4$•$5H_2O$ (0.2 mmol) was added to a 20 mL scintillation vial and dissolved in ca. 3 mL of 20% glycerol 80% water mixture. The solution was then transferred to a 10 mL volumetric flask and diluted accordingly to afford a 20 mM stock solution; calibration standards were then prepared from the stock solution. Briefly, the 1 mM and the 2 mM calibration standard were prepared directly from the stock solution. The remaining standards were prepared by diluting the 1 mM or 2 mM solution once more

using volumetric pipettes and volumetric flasks of varying sizes. The error associated with concentration is estimated to be ≤ 2%. Given its relatively small size compared to other sources of error, we have excluded this random error from further consideration and have assumed the concentration to be absolute.

77K X-band EPR spectra were then obtained on a variety of samples with variable Cu^{II} concentrations at 0.5 mW microwave power. A linear baseline correction was performed on the resulting EPR spectra to give a zero baseline. Double integration was performed from 260 to 340 mT. The end point of integration was chosen to minimize any higher-order baseline contribution; we found this results in a 2% definition error to the double integrated intensity of the analyte. Moreover, we collected multiple spectra for a selected number of samples by first removing the sample dewar from the EPR resonator and then collecting a new set of spectra. We estimate instrument variations and the operator errors contribute 3000 to the total integrated intensity. The calibration curve and relevant statistics have been reported in Figure S2.

Three batches of **L8•CuCl$_2$** were prepared independently using Method C and diluted to 2.1 mM in Cu. For ESI-MS (negative ion mode), this solution was further diluted with acetonitrile. HRMS (MM) *m/z* calc'd for $C_{29}H_{22}Cl_2CuN_3O_2$ $[M+H]^-$ = 577.0385, found 577.0364. An aliquot of the sample was loaded into a 4.0 mm standard quartz Norell EPR tube and immediately immersed in liquid nitrogen to avoid sample decomposition. Rapid freezing also ameliorates the adverse effect from the non-glassiness of THF, as we found preparing the complex in the glassy 2-MeTHF solvent led to a yellow solution with a different EPR spectrum (Figure S3). 2 mL of the same solution of each sample was then loaded into a 1 cm borosilicate cuvette to obtain its absorption spectrum. All three samples

gave optical spectra similar to that reported herein (Figure S4) and the manuscript, albeit small variations exist. As a result, we estimate a 5% error associated with the concentrations of the analyte (± 0.1 mM).

Three **L8•CuCl$_2$** samples give double integrated intensity of 3.00 *10^5, 2.87*10^5, and 2.68*10^5. The averaged concentration was 1.81 mM with a standard deviation of 0.1 mM. Moreover, combing various sources of error with standard error of regression, standard error of the slope, and the standard error of the intercept resulted in a 6 % error associated with the calibration method described herein. Adding calibration error and the standard deviation in quadrature, we report the average concentration of monomeric, divalent copper in **L8•CuCl$_2$** to be 1.81 (± 0.14) mM.

Additionally, we quantified the amount of monomeric, divalent copper after the addition of 1.5 equivalents of silyl ketene acetal **2** (Figure 2, black dotted line) and found the concentration to be 0.29 (± 0.02) mM.

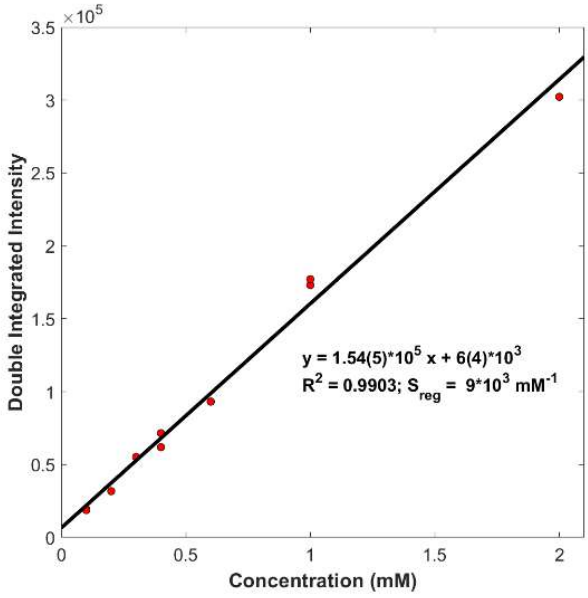

Figure S2. *Calibration Curve for Spin Quantification.*

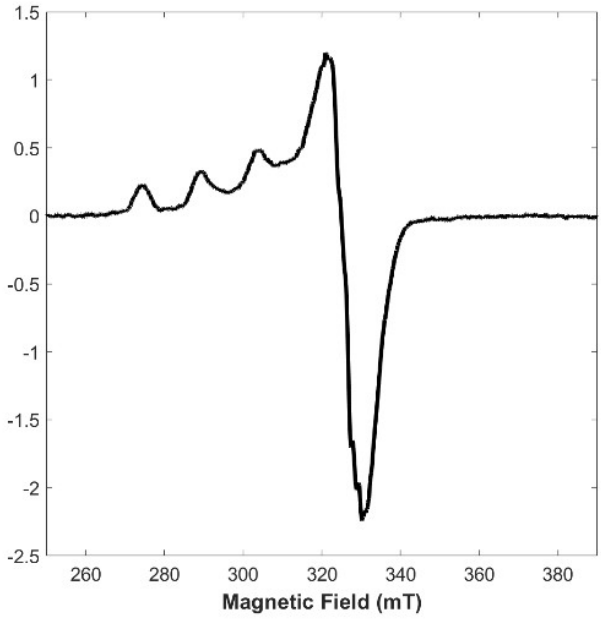

Figure S3. *77 K EPR Spectrum of* ***L8•CuCl₂*** *in 2-MeTHF.*

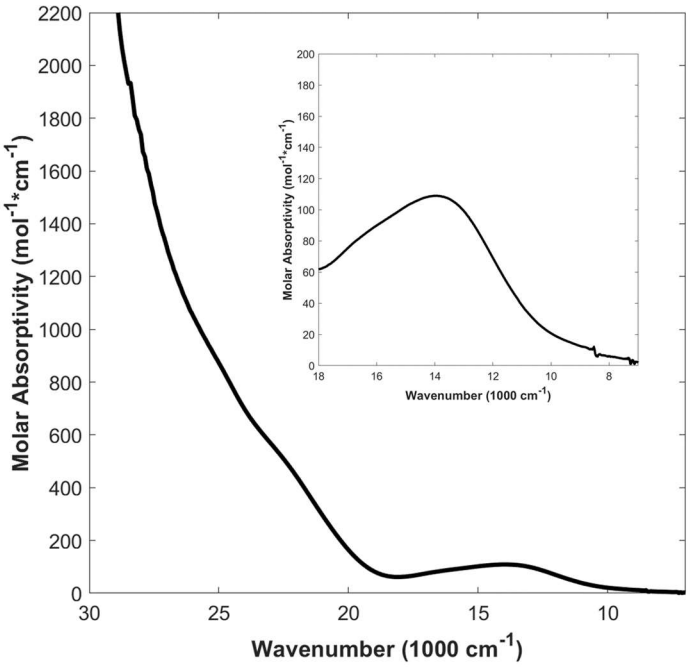

Figure S4. *Absorption Spectrum of* ***L8•CuCl₂.***

Preliminary Evidence for the Dissociation of Benzamide

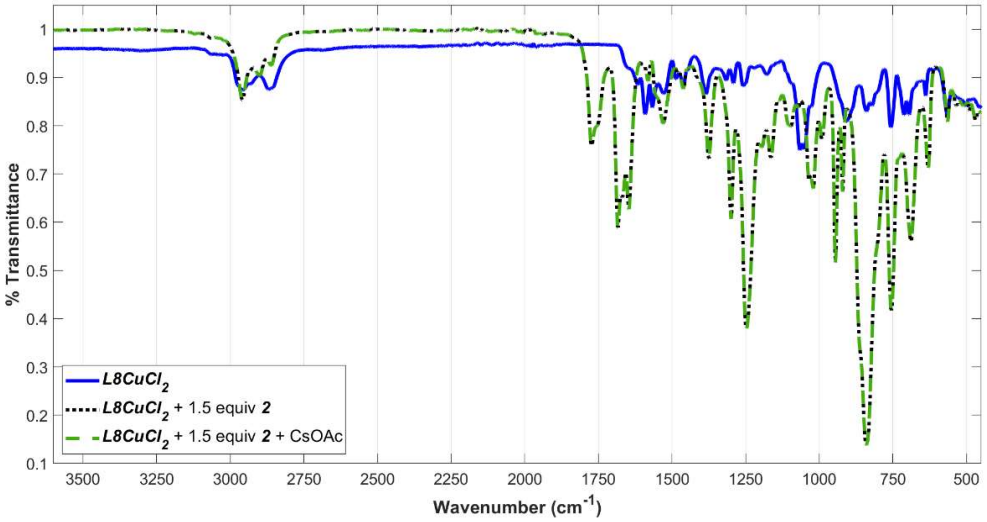

Figure S5: *IR Spectra.*

Compared to that of the free ligand, the pyridine ring bending mode shifted from 748 to 756 cm^{-1}, indicating the coordination of pyridine to copper center. [26] For **L8•CuCl₂** (blue trace) we consistently noted high transmittance. Upon adding silyl ketene acetal **2**, we observed the reappearance of amide bands at 1683, 1669, and 1646 cm^{-1}. A ketone band was also observed at 1774 cm^{-1}. The pyridine remained bound to the copper center as the ring bending mode occurred at 755 cm^{-1}. Interestingly, we observed an intense ring C-H bend from the phenyl moiety. These results suggest that the benzamide moiety may have dissociated upon addition of silyl ketene acetal **2**.

1.5 Notes and References

1. (a) Seitz, M.; Reiser, O. Synthetic approaches towards structurally diverse γ - butyrolactone natural-product-like compounds. *Curr. Opin., Chem. Biol***. 2005** , *9*, 285–292. (b) A. I. Meyers, Y. Yamamoto, E. D. Mihelich, R. A. Bell, Asymmetric Synthesis of 2-Subsituted Butyrolactones and Valerolactones. *J. Org. Chem.* **1980**, *45*, 2792–2796. (c) Madelaine, C.; Valerio, V.; Maulide, N. Unexpected Electrophilic Rearrangements of Amides: Challenging Substituted Lactones. *Angew. Chem. Int. Ed.* **2010**, *49*, 1583–1586.
2. (a) Evans, D. A.; Kozlowski, M. C.; Murry, J. A.; Burgey, C. S.; Campos, K. R.; Connell, B. T.; Staples, R. J. C_2–Symmetric Copper(II) Complexes as Chiral Lewis Acids. Scope and Mechanism of Catalytic Enantioseletive Aldol Additions of Enolsilanes to (Benzyloxy)acetaldehyde. *J. Am. Chem. Soc***. 1999**, *121*, 669–685. (b) Evans, D. A.; Murry, J. A.; Kozlowski, M. C. C2-Symmetric Copper(II) Complexes as Chiral Lewis Acids. Catalytic Enantioselective Aldol Additions of Silylketene Acetals to (Benzyloxy)acetaldehyde. *J. Am. Chem. Soc.* **1996**, *118*, 5814–5815. (c) Saaby, S.; Nakama, K.; Lie, M. A.; Hazell, R. G.; Jørgensen, K. A. The First Catalytic Highly Enantioselective Alkylation of Ketimines A Novel Approach to Optically Active Quaternary α-Amino Acids. *Chem. Eur. J.* **2003**, *9*, 6145−6154. (b) For enantioselective □-arylation of silyl ketene acetals: Huang, Z.; Chen, Z.; Lim, L. H.; Quang, G. C. P.; Hirao, H.; Zhou, J. Weak Arene C–H●●●O Hydrogen Bonding in Palladium-Catalyzed Arylation of Lactones. *Angew. Chem. Int. Ed*. **2013**, *52*, 5807–5812.
3. For Lewis acid-catalyzed Aldol reactions: Tsuji, J.;Takahashi, H.; Morikawa, M.

Organic Syntheses by Means of Noblemetal Compounds XVIII. Reaction of π-Allyl Palladium Chloride with Nucleophiles. *Tetrahedron Lett.*, **1965**, *6*, 4387–4388.

4. (a) James, J.; Guiry, P. J.; Highly Enantioselective Construction of Sterically Hindered α-Allyl-α-Aryl Lactones via Palladium-Catalyzed Decarboxylative Asymmetric Allylic Alkylation. *ACS Catal*. **2017**, *7*, 1397–1402. (b) Nascimiento de Oliveira, M.; Fournier, J.; Arseniyadis, S.; Cossy, J. A Palladium-Catalyzed Asymmetric Allylic Alkylation Appraoch to α-Quaternary γ-Butyrolactones. *Org. Lett.* **2017**, *19*, 14–17. (c) P. Meletis, M. Patil, W. Thiel, W. Frank, M. Braun. Enantioselective and Diastereoselective Tsuji–Trost Allylic Alkylation of Lactones: An Experimental and Computational Study *Chem. Eur. J.* **2011**, *17*, 11243–11249. (d) X. Jiang, J. F. Hartwig. Iridium-Catalyzed Enantioselective Allylic Substitution of Aliphatic Esters with Silyl Ketene Acetals as the Ester Enolates. *Angew. Chem. Int. Ed.* **2017**, *56*, 8887–8891;
5. (a) Ngamnithiporn, A.; Jette, C.; Bachman, S.; Virgil, S.; Stoltz, B. M. Nickel-Catalyzed Enantioselective Allylic Alkylation of Lactones and Lactams with Unactivated Alcohols. *Chem. Sci*. **2018**, *9*, 2547–2551. (b) Hayashi, M.; Bachman, S.; Hashimoto, S.; Eichman, C. C.; Stoltz, B.M. Ni-Catalyzed Enantioselective C-Acylation of α-Substituted Lactams. *J. Am. Chem. Soc.* **2016**, *138*, 8997–9000. (c) Han, S.–J.; Doi, R.; Stoltz, B. M. Nickel-Catalyzed Intramolecular C–O Bond Formation: Synthesis of Cyclic Enol Ethers. *Angew. Chem. Int. Ed.* **2016**, *55*, 7437–7440.
6. Li, D.; Ohmiya, H.; Sawamura, M. Copper-Catalyzed γ-Selective and Stereospecific Allylic Alkylation of Ketene Silyl Acetals. *J. Am. Chem. Soc*. **2011**, *133*, 5672–5675.

7. (a) Falciola, C. A.; Alexakis, A. Copper Catalyzed Asymmetric Allylic Alkylation. *Eur. J. Org. Chem.* **2008**, 3765–3780. (b) Alexakis, A.; Bäckvall, J. E.; Krause, N.; Pàmies, O.; Diéguez, M. Enantioselective Copper-Catalyzed Conjugate Addition and Allylic Substitution Reactions. *Chem. Rev.* **2008**, *108*, 2796–2823. (c) Harutyunyan, S. R.; den Hartog, T.; Geurts, K.; Minnaard, A. J.; Feringa, B. L. Catalytic Asymmetric Conjugate Addition and Allylic Alkylation with Grignard Reagents. *Chem. Rev.* **2008**, *108*, 2824–2852.
8. For Cu^{II} catalysts with 1,3-dicarbonyls see (a) Trillo, P.; Baeza, A. Copper-Catalyzed Asymmetric Allylic Alkylation of β -Keto Esters with Allylic Alcohols. *Adv. Synth. Catal.* **2017**, *359*, 1735–1741. (b) Deng, Q.–H.; Wadepohl, H.; Gade, L. H. Highly Enantioselective Copper-Catalyzed Alkylation of β-Ketoesters and Subsequent Cyclization to Spiro lactones/Bi-Spirolactones. *J. Am. Chem. Soc.* **2012**, *134*, 2946–2949.
9. The use of first row transition metals in allylation is mainly limited to 1,3-dicarbonyls: (a) Alexakis, A.; Begouin, J. M.; Crawley, M. L.; Guiry, P. J.; Kammerer-Pentier, C.; Kleimark, J.; Klein, J. E M. N.; Langlois, J. –B.; Liron, F.; Liu, W. –B.; Milhau, L.; Moberg, C.; Norrby, P. –O.; Plietker, B.; Poli, G.; Prestat, G.; Trost, B. M. Weickmann, D.; Xia, J.–B.; You, S. –L. Transition Metal Catalyzed *Enantioselective Allylic Substitution in Organic Synthesis*; Kazmeier, U., Eds.; Springer, New York, **2012**, vol. 38, pp1-341.To our knowledge, there is only one report on the enantioselective allylic alkylation of a non-stabilized enolate nucleophile using Ni (b)Wang, J.; Wang, P.; Wang, L.; Li, D.; Wang, K.; Wang, Y.; Zhu, H.; Yang, D.; Wang, R. Nickel-Mediated Asymmetric Allylic Alkylation

between Nitroallylic Acetates and Acyl Imidazoles. *Org. Lett*. **2017**, *19*, 4826–4829.

10. For additional commercial and chiral picolinyl ligands, bases, and copper sources tested, see the supporting information associated with the published article.
11. With LiHMDS as the base, complexation could be carried out at room temperature, allowing for an operational simpler reaction set-up. For Cu/L complexation using different bases, see the supporting information associated with the published article.
12. (a) Harada, A.; Makida, Y.; Sato, T.; Ohmiya, H.; Sawamura, M. Copper-Catalyzed Enantioselective Allylic Alkylation of Terminal Alkyne Pronucleophiles. *J. Am. Chem. Soc.* **2014**, *136*, 13932–13939. (b) Yoshikai, N.; Zhang, S.-L.; Nakamura, E. Origin of Regio- and Stereoselectivity of Allylic Subsititution of Organocopper Reagents. *J. Am. Chem. Soc.* **2008**, *130*, 12862–12863. (c) Yamanaka, M.; Kato, S.; Nakamura, E. Mechanism and Regioselectivity of Reductive Elimination of π-Allylcopper(III) Intermediates. *J. Am. Chem. Soc.* **2004**, *126*, 6287–6293. (d) Yoshikai, N.; Nakamura, E. Mechanisms of Nucleophilic Organocopper (I) Reactions. *Chem. Rev.* **2012**, *112*, 2339–2372.
13. (a) Mulqi, M.; Stephens, F. S.; Vagg, R. S. Studies on the Metal–Amide Bond. V*. The Structure of Aqua[N,N'-bis(2'-pyridinecarboxamido)-*trans*-1,2-cyclohexane]copper(II) Monohydrate. *Inorg. Chim. Acta*, **1981**, *51*, 9–14. (b) Mulqi, M.; Stephens, F. S.; Vagg, R. S. Studies on the Metal–Amide Bond. XI*. The Structure of Aqua[N,N'-bis(2'-pyridinecarboxamido)-*trans*-1,2-cyclohexane]copper(II) Dihydrate. *Inorg. Chim. Acta*, **1981**, *52*, 177–182. There is only one report on the use of **L1** in combination with Cu in catalysis: (c) Fan, X.; Zhang, X.; Li, C.; Gu, Z. Enantioselective Atropisomeric Anilides Synthesis via Cu-

Catalyzed Intramolecular Adjacent C–N Coupling. *ACS Catal*. **2019**, *9*, 2286–2291. For the synthesis and use of mono-picolinyl ligands in Cu catalysis: (d) Carlo Sambiagio. Investigations on the use of Amidic Ligands in Copper-Catalyzed Arylation Reactions, Ph.D. Dissertation, University of Leeds, Leeds, West Yorkshire, England, 2015.

14. (a) Trost, B. M.; Hachiya, I.; Asymmetric Molybdenum–Catalyzed Alkylations. *J. Am. Chem. Soc.* **1998**, *120*, 1104–1105. (b) Trost, B. M.; Dogra, K.; Hachiya, I.; Emura, T.; Hughes, D. L.; Krska, S.; Reamer, R. A.; Palucki, M.; Yasuda, N.; Reider, P. Designed Ligands as Probes for the Catalytic Binding Mode in Mo-Catalyzed Asymmetric Allylic Alkylation. *Angew. Chem. Int. Ed*. **2002**, *114*, 2009–2012. (c) Luft, J. A. R.; Yu, Z.–X. Hughes, D. L.; Lloyd–Jones, G. C. Krska, S. W.; Houk, K. N. On the Stability of the π–Allyl Intermediate in Molybdenum–Catalyzed Asymmetric Alkylations. *Tetrahedron: Asymmetry*, **2006**, *17*, 716–724.
15. See SI for more information.
16. Okuniewski, A.; Rosiak, D.; Chojnacki, J.; Becker, B.; Coordination Polymers and Molecular Structures among Complexes of Mercury(II) Halides with Selected 1-Benzoylthioureas. *Polyhedron*. **2015**, *90*, 47–57.
17. A reduced energy gap was observed for the more flexible ligand **L2**
18. We also observed a diamagnetic species by ^{1}H NMR (S234 under supporting information associated with the published article).
19. Ito, Y.; Konoike, T.; Saegusa, T. Reaction of Ketone Enolates with Copper Dichloride: Synthesis of 1,4 Diketones. *J. Am. Chem. Soc.* **1975**, *97*, 2912–2914. Via □-Halogenation (b) Evans, R. W.; Zbieg, J. R.; Zhu, S.; Li, W.; MacMillan, D. W. C.

Simple Catalytic Mechanism for the Direct Coupling of □-Carbonyls with Functionalized Amines: A One-Step Synthesis of Plavix. *J. Am. Chem. Soc*. **2013**, *135*, 16074–16077. (c) Rathke, M.; Lindert, A.; Reaction of Ester Enolates with Copper(II) Salts: Synthesis of Substituted Succinate Esters. *J. Am. Chem. Soc.* **1971**, *93*, 4605–4606. (d) Kochi, J. K.; The Reduction of Cupric Chloride by Carbonyl Compounds. *J. Am. Chem. Soc*. **1955**, *77*, 5724–5728. (e) Kosower, E. M.; Cole, W. J.; Wu, G. –S, Cardy, D. E.; Meisters, G.; Halogenation with Copper (II). I. Saturated Ketones and Phenol. *J. Org. Chem*. **1963**, *28*, 630–633. (f) Kosower, E. M.; Wu, G. –S. Halogenation with Copper(II). II. Unsaturated Ketones. *J. Org. Chem.* **1963**, *28*, 633–638.

20. The the NNO binding mode preference was retained for a number of different Cu^{II} and Cu^{I} intermediates (See Table S4).
21. IR data of our Cu^{I} catalyst indicates that the benzamide portion of the ligand dissociates upon exposure to silyl ketene acetal **2**. In addition, DFT data also indicates that a C-bound Cu^{I} enolate is lower in energy than the O-bound enolate. Future work will focus on expanding on these results.
22. We believe that oxidative addition to the branched electrophile **1u** generates a sterically congested $Cu^{III}[\alpha+\pi]$ allyl species, which undergoes a 1,3-allyl migration [12a]

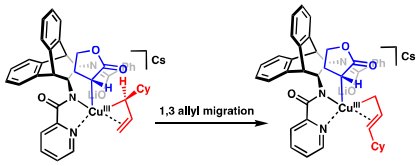

23. For other potential applications of chiral α-allyl γ-butyrolactones, see S76 under supplementary information associated with the published article.

24. For other nucleophiles tested, see S23 under supplementary information associated with the published article

25. Neese, F. Software update: the ORCA program system, version 4.0. WIREs. Comput. Mol. Sc. 2017, 8, e1327. S55 3.

26. (a) Solomon, E. I.; Szilagyi, R. K.; DeBeer George, S.; Basumallick, L. Chem. Rev. 2004, 104, 419–458. (b) Szilagyi, R. K.; Metz, M.; Solomon, E. I. J. Phys. Chem. A. 2002, 106, 2994–3007.

27. Bowmaker, G.A.; Di Nicola, C.; Pettinari, C.; Skelton, B.W.; Somers, N.; White, A.H. Dalton Trans., 2011, 40, 5102-5115

Chapter 2

Electronic structures of nickel(II)-bis(indanyloxazoline)-dihalide catalysts: Understanding ligand field contributions that promote C(sp^2)–C(sp^3) cross-coupling[†]

2.1 Introduction

The number of accessible oxidation states and the possibility of both one- and two-electron redox reactions make nickel a well-suited alternative to precious metals such as iridium and platinum for cross-coupling catalysis. Since the first report of reductive coupling of aryl halides to biaryl products by bis(1,5-cyclooctadiene)nickel^0 in 1971,[1] numerous reports of coupling reactions, including enantioselective cross-coupling, have appeared.[2] Early studies used electrochemistry to render these reactions catalytic in nickel,[3] and in 2007 Durandetti *et al.* demonstrated that elemental manganese could be used as the terminal reductant for the Ni(bipyridine)Br_2-catalyzed reductive cross-coupling of

[†] This chapter was reproduced from a published manuscript.

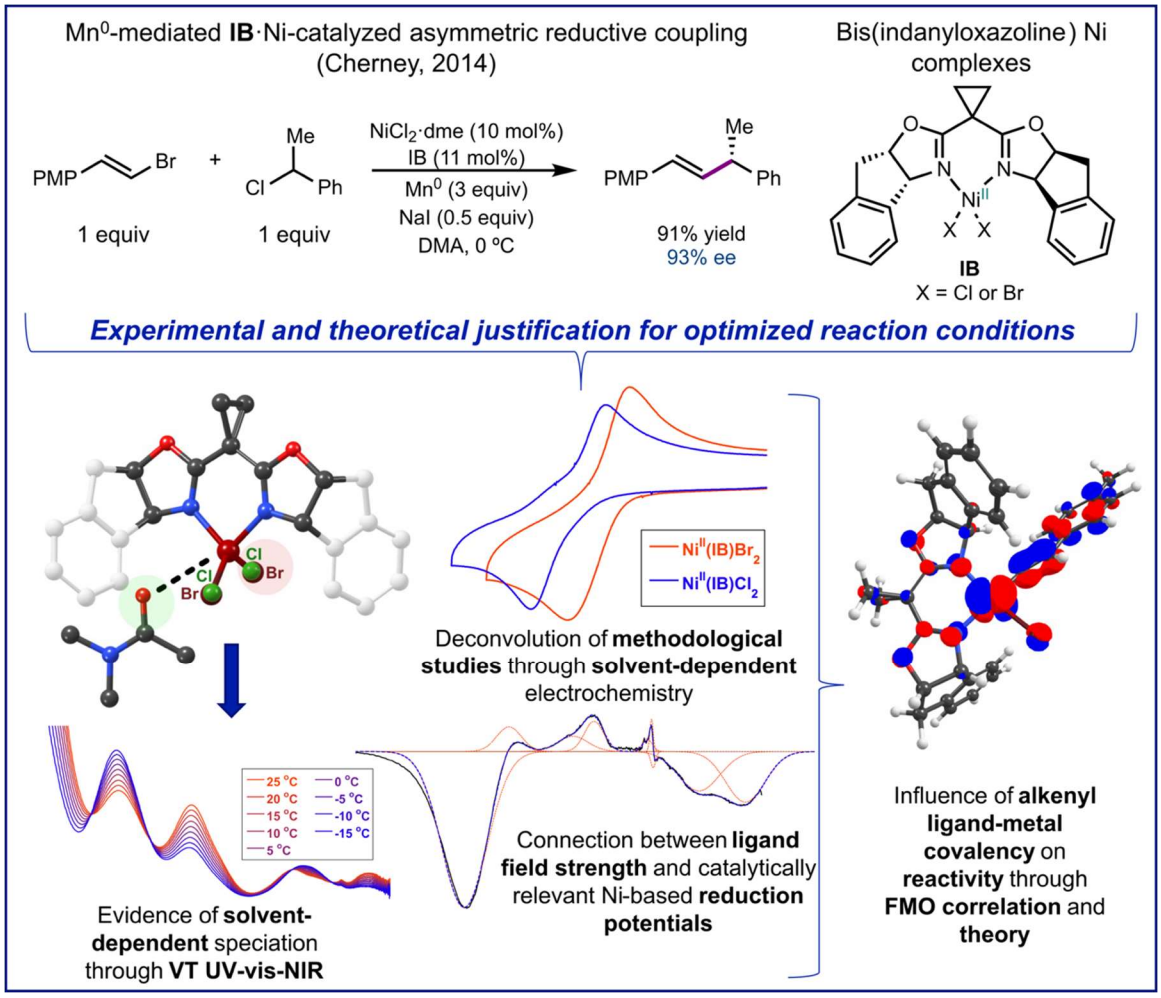

Scheme 1. *Outline of key findings from this comprehensive spectroscopic, electrochemical, and computational study of Ni^{II} precatalysts for enantioselective reductive alkenylation. FMO = frontier molecular orbital.*

iodobenzene with α-chloroesters in up to 87% yield.[4] The first highly selective enantioconvergent reductive cross-coupling was reported by one of our groups in 2013.[5] Using bis(4-phenyloxazoline) (PhBOX), elemental manganese, and a 30% DMA/THF solvent mixture, high yields and enantioselectivity were obtained for cross-coupling of acyl chlorides and benzyl chlorides. Following this, a variety of chiral ligand frameworks were shown to be effective for the reductive cross-coupling of different electrophile pairs.[2] For example, bis(indanyloxazoline) (**Scheme 1**, bottom, **IB**) Ni complexes catalyze a variety

of reductive alkenylation reactions, including formation of enantioenriched allylic silanes and alkenes with aryl-substituted tertiary stereogenic centers (**Scheme 1**, bottom).[6,7] More recently, one of our groups has also demonstrated electrocatalytic competency of these Ni^{II} complexes for cross-coupling reactions.[8]

A fundamental and detailed description of both the ground- and excited-state electronic properties of transition metal complexes can help infer catalytic operativity and competency. For example, one of our groups has recently provided detailed electronic structural and mechanistic studies of the ground- and excited-state properties of low-spin Ni^{II} bipyridine aryl halide complexes and their Ni^{I} photogenerated intermediates. These studies identified key structure-function relationships relevant for excited state bond homolysis and oxidative addition reactivity, which allowed for the mechanistic analysis of Ni^{I}-mediated activation of strong $C(sp^2)$–Cl bonds.[9,10] Our groups also recently participated in collaborative work that utilized cyclic voltammetry under catalytic conditions and UV-vis-NIR spectroelectrochemistry to better understand the interplay of Ni and Cr oxidation states for Nozaki-Hiyama-Kishi coupling.[11] Another study by Neidig *et al.* utilized a combination of Mössbauer spectroscopy, magnetic circular dichroism, and computations to demonstrate that the kinetic competency of four-coordinate organoiron toward halogen abstraction is dependent on the accessibility and relative energy of iron-based orbitals.[12]

Despite the rapidly growing number of Ni-catalyzed reductive cross-coupling reactions being developed, there have been relatively few detailed mechanistic studies, particularly of bis(oxazoline) Ni complexes. Additionally, although solvent typically has a profound influence on the yield and selectivity of these reactions,[13–18] the influence of

solvent coordination to the active catalyst has not been thoroughly studied. A previous study has crystallographically characterized a five-coordinate, DMSO-bound Ni^{II} phenanthroline complex, also suggesting the potential influence of solvent in the catalytic cycle.[19] A recent study by Diao *et al.* has suggested a $Ni^{I/III}$ redox cycle and radical formation and capture are pertinent for catalysis by (biOx)Ni^{II}ArX catalysts, which revised previous suggestions of involvement of $Ni^{0/II}$ oxidation states.[20] In general, uncertainty still exists regarding how the specific ligand, as well as the potential role of solvent coordination, influence both low-spin and high-spin Ni^{II} cross-coupling catalysis.

To this end, we provide the first comprehensive spectroscopic and electrochemical investigation of two reductive cross-coupling catalysts, **Ni^{II}(IB)Cl_2** and **Ni^{II}(IB)Br_2** [**IB** = (3a*R*,3a'*R*,8a*S*,8a'*S*)-2,2'-(cyclopropane-1,1-diyl)bis(3a,8a-dihydro-8*H*-indeno[1,2-*d*]-oxazole)], to provide broad insight into the complex conditions and mechanism (**Scheme 1**). Although studies related to these complexes by one of our groups were primarily in the context of developing reductive alkenylation, we note that these and similar complexes have also been reported for a number of other reactions, including reductive arylation, 1,2-alkynylboration, and 1,2-vinylboration, further motivating their detailed experimental and computational investigation.[21–31] Here we use variable-temperature (VT) UV-vis-NIR absorption, circular dichroism (CD), vibrational CD (VCD), and magnetic CD (MCD) spectroscopies, coupled with cyclic voltammetry, spectroelectrochemistry, and DFT/TDDFT and multi-reference (CASSCF/CASPT2) calculations to elucidate specific electronic structure contributions to reactivity, as well as the influence of solvent on the efficacy of catalytic transformations (**Scheme 1**). Quantifying halide-dependent spectral features directly connects ligand field strength and redox potentials. Similarly, studying

three solvents with different donor numbers (DNs) provides a route toward understanding previously reported empirical solvent optimization studies. We demonstrate that DMA solvent can coordinate to catalytically-relevant Ni species and evaluate the potential role of solvent coordination in their reactivity. Based on previously reported yields and findings reported here, we suggest solvent coordination and low temperature can favorably influence driving forces and kinetic barriers of key reaction steps leading to cross-coupled product. These studies provide new insights relevant to the catalytic reactivity of chiral bis(oxazoline) Ni catalysts that have been recently popularized for a variety of asymmetric Ni-catalyzed cross-coupling reactions (**Scheme 1**).

2.2 Results and Analysis

2.2.1 Room-Temperature UV-Vis-NIR, CD, and MCD Characterization of $Ni^{II}(IB)Cl_2$ and $Ni^{II}(IB)Br_2$ in a Non-Coordinating Solvent

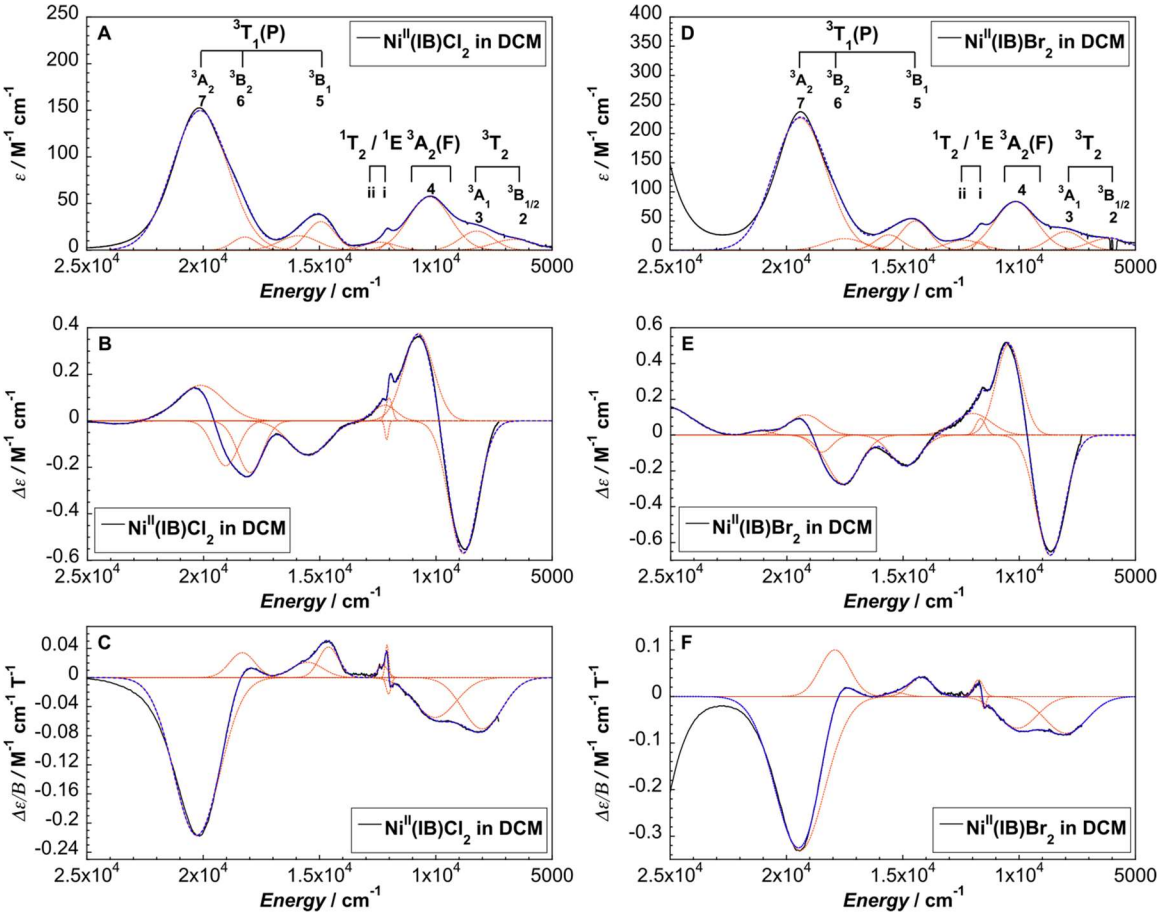

***Figure 1**. Spectroscopic characterization of the Ni complexes. Room temperature (**A, D**) UV-vis-NIR absorption, (**B, E**) CD, and (**C, F**) MCD spectra of **$Ni^{II}(IB)Cl_2$** and **$Ni^{II}(IB)Br_2$** in DCM with Gaussian resolutions of individual transitions (orange). Overall fit to each spectrum given in dashed blue.*

Due to the absence of low-energy charge transfer bands in the UV-vis-NIR, electronic absorption spectra of **$Ni^{II}(IB)Cl_2$** and **$Ni^{II}(IB)Br_2$** in DCM (donor number, DN = 2.4)[32,33] (**Figures 1A-C** and **1D-F**, respectively) provide rich insights into the Ni^{II} ligand field through observation of numerous spin-allowed and spin-forbidden ligand field

transitions (**Table 1**). These transitions arise from the orbital triplet ground state (i.e., $^3T_1(F)$ in an idealized T_d geometry) of the S = 1 d^8 Ni^{II} complexes and exhibit correspondingly weak molar absorptivities at 294 K. CD and MCD spectroscopies provide complementary, signed, spectroscopic methods to resolve overlapping ligand field transitions. Due to the presence of the chiral **IB** ligand, the Ni^{II}-based ligand field transitions exhibit CD intensity (**Figures 1B** and **1E**), and both complexes exhibit room temperature MCD signals at 1.4 T (**Figures 1C** and **1F**, respectively). A detailed discussion of band assignments can be found in Supporting Information **Section S3**.

Table 1*. Band maxima and full widths at half maxima (FWHM) for* ***Ni^{II}(IB)Cl_2*** *and* ***Ni^{II}(IB)Br_2*** *in DCM obtained from simultaneous Gaussian resolution of UV-vis-NIR, CD, MCD, and vibrational CD spectra. Numbered states correspond to spin-allowed ligand field transitions.*

Ni^{II}(IB)Cl_2							
	Absorption (cm^{-1})		**CD (cm^{-1})**		**MCD (cm^{-1})**		**Assignment**
#	**Band max.**	**FWHM**	**Band max. (Sign)**	**FWHM**	**Band max. (Sign)**	**FWHM**	***T_d*: *C_{2v}* Geometry**
1	---	---	2170 (+)	730	---	---	$^3T_1(F)$: $^3B_1(F) \rightarrow {}^3A_2(F)$
2	6640	2160	---	---	---	---	$^3T_2$: $^3B_1(F) \rightarrow {}^3B_1/{}^3B_2$
3	8240	1680	8820 (−)	1480	8010 (−)	2000	$^3T_2$: $^3B_1(F) \rightarrow {}^3A_1$
4	10 270	2110	10 750 (+)	1500	10 030 (−)	2110	$^3A_2(F)$: $^3B_1(F) \rightarrow {}^3A_2(F)$
i	12 100	400	12 020 (+)	330	12 030 (−)	250	$^3B_1(F) \rightarrow {}^1T_2/{}^1E$
	---	---	12 120 (−)	180	12 100 (+)	170	$^3B_1(F) \rightarrow {}^1T_2/{}^1E$

ii	12 400	1630	12 200 (+)	1150	---	---	Spin-forbidden LF
5	14 940	1430	---	---	14 610 (+)	1000	$^3T_1(P)$: $^3B_1(F) \rightarrow {}^3B_1(P)$
iii	15 890	1910	15 500 (−)	1950	15 530 (+)	1570	---
6	18 210	1220	18 000 (−)	1250	18 320 (+)	1280	$^3T_1(P)$: $^3B_1(F) \rightarrow {}^3B_2(P)$
iv	---	---	19 050 (−)	1250	---	---	---
7	20 130	2800	20 130 (+)	2300	20 270 (−)	2330	$^3T_1(P)$: $^3B_1(F) \rightarrow {}^3A_2(P)$
v	---	---	23 740 (−)	1600	---	---	LF of Trimer
$Ni^{II}(IB)Br_2$							
	Absorption (cm^{-1})		**CD (cm^{-1})**		**MCD (cm^{-1})**		**Assignment**
#	**Band max.**	**FWHM**	**Band max. (Sign)**	**FWHM**	**Band max. (Sign)**	**FWHM**	***T_d*: *C_{2v}* Geometry**
1	---	---	2210 (+)	970	---	---	$^3T_1(F)$: $^3B_1(F) \rightarrow {}^3A_2(F)$
2	6150	2000	---	---	---	---	$^3T_2$: $^3B_1(F) \rightarrow {}^3B_1/{}^3B_2$
3	7980	1670	8670 (−)	1450	7980 (−)	2150	$^3T_2$: $^3B_1(F) \rightarrow {}^3A_1$
4	10 150	2080	10 460 (+)	1280	10 060 (−)	1930	$^3A_2(F)$: $^3B_1(F) \rightarrow {}^3A_2(F)$
	---	---	---	---	11 500 (−)	180	$^3B_1(F) \rightarrow {}^1T_2/{}^1E$
i	11 670	500	11 660 (+)	500	11 750 (+)	500	$^3B_1(F) \rightarrow {}^1T_2/{}^1E$
ii	12 380	1750	12 000 (+)	1830	---	---	Spin-forbidden LF

5	14 460	1450	14 900 (−)	1530	14 210 (+)	1280	$^3T_1(P)$: $^3B_1(F) \rightarrow {}^3B_1(P)$
iii	15 600	1330	---	---	15 290 (+)	970	---
6	17 500	2000	17 560 (−)	1650	17 920 (+)	1500	$^3T_1(P)$: $^3B_1(F) \rightarrow {}^3B_2(P)$
iv	---	---	18 500 (−)	1030	---	---	---
7	19 410	2660	19 200 (+)	1670	19 420 (−)	2500	$^3T_1(P)$: $^3B_1(F) \rightarrow {}^3A_2(P)$
v	---	---	21 130 (+)	1030	---	---	$^3B_1(F) \rightarrow {}^1T_{1g}$, $^1T_{2g}$, $^1A_{1g}$, ^1E_g
vi	---	---	25 100 (+)	2400	---	---	LMCT

The ligand field transitions of **Ni^{II}(IB)Cl_2** relative to **Ni^{II}(IB)Br_2** are blueshifted by ~120 – 710 cm^{-1} in DCM (overlaps in **Figure S17**), consistent with stronger donation from chloride relative to bromide. To estimate the relative ligand field strengths, we average the assigned spin-allowed transitions (bands 1 – 7). Doing so provides relative ligand field strengths of ~12 365 cm^{-1} and ~11 975 cm^{-1} (Δ = ~390 cm^{-1}) for **Ni^{II}(IB)Cl_2** and **Ni^{II}(IB)Br_2**, respectively, in accord with the greater ligand field strength in the chloride complex relative to bromide. As will be shown below, the ligand field bands and ligand field strengths can be directly related to the energies of the Ni^{II}-based redox active molecular orbitals (RAMOs) and, thus, complex redox potentials (*vide infra*, **Section 3.3**). To the best of our knowledge, this provides the first experimental connection between ligand field spectroscopy and the electrochemical potentials of Ni^{II}-based enantioselective cross-coupling catalysts.

2.2.2 Vibrational CD Spectroscopy of $Ni^{II}(IB)Cl_2$ and $Ni^{II}(IB)Br_2$

Pseudo-T_d Ni(II)/Co(II) and pseudo-O_h V(III) complexes can exhibit large splittings of their orbital triplet ground states. These splittings can be observed using techniques such as electronic Raman or VCD. The latter is the infrared analogue of electronic CD spectroscopy and provides a means to determine absolute stereochemical configurations or probe low-energy electronic transitions in chiral transition metal complexes.[34,35] VCD signals are observed for both **$Ni^{II}(IB)Cl_2$** and **$Ni^{II}(IB)Br_2$** complexes dissolved in d^2-DCM (**Figure 2**). Note high sample concentrations are necessary for VCD measurements. Despite substantial trimerization of **$Ni^{II}(IB)Cl_2$** at these concentrations (*vide infra*, **Section 2.4**), the observed VCD transition is still assigned to the four-coordinate species, as evidenced by calculations (**Figure S121**) and spectral consistency with the **$Ni^{II}(IB)Br_2$** analogue, which does not undergo trimerization at high concentrations in DCM. Furthermore, to confirm the observed VCD spectral intensity for **$Ni^{II}(IB)X_2$** complexes corresponds to a ligand field transition, the d^{10} complex, **$Zn^{II}(IB)Cl_2$**, was synthesized in a manner analogous to the Ni^{II} complexes. Note that an analogous complex, $Cu^{II}(IB)Cl_2$, has been previously reported.[36] The VCD spectrum of **$Zn^{II}(IB)Cl_2$** in d^2-DCM does not exhibit electronic absorption in the region of 1800 – 3200 cm^{-1} (**Figure 2**). **$Ni^{II}(IB)Cl_2$** exhibits a moderately sharp (FWHM = ~730 cm^{-1}) ligand field transition at ~2170 cm^{-1}, while **$Ni^{II}(IB)Br_2$** exhibits a transition (FWHM = ~970 cm^{-1}) at ~2210 cm^{-1}. For both complexes, this band (band 1, $^3B_1(F) \rightarrow {}^3A_2$ transition in C_{2v}) arises from a transition within the orbital triplet ground state ($^3T_1(F)$ in T_d), which is split by low symmetry distortions and spin-orbit coupling. Note the positive sign of the VCD band is consistent with the other $^3A_2$ states observed with CD (**Figure 1B** and **1E**). While the

relative ground state splittings are quite similar between the two complexes, the small increase in splitting for **Ni^{II}(IB)Br_2** is likely due to the greater spin-orbit coupling constant for Br relative to Cl.

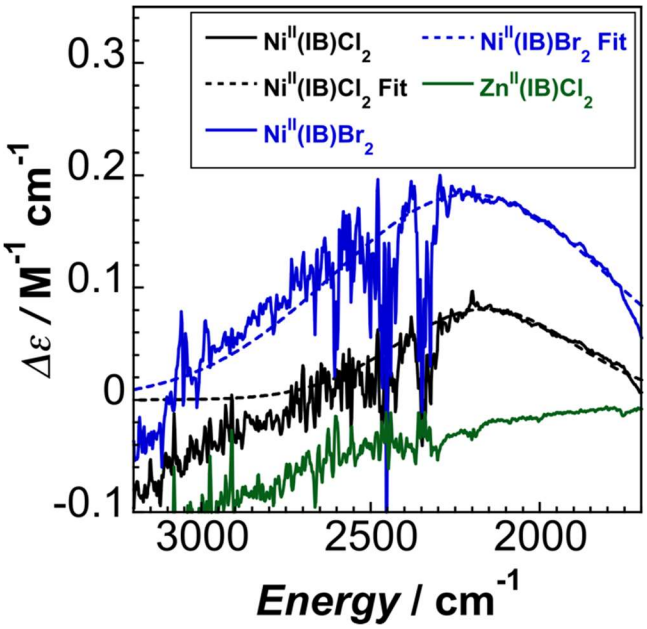

***Figure 2**. Background-corrected vibrational CD spectra of 160.0 mM **Ni^{II}(IB)Cl_2**, 139.0 mM **Ni^{II}(IB)Br_2**, and 115.2 mM **Zn^{II}(IB)Cl_2** in d^2-DCM.*

This application of VCD determines electronic excited state energies of the low-symmetry split orbital triplet ground state of transition metal-based enantioselective cross-coupling catalysts for the first time. These data, combined with the UV-vis-NIR, electronic CD, and MCD data, have allowed for the experimental determination of a complete ligand field energy level diagram for the **Ni^{II}(IB)X_2** complexes. All transitions to individual excited states in T_d and C_{2v} symmetry are assigned in the correlation diagram in **Figure 3**.

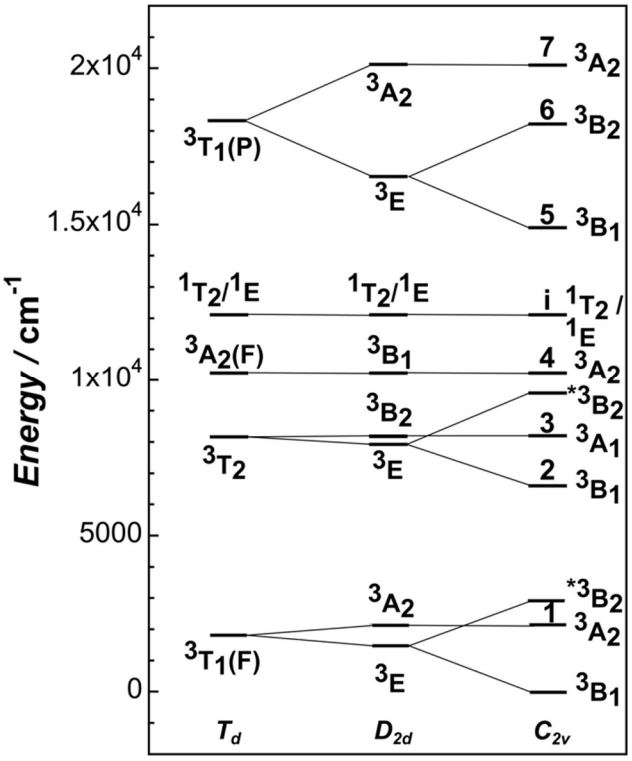

Figure 3. *Descent in symmetry state diagram for $Ni^{II}(IB)Cl_2$. Starred states are derived from CASSCF/CASPT2 calculations and shifted by the average ratio of the seven experimental spin-allowed transitions vs. seven calculated ligand field energies. Numbered states given in* ***Table 1****.*

2.2.3 Room Temperature UV-Vis-NIR, CD, and MCD Characterization of $Ni^{II}(IB)Cl_2$ and $Ni^{II}(IB)Br_2$ in Coordinating Solvents

To complement data obtained in DCM (poor σ and π donor) and to assess the solvent-dependent behavior of $\mathbf{Ni^{II}(IB)X_2}$ complexes, room temperature UV-vis-NIR absorption, CD, and 1.4 T MCD spectra were also acquired in MeCN (moderate σ donor and moderate π acceptor) and DMA (very strong σ donor and moderate π acceptor). These solvents were selected for their relative differences in dielectric constant and Lewis basicity/acidity to assess the effects of solvent environment on geometric and electronic structure, which can subsequently be correlated with catalytic activity and selectivity.

UV-vis-NIR spectra of **$Ni^{II}(IB)Cl_2$** and **$Ni^{II}(IB)Br_2$** exhibit significant solvent dependence (**Figures S9** and **S10**). In addition to decreased overall intensities compared to transitions observed in DCM, new spectral intensity grows in at ~23 000 cm^{-1}, with weak intensity in MeCN and greatest intensity in DMA. These spectral changes are also manifested in the solvent-dependent CD and MCD spectra (**Figures S44-S47**), with the new spectral intensity at ~23 000 cm^{-1} corresponding to a new negative band in CD and MCD. As demonstrated in **Section 2.4** below, this new band reflects an equilibrium between the four- and five-coordinate, solvent coordinated species. Thus, electronic spectroscopies provide a direct handle on DMA coordination to Ni^{II} dihalide complexes relevant to catalysis.

2.2.4 Variable-Concentration and Variable-Temperature UV-Vis-NIR Spectroscopy of $Ni^{II}(IB)Cl_2$ and $Ni^{II}(IB)Br_2$

Solvent and additive evaluation are necessary steps in the optimization of transition metal-catalyzed organic reactions. However, these steps can be somewhat arbitrary and rely on a large empirical screening matrix. Previous studies of **$Ni^{II}(IB)X_2$** demonstrated catalytic yields are maximized in DMA and when the reaction is cooled to 0–5 °C.[6–8] By obtaining VT UV-vis-NIR spectra for both **$Ni^{II}(IB)Cl_2$** and **$Ni^{II}(IB)Br_2$** in DCM and DMA, we aimed to provide insight into precatalyst speciation and, in turn, to provide experimental thermodynamic data for rational catalyst and condition design.

As the concentration of **$Ni^{II}(IB)Cl_2$** is increased in DCM, a noticeable color change from pink to orange is observed. Correspondingly, new electronic absorption bands are observed at 13 100 cm^{-1} and 22 840 cm^{-1} with increasing concentration (**Figure S16**). These additional absorption bands are ascribed to the formation of a **$[Ni^{II}(IB)Cl_2]_3$ μ-Cl**

trimer. A previously obtained crystal structure of this species shows it possesses both five- and six-coordinate formal Ni^{II} centers.[37]

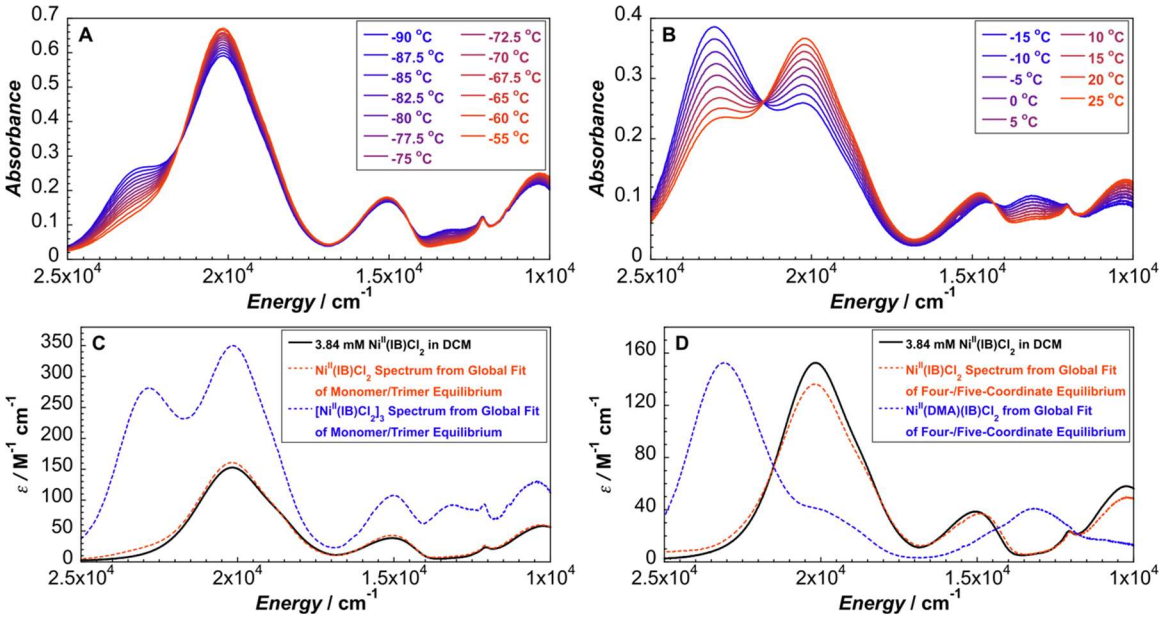

***Figure 4**. VT studies of Ni^{II} precatalysts. VT UV-vis-NIR spectra of (**A**) 4.3 mM **Ni^{II}(IB)Cl$_2$** in DCM and (**B**) 3.6 mM **Ni^{II}(IB)Cl$_2$** in DMA, as well as corresponding resolved spectra from global nonlinear regression for (**C**) **Ni^{II}(IB)Cl$_2$** monomer and trimer and (**D**) four- and five-coordinate **Ni^{II}(IB)Cl$_2$** monomer. Note analogous spectra for **Ni^{II}(IB)Br$_2$** are presented in **Figures S11-12**.*

The UV-vis-NIR spectra of **Ni^{II}(IB)Cl$_2$** in DCM (4.3 mM) and DMA (3.6 mM) also depend on temperature (**Figure 4A** and **4B**). Because of the number of overlapping transitions present in each spectrum, the VT spectra were resolved using global modeling of the temperature dependence through nonlinear regression at multiple wavelengths and bootstrapping (**Figures S13-S15**).[38,39] In DMA, the VT UV-vis-NIR spectra reflect an equilibrium between the four- and five-coordinate, DMA coordinated species for **Ni^{II}(IB)Cl$_2$** (five-coordinate absorption maximum at 22 840 cm^{-1}) and **Ni^{II}(IB)Br$_2$** (five-coordinate absorption maximum at 23 230 cm^{-1}). In DCM, the VT UV-vis-NIR spectra reflect an equilibrium between a monomeric and trimeric form (trimer absorption maxima

at 22 840 cm^{-1} and 20 160 cm^{-1}). We note the excellent agreement between the resolved spectra of the four-coordinate species and the spectra of isolated **Ni^{II}(IB)Cl_2** and **Ni^{II}(IB)Br_2** obtained in DCM (**Figure 4** and **S12**). In contrast to **Ni^{II}(IB)Cl_2**, **Ni^{II}(IB)Br_2** exhibited no trimerization up to 152.1 mM or in VT studies down to –85 °C (**Figures S18-S19**).

In addition to resolving the spectra for four-coordinate, five-coordinate, and trimeric species, these fits provide thermodynamic parameters based on the two equilibrium expressions,

$$K_{eq} = \frac{[(Ni(IB)X_2)_3]}{[Ni(IB)X_2]^3}\ , K_{eq} = \frac{[Ni(Solv.)(IB)X_2]}{[Ni(IB)X_2]} \quad (1)$$

K_{eq} values for DMA coordination to **Ni^{II}(IB)Cl_2** and **Ni^{II}(IB)Br_2** are similar (0.58 and 0.97, respectively, **Table 2**). Furthermore, K_{eq} = 16.7 is calculated at 294 K for formation of the **[Ni^{II}(IB)Cl_2]$_3$ μ-Cl** trimer in DCM. Despite the exergonicity of this process (**Table 2**), the extent of reaction is only 0.09% at 4.3 mM, which is why essentially no trimer is observed at room temperature at low Ni^{II} concentrations. As expected for associative reactions, all entropy values for solvent coordination and trimerization are negative. Note that the extent of temperature-dependent reaction is primarily sensitive to the ratio of the enthalpy to entropy, and the global fitting can extract this value with <1% uncertainty. However, global fitting can additionally extract the absolute standard enthalpies and entropies, albeit with higher uncertainty. From K_{eq} values, we estimate concentrations of ~37% and ~49% for DMA-coordinated **Ni^{II}(IB)Cl_2** (3.6 mM) and **Ni^{II}(IB)Br_2** (3.5 mM), respectively, at 294 K. Upon cooling to 273 K, these values increase significantly to ~53% and ~69%, respectively.

***Table 2**. Thermodynamic reaction parameters for transition metal oligomers and solvent adducts of **$Ni^{II}(IB)X_2$** species. 95% confidence intervals of global fitting given in brackets.*

Complex	**Standard Enthalpy [Range]**	**Standard Entropy [Range]**	**Free Energy (294 K)**	**K_{eq} (294 K)**
$Ni^{II}(IB)(DMA)Cl_2$	−5.0 kcal mol^{-1} [−4.3, −7.1]	−18.1 cal mol^{-1} K^{-1} [−15.4, −25.1]	0.3 kcal mol^{-1}	0.58
$Ni^{II}(IB)(DMA)Br_2$	−6.1 kcal mol^{-1} [−4.2, −8.3]	−20.8 cal mol^{-1} K^{-1} [−13.4, −28.9]	0.02 kcal mol^{-1}	0.97
$[Ni^{II}(IB)Cl_2]_3$	−8.2 kcal mol^{-1} [−4.1, −12.5]	−22.3 cal mol^{-1} K^{-1} [−1.5, −43.7]	−1.6 kcal mol^{-1}	16.7

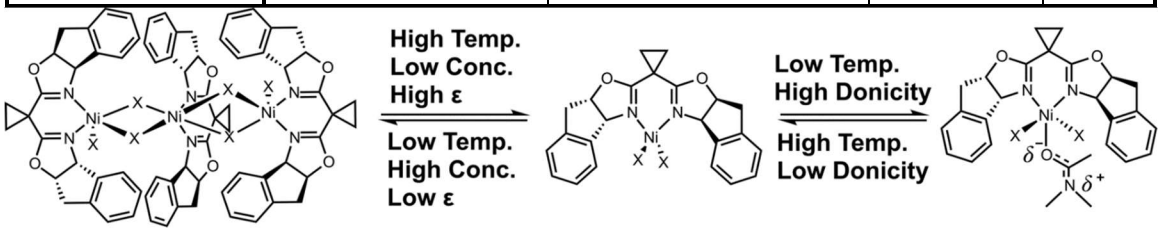

***Figure 5**. Equilibrium behavior of **$Ni^{II}(IB)X_2$** based on solvent conditions and concentration. Note while trimerization is not observed for **$Ni^{II}(IB)Br_2$**, it may form at higher concentrations or lower temperatures accessed herein.*

As depicted in **Figure 5**, the preceding analysis provides the first detailed view of the effects of dielectric constant, concentration, and solvent donicity on the speciation equilibria of Ni^{II} precatalyst solutions. With high solvent donicity, the equilibrium shifts toward a five-coordinate, solvent coordinated species for both **$Ni^{II}(IB)Cl_2$** and **$Ni^{II}(IB)Br_2$**. Increasing concentration and low dielectric constant shifts the equilibrium toward a trimeric species for **$Ni^{II}(IB)Cl_2$**. Thus, solvent coordination, temperature, and catalyst

concentration are important effects that contribute to catalyst speciation and activity under reaction conditions (*vide infra*, **Discussion**). VT spectroscopies provide a direct handle on the speciation and the associated thermodynamics.

2.2.5 Cyclic Voltammetry of $Ni^{II}(IB)Cl_2$ and $Ni^{II}(IB)Br_2$ in DCM, MeCN, and DMA

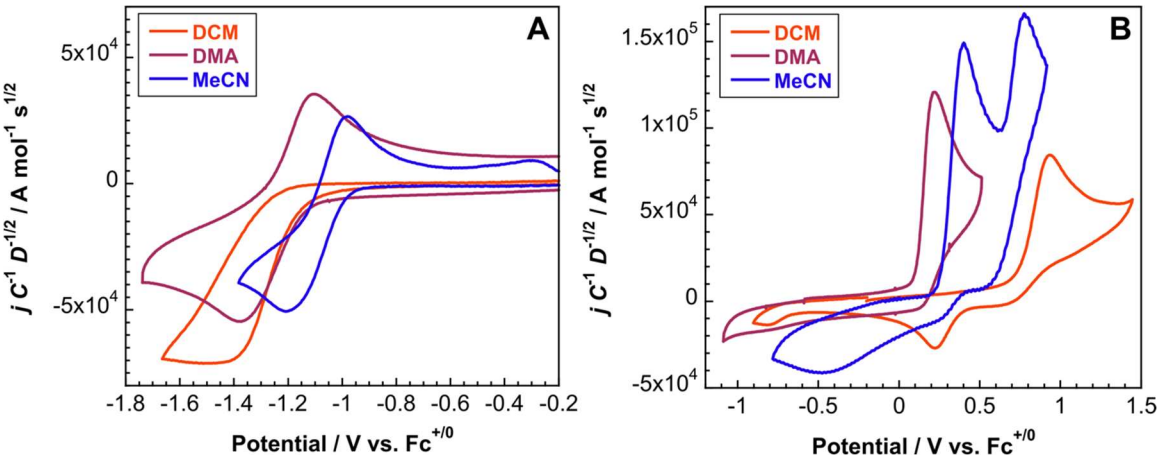

***Figure 6**. Solvent-dependent, diffusion- and concentration-normalized voltammetry of $Ni^{II}(IB)Br_2$ (details of normalization are provided in **Section S5** in the Supporting Information). All electrochemistry acquired in 0.1 M $TBAPF_6$ solution at a scan rate of 100 mV s^{-1}.*

To assess the effects of solvent donicity and dielectric constant on the electrochemical properties of $\mathbf{Ni^{II}(IB)X_2}$ complexes, scan rate-dependent cyclic voltammetry data were acquired in DCM, MeCN, and DMA (**Figure 6** and **Figures S48-S59**). **Table 3** provides peak and formal potentials for initial redox events, while **Table S1** provides peak and formal potentials for unique re-oxidation and re-reduction events that result from chemical reactions following initial electron transfers. Additional details and discussions are provided in Supporting Information **Section S5**.

***Table 3**. Electrochemical parameters for $Ni^{II}(IB)Cl_2$ and $Ni^{II}(IB)Br_2$ in 0.1 M $TBAPF_6$ electrolyte solution using a glassy carbon working electrode, 0.01 M $Ag^{+/0}$ non-aqueous*

reference electrode, and platinum wire counter electrode. All peak and formal potentials are given in volts, obtained using a 100 mV s^{-1} scan rate (unless otherwise stated), and referenced to $Fc^{+/0}$.

Complex	**Solvent**	$E_{p,a,1}$	$E_{p,a,2}$	$E_{p,c}$	$E_{p/2,c}$	$E_c^{0\prime a}$	$E_a^{0\prime a}$	**D_0 (cm^2 s^{-1})[b]**
Ni^{II}(IB)Cl_2	DCM	1.51	---	−1.5	−1.4	−1.4	1.38[d]	9.25
Ni^{II}(IB)Br_2	DCM	0.94	---	−1.4	−1.2	−1.2	0.85	9.25
Ni^{II}(IB)Cl_2	MeCN	0.96	---	−1.4	−1.2	−1.3	0.81	1.05
Ni^{II}(IB)Br_2	MeCN	0.36	0.75	−1.2	−1.0	−1.0	0.30/0.6	9.55
Ni^{II}(IB)Cl_2	DMA	0.67	---	−1.5	−1.4	−1.4	0.48	2.81
Ni^{II}(IB)Br_2	DMA	0.22	---	−1.3	−1.2	−1.2	0.15	3.06
Ni^{II}(^{diBn}biOx)Br_2[c]	1,2-	---	---	−1.9	−1.5	---	---	---
Ni^{II}(^{iPr}biOx)Br_2[c]	1,2-	---	---	−1.6	−1.4	---	---	---
Ni^{II}(^{diMe}biOx)(Dipp)B	THF	---	---	−2.3	−2.1	---	---	---

[a]From the inflection potential of the redox process at 100 mV s^{-1}, which approximates the formal potential. [b]Derived from mass transport-controlled current at a disk microelectrode. [c]See reference 40. [d]Estimated from the local minimum of dj/dV at 25 mV s^{-1}. [e]Estimated from the local minimum of dj/dV at 100 mV s^{-1}. $E_{p/2,c}$ is the potential at half of the peak current.

Previous studies have provided formal potentials for both aromatic and non-aromatic Ni^{II} diimine systems, with many reports providing kinetic analyses with substrate present.[41,20] However, to our knowledge, this is the first example of detailed solvent-dependent electroanalytical chemistry for non-aromatic Ni^{II} cross-coupling catalysts. In general, precatalyst electrochemical responses are remarkably solvent dependent. In all three solvents, **Ni^{II}(IB)Cl_2** and **Ni^{II}(IB)Br_2** both exhibit single, electrochemically irreversible reduction events with significantly shifted oxidative waves (**Figures 6**, and

S50, S54, S58). The general irreversibility required use of peak potentials ($E_{p,a}$ or $E_{p,c}$), potentials at half of the peak current value ($E_{p/2}$), and inflection potentials (accurate estimate of formal potential, $E^{0'}$) for analysis.[42] Our measured Fc formal potentials in DMA and MeCN are 85 and 91 mV vs 0.01 M $Ag^{+/0}$, respectively, indicating accurate conclusions can be drawn regarding solvent effects on measured formal potentials of the Ni complexes in these solvents. In DCM, the measured Fc formal potential is 215 mV. Therefore, measured formal potentials in DCM will appear negatively shifted relative to values in DMA and MeCN.

Based on shifts in peak potential as a function of scan rate and scan rate normalized voltammetry (current function) in all three solvents (**Figures S48-S58**), as well as differential pulse voltammetry and variable temperature voltammetry in DMA for **Ni^{II}(IB)Cl_2** (**Figure S58**), we can draw some insightful conclusions regarding the reduction mechanism, as the current function and shift in peak potential are dictated by the particular chemical and electrochemical mechanism. These conclusions also apply to **Ni^{II}(IB)Br_2**. We ascribe the reduction of both complexes to a concerted E_qC_i (in DMA and MeCN, solvent coordination and/or halide loss occur in concert) or step-wise E_iC_i mechanism (DCM), where slow electron transfer is followed by rapid halide loss. In DCM, three-coordinate **Ni^{I}(IB)X** will be generated upon reduction, with no subsequent solvent coordination. The lack of return current, shift in peak potential as a function of the logarithm of the scan rate near 29.6 mV, with ~33 mV observed here, and decrease in the current function toward a limiting value as the scan rate is increased supports a kinetically-controlled, stepwise reduction followed by rapid halide loss (**Figures S48** and **S50**). Activation of DCM by other nickel complexes supported by naphthyridine-diimine ligands

has been observed previously.[43] However, spectroelectrochemical data obtained in DCM do not support reactivity of the **Ni^{I}(IB)X** with solvent (**Figures S73 - S75**). Overall, this analysis featuring electron transfer coupled to rapid halide loss is consistent with halide dissociation observed previously using extended X-ray absorption fine structure (EXAFS) for a low-spin Ni^{II} biOx aryl halide complex upon reduction with potassium graphite.[20] Experimental formal potentials for chemically-coupled reduction of **Ni^{II}(IB)Cl$_2$** and **Ni^{II}(IB)Br$_2$** to **Ni^{I}(IB)Cl** and **Ni^{I}(IB)Br** in DCM are −1.47 V and −1.26 V vs. $Fc^{+/0}$, respectively (**Table 3**). It is therefore ~0.21 V (~1695 cm^{-1}) harder to reduce **Ni^{II}(IB)Cl$_2$** relative to **Ni^{II}(IB)Br$_2$**. This observation is consistent with the energetic shifts in the spin-allowed ligand field bands in DCM in experiment (*vide supra*, **Section 2.1**) and calculations (*vide infra*, **Section 3.2** and **3.3**). In MeCN and DMA, **Ni^{II}(IB)Cl$_2$** (**Figures S54** and **S58**) and **Ni^{II}(IB)Br$_2$** (**Figure 6**, left) both exhibit superficially quasi-reversible voltammetry for the reduction. Experimental formal potentials for chemically-coupled reduction in MeCN/DMA of **Ni^{II}(IB)Cl$_2$** and **Ni^{II}(IB)Br$_2$** are −1.32/−1.47 V and −1.05/−1.23 V vs. $Fc^{+/0}$, respectively (Δ = ~0.27/~0.24 V (~2180/1935 cm^{-1})). Thus, for all solvents used here, it is harder to reduce **Ni^{II}(IB)Cl$_2$** relative to **Ni^{II}(IB)Br$_2$**.

Based on the VT UV-vis-NIR data in DMA (*vide supra*, **Section 2.4**), both the Ni^{II} four-coordinate and five-coordinate solvent adducts exist in equilibrium, and this can potentially influence the electrochemistry measured in this solvent. One possibility for the reduction mechanism for these species is reduction followed by halide loss and, for the four-coordinate portion of the complex, coordination of DMA to the Ni^{I} center, which could occur in a concerted or stepwise fashion. For a concerted mechanism, the anticipated shift in peak potential as a function of log(v) is 29.6/α mV, where α is the transfer

coefficient for electron transfer.[42] Based on the observation of only one differential pulsed voltammetry wave on the forward scan and the shift in peak potential with log(*v*) (~77-104 mV), we propose that the reduction and chemical follow up reaction in both MeCN and DMA (i.e., solvent coordination at Ni^{I}) is a concerted process. The two return waves observed scanning oxidatively suggest generation of a halide-dissociated species that is re-oxidized at more positive potentials. This conclusion is supported by VT differential pulse voltammetry (**Figure S58**), where the differential current at the more positive wave decreases as temperature is decreased, while the differential current at the wave ascribed to re-oxidation of five-coordinate Ni^{I} increases. Based on behavior previously observed for these systems and our computed formal potentials,[20] the more positive re-oxidation could arise from re-oxidation of a Ni^{I}/Ni^{I} dimer that forms after the initial reduction. However, we favor the interpretation featuring re-oxidation of the halide-dissociated species based on computed formal potentials (*vide infra*, **Section 3.3**) and lack of return oxidation near the reduction event in DCM, where Ni^{I} is anticipated to dimerize rapidly. Further supporting our hypothesis, an additional wave near where three-coordinate Ni^{I} is predicted to oxidize is present in MeCN, but not in DMA (**Figures S52** and **S54**), supporting the weaker coordination affinity of MeCN and our assignment of the species generated upon reduction.

Potentials for chemically-coupled reductions in DMA are more negative relative to MeCN by ~200 mV for both complexes. As discussed further in **Section 3.3**, this difference is ascribed to DMA being a higher donicity solvent and coordinating to the Ni^{II} center. Note that solvent coordination is not observed in DCM and only weakly so in MeCN. It is further interesting to note that the reduction potential for **Ni^{II}(IB)Cl_2** in both DCM and

DMA is −1.47 V vs. $Fc^{+/0}$, respectively; for **Ni^{II}(IB)Br_2**, these are −1.26 V and −1.23 V vs. $Fc^{+/0}$, respectively. The similarity in reduction potentials in DCM and DMA is ascribed to the relative Fc formal potentials in DCM vs. DMA and the role of solvent in facilitating the Ni–X bond rupture upon one-electron reduction, with the anionic halide loss more facile in DMA relative to DCM. Because of these considerations and the electronic structure calculations presented in **Section 3.3**, the more quantitative comparison of potentials for the reduction with and without coordinated solvent is that between MeCN and DMA. Furthermore, the temperature-dependent cyclic voltammetry demonstrates a negatively shifted reduction potential as the temperature is lowered, which may be due to increasing the relative amount of five-coordinate species. Thus, overall, solvent coordination results in a harder to reduce Ni^{II} center. By extension, this can be further translated to a more reducing Ni^{I} species, which, under catalytic conditions, can facilitate oxidative addition (*vide infra*, **Discussion**).[44]

Ligand field and bonding effects on Ni^{II}-based redox potentials can be further elucidated using electronic structure calculations (*vide infra*, **Section 3.3**) and through correlations to electronic spectroscopy, as transitions to the RAMO are also observed experimentally. Differences in measured redox potentials correlate directly with specific structural influences on the energy of the RAMO.

Finally, based on the measured formal potentials, proposed electrochemical mechanisms, and additional electronic structure calculations of redox potentials (*vide infra*, **Section 3.3**), we do not believe **Ni^0(IB)X_2** (or Ni^0 in any form) is thermodynamically accessible in the electrochemical window of common electrochemistry solvents, which supports a $Ni^{I/III}$ catalytic cycle for reductive alkenylation and potentially related reactions involving

bis(oxazoline)–Ni complexes.[20] No additional reduction beyond Ni^{I} is required for oxidative addition of substrates for which this catalyst has been previously demonstrated to be competent, and this finding has important mechanistic implications for bis(oxazoline)–Ni-catalyzed reactions more generally.

2.2.6 Spectroelectrochemistry of $Ni^{II}(IB)Cl_2$ and $Ni^{II}(IB)Br_2$ in DCM and DMA

To rationalize the noticeable difference in electrochemical response of **$Ni^{II}(IB)X_2$** in DCM vs. DMA and to further understand the solvent-dependent catalytic activity, time-based spectroelectrochemical measurements were performed for both negative and positive polarizations. These measurements are the first comprehensive solvent-dependent spectroelectrochemistry for Ni^{II} cross-coupling catalysts. All experimental plots are shown in **Figures S61-S87**. In conjunction with calculations (*vide infra*, **Figures S133-S140**), we can assign transient spectra to possible species generated under polarized conditions. In DCM, polarization negative of the first reduction generates a spectrum with a slightly blue-shifted, higher-energy ligand field transition, consistent with calculated spectra for **$Ni^{I}(IB)X$** (**Figures S133** and **S135**).

Reduction of both **$Ni^{II}(IB)Br_2$** and **$Ni^{II}(IB)Cl_2$** in DMA generates spectra consistent with calculated spectra corresponding to a solvent-coordinated Ni^{I} species, **$Ni^{I}(IB)(DMA)X$** (**Figures S134** and **S136**). All ligand field bands decay in intensity upon oxidation, which is ascribed to oxidative degradation or oligomerization. Spectra obtained after positive polarization of **$Ni^{II}(IB)Br_2$** are consistent with bromide speciation.[45]

2.3 Computational Results

In this section, we sought to gain further insights into the electronic structures of the precatalysts by comparing experimental spectra and redox potentials with computed ground- and excited-state properties obtained from a combination of DFT, time-dependent DFT (TDDFT), and multireference CASSCF/CASPT2 calculations. TDDFT and multireference methods predict electronic transitions below ~25 000 cm^{-1} are ligand field excitations, and differences between computed electronic spectra of **Ni^{II}(IB)X_2** complexes arise from differences in ligand field strength. Generally, increased ligand field strength destabilizes the β lowest unoccupied molecular orbitals (β-LUMOs), which negatively shifts the reduction potential of **Ni^{II}(IB)Cl_2** relative to **Ni^{II}(IB)Br_2**. DFT calculations also corroborate that, depending on reaction conditions (such as the choice of coordinating/non-coordinating solvent or Ni^{II} concentration), precatalysts can exist in complex equilibria featuring four-coordinate **Ni^{II}(IB)X_2**, five-coordinate **Ni^{II}(IB)(solv.)X_2**, or trimeric [**Ni^{II}(IB)X_2**]$_3$ **μ-X** species. Finally, we demonstrate the role of ligand–metal covalency in tuning the relative reactivity of the catalyst resting state; the bonding of this species further manifests in a correlation between reaction yield and its oxidation potential relative to those of C(sp^3) radicals.

2.3.1 DFT and TDDFT Calculated Thermodynamics and Spectra of Ni^{II}(IB)Cl_2 and Ni^{II}(IB)Br_2 Precatalysts

Using a TPSSh functional with a conductor-like polarizable continuum model (CPCM) (see Computational Details in **Section S8** of the Supporting Information), the ground state wave functions of **Ni^{II}(IB)Cl_2** and **Ni^{II}(IB)Br_2** are high-spin (S = 1) Ni^{II}. TDDFT was used to calculate the electronic transition energies (**Table 4**). The intensities

of the lower-energy ligand field bands are underestimated relative to experiment and do not contribute significantly to the overall predicted spectra (**Figures S92-S93**). Additionally, two-electron excitations and spin-flip transitions are inaccessible through conventional TDDFT and, thus, are not observed in the spectral predictions (e.g., $^3A_2(F)$, band 4 and $^1T_2/^1E$, band i excited states in T_d). For d^8 Ni^{II}, there are only six spin-allowed ligand field transitions accessible using TDDFT (**Table 4**). Therefore, full assignment of all absorption bands from **Section 2.1** cannot be achieved using this approach. A more detailed analysis must be obtained from the multi-reference CASSCF/CASPT2 calculations (*vide infra*, **Section 3.2**). Nonetheless, qualitative correlations can be made by comparing to assignments in the parent T_d point group (**Table 4**). While the absolute calculated energies of the ligand field transitions are not well-reproduced with TDDFT, the average energies agree well with the experimentally determined relative ligand field strengths (*vide supra*, **Section 2.1**). For example, experimental values of ~12 365 cm^{-1} and ~11 975 cm^{-1} (Δ = ~390 cm^{-1}) were determined for **Ni^{II}(IB)Cl_2** and **Ni^{II}(IB)Br_2**, respectively, and are computationally estimated to be ~13 780 cm^{-1} and ~13 370 cm^{-1} (Δ = ~410 cm^{-1}) .

Table 4*. Experimental (UV-vis-NIR absorption) and predicted electronic transition energies for* ***Ni^{II}(IB)Cl_2*** *and* ***Ni^{II}(IB)Br_2****.*

Predicted transition energies (cm^{-1})						**Assignment, (#)[b]**
Ni(IB)Cl_2			**Ni(IB)Br_2**			
Experiment	***DFT***	***CASPT2***	***Experiment***	***DFT***	***CASPT2***	
2170[a]	7629	2009	2210[a]	7242	1824	$^3T_1(F)$: $^3B_1(F) \rightarrow A_2(F)$, (1)
---	10056	3318	---	9730	2974	$^3T_2$: $^3B_1(F) \rightarrow {}^3B_1/{}^3B_2$
6640	14393	7443	6150	13924	7229	$^3T_2$: $^3B_1(F) \rightarrow {}^3B_1/{}^3B_2$, (2)

8240	14991	9786	7980	14972	9322	$^3T_2$: $^3B_1(F) \rightarrow {}^3A_1$, (3)
---	---	10 810	---	---	10244	$^3T_2$: $^3B_1(F) \rightarrow {}^3B_1/{}^3B_2$
10 270	---	12709	10150	---	12382	$^3A_2(F)$: $^3B_1(F) \rightarrow {}^3A_2(F)$, (4)
14 940	18462	16354	14460	17529	16112	$^3T_1(P)$: $^3B_1(F) \rightarrow {}^3B_1(P)$, (5)
18 210	---	20 607	17 500	---	19514	$^3T_1(P)$: $^3B_1(F) \rightarrow {}^3B_2(P)$, (6)
20 130	17166	21586	19410	16834	19561	$^3T_1(P)$: $^3B_1(F) \rightarrow {}^3A_2(P)$, (7)

[a]Experimental energies for the $^3B_1(F) \rightarrow A_2(F)$ band were taken from the VCD spectroscopy. [b]Numbered states correspond to spin-allowed ligand field transitions observed in experiments.

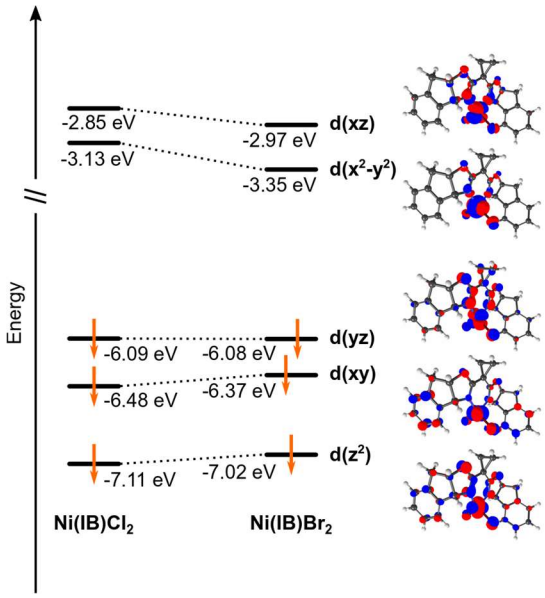

***Figure 7**. Comparison between 3d β-orbital manifolds of **Ni^{II}(IB)X$_2$** precatalysts demonstrating the destabilization of the β-LUMOs due to differences in Cl vs. Br ligand field strength.*

In addition to correlating TDDFT calculations to experimental precatalyst spectra, they can be further utilized to understand the equilibria discussed in **Section 2.4** (see Supporting Information **Section S8.1**). The calculations corroborate that precatalysts can

exist in complex equilibria featuring four-coordinate **$Ni^{II}(IB)X_2$**, five-coordinate **$Ni^{II}(IB)(solv.)X_2$**, or trimeric **$[Ni^{II}(IB)X_2]_3$ μ-X** species. Consistent with experiment, the calculated spectra for five-coordinate species and trimeric species exhibit a significant blue shift for the most intense calculated ligand field band (band 7; **Figures S130-S132**).

2.3.2 Ab initio Multireference Calculations of the $Ni^{II}(IB)Cl_2$ and $Ni^{II}(IB)Br_2$ Precatalysts

Due to the inherent complications with TDDFT described above, we have also used *ab initio* multireference calculations to compute and assign the experimentally observed ligand field excitations. First, we have systematically probed the effects of active space variation in CASSCF calculations (see Computational Details in **Section S8** of the Supporting Information) on the qualitative agreement of **$Ni^{II}(IB)Cl_2$** and **$Ni^{II}(IB)Br_2$** with experimental spectra. Regardless of active space size (**Tables S24-S39**), the ground state is exclusively high spin. Notably, the largest active space used in this work, 22e,12o (five Ni 3*d* orbitals, six halide 2*p*/3*p* orbitals, and the Ni(IB) σ bonding orbital), results in a single-reference ground-state solution, with the highest weight of a single configuration in the CI vector of ~95% for both **$Ni^{II}(IB)Cl_2$** and **$Ni^{II}(IB)Br_2$** (**Tables S29** and **S35**). This configuration corresponds to an $S = 1$ triplet ground state with unpaired electrons in the $d(x^2\text{-}y^2)$ and $d(xz)$ orbitals (i.e., the same configuration as obtained from DFT calculations; *cf.* **Figure 7**). We note that inclusion of the occupied halide 2*p*/3*p* orbitals and the Ni(IB) σ bonding orbital in the active space was essential to reproduce the experimental spectra. With this optimized active space, UV-vis-NIR absorption, CD, and MCD spectra of **$Ni^{II}(IB)Cl_2$** and **$Ni^{II}(IB)Br_2$** were calculated (**Figure 8** and **S141-S142**). These calculations generally support assignments of experimental data given in **Section 2.1** (**Table 4**).

Individual states can be assigned based on the configuration state function with the largest weight in the CI vector, in conjunction with the location of the 3*d* holes (see Supporting Information **Section S8.2**).

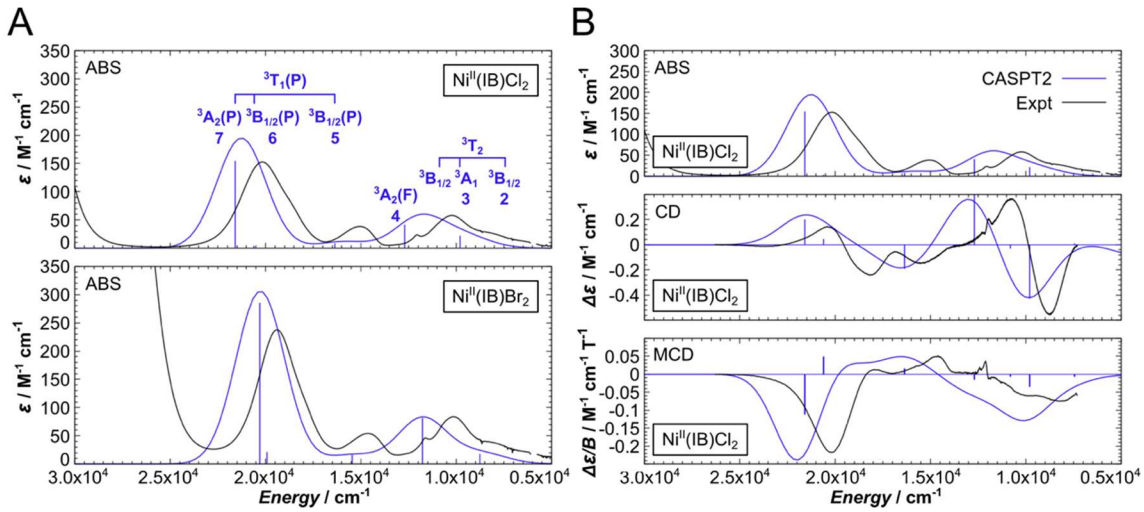

***Figure 8**. Comparison between calculated (CASPT2, 22e,12o; blue) and experimental (black) spectra. (**A**) UV-vis-NIR absorption spectra of **Ni^{II}(IB)Cl$_2$** (top) and **Ni^{II}(IB)Br$_2$** (bottom). Group theory assignments are given along with bands numbered as in experiment. The state ordering is the same for **Ni^{II}(IB)Br$_2$**. (**B**) UV-vis-NIR absorption, CD, and MCD spectra of **Ni^{II}(IB)Cl$_2$**. Note absorption and CD spectra are not normalized, while the computed MCD spectrum has normalized intensities to match experiment. Corresponding data for **Ni^{II}(IB)Br$_2$** are presented in **Figure S142** in the Supporting Information.*

Calculated signs for CD and MCD transitions are also consistent with experiment. All $^3A_2$ excited states exhibit experimental and calculated positive CD bands and negative MCD bands. The $^3A_1$ excited state (band 3 in experiment) exhibits negative bands for both CD and MCD. As supported by theory, the $^3B_1$ excited state exhibits a negative CD band and a positive MCD band. In contrast, the predicted sign for CD does not match that observed experimentally for the higher-energy $^3B_2$ excited state, though this is likely due to this transition being formally forbidden and gaining intensity through either spin-orbit or vibronic coupling, which can give either positive or negative differential intensity in CD.[46]

The overall success of the CASSCF/CASPT2 approach in calculating UV-vis-NIR, and in particular CD/MCD spectra, is especially encouraging for future analyses of experimental spectra for other chiral first-row transition metal cross-coupling catalysts.

2.3.3 Computed Electrochemical Properties

Since the CASSCF CI vector indicates that the ground-state solutions are single-referent, we can use DFT to interpret the effects of different halide ligands on the $Ni^{III/II}$, $Ni^{II/I}$, and $Ni^{I/0}$ reduction potentials of the **Ni^{II}(IB)X_2** complexes and connect them to thermodynamically accessible redox pathways of Ni-based reductive cross-coupling catalysis. **Table 5** provides computed potentials for various electrochemical processes (*vide supra*, **Section 2.5**). Experimentally, the reduction of **Ni^{II}(IB)X_2** complexes is chemically irreversible due to halide dissociation. DFT calculations predict slightly positive halide dissociation energies of ΔG_{dissoc}(CPCM) of ~6 kcal mol^{-1} and ~7 kcal mol^{-1} for Cl and Br **Ni^{I}(IB)X_2** complexes, respectively. The positive ΔG_{dissoc} may be associated with inaccuracies in halide solvation energy when using a simple CPCM. The high electrolyte concentration in electrochemical experiments, which is not accounted for in the computations, may also further shift the equilibrium toward dissociation. For comparison, the calculated ΔG_{dissoc} of halide loss from **Ni^{II}(IB)X_2** is significantly higher in energy (ΔG_{dissoc}(CPCM) = ~30 kcal mol^{-1} and ~29 kcal mol^{-1} for Cl and Br, respectively), indicating much stronger ligand–metal bonds for the Ni^{II} species.

The computed one-electron reduction potentials coupled to halide loss are –1.49 V and –1.39 V vs. $Fc^{+/0}$ for **Ni^{II}(IB)Cl_2** and **Ni^{II}(IB)Br_2**, respectively, with no additional coordinated solvent ligand (**Table 5**). The absolute calculated values compare well with those measured experimentally (**Table 3**), as does the calculated potential difference

between the two complexes (Δ = ~0.10 V (~805 cm^{-1}) (calculated) vs. Δ = ~0.24 V (~1960 cm^{-1}) (experiment – average for all three solvents)). Thus, DFT calculations support the idea that stronger ligand fields generally lead to a more negative potential for Ni^{I} formation. In that regard, more facile reduction of **Ni^{II}(IB)Br_2** is attributed to the lower energy of the β-LUMOs by ~0.2 eV (**Figure 7**).

***Table 5**. Computed formal potentials for **Ni^{II}(IB)Cl_2** and **Ni^{II}(IB)Br_2**. All potentials referenced to $Fc^{+/0}$ with computed absolute potential of –4.55 eV to compare the effect of solvent coordination without the shift induced by $Fc^{+/0}$ in different solvents. Note that MeCN and DMA are essentially indistinguishable in the CPCM and produce the same computed value of $Fc^{+/0}$ absolute potential.*

Coordinated Solvent	**Reaction**	**V vs. $Fc^{+/0}$**
None	$Ni^{II}(IB)Cl_2 + e^- \rightarrow Ni^{I}(IB)Cl_2$	−1.24
	$Ni^{II}(IB)Cl + e^- \rightarrow Ni^{I}(IB)Cl$	−0.20
	$Ni^{II}(IB)Cl_2 + e^- \rightarrow Ni^{I}(IB)Cl + Cl^-$	−1.49
	$Ni^{II}Ni^{I}(IB)_2Cl_4$ Dimer + $e^- \rightarrow [Ni^{I}(IB)Cl_2]_2$ Dimer	−1.28
	$Ni^{II}(IB)Br_2 + e^- \rightarrow Ni^{I}(IB)Br_2$	−1.11
	$Ni^{II}(IB)Br + e^- \rightarrow Ni^{I}(IB)Br$	−0.13
	$Ni^{II}(IB)Br_2 + e^- \rightarrow Ni^{I}(IB)Br + Br^-$	−1.39
	$Ni^{II}Ni^{I}(IB)_2Br_4$ Dimer + $e^- \rightarrow [Ni^{I}(IB)Br_2]_2$	−1.26
MeCN	$Ni^{II}(IB)Cl(MeCN) + e^- \rightarrow Ni^{I}(IB)Cl(MeCN)$	−0.59
	$Ni^{II}(IB)Cl_2(MeCN) + e^- \rightarrow Ni^{I}(IB)Cl(MeCN) + Cl^-$	−1.65
	$Ni^{II}(IB)Cl_2(MeCN) + e^- \rightarrow Ni^{I}(IB)Cl_2 + MeCN$	−1.03
	$Ni^{II}(IB)Br(MeCN) + e^- \rightarrow Ni^{I}(IB)Br(MeCN)$	−0.90
	$Ni^{II}(IB)Br_2(MeCN) + e^- \rightarrow Ni^{I}(IB)Br(MeCN) +$	−1.48
	$Ni^{II}(IB)Br_2(MeCN) + e^- \rightarrow Ni^{I}(IB)Br_2 + MeCN$	−0.85
DMA	$Ni^{II}(IB)Cl(DMA) + e^- \rightarrow Ni^{I}(IB)Cl(DMA)$	−1.17
	$Ni^{II}(IB)Cl_2(DMA) + e^- \rightarrow Ni^{I}(IB)Cl(DMA) + Cl^-$	−1.66

	$Ni^{II}(IB)Cl_2(DMA) + e^- \rightarrow Ni^{I}(IB)Cl_2 + DMA$	−1.06
	$Ni^{II}(IB)Br(DMA) + e^- \rightarrow Ni^{I}(IB)Br(DMA)$	−1.09
	$Ni^{II}(IB)Br_2(DMA) + e^- \rightarrow Ni^{I}(IB)Br(DMA) + Br^-$	−1.44
	$Ni^{II}(IB)Br_2(DMA) + e^- \rightarrow Ni^{I}(IB)Br_2 + DMA$	−0.86

The computed one-electron reduction potentials coupled to halide loss also shift negatively upon solvent coordination. For the Cl complex, calculated values are –1.49 V, –1.65 V, and –1.66 V vs. $Fc^{+/0}$ for no solvent, MeCN, and DMA coordination, respectively. For the Br complex, analogous calculated values are –1.39 V, –1.48 V, and –1.44 V vs. $Fc^{+/0}$. These negative potential shifts due to solvent coordination are also ascribed to modifications of the Ni^{II} β-LUMOs. For example, average energy destabilizations of 0.40 eV and 0.47 eV are observed for **Ni^{II}(IB)Cl_2** and **Ni^{II}(IB)Br_2** complexes, respectively, upon MeCN or DMA coordination. Together, these calculations and the ligand field spectroscopy both indicate for the first time that the RAMO energy is an excellent descriptor of the redox properties of these metal-based cross-coupling catalysts, and DFT calculations provide a useful approach for analyzing ligand contributions to potentials.

Finally, further extending these calculations to additional species, the computed reduction of **Ni^{I}(IB)X** to **Ni^{0}(IB)X** or **Ni^{0}(IB)** is calculated to occur at exceedingly negative formal potentials (∼–3 V to –4 V). These calculated potentials for Ni^0 formation are significantly more negative than the reduction potentials of typical reductants used in cross-coupling reactions (e.g., ∼–1.11 V vs. $Fc^{+/0}$ in DMA for tetrakis(dimethylamino)ethylene (TDAE) or ∼–1.94 V vs $Fc^{+/0}$ in DMF for Mn^0).[47,48] Similarly, the disproportionation of **Ni^{I}(IB)X** to **Ni^{II}(IB)X_2** and **Ni^{0}(IB)** is thermodynamically highly unfavorable, with a ΔG(CPCM) of ∼+57 kcal mol^{-1} for both X = Cl and Br. Thus, Ni^0 is unlikely to be a catalytically relevant

redox state. Bis(1,5-cyclooctadiene)nickel^0 (**Ni(COD)$_2$**), when used as the nickel source, likely first generates **Ni^{II}(IB)X$_2$** to commence the catalytic cycle. It is possible that **Ni^0(IB)** can be formed by mixing **IB** and **Ni(COD)$_2$**, and that this Ni^0 complex might oxidatively add one of the electrophiles to give **Ni^{II}(IB)RX** and initiate the first turnover. However, it is unlikely that the catalytic cycle involves reduction back to **Ni^0(IB)**.

2.3.4 Resting State Electronic Structure and its Contributions to Reactivity

The electronic structure and electrochemical properties determined herein for **Ni^{II}(IB)X$_2$** complexes support a Ni$^{I/III}$ cross-coupling reaction cycle. A low-spin square planar Ni^{II} phenanthroline (phen) aryl halide (**Ni^{II}(phen)(Ar)X**) resting state has been proposed by Diao *et al.* for Ni-catalyzed reductive 1,2–dicarbofunctionalization of alkenes.[49] This resting state is thought to form from **Ni^{I}(phen)X** bimolecular oxidative addition of the aryl halide. The **Ni^{II}(phen)(Ar)X** is anticipated to react rapidly with C(sp^3) radicals to produce a five-coordinate **Ni^{III}(phen)(Ar)X** intermediate.[31] The 'R–Ar' cross-coupled product can then form via reductive elimination. The analogous reactivity considerations for **IB** complexes and vinyl halides are given in **Figure 9**.[44]

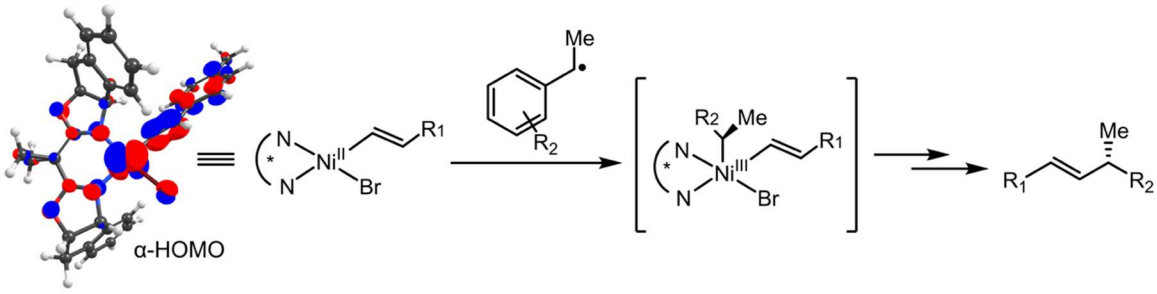

***Figure 9**. RAMO of the resting **Ni^{II}(IB)(Vn)X** for the Ni$^{II/III}$ redox couple and radical capture with Vn = 1-methyl-4-vinylbenzene and X = Br.*

Given the ability to accurately calculate and reproduce experimental formal

potentials, the same approach can be used to investigate the bonding and redox properties of the **Ni^{II}(IB)(Vn)Br** (Vn = 1-methyl-4-vinylbenzene; **Figure 9**) resting state, which we were unable to isolate and study electrochemically due to instability.[44] The calculated reduction potential of this species coupled to halide loss is –1.82 V vs. $Fc^{+/0}$ in DMA. Interestingly, this is ~0.4 V more negative than that calculated for reduction of **Ni^{II}(IB)Br$_2$**. The less facile reduction of **Ni^{II}(IB)(Vn)Br** relative to **Ni^{II}(IB)Br$_2$** likely stems from the increased donor strength of the Vn co-ligand (relative to Br). In the low-spin state of **Ni^{II}(IB)(Vn)Br**, the Ni^{II} $d(x^2\text{-}y^2)$ orbital is the RAMO for the $Ni^{II/I}$ couple. Strong antibonding interactions within the RAMO will destabilize the energy of this orbital, which will decrease the electron affinity and, thus, result in a more negative reduction potential. In this respect, it is also noted that, across a series of various para-substituted styrenyl derivatives, the calculated $Ni^{II/I}$ reduction potentials of the **Ni^{II}(IB)(Vn)Br** species (coupled to halide dissociation) trend with the Hammett parameters of the substituent and the Ni^{II} character in the $d(x^2\text{-}y^2)$ RAMO obtained from Löwdin population analysis (**Figure S90**).

It is also instructive to consider the role of the Vn ligand in the benzyl-C(sp^3) radical recombination with **Ni^{II}(IB)(Vn)X**. The high donation of the Vn co-ligand in **Ni^{II}(IB)(Vn)X** would make this intermediate more oxidizable and readily available for the less-exergonic radical coupling; this variation in donation should also be correlated to changes in Ni^{II}–ligand bond covalency. Indeed, the calculated ligand–metal covalency of **Ni^{II}(IB)(Vn)Br** varies linearly with the calculated energy of the RAMO (**Figure 10A**). **Ni^{II}(IB)(Vn)Br** styrenyl systems with either dimethylamino or carbomethoxy substituents at the four position feature ~62% 3*d* character vs. ~10% 3*d* character in the RAMO, which

correlate to more negative and less negative RAMO energies, respectively. Previous studies have also observed a linear correlation between redox potential and covalency in metalloproteins and model complexes.[50–53]

The less-donating halide ligands (relative to the Vn ligand) could electronically disfavor trapping of **Ni^{II}(IB)X_2** with benzylic radicals; this interpretation is supported by DFT calculations with **$Ni^{II/III}$(IB)X_2** oxidation potentials that are >1 V negative of oxidation potentials of **$Ni^{II/III}$(IB)(Vn)Br** (**Figure 10B**). The electronic influence of the Vn co-ligand can thus be envisioned as enhancing the kinetically competent radical recombination relative to deleterious side reactivity of the free benzylic radical. Indeed, there is a reasonable match between the calculated oxidation energies of the benzylic radicals and **Ni^{II}(IB)(Vn)Br** species, leading to favorable (near-ergoneutral) radical recombination reactions (**Table S9**). Additionally, there is a direct correlation between calculated oxidation potential gaps (ΔE_{ox} between the benzyl-C(sp^3) radical and **Ni^{II}(IB)(Vn)Br** species) and reaction yields obtained from coupling the benzylic radicals generated from the NHP esters (NHP = *N*-hydroxyphthalimide),[54] with the highest yields observed for reactions between benzyl-C(sp^3) radicals and **Ni^{II}(IB)(Vn)Br** species with calculated oxidation potential gaps (ΔE_{ox}) of ~–0.4 V (**Figure 10C**). Although care must be taken drawing mechanistic conclusions from reaction yields, given that 1) **Ni^{II}(IB)(Vn)X** is the catalyst resting state[44] (*vide infra*), and 2) Ni is not involved in generating the radical from the NHP ester, the correlation between reaction yield and ΔE_{ox} reflects the favorability of the radical addition to **Ni^{II}(IB)(Vn)Br**.

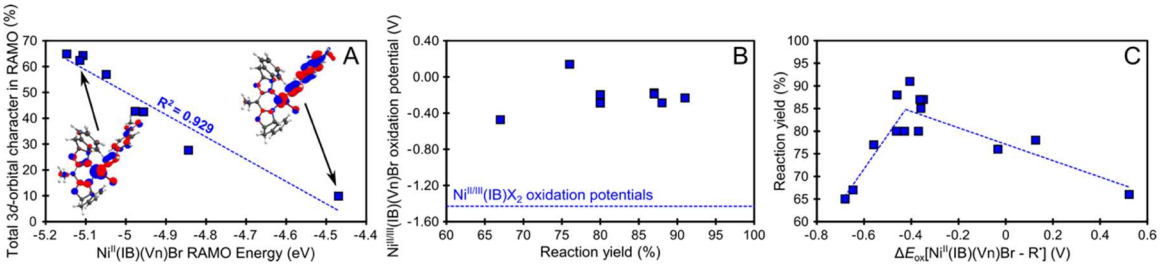

***Figure 10**. Electronic structure and reactivity considerations for precatalysts and resting states. (**A**) Correlation between the total 3d orbital character in the RAMO of the **Ni^{II}(IB)(Vn)Br** and the RAMO energy. (**B**) Comparison between the **Ni$^{II/III}$(IB)(Vn)Br** oxidation potentials vs. reaction yields of the Vn/ethylbenzene C–C coupling with benzyl-C(sp^3) radicals generated by reduction of NHP esters. Blue line indicates the oxidation potentials of **Ni$^{II/III}$(IB)X$_2$** precatalysts to demonstrate insufficient reactivity to compete with **Ni^{II}(IB)(Vn)Br** to quench benzyl-C(sp^3) radicals. (**C**) Reaction yields of various Vn/benzyl-C(sp^3) C–C coupling reactions plotted against the difference between computed oxidation potentials of **Ni$^{II/III}$(IB)(Vn)Br** and benzyl-C(sp^3) radicals. Note all values are also tabulated in **Table S8**. Reaction yields plotted from Reference 54.*

2.4 Discussion

Due to their disparate electronic structures relative to precious metal analogs, first-row transition metal catalysts unlock a rich area of exploration for the discovery of new organic reactions. Indeed, many novel bond constructions have been discovered recently.[2] Exciting mechanistic studies have also highlighted a variety of inorganic species of relevance to reactivity, many of which feature interesting metal- and ligand-based redox events. Furthermore, ground state cross-coupling reaction mechanisms of first-row transition metal complexes have direct relevance to the thermal components of photoredox catalysis. Unlike their bipyridine and terpyridine analogues, which feature intense MLCT transitions, non-conjugated ligands (e.g., **IB**) exhibit rich ligand field spectral features that can be utilized to interrogate Ni-based electronic structure, and just as transient spectroscopic methods can provide insights into the light-induced components of photoredox mechanisms,[55] steady state spectroscopic methods can also provide direct insights into electronic structure contributions to transition metal reactivity.[12,56,57]

Here we have provided several new insights into the area of cross-coupling catalysis: 1) a combination of electronic and magneto-optical spectroscopic methods has allowed for a detailed analysis and definition of the ligand field excited state manifolds of two previously employed cross-coupling catalysts, $\mathbf{Ni^{II}(IB)Cl_2}$ and $\mathbf{Ni^{II}(IB)Br_2}$. This analysis has allowed for the quantification of relative ligand field strengths. As discussed further below, we demonstrate how ligand field strength is linked directly to changes in the energy of the Ni-based RAMO and, thus, to reduction potentials. 2) VT UV-vis-NIR spectroscopy has uncovered and identified two equilibrium processes that we believe to be significant for cross-coupling reaction mechanisms and yields. These equilibria feature a)

four-coordinate and five-coordinate Ni^{II} complexes when in DMA, and b) a monomeric and trimeric species in the Cl complex when in DCM. 3) The Vn ligand involved in cross-coupling plays a critical role in directing the reactivity of the putative resting Ni^{II} complex. Specifically, the electronic nature of the Vn ligand tunes the Ni-based covalency over a large range. In doing so, the covalent character modulates the reactivity of this species toward $C(sp^3)$ radicals, and we have observed a direct correlation between previously reported reaction yields[58] and the difference in oxidation potential between the Ni^{II} resting state and the $C(sp^3)$ radicals, which reflects the driving force for the radical recombination reaction between these species.

Averaging all assignable, spin-allowed ligand field excited states, it was demonstrated in **Section 2.1** that the ligand field strength of the Cl complex is ~390 cm^{-1} stronger than the Br complex. In **Section 2.5**, it was shown that one-electron reduction of **Ni^{II}(IB)X_2** complexes is coupled to rapid halide dissociation, and it is on average (over three solvents) ~0.24 V (~1960 cm^{-1}) harder to reduce the Cl complex relative to the Br complex. In **Section 3.3**, it was also demonstrated that electronic structure calculations can accurately reproduce the experimental one-electron reduction potentials and that the origin of the relative reduction potential arises from ligand field (de)stabilization of the Ni^{II}-based RAMO. Thus, combining ligand field spectroscopies with electrochemistry and electronic structure calculations provides a direct means to dissect geometric and electronic structure contributions to catalytically-relevant redox potentials and allows for an experimentally calibrated approach to extend computations to reaction intermediates.

While the ligand perturbations studied here are halide-based, the ligand field spectral features of Ni-catalysts will also be highly sensitive to ligand perturbations. For

example, in **Table 6**, we have compiled electronic transitions for the **IB** complexes and a series of previously reported pseudo-T_d Ni^{II} complexes, with structures shown in **Figure 11**.[59–63] In general, the second $^3B_1 \rightarrow {}^3A_2(F)$ transition, which is the most intense observed in the lower-energy ligand field manifold, tracks roughly with the overall ligand field strength, with $Ni^{II}(PPh_3)_2Cl_2$ exhibiting the highest transition energy. Another noticeable trend, the variability in $^3B_1/^3B_2$ transition energies, stems from high variability in geometric distortions. We also note the similarity in blueshifts in transition energies for **Ni^{II}(IB)X_2** and $Ni^{II}(L+)X_3$ as a function of halide identity. Thus, measured ligand field transitions can provide a means to estimate specific ligand contributions to catalyst electronic structure and ultimately redox potentials and reactivity in future studies.

***Table 6**. Comparison between spin-allowed transition energies for **Ni^{II}(IB)Cl_2** and **Ni^{II}(IB)Br_2** in DCM and previously studied pseudo-T_d Ni^{II} complexes (units of cm^{-1}).*

Complex	$^3B_1(F) \rightarrow {}^3A_2(F)$	$^3B_1(F) \rightarrow {}^3B_1/{}^3B_2(F)$	$^3B_1(F) \rightarrow {}^3A_1(F)$	$^3B_1(F) \rightarrow {}^3A_2(F)$	$^3B_1(F) \rightarrow {}^3B_1(P)$	$^3B_1(F) \rightarrow {}^3B_2(P)$	$^3B_1(F) \rightarrow {}^3A_2(P)$
$Ni^{II}(IB)Cl_2$[a]	2170	6640	8240	10270	14940	18210	20130
$Ni^{II}(IB)Br_2$[a]	2210	6140	7970	10140	14570	17420	19380
$Ni^{II}(PPh_3)_2Cl_2$[b]	4500	10 200	8000	1 200	18100	14600 – 16400*	1600
Ni^{II}(biquinoline)Br_2[c]	3740	4941	6020	9810	18450	17300	19430
$[Ni^{II}Cl_4]^{2-}$[d]	4440	3970	4440	6870	14250	14250	15240
$Ni^{II}(L+)Cl_3$[e]	4660*	5260	6410	9090	16 000	16000	17240
$Ni^{II}(L+)Br_3$[e]	4530	5100	6410	8700	15 200 –	15200 –	16250

					16100	16100	

[a]This work. [b]Reference 64. [c]Reference 65. [d]References 66 and 67 . [e]Reference 68. Starred transition energies are obtained from crystal field analysis of other experimentally observed transitions.

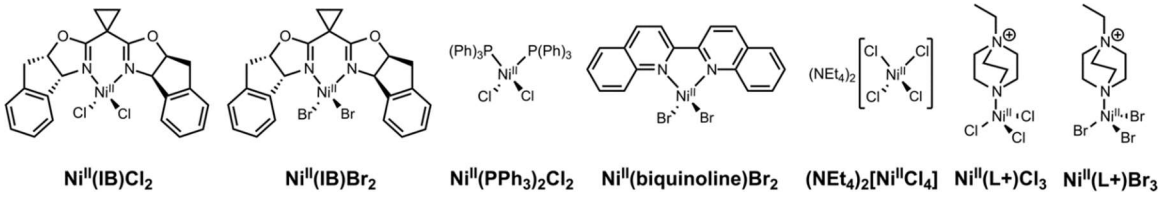

***Figure 11**. Structures of pseudo-T_d Ni^{II} complexes used for comparison in **Table 6**.*

VT electronic absorption spectra reported here are also particularly illuminating and provide 1) direct evidence of variable speciation for **IB** complexes as a function of solvent and temperature and 2) direct thermodynamic parameters describing these equilibria. For **Ni^{II}(IB)Cl$_2$** and **Ni^{II}(IB)Br$_2$** in DMA, a significant fraction of DMA coordinated complex is present at room temperature (~37% and 49%, respectively, at 3.6 mM (Cl) and 3.5 mM (Br)). At lower temperatures (273 K), DMA coordination is strongly favored (~53% and 69%, respectively). Generally, amide-based solvents can coordinate to metal centers through the carbonyl oxygen, preference for which is further influenced by steric hindrance at the nitrogen center. The $n_N \rightarrow \pi^*_{CO}$ delocalization of the amide results in increased electron density on oxygen (**Figure 5**), leading to a strong donor and a partial negative charge near the Ni^{II} center.[69] As demonstrated herein for the first time by a combination of electrochemistry and electronic structure calculations, DMA coordination can lead to a more difficult to reduce Ni^{II} center, with negatively shifted potentials of ~200 mV in DMA vs. MeCN for the Cl and Br complexes. The single electron reduction leads

to rupture of the halide–metal bond; we propose that halide solvation and solvent coordination to Ni can also contribute significantly to the measured reduction potential (e.g., –1.47 V vs. $Fc^{+/0}$ in DMA/DCM for **Ni^{II}(IB)Cl_2**). Of further note, yields for reductive alkenylation are maximized when 1) DMA or another amide solvent is utilized, and 2) the reaction temperature is lowered to 0–5 °C, with both considerations favoring nickel coordination by the solvent.

Scheme 2 provides boron trifluoride (BF_3) donor numbers, acceptor numbers, substrate conversion percentage, and cross-coupled yield percentages for the reaction between (1-chloroethyl)benzene and (*E*)-1-(2-bromovinyl)-4-methoxybenzene. Previous studies determined the optimized conditions based on systematic screening of reaction parameters.[7] We conducted triplicate measurements of this reaction in several solvents with a range of Lewis basicities. Generally, as the donicity of the solvent decreases, the substrate consumption and cross-coupled product yield decrease significantly. As discussed further below, we believe this reflects a significant steric effect at play, which can protect Ni^{II} and/or reduced Ni^{I} species from off-cycle reactivity. Based on these considerations, we also purport that amide coordination results in a more oxidizable Ni^{I} species, which increases oxidative addition reactivity.

The VT UV-vis-NIR and spectroelectrochemistry studies, when compared with experimental conditions often utilized for nickel-catalyzed reductive cross-coupling (i.e., low temperatures, use of coordinating solvents, relatively mild reducing agents, etc.),[2,7,8] are consistent with the mechanistic investigation of this reaction by Turro and coworkers,[44] which suggests this reaction proceeds via a $Ni^{I/III}$ redox cycle (**Scheme 3**), similar to that proposed by Diao and coworkers for the related cross-coupling of aryl halides.[20] Additional

aspects of the optimized reaction conditions can be commented on, however, as derived from the findings in the present study.

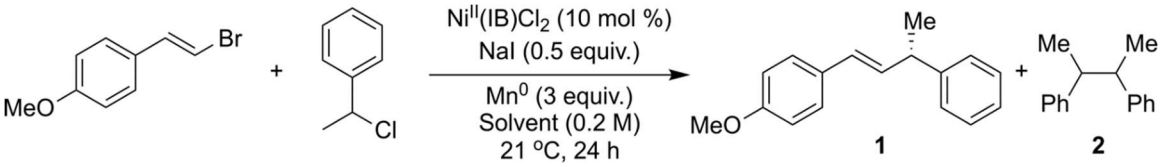

Solvent	**Donor Number (kcal mol⁻¹) (BF_3 Affinity)**	**Acceptor Number**	**Yield of 1**	**Ratio of Yields for 1 to 2**
N-Methyl-2-pyrrolidone (NMP)	26.9	13.3	52%± 1%	2.1
N,N'-Dimethylpropyleneurea	26.8	---	38%± 1%	1.2
N,N'-Dimethylacetamide (DMA)	26.8	13.6	72%± 2%	4.1
N'N'-Dimethylformamide (DMF)	26.4	16.0	50%± 2%	1.6
Tetrahydrofuran (THF)	21.6	8.0	30%± 1%	0.9
Ethyl Acetate (EtOAc)	18.1	9.3	33%± 3%	1.1
1,2-Dimethoxyethane (DME)	17.8	10.2	34%± 2%	1.1
1,4-Dioxane	17.7	10.8	---	---
Acetonitrile (MeCN)	14.4	18.9	16%± 1%	0.4
Dichloromethane (DCM)	2.4	20.4	---	---

Scheme 2*. Conversion and cross-coupled yields for a representative reductive cross-coupling of (1-chloroethyl)benzene and (E)-1-(2-bromovinyl)-4-methoxybenzene using* ***$Ni^{II}(IB)Cl_2$****, along with donor and acceptor numbers for solvents tested in optimization studies. Standard errors were calculated from three trials. Experimental procedure given in Supporting Information Section S1. D-BF_3 donor numbers taken from References 32 and 33. Acceptor numbers (ANs) taken from Reference 33. All ANs measured with respect to the affinity of antimony pentachloride towards triethylphosphine oxide.*

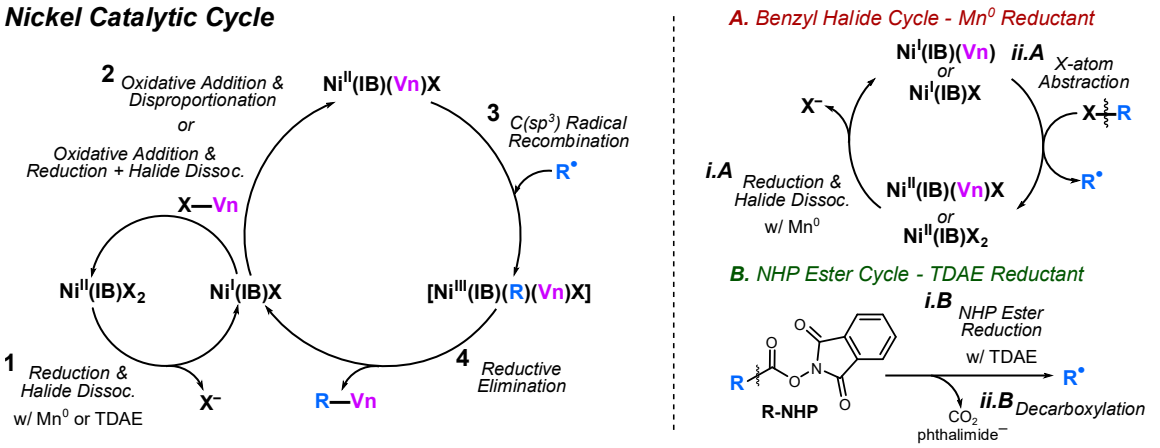

Catalytic Cycle Resting State

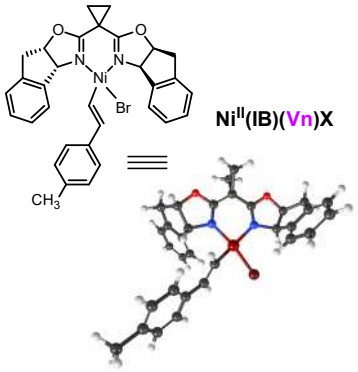

Energetics of Nickel Cross-Coupling Catalysis

		ΔG (298 K)
1	$Ni^{II}(IB)Br_2 + e^- \longrightarrow Ni^{I}(IB)Br + Br^-$	–12.7 kcal/mol (Mn^0)
		+1.1 kcal/mol (TDAE)
2	$Ni^{I}(IB)Br + Br–Vn \longrightarrow [Ni^{III}(IB)(Vn)Br_2]$	+4.8 kcal/mol
	$[Ni^{III}(IB)(Vn)Br_2] + Ni^{I}(IB)Br \longrightarrow Ni^{II}(IB)Br_2 + Ni^{II}(IB)(Vn)Br$	–20.4 kcal/mol
	or $[Ni^{III}(IB)(Vn)Br_2] + e^- \longrightarrow Ni^{II}(IB)(Vn)Br + Br^-$	–33.0 kcal/mol (Mn^0)
		–19.2 kcal/mol (TDAE)
3	$Ni^{II}(IB)(Vn)Br + R^\bullet \longrightarrow [Ni^{III}(IB)(Vn)(R)Br]$	+4.6 kcal/mol
4	$[Ni^{III}(IB)(Vn)(R)Br] \longrightarrow Ni^{I}(IB)Br + R–Vn$	–40.5 kcal/mol
i.A	$Ni^{II}(IB)(Vn)Br + e^- \longrightarrow Ni^{I}(IB)(Vn) + Br^-$	–2.8 kcal/mol (Mn^0)
	or $Ni^{II}(IB)Br_2 + e^- \longrightarrow Ni^{I}(IB)Br + Br^-$	–12.7 kcal/mol (Mn^0)
ii.A	$Ni^{I}(IB)(Vn) + Br–R \longrightarrow Ni^{II}(IB)(Vn)Br + R^\bullet$	–19.1 kcal/mol
	or $Ni^{I}(IB)Br + Br–R \longrightarrow Ni^{II}(IB)Br_2 + R^\bullet$	–9.3 kcal/mol
i.B	$R\text{-}NHP + e^- \longrightarrow [R\text{-}NHP]^{\bullet-}$	+1.1 kcal/mol (TDAE)
ii.B	$[R\text{-}NHP]^{\bullet-} \longrightarrow R^\bullet + CO_2 + phthalimide^-$	–56.4 kcal/mol

***Scheme 3**. Representative computed $Ni^{I/III}$ catalytic cycle for the cross-coupling of $C(sp^2)$ vinyl and $C(sp^3)$ benzyl electrophiles. Relative Gibbs free energy values were computed at the TPSSh (CPCM) level for X = Br. Reactions involving electron transfers were corrected by adding the energy of $Mn^{0/2+}$ redox couple or $TDAE^{0/+}$, which were used as the external reducing agents in refs. [54] and [7]. Note that we have adopted values of $E° = -1.94$ V vs. $Fc^{+/0}$ for $Mn^{2+/0}$ obtained from the experiments in refs. [48] and [70] and $E° = -1.34$ V vs. $Fc^{+/0}$ for $TDAE^{+/0}$ from computations in this article.*

To better understand their role in the cross-coupling of (*E*)-1-(2-bromovinyl)-4-methylbenzene (Vn $C(sp^2)$ component) and (1-bromoethyl)benzene ($C(sp^3)$ radical), DFT computed stable intermediates along the nickel catalytic cycle are shown in **Scheme 3** for **$Ni^{II}(IB)Br_2$**. Free energies of individual steps are energetically accessible, suggesting favorable cross-coupling reactivity. Note that the C–C bond forming cycle is identical regardless of the $C(sp^3)$ benzyl radical source. However, two distinct pathways to

generating these radicals have been proposed by Turro *et al.*, which differ in terms of substrate (i.e., benzyl halide, pathway A, or NHP ester, pathway B) and reductant (i.e., Mn^0 vs. TDAE reductants) (**Scheme 3**).[44] We also note **Scheme 3** only features computed free energies, and we have restricted our discussion of the possible effects of DMA to these steps/energies. It is also possible for DMA coordination to influence reaction barriers. More detailed mechanistic aspects and reaction kinetics are discussed in reference 44 by Turro *et al.*. More broadly, results described herein suggest future computational studies should also consider explicit solvent coordination in calculated reaction mechanisms.

With benzyl bromide and a Mn^0 reductant, the only computed endergonic reaction in the catalytic cycle is the radical recombination of the C(sp^3) radical with **Ni^{II}(IB)(Vn)Br** to form **Ni^{III}(IB)(Vn)(R)Br** (**Scheme 3**, reaction 3, ΔG^0(CPCM) = 4.6 kcal/mol). Notably, **Ni^{II}(IB)(Vn)Br** and related species have been assigned as the catalytic resting state.[49,20,44] The generation of C(sp^3) benzyl radical from benzyl bromide is a favorable process through Br-atom abstraction (reaction ii.A) with either **Ni^{I}(IB)Vn** (ΔG^0(CPCM) = –19.1 kcal mol^{-1}) or **Ni^{I}(IB)Br** (–9.3 kcal mol^{-1}), thus suggesting there might be a balance between this reactivity pathway and reactions *i.A* and *ii.A* in **Scheme 3**. The detailed kinetic analysis presented in ref. [44], however, suggests that XAT from Ni^{II}(IB)X is a more likely alternative, as also evidenced by the observed reactivity of Ni^{I}(IB)X with both C(sp^2) vinyl- and C(sp^3) benzyl-halides.

With the NHP ester substrate and TDAE as a reductant, the **Ni^{I}(IB)Br** formation from **Ni^{II}(IB)Br_2** becomes slightly disfavored with ΔG^0(CPCM) = 1.1 kcal/mol, in addition to the only endergonic reaction 3 in pathway A. In this scenario, the C(sp^3) benzyl radical can be generated from NHP ester without Ni involvement through a direct reduction with

TDAE (reaction *i.B*, $E_{1/2}$ = –1.39 V vs. $Fc^{+/0}$)) followed by a highly exergonic decomposition, yielding CO_2, phthalimide anion, and C(sp^3) benzyl radical (pathway *i.B*). As discussed, higher yields of cross-coupled product are typically obtained at lower temperatures and in coordinating solvents, supporting solvent coordination as a key component for the catalytic cycle.[2,7,8] The computed free energies indeed suggest an equilibrium might exist between the **Ni^{I}(IB)Br** and the **[Ni^{I}(IB)Br]$_2$ μ-Br** dimeric species (ΔG^0(CPCM) = +4.1 kcal/mol). We speculate low temperature, which entropically favors solvent coordination, might prevent highly reactive Ni^{I} intermediates from entering off-cycle pathways, especially toward forming oligomeric (e.g., dimeric/trimeric) species. The same could be true for Ni^{II} species. Coordinating solvents can similarly protect Ni^{I} from dimerization by forming a more favorable equilibrium between **Ni^{I}(IB)Br** ↔ **Ni^{I}(IB)(S)Br**, where S = solvent, since formation of the dimer from **Ni^{I}(IB)(S)Br** intermediate may be disfavored sterically. Although the ΔG^0 for DMA coordination to **Ni^{I}(IB)Br** is computed to be higher than ΔG^0 for dimerization (~6.9 kcal mol^{-1} vs. ~4.1 kcal mol^{-1}), the large excess of DMA (especially relative to the rather low concentration of **Ni^{I}(IB)Br** under catalytic conditions) will favor solvent coordination and further perturb the relative concentrations/equilibria for both processes.

DMA coordination to **Ni^{I}(IB)X** could also lower the kinetic barrier for bimolecular oxidative addition reactivity in reaction 2 (**Scheme 3**): 1) the **Ni^{I}(IB)X** oxidation to **Ni^{II}(IB)X$_2$** is favored in DMA, as observed by the negative shift in reduction potential in the experimental cyclic voltammetry, and 2) oxidative addition of vinyl-halide to **Ni^{I}(IB)X** forming **Ni^{II}(IB)(Vn)X** is favored due to increased electron density on the Ni center and destabilized frontier molecular orbitals upon DMA coordination.

In addition to insights into the role of solvent coordination, the Vn ligand itself can strongly contribute to the reactivity of the resting state. Indeed, there is a linear trend between the amount of metal character in the RAMO and its energy (**Figure 10A**). In general, ligand contributions to the destabilization of the energy of the RAMO will result in greater reactivity and easier oxidation. Notably, we observed a correlation between the reaction yields and the difference in oxidation potentials of **Ni^{II}(IB)(Vn)Br** and benzyl-C(sp^3) radical (ΔE_{ox}). The same metric was recently proposed by Okamoto *et al.* as a measure of the probability of intramolecular redox reactions, showing the most favorable radical recombination for ΔE_{ox} ~0 V.[71] In our case, the coupling efficiency and resulting yields maximize when the benzyl-C(sp^3) radical oxidation potential is slightly higher (by ~0.4 V) than the oxidation potential of **Ni^{II}(IB)(Vn)Br**. A higher reactivity of the benzyl-C(sp^3) radical might be necessary to overcome the reorganization energy required for the change in coordination geometry of the Ni catalyst upon formation of a five-coordinate **Ni^{III}(IB)(R)(Vn)Br** intermediate. Lower yields at higher oxidation potentials of the benzyl-C(sp^3) radicals could be similarly justified by accessing side-reaction radical pathways (e.g., homocoupling). The calculated mismatch in the oxidation potentials may also be a computational artifact. Although we have demonstrated a reasonable correlation between computed and experimental electrochemical data, the nature of Ni catalysts and small organic radicals is quite different and could result in varied relative accuracy of the computed oxidation potentials. The computational model also neglects explicit solvation, whereas DMA solvation and/or coordination to the Ni catalyst (as demonstrated in the present study) could shift the observed oxidation potentials. Regardless, there is a clear trend between the calculated ΔE_{ox} and reaction yields, which indicates the relative

oxidation potentials and frontier molecular orbitals of the **Ni^{II}(IB)(Vn)Br** resting state and the benzyl-C(sp^3) radicals may be a useful predictor for reactivity and can be utilized to computationally screen and guide the synthesis of new Ni complexes for reductive cross-coupling catalysis.

2.5 Concluding Remarks

We have presented the first comprehensive spectroscopic, electrochemical, and computational study of Ni^{II}-based chiral reductive cross-coupling catalysts, **Ni^{II}(IB)Cl_2** and **Ni^{II}(IB)Br_2**. This combination of methods has established 1) there is a direct connection between ligand field strength and catalytically relevant Ni-based reduction potentials, 2) there exists variable speciation for **IB** complexes as a function of solvent and temperature, and VT spectroscopy provides a means to directly measure thermodynamic parameters describing these equilibria, and 3) the Vn ligand involved in cross-coupling plays a critical role in directing the reactivity of the putative resting Ni^{II} complex through strong modulation of ligand–metal covalency. These experimental findings strongly support a critical steric and electronic role that amide-based solvents play in the cross-coupling catalytic cycle. Through this electronic structural characterization, we suggest that dimerization or oligomerization of the catalyst is inhibited by solvent coordination. Furthermore, the modification of electronic structure through solvent coordination increases the driving force for oxidative addition, as evidenced by formal potentials from voltammetry. These results highlight the importance of reaction conditions on catalytic efficiencies and will guide future methodology studies, as well as the development of new ligand scaffolds for Ni-based reductive cross-coupling catalysis.

2.6 Experimental Section

2.6.1 General Considerations

Anhydrous zinc(II) chloride (Millipore Sigma) and electrochemical grade tetrabutylammonium hexafluorophosphate (Millipore Sigma) were used as received. Anhydrous N,N-dimethylacetamide (Millipore Sigma) and d^2-dichloromethane (Cambridge Isotope Laboratories, Inc.) were stored in a nitrogen-filled glove box over activated 3 Å molecular sieves. Acetonitrile and dichloromethane were taken from degassed, dry solvent systems and stored over activated 3 Å molecular sieves in a nitrogen-filled glove box. Nickel(II) dichloride (3a*R*,3a'*R*,8a*S*,8a'*S*)-2,2'-(cyclopropane-1,1-diyl)bis(3a,8a-dihydro-8*H*-indeno[1,2-*d*]oxazole) [**Ni(IB)Cl$_2$**] and nickel(II) dibromide (3a*R*,3a'*R*,8a*S*,8a'*S*)-2,2'-(cyclopropane-1,1-diyl)bis(3a,8a-dihydro-8*H*-indeno[1,2-*d*]oxazole) [**Ni(IB)Br$_2$**] were synthesized according to literature precedent and doubly recrystallized from a mixture of DCM/hexanes.[1,2] All solvents were dried and stored over activated 3 Å molecular sieves in a nitrogen-filled glove box. All NMR spectra were collected on a Varian 400 MHz or Bruker 400 MHz spectrometer (δ in ppm, m: multiplet). ^{13}C NMR spectra were ^{1}H decoupled.

UV-vis-NIR spectra were acquired using a Varian Cary 500 spectrophotometer, while electronic CD and MCD spectra were acquired using a Jasco J1700 CD spectrometer and 1.4 T permanent magnet. MCD spectra were generated by taking the difference between spectra with field direction parallel and field direction antiparallel to the direction of light propagation. Vibrational circular dichroism data (VCD) were collected using a Chiral*IR*-2X (BioTools, Inc.) spectrometer. Spectra were background-corrected for both cell and solvent signals. All spectra were collected in a 0.1 mm path length calcium fluoride

cell. Variable temperature UV-vis-NIR spectra were acquired using a Varian Cary 50 spectrophotometer equipped with a USP-203 series cryostat (UNISOKU Co.) cooled with liquid nitrogen. Samples were equilibrated at each temperature for five minutes prior to acquisition. Spectroelectrochemical measurements were performed in a nitrogen-filled glovebox with a quartz spectroelectrochemical cell with a 0.17 cm path length from Pine Research Instrumentation (AKSTCKIT3), a gold honeycomb electrode (Pine Instruments), and a platinum wire counter electrode. Measurements were recorded using an Analytical Instrument Systems, Inc. DT2000 deuterium-tungsten UV-vis-NIR light source coupled to Stellarnet Black Comet UV-vis and DWARF-Star NIR spectrometers. All room-temperature UV-vis-NIR spectra and low-temperature magnetic circular dichroism spectra were deconvolved simultaneously using Gaussian functions with fixed absorption maxima if possible or by letting values float within 10% for each set of spectra. All deconvolutions were performed in Matlab 2018b.

Homogeneous voltammetry experiments were conducted in a nitrogen-filled glove box using either a 3 mm diameter glassy carbon (CH Instruments) or an 11 μm carbon fiber microdisk working electrode (Gamry Instruments). The real surface areas of these electrodes were determined using averaged values of decay currents from chronoamperometry (macro-disk) or steady-state currents from low scan rate linear sweep voltammetry (micro-disk) in acetonitrile with 0.1 M $TBAPF_6$ and ferrocene as the redox-active standard ($D_0 = 2.24 \times 10^{-5}$ cm^2 s^{-1}).[3] Based on the Cottrell equation (macroelectrode) or the steady-state current equation (microelectrode), the real surface areas were determined to be 0.0877 cm^2 and 1.79×10^{-6} cm^2, respectively.[4] A 0.01 M $Ag^{+/0}$ non-aqueous reference electrode and platinum wire counter electrode were used for all

voltammetry experiments. 0.01 M $AgNO_3$/0.1 M $TBAPF_6$ in MeCN was used as the filling solution for the non-aqueous reference electrode (Bioanalytical Systems, Inc.). Linear fitting to the intercept of a Nyquist plot obtained from potentiostatic electrochemical impedance spectroscopy at the open circuit potential was used to determine the uncompensated resistance, and 95% of this value was compensated. All voltammetry was internally referenced to the $Fc^{+/0}$ redox couple. All experiments utilized a Gamry Reference 600 or Biologic SP-200 potentiostat. Low-temperature voltammetry was conducted using a temperature-controlled 50:50 ethylene glycol:water bath. Solutions were degassed with N_2 prior to measurement. A silver wire pseudo-reference electrode was used in place of $Ag^{+/0}$.

***Zinc(II) bis(chloride) (3aR,3a'R,8aS,8a'S)-2,2'-(cyclopropane-1,1-diyl)bis(3a,8a-dihydro-8H-indeno[1,2-d]oxazole)* [Zn(IB)(Cl)$_2$]:**

Previous syntheses of Ni(II) complexes were used as a template. (3a*R*,3a'*R*,8a*S*,8a'*S*)-2,2'-(cyclopropane-1,1-diyl)bis(3a,8a-dihydro-8*H*-indeno[1,2-*d*]-oxazole) (0.126 g, 0.354 mmol) and zinc(II) chloride (0.056 g, 0.412 mmol) were dissolved in 6.5 mL MeCN/0.1 mL H_2O in a 20 mL scintillation vial under N_2. The solution was heated at 80 ºC for six hours and then cooled to room temperature. The solvent was evaporated *in vacuo*, and the resulting solid was redissolved in dichloromethane. The solution was filtered through a microfiber pipet filter, and the complex was precipitated with excess pentane. The solid was filtered, dried, and weighed to yield the product as a colorless powder (137.8 mg, 79% yield). ^{13}C NMR (100 MHz, CD_2Cl_2) δ 169.0, 139.5, 138.7, 130.1, 128.3, 127.5, 125.5, 86.1, 74.9, 39.3, 21.8, 19.3; ^1H NMR (400 MHz, CD_2Cl_2) δ 7.95 (m, 2H), 7.34 (m, 6H), 5.89 (m, 2H), 5.52 (m, 2H), 3.48 (m, 2H), 3.28 (m, 2H), 1.96 (m, 2H), 1.76 (m, 2H).

Solvent-dependent Yields for Reductive Heterocoupling

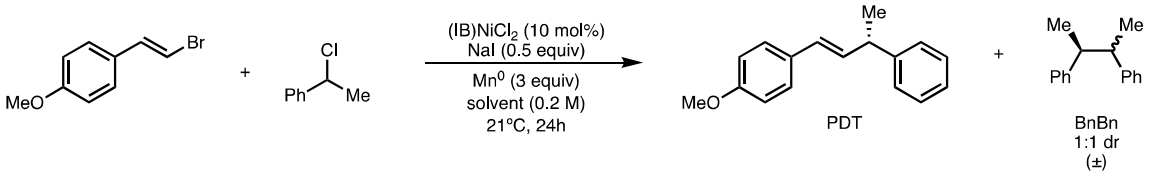

Procedure: To an oven-dried 1 dram vial equipped with a stir bar was added (*E*)-1-(2-bromovinyl)-4-methoxybenzene (21.3 mg, 0.10 mmol, 1 equiv), Mn^0 powder (7.5 mg, 0.30 mmol, 3 equiv), and $Ni^{II}(IB)Cl_2$ (4.9 mg, 0.010 mmol, 0.1 equiv). The vial was then brought into a N_2-filled glovebox where NaI (7.5 mg, 0.050 mmol, 0.5 equiv) was added followed by a careful (as to not disturb Mn^0 powder) addition of 500 μL (0.2 M) of the appropriate solvent. 1-chloroethyl)benzene (13.3 μL, 0.10 mmol, 1 equiv) was then added followed by *n*-dodecane internal standard. The vial was sealed with a Teflon-lined cap and further sealed with electrical tape then removed from the glovebox where it was allowed to stir at 1500 rpm for 24 h. Upon completion, the reaction was quenched with 1 mL of H_2O and extracted with 1 mL EtOAc then filtered through a $MgSO_4$ plug where the filtrate was further diluted with EtOAc and analyzed by GC-FID. Procedure was repeated 3x for each solvent.

2.6.2 NMR Spectra

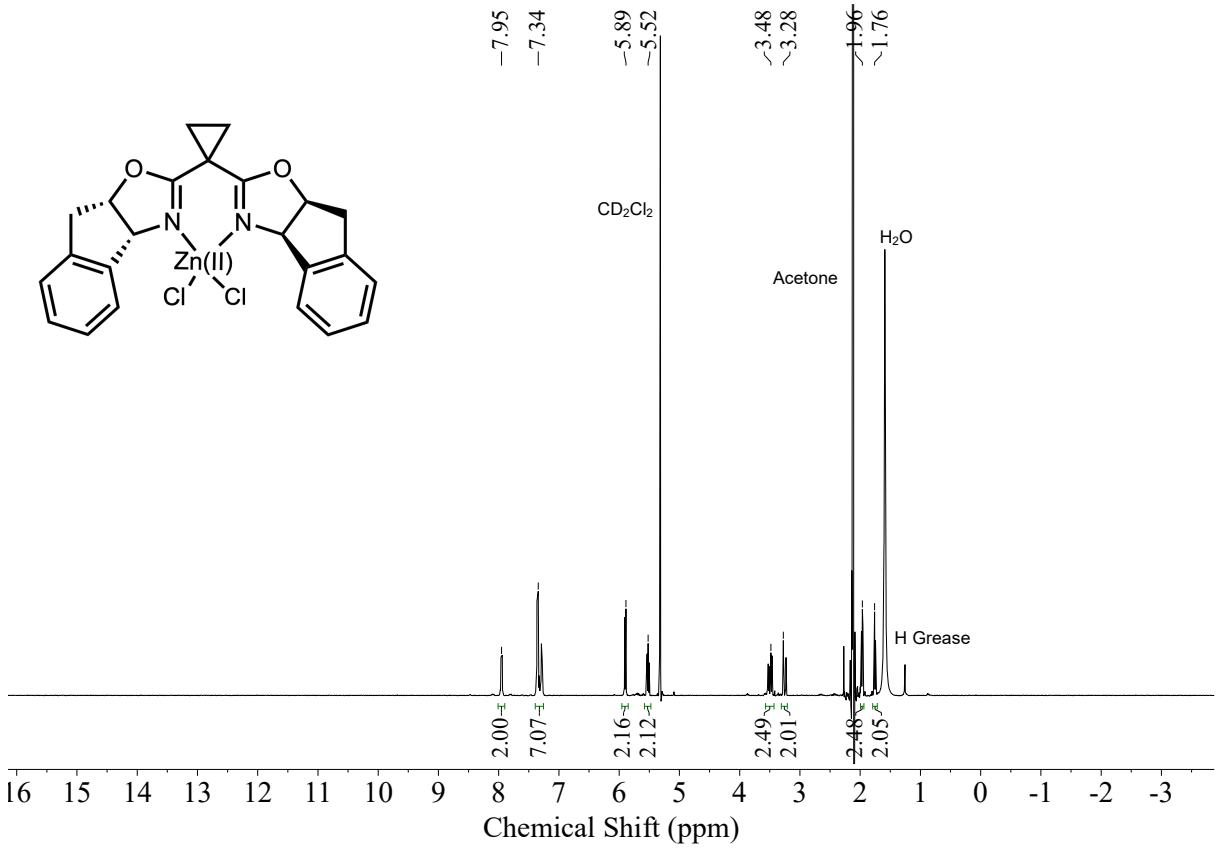

***Figure S1**. ^{1}H NMR of **Zn(IB)Cl$_2$** in d^2-dichloromethane.*

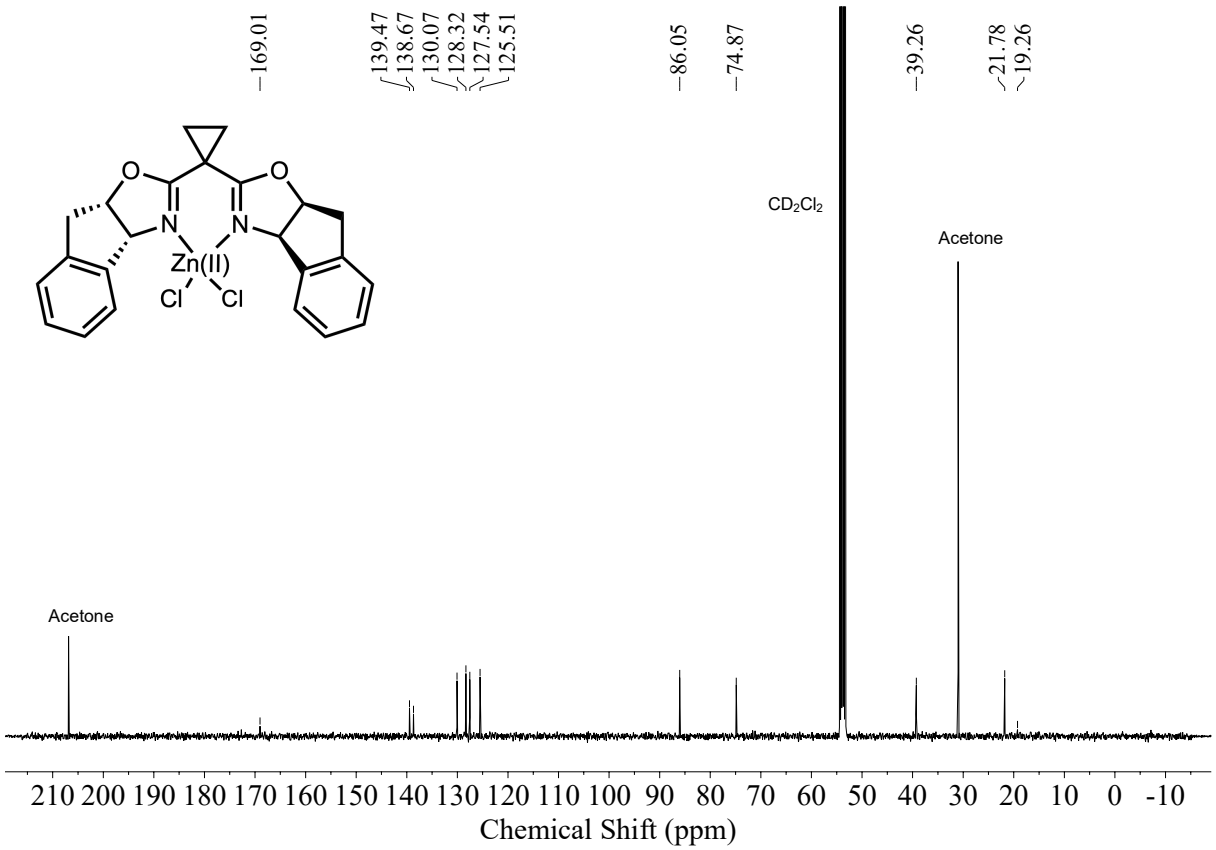

***Figure S2**. ^{13}C NMR of **Zn(IB)Cl$_2$** in d^2-dichloromethane.*

2.6.3 UV-vis-NIR Spectra and Expanded Main Text Dicussion

Briefly, MCD spectroscopy relies on the differential absorption of left- and right-circularly polarized light in the presence of a longitudinal magnetic field. The general intensity of an MCD spectrum can be defined by **Equation 1**:

$$I \propto \left[A_1\left(\frac{-\partial f(E)}{\partial E}\right) + \left(B_0 + \frac{C_0}{kT}\right) f(E)\right] \quad (1)$$

where *A*-terms and *B*-terms are temperature independent, while *C*-terms are temperature dependent. Based on the magnitude of low-symmetry distortions from ideal T_d, consideration of first-order spin-orbit coupling on the Ni^{II} center, and acquisition temperature, the observed MCD intensity is tentatively assigned to *B*-term intensity due to

magnetic field-induced mixing of excited states. A future study utilizing variable-temperature variable-field MCD will be used to define this, along with the nature of the ground state zero-field splittings in these and other Ni^{II} cross-coupling catalysts.

Full Gaussian resolutions obtained from collective fits of the absorption, CD, and MCD spectra of **Ni^{II}(IB)Cl_2** and **Ni^{II}(IB)Br_2** in DCM are given in **Figure 1** and summarized in **Table 1**. Both complexes are pseudo-T_d, a geometry that has been studied extensively for high-spin Ni^{II} complexes using ligands spanning a range of ligand field strengths.[5–7] Chloride and bromide are weak σ donors and π donors, while the bidentate **IB** is a moderate σ donor. Thus, these four-coordinate complexes are expected to follow a weak-field excited state ordering. Band assignments in idealized T_d and C_{2v} symmetry are provided in **Figure 1** and **Table 1**.

By group theory, the $^3T_1$(F) ground state (in T_d) will split due to low symmetry distortions. Descending in symmetry, and depending on the specific distortion angles and bond compression/elongation, the ground state can be $^3A_2$, $^3B_1$, or $^3B_2$ in C_{2v}.[8] Based on multiconfigurational calculations and previous assignments for complexes with similar primary ligand coordination spheres, the low symmetry distorted ground state is tentatively assigned as $^3B_1$ in both complexes. For this assignment, transitions to $^3B_2$ excited states are forbidden by group theory; transitions to $^3A_1$, $^3A_2$, or $^3B_1$ excited states are electric dipole allowed.[5] Based on calculations and assigned $^3B_1$ ground state, the two holes lie in the $d(x^2-y^2)$ and d(xz) 3d orbitals, consistent with previous angular overlap calculations on similar complexes.[9] We assign states for **Ni^{II}(IB)Cl_2** from low to high energy; these assigned states correlate directly with those in **Ni^{II}(IB)Br_2**. Bands 2, 3, and 4 fall in the ~5000 – 11 000 cm^{-1} region (**Figure 1**). Note band 1 is observed at low energy in

vibrational CD (Main Text, **Section 2.2**). Bands 2 and 3 are assigned as the $^3B_1$ and $^3A_1$ components (in C_{2v}), respectively, of the parent $^3T_1(F) \rightarrow {}^3T_2$ (in T_d) excited state. One component from the $^3T_1(F) \rightarrow {}^3T_2$ (i.e., the $^3B_2$) does not seem to be observed, consistent with its electric dipole forbidden nature and proximity to other transitions. Assignment of these transitions can be made with more certainty based on calculations (**Section 8.2**), which suggest both states should yield negative differential CD and MCD intensity. This is the case for band 3. Since $^3B_1 \rightarrow {}^3B_2$ is electric dipole forbidden, the higher oscillator strength observed for band 3 is consistent with calculated values, supporting assignment of this band as the $^3B_1 \rightarrow {}^3A_1$ transition. Band 4, the most intense transition in this lower energy manifold, is assigned to the $^3A_2(F)$ term (in T_d) ($^3B_1(F) \rightarrow {}^3A_2$ in C_{2v}), consistent with previously reported spectra for a large number of high-spin, pseudo-tetrahedral Ni^{II} complexes.[5]

A sharp spin-forbidden ligand field transition is observed at ~12 100 cm^{-1} (band i) and can be assigned to a component of the $^3T_1(F) \rightarrow {}^1E,{}^1T_2$ (in T_d) spin-flip transitions. This region consists of additional intensity (band ii), which is tentatively ascribed to additional overlapping spin-forbidden components that are broadened due to low-symmetry distortions. This assignment is also consistent with the additional structure present in this spectral region in the MCD spectrum (**Figure 1C**).

The higher energy manifold of components (~14 000 – ~22 000 cm^{-1}) is assigned to the next orbital triplet, $^3T_1(F) \rightarrow {}^3T_1(P)$ (in T_d), which is comprised of bands at 14 940 cm^{-1} [band 5 ($^3B_1(F) \rightarrow {}^3B_1(P)$)], 18 210 cm^{-1} [band 6 ($^3B_1(F) \rightarrow {}^3B_2(P)$)], and 20 130 cm^{-1} [band 7 ($^3B_1(F) \rightarrow {}^3A_2(P)$)]. The oscillator strengths for these bands track with electric dipole selection rules predicted by theory (i.e., bands 7, 6 > band 5).

The similarity in the signs of vibrational CD (*vide infra*), CD, and MCD signals between **Ni^{II}(IB)Cl$_2$** and **Ni^{II}(IB)Br$_2$** lead us to conclude that they exhibit the same state orderings for observed spin-allowed ligand field transitions. All assignments are also self-consistent based on differential intensity in CD and MCD. For example, $^3B_1 \rightarrow {}^3A_2$ transitions all display positive CD intensity and negative MCD intensity. For **Ni^{II}(IB)Cl$_2$**, additional bands are present at 12 400 cm^{-1} (band ii, UV-vis-NIR/CD), 15 890 cm^{-1} (band iii, UV-vis-NIR/CD/MCD), 19 050 cm^{-1} (band iv, CD), and 23 740 cm^{-1} (band v, UV-vis-NIR/CD/MCD). As partially described above, these are tentatively ascribed to the geometric and spin-orbit splitting of spin-forbidden transitions that broaden components (12 400 and 19 050 cm^{-1}) and small amounts of trimer formation (23 740 cm^{-1}) (Main text, **Section 2.4**). Note the band at 19 050 cm^{-1} in CD is required to adequately fit the CD data. However, the UV-vis-NIR and MCD data are fit well without inclusion of the 19 050 cm^{-1} band. Therefore, this band has not been included in the UV-vis-NIR and MCD fits.

The ligand field transitions of **Ni^{II}(IB)Cl$_2$** relative to **Ni^{II}(IB)Br$_2$** are blueshifted by ~120 – 710 cm^{-1} in DCM (overlaps in **Figure S17**), consistent with stronger donation from chloride relative to bromide. 10*Dq* in idealized T_d is given by the gap between the $^3A_2$(F) and the center of gravity of the $^3T_2$(F) manifold.[7] Using band 4 and the average of bands 2 and 3 for these energies, respectively, provides values of 2830 cm^{-1} and 3085 cm^{-1} for **Ni^{II}(IB)Cl$_2$** and **Ni^{II}(IB)Br$_2$**. While these estimates are consistent with previous 10*Dq* values of < 4000 cm^{-1} for various pseudo-T_d Ni(II) complexes with weak σ donor ligands,[10] this approach does not provide a meaningful result for the **Ni^{II}(IB)X$_2$** comparison here. For highly distorted complexes, greater configuration interaction between states due to lower symmetry can lead to significant splitting of orbital triplets, which can make it difficult to

extract accurate values of 10*Dq*. To estimate the relative ligand field strength, we average the assigned spin-allowed transitions (bands 1 – 7). Doing so provides relative ligand field strengths of ~12 365 cm^{-1} and ~11 975 cm^{-1} (Δ = ~390 cm^{-1}) for **Ni^{II}(IB)Cl_2** and **Ni^{II}(IB)Br_2**, respectively, in better accord with the greater ligand field strength in the chloride complex relative to bromide. For one of the first times in this field, we demonstrate the direct connection of ligand field transitions exciting into the Ni^{II}-based redox active molecular orbitals (RAMOs), which allows for correlations between transition energies and redox potentials to be made (Main text, **Section 3.3**).

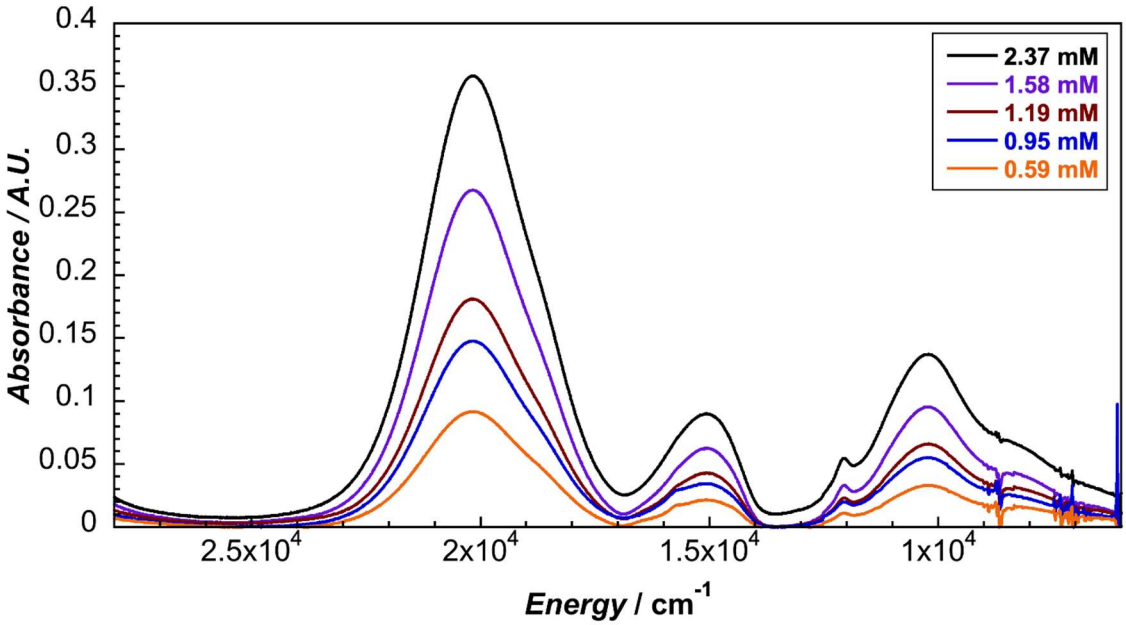

***Figure S3**. UV-vis-NIR spectra of **Ni^{II}(IB)Cl_2** in DCM.*

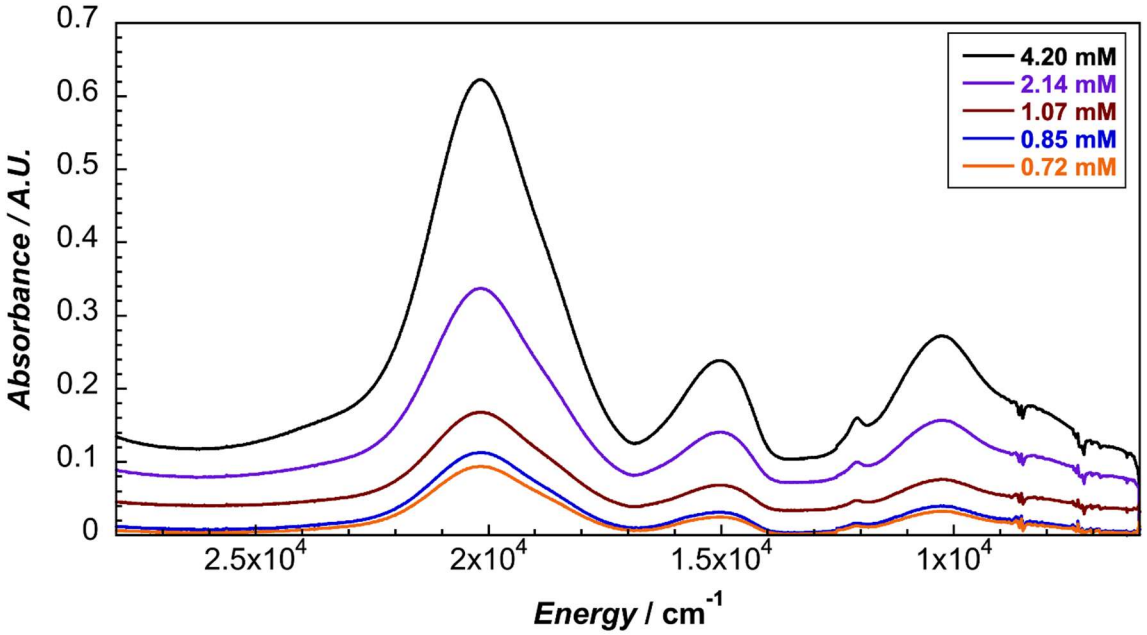

***Figure S4**. UV-vis-NIR spectra of **$Ni^{II}(IB)Cl_2$** in MeCN.*

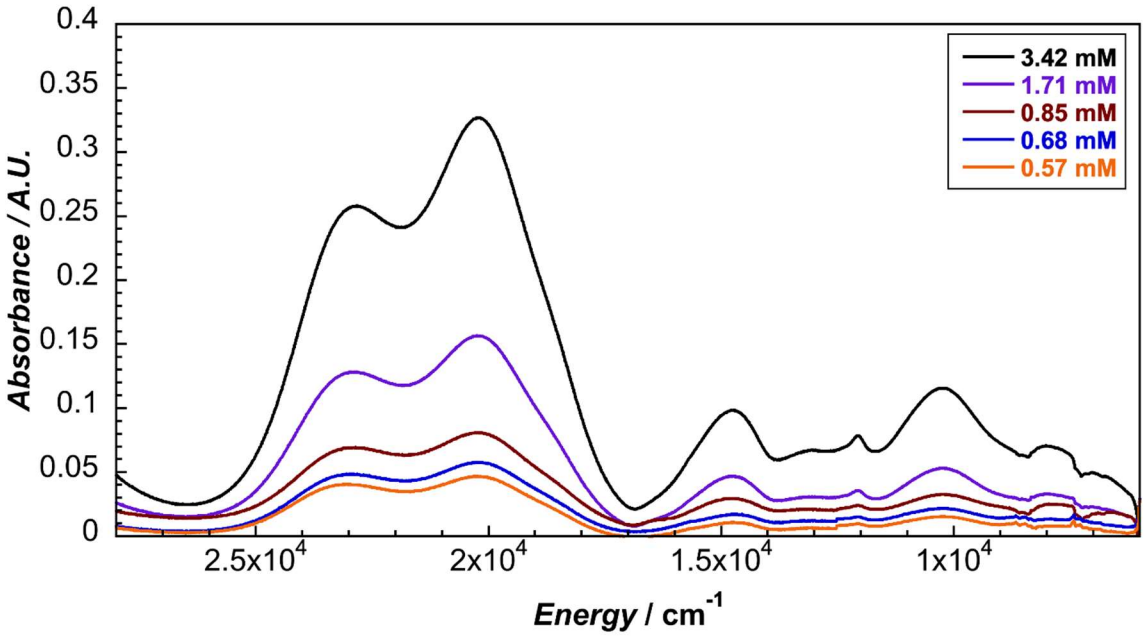

***Figure S5**. UV-vis-NIR spectra of NiII(IB)Cl2 in DMA.*

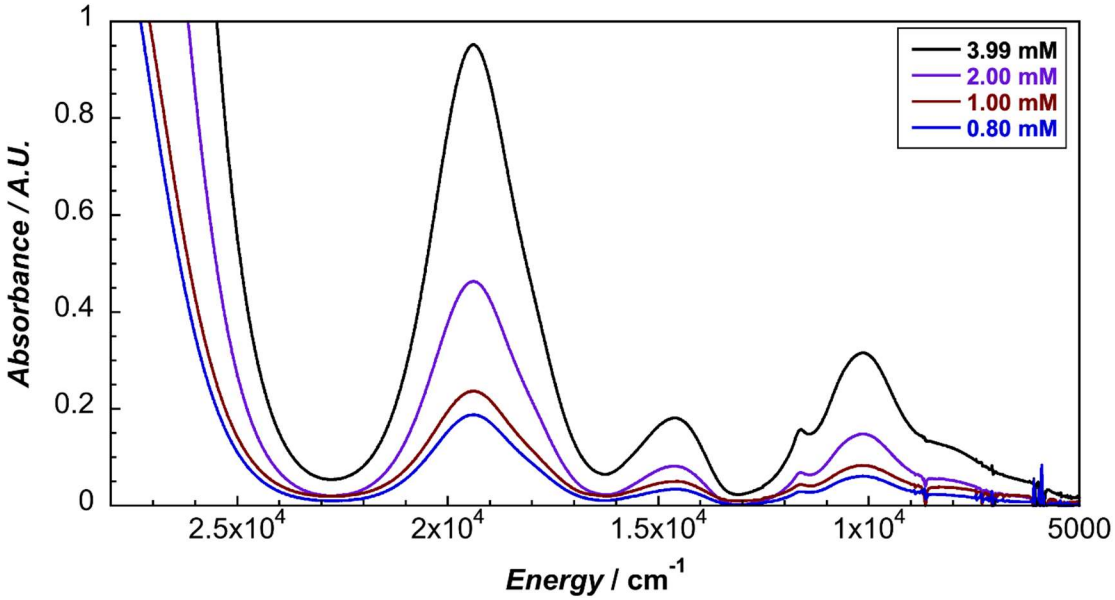

***Figure S6**. UV-vis-NIR spectra of **$Ni^{II}(IB)Br_2$** in DCM.*

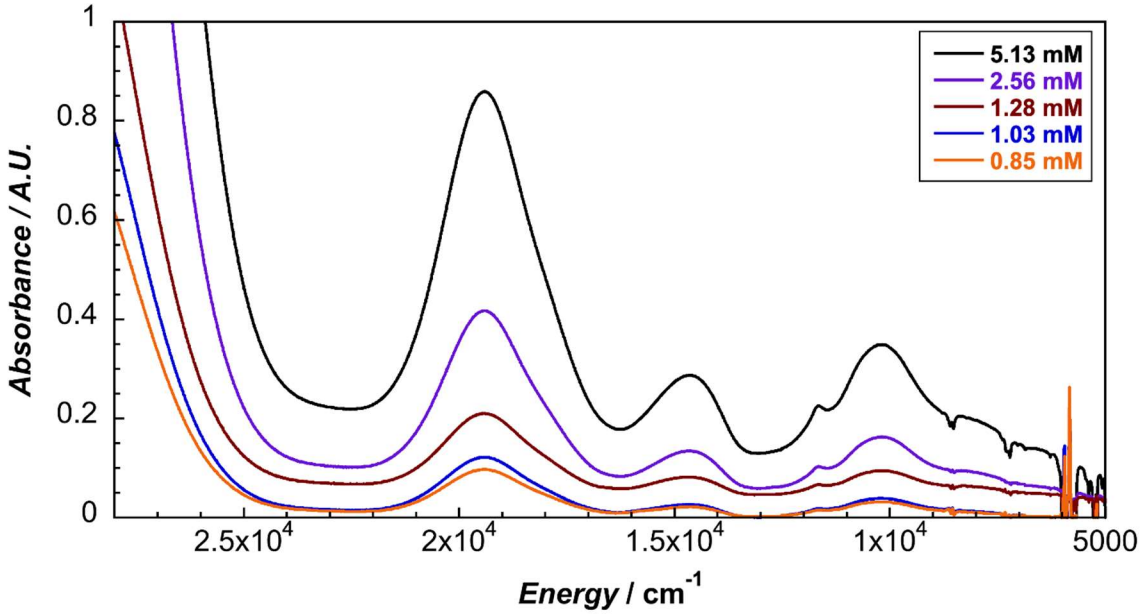

***Figure S7**. UV-vis-NIR spectra of **$Ni^{II}(IB)Br_2$** in MeCN.*

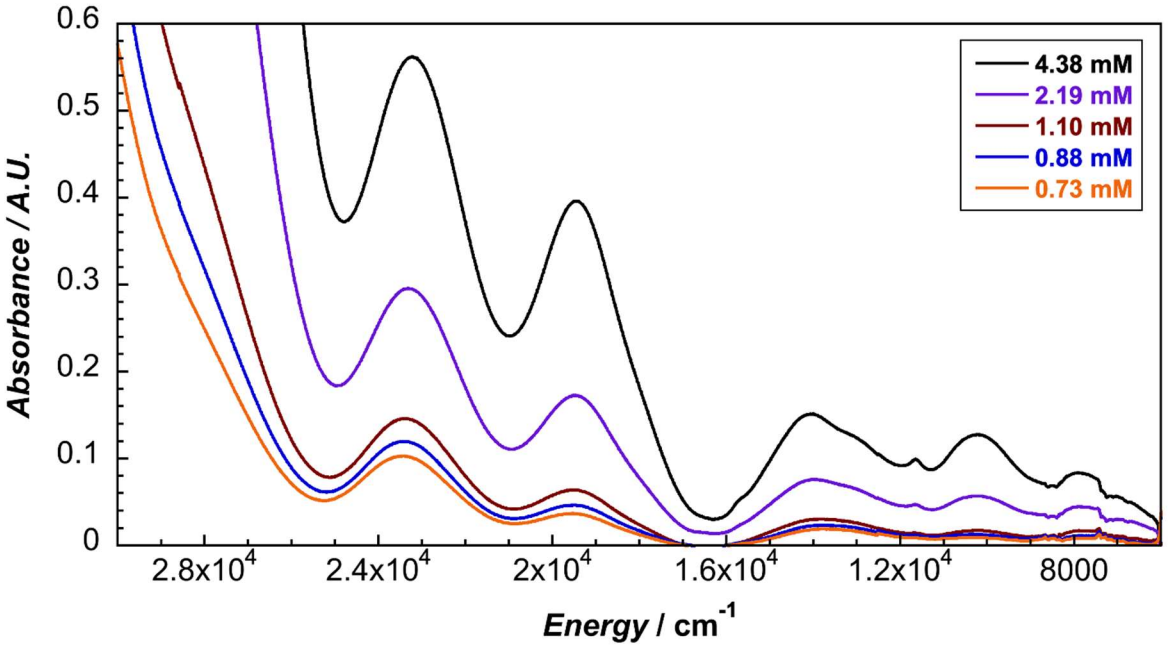

***Figure S8**. UV-vis-NIR spectra of **$Ni^{II}(IB)Br_2$** in DMA.*

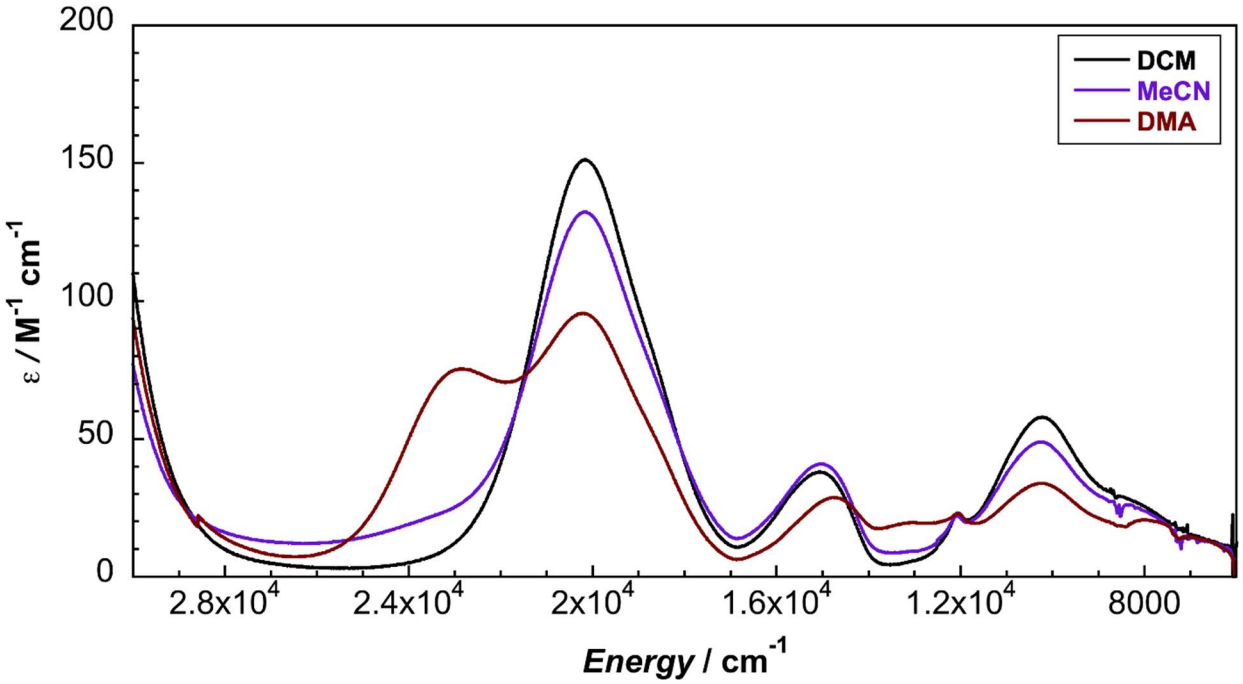

***Figure S9**. Solvent comparison of UV-vis-NIR spectra of **$Ni^{II}(IB)Cl_2$**.*

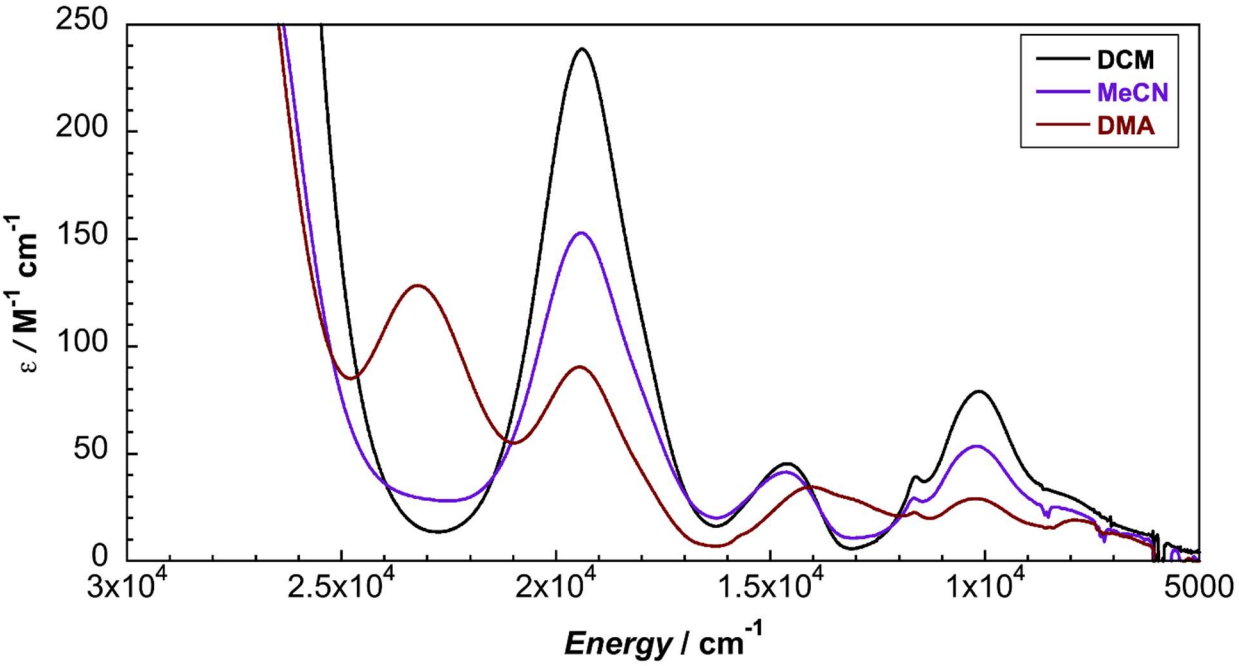

***Figure S10**. Solvent comparison of UV-vis-NIR spectra of **Ni^{II}(IB)Br$_2$**.*

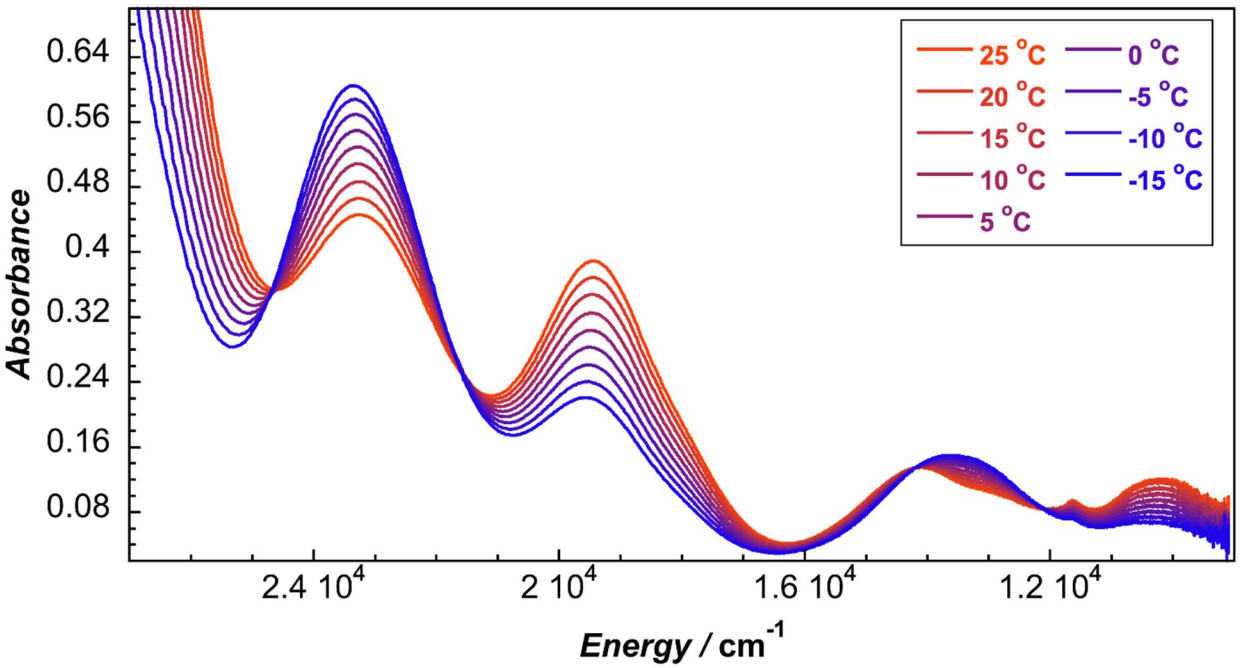

***Figure S11**. Variable-temperature UV-vis-NIR spectra of 3.5 mM **Ni^{II}(IB)Br$_2$** in DMA.*

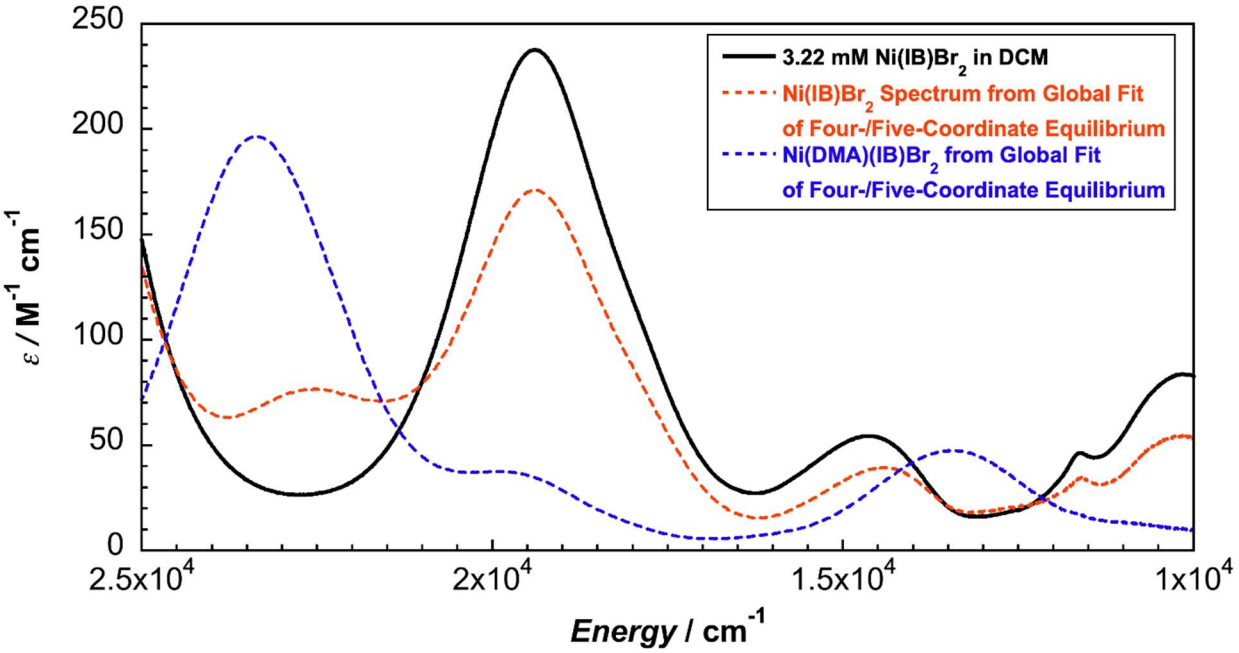

***Figure S12**. Global fitting and deconvolution into four- and five-coordinate species of the UV-vis-NIR spectra of **Ni^{II}(IB)Br$_2$** in DMA.*

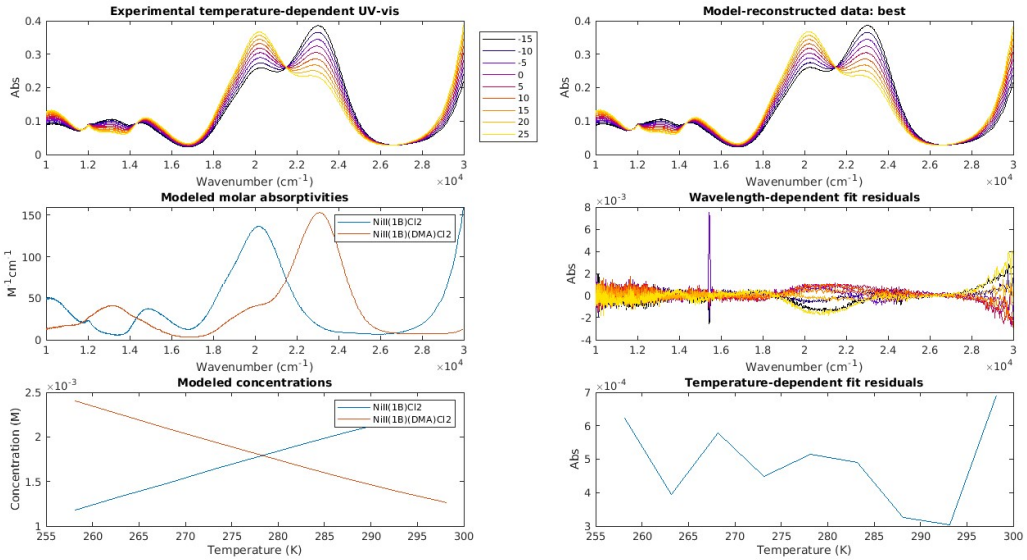

***Figure S13**. Global fitting and deconvolution into four- and five-coordinate species of the UV-vis-NIR spectra of 3.6 mM **Ni^{II}(IB)Cl$_2$** in DMA.*

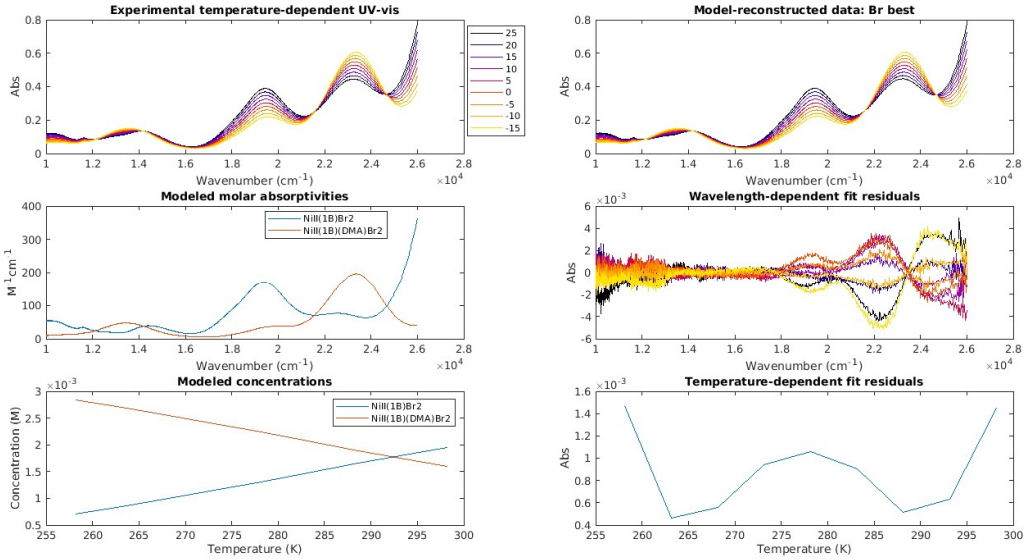

***Figure S14**. Global fitting and deconvolution into four- and five-coordinate species of the UV-vis-NIR spectra of 3.5 mM **$Ni^{II}(IB)Br_2$** in DMA.*

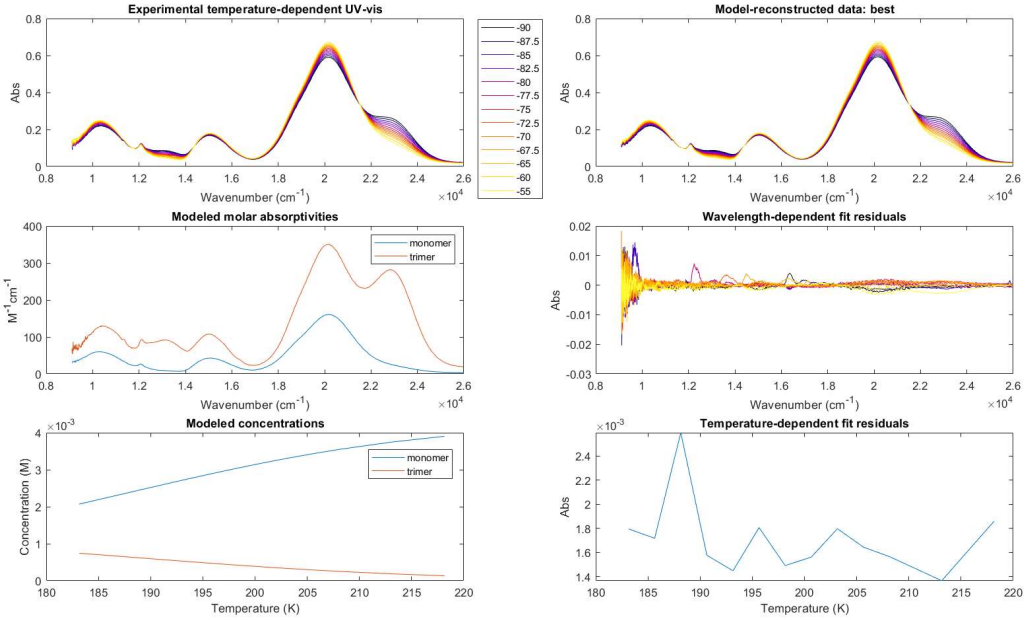

***Figure S15**. Global fitting and deconvolution into monomer and trimer species of the UV-vis-NIR spectra of 4.3 mM **$Ni^{II}(IB)Cl_2$** in DCM.*

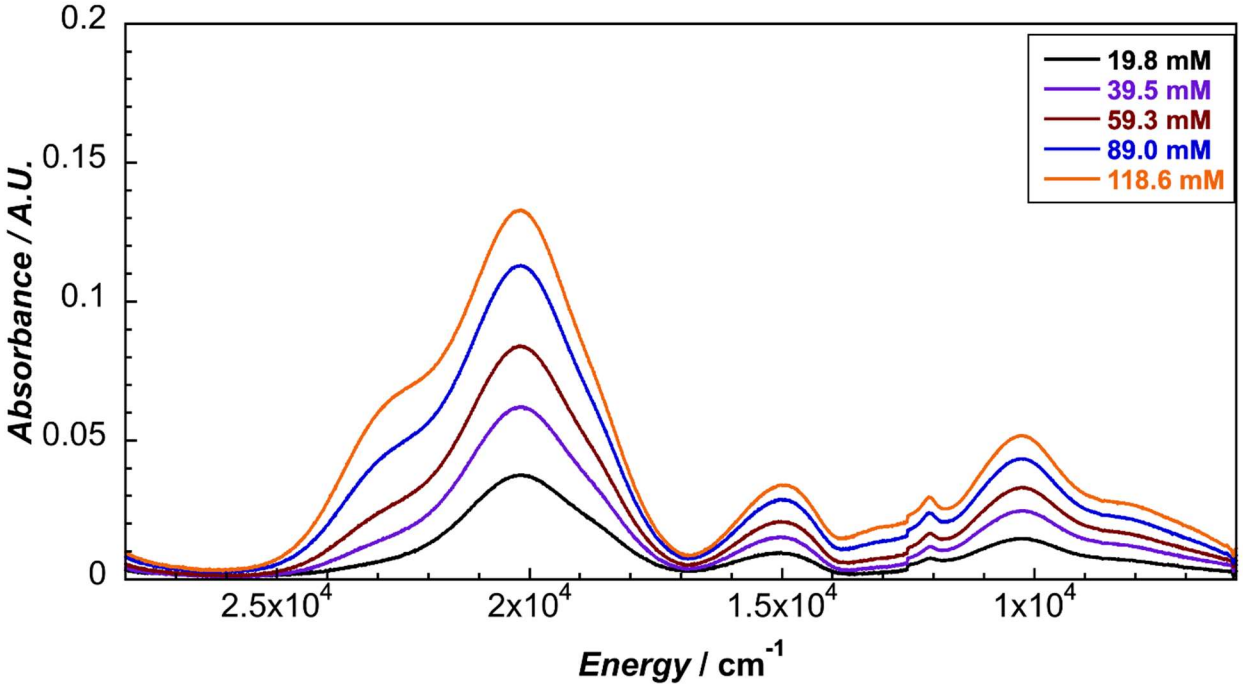

***Figure S16**. Variable-concentration UV-vis-NIR spectra of **$Ni^{II}(IB)Cl_2$** in d^2-dichloromethane in a 0.1 mM calcium fluoride optical cell.*

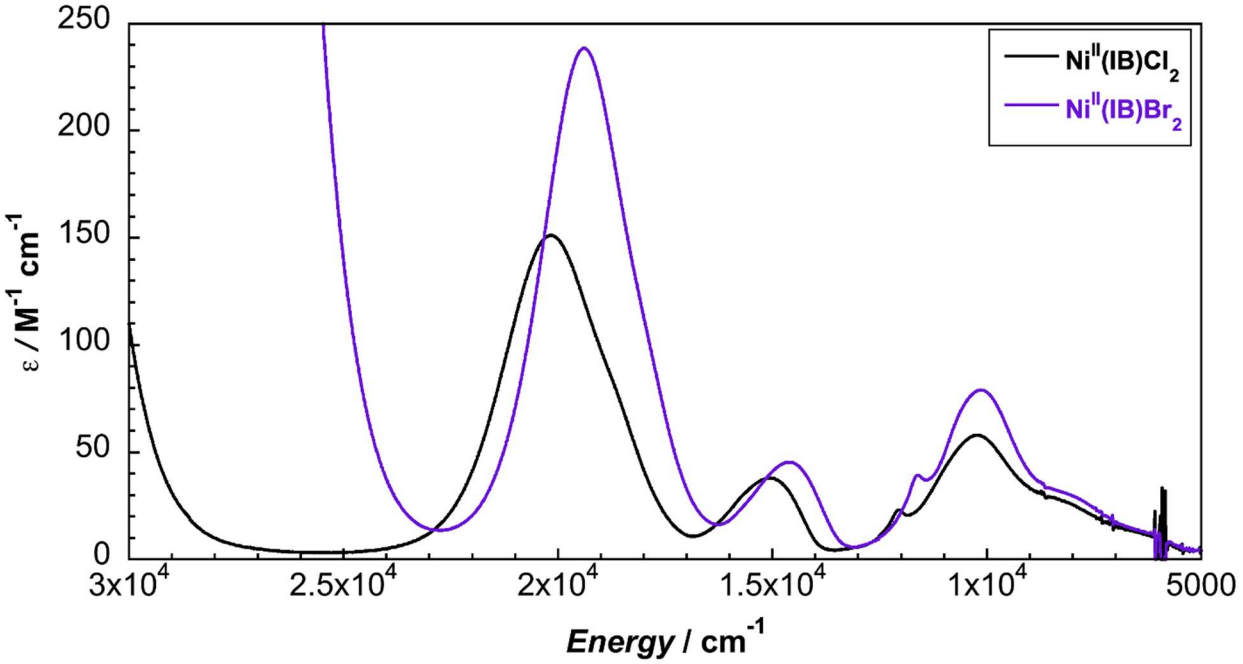

***Figure S17**. Comparison of $Ni^{II}(IB)Cl_2$ and $Ni^{II}(IB)Br_2$ in DCM.*

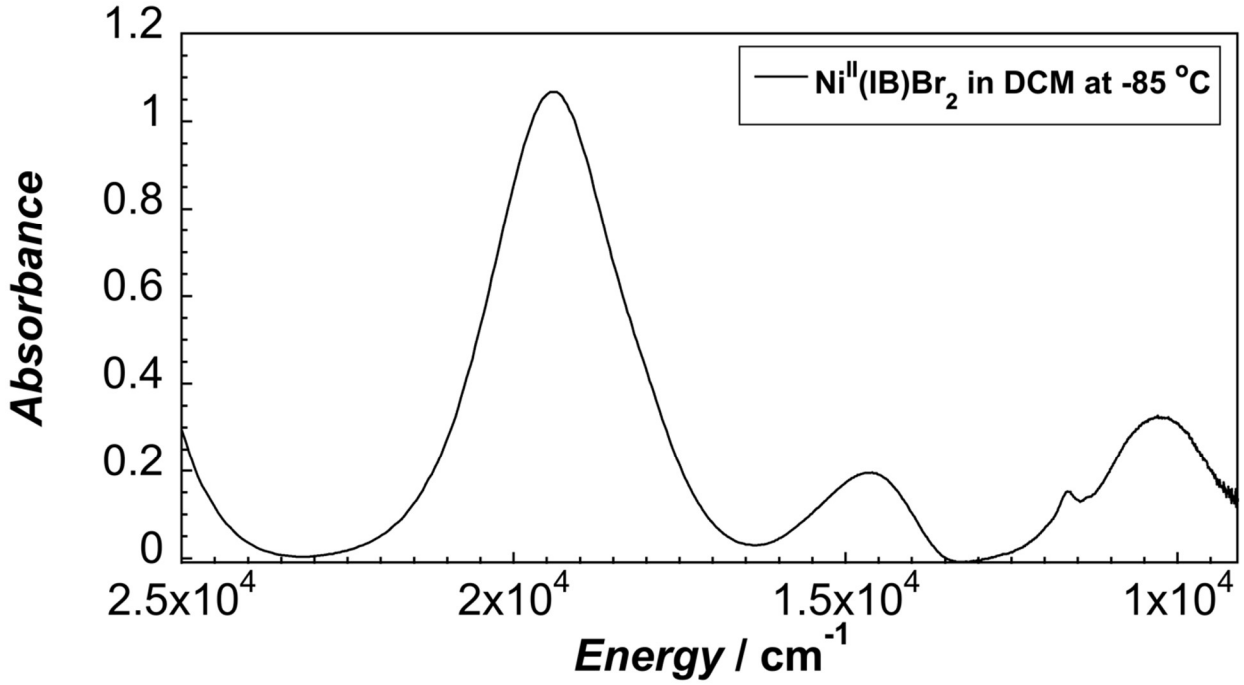

***Figure S18**. UV-vis-NIR spectra of $Ni^{II}(IB)Br_2$ at −85 °C in DCM solution.*

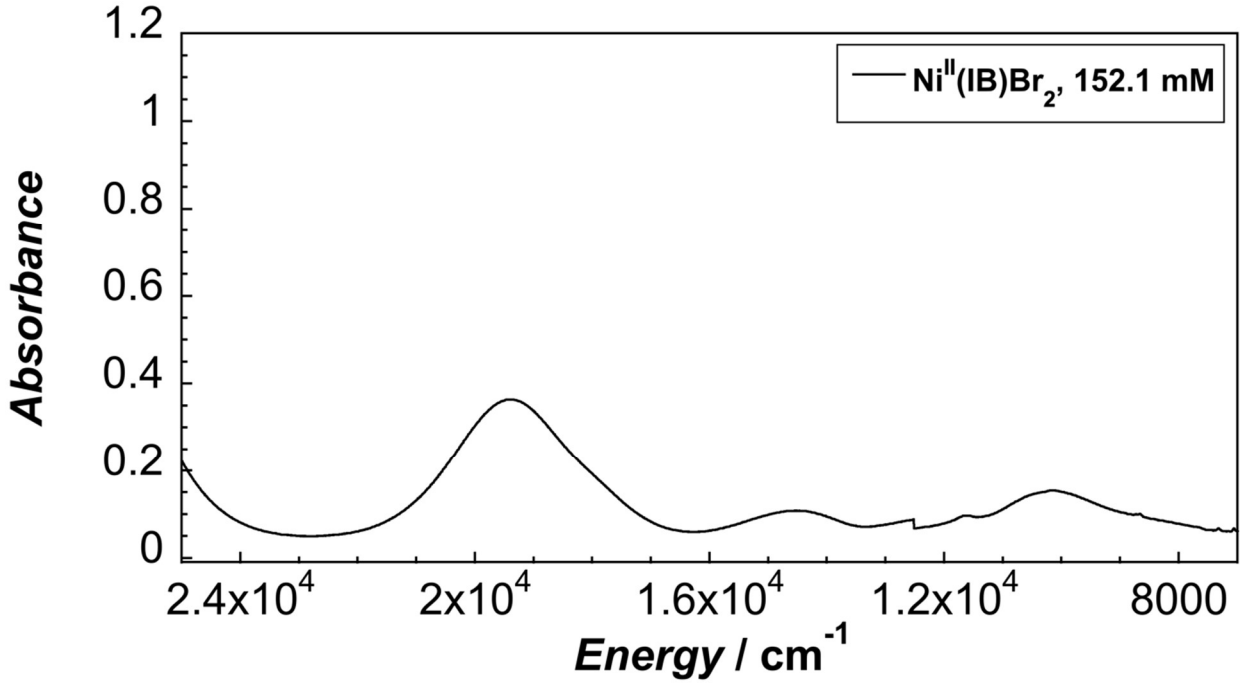

***Figure S19**. UV-vis-NIR spectra of 152.1 mM $Ni^{II}(IB)Br_2$ in DCM solution.*

2.6.4 Circular Dichroism and Magnetic Circular Dichroism Spectra

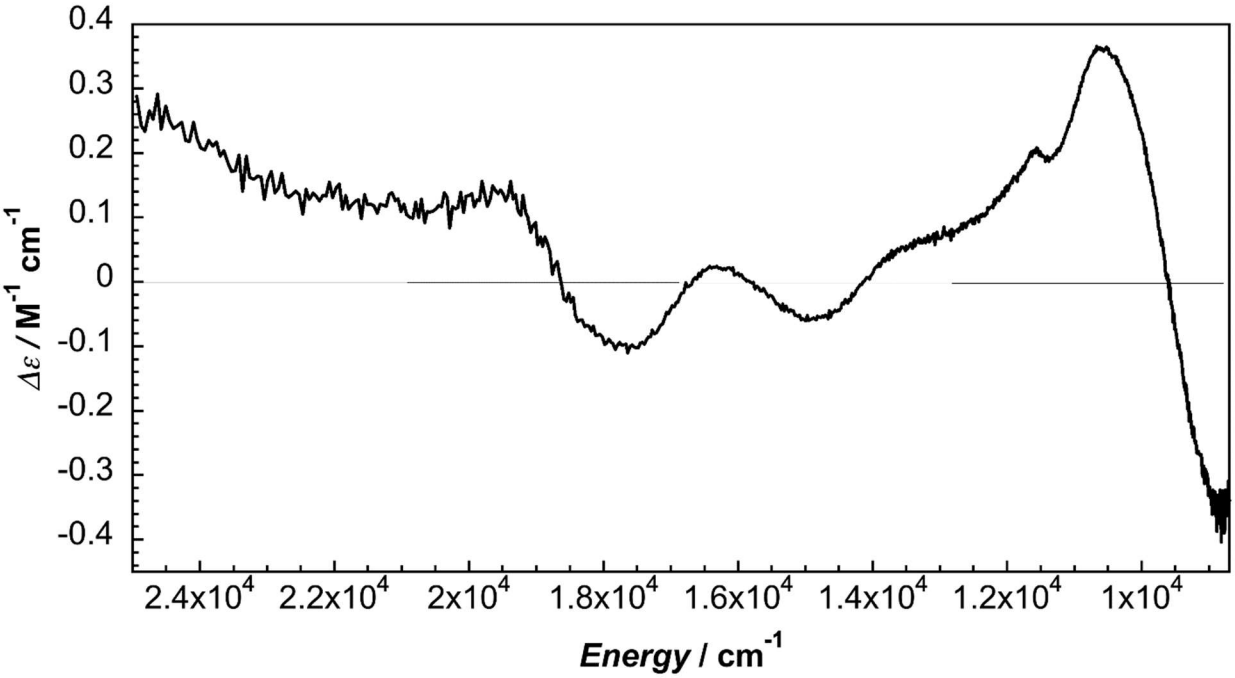

***Figure S20**. Circular dichroism of $Ni^{II}(IB)Br_2$ in DCM at 294 K.*

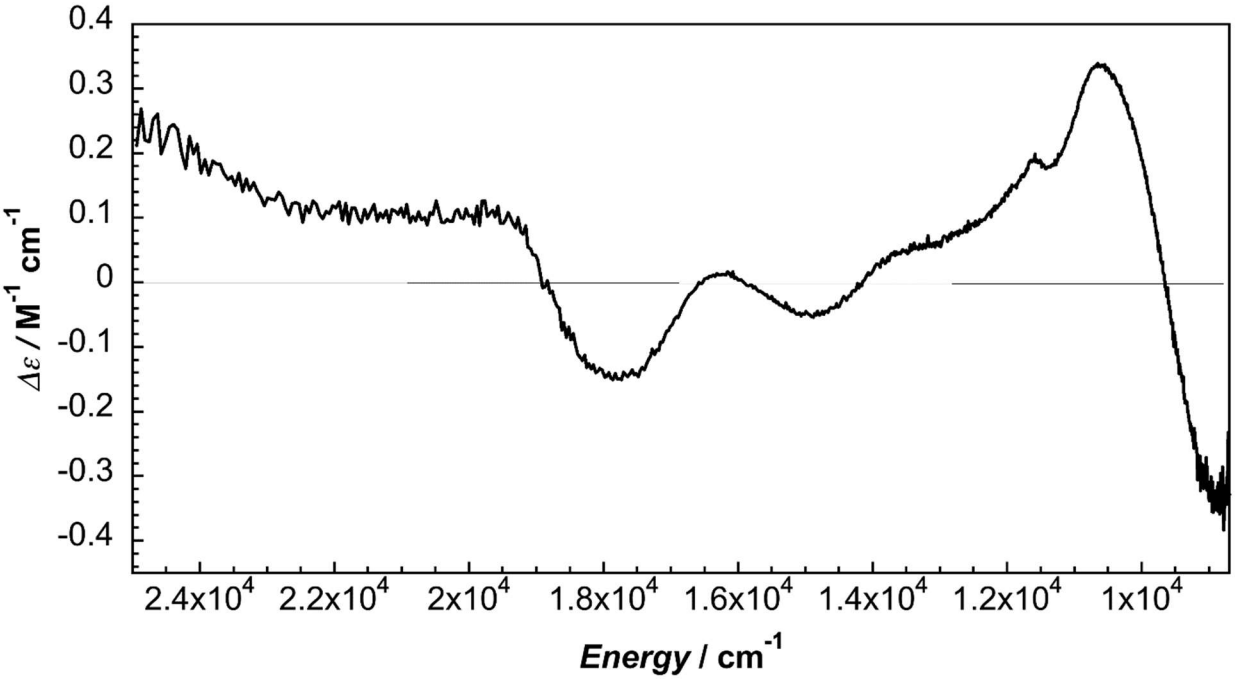

***Figure S21**. Circular dichroism of **$Ni^{II}(IB)Br_2$** in 0.1 M $TBAPF_6$ in DCM solution at 294 K.*

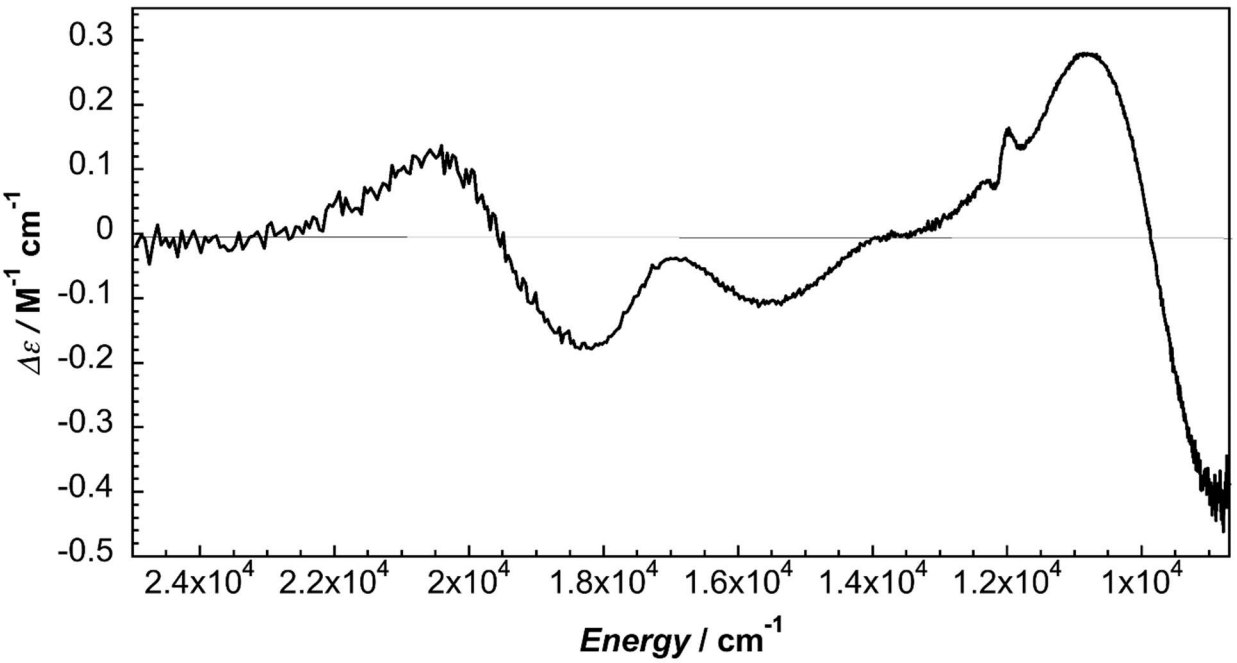

***Figure S22**. Circular dichroism of $Ni^{II}(IB)Cl_2$ in DCM at 294 K.*

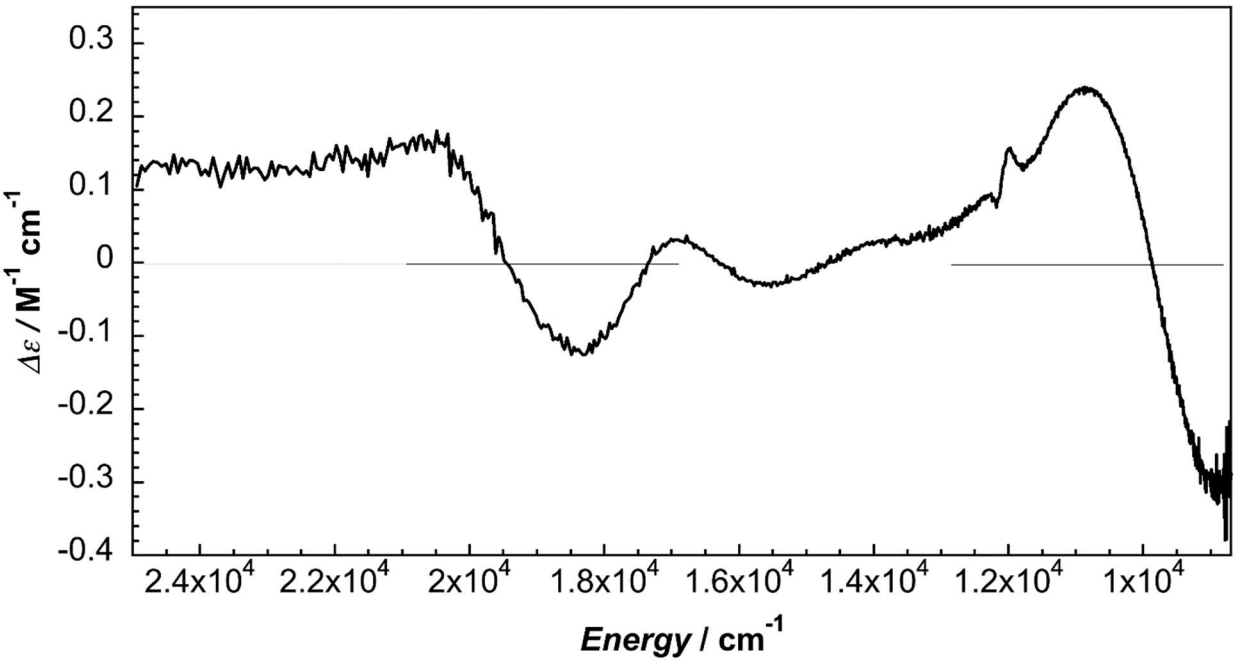

***Figure S23**. Circular dichroism of **$Ni^{II}(IB)Cl_2$** in 0.1 M $TBAPF_6$ in DCM solution at 294 K.*

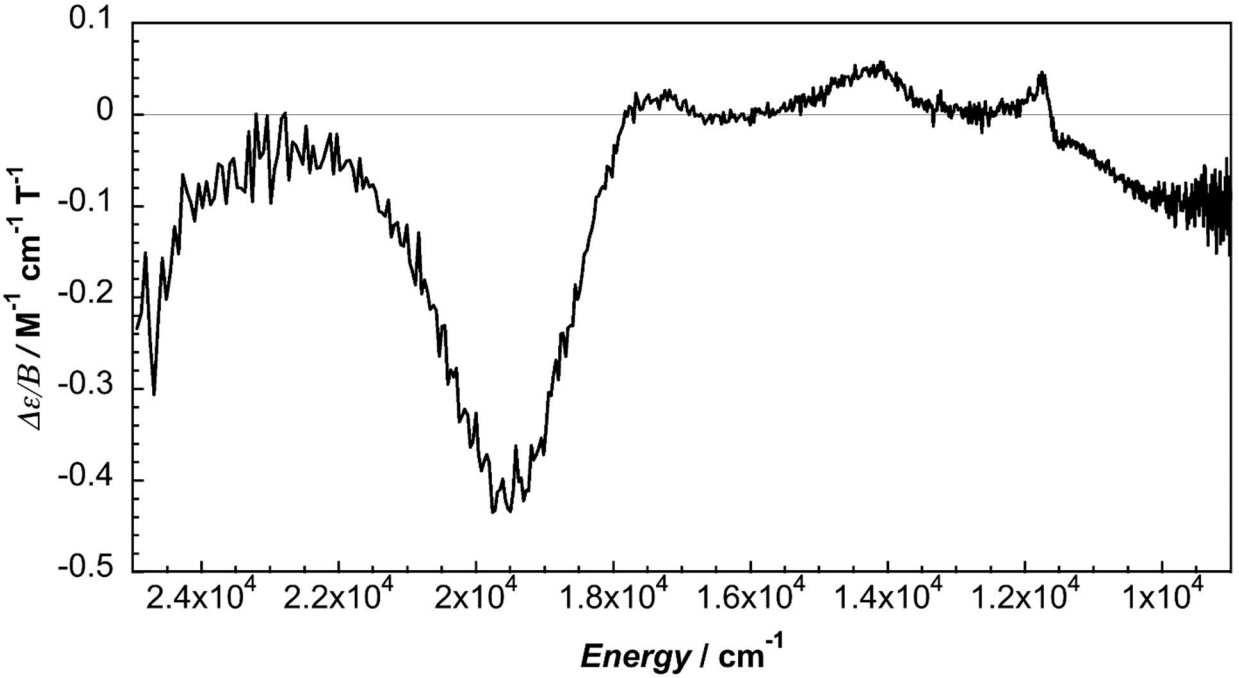

***Figure S24**. Magnetic circular dichroism of **Ni^{II}(IB)Br_2** in DCM at 294 K.*

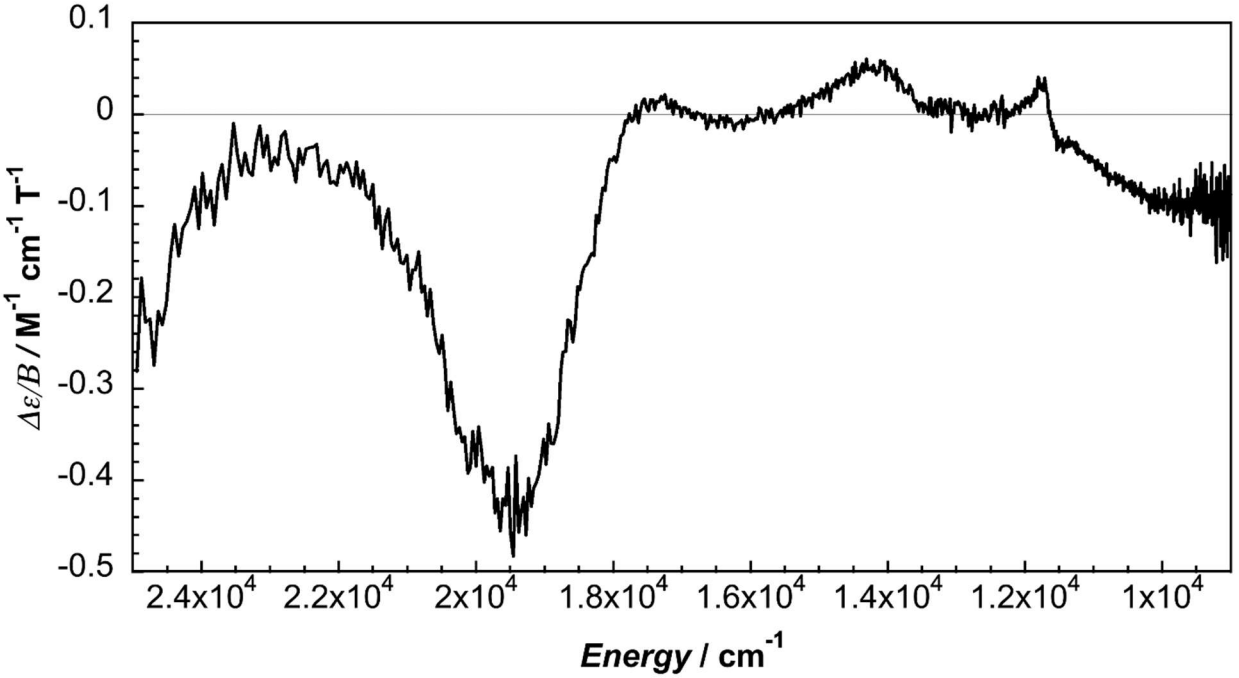

***Figure S25**. Magnetic circular dichroism of NiII(IB)Br2 in 0.1 M TBAPF6 in DCM solution at 294 K.*

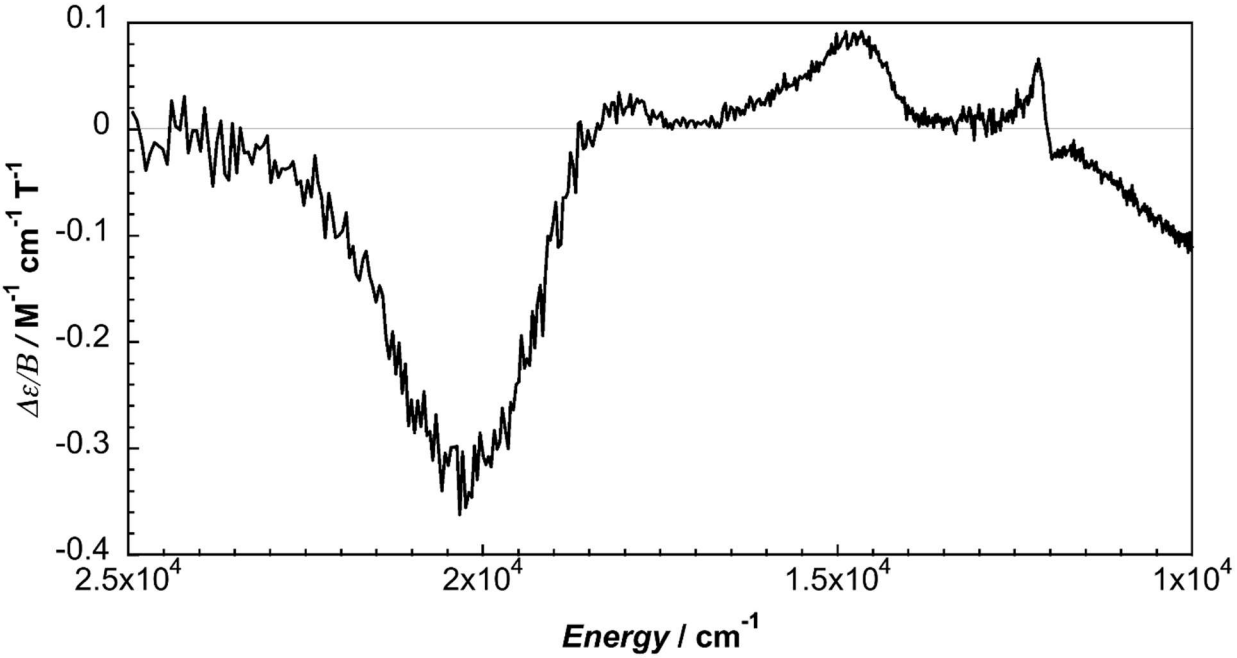

***Figure S26**. Magnetic circular dichroism of $Ni^{II}(IB)Cl_2$ in DCM at 294 K.*

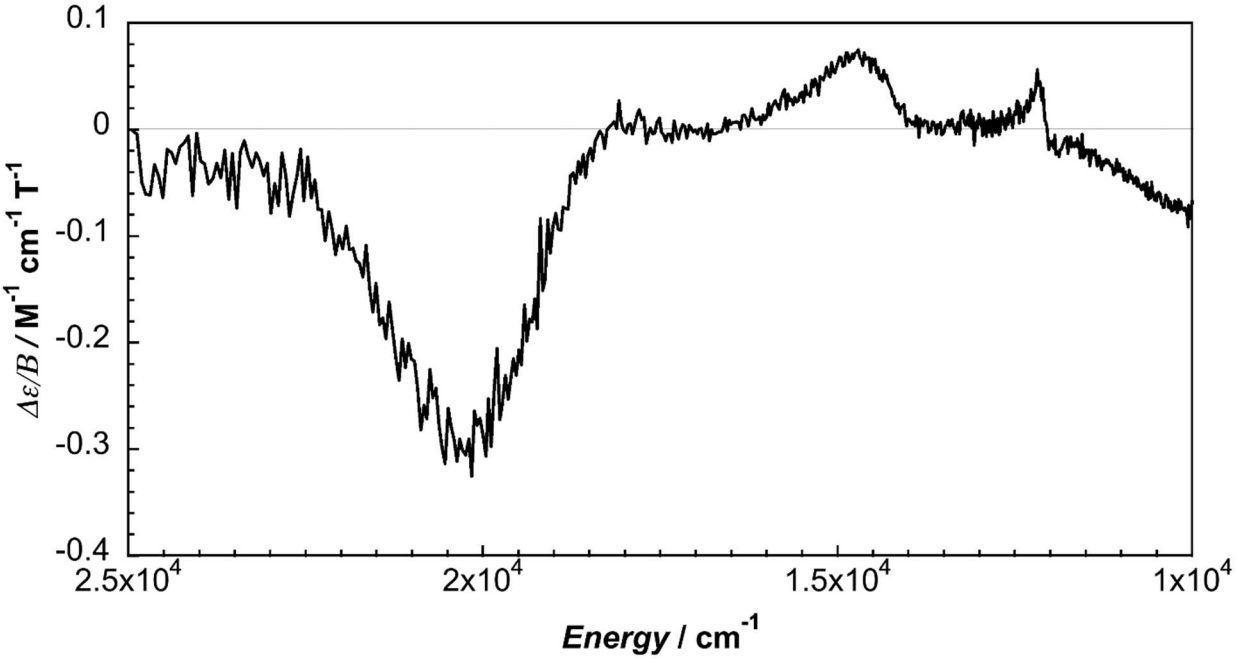

***Figure S27**. Magnetic circular dichroism of **$Ni^{II}(IB)Cl_2$** in 0.1 M $TBAPF_6$ in DCM solution at 294 K.*

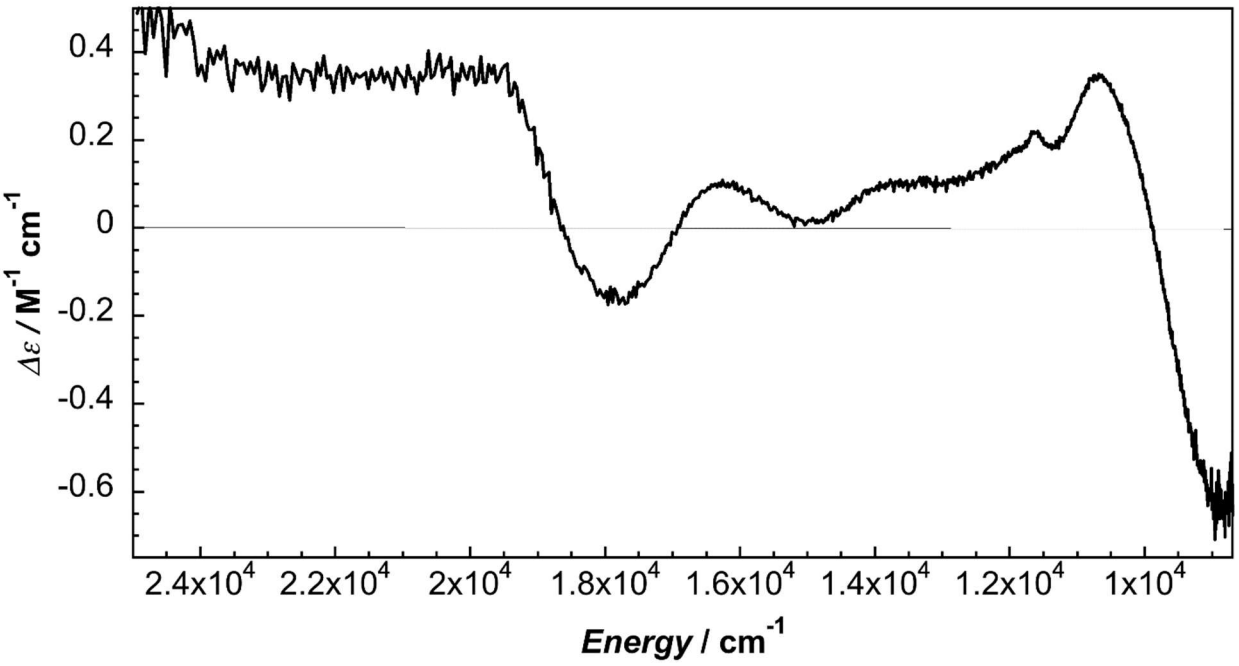

***Figure S28**. Circular dichroism of **Ni^{II}(IB)Br$_2$** in MeCN at 294 K.*

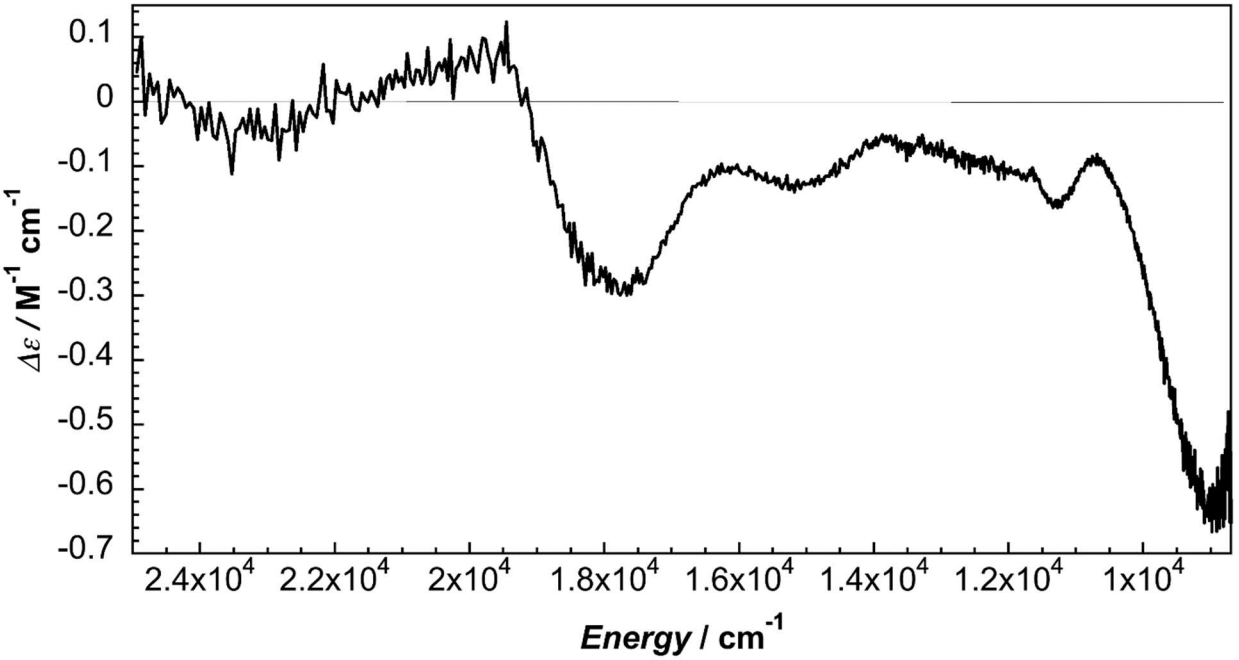

***Figure S29**. Circular dichroism of **Ni^{II}(IB)Br$_2$** in 0.1 M TBAPF$_6$ in MeCN at 294 K.*

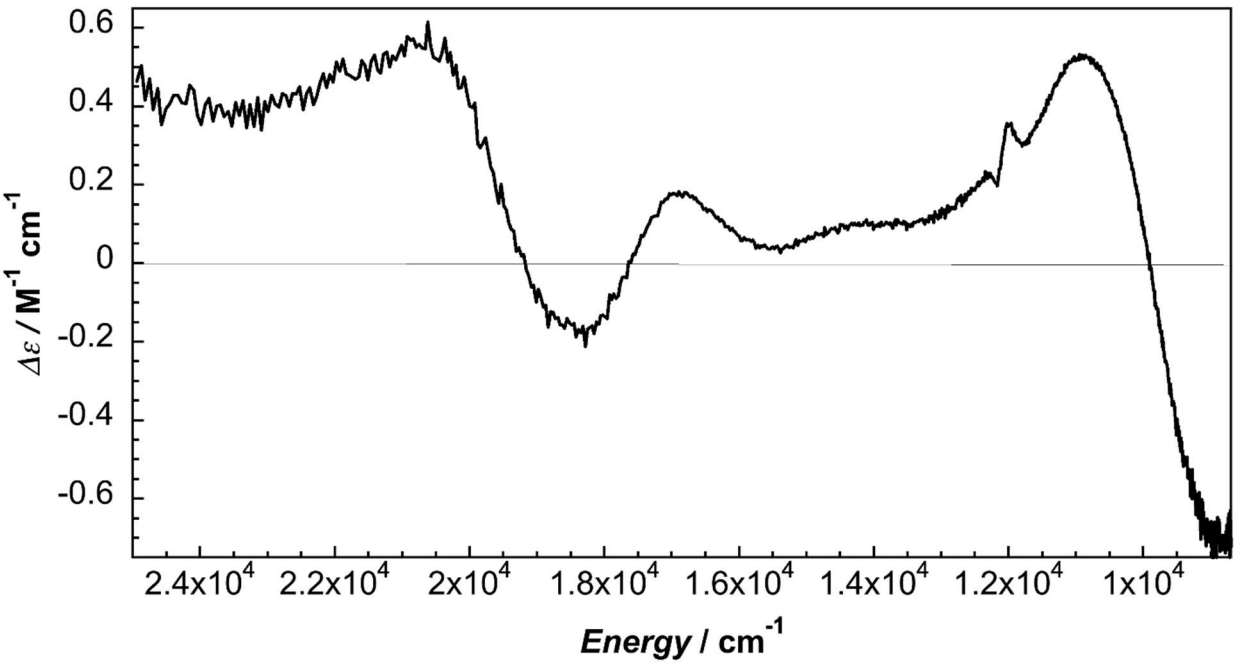

***Figure S30**. Circular dichroism of **$Ni^{II}(IB)Cl_2$** in MeCN at 294 K.*

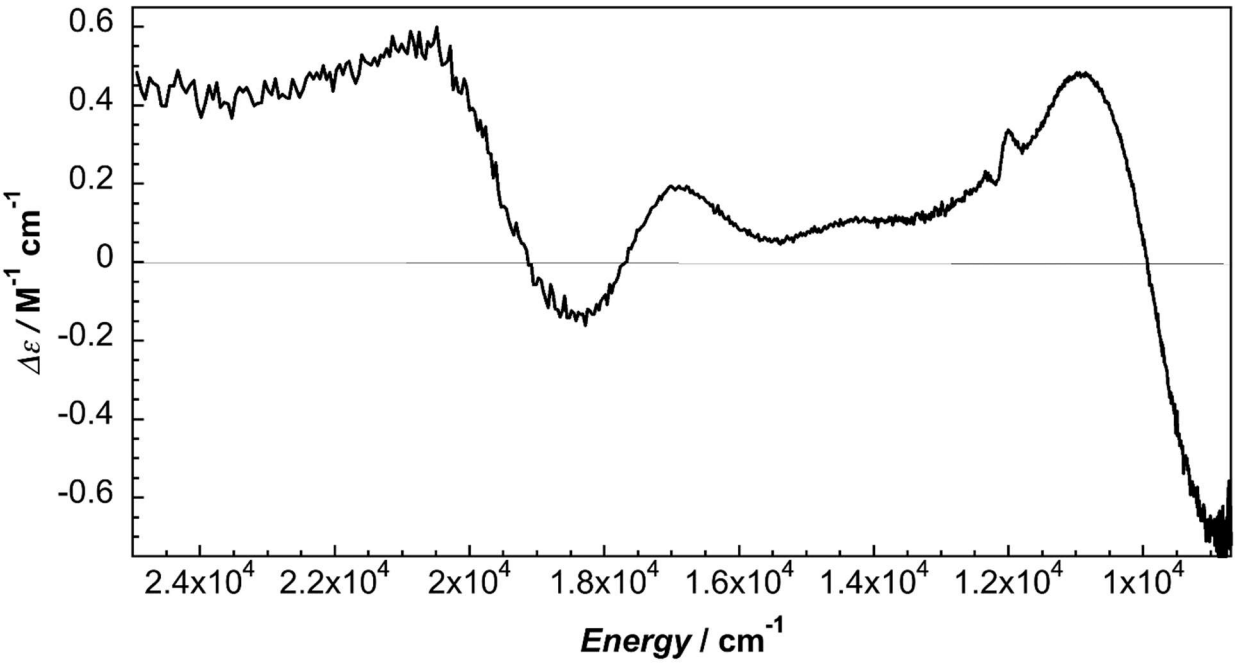

***Figure S31.** Circular dichroism of $Ni^{II}(IB)Cl_2$ in 0.1 M $TBAPF_6$ in MeCN solution at 294 K.*

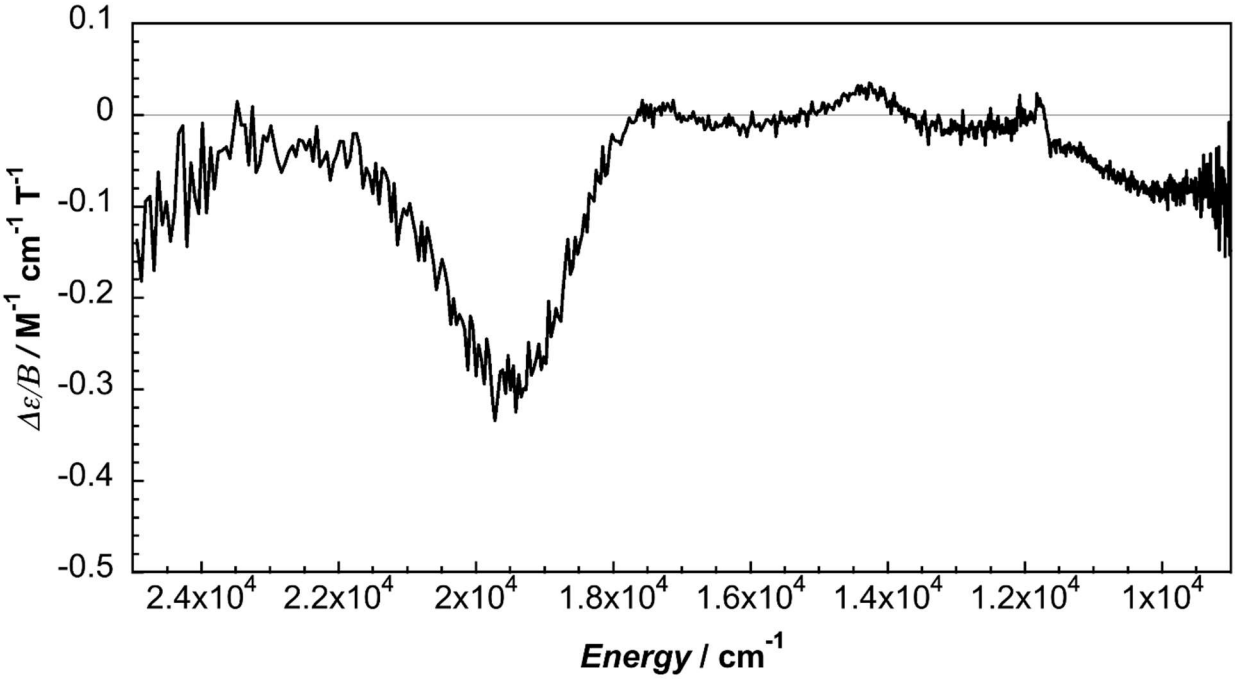

***Figure S32**. Magnetic circular dichroism of $Ni^{II}(IB)Br_2$ in MeCN.*

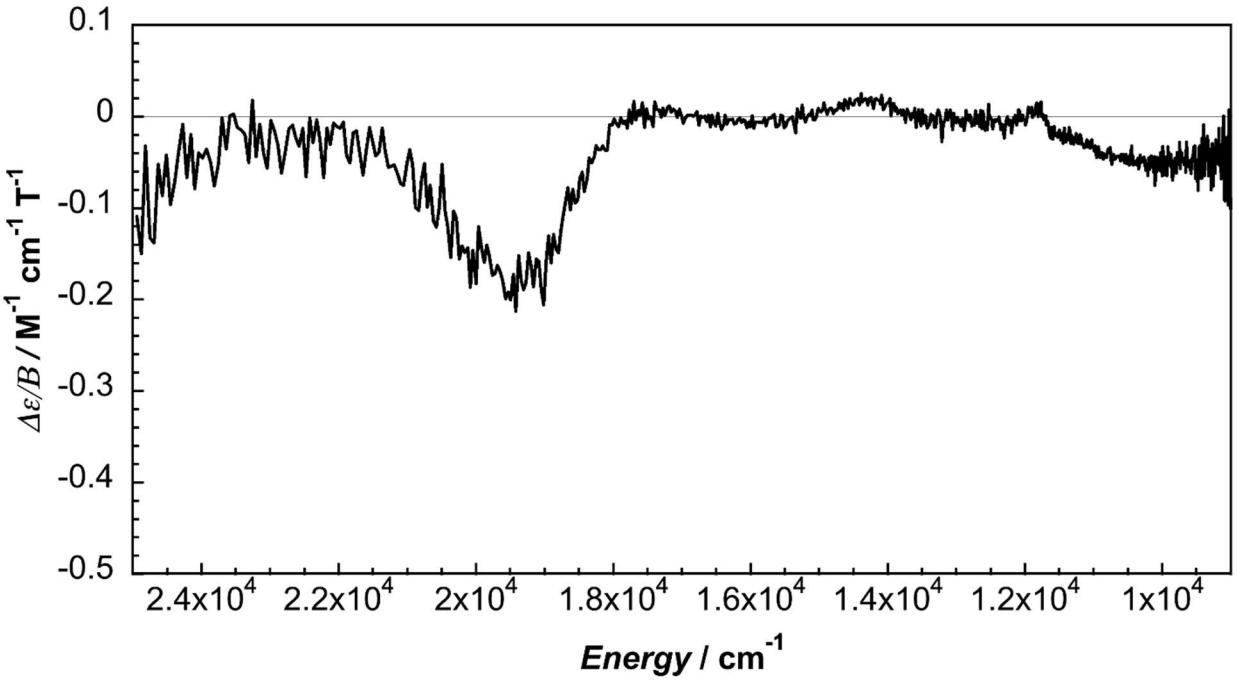

***Figure S33**. Magnetic circular dichroism of $\mathbf{Ni^{II}(IB)Br_2}$ in 0.1 M $TBAPF_6$ in MeCN solution at 294 K.*

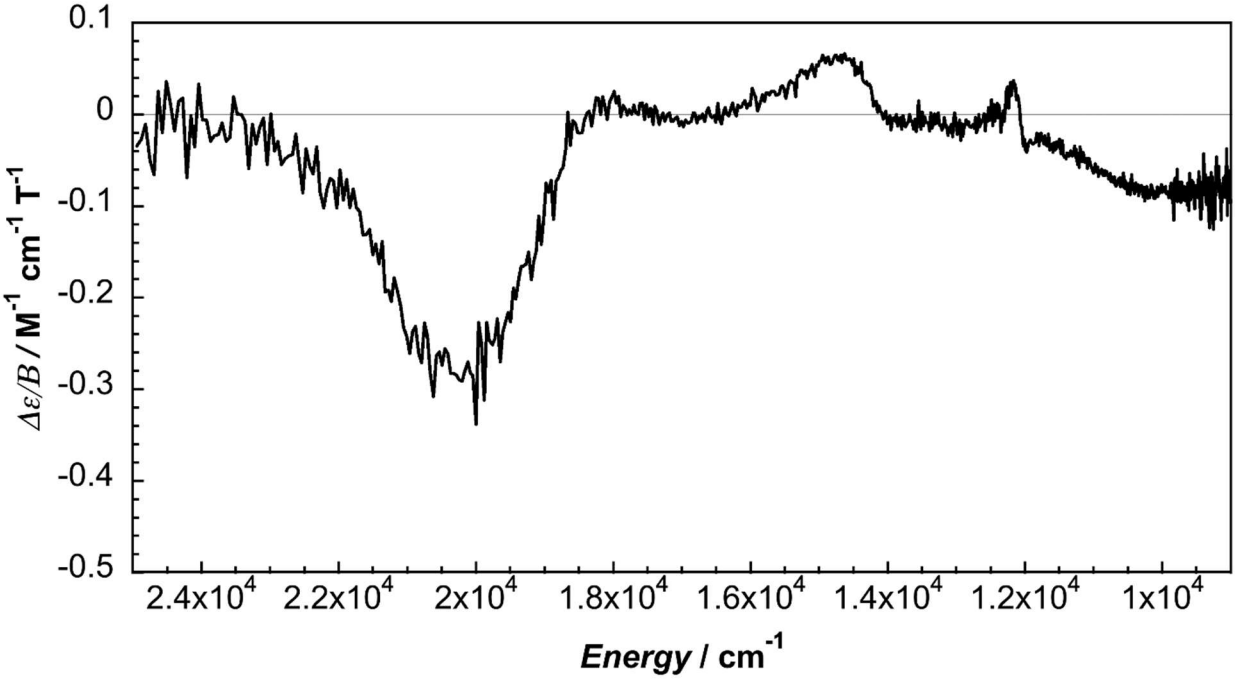

***Figure S34**. Magnetic circular dichroism of **Ni^{II}(IB)Cl$_2$** in MeCN.*

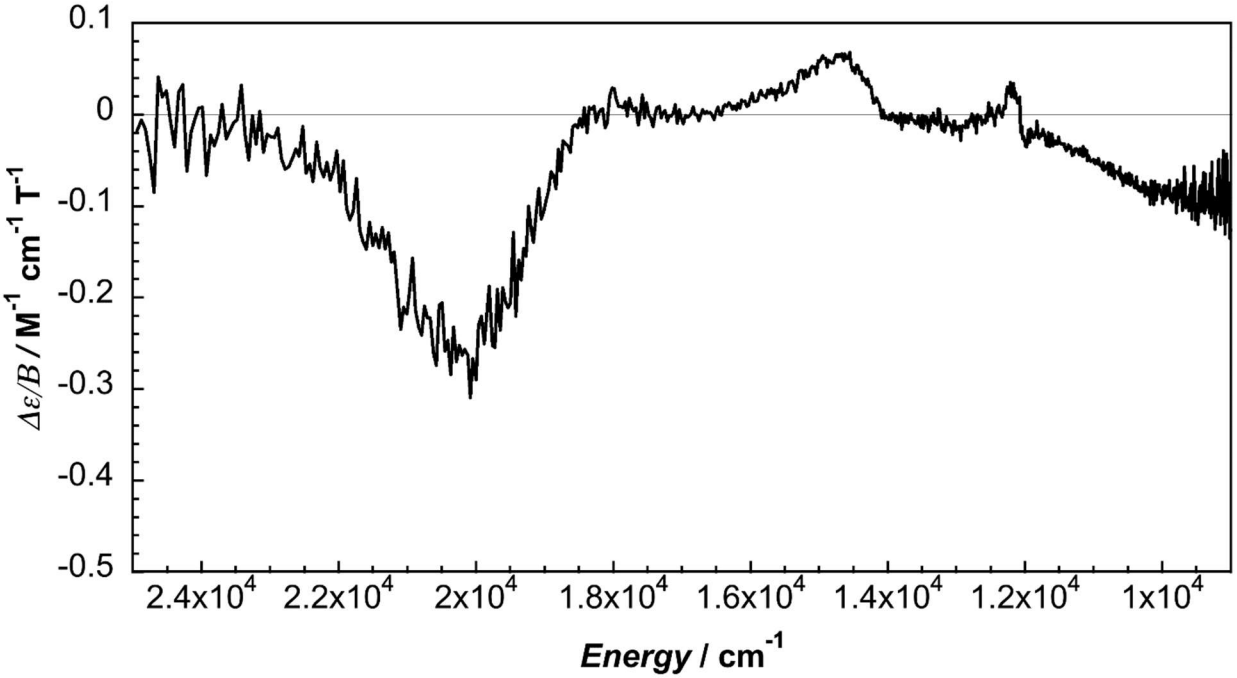

***Figure S35**. Magnetic circular dichroism of **Ni^{II}(IB)Cl$_2$** in 0.1 M $TBAPF_6$ in MeCN solution at 294 K.*

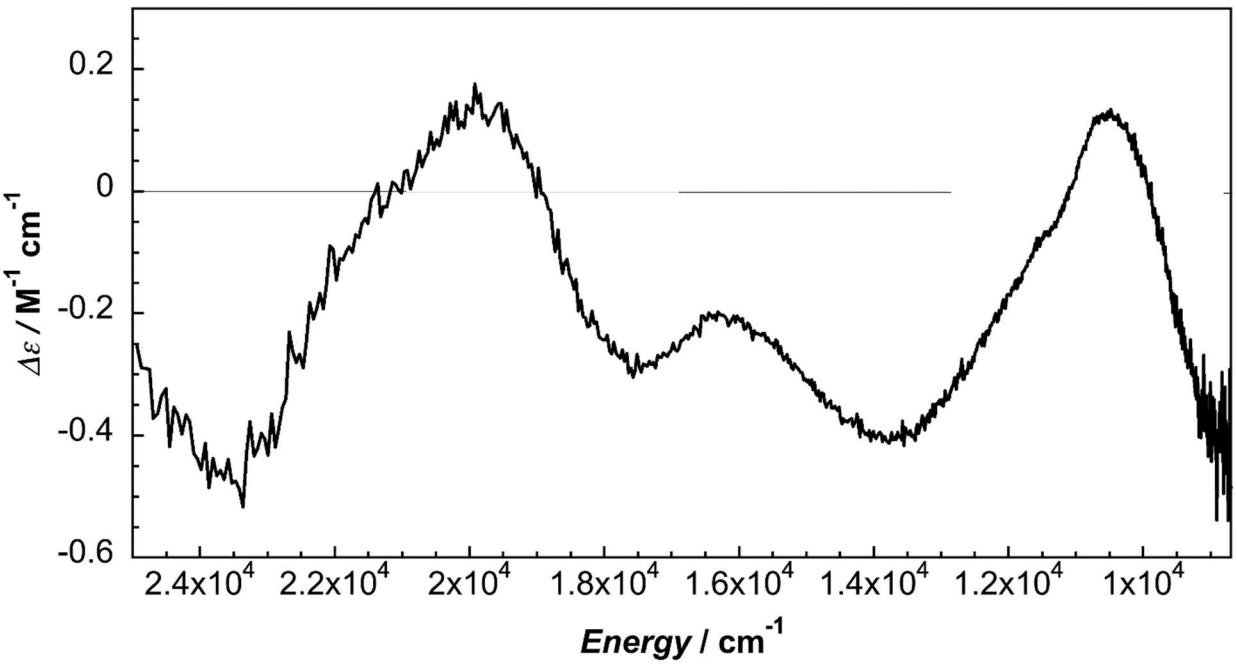

***Figure S36**. Circular dichroism of **Ni^{II}(IB)Br$_2$** in DMA at 294 K.*

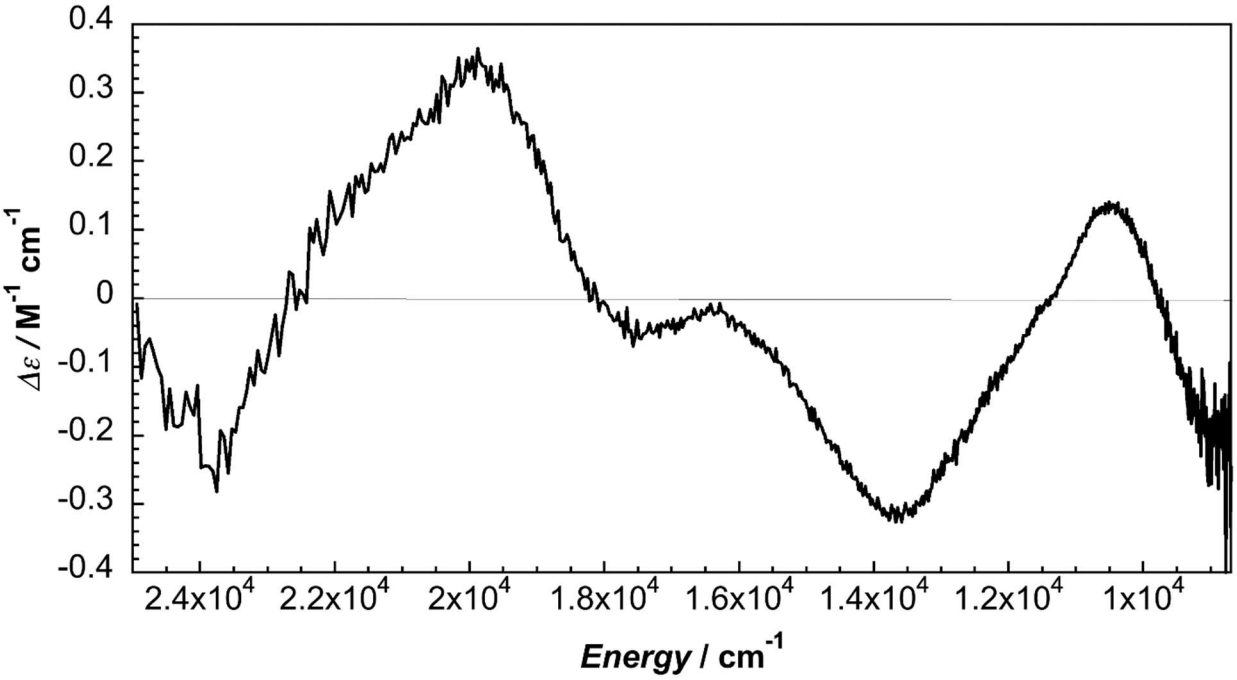

***Figure S37**. Circular dichroism of **Ni^{II}(IB)Br$_2$** in 0.1 M $TBAPF_6$ in DMA solution at 294 K.*

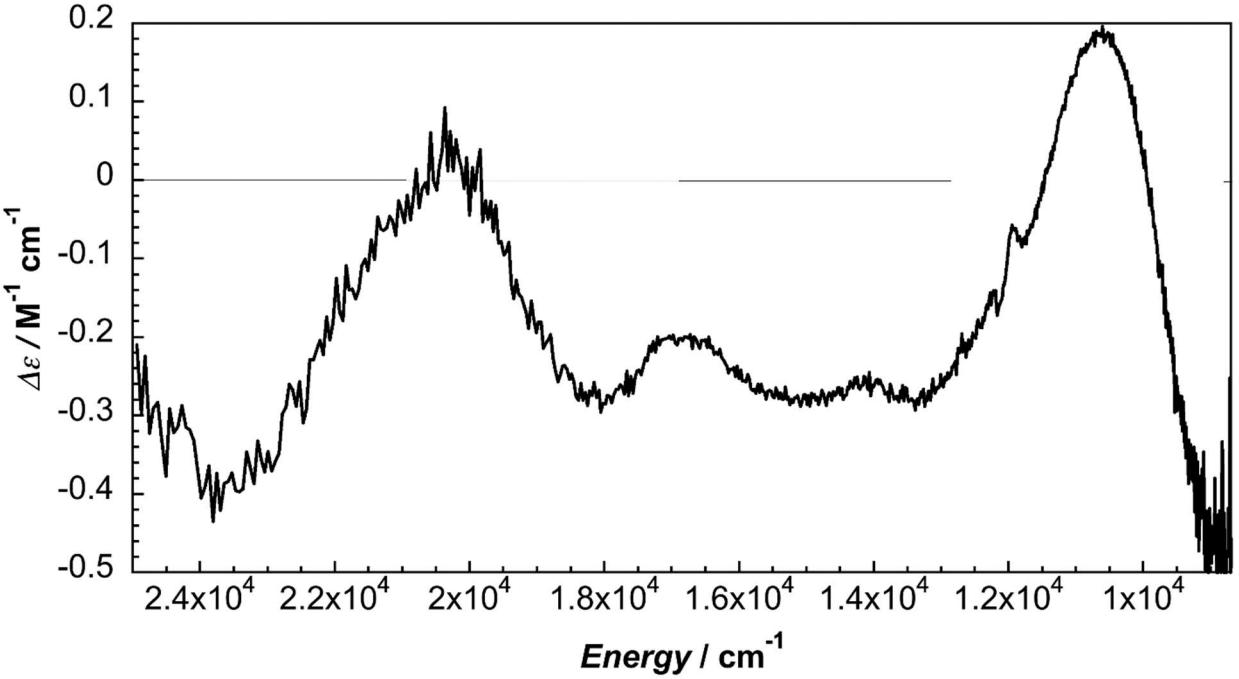

***Figure S38**. Circular dichroism of **Ni^{II}(IB)Cl$_2$** in DMA at 294 K.*

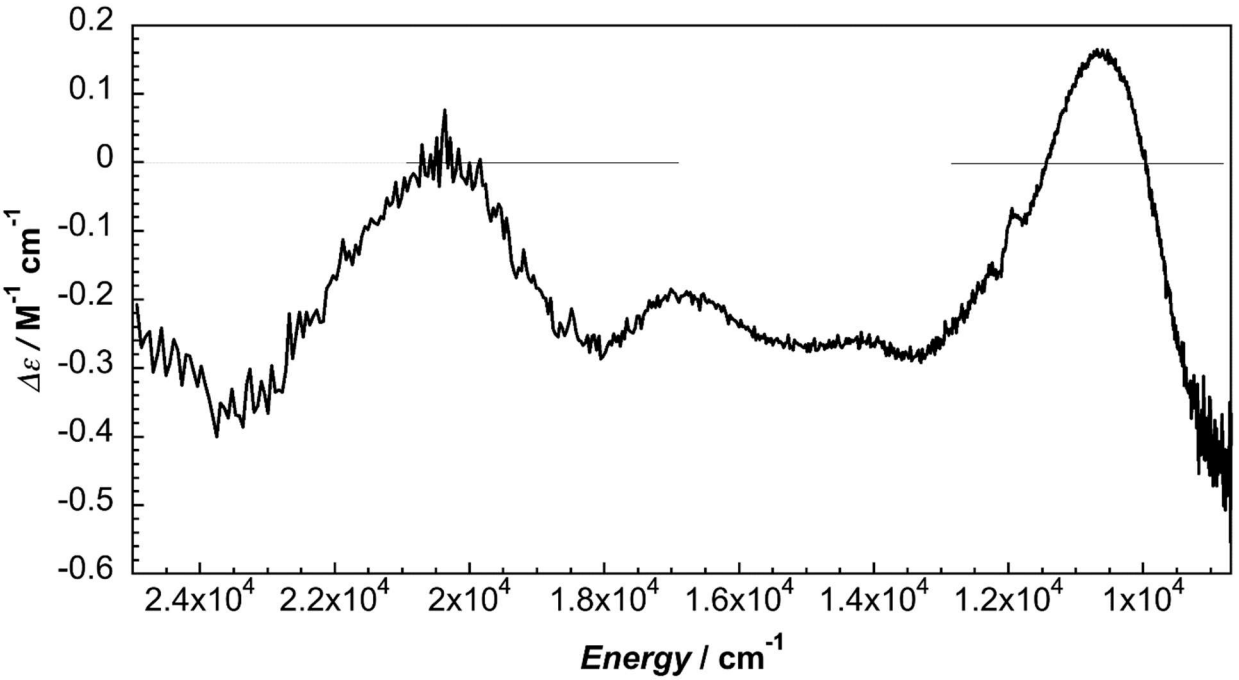

***Figure S39**. Circular dichroism of **Ni^{II}(IB)Cl$_2$** in 0.1 M TBAPF$_6$ in DMA solution at 294 K.*

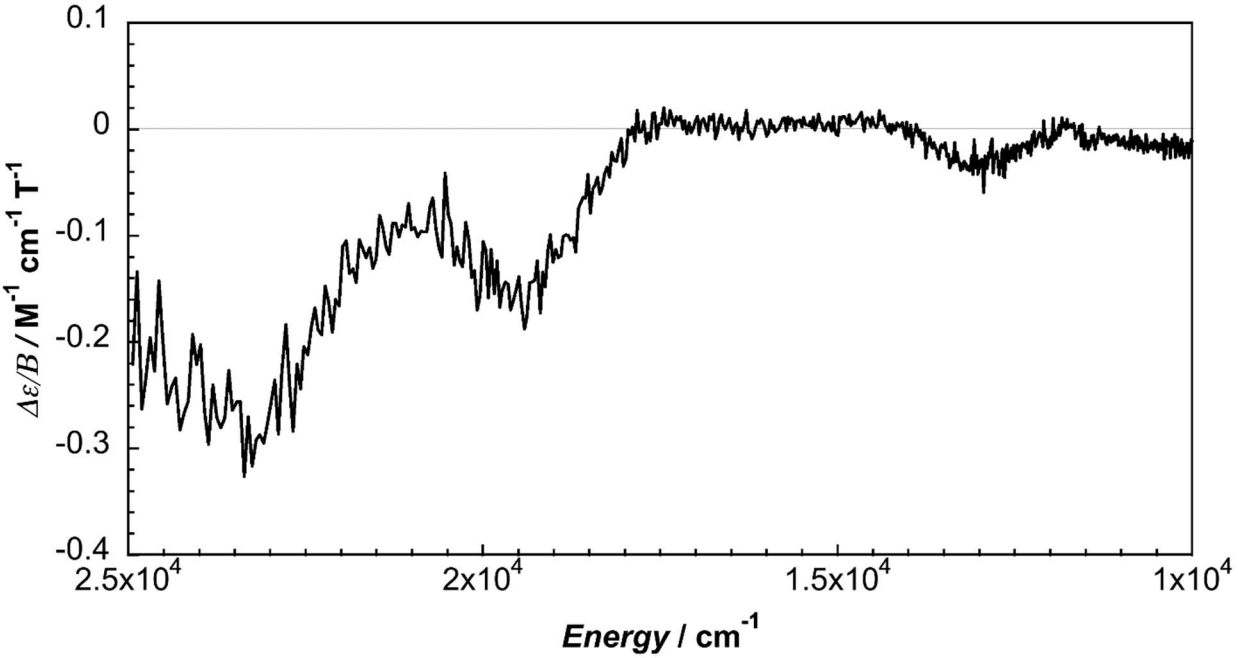

***Figure S40**. Magnetic circular dichroism of **$Ni^{II}(IB)Br_2$** in DMA at 294 K.*

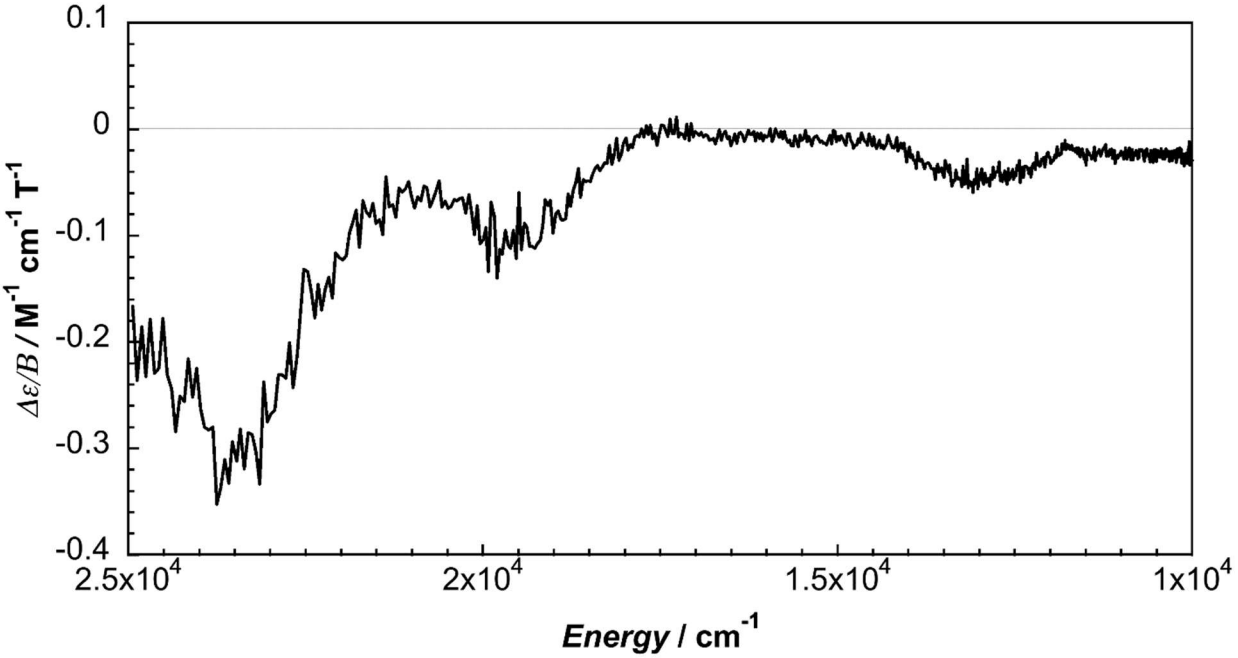

***Figure S41**. Magnetic circular dichroism of **$Ni^{II}(IB)Br_2$** in 0.1 M $TBAPF_6$ in DMA solution at 294 K.*

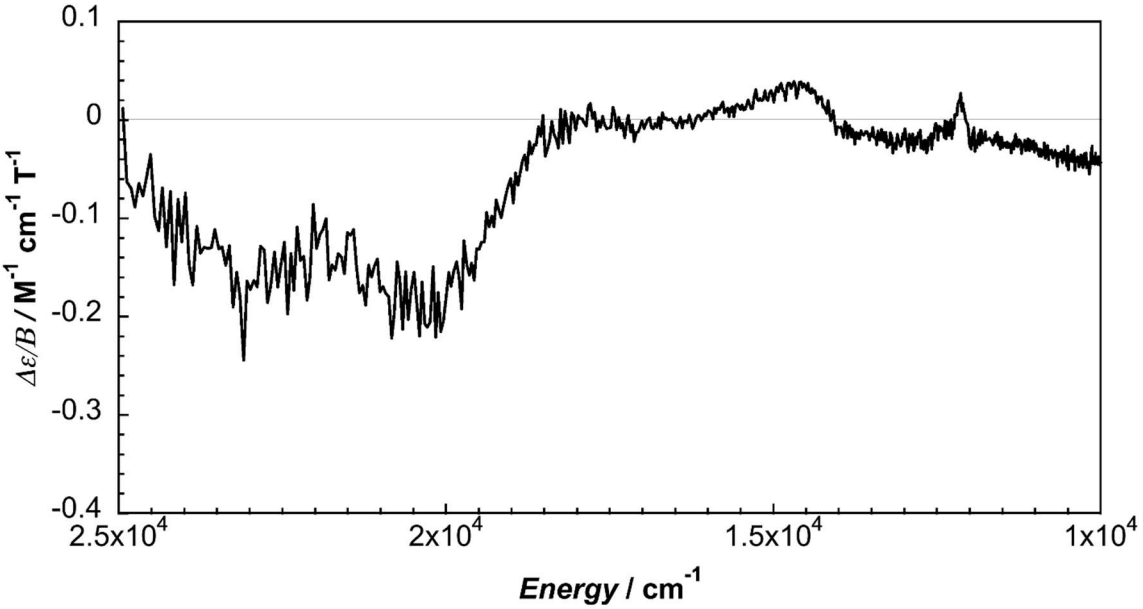

***Figure S42**. Magnetic circular dichroism of **$Ni^{II}(IB)Cl_2$** in DMA at 294 K.*

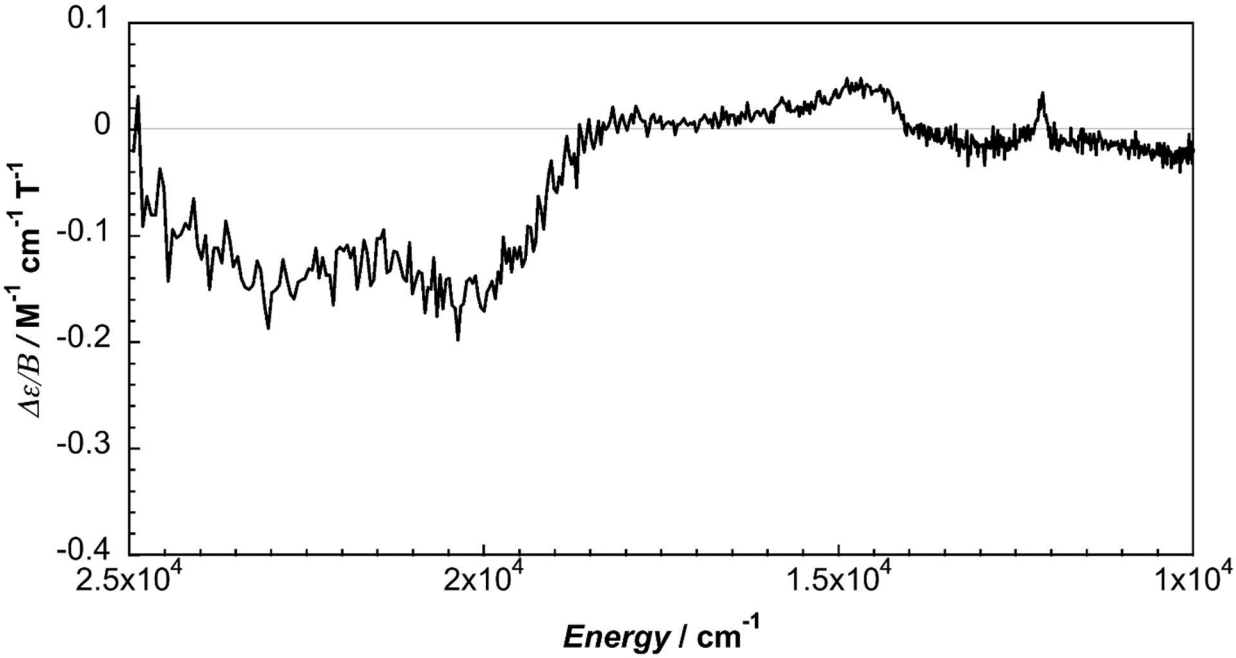

***Figure S43**. Magnetic circular dichroism of **$Ni^{II}(IB)Cl_2$** in 0.1 M $TBAPF_6$ in DMA solution at 294 K.*

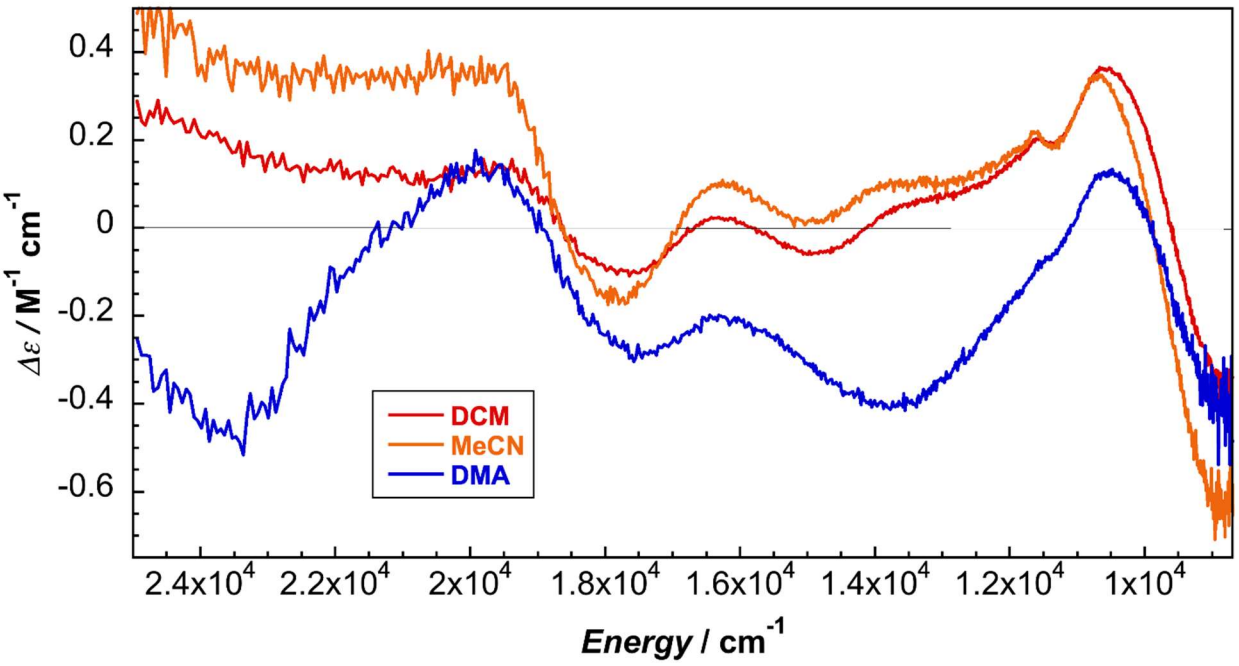

***Figure S44**. Solvent comparison of circular dichroism of $Ni^{II}(IB)Br_2$ at 294 K.*

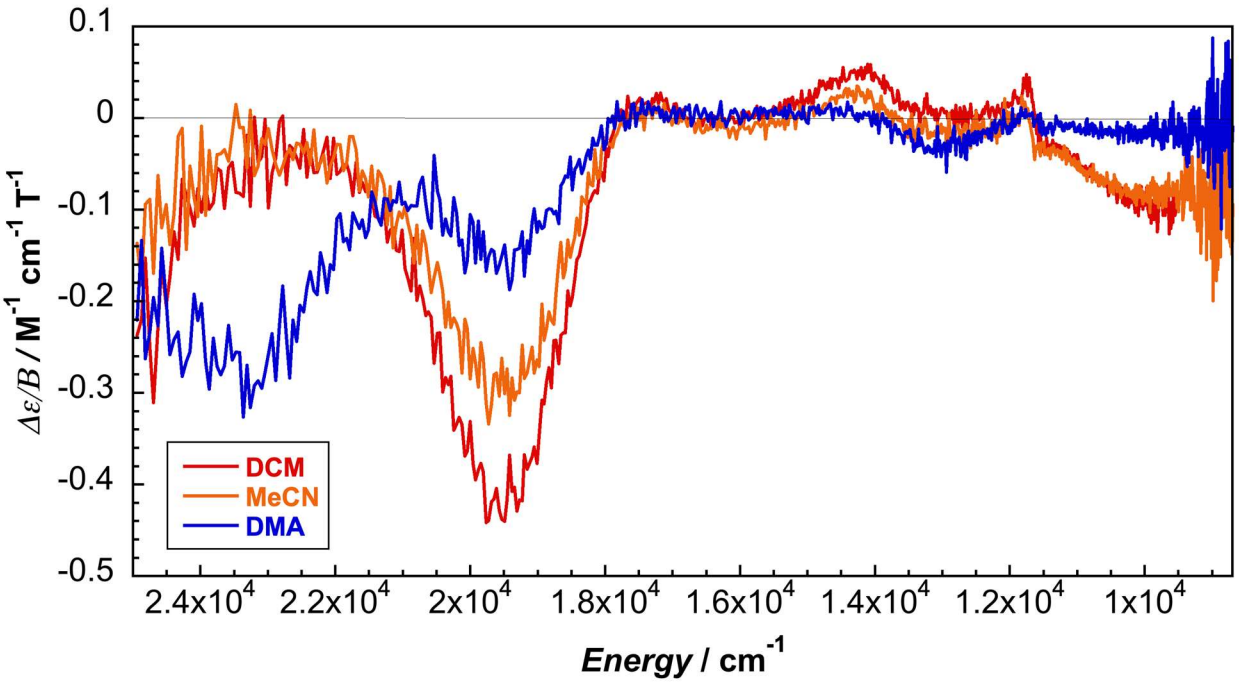

***Figure S45**. Solvent comparison of magnetic circular dichroism of **$Ni^{II}(IB)Br_2$** at 294 K.*

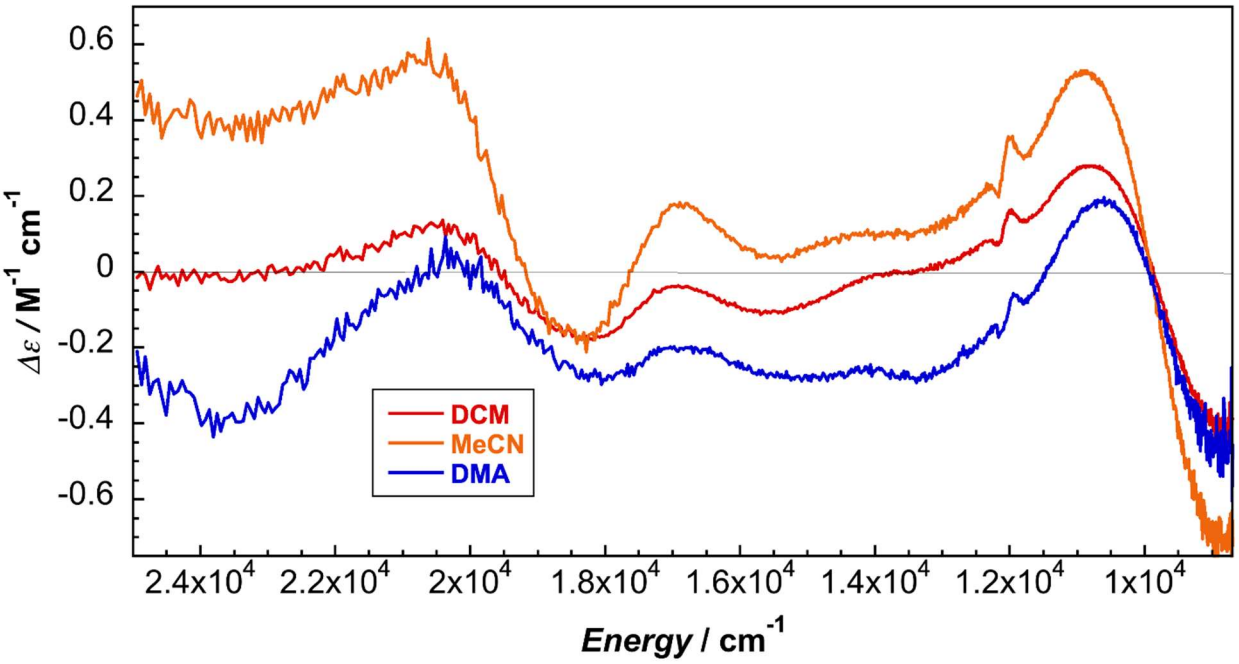

***Figure S46**. Solvent comparison of circular dichroism of $Ni^{II}(IB)Cl_2$ at 294 K.*

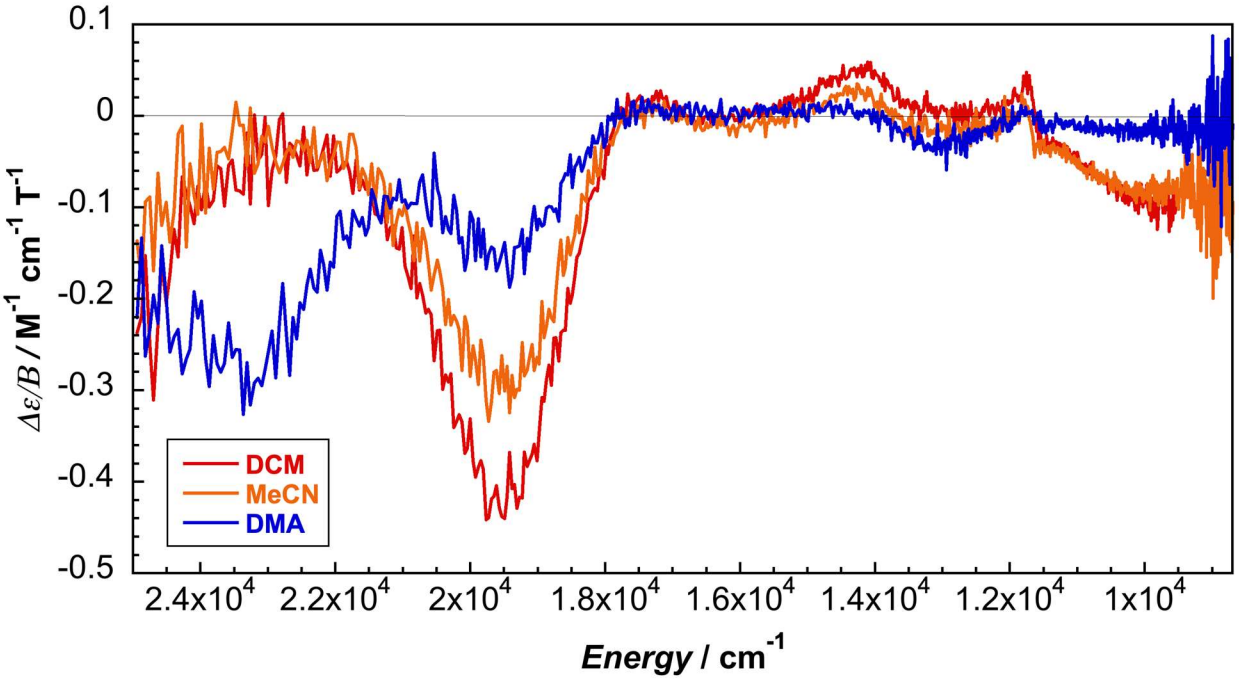

***Figure S47**. Solvent comparison of magnetic circular dichroism of **$Ni^{II}(IB)Cl_2$** at 294 K.*

2.6.5 Electrochemistry

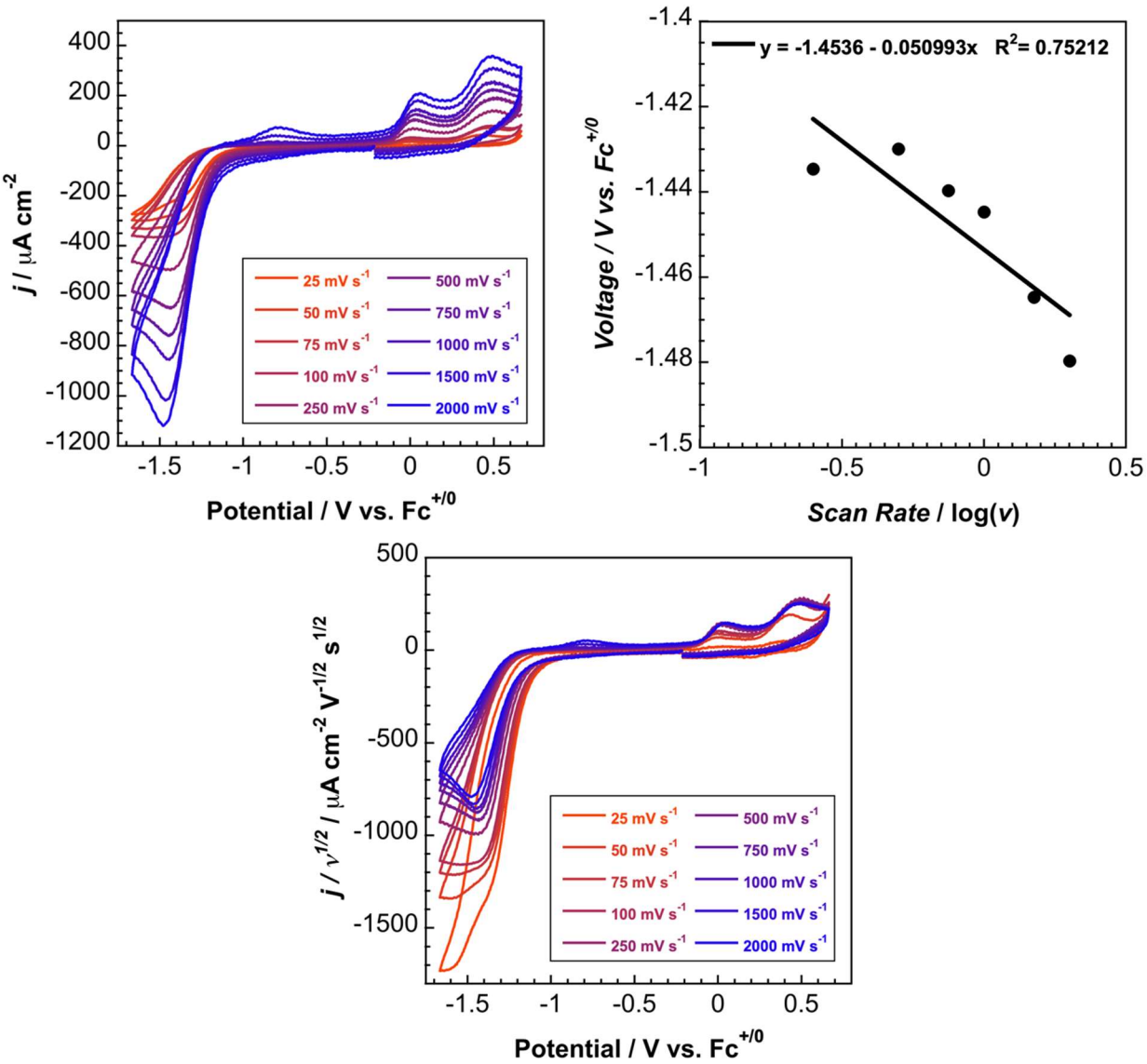

***Figure S48**. (**Upper Left**) Scan-rate dependence of reduction of 1.64 mM **$Ni^{II}(IB)Br_2$** in 0.1 M $TBAPF_6$ in DCM solution. (**Upper Right**) Peak reduction potential versus the logarithm of the scan rate ($V\ s^{-1}$). (**Lower**) Scan rate normalized voltammetry of 1.64 mM **$Ni^{II}(IB)Br_2$** in 0.1 M $TBAPF_6$ in DCM solution.*

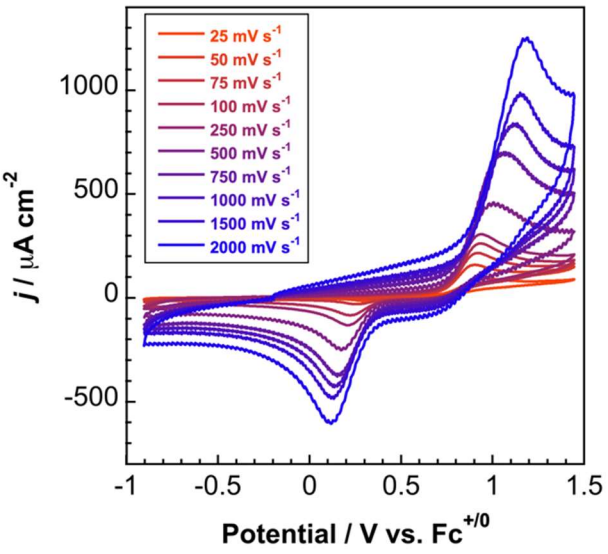

***Figure S49**. Scan-rate dependence of oxidation of 1.0 mM **Ni^{II}(IB)Br_2** in DCM in 0.1 M $TBAPF_6$ solution.*

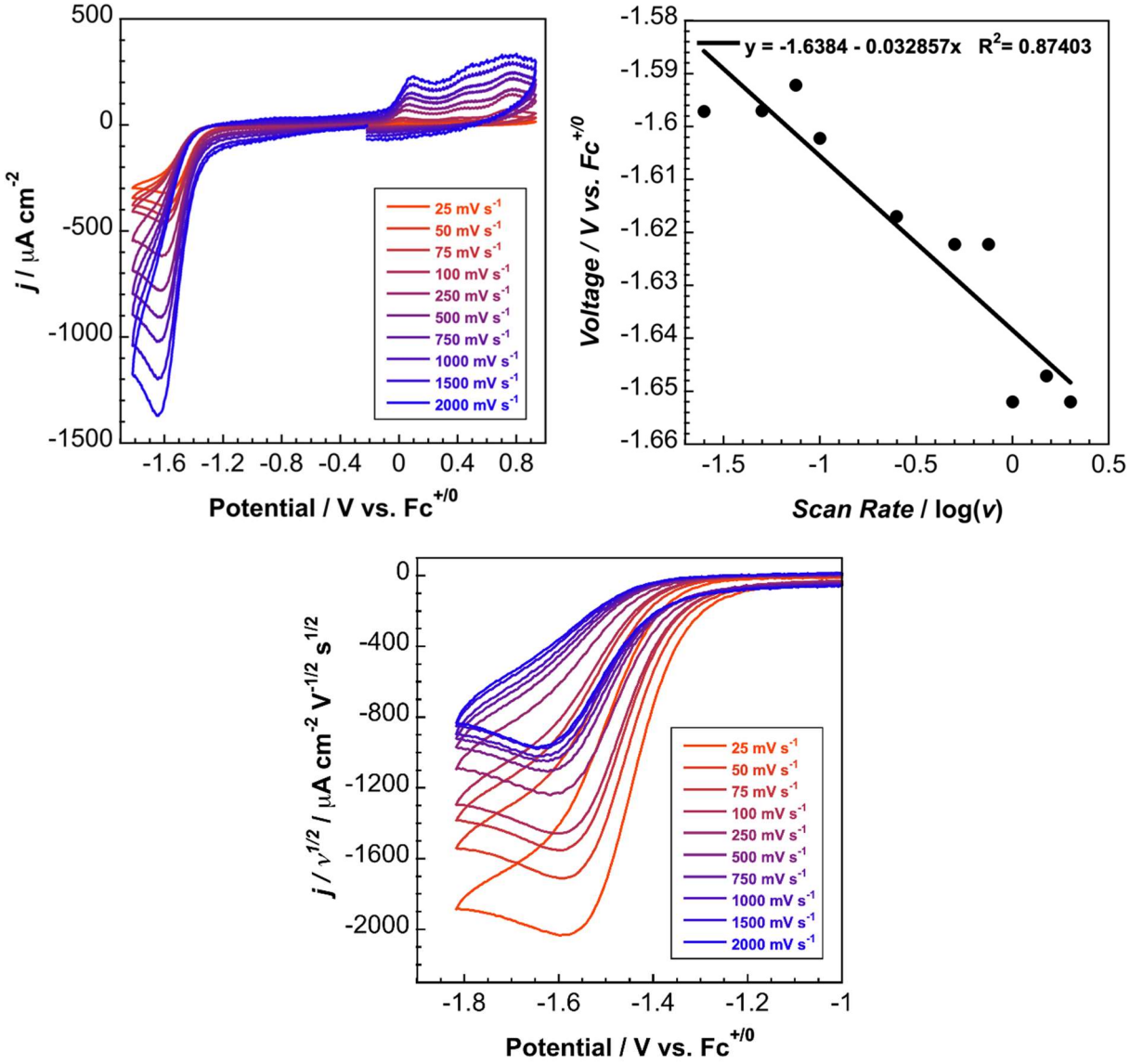

***Figure S50**. (**Upper Left**) Scan-rate dependence of reduction of 1.69 mM **Ni^{II}(IB)Cl$_2$** in 0.1 M TBAPF$_6$ in DCM solution. (**Upper Right**) Peak reduction potential versus the logarithm of the scan rate (V s^{-1}). (**Lower**) Scan rate normalized voltammetry of 1.69 mM **Ni^{II}(IB)Cl$_2$** in 0.1 M TBAPF$_6$ in DCM solution.*

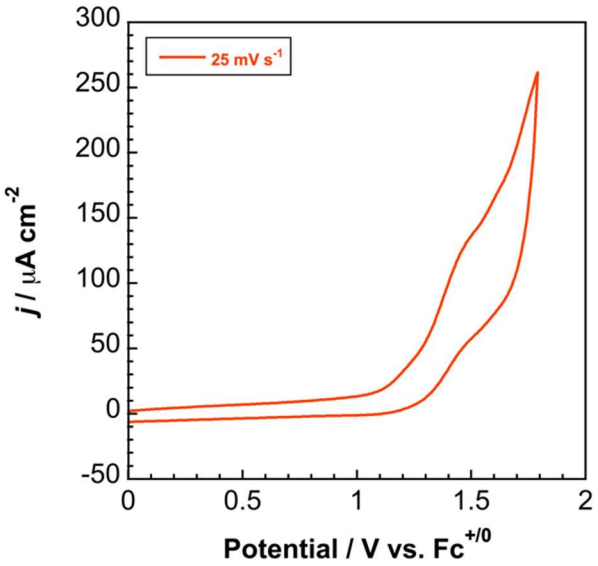

***Figure S51**. 25 mV s^{-1} scan of oxidation of 1.21 mM **$Ni^{II}(IB)Cl_2$** in 0.1 M $TBAPF_6$ in DCM solution.*

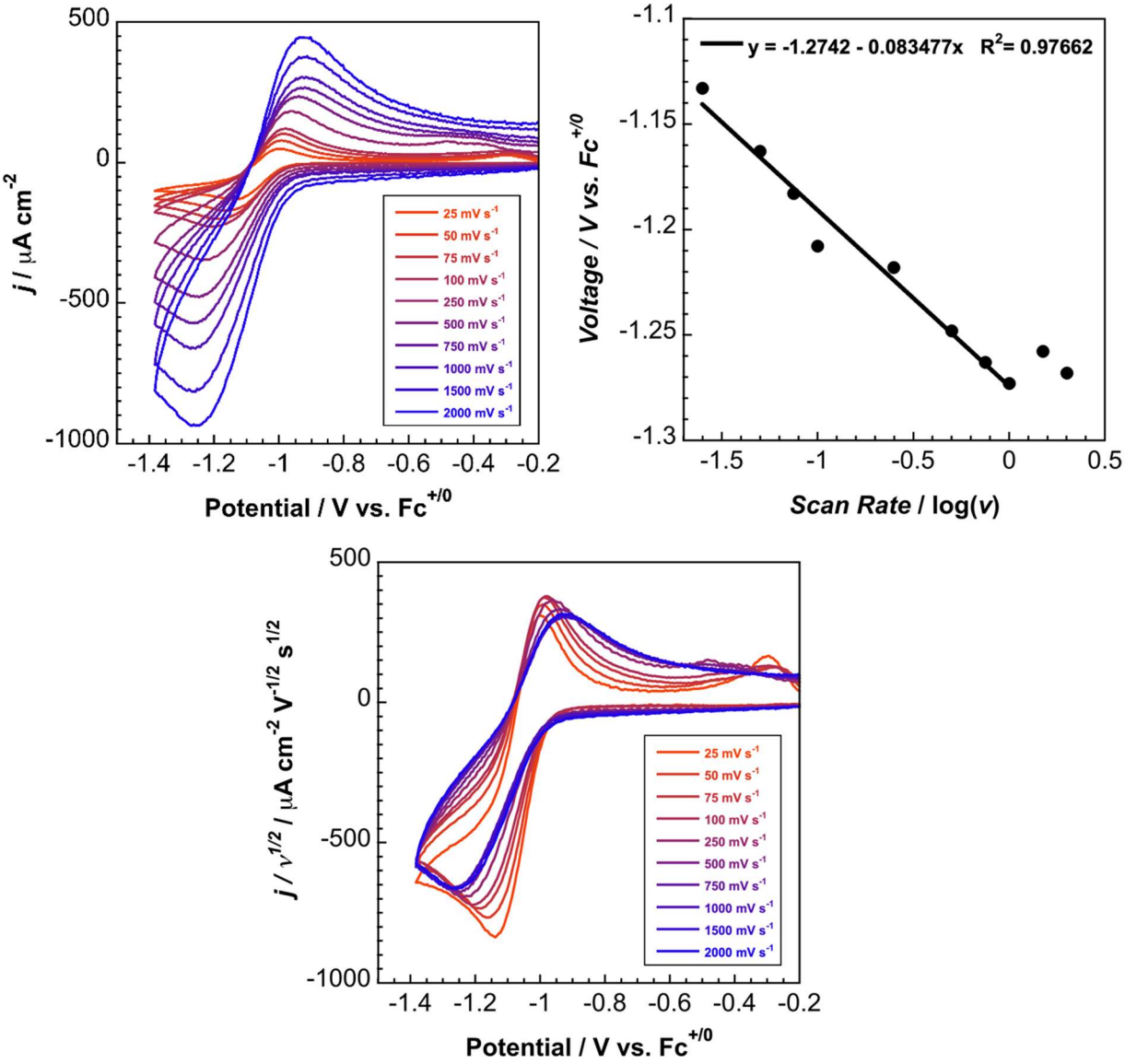

Figure S52. (***Upper Left***) *Scan-rate dependence of reduction of 1.46 mM* ***Ni^{II}(IB)Br$_2$*** *in 0.1 M TBAPF$_6$ in MeCN solution. (****Upper Right****) Peak reduction potential versus the logarithm of the scan rate (V s^{-1}). (****Lower****) Scan rate normalized voltammetry of 1.46 mM* ***Ni^{II}(IB)Br$_2$*** *in 0.1 M TBAPF$_6$ in MeCN solution.*

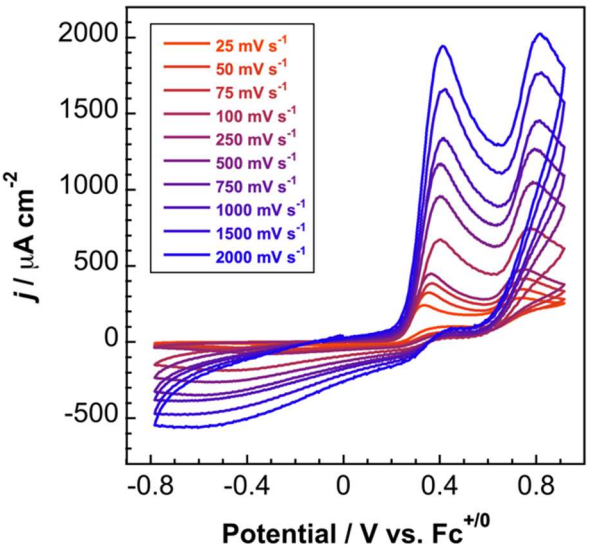

***Figure S53**. Scan-rate dependence of oxidation of 1.46 mM **Ni^{II}(IB)Br_2** in 0.1 M $TBAPF_6$ in MeCN solution.*

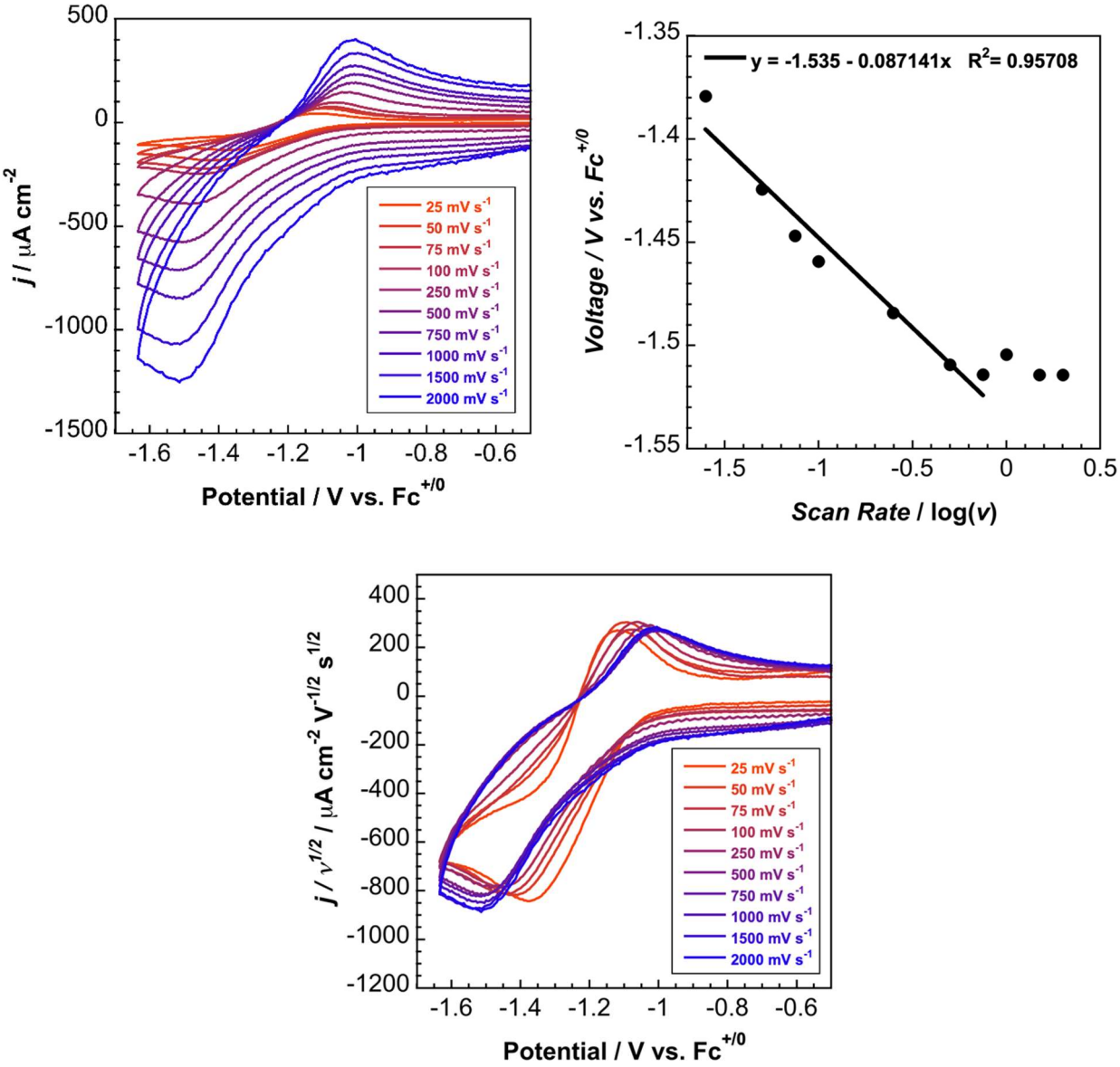

Figure S54. (***Upper Left***) *Scan-rate dependence of reduction of 1.44 mM* ***Ni^{II}(IB)Cl$_2$*** *in 0.1 M TBAPF$_6$ in MeCN solution. (****Upper Right****) Peak reduction potential versus the logarithm of the scan rate (V s^{-1}). (****Lower****) Scan rate normalized voltammetry of 1.44 mM* ***Ni^{II}(IB)Cl$_2$*** *in 0.1 M TBAPF$_6$ in MeCN solution.*

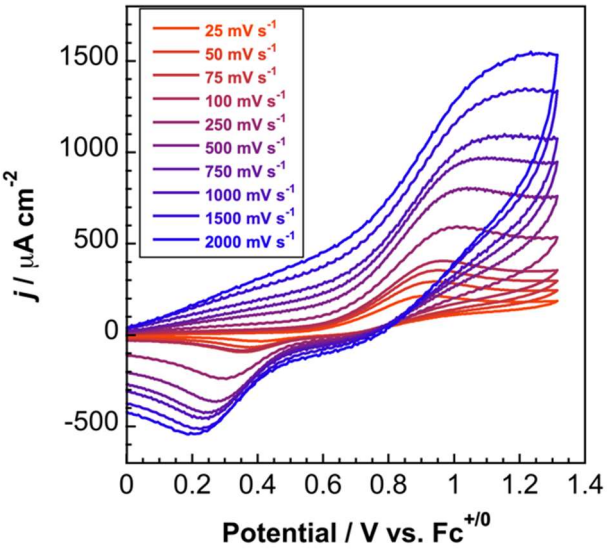

***Figure S55**. Scan-rate dependence of oxidation of 1.44 mM **$Ni^{II}(IB)Cl_2$** in 0.1 M $TBAPF_6$ in MeCN solution.*

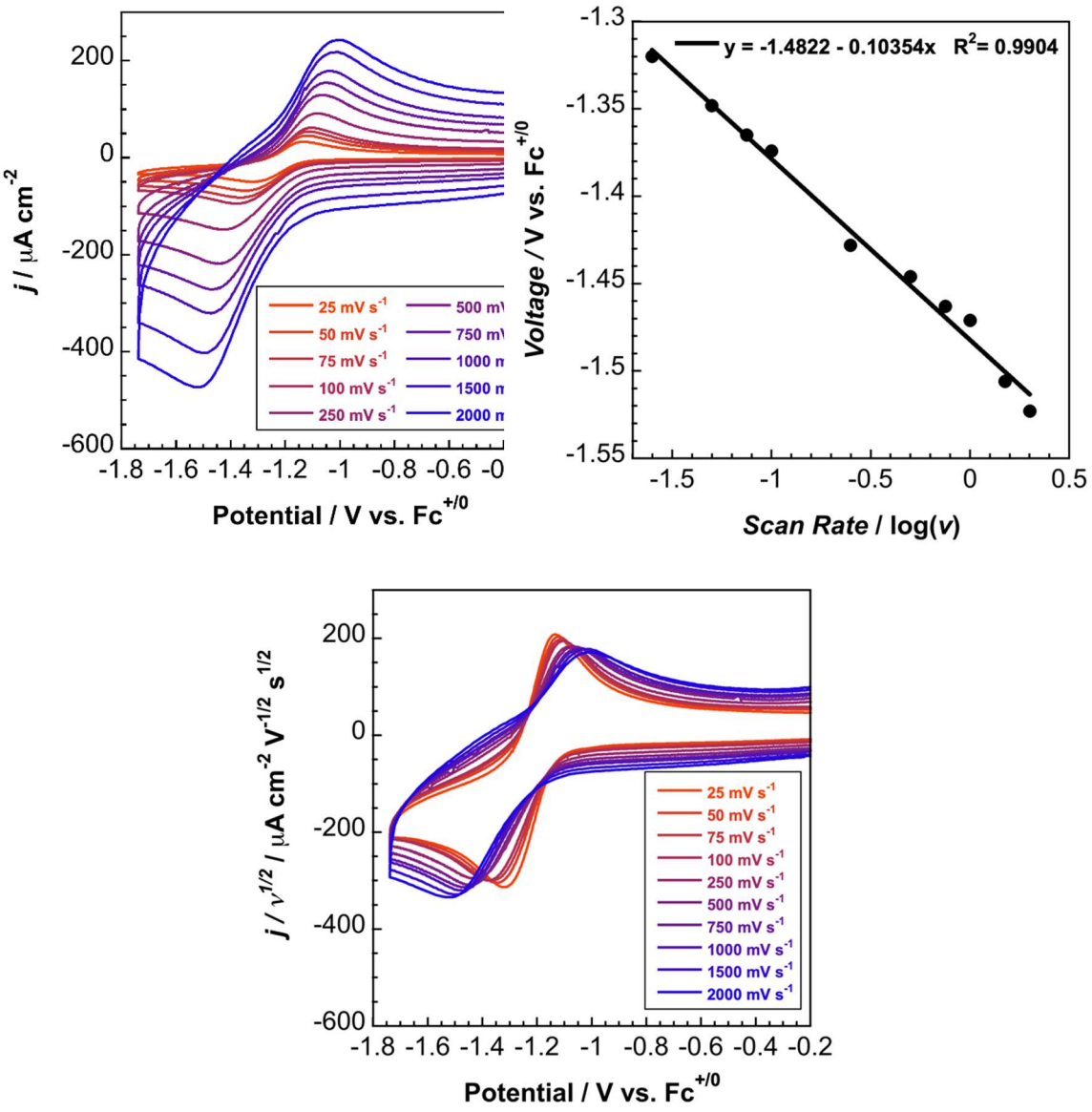

***Figure S56**. (**Upper Left**) Scan-rate dependence of reduction of 1.00 mM **Ni^{II}(IB)Br$_2$** in 0.1 M TBAPF$_6$ in DMA solution. (**Upper Right**) Peak reduction potential versus the logarithm of the scan rate (V s^{-1}). (**Lower**) Scan rate normalized voltammetry of 1.00 mM **Ni^{II}(IB)Br$_2$** in 0.1 M TBAPF$_6$ in DMA solution.*

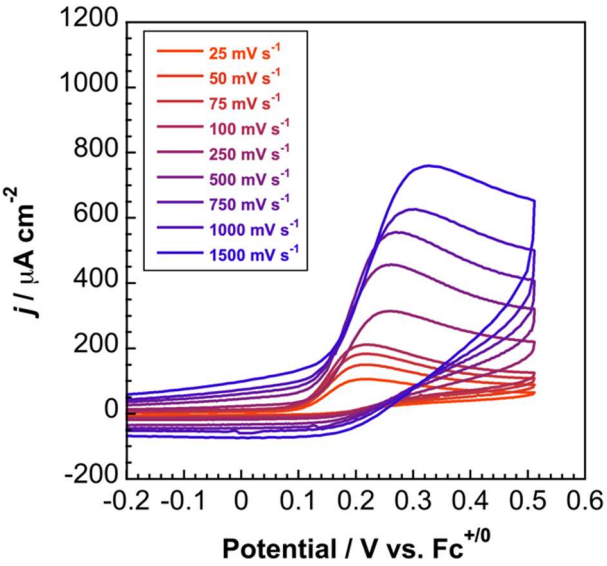

Figure S57. Scan-rate dependence of oxidation of 1.00 mM $Ni^{II}(IB)Br_2$ in 0.1 M $TBAPF_6$ in DMA solution.

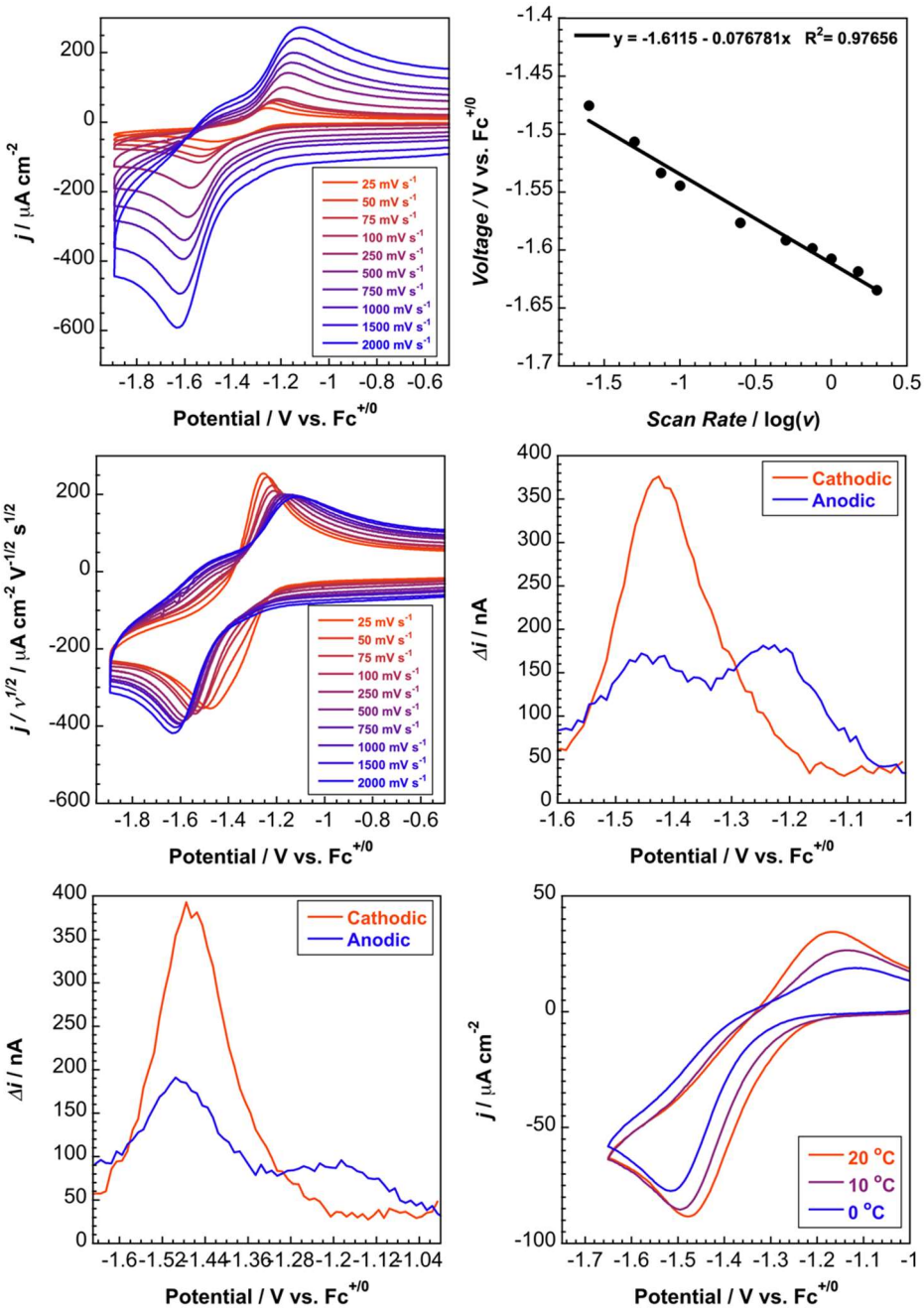

Figure S58. (***Upper Left***) *Scan-rate dependence of reduction of 1.39 mM* ***Ni^{II}(IB)Cl$_2$*** *in 0.1 M TBAPF$_6$ in DMA solution. (****Upper Right****) Peak reduction potential versus the logarithm of the scan rate (V s^{-1}). (****Middle Left****) Scan rate normalized voltammetry of 1.39 mM* ***Ni^{II}(IB)Cl$_2$*** *in 0.1 M TBAPF$_6$ in DCM solution. (****Middle Right****) Cathodic and return anodic differential pulse voltammetry of 1.79 mM* ***Ni(IB)Cl$_2$*** *in 0.1 M TBAPF$_6$ in DMA solution at 20 °C . (****Bottom Left****) Cathodic and return anodic differential pulse voltammetry of 1.79 mM* ***Ni^{II}(IB)Cl$_2$*** *in 0.1 M TBAPF$_6$ in DMA solution at 0 °C . (****Bottom Right****) Variable temperature voltammetry of the first reduction and re-oxidation of 1.79 mM* ***Ni^{II}(IB)Cl$_2$*** *in 0.1 M TBAPF$_6$ in DMA solution. Potentials shifted to the peak potential of* ***Ni^{II}(IB)Cl$_2$*** *in DMA*

at 25 mV s^{-1} from scan rate dependent voltammetry. DPV Parameters: 10 mV step size, 0.5 s sample period, 0.1 s pulse time, 5 mV pulse height.

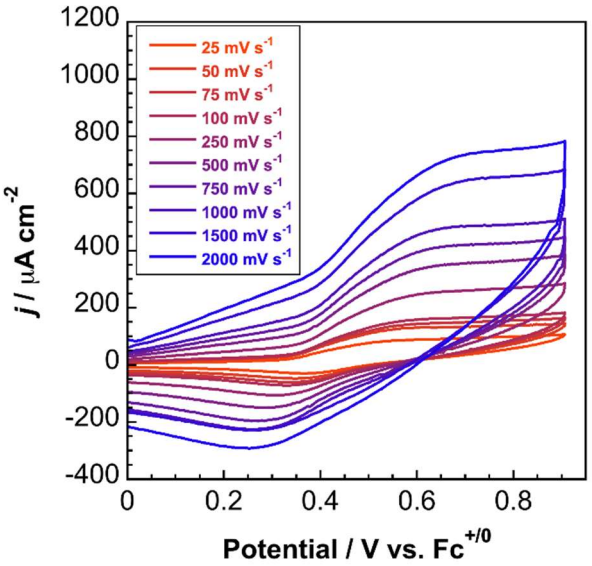

***Figure S59**. Scan-rate dependence of oxidation of 1.39 mM **$Ni^{II}(IB)Cl_2$** in 0.1 M $TBAPF_6$ in DMA solution.*

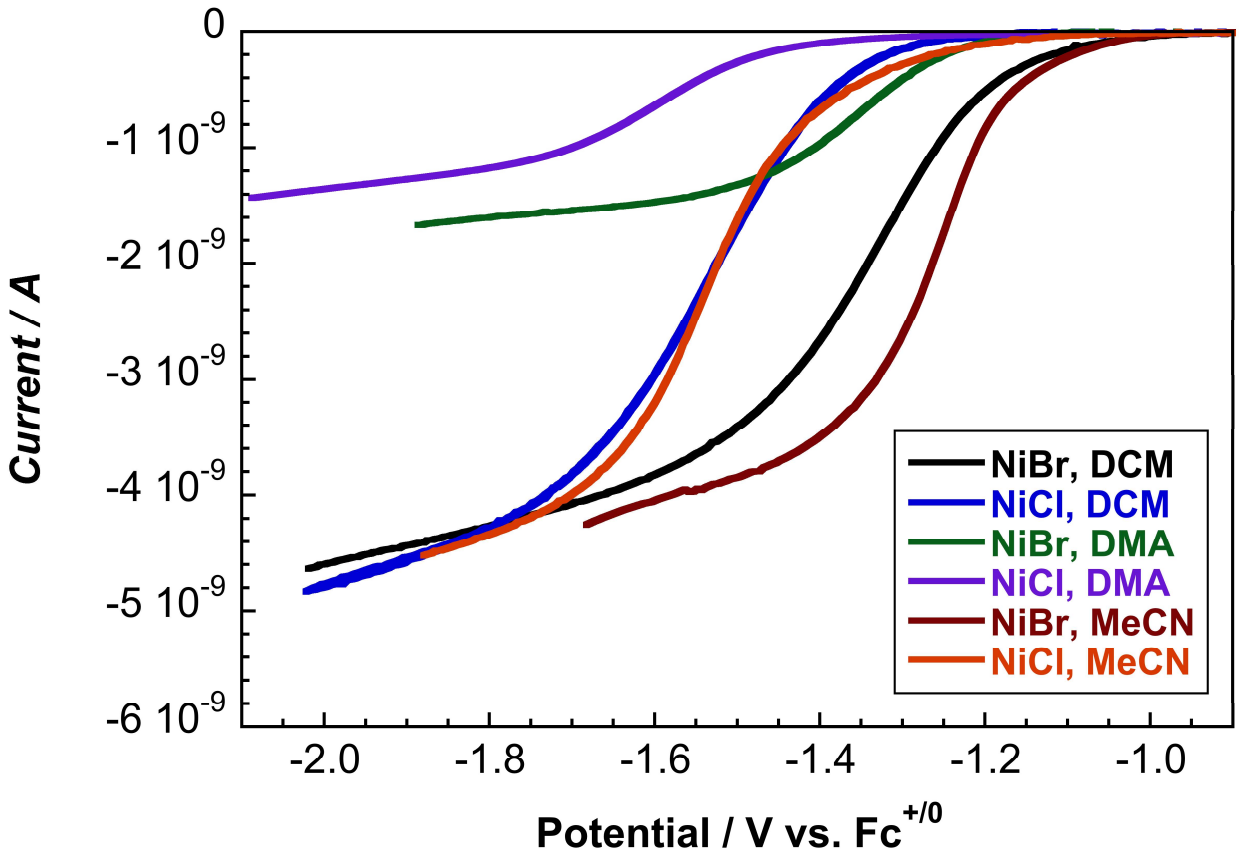

***Figure S60**. Summary overlay of microelectrode scans for determination of diffusions coefficients of **$Ni^{II}(IB)Br_2$** and **$Ni^{II}(IB)Cl_2$** in DCM, MeCN, and DMA solution.*

***Table S1**. Return electrochemical parameters (upper, oxidation; lower, reduction) for **$Ni^{II}(IB)Cl_2$** and **$Ni^{II}(IB)Br_2$** and electrochemical parameters (oxidation) for tetrabutylammonium bromide (**TBABr**) in 0.1 M $TBAPF_6$ electrolyte solution using a glassy carbon working electrode, 0.01 M $Ag^{+/0}$ non-aqueous reference electrode, and platinum wire counter electrode. All peak and formal potentials are given in volts, obtained using a 1000 mV s^{-1} scan rate (unless otherwise stated), and referenced to $Fc^{+/0}$.*

Complex	Solvent	$E_{p,an.,1}$	$E_{p,an.,2}$	$E_{p,an.,3}$	$E_{p,an.,4}$	$E^{0'}_{an.,1}$ [a]	$E^{0'}_{an.,2}$ [a]	$E^{0'}_{an.,3}$ [a]	$E^{0'}_{an.,4}$ [a]
$Ni^{II}(IB)Cl_2$	DCM	−0.78[b]	0.09	0.42[c]	0.78	−0.95[b]	0.00	0.33	0.63
$Ni^{II}(IB)Br_2$	DCM	−0.79[b]	0.04	---	0.48	−0.85[b]	−0.02	---	0.38
$Ni^{II}(IB)Cl_2$	MeCN	−1.01	−0.44[d]	---	---	−1.10	−0.55	---	---
$Ni^{II}(IB)Br_2$	MeCN	−0.92	---	---	---	−1.02	−0.36[c]	---	---
$Ni^{II}(IB)Cl_2$	DMA	−1.15	---	---	---	−1.24	---	---	---
$Ni^{II}(IB)Br_2$	DMA	−1.03	---	---	---	−1.15	---	---	---
TBABr	DCM	---	---	0.24[c]	0.56[c]	---	---	0.18[c]	0.48[c]

[a]Taken from the inflection potential of the redox process at 1000 mV s^{-1}, which approximates the formal potential. [b]Values at 2000 mV s^{-1}. [c]Values at 100 mV s^{-1}. [d]Values at 75 mV s^{-1}.

Complex	Solvent	$E_{p,cat.,1}$	$E_{p,cat.,2}$	$E_{p,cat.,3}$	$E^{0\prime}_{cat.,1}$ [a]	$E^{0\prime}_{cat.,2}$ [a]	$E^{0\prime}_{cat.,3}$ [a]
$Ni^{II}(IB)Cl_2$	DCM	---	---	---	---	1.38	---
$Ni^{II}(IB)Br_2$	DCM	0.16	---	---	0.24	---	0.86
$Ni^{II}(IB)Cl_2$	MeCN	0.24	---	---	0.36	0.86	---
$Ni^{II}(IB)Br_2$	MeCN	−0.61	---	---	−0.45	0.35	0.72
$Ni^{II}(IB)Cl_2$	DMA	0.27	---	---	0.41	---	---
$Ni^{II}(IB)Br_2$	DMA	0.00	---	---	0.26	---	---
TBABr	DCM	−0.06[b]	---	0.36[c]	0.00	0.20	0.52[b]

[a]Taken from the inflection potential of the redox process at 1000 mV s^{-1}, which approximates the formal potential. [b]Values at 100 mV s^{-1}.

***Table S2**. Electrochemical parameters for **$Ni^{II}(IB)Cl_2$** and **$Ni^{II}(IB)Br_2$** in 0.1 M $TBAPF_6$*

electrolyte solution using a glassy carbon working electrode, 0.01 M $Ag^{+/0}$ non-aqueous reference electrode, and platinum wire counter electrode. All peak and formal potentials are given in volts, obtained using a 1000 mV s^{-1} scan rate (unless otherwise stated), and referenced to $Fc^{+/0}$.

Complex	***Solvent***	$E_{p,a,1}$	$E_{p,a,2}$	$E_{p,c}$	$E_{p/2,\,c}$	$E_c^{0\prime a}$	$E_a^{0\prime a}$	D_0 ($cm^2\ s^{-1}$)[b]
$Ni^{II}(IB)Cl_2$	*DCM*	*1.51*[d]	---	*−1.62*	*−1.49*	*−1.53*	*1.38*	*9.25 x 10^{-6}*
$Ni^{II}(IB)Br_2$	*DCM*	*1.11*	---	*−1.45*	*−1.30*	*−1.32*	*1.00*	*9.25 x 10^{-6}*
$Ni^{II}(IB)Cl_2$	*MeCN*	*1.10*	---	*−1.50*	*−1.34*	*−1.40*	*0.93*	*1.05 x 10^{-5}*
$Ni^{II}(IB)Br_2$	*MeCN*	*0.42*	*0.82*	*−1.26*	*−1.10*	*−1.10*	*0.34/0.74*	*9.55 x 10^{-6}*
$Ni^{II}(IB)Cl_2$	*DMA*	*0.75*[d,e]	---	*−1.63*	*−1.52*	*−1.56*	*0.62*	*2.81 x 10^{-6}*
$Ni^{II}(IB)Br_2$	*DMA*	*0.33*[d,e]	*0.44*[e]	*−1.45*	*−1.31*	*−1.34*	*0.24/0.39*	*3.06 x 10^{-6}*
$Ni^{II}(^{diBn}biOx)Br_2$[c]	*1,2-DFB*	---	---	*−1.90*	*−1.55*	---	---	---
$Ni^{II}(^{iPr}biOx)Br_2$[c]	*1,2-DFB*	---	---	*−1.64*	*−1.46*	---	---	---
$Ni^{II}(^{diMe}biOx)(Dipp)Br$[c]	*THF*	---	---	*−2.39*	*−2.12*	---	---	---

[a]From the inflection potential of the redox process at 1000 mV s^{-1}, which approximates the formal potential. [b]Derived from mass transport-controlled current at a disk microelectrode. [c]See reference [11]. [d]Estimated from the local minimum of dj/dV. [e]Values at 75 mV s^{-1}. $E_{p/2,\,c}$ is the potential at half of the peak current.

In DCM, four re-oxidations are observed for **$Ni^{II}(IB)Cl_2$** and **$Ni^{II}(IB)Br_2$** after initial one-electron reduction. The first re-oxidation only appears at fast scan rates, indicative of a transient species that quickly decays on the CV time scale, and is tentatively assigned as the four-coordinate Ni^{I} species that has not yet lost a halide. Experimental re-oxidation potentials for **$Ni^{I/II}(IB)Cl_2$** and **$Ni^{I/II}(IB)Br_2$** are −0.95 V and −0.85 V vs. $Fc^{+/0}$, respectively, indicating the former species is easier to oxidize, consistent with relative initial reduction potentials. The second re-oxidation (0.00 V (Cl) and −0.02 V (Br) vs. $Fc^{+/0}$) is assigned to the three-coordinate Ni^{I} complexes (i.e., **$Ni^{I/II}(IB)X$**) (**Figures S48** and **S50**). The third and fourth re-oxidations are assigned to bromide/chloride re-oxidations that ultimately lead to the dihalide. Anodically, the complexes in DCM exhibit the most positive

formal potentials, consistent with solvent-assisted oxidation that is likely coupled to a follow-up chemical reaction. The waveform and peak-to-peak separation are consistent with oxidation of bromide to tribromide, as evidenced by previous mechanistic studies on this complex reaction, specifically the observed return reduction at 0.24 V vs. $Fc^{+/0}$.

In DMA, the anodically shifted re-oxidation is likely associated with a one-electron reduced, halide-dissociated, solvent-associated species, as evidenced by the potentials for **Ni^{I}(IB)Cl(DMA)** and **Ni^{I}(IB)Br(DMA)** of −1.15 V and −1.14 V vs. $Fc^{+/0}$, respectively. This behavior is supported by the subtle shifts in anodic peak potential as a function of scan rate that are observed in **Figures S56** and **S58**. Similarly, the potentials for **Ni^{I}(IB)Cl(MeCN)** and **Ni^{I}(IB)Br(MeCN)** are −1.10 V and −1.02 V vs. $Fc^{+/0}$. Behavior similar to re-oxidation in DMA is observed in **Figures S52** and **S54**. Less return current at the more anodic wave suggests weaker binding of MeCN relative to DMA, consistent with the spectroscopic data.

Anodically, the normalized voltammetry in **Figure 6** indicates that oxidation in both solvents removes multiple electrons, which suggests formation of elemental bromine or bromine speciation. The return reduction in MeCN further supports this behavior. The oxidation of bromide to bromine on a platinum electrode in MeCN occurs at 0.12, 0.72 V vs. $Fc^{+/0}$, while oxidations of **Ni^{II}(IB)Br_2** occur at 0.34, 0.74 V vs. $Fc^{+/0}$.

To assess the effects of solvent donicity and dielectric constant on the electrochemical properties of **Ni^{II}(IB)X_2** complexes, scan rate-dependent cyclic voltammetry data were acquired in DCM, MeCN, and DMA (**Figure 6** and **Figures S48-S59**). **Table 3** provides peak and formal potentials for initial redox events, while **Table S1**

provides peak and formal potentials for unique re-oxidation and re-reduction events that result from chemical reactions following initial electron transfers.

To minimize unknown parameters for the analysis given below, real surface areas of a 3-mm diameter glassy carbon electrode and an 11-μm diameter carbon fiber disk microelectrode were determined by measuring ferrocene (Fc) voltammetry. To ensure consistent mass transport behavior, diffusion coefficients were measured for $\mathbf{Ni^{II}(IB)X_2}$ complexes in the three solvents using the steady-state current for a disk microelectrode. This current can be used to determine the diffusion coefficients for both reversible and irreversible processes.[12] Since both complexes are neutral, the diffusion coefficients approximately follow the Stokes-Einstein equation, which inversely correlates the diffusion coefficient of a spherical particle and the viscosity of the solvating medium, as given by **Equation 2**:

$$D_0 = \frac{k_B T}{6\pi\eta r} \tag{2}$$

where D_0 is the particle diffusion coefficient, k_B is Boltzmann's constant, T is temperature, η is the viscosity of the solvent, and r is the hydrodynamic radius of the diffusing particle. Slightly smaller diffusion coefficients are observed for both complexes in DCM (η = 0.40 mPa s)[13] relative to MeCN (η = 0.34 mPa s),[14] consistent with small differences in solvent viscosity and comparable hydrodynamic radii for both complexes. Consistent results are also obtained for coefficients in DMA (η = 0.94 mPa s), which has a viscosity nearly three times that of MeCN.[15] With accurate D_0 values, the voltammetry data can be normalized to provide a more meaningful comparison between solvent and scan rate-dependent effects (**Figure 6**).

Previous studies have provided formal potentials for both aromatic and non-aromatic Ni(II) diimine systems, with many reports providing kinetic analyses with substrate present.[16,17] However, to our knowledge, this is one of the first examples of detailed solvent-dependent electroanalytical chemistry for non-aromatic Ni(II) cross-coupling catalysts, with findings here rationalizing the parameters optimized through methodological studies. In general, precatalyst electrochemical responses are remarkably solvent dependent. In all three solvents, **Ni^{II}(IB)Cl_2** and **Ni^{II}(IB)Br_2** both exhibit single, electrochemically irreversible reduction events with significantly shifted oxidative waves (**Figures 6**, and **S50, S54, S58**). The general irreversibility required use of peak potentials ($E_{p,a}$ or $E_{p,c}$), potentials at half of the peak current value ($E_{p/2}$), and inflection potentials (accurate estimate of formal potential, $E^{0'}$) for analysis.[12] These data are analyzed with a caveat that the ferrocene (Fc) formal potential exhibits solvent dependence. However, Our measured Fc formal potentials in DMA and MeCN are 85 and 91 mV vs 0.01 M $Ag^{+/0}$, respectively, indicating accurate conclusions can be drawn regarding solvent effects on measured formal potentials of the Ni complexes in these solvents. In DCM, the measured Fc formal potential is 215 mV. Therefore, measured formal potentials in DCM will appear negatively shifted relative to values in DMA and MeCN.

Based on shifts in peak potential as a function of scan rate and scan rate normalized voltammetry (current function) in all three solvents (**Figures S48-S58**), as well as differential pulse voltammetry and variable temperature voltammetry in DMA for **Ni^{II}(IB)Cl_2** (**Figure S58**), we can draw some insightful conclusions regarding the reduction mechanism, as the current function and shift in peak potential are dictated by the particular chemical and electrochemical mechanism. These conclusions also apply to **Ni^{II}(IB)Cl_2**.

We ascribe the reduction of both complexes to a concerted E_qC_i (in DMA and MeCN, solvent coordination and/or halide loss occur in concert) or step-wise E_iC_i mechanism (DCM), where slow electron transfer is followed by rapid halide loss. In DCM, three-coordinate **Ni^{I}(IB)X** will be generated upon reduction, with no subsequent solvent coordination. The lack of return current, shift in peak potential as a function of the logarithm of the scan rate near 29.6 mV, with ~33 mV observed here, and decrease in the current function toward a limiting value as the scan rate is increased supports a kinetically-controlled, stepwise reduction followed by rapid halide loss (**Figures S48** and **S50**). Activation of DCM by other nickel complexes supported by naphthyridine-diimine ligands has been observed previously.[18] However, spectroelectrochemical data obtained in DCM do not support reactivity of the **Ni^{I}(IB)X** with solvent (**Figures S73 - S75**). Overall, this analysis featuring electron transfer coupled to rapid halide loss is consistent with halide dissociation observed previously using extended X-ray absorption fine structure (EXAFS) for a low-spin Ni^{II} biOx aryl halide complex upon chemical reduction with potassium graphite.[17]

Experimental formal potentials for chemically-coupled reduction of **Ni^{II}(IB)Cl$_2$** and **Ni^{II}(IB)Br$_2$** to **Ni^{I}(IB)Cl** and **Ni^{I}(IB)Br** in DCM are −1.47 V and −1.26 V vs. $Fc^{+/0}$, respectively (**Table 3**). It is therefore ~0.21 V (~1695 cm^{-1}) harder to reduce **Ni^{II}(IB)Cl$_2$** relative to **Ni^{II}(IB)Br$_2$**. This observation is consistent with the energetic shifts in the spin-allowed ligand field bands in DCM in experiment (Main text, **Section 2.1**) and calculations (**Section 3.1** and **3.2**). In MeCN and DMA, **Ni^{II}(IB)Cl$_2$** (**Figures S54** and **S58**) and **Ni^{II}(IB)Br$_2$** (**Figure 6**, left) both exhibit superficially quasi-reversible voltammetry for the reduction. Experimental formal potentials for chemically-coupled reduction in

MeCN/DMA of **Ni^{II}(IB)Cl_2** and **Ni^{II}(IB)Br_2** are −1.32/−1.47 V and −1.05/−1.23 V vs. $Fc^{+/0}$, respectively (Δ = ~0.27/~0.24 V (~2180/1935 cm^{-1})). Thus, for all solvents used here, it is harder to reduce **Ni^{II}(IB)Cl_2** relative to **Ni^{II}(IB)Br_2**.

Based on the VT UV-vis-NIR data in DMA (**Section 2.4**), both the Ni^{II} four-coordinate and five-coordinate solvent adducts exist in equilibrium, and this can potentially influence the electrochemistry measured in this solvent. One possibility for the reduction mechanism for these species is reduction followed by halide loss and, for the four-coordinate portion of the complex, coordination of DMA to the Ni^{I} center, which could occur in a concerted or stepwise fashion. For a concerted mechanism, the anticipated shift in peak potential as a function of log(*v*) is 29.6/α mV, where α is the transfer coefficient for electron transfer.[12] Based on the observation of only one differential pulsed voltammetry wave on the forward scan and the shift in peak potential with log(*v*) (~77-104 mV), we propose that the reduction and chemical follow up reaction in both MeCN and DMA (i.e., solvent coordination at Ni^{I}) is a concerted process. The two return waves observed scanning oxidatively suggest generation of a halide-dissociated species that is re-oxidized at more positive potentials. This conclusion is supported by VT differential pulse voltammetry (**Figure S58**), where the differential current at the more positive wave decreases as temperature is decreased, while the differential current at the wave ascribed to re-oxidation of five-coordinate Ni^{I} increases. Based on behavior previously observed for these systems and our computed formal potentials,[17] the more positive re-oxidation could arise from re-oxidation of a Ni^{I}/Ni^{I} dimer that forms after the initial reduction. However, we favor the interpretation featuring re-oxidation of the halide-dissociated species based on computed formal potentials (**Table 5**) and lack of return oxidation near the reduction

event in DCM, where Ni^{I} is anticipated to dimerize rapidly. Further supporting our hypothesis, an additional wave near where three-coordinate Ni^{I} is predicted to oxidize is present in MeCN, but not in DMA (**Figures S52** and **S54**), supporting the weaker coordination affinity of MeCN and our assignment of the species generated upon reduction.

Potentials for chemically-coupled reductions in DMA are more cathodic relative to MeCN by ~200 mV for both complexes. As discussed in **Section 3.3** of the main text, this difference is ascribed to DMA being a higher donicity solvent and coordinating to the Ni^{II} center. Note that solvent coordination is not observed in DCM and only weakly so in MeCN. Indeed, DFT calculations suggest the chemically-coupled reductions of DMA-coordinated **Ni^{II}(IB)Cl_2** and **Ni^{II}(IB)Br_2** are ~0.17 V and ~0.05 V more negative. It is further interesting to note that the reduction potential for **Ni^{II}(IB)Cl_2** in both DCM and DMA is −1.47 V vs. $Fc^{+/0}$, respectively; for **Ni^{II}(IB)Br_2**, these are −1.26 V and −1.23 V vs. $Fc^{+/0}$, respectively. The similarity in reduction potentials in DCM and DMA is ascribed to the relative Fc formal potentials in DCM vs. DMA and the role of solvent in facilitating the Ni–X bond rupture upon one-electron reduction, with the anionic halide loss more facile in DMA relative to DCM. Because of these considerations and the electronic structure calculations presented in **Section 3.3**, the more quantitative comparison of potentials for the reduction with and without coordinated solvent is that between MeCN and DMA. Furthermore, the temperature-dependent cyclic voltammetry demonstrates a cathodically shifted reduction potential as the temperature is lowered, which may be due to increasing the relative amount of five-coordinate species. Thus, overall, solvent coordination results in a harder to reduce Ni^{II} center. By extension, this can be further

translated to a more reducing Ni^{I} species, which, under catalytic conditions, can facilitate oxidative addition (see **Discussion** in the main text).[19]

Ligand field and bonding effects on Ni^{II}-based redox potentials can be further elucidated using electronic structure calculations (**Section 3.3**) and through correlations to electronic spectroscopy, as transitions to the RAMO are also observed experimentally. Differences in measured redox potentials correlate directly with specific structural influences on the energy of the RAMO.

Finally, based on the measured formal potentials, proposed electrochemical mechanisms, and additional electronic structure calculations of redox potentials (**Section 3.3**), we do not believe $\mathbf{Ni^{0}(IB)X_2}$ (or Ni^{0} in any form) is thermodynamically accessible in the electrochemical window of common electrochemistry solvents, which supports a $Ni^{I/III}$ catalytic cycle for reductive alkenylation and potentially related reactions involving bis(oxazoline)–Ni complexes.[17] No additional reduction beyond Ni^{I} is required for oxidative addition of substrates for which this catalyst has been previously demonstrated to be competent.

2.6.6 Spectroelectrochemistry

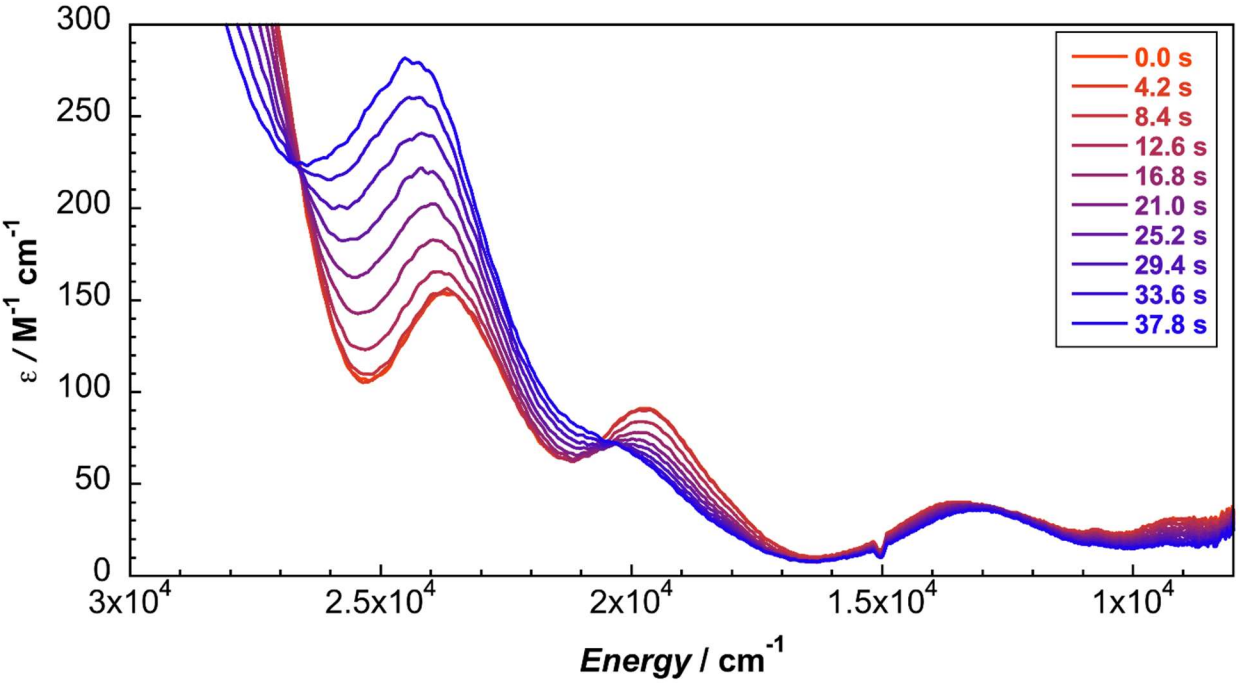

Figure S61. UV-vis-NIR spectral changes during the first 40 s of controlled potential *electrolysis at 0.24 V vs. $Fc^{+/0}$ of* ***$Ni^{II}(IB)Br_2$*** *in 0.1 M $TBAPF_6$ in DMA solution.*

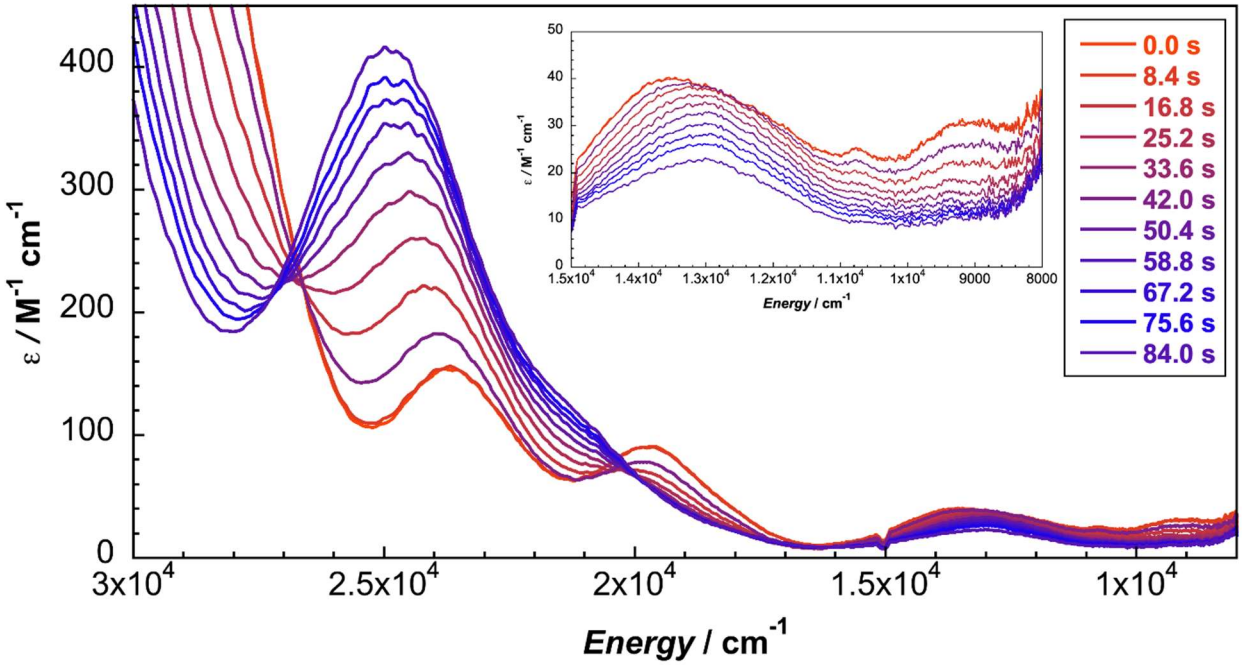

Figure S62*. UV-vis-NIR spectral changes during the first 80 s of controlled potential electrolysis at 0.24 V vs. $Fc^{+/0}$ of* ***$Ni^{II}(IB)Br_2$*** *in 0.1 M $TBAPF_6$ in DMA solution.*

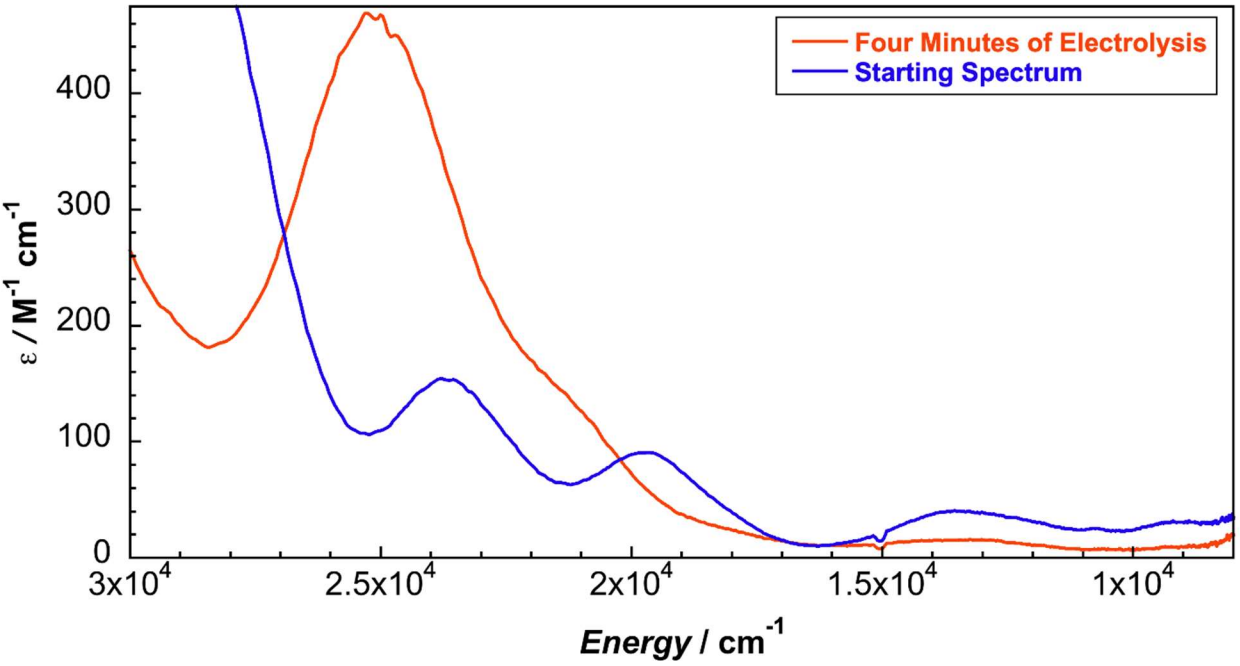

Figure S63. *Starting and ending UV-vis-NIR spectra for four minutes of controlled potential electrolysis at 0.24 V vs. $Fc^{+/0}$ of* ***$Ni^{II}(IB)Br_2$*** *in 0.1 M $TBAPF_6$ in DMA solution.*

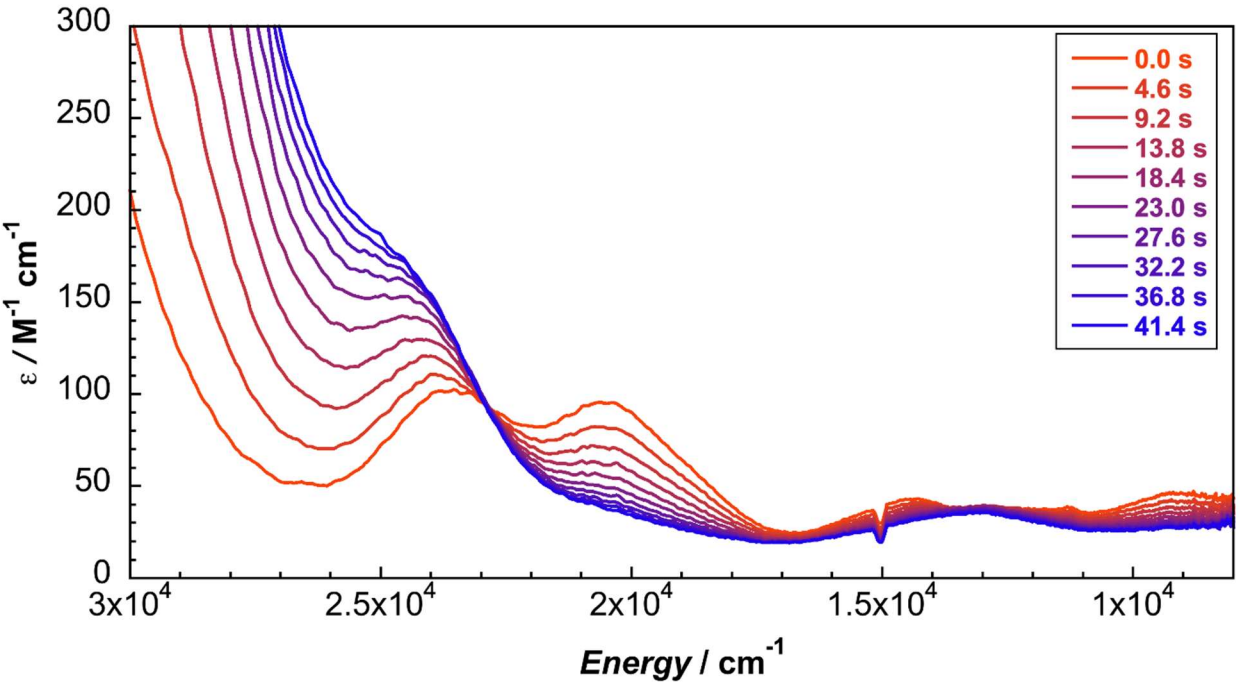

Figure S64. *UV-vis-NIR spectral changes during the first 40 s of controlled potential electrolysis at 0.70 V vs. $Fc^{+/0}$ of* ***$Ni^{II}(IB)Cl_2$*** *in 0.1 M $TBAPF_6$ in DMA solution.*

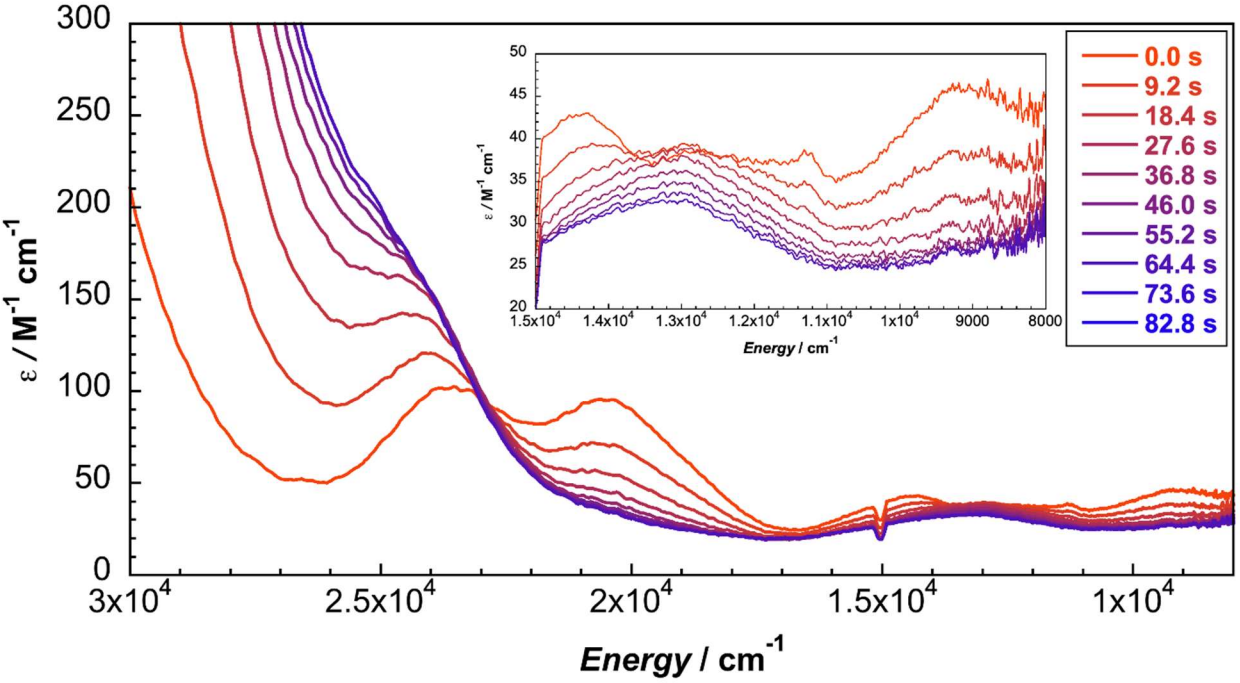

Figure S65. *UV-vis-NIR spectral changes during the first 80 s of controlled potential electrolysis at 0.70 V vs. $Fc^{+/0}$ of* ***$Ni^{II}(IB)Cl_2$*** *in 0.1 M $TBAPF_6$ in DMA solution.*

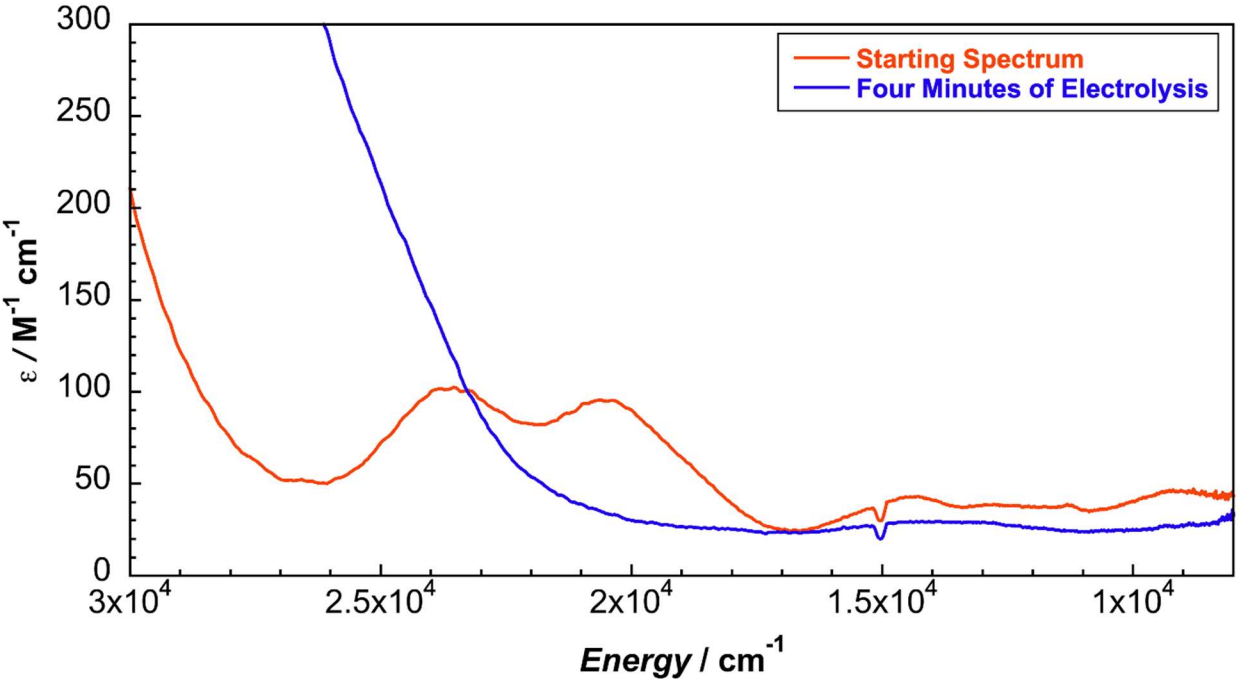

Figure S66. Starting and ending UV-vis-NIR spectra for four minutes of controlled potential electrolysis at 0.70 V vs. Fc+/0 of NiII(IB)Cl2 in 0.1 M TBAPF6 in DMA solution.

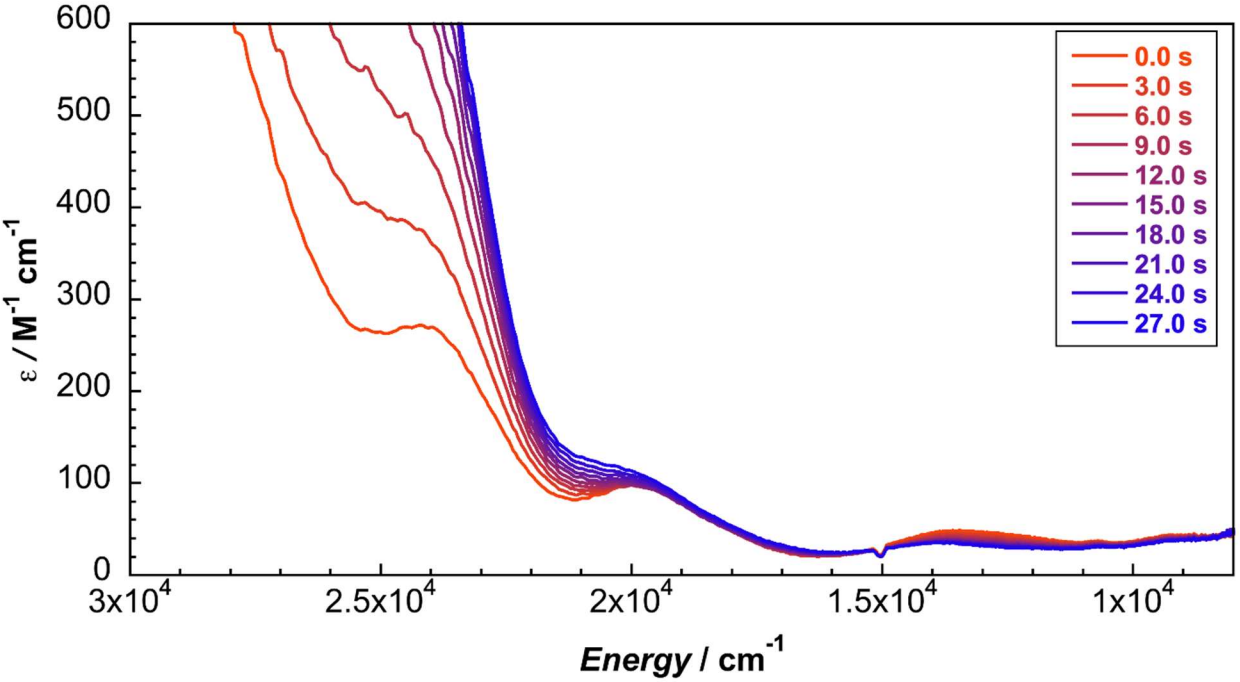

Figure S67. *UV-vis-NIR spectral changes during the first 30 s of controlled potential electrolysis at −1.60 V vs. $Fc^{+/0}$ of $Ni^{II}(IB)Br_2$ in 0.1 M $TBAPF_6$ in DMA solution.*

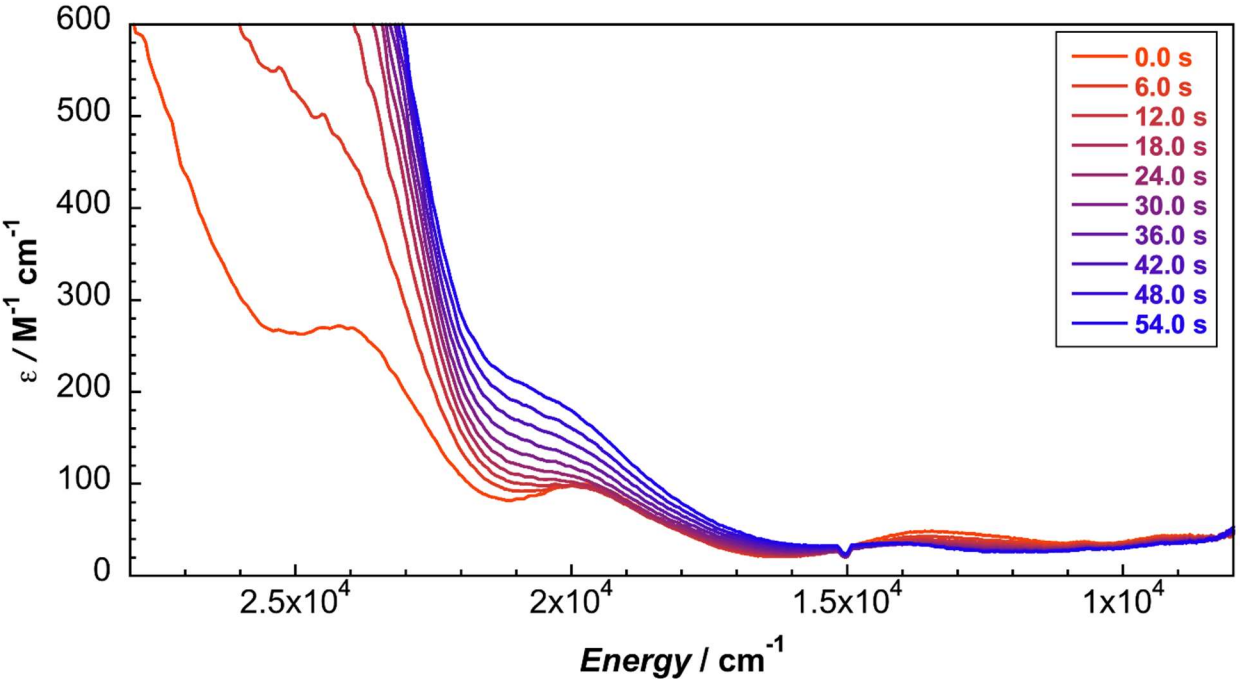

Figure S68*. UV-vis-NIR spectral changes during the first 55 s of controlled potential electrolysis at −1.60 V vs. $Fc^{+/0}$ of* ***$Ni^{II}(IB)Br_2$*** *in 0.1 M $TBAPF_6$ in DMA solution.*

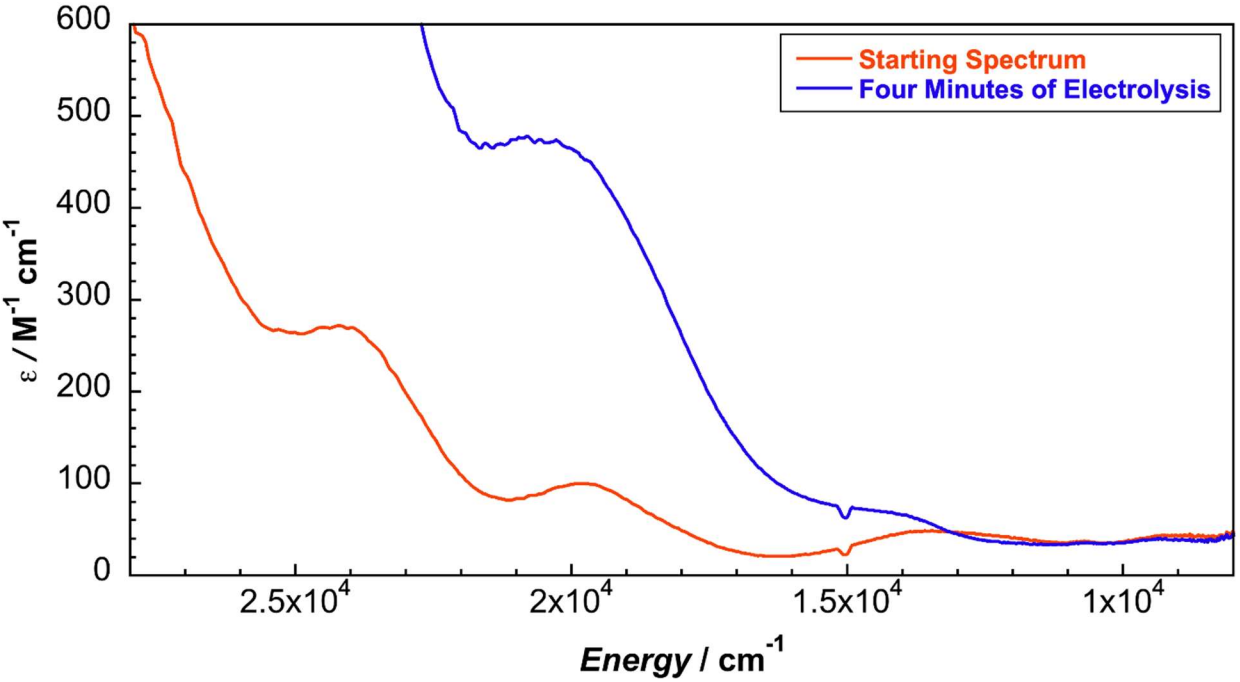

Figure S69. *Starting and ending UV-vis-NIR spectra for four minutes of controlled potential electrolysis at −1.60 V vs. $Fc^{+/0}$ of* ***Ni^{II}(IB)Br_2*** *in 0.1 M $TBAPF_6$ in DMA solution.*

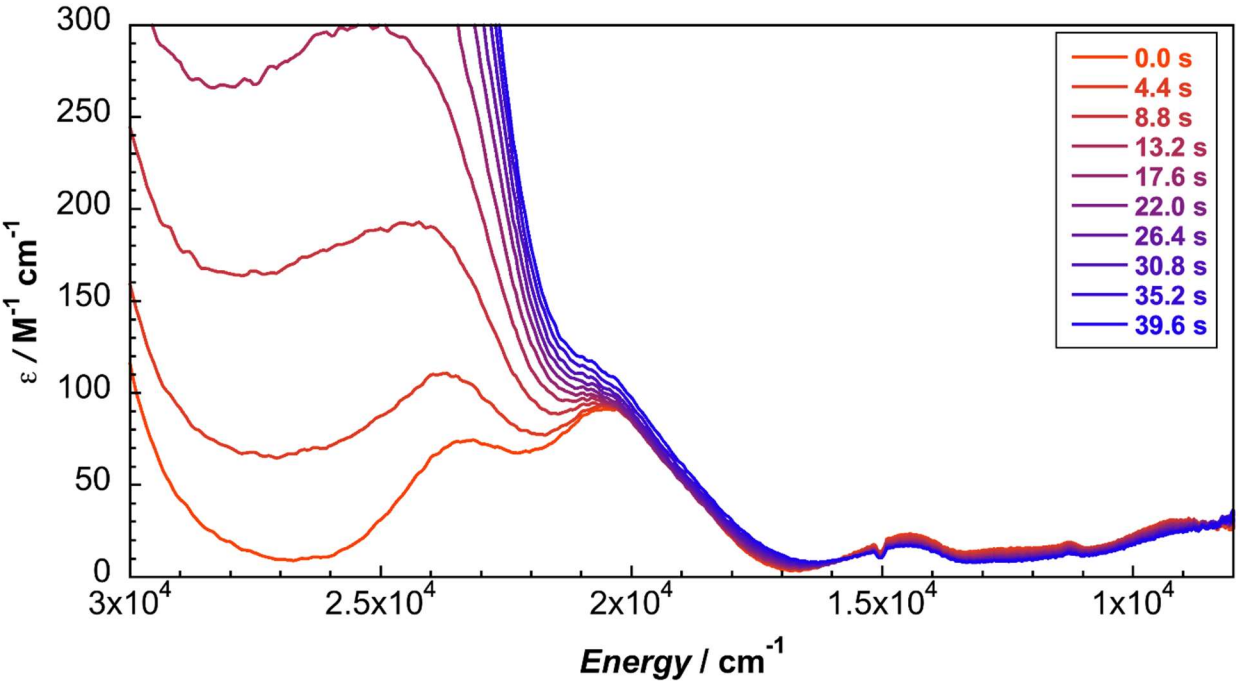

Figure S70. *UV-vis-NIR spectral changes during the first 40 s of controlled potential electrolysis at −1.80 V vs. $Fc^{+/0}$ of* ***Ni^{II}(IB)Cl_2*** *in 0.1 M $TBAPF_6$ in DMA solution.*

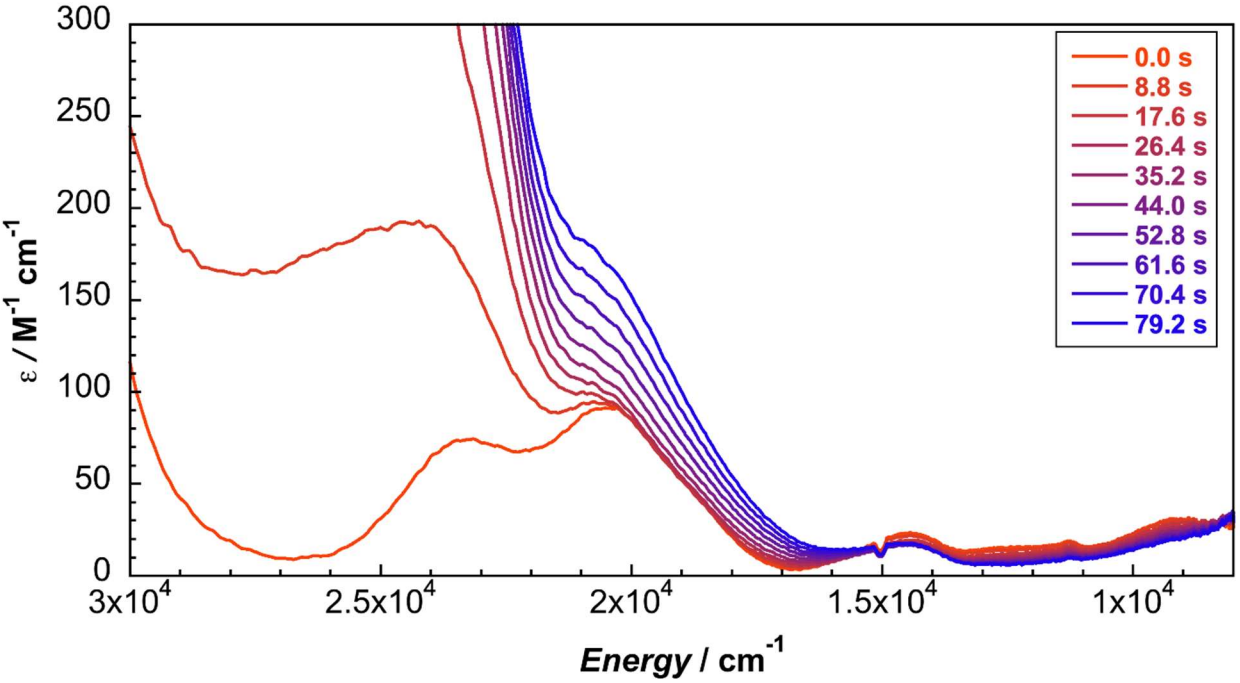

Figure S71. *UV-vis-NIR spectral changes during the first 40 s of controlled potential electrolysis at −1.80 V vs. $Fc^{+/0}$ of* ***$Ni^{II}(IB)Cl_2$*** *in 0.1 M $TBAPF_6$ in DMA solution.*

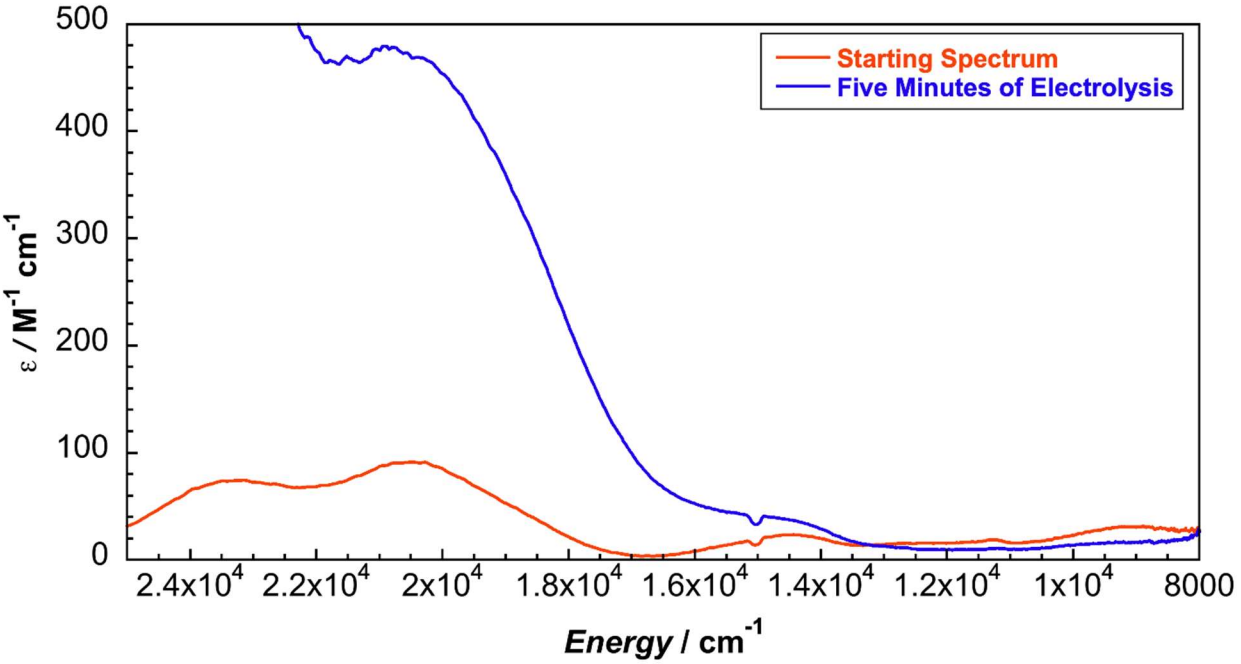

Figure S72. *Starting and ending UV-vis-NIR spectra for four minutes of controlled potential electrolysis at −1.80 V vs. $Fc^{+/0}$ of* ***$Ni^{II}(IB)Cl_2$*** *in 0.1 M $TBAPF_6$ in DMA solution.*

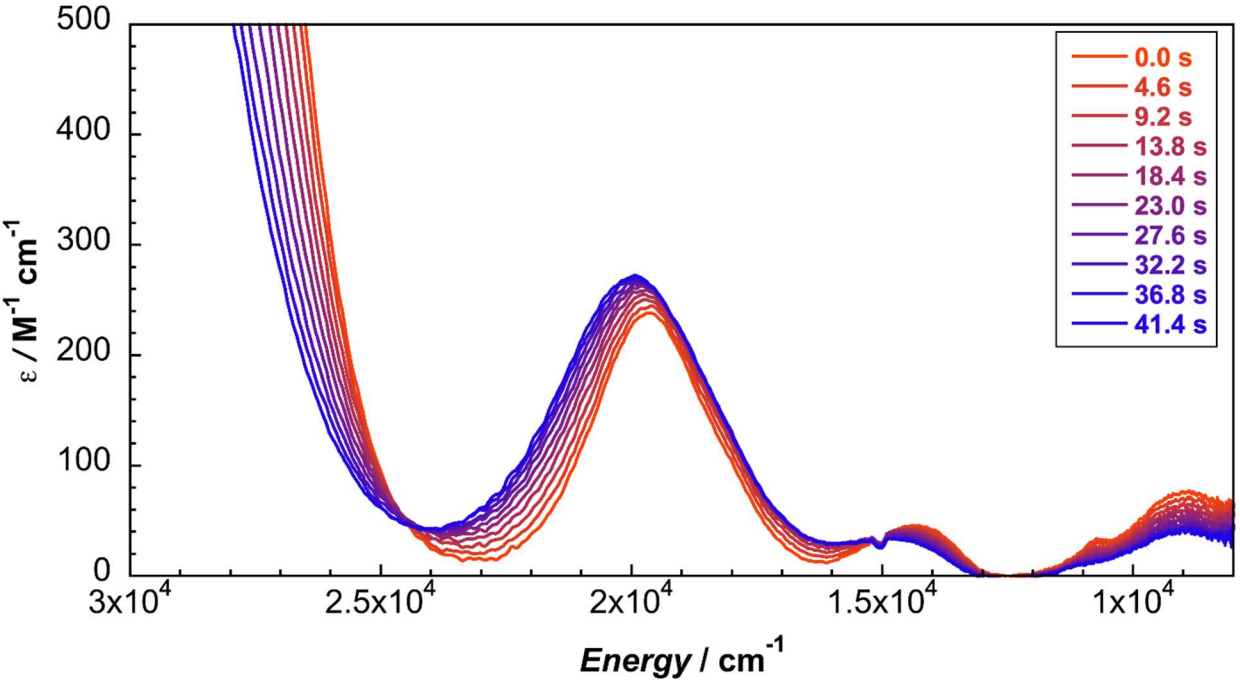

***Figure S73**. UV-vis-NIR spectral changes during the first 40 s of controlled potential electrolysis at −1.50 V vs. $Fc^{+/0}$ of **$Ni^{II}(IB)Br_2$** in 0.2 M $TBAPF_6$ in DCM solution.*

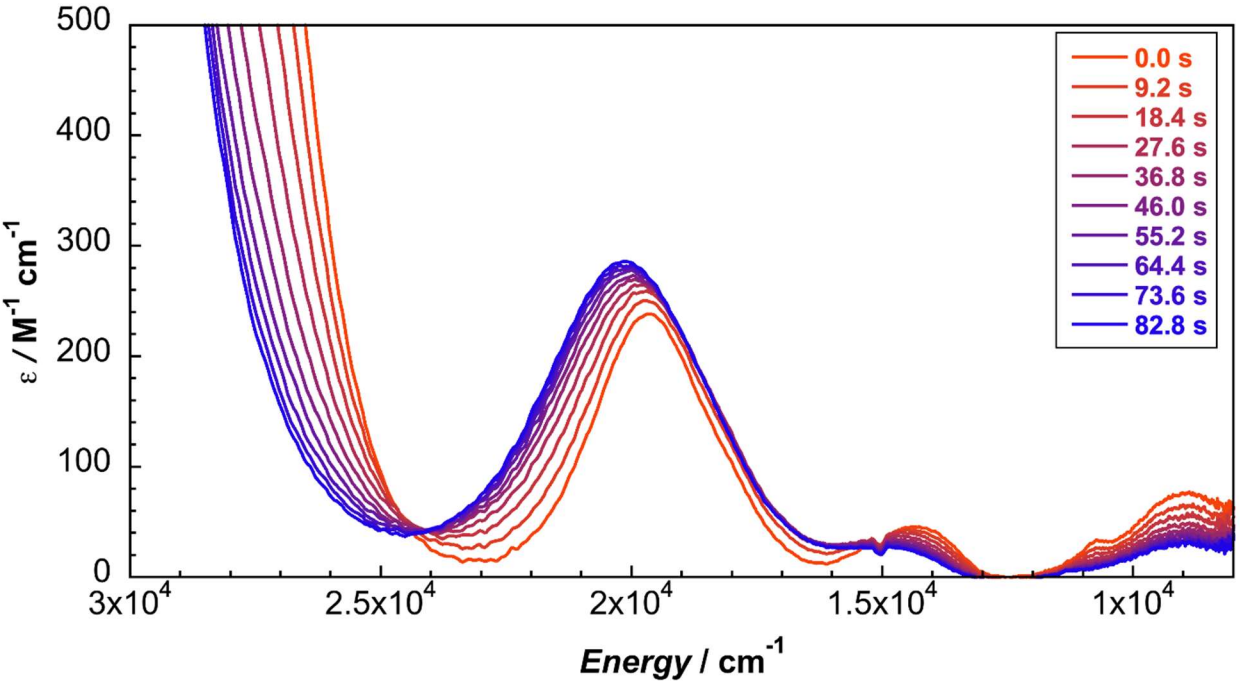

***Figure S74**. UV-vis-NIR spectral changes during the first 80 s of controlled potential electrolysis at −1.50 V vs. $Fc^{+/0}$ of **$Ni^{II}(IB)Br_2$** in 0.2 M $TBAPF_6$ in DCM solution.*

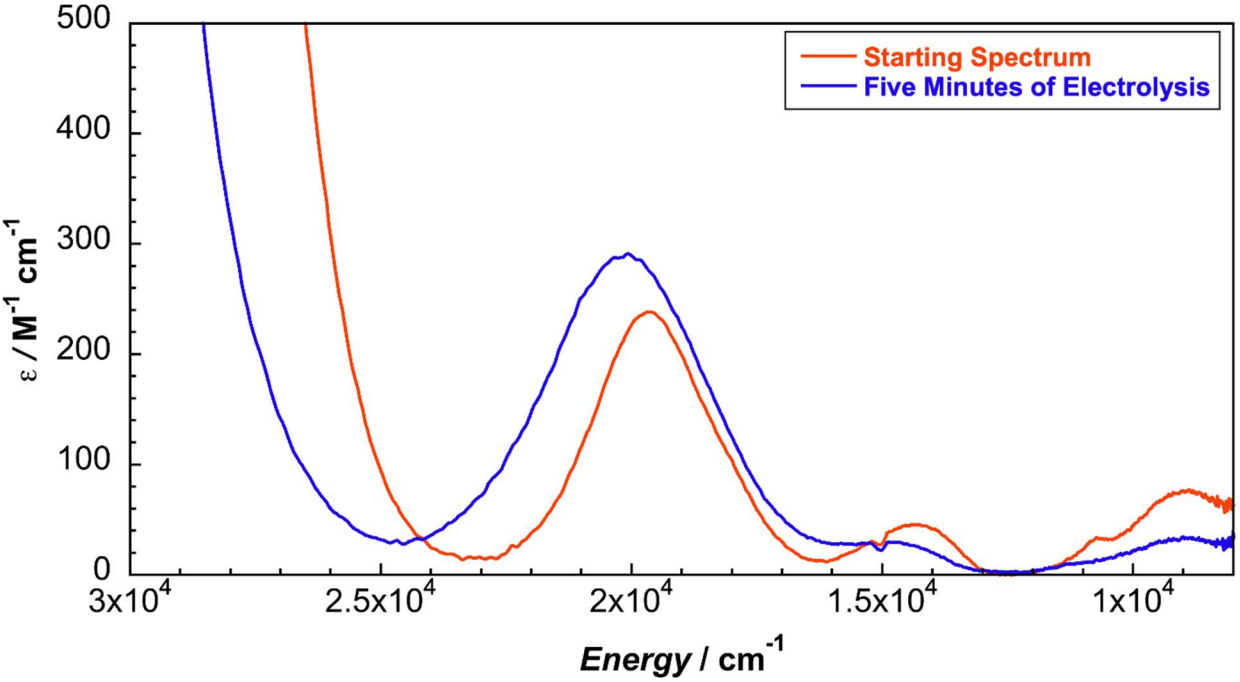

***Figure S75**. Starting and ending UV-vis-NIR spectra for five minutes of controlled potential electrolysis at −1.50 V vs. $Fc^{+/0}$ of **Ni^{II}(IB)Br_2** in 0.2 M $TBAPF_6$ in DCM solution.*

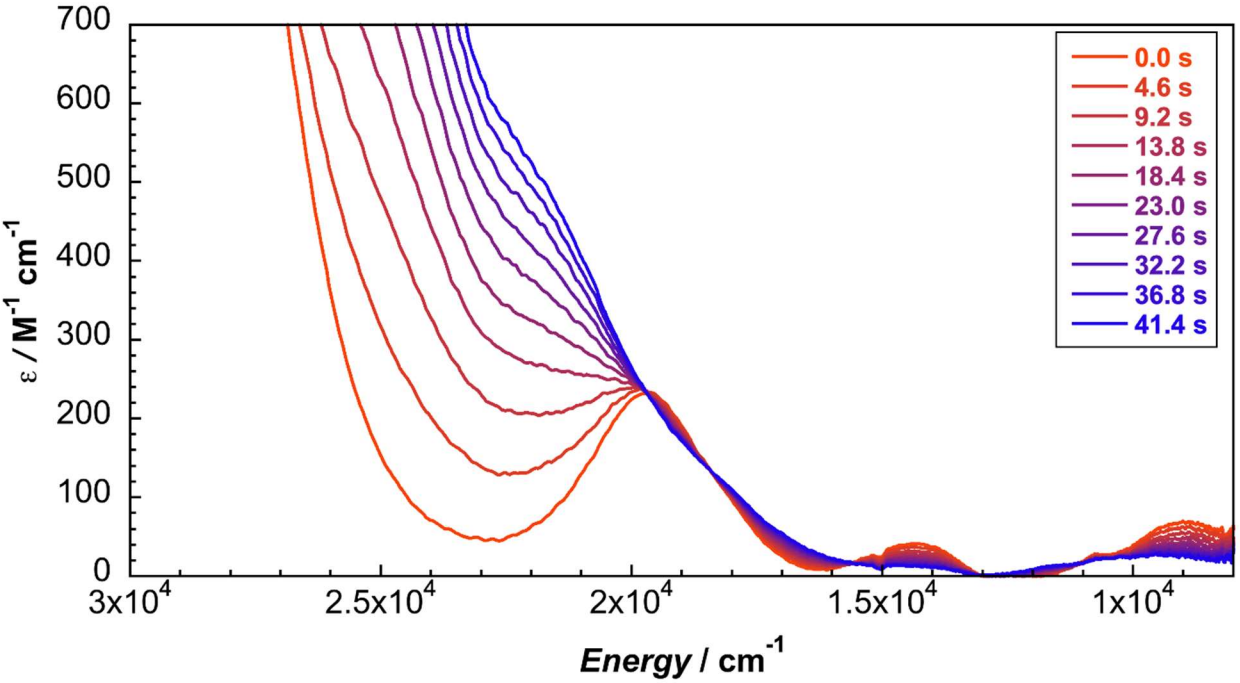

***Figure S76**. UV-vis-NIR spectral changes during the first 40 s of controlled potential electrolysis at 1.20 V vs. $Fc^{+/0}$ of **Ni^{II}(IB)Br_2** in 0.2 M $TBAPF_6$ in DCM solution.*

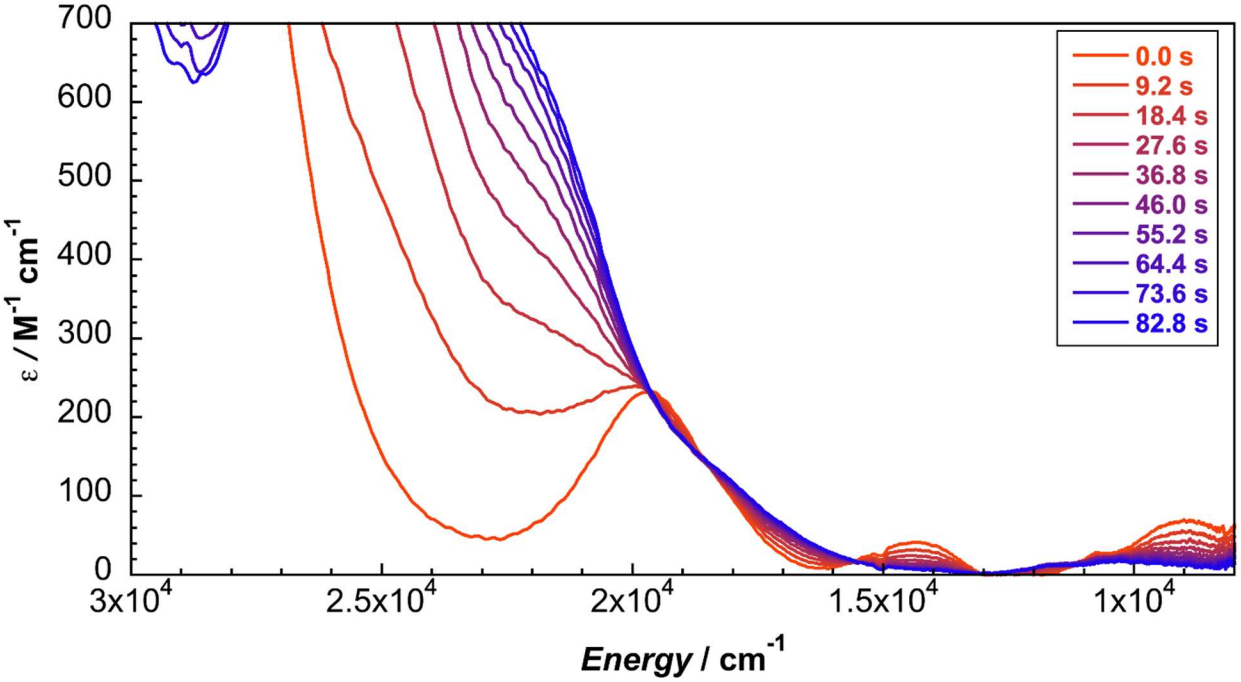

***Figure S77**. UV-vis-NIR spectral changes during the first 80 s of controlled potential electrolysis at 1.20 V vs. $Fc^{+/0}$ of **$Ni^{II}(IB)Br_2$** in 0.2 M $TBAPF_6$ in DCM solution.*

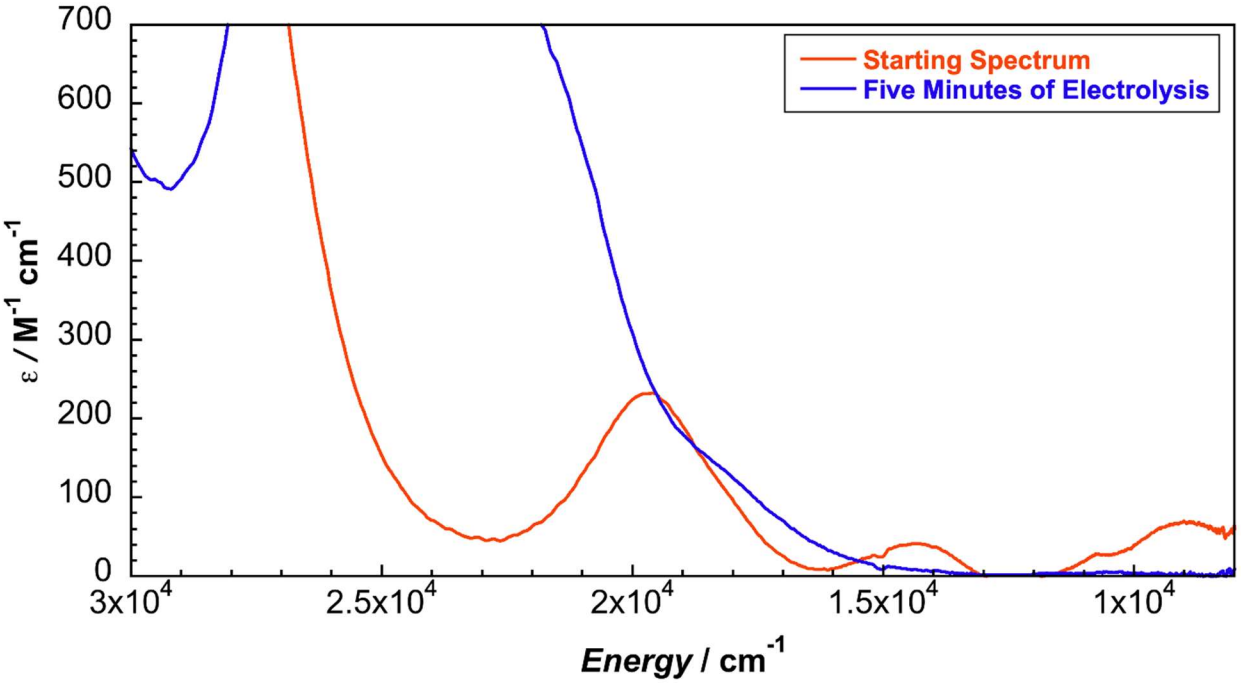

***Figure S78**. Starting and ending UV-vis-NIR spectra for five minutes of controlled potential electrolysis at 1.20 V vs. $Fc^{+/0}$ of **$Ni^{II}(IB)Br_2$** in 0.2 M $TBAPF_6$ in DCM solution.*

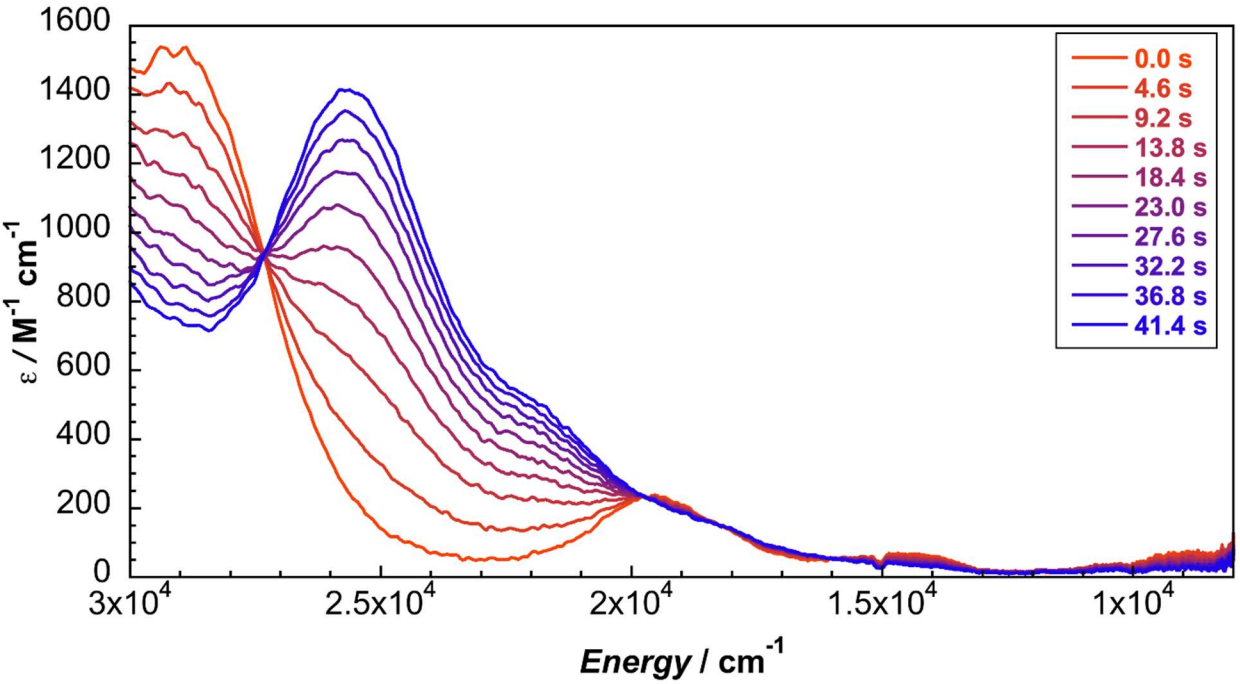

***Figure S79**. UV-vis-NIR spectral changes (diluted) during the first 40 s of controlled potential electrolysis at 1.20 V vs. $Fc^{+/0}$ of **$Ni^{II}(IB)Br_2$** in 0.1 M $TBAPF_6$ in DCM solution.*

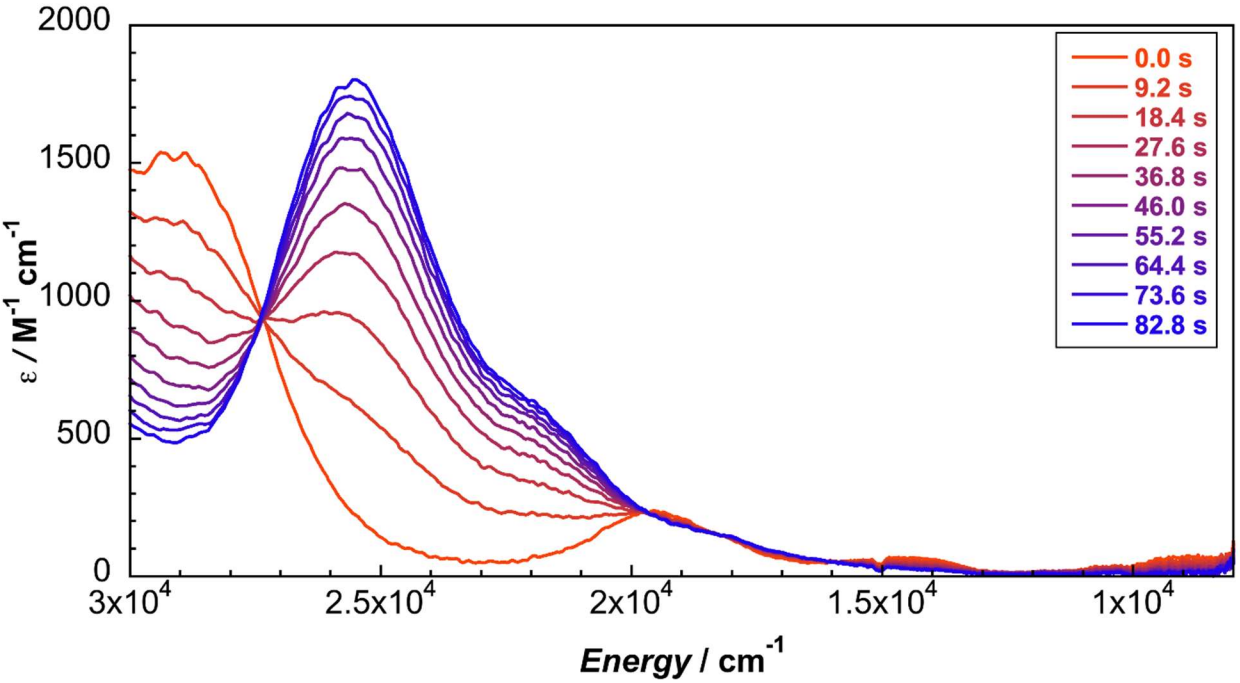

***Figure S80**. UV-vis-NIR spectral changes (diluted) during the first 80 s of controlled potential electrolysis at 1.20 V vs. $Fc^{+/0}$ of **$Ni^{II}(IB)Br_2$** in 0.1 M $TBAPF_6$ in DCM solution.*

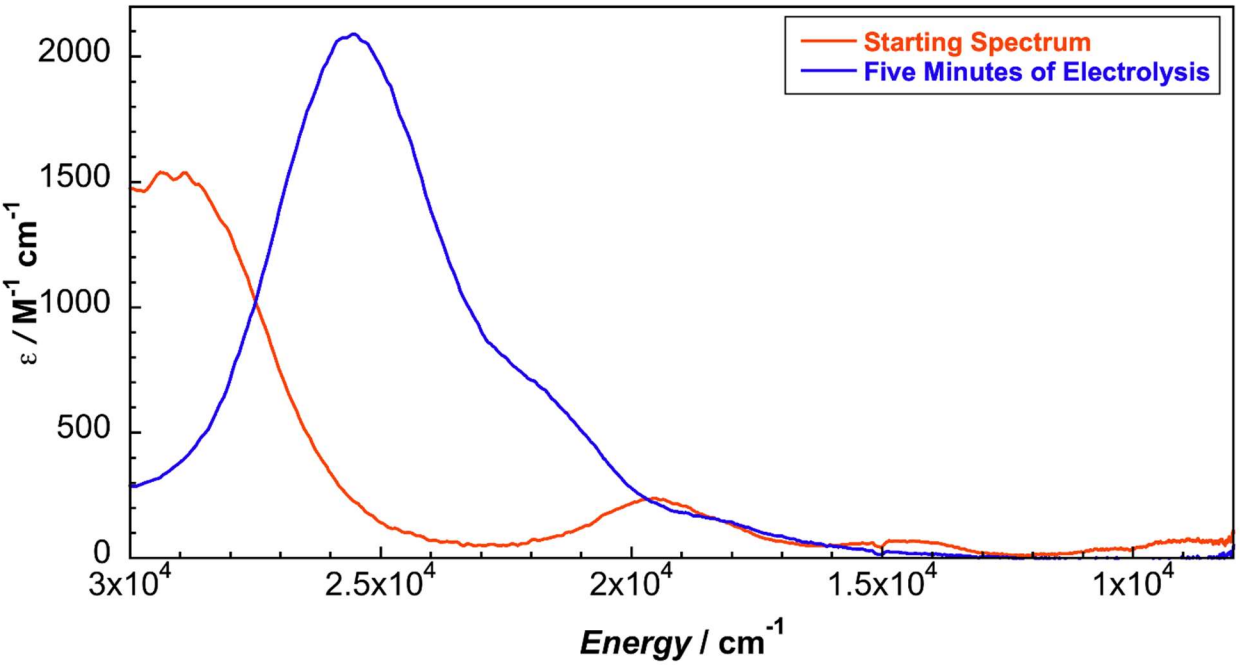

***Figure S81**. Starting and ending UV-vis-NIR spectra for five minutes of controlled potential electrolysis at 1.20 V vs. $Fc^{+/0}$ of **Ni^{II}(IB)Br_2** in 0.1 M $TBAPF_6$ in DCM solution.*

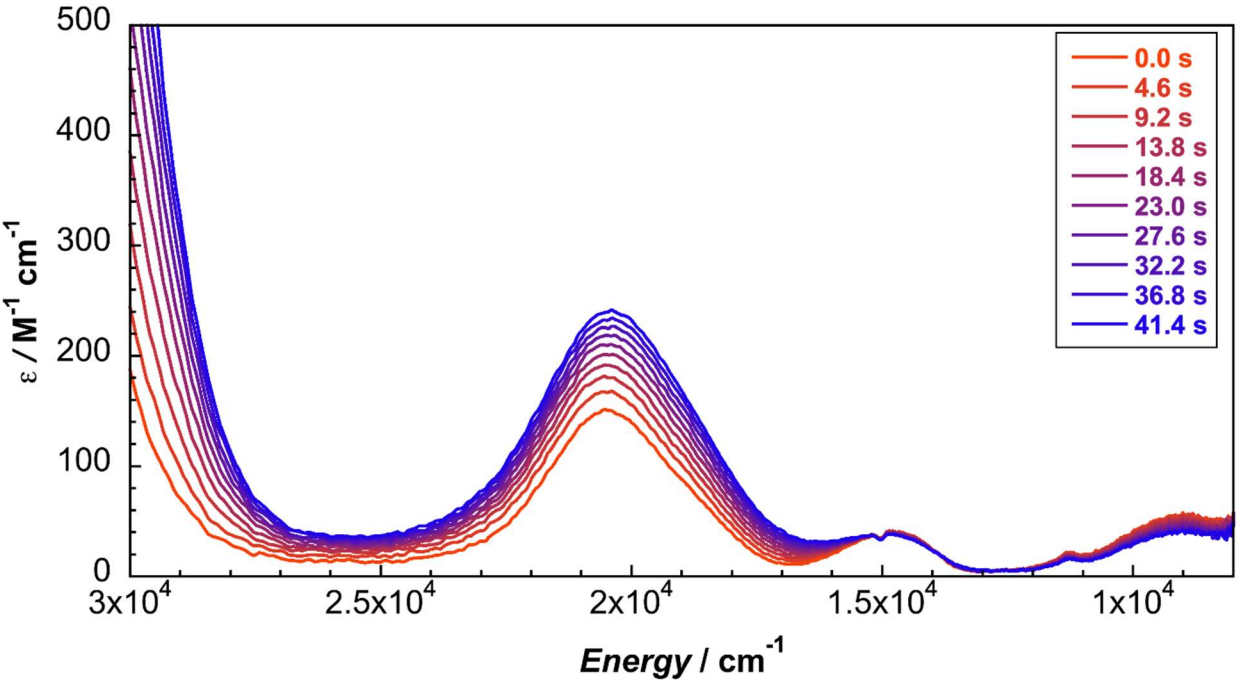

***Figure S82.** UV-vis-NIR spectral changes during the first 40 s of controlled potential electrolysis at −1.50 V vs. $Fc^{+/0}$ of Ni^{II}(IB)Cl_2 in 0.2 M $TBAPF_6$ in DCM solution.*

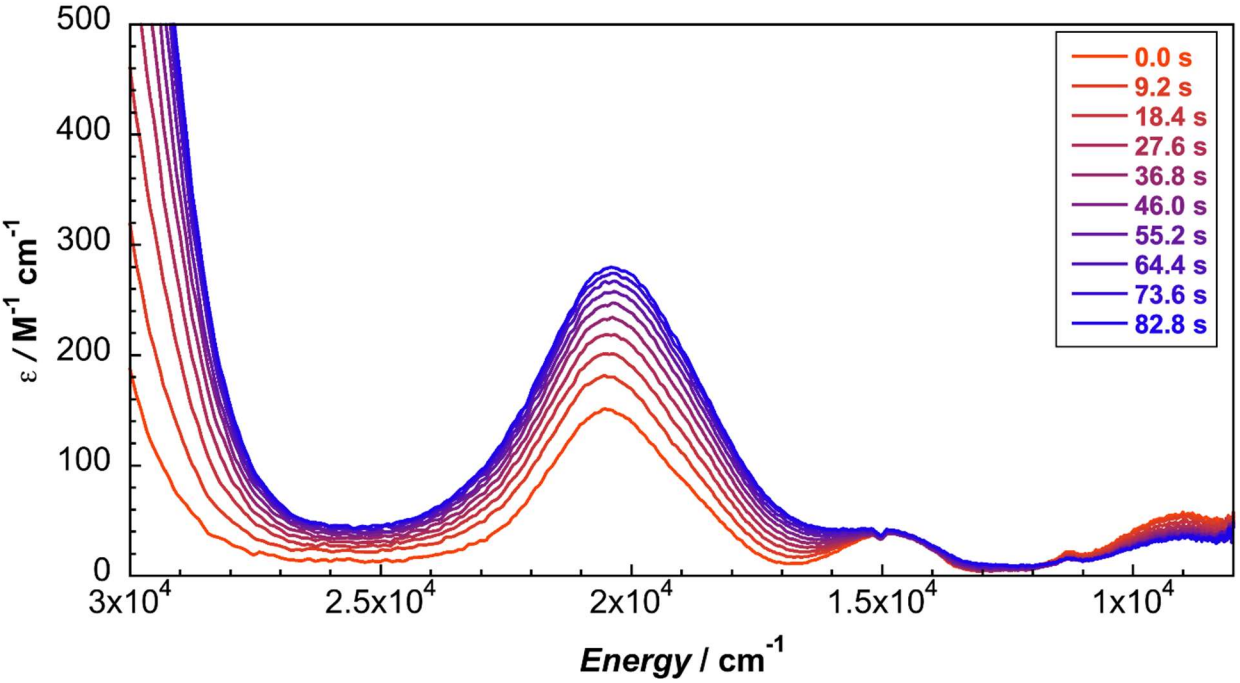

***Figure S83**. UV-vis-NIR spectral changes during the first 80 s of controlled potential electrolysis at −1.50 V vs. $Fc^{+/0}$ of **$Ni^{II}(IB)Cl_2$** in 0.2 M $TBAPF_6$ in DCM solution.*

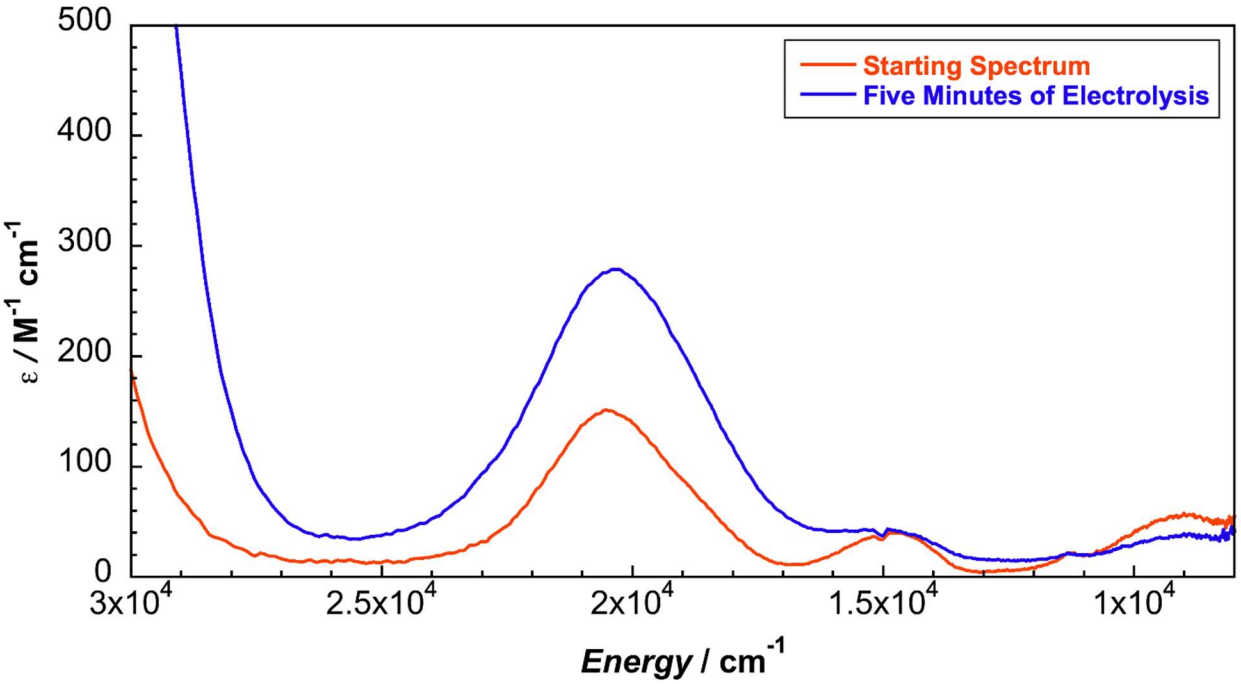

***Figure S84**. Starting and ending UV-vis-NIR spectra for five minutes of controlled potential electrolysis at −1.50 V vs. $Fc^{+/0}$ of **$Ni^{II}(IB)Cl_2$** in 0.2 M $TBAPF_6$ in DCM solution.*

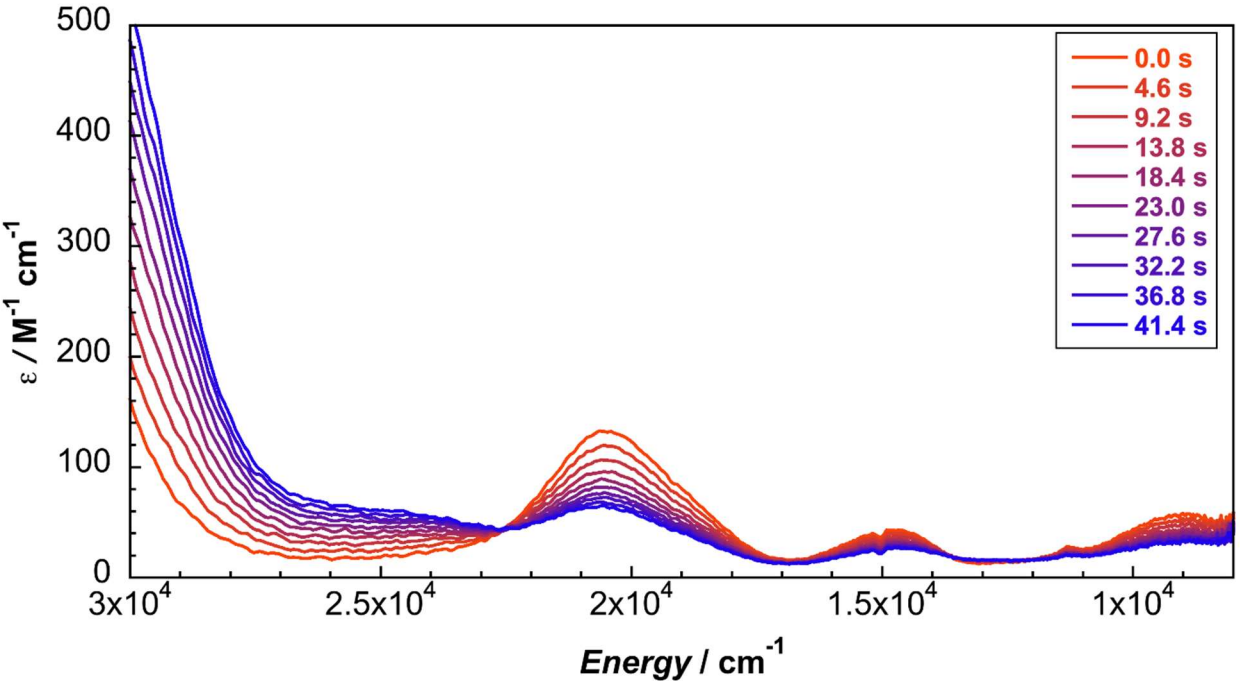

Figure S85. UV-vis-NIR spectral changes during the first 40 s of controlled potential electrolysis at 1.50 V vs. $Fc^{+/0}$ of $Ni^{II}(IB)Cl_2$ in 0.2 M $TBAPF_6$ in DCM solution.

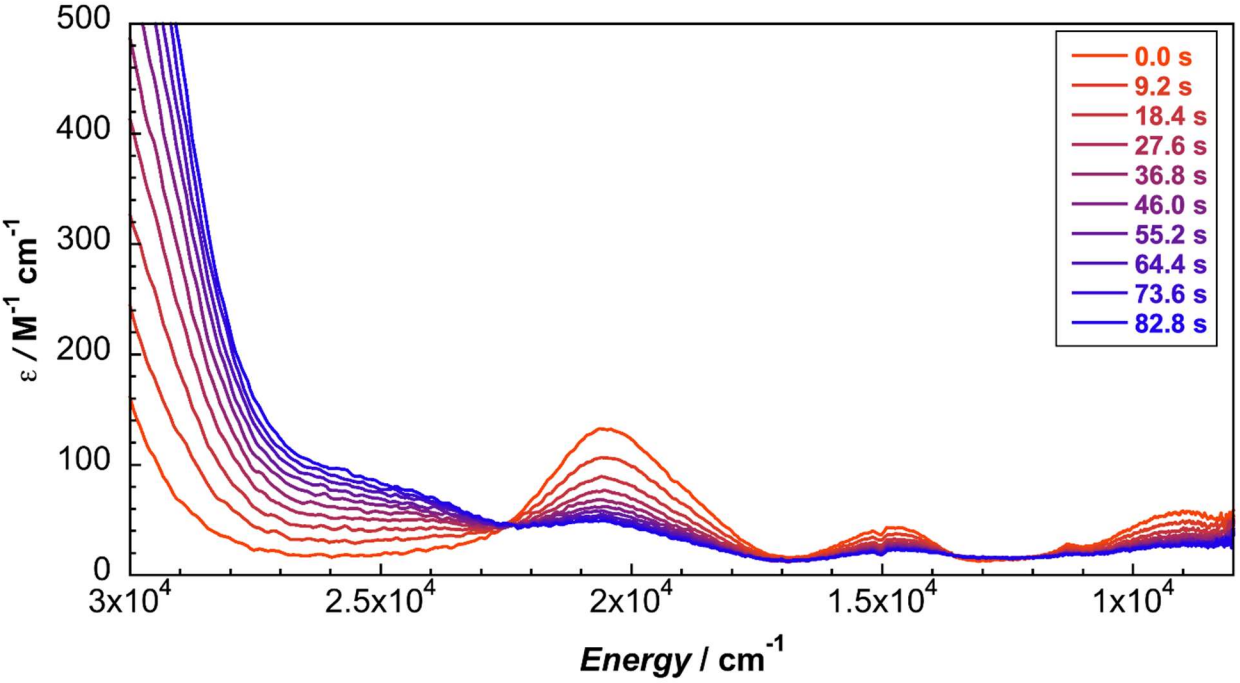

***Figure S86**. UV-vis-NIR spectral changes during the first 80 s of controlled potential electrolysis at 1.50 V vs. $Fc^{+/0}$ of **$Ni^{II}(IB)Cl_2$** in 0.2 M $TBAPF_6$ in DCM solution.*

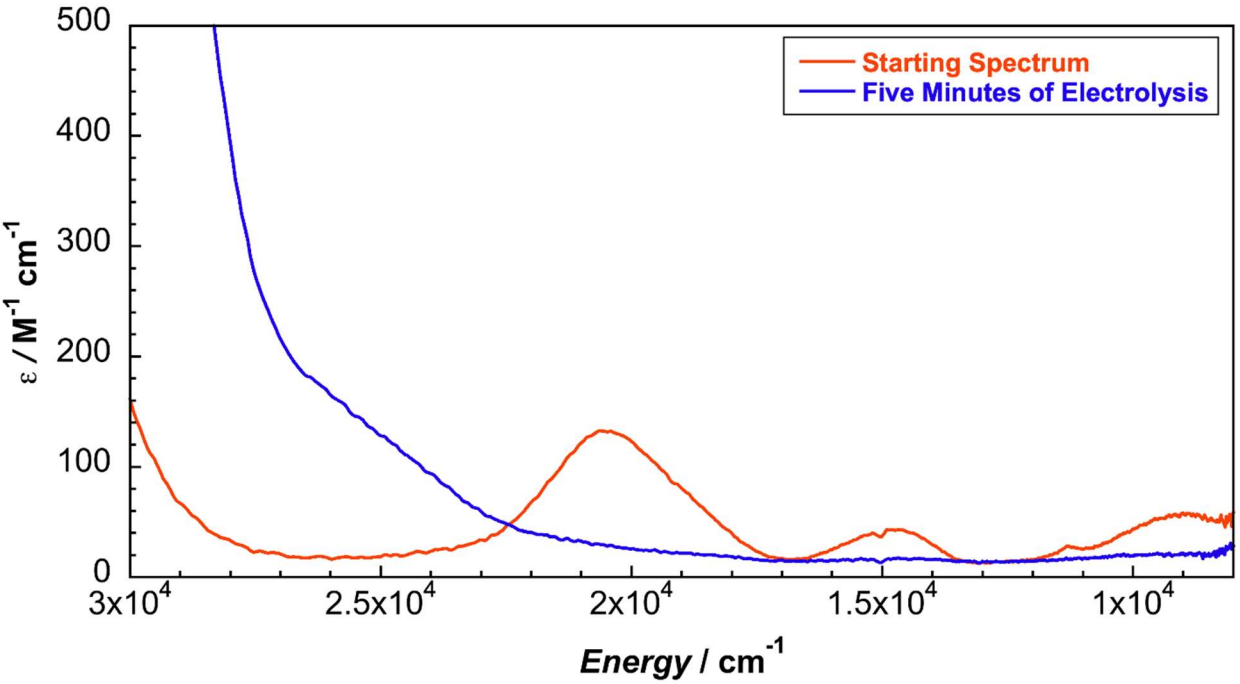

Figure S87. *Starting and ending UV-vis-NIR spectra for five minutes of controlled potential electrolysis at 1.50 V vs. $Fc^{+/0}$ of $Ni^{II}(IB)Cl_2$ in 0.2 M $TBAPF_6$ in DCM solution.*

2.6.7 X-ray Crystalographic Data

Collection and Refinement of Zinc(II) bis(chloride) (3a*R*,3a'*R*,8a*S*,8a'*S*)-2,2'-(cyclopropane-1,1-diyl)bis(3a,8a-dihydro- 8*H*-indeno[1,2-*d*]oxazole) [Zn(IB)Cl$_2$]

Low-temperature diffraction data (ϕ-and ω-scans) were collected on a Bruker AXS KAPPA APEX II diffractometer coupled to a PHOTON 100 CMOS detector with graphite monochromated Mo K_α radiation (λ = 0.71073 Å) for the structure of compound **Zn^{II}(IB)Cl$_2$**. The structure was solved by direct methods using SHELXL[20] and refined against F^2 on all data by full-matrix least squares with SHELXL-2019[21] using established refinement techniques.[22] All non-hydrogen atoms were refined anisotropically. All hydrogen atoms were included into the model at geometrically calculated positions and refined using a riding model. The isotropic displacement parameters of all hydrogen atoms

were fixed to 1.2 times the *U* value of the atoms they are linked to (1.5 times for methyl groups). All disordered atoms were refined with the help of similarity restraints on the 1,2- and 1,3-distances and displacement parameters as well as rigid bond restraints for anisotropic displacement parameters. **Zn^{II}(IB)Cl_2** crystallizes in the orthorhombic space group $P2_12_12_1$ with one molecule in the asymmetric unit. A Dow Next Generation Instrumentation Grant supported this work performed by the X-Ray Crystallography Facility (XRCF) in the Beckman Institute (BI) at Caltech.

The B Level Alert results from a very small ESD value (0.003). Since the Flack value (0.05) is very small, the absolute configuration of the molecule is correct. We attempted to add TWIN and BASF and refine the structure, which did not remove the alert.

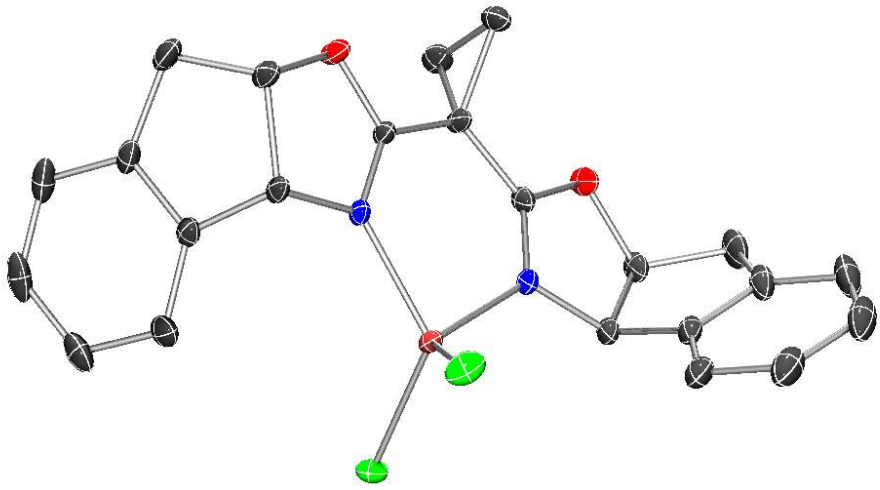

Figure S88. *Molecular structure of the asymmetric unit of* ***$Zn^{II}(IB)Cl_2$****. Thermal ellipsoids set at 50% probability. Hydrogens omitted for clarity.*

Table S3. *Crystal data and structure refinement for* ***Zn(IB)Cl$_2$.***

Empirical formula	C23 H20 N2 O2 Cl2 Zn	
Formula weight	492.68	
Temperature	100(2) K	
Wavelength	0.71073 Å	
Crystal system	orthorhombic	
Space group	$P2_12_12_1$	
Unit cell dimensions	a = 9.323(3) Å	α= 90°.
	b = 10.617(3) Å	β= 90°.
	c = 21.782(3) Å	γ = 90°.
Volume	2156.1(9) Å^3	
Z	4	
Density (calculated)	1.518 g/cm^3	
Absorption coefficient	1.401 mm^{-1}	
F(000)	1008.0	
Crystal size	0.200 x 0.250 x 0.300 mm^3	
Theta range for data collection	3.74 to 72.68°.	
Index ranges	$-15 \leq h \leq 15$, $-17 \leq k \leq 17$, $-36 \leq l \leq 33$	
Reflections collected	54043	
Independent reflections	10439 [R_{int} = 0.0392]	
Completeness to theta = 50.5°	99.40 %	
Absorption correction	Semi-empirical from equivalents	
Max. and min. transmission	0.7471 and 0.6611	
Refinement method	Full-matrix least-squares on F^2	
Data / restraints / parameters	10439 / 0 / 271	
Goodness-of-fit on F^2	1.066	
Final R indices [I > 2σ(I)]	R_1 = 0.0314, wR_2 = 0.0775	
R indices (all data)	R_1 = 0.0349, wR_2 = 0.0789	
Extinction coefficient	n/a	
Largest diff. peak and hole	1.03 and −0.43 e A^{-3}	

2.6.8 TDDFT and CASSCF+NEVPT2 Results and Inputs

Density Functional Theory

All DFT calculations were carried out using ORCA 5.0.3.[23] The structures were optimized using the BP86 functional,[9] the hybrid basis set def2-TZVP/def2-TZVPP(Ni),[24] and the D3BJ dispersion correction.[25,26] The effect of solvation on geometry optimizations was included by employing the conductor-like polarizable continuum model (CPCM)[27,28]

with a dielectric constant of ε = 38 to model DMA solvent. The calculations were accelerated by resolution-of-identity approximation (RI).[29]

For the equilibrium geometries, the terms contributing to Gibbs free energy were calculated as follows:

$$G = E_{el} + G_{solv} + [E_{ZPVE} + RT - RTlnQ], \quad (3)$$

where:

i) E_{el} is the *in vacuo* electronic energy, calculated using RI-TPSSh-D3BJ method,

ii) G_{solv} is the free energy of solvation; calculated using the conductor-like polarizable continuum model (CPCM),

iii) $[E_{ZPVE} + RT - RT \ln Q]$ corresponds to the thermal enthalpic and entropic contributions to the solute energy with E_{ZPVE} and Q being the zero-point vibrational energy and the molecular partition function, respectively; obtained from frequency calculations with the rigid rotor/harmonic oscillator approximation (for p = 1 bar, T = 298 K).

The standard one-electron reduction potentials ($E°$ in V) were calculated from the change of the Gibbs free energy from eq. 3 upon 1e$^-$ reduction of the solute, Ox (aq) + e^- → Red (aq):

$$E° \text{ [V]} = G_{\text{Ox}} \text{ [eV]} - G_{\text{Red}} \text{ [eV]} + \Delta E°_{\text{abs}}(\text{reference}) \text{ [eV]}, \quad (4)$$

where G_{Ox}/G_{Red} are the Gibbs free energies of the oxidized/reduced state of a solute, and $\Delta E°_{abs}$(reference) is the absolute potential of a reference electrode, which is required to compare computations with experiment. We have referenced the potentials to the $Fc^{+/0}$ absolute potential calculated using the same methodology as for the calculations of the

Gibbs free energies of the Ni catalysts (*vide infra*), yielding a value of –4.55 eV in DMA solvent.

Time-Dependent Density Functional Theory

To compare computed electronic absorption spectra with experimental UV-vis-NIR spectra, we have performed TD-DFT calculations using TPSSh[30,31] on top of the DFT optimized (BP86) geometries.

Multiconfiguration Self-Consistent Field (MCSCF) Calculations

As implemented in the ORZ code, multiconfigurational/multireference approximations to wave function theory: CASSCF/MS-CASPT2[32–37] were performed in combination with the ANO-RCC basis set[38,39] for DFT-optimized structures of Ni catalysts. The ANO-RCC basis set, contracted to ANO-RCC-VTZP for Ni and coordinating atoms and ANO-RCC-VDZP for the rest was used. The second-order Douglas−Kroll−Hess (DKH2) one-electron spin-less Hamiltonian was applied for all WFT-based calculations to allow for spin-free relativistic effects.[40–42] The complete active space used in CASSCF calculations is specified in **Figure S91**, with the largest active space investigated herein comprising 22 electrons in 12 orbitals (denoted as 22e,12o) for **Ni^{II}(IB)X_2** complexes. This active space includes 5 x Ni_{3d}, 3 x $halide_{3p/4p}$ (per each halide; i.e., 6 orbitals for dihalide complexes), and 1 x $IB_{\sigma\text{-bonding}}$ orbitals.

Optimized structures of all studied complexes are provided in a separate zip file.

S.8.1. Ground- and Excited-States Calculations with DFT/TDDFT.

Three different DFT functionals with varying amounts of exact exchange were used for comparison of the calculated bond distances of **Ni^{II}(IB)Cl_2** and **Ni^{II}(IB)Br_2** ground states (**Table S4**) and TDDFT electronic transition energies (**Table S5**). We note that the TPSSh functional provides the best overall agreement (considering bond lengths, transition energies, and oscillator strengths) and is used throughout this study for comparison to experiment.

***Table S4**: Comparison of selected bond distances and angles from X-ray crystallography with computed values at various DFT levels (BP86, TPSSh, and B3LYP).*

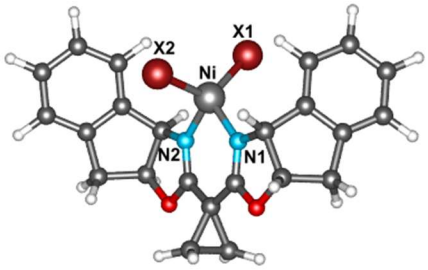

Ni^{II}(IB)Cl_2:

Bond Length (Å)				
Bond	Crystal Structure	BP86	TPSSh	B3LYP
Ni-Cl1	2.2254(6)	2.24	2.25	2.27
Ni-Cl2	2.2330(6)	2.24	2.25	2.28
Ni-N1	1.987(1)	1.96	1.98	2.00
Ni-N2	1.971(1)	1.96	1.97	1.99
Bond Angle (°)				
Angle	Crystal Structure	BP86	TPSSh	B3LYP
Cl1-Ni-Cl2	115.80(2)	129	130	126
Cl1-Ni-N1	118.49(4)	117	119	122
Cl1-Ni-N2	98.70(4)	98	102	103
Cl2-Ni-N1	105.42(4)	98	98	98

Cl2-Ni-N2	126.48(4)	117	102	112
N1-Ni-N2	90.52(5)	92	92	91

$Ni^{II}(IB)Br_2$:

Bond Length (Å)				
Bond	Crystal Structure	BP86	TPSSh	B3LYP
Ni-Br1	2.358(1)	2.39	2.40	2.43
Ni-Br2	2.3749(9)	2.37	2.39	2.42
Ni-N1	1.974(5)	1.95	1.97	1.99
Ni-N2	1.981(5)	1.96	1.97	1.99
Bond Angle (°)				
Angle	Crystal Structure	BP86	TPSSh	B3LYP
Br1-Ni-Br2	117.13(4)	127	132	124
Br1-Ni-N1	124.1(1)	111	111	112
Br1-Ni-N2	101.1(1)	97	99	98
Br2-Ni-N1	100.2(1)	101	100	102
Br2-Ni-N2	122.2(1)	122	115	125
N1-Ni-N2	90.8(2)	92	93	92

An appreciable Ni^{II}–X covalency is observed in these calculated Ni^{II} ground states, with Mulliken spin populations of ~0.17e (summation over Cl atoms) and ~0.19e (summation over Br atoms) resulting from mixing of halide 2*p*/3*p* and Ni 3*d* orbitals. The slightly higher covalency of **Ni^{II}(IB)Br_2** is apparent from the smaller 3*d* orbital character in the β-LUMOs (β-LUMO: 75.5% vs. 73.8%, β-LUMO+1: 73.9% vs. 73.1% for **Ni^{II}(IB)Cl_2** vs. **Ni^{II}(IB)Br_2**). β-LUMO energies are destabilized and less negative for **Ni^{II}(IB)Cl_2** vs. **Ni^{II}(IB)Br_2** (**Figure S89**; β-LUMO: –3.13 eV vs. –3.35 eV, β-LUMO+1: –2.85 eV vs. –2.97 eV, respectively). Since the covalency difference is small, the destabilized β-LUMO energies likely arise from the shorter Ni^{II}–X bonds and the resulting stronger ligand field of the chloride ligands (2.25 Å (Ni–Cl) vs. 2.40 Å (Ni–Br); **Table S4**).

Table S5. TDDFT predicted electronic transitions and their energies for **Ni^{II}(IB)Cl_2** and **Ni^{II}(IB)Br_2** using BP86, TPSSh, and B3LYP functionals.

Predicted Transition	**Predicted Transition Energies (cm^{-1})**					
	Ni^{II}(IB)Cl_2			**Ni^{II}(IB)Br_2**		
	BP86	TPSSh	B3LYP	BP86	TPSSh	B3LYP
$^3T_1(F)$: $^3B_1(F) \rightarrow {}^3A_2(F)$	5860	7629	6096	5408	7242	5823
$^3T_1(F)$: $^3B_1(F) \rightarrow {}^3B_2(F)$	8259	10 056	8188	7865	9730	7998
$^3T_2$: $^3B_1(F) \rightarrow {}^3B_2$	10 474	14 393	12 418	10 003	13 924	12 080
$^3T_2$: $^3B_1(F) \rightarrow {}^3A_1$	13 366	14 991	12 693	12 854	14 972	12 868
$^3T_1(P)$: $^3B_1(F) \rightarrow {}^3A_2(P)$	13 575	17 116	15 481	13 340	16 834	15 420
$^3T_1(P)$: $^3B_1(F) \rightarrow {}^3B_1(P)$	14 788	18 462	16 565	13 736	17 529	15 814
LMCT	16 214	25 014	29 283	15 173	22 628	25 301
LMCT	16 736	25 082	29 443	15 613	23 086	26 003
LMCT	17 317	25 737	29 699	15 837	23 212	26 564

The six lowest-energy transitions from **Table S5** correspond to ligand field transitions (**Figure S89**), four of which are also observed in experiment and can be used to compare energies. Namely, from the $^3T_1(F)$ state, the experimental $^3B_1(F) \rightarrow {}^3A_2(F)$ transition (band 1) is observed at ~2000 cm^{-1} (Cl) and ~2200 cm^{-1} (Br) in the vibrational

CD data; these transitions are highly overestimated in TDDFT (TPSSh/CPCM) with energies of ~7600 cm^{-1} (Cl) and ~7200 cm^{-1} (Br). The $^3B_1(F) \rightarrow {}^3A_1$ (band 3) maxima are at ~8200 cm^{-1} (Cl) and ~8000 cm^{-1} (Br) in experiment and at ~10 100 cm^{-1} (Cl) and ~9700 cm^{-1} (Br) in the calculation. Finally, two bands arising from the $^3T_1(P)$ excited state are observed experimentally: $^3B_1(F) \rightarrow {}^3B_1(P)$ (band 5) and $^3B_1(F) \rightarrow {}^3A_2(P)$ (band 7). The TDDFT predicted energy of band 5 is again too high (band 5: ~14 900 cm^{-1} (experiment, Cl) and ~14 500 cm^{-1} (experiment, Br) vs. 18 500 cm^{-1} (TDDFT, Cl) and ~17 500 cm^{-1} (TDDFT, Br)). Conversely, band 7 is underestimated in TDDFT, leading to an incorrect predicted ordering of the $^3T_1(P)$ states (band 7: ~20 100 cm^{-1} (experiment, Cl) and ~19 400 cm^{-1} (experiment, Br) vs. 17 100 cm^{-1} (TDDFT, Cl) and ~16 800 cm^{-1} (TDDFT, Br)). The $^3B_1(F) \rightarrow {}^3A_2(P)$ band is, however, correctly predicted as the transition with the highest oscillator strength.

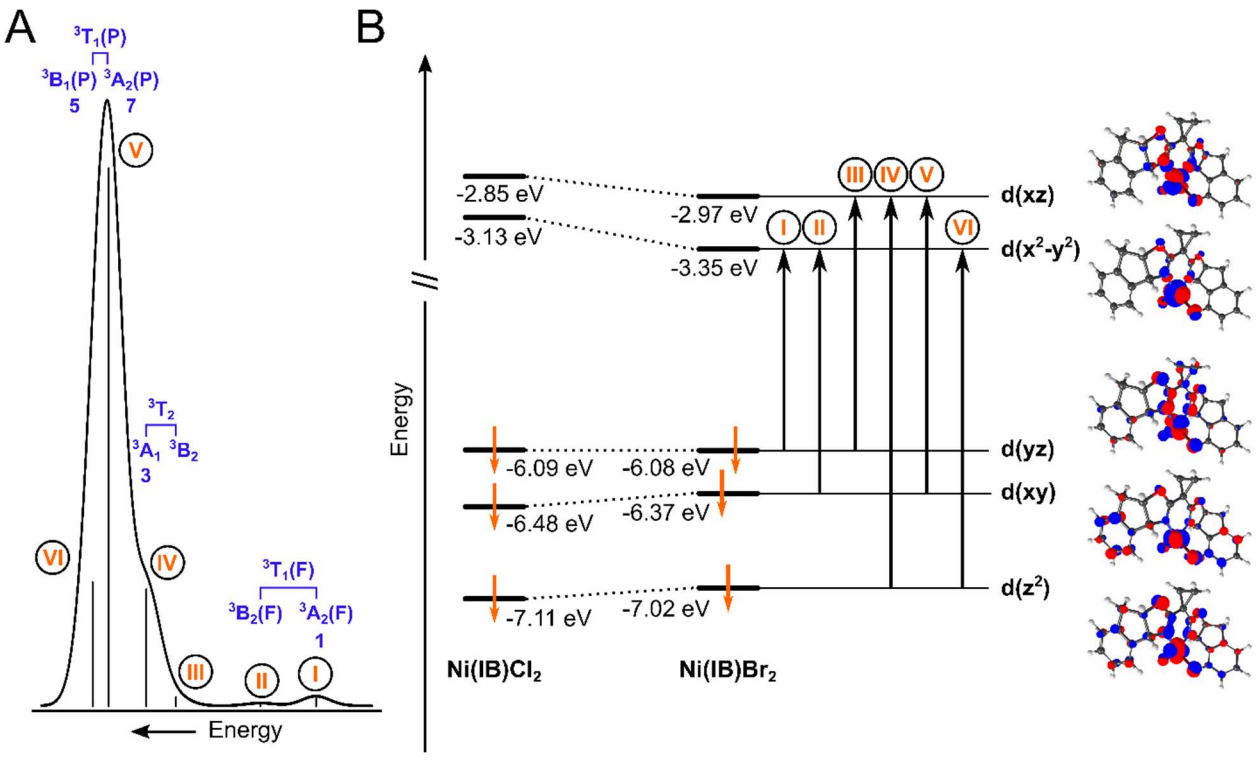

***Figure S89**. TDDFT calculations for **$Ni^{II}(IB)X_2$** precatalysts. (**A**) An illustrative spectrum for **$Ni^{II}(IB)Br_2$** (TPSSh/CPCM). Transition assignments from group theory (blue text) are provided along with bands numbered as in experiment. (**B**) Individual transitions from **A** depicted on the 3d ϐ-orbital manifold of **$Ni^{II}(IB)Br_2$** (right). Comparison between 3d ϐ-orbital manifolds of **$Ni^{II}(IB)Cl_2$** vs. **$Ni^{II}(IB)Br_2$** demonstrating destabilization of the ϐ-LUMOs due to differences in Cl vs. Br ligand field strength.*

In addition to correlating TDDFT calculations to experimental precatalyst spectra, they can be further utilized to understand the equilibria discussed in **Section 2.4**. The TDDFT calculated spectra of **$Ni^{II}(IB)X_2$** complexes do not change significantly with different CPCM dielectric constants (e.g., DMA (ε = 38) or DCM (ε = 9), **Figures S92-S93**), consistent with weak experimental solvatochromism of the ligand field bands for these neutral complexes (**Figures S3-S4** and **S6-S7**). Calculated spectra also do not display the additional ~23 000 cm^{-1} band observed in DMA; this band is proposed to originate from a five-coordinate **$Ni^{II}(IB)(DMA)X_2$** species. Indeed, calculated spectra for five-coordinate species exhibit a significant blue shift for the most intense calculated ligand field band (band 7, $^3B_1(F) \rightarrow {}^3A_2(P)$) by ~3000 - 4000 cm^{-1} (**Figures S130-S131**). For this species, DMA preferentially coordinates to Ni^{II} via the oxygen atom, consistent with literature precedent[43] (see the comparison between TDDFT calculated spectra of oxygen- and nitrogen-coordinated DMA species, **$Ni^{II}(IB)(O\text{-}DMA)X_2$** and **$Ni^{II}(IB)(N\text{-}DMA)X_2$**, in **Figures S94-S95**). The computed free energies (in CPCM) of **$Ni^{II}(IB)(DMA)X_2$** formation are only ~4 kcal mol^{-1} (X = Cl) and ~6 kcal mol^{-1} (X = Br), qualitatively consistent with a possible equilibrium between **$Ni^{II}(IB)X_2$** and **$Ni^{II}(IB)(DMA)X_2$** at room temperature and further consistent with strongly temperature-dependent UV-vis-NIR data (**Figure 4**). While the computed free energies are higher than those derived experimentally, this difference likely stems from deviations in solvation free energies, and/or solute and solvent entropic contributions to the calculated free energies, which are difficult to capture

accurately as the problem involves multi-molecular association process. As such, the disagreement is only ~3.7 kcal mol^{-1} (**Ni(IB)Cl$_2$**) and ~5.8 kcal mol^{-1} (**Ni(IB)Br$_2$**), which does not seem to be unprecedented for current state-of-the-art computational modeling techniques.[44]

***Table S6**. Calculated formation energies of precatalyst structures proposed to be involved under different reaction conditions. All energies are in units of kcal mol^{-1}.*

Equilibrium Reaction	Δ*H*(gas-phase)	Δ*G*(gas-phase)	Δ*G*(CPCM)
$Ni^{II}(IB)Cl_2$ + DMA ⇌ $Ni^{II}(IB)(DMA)Cl_2$	-5.2	10.1	4.0
$Ni^{II}(IB)Br_2$ + DMA ⇌ $Ni^{II}(IB)(DMA)Br_2$	-5.8	10.9	5.8
2 $Ni^{II}(IB)Cl_2$ ⇌ $[Ni^{II}(IB)Cl_2]_2$ dimer	-15.1	-6.5	-0.7
2 $Ni^{II}(IB)Br_2$ ⇌ $[Ni^{II}(IB)Br_2]_2$ dimer	-14.7	-4.7	1.1
3 $Ni^{II}(IB)Cl_2$ ⇌ $[Ni^{II}(IB)Cl_2]_3$ trimer	-24.4	-12.0	-3.5
3 $Ni^{II}(IB)Br_2$ ⇌ $[Ni^{II}(IB)Br_2]_3$ trimer	-22.5	-9.0	-0.7

The concentration-dependent electronic absorption data for **Ni^{II}(IB)Cl$_2$** in DCM (**Figure S16**) suggest there is also an appreciable equilibrium between **Ni^{II}(IB)Cl$_2$** and an aggregated species (e.g., dimer or trimer). Concentration-dependent data are not observed for **Ni^{II}(IB)Br$_2$** up to ~150 mM (*vide supra*, **Section 2.4**, **Figure S19**). For comparison, we have calculated the energy of [**Ni^{II}(IB)X$_2$**]$_2$ **μ-X** dimer and [**Ni^{II}(IB)X$_2$**]$_3$ **μ-X** trimer formation. From the calculated free energies, the [**Ni^{II}(IB)Cl$_2$**]$_3$ and [**Ni^{II}(IB)Br$_2$**]$_3$ trimers are predicted to be the most thermodynamically stable species (Δ*G*(CPCM) = –3.5 kcal mol^{-1} and –0.7 kcal mol^{-1} vs. the monomer for X = Cl and Br, respectively) (**Table S7**), and should thus be accessible at room temperature. While still negative, the calculated free

energy of trimer formation is less negative for X = Br, in qualitative accord with experimental observations.

Finally, the calculated TDDFT spectra of the trimers qualitatively resemble the monomeric species (**Figures S96-S97**), but with blue-shifted ligand field bands relative to the monomers. This compares well with the experimental spectrum of the oligomeric species obtained from the variable-concentration and variable-temperature spectra of **Ni^{II}(IB)Cl_2** (**Section 2.4**), with experimental and computed spectra overlaid in **Figure S132**.

***Table S7**: Calculated standard reduction potentials of various Ni-indabox complexes using DFT (TPSSh) methodology. All reduction potentials of the Ni complexes are referenced to the absolute potential of the reference electrode ($Fc^{+/0}$).*

Reference electrode	
Ferrocenium / Ferrrocene ($Fc^{+/0}$)	4.55 V
Ni^{III} Oxidation State	Reduction potential (vs. $Fc^{+/0}$)
$Ni^{III}(IB)Cl_2$ / $Ni^{II}(IB)Cl_2$	1.41 V
$Ni^{III}(IB)Br_2$ / $Ni^{II}(IB)Br_2$	1.42 V
Ni^{II} Oxidation State	Reduction potential (vs. $Fc^{+/0}$)
$Ni^{II}(IB)Cl_2$ / $Ni^{I}(IB)Cl_2$	–1.24 V
$Ni^{II}(IB)Cl_2$ / $Ni^{I}(IB)Cl$ + Cl	–1.48 V
$Ni^{II}(IB)Cl$ / $Ni^{I}(IB)Cl$	–0.20 V
$Ni^{II}(IB)Br_2$ / $Ni^{I}(IB)Br_2$	–1.11 V
$Ni^{II}(IB)Br_2$ / $Ni^{I}(IB)Br$ + Br	–1.39 V
$Ni^{II}(IB)Br$ / $Ni^{I}(IB)Br$	–0.13 V
Ni^{I} Oxidation State	Reduction potential (vs. $Fc^{+/0}$)
$Ni^{I}(IB)Cl$ / $Ni^{0}(IB)Cl$	–3.10 V

$Ni^{I}(IB)Cl / Ni^{0}(IB) + Cl$	–3.97 V
$Ni^{I}(IB)Br / Ni^{0}(IB)Br$	–3.07 V
$Ni^{I}(IB)Br / Ni^{0}(IB) + Br$	–3.87 V

***Table S8**: Ni-3d atomic orbital character in the β-LUMO of **Ni^{II}(IB)Cl_2**, **Ni^{II}(IB)Br_2** and α-HOMO of different **Ni^{II}(IB)(Vn)Br** complexes (Vn = substituted p-vinylbenzene derivative).*

$Ni^{II}(IB)X_2$ (S = 1); X =	β-LUMO Ni-3d orbital character
Cl	75.5 %
Br	73.8 %
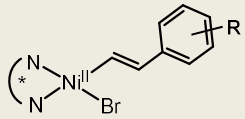 $Ni^{II}(IB)(^{R}Vn)Br$ (S = 0); R =	α-HOMO Ni-3d orbital character
p-CF_3	64.3 %
p-CN	64.9 %
p-CO_2Me	62.4 %
p-Me	42.5 %
p-NMe_2	9.9 %
p-OMe	27.6 %
p-OTs	57.0 %
Pyp-OMe	42.7 %

***Table S9**: Calculated oxidation potentials of various **Ni^{II}(IB)(Vn)Br** and benzyl-C(sp^3) radicals (Vn = substituted p-vinylbenzene derivative). All oxidation potentials are referenced to the absolute potential of the reference electrode ($Fc^{+/0}$).*

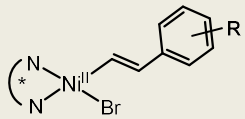 $Ni^{II}(IB)(^{R}Vn)Br$ (S = 0); R =	Oxidation Potential (vs. $Fc^{+/0}$)
p-CF_3	–0.17 V
p-CN	–0.23 V
p-CO_2Me	–0.19 V

p-Me	–0.29 V
p-NMe_2	+0.14 V
p-OMe	–0.20 V
p-OTs	–0.29 V
Pyp-OMe	–0.47 V

R =	Oxidation Potential (vs. $Fc^{+/0}$)
H	+0.17 V
p-Br	+0.23 V
p-CF_3	+0.48 V
p-F	+0.16 V
p-NMe_2	–0.72 V
p-OMe	–0.32 V
p-Cl-*m*-Cl	+0.36 V

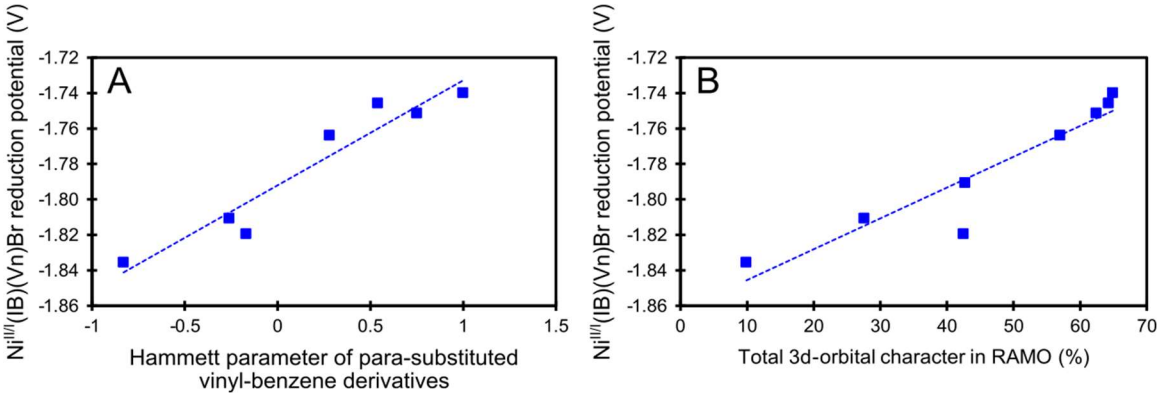

Figure S90: (A) *Calculated $Ni^{II/I}$ reduction potentials of the* ***Ni^{II}(IB)(Vn)Br*** *species (coupled to halide dissociation) vs. the vinyl substituent Hammett parameters.* ***(B)*** *Calculated $Ni^{II/I}$ reduction potentials of the* ***Ni^{II}(IB)(Vn)Br*** *species (coupled to halide dissociation) vs. the 3d-orbital character in the Ni^{II} $d(x^2-y^2)$ RAMO.*

S8.2. Ground- and Excited-States Calculations with CASSCF/CASPT2

The ground-state wave function character of **Ni^{II}(IB)Cl_2** and **Ni^{II}(IB)Br_2** depends on the active space variation in CASSCF calculations (**Figure S91**). Regardless of active space size, the ground state is exclusively high spin (at the ΔH level, the lowest-energy low-spin states are ~36-49 kcal mol^{-1} (CASSCF) and ~28-39 kcal mol^{-1} (CASPT2) higher in energy). An appreciable multiconfigurational character is observed, however, with a minimal active space (8e,5o; consisting of five Ni 3*d* orbitals), with contributions to the ground state configuration interaction (CI) vector from several different $3d^8$ Ni^{II} electronic configurations (**Tables S24** and **S30**). With the 22e,12o active space (five Ni 3*d* orbitals, six halide 2*p*/3*p* orbitals, and the Ni(IB) σ bonding orbital), the ground-state solution is single-referent, with the highest weight of a single configuration in the CI vector of ~95% for both **Ni^{II}(IB)Cl_2** and **Ni^{II}(IB)Br_2** (**Tables S28** and **S34**). This configuration corresponds to an $S = 1$ triplet ground state with unpaired electrons in the $d(x^2\text{-}y^2)$ and $d(xz)$ orbitals. The orbital compositions also reflect the covalent interaction between the halide 2*p*/3*p* atomic orbitals and the Ni 3*d* orbitals, with Mulliken spin populations of ~0.14e (summation over Cl atoms) and ~0.17e (summation over Br atoms).

With this optimized active space, we have calculated the UV-vis-NIR absorption, CD, and MCD spectra of **Ni^{II}(IB)Cl_2** and **Ni^{II}(IB)Br_2** (**Figure 8** and **S142**). These calculations generally support assignments of experimental data given in **Section 2.1** (**Table 4**). Individual states can be assigned based on the configuration state function with the largest weight in the CI vector, in conjunction with the location of the 3*d* holes. For example, the ground-state wave functions for both complexes can be described as having ~95% character of the configuration state function with holes in $d(x^2\text{-}y^2)$ and $d(xz)$ orbitals.

From group theory, this corresponds to the $^3B_1$ state in C_{2v} (i.e., direct product between A_1 and B_1). The first observed transition, calculated at ~2000 cm^{-1} (**Ni^{II}(IB)Cl$_2$**) and ~1800 cm^{-1} (**Ni^{II}(IB)Br$_2$**), has ~82% and ~84% character of the configuration state function with holes in *d*(yz) and *d*(xz) orbitals, corresponding to the $^3B_1(F) \rightarrow {}^3A_2$ transition (band 1 in **Table 1**), matching the energy in the experimental vibrational CD (~2200 cm^{-1} for both complexes). The next computed transition (~3300 cm^{-1} and ~3000 cm^{-1} for **Ni^{II}(IB)Cl$_2$** and **Ni^{II}(IB)Br$_2$**) is assigned as the forbidden $^3B_1(F) \rightarrow {}^3B_2(F)$ transition and is not observed in experiment. In the $^3T_2$ manifold (in T_d), we observe band 2 ($^3B_1(F) \rightarrow {}^3B_1/{}^3B_2$; calculated: ~7400 cm^{-1} (Cl) and ~7200 cm^{-1} (Br), experimental: ~6200 cm^{-1} (Cl) and ~6600 cm^{-1} (Br)) and band 3 ($^3B_1(F) \rightarrow {}^3A_1$; calculated: ~9800cm^{-1} (Cl) and ~9300 cm^{-1} (Br), experimental: ~8000 cm^{-1} (Cl) and ~8200 cm^{-1} (Br)), as well as the forbidden $^3B_1(F) \rightarrow {}^3B_1/{}^3B_2$ transition (calculated: 10 800 cm^{-1} (Cl) and 10 200 cm^{-1} (Br)). Note we cannot unambiguously differentiate between $^3B_1/{}^3B_2$ assignments in all cases, as the states with holes in different orbitals mix in the multiconfigurational wavefunctions and exhibit similar CI weights. The most intense transition in the low-energy region, band 4 (experimental: 10 270 cm^{-1} (Cl) and 10 150 cm^{-1} (Br), calculated: ~12 700 cm^{-1} (Cl) and ~12 400 cm^{-1} (Br)), is assigned as the double-electron $^3B_1(F) \rightarrow {}^3A_2(F)$ transition with the holes in the $d(z^2)$ and *d*(xy) orbitals. Finally, transitions to the $^3T_1(P)$ manifold (in T_d) are calculated in the range of ~16 100 cm^{-1} to ~21 600 cm^{-1} (experiment: ~14 500 cm^{-1} to ~20 100 cm^{-1}) with the same ordering as experiment (band 5: $^3B_1(F) \rightarrow {}^3B_1(P)/{}^3B_2(P)$, band 6: $^3B_1(F) \rightarrow {}^3B_1(P)/{}^3B_2(P)$, and the most intense band 7: $^3T_1(P)$: $^3B_1(F) \rightarrow {}^3A_2(P)$) (see **Tables S22** and **S23** for tabulated energies and assignments).

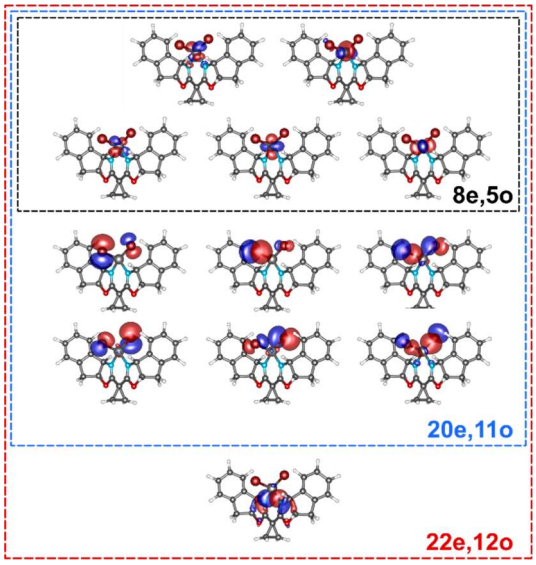

***Figure S91**: Different active spaces investigated in the multireference calculations. The largest active space comprising 22 electrons in 12 orbitals (denoted as 22e,12o) includes 5 x Ni_{3d} (black box), 3 x $Halide_{3p/4p}$ (per each halide; i.e., 6 orbitals for dihalide complexes, blue box), and 1 x $IB_{\sigma\text{-}bonding}$ orbitals (red box).*

S8.3. Additional Figures

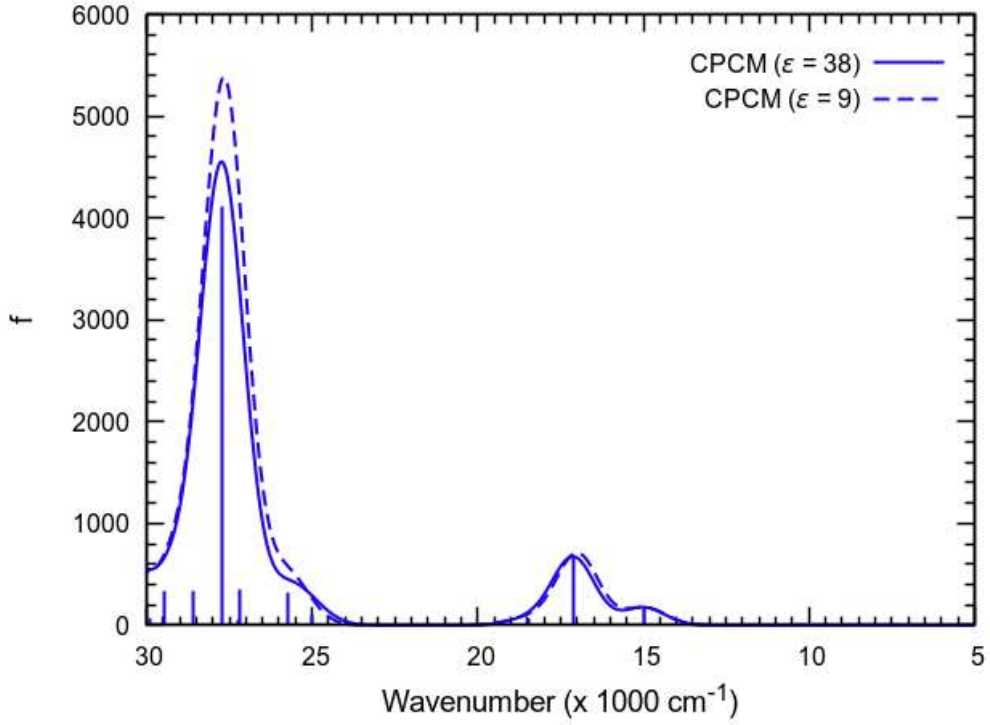

***Figure S92**: Calculated UV-vis-NIR spectra of **Ni^{II}(IB)Cl_2** at the TDDFT (TPSSh) level.*

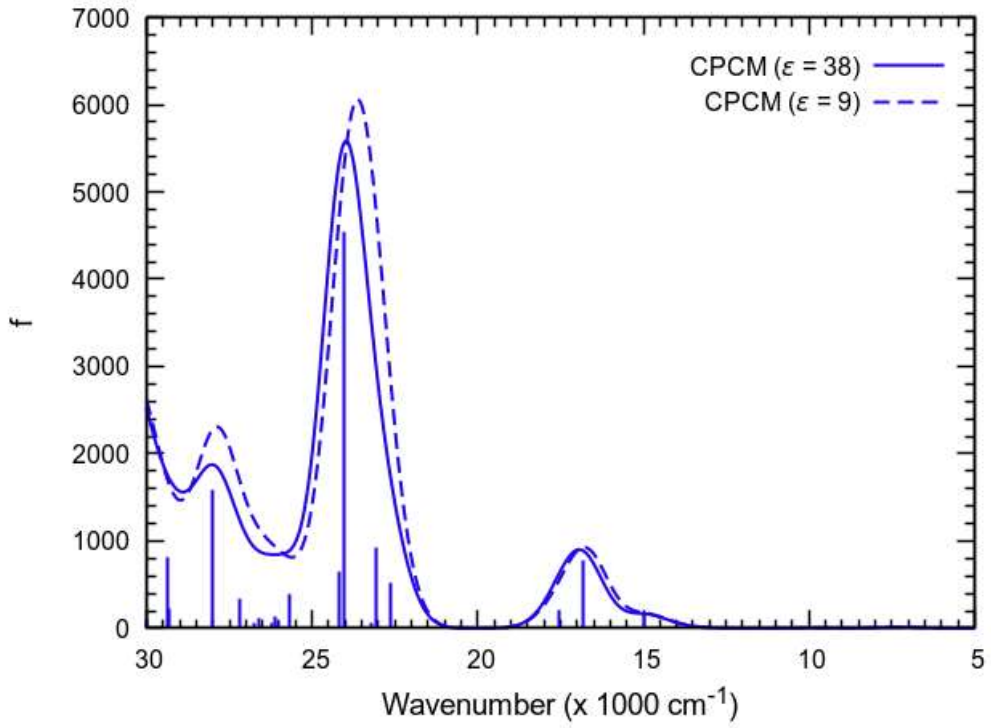

***Figure S93**: Calculated UV-vis-NIR spectra of **Ni^{II}(IB)Br$_2$** at the TDDFT (TPSSh) level.*

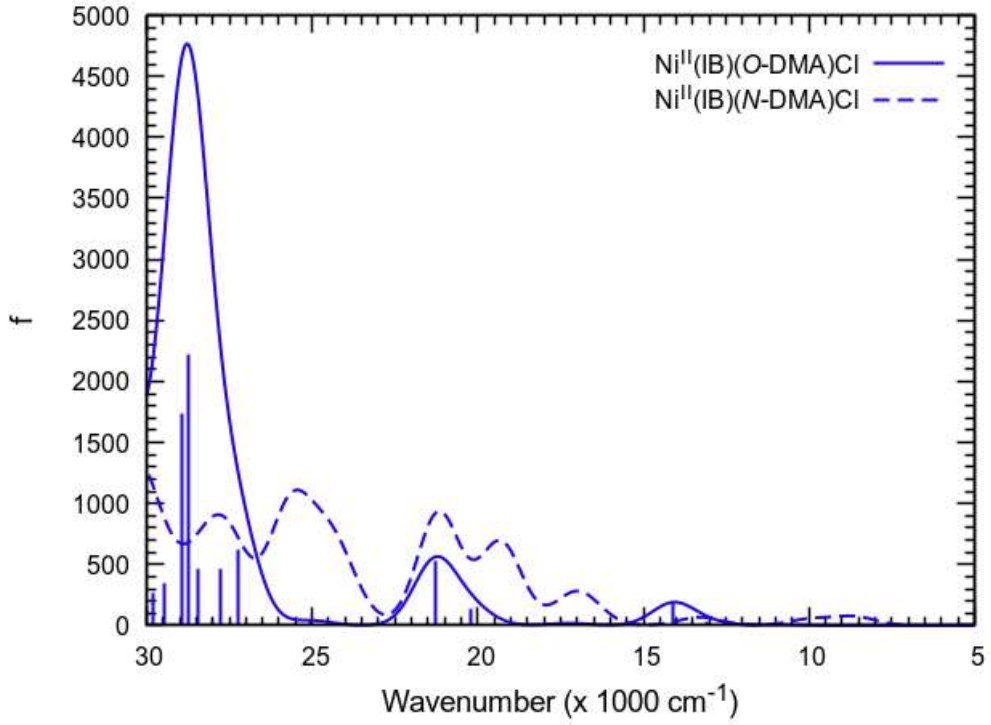

***Figure S94**: Calculated UV-vis-NIR spectra of solvent(DMA)-bound complexes **Ni^{II}(IB)(O-DMA)Cl$_2$** and **Ni^{II}(IB)(N-DMA)Cl$_2$** at the TDDFT (TPSSh) level and CPCM solvation model (ε = 38).*

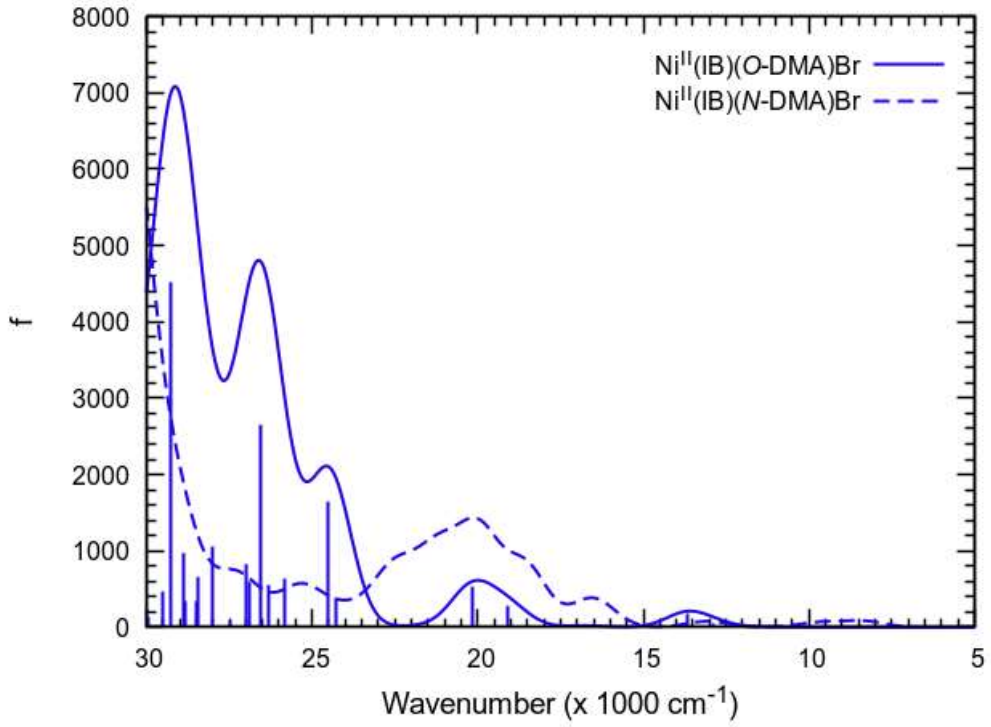

***Figure S95**: Calculated UV-vis-NIR spectra of solvent(DMA)-bound complexes **Ni^{II}(IB)(O-DMA)Br$_2$** and **Ni^{II}(IB)(N-DMA)Br$_2$** at the TDDFT (TPSSh) level and CPCM solvation model (ε = 38).*

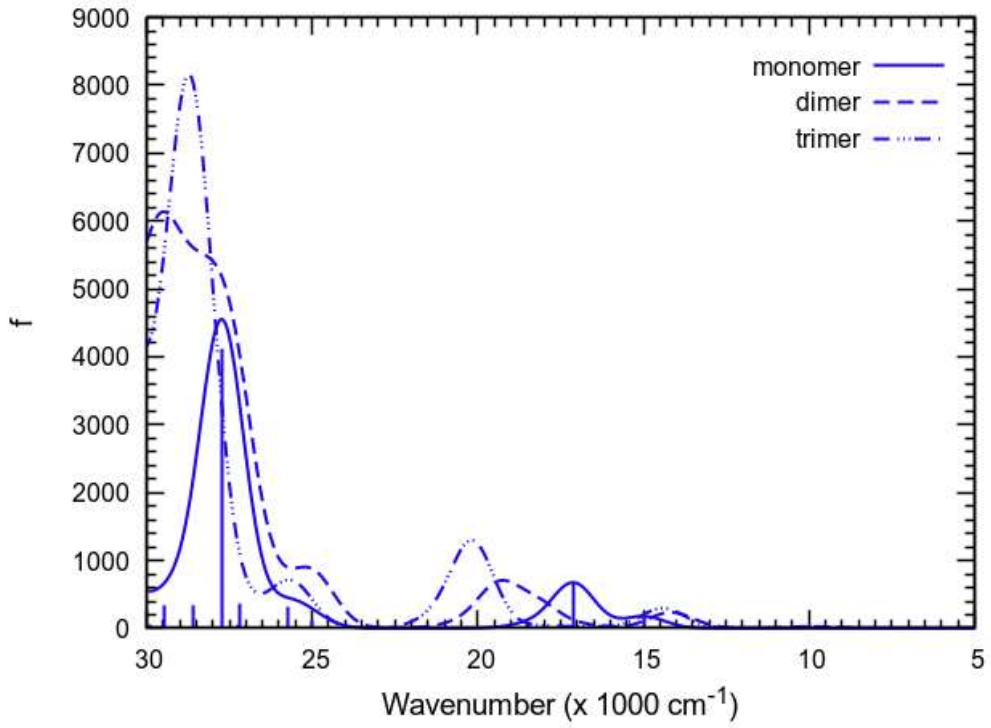

***Figure S96**: Calculated UV-vis-NIR spectra **$Ni^{II}(IB)Cl_2$** in its monomeric, dimeric, and trimeric forms at the TDDFT (TPSSh) level and CPCM solvation model (ε = 38).*

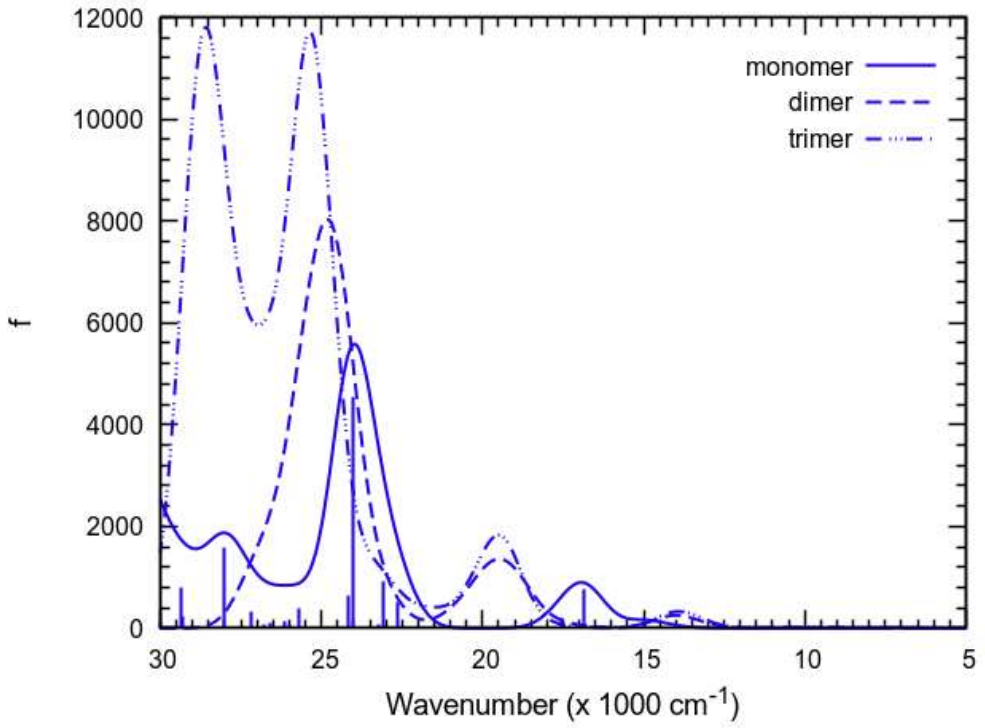

***Figure S97**: Calculated UV-vis-NIR spectra of **Ni^{II}(IB)Br_2** in its monomeric, dimeric, and trimeric forms at the TDDFT (TPSSh) level and CPCM solvation model (ε = 38).*

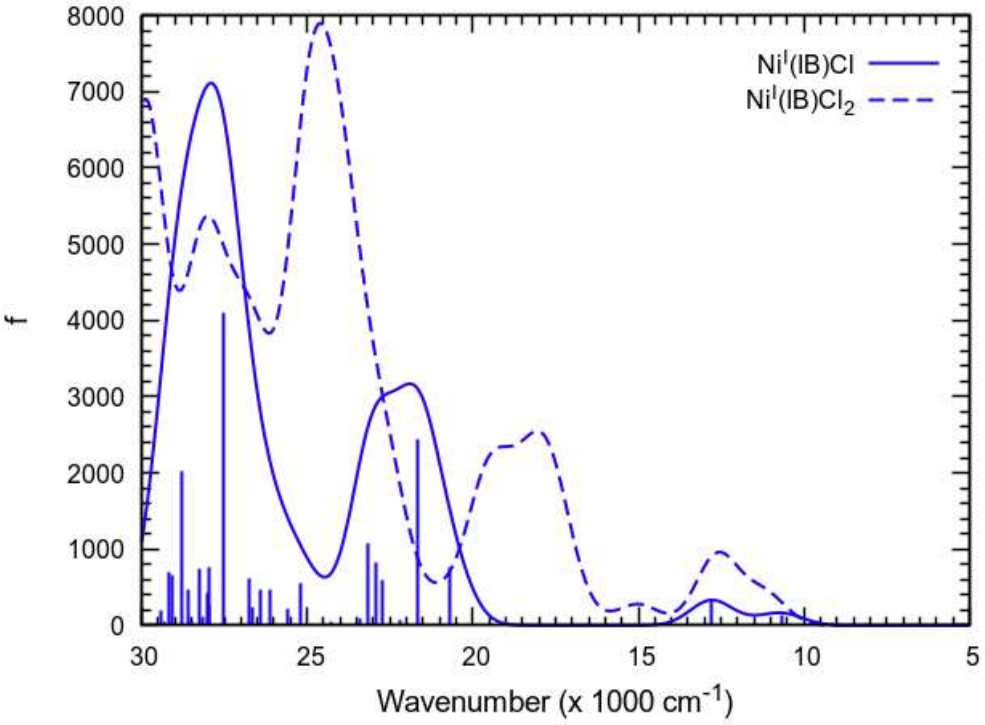

***Figure S98**: Calculated UV-vis-NIR spectra of **Ni^{I}(IB)Cl_2** and **Ni^{I}(IB)Cl** at the TDDFT (TPSSh) level and CPCM solvation model (ε = 38).*

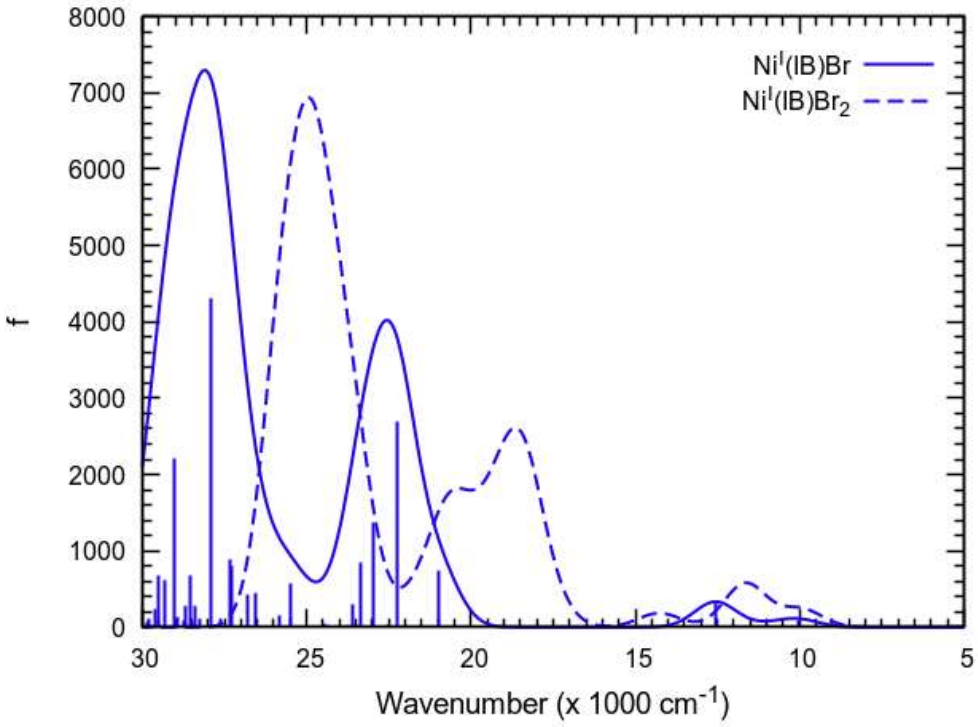

***Figure S99**: Calculated UV-vis-NIR spectra of **Ni^{I}(IB)Br_2** and **Ni^{I}(IB)Br** at the TDDFT (TPSSh) level and CPCM solvation model (ε = 38).*

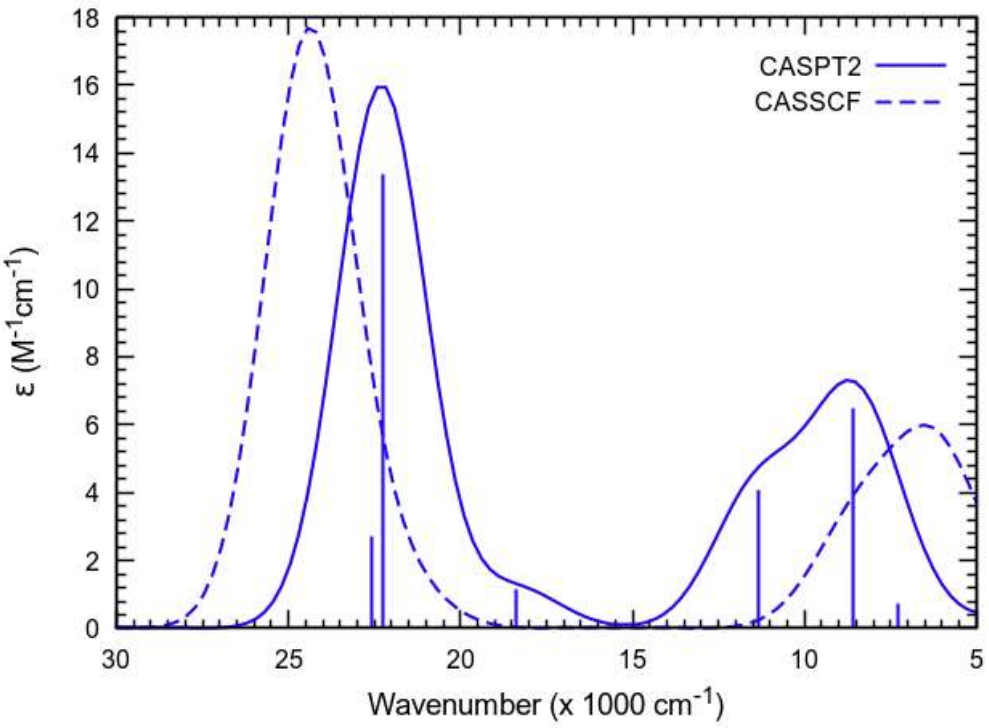

***Figure S100**: Calculated UV-vis-NIR spectra of **Ni^{II}(IB)Cl_2** at the CASSCF and MS-CASPT2 levels with 8e,5o active space (cf. Figure S91) in the gas phase.*

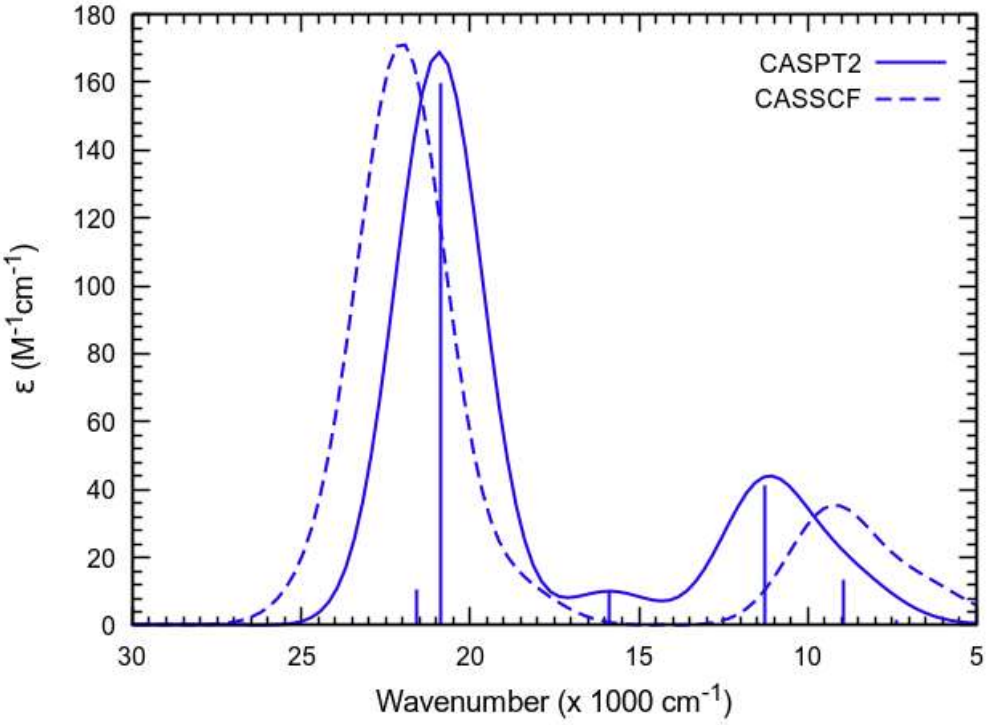

***Figure S101**: Calculated UV-vis-NIR spectra of **Ni^{II}(IB)Cl_2** at the CASSCF and MS-CASPT2 levels with 20e,11o active space (cf. Figure S91) in the gas phase.*

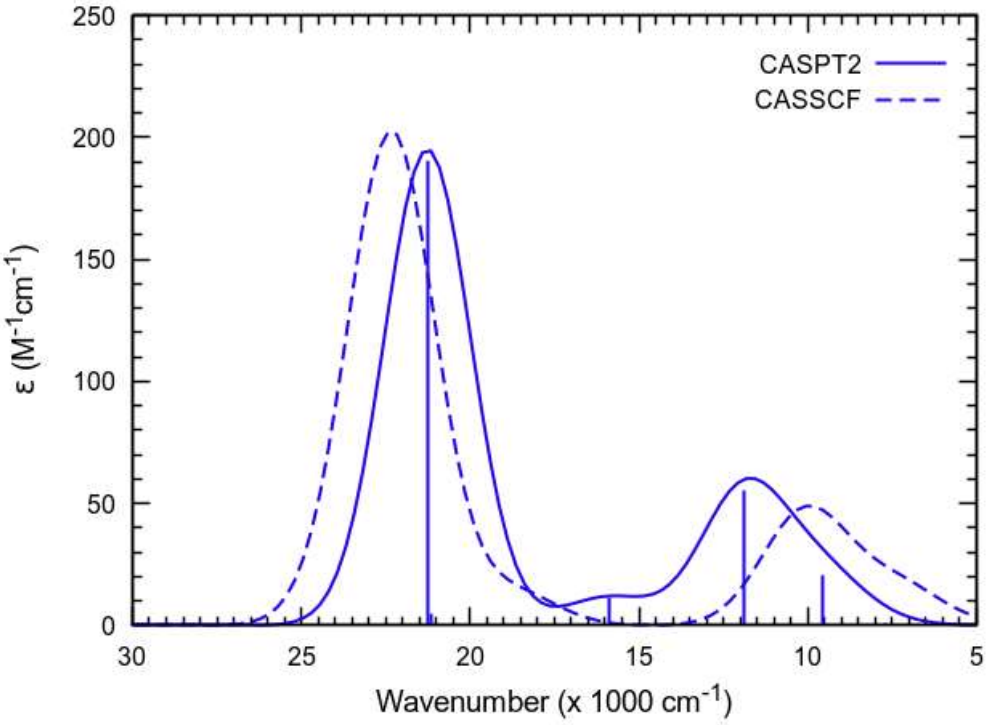

***Figure S102**: Calculated UV-vis-NIR spectra of **$Ni^{II}(IB)Cl_2$** at the CASSCF and MS-CASPT2 levels with 22e,12o active space (cf. Figure S91) in the gas phase.*

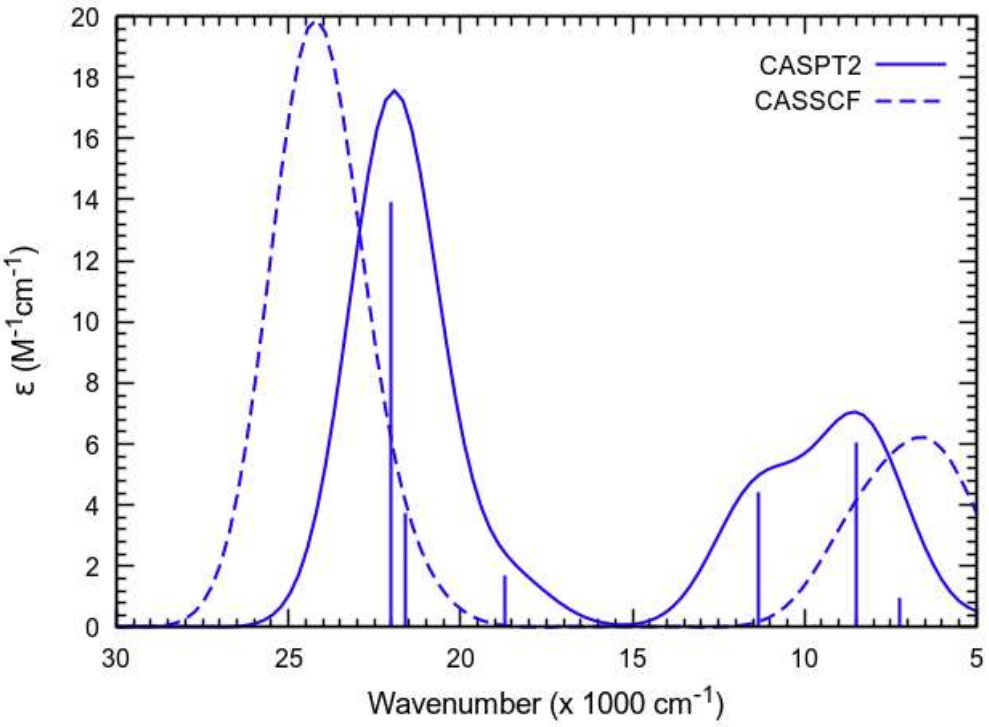

***Figure S103**: Calculated UV-vis-NIR spectra of **$Ni^{II}(IB)Br_2$** at the CASSCF and MS-CASPT2 levels with 8e,5o active space (cf. Figure S91) in the gas phase.*

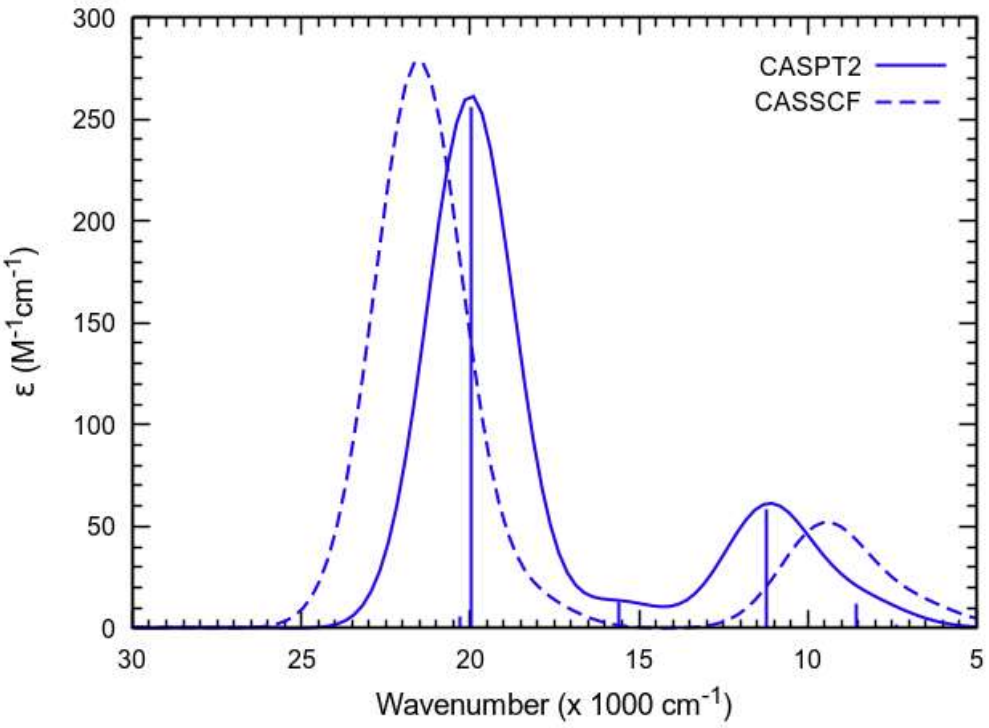

***Figure S104**: Calculated UV-vis-NIR spectra of **Ni^{I}(IB)Br$_2$** at the CASSCF and MS-CASPT2 levels with 20e,11o active space (cf. Figure S91) in the gas phase.*

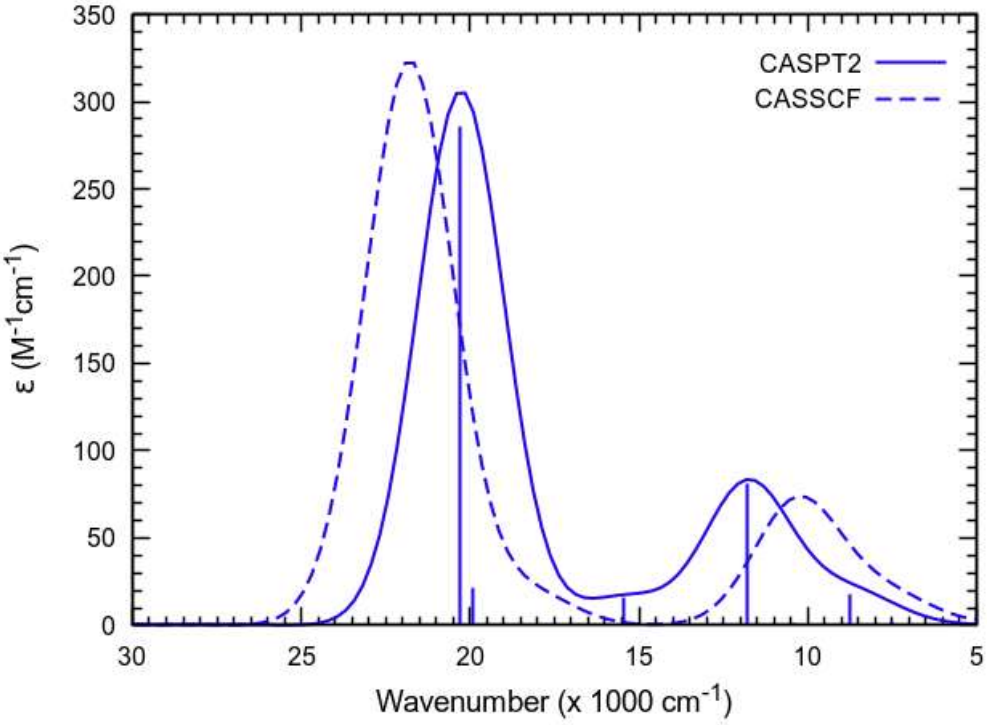

***Figure S105**: Calculated UV-vis-NIR spectra of **Ni^{II}(IB)Br_2** at the CASSCF and MS-CASPT2 levels with 22e,12o active space (cf. Figure S91) in the gas phase.*

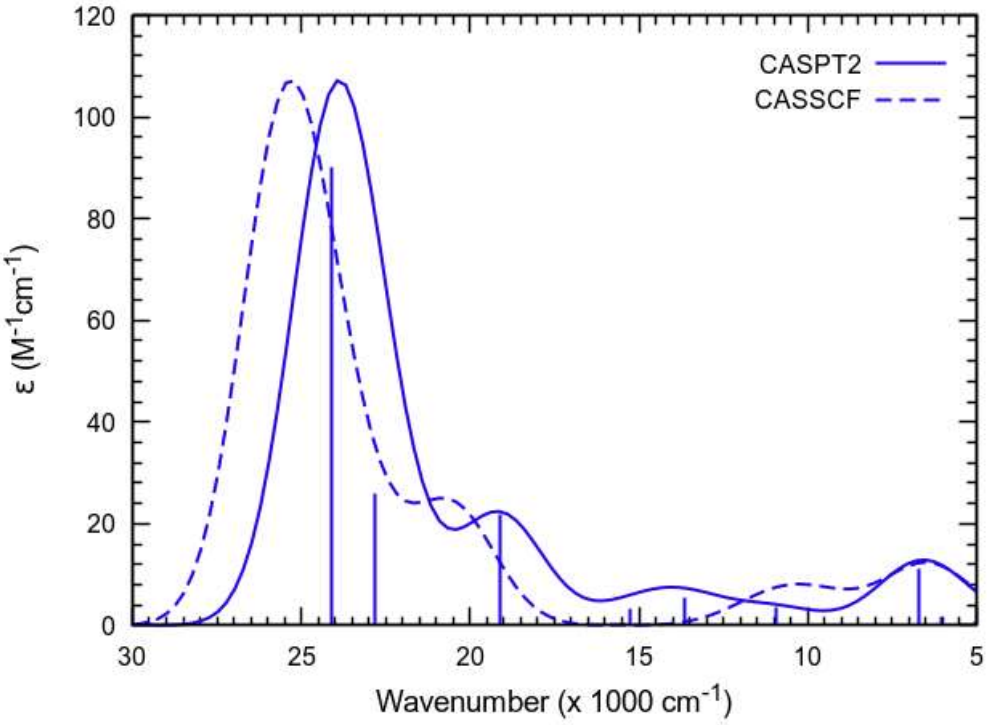

***Figure S106**: Calculated UV-vis-NIR spectra of solvent(DMA)-bound complex Ni^{II}(IB)(O-DMA)Cl_2 at the CASSCF and MS-CASPT2 levels with 22e,12o active space (cf. Figure S91).*

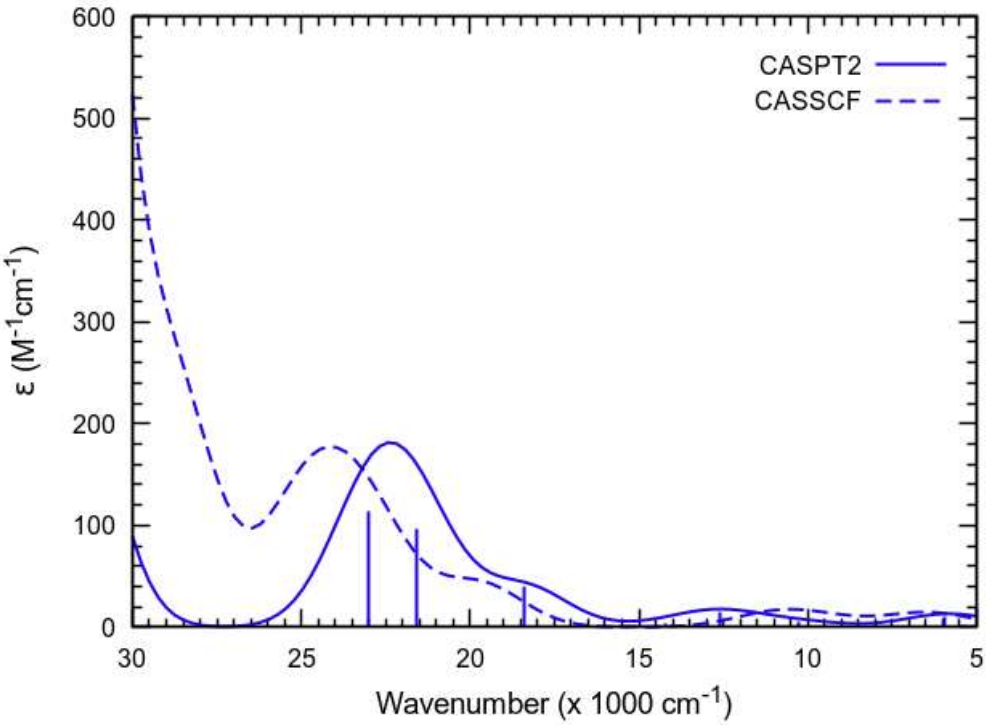

***Figure S107**: Calculated UV-vis-NIR spectra of solvent(DMA)-bound complex Ni^{II}(IB)(O-DMA)Br_2 at the CASSCF and MS-CASPT2 levels with 22e,12o active space (cf. Figure S91).*

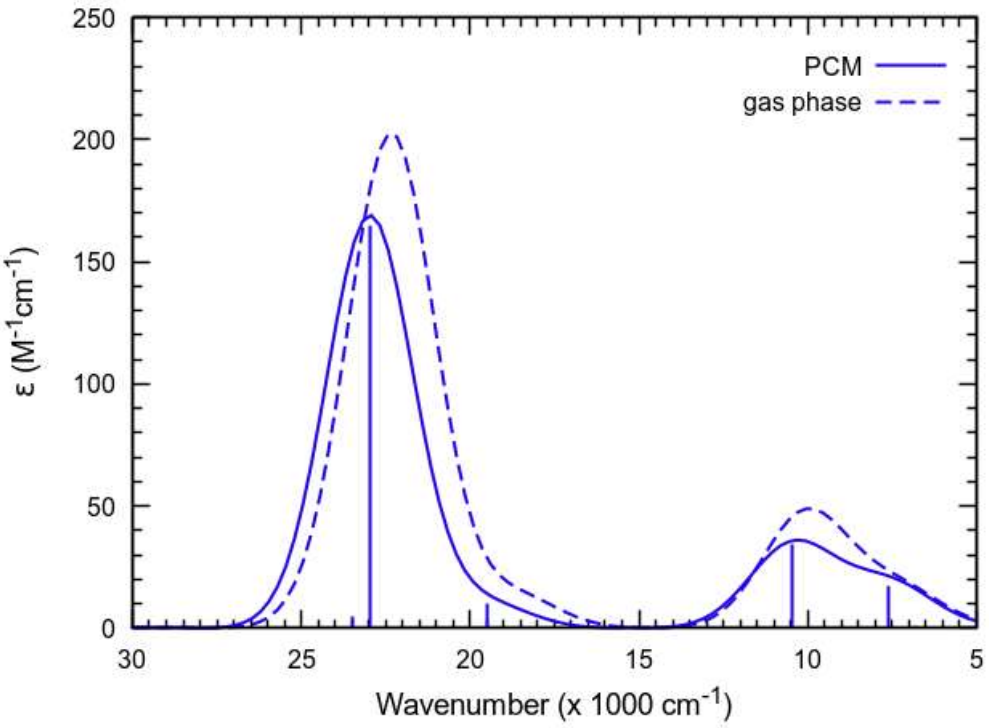

***Figure S108**: Calculated UV-vis-NIR spectra of **$Ni^{II}(IB)Cl_2$** at the CASSCF level with 22e,12o active space (cf. Figure S91) in the gas phase vs. PCM (ε = 38) solvation model.*

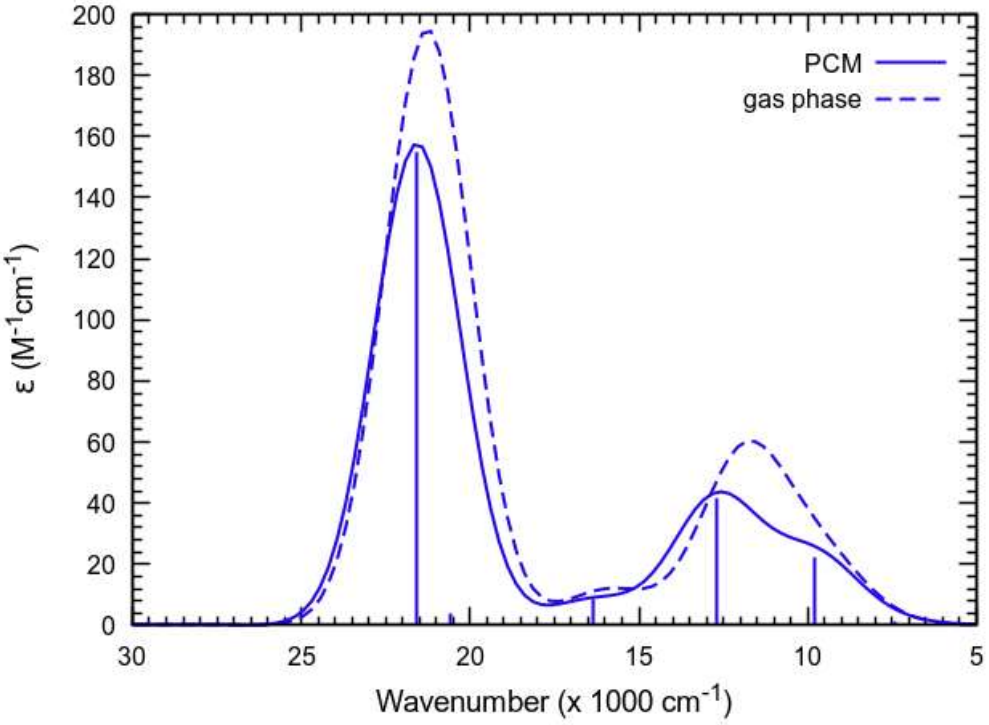

***Figure S109**: Calculated UV-vis-NIR spectra of **$Ni^{II}(IB)Cl_2$** at the MS-CASPT2 level with 22e,12o active space (cf. Figure S91) in the gas phase vs. PCM (ε = 38) solvation model.*

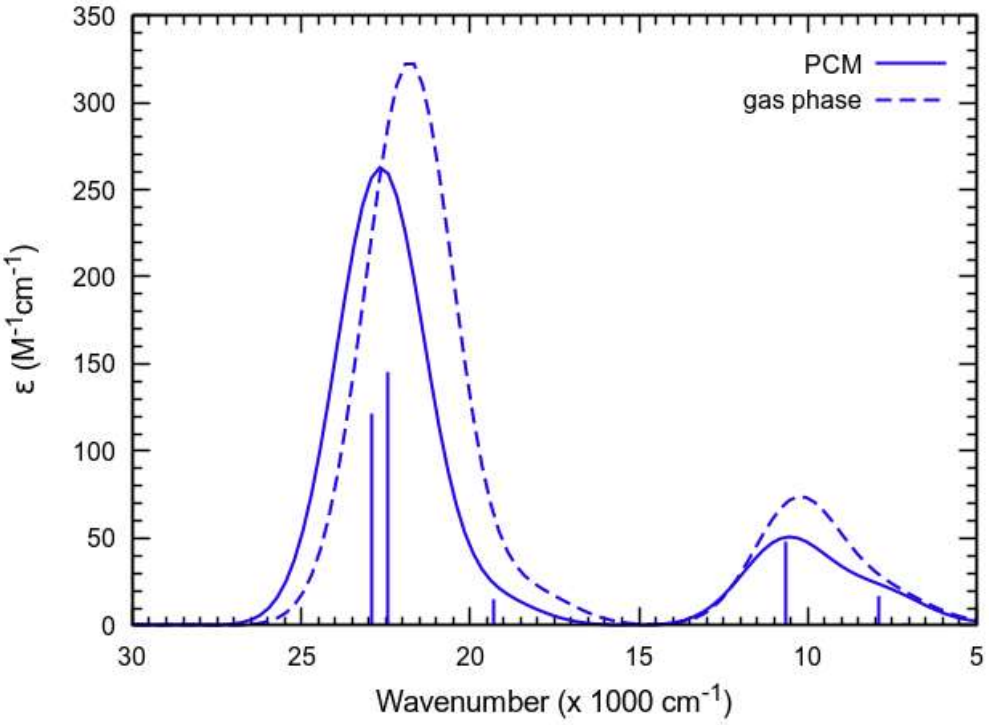

***Figure S110**: Calculated UV-vis-NIR spectra of **$Ni^{II}(IB)Br_2$** at the CASSCF level with 22e,12o active space (cf. Figure S91) in the gas phase vs. PCM (ε = 38) solvation model.*

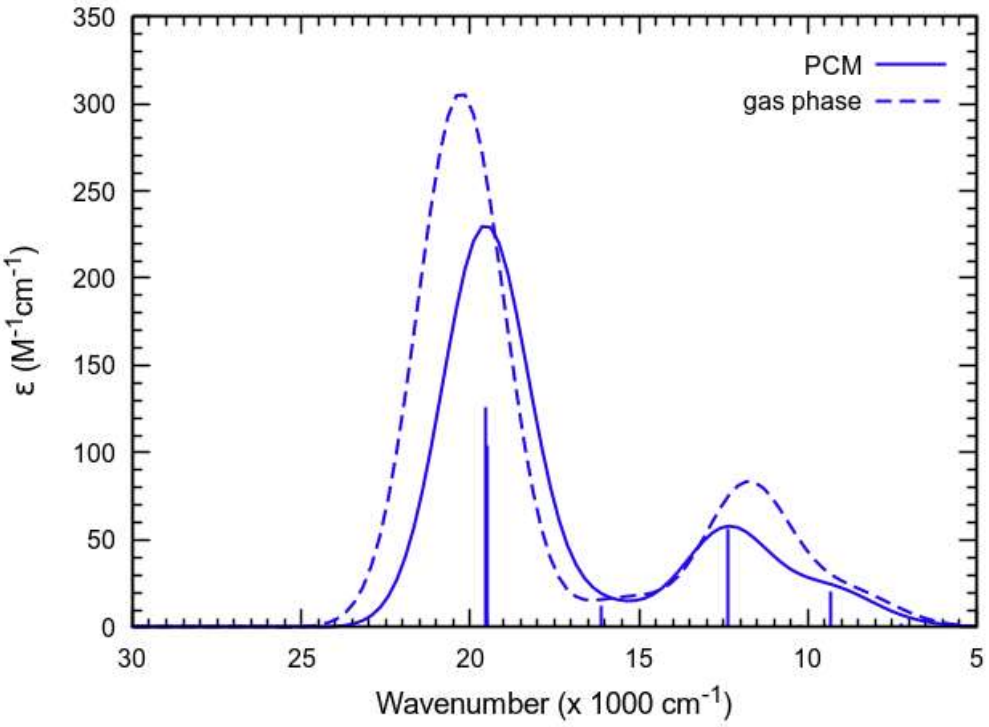

***Figure S111**: Calculated UV-vis-NIR spectra of **$Ni^{II}(IB)Br_2$** at the MS-CASPT2 level with 22e,12o active space (cf. Figure S91) in the gas phase vs. PCM (ε = 38) solvation model.*

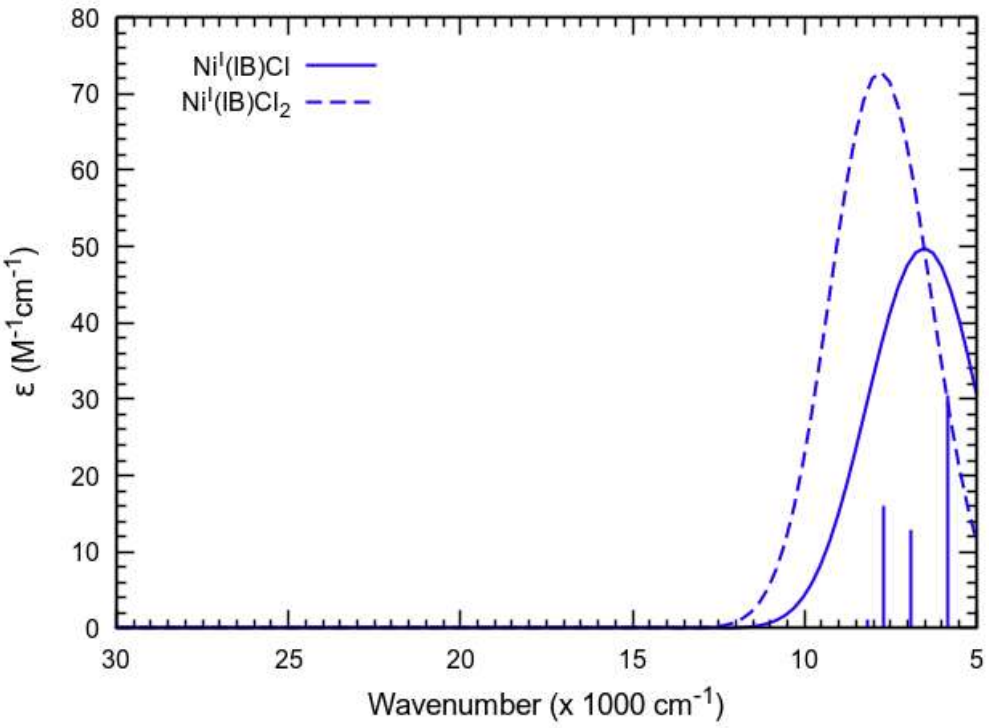

***Figure S112**: Calculated UV-vis-NIR spectra of Ni^{I}(IB)Cl$_2$ and Ni^{I}(IB)Cl at the CASSCF level with 23e,12o and 17e,9o active spaces.*

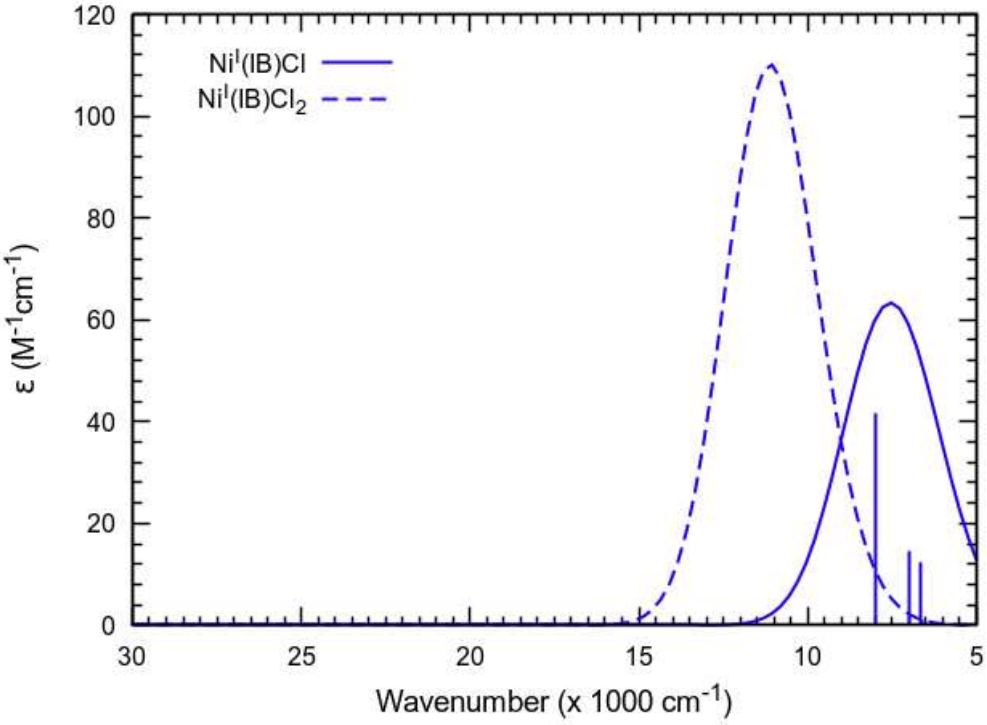

***Figure S113**: Calculated UV-vis-NIR spectra of Ni^{I}(IB)Cl$_2$ and Ni^{I}(IB)Cl at the MS-CASPT2 level with 23e,12o and 17e,9o active spaces.*

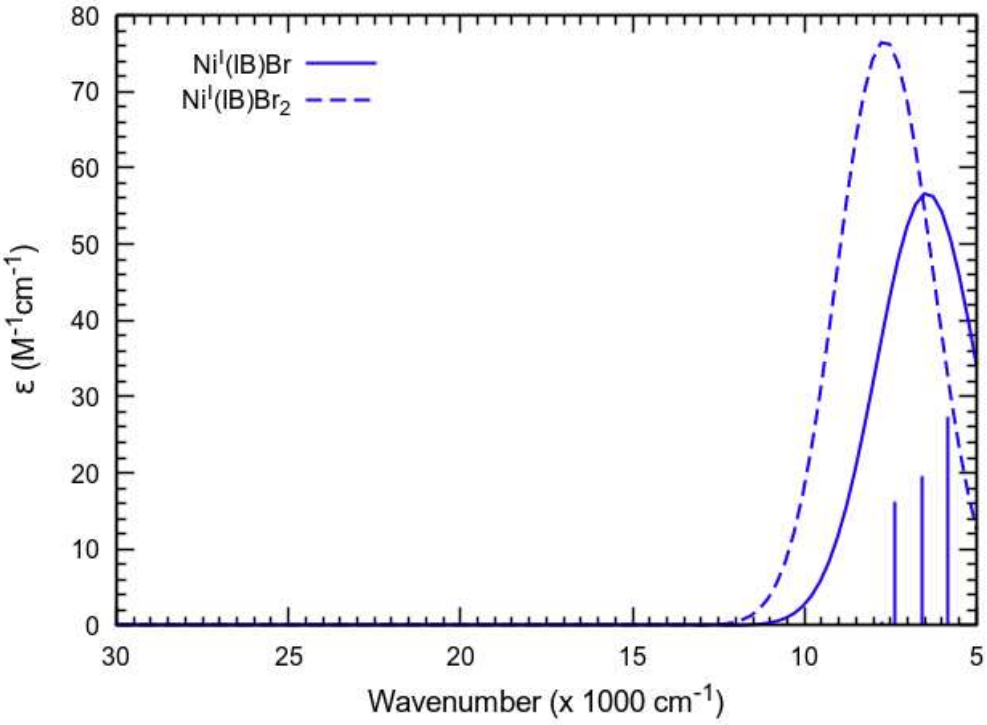

***Figure S114**: Calculated UV-vis-NIR spectra of $Ni^{I}(IB)Br_2$ and $Ni^{I}(IB)Br$ at the CASSCF level with 23e,12o and 17e,9o active spaces.*

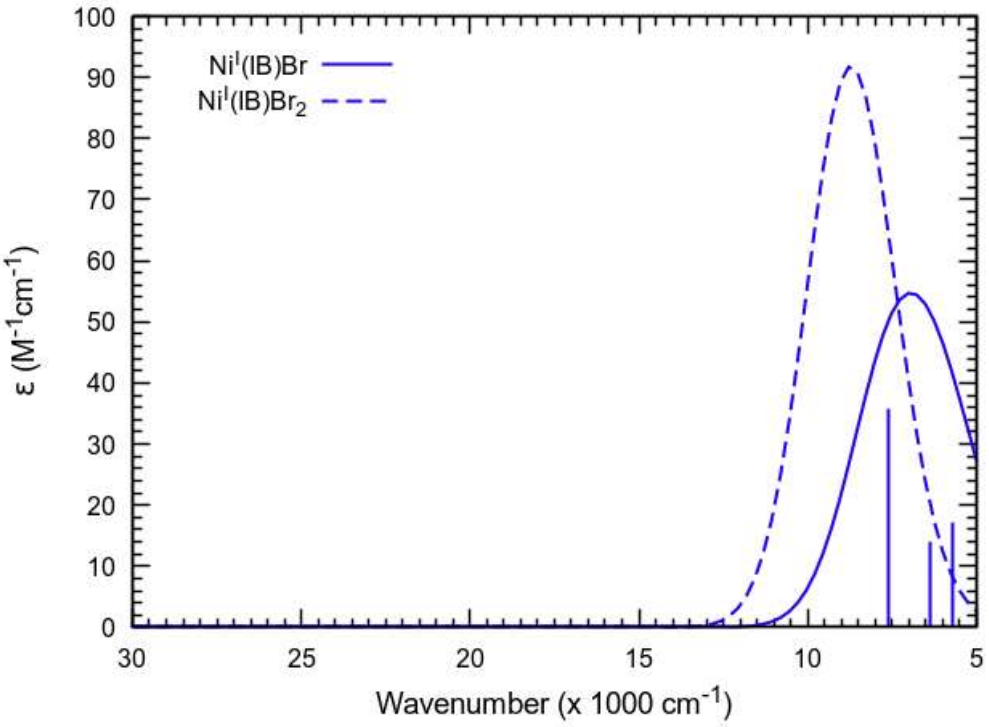

***Figure S115**: Calculated electronic absorption spectra of $Ni^{I}(IB)Br_2$ and $Ni^{I}(IB)Br$ at the MS-CASPT2 level with 23e,12o and 17e,9o active spaces.*

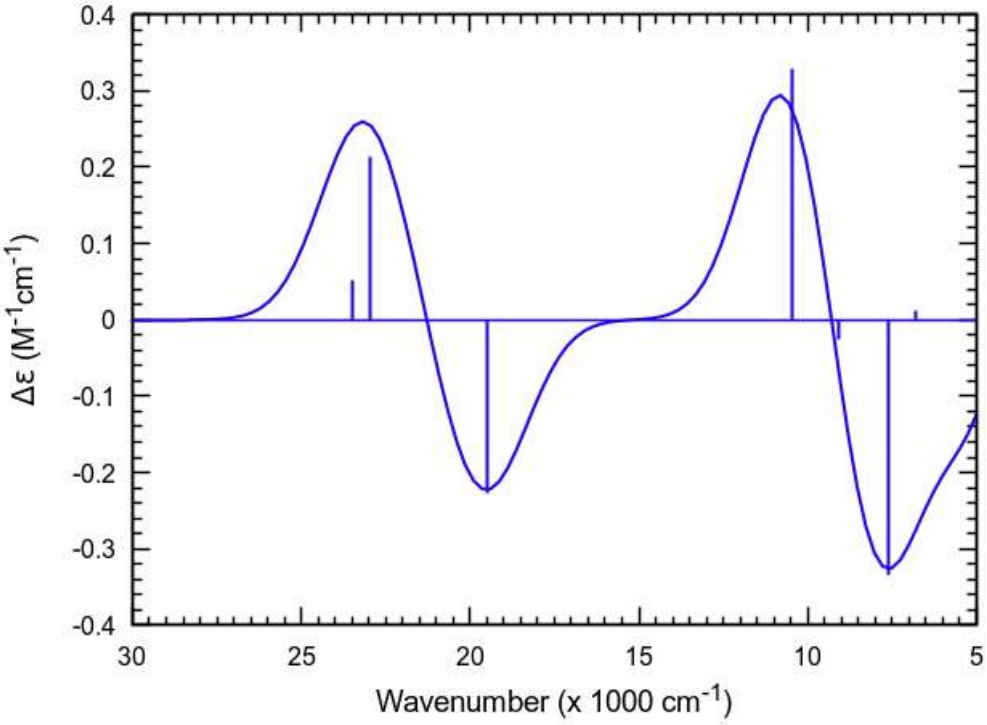

***Figure S116**: Calculated circular dichroism spectrum of **$Ni^{II}(IB)Cl_2$** at the CASSCF level with 22e,12o active space (cf. Figure S91).*

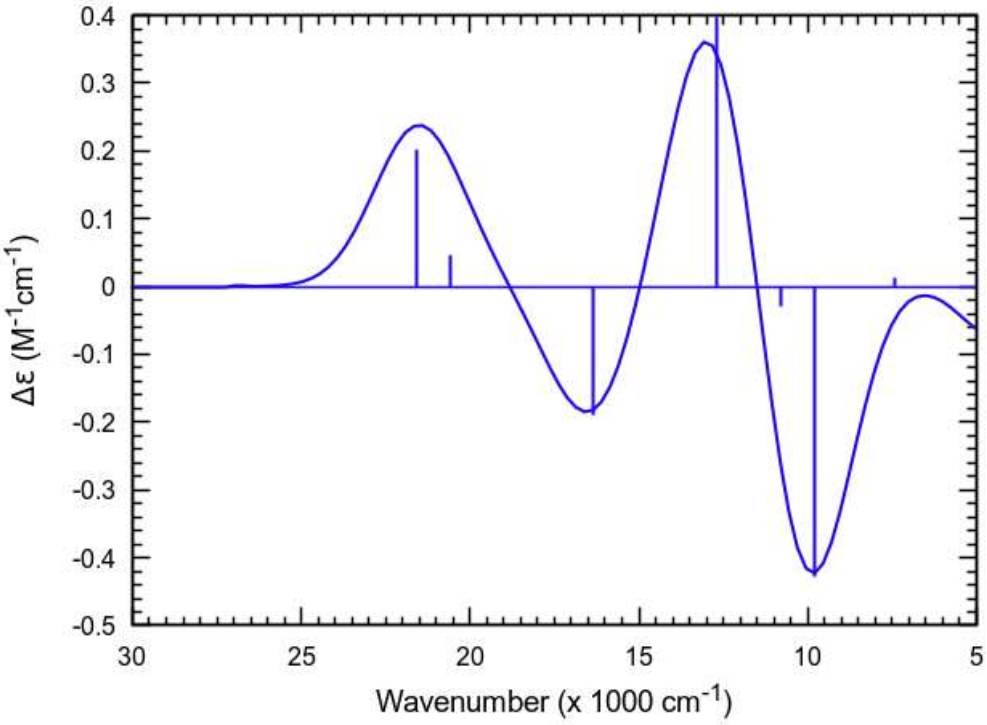

***Figure S117**: Calculated circular dichroism spectrum of **Ni^{II}(IB)Cl_2** at the MS-CASPT2 level with 22e,12o active space (cf. Figure S91).*

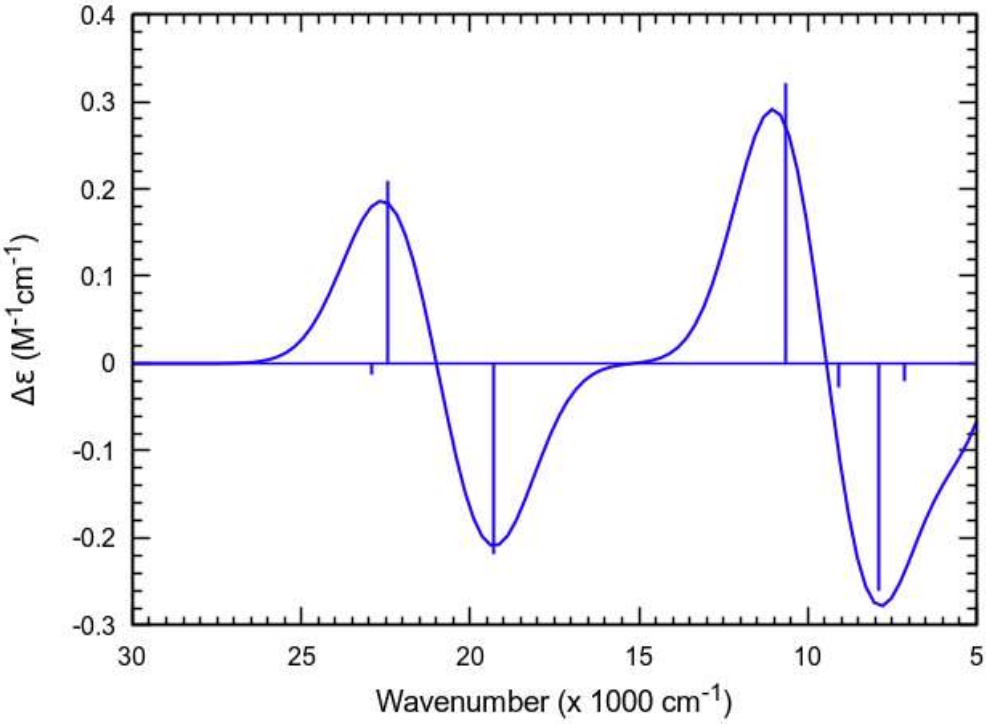

Figure S118: Calculated circular dichroism spectrum of **Ni(IB)Br_2** at the CASSCF level with 22e,12o active space (*cf.* Figure S91).

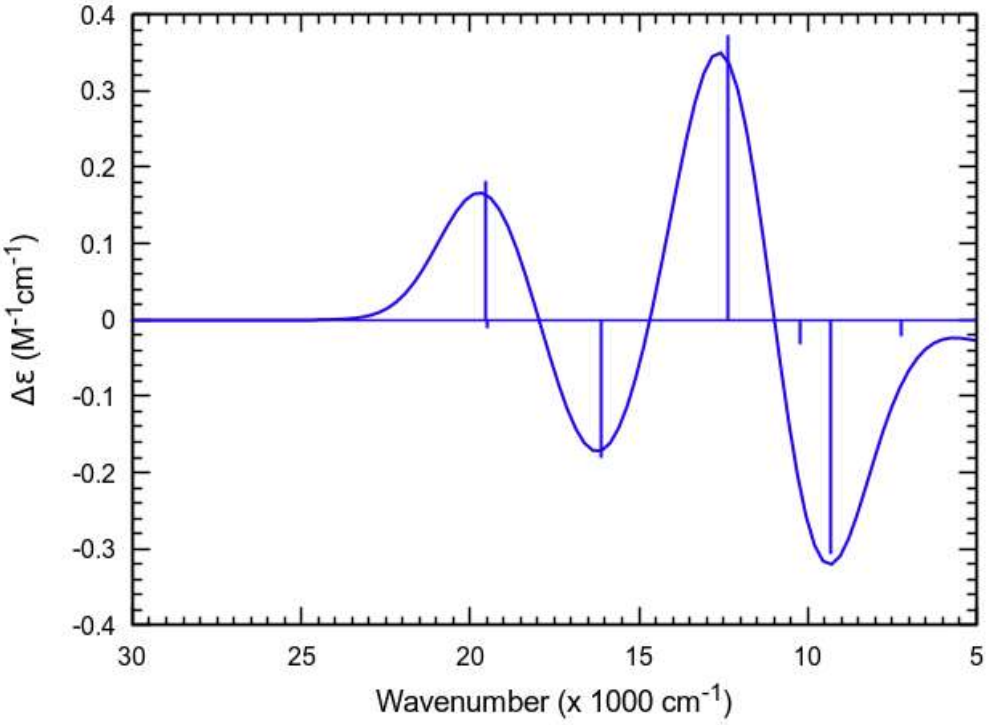

***Figure S119**: Calculated circular dichroism spectrum of **Ni^{II}(IB)Br$_2$** at the MS-CASPT2 level with 22e,12o active space (cf. Figure S91).*

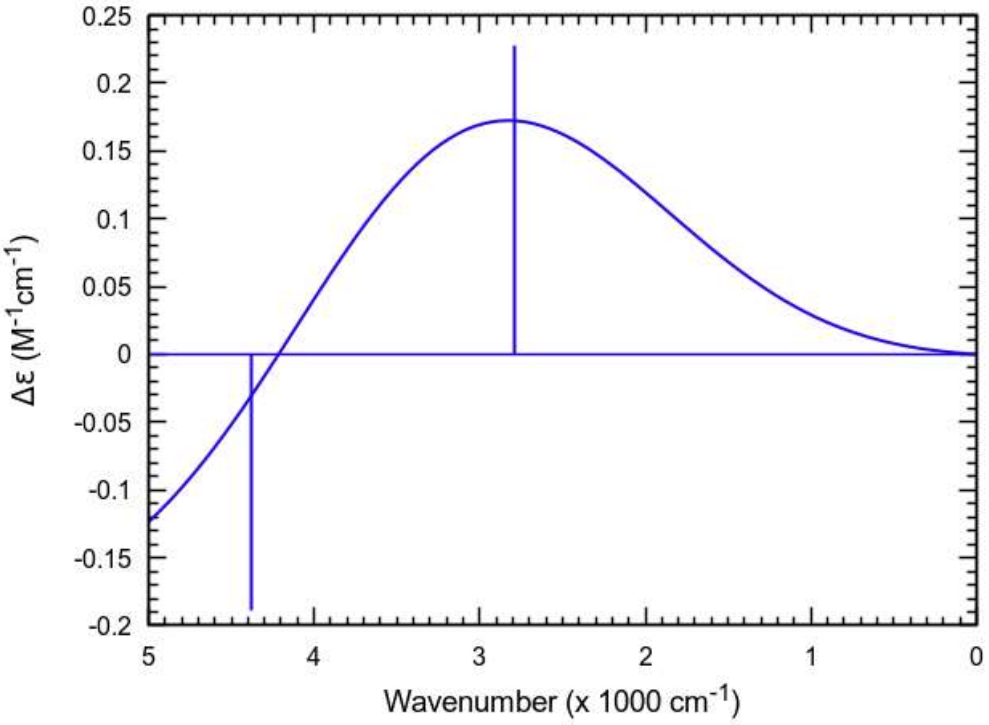

***Figure S120**: Calculated circular dichroism spectrum of **$Ni^{II}(IB)Cl_2$** at the CASSCF level with 22e,12o active space (cf. Figure S91) in the 0-5000 cm^{-1} energy region.*

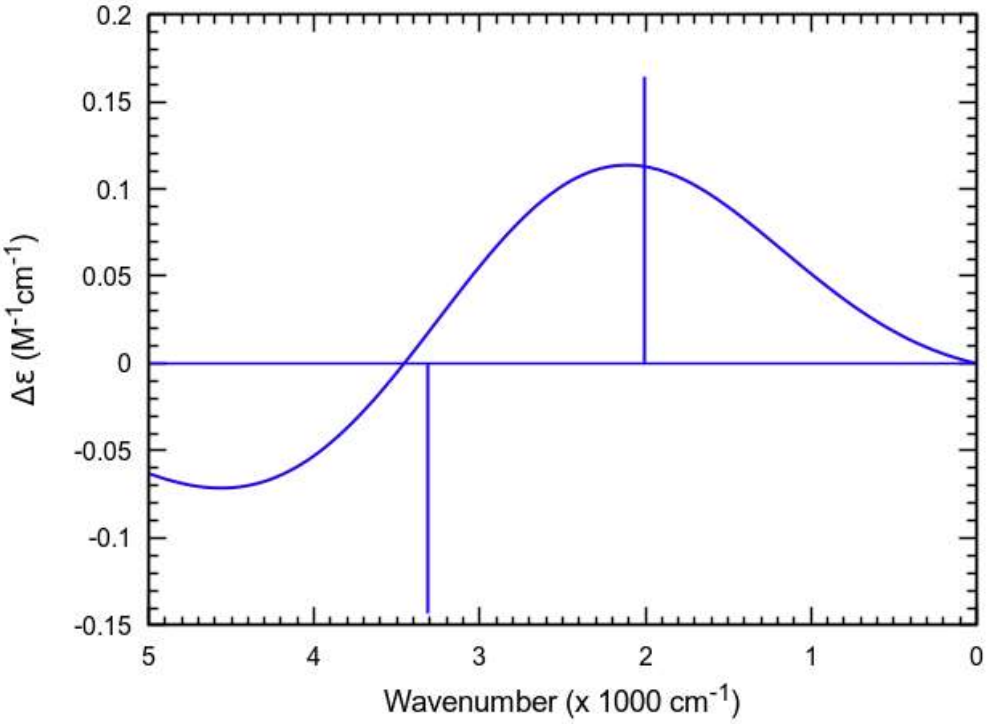

***Figure S121**: Calculated circular dichroism spectrum of **$Ni^{II}(IB)Cl_2$** at the MS-CASPT2 level with 22e,12o active space (cf. Figure S91) in the 0-5000 cm^{-1} energy region.*

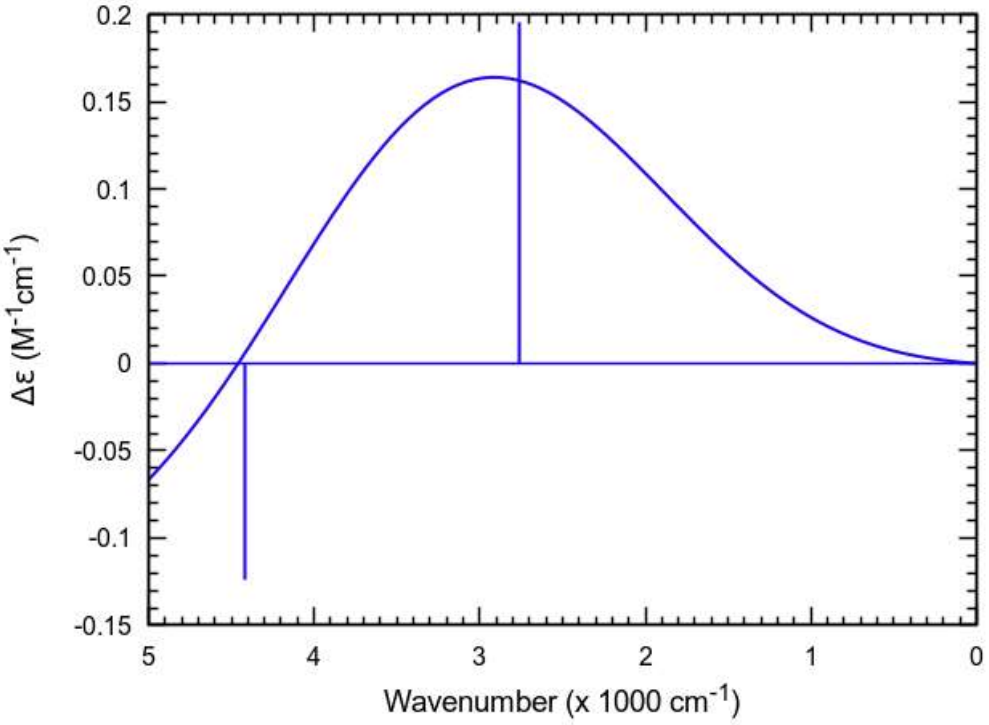

***Figure S122**: Calculated circular dichroism spectrum of **Ni^{II}(IB)Br_2** at the CASSCF level with 22e,12o active space (cf. Figure S91) in the 0-5000 cm^{-1} energy region.*

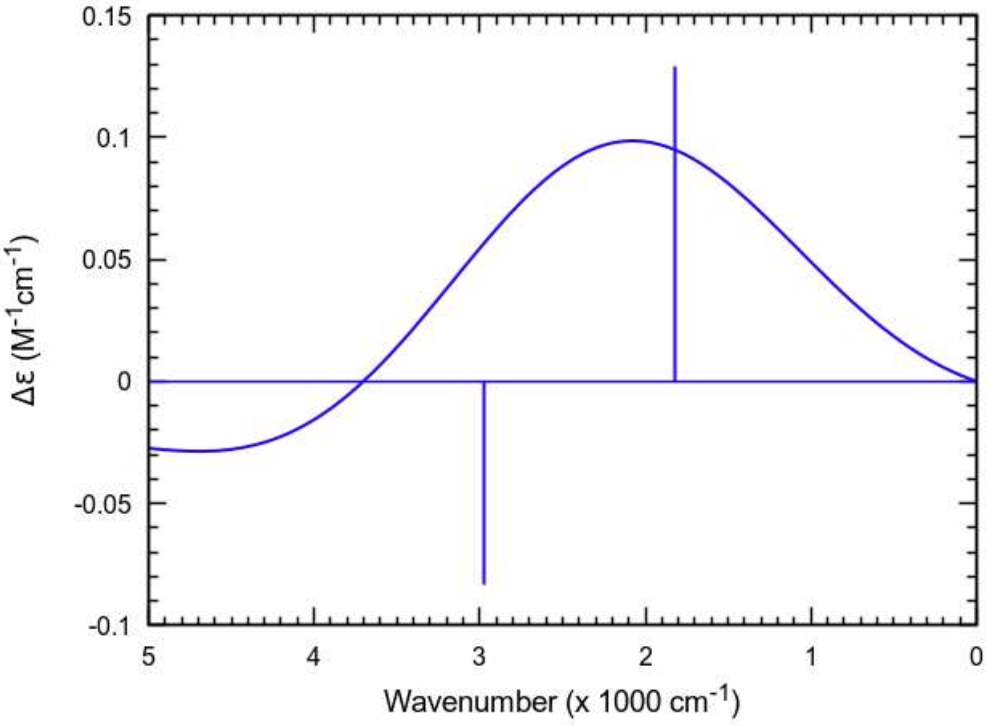

***Figure S123**: Calculated circular dichroism spectrum of **$Ni^{II}(IB)Br_2$** at the MS-CASPT2 level with 22e,12o active space (cf. Figure S91) in the 0-5000 cm^{-1} energy region.*

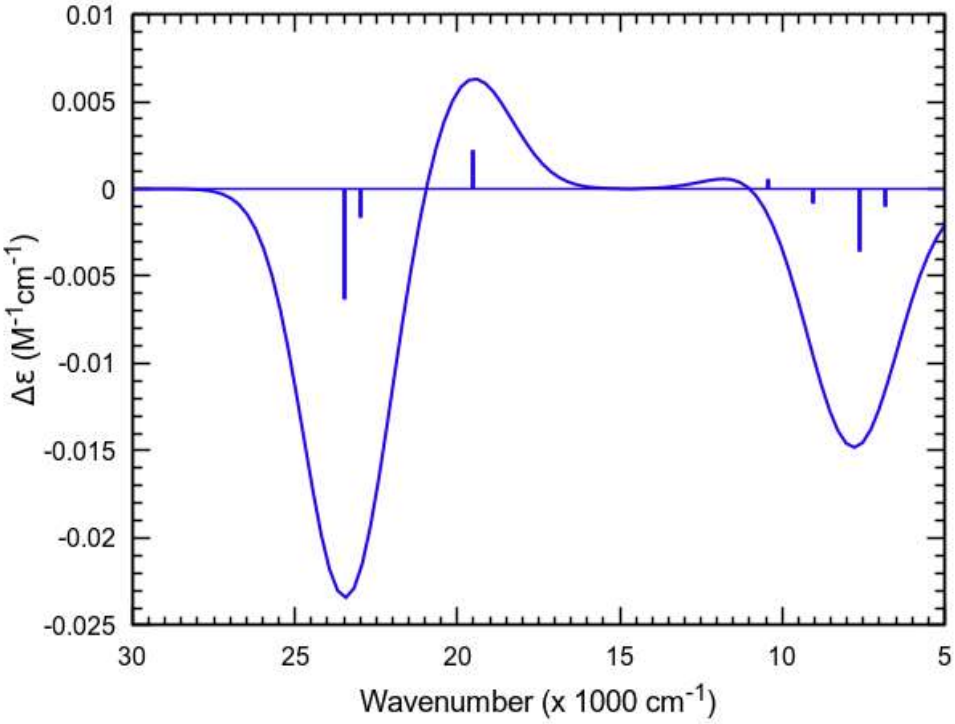

***Figure S124**: Calculated magnetic circular dichroism spectrum of **$Ni^{II}(IB)Cl_2$** at the CASSCF level with 22e,12o active space (cf. Figure S91).*

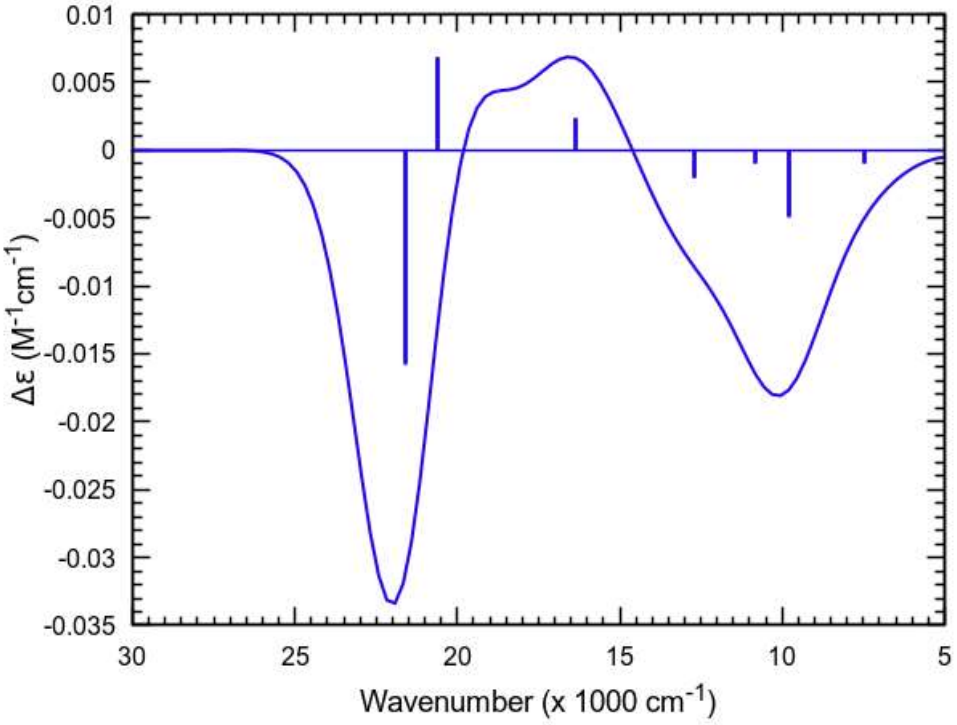

***Figure S125**: Calculated magnetic circular dichroism spectrum of **$Ni^{II}(IB)Cl_2$** at the MS-CASPT2 level with 22e,12o active space (cf. Figure S91).*

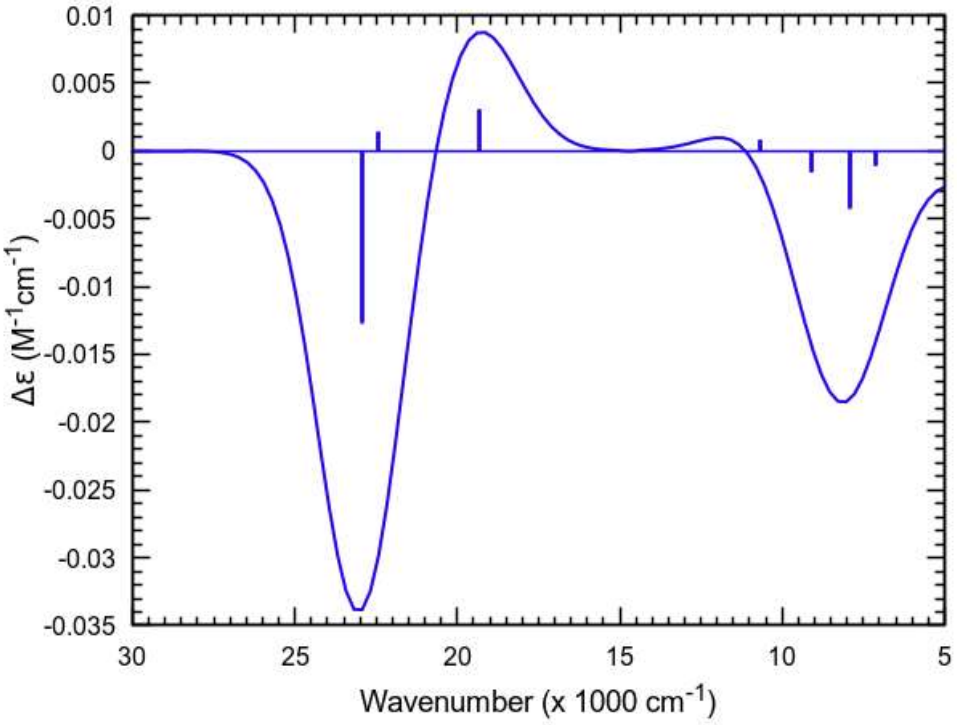

***Figure S126**: Calculated magnetic circular dichroism spectrum of **$Ni^{II}(IB)Br_2$** at the CASSCF level with 22e,12o active space (cf. Figure S91).*

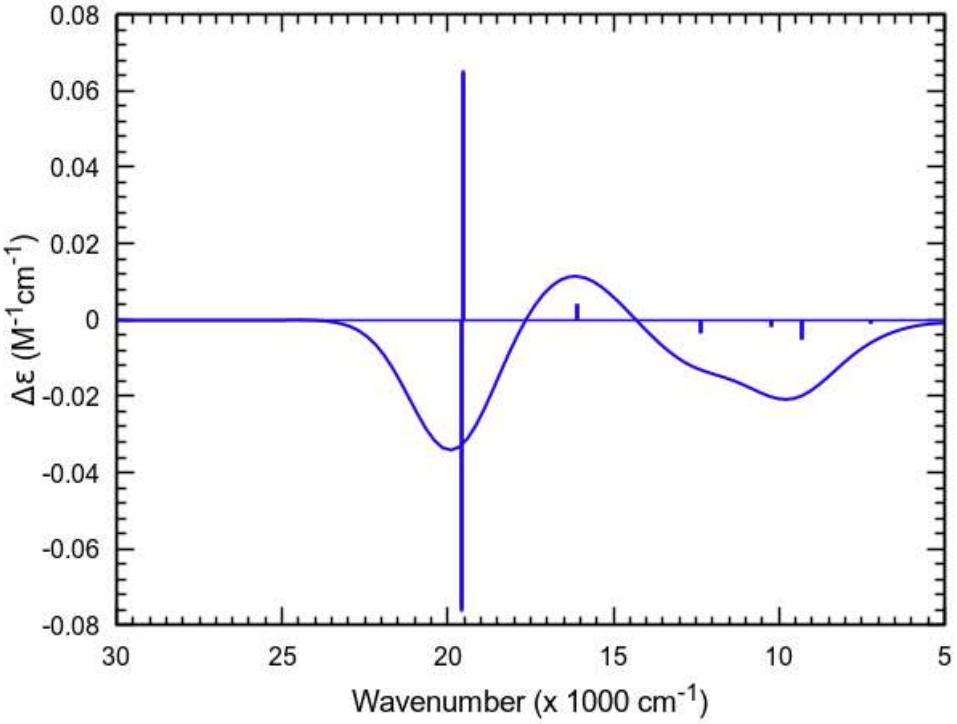

***Figure S127**: Calculated magnetic circular dichroism spectrum of **$Ni^{II}(IB)Br_2$** at the MS-CASPT2 level with 22e,12o active space (cf. Figure S91).*

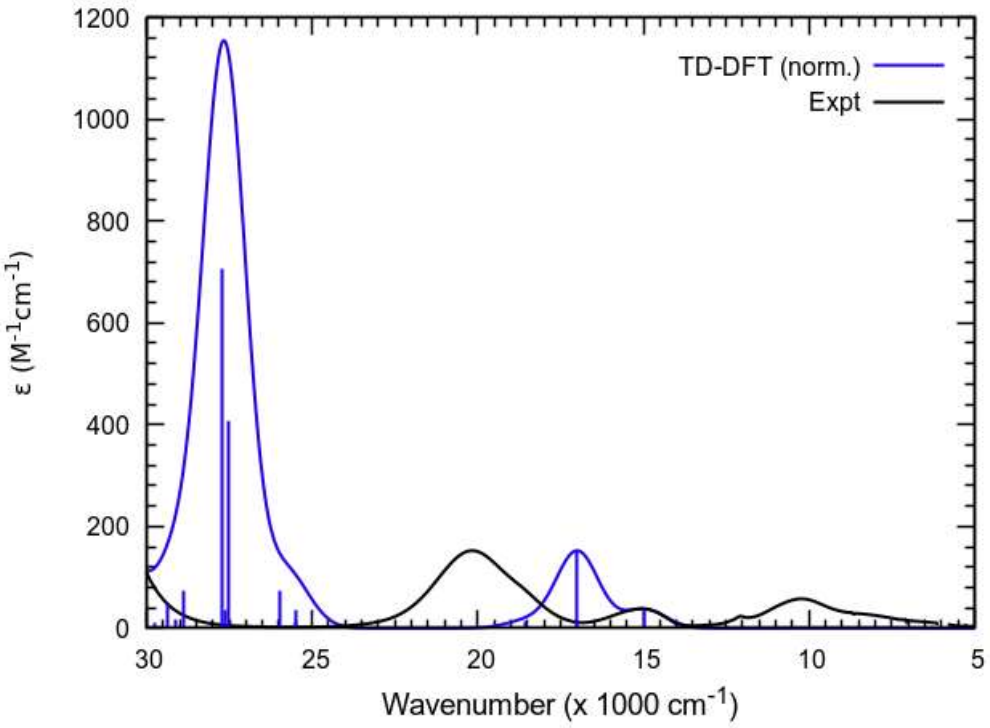

***Figure S128**: Comparison of experimental vs. calculated UV-vis-NIR spectrum of **Ni^{II}(IB)Cl_2** at the TDDFT (TPSSh) level with CPCM solvation model (ε = 38).*

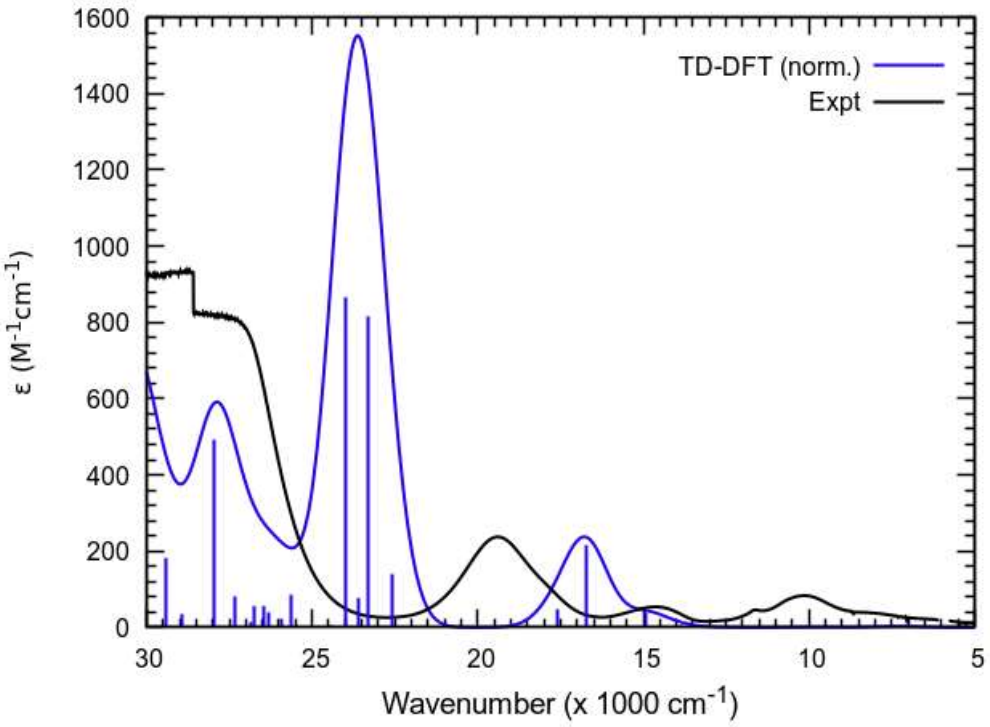

***Figure S129**: Comparison of experimental vs. calculated UV-vis-NIR spectrum of **$Ni^{II}(IB)Br_2$** at the TDDFT (TPSSh) level with CPCM solvation model (ε = 38).*

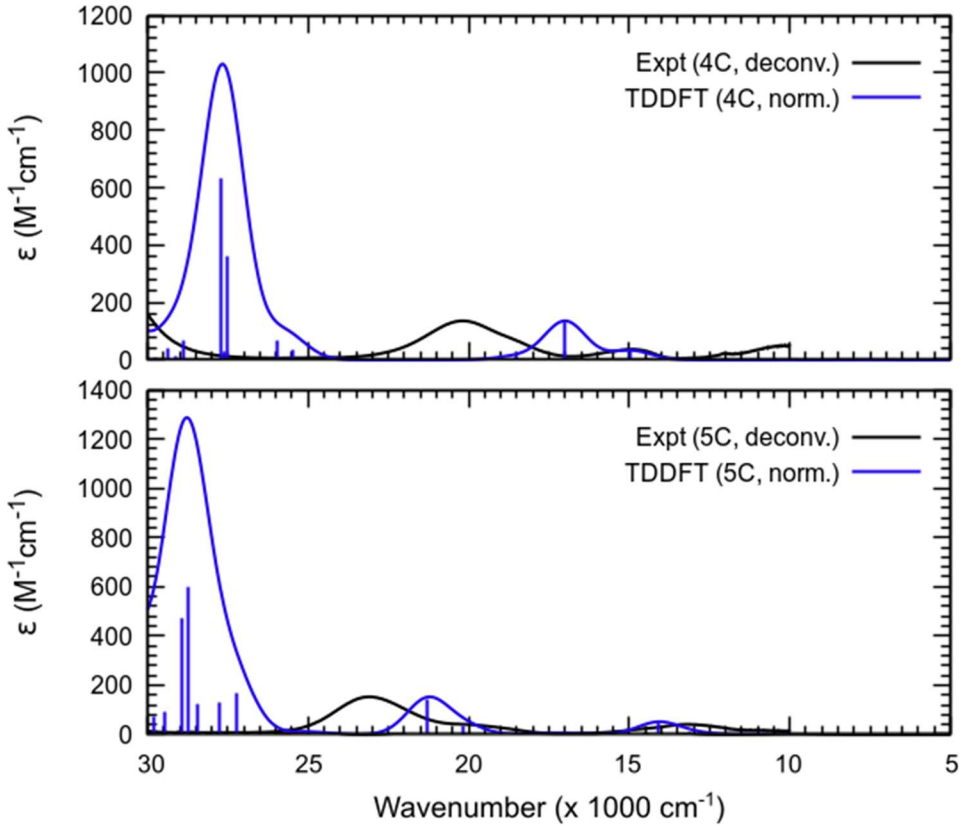

***Figure S130**: Comparison of UV-vis-NIR spectra of four-coordinate **$Ni^{II}(IB)Cl_2$** (4C) and five-cooordinate (5C) $Ni^{II}(IB)(DMA)Cl_2$, as deconvolved from variable-temperature UV-vis-NIR spectra in **Figure 7** vs. calculated spectra of **$Ni^{II}(IB)Cl_2$** and $Ni^{II}(IB)(O\text{-}DMA)Cl_2$ at the TDDFT (TPSSh) level with CPCM solvation model (ε = 38).*

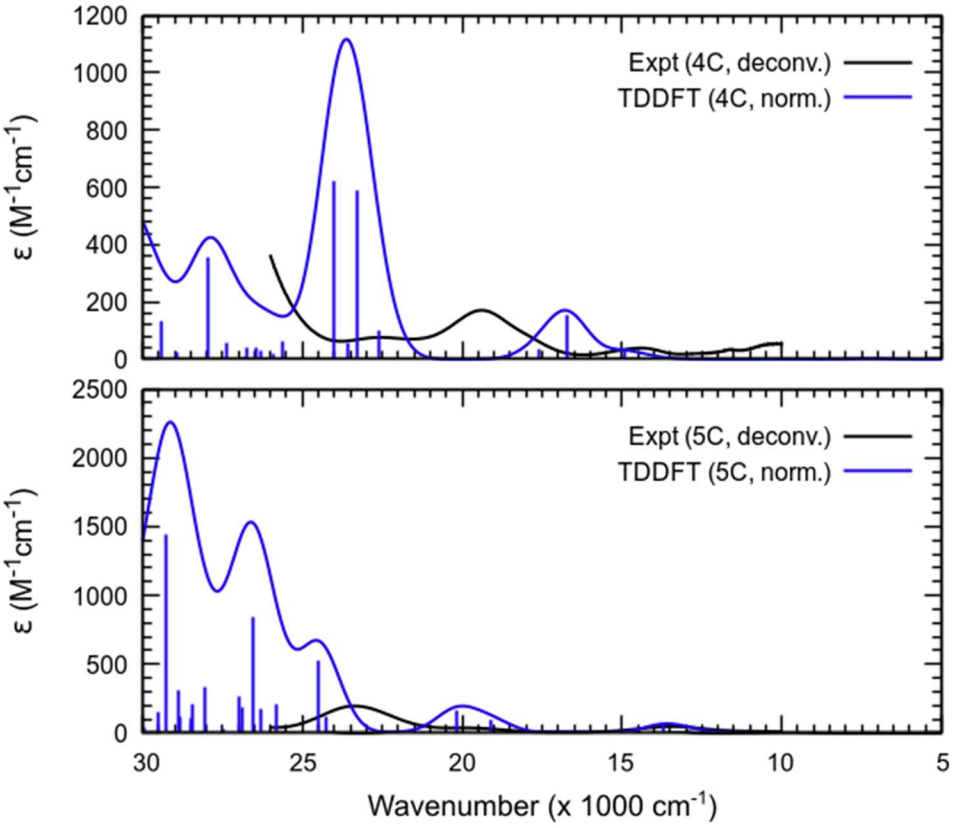

***Figure S131**: Comparison of UV-vis-NIR spectra of four-coordinate **$Ni^{II}(IB)Br_2$** (4C) and five-cooordinate (5C) $Ni^{II}(IB)(DMA)Br_2$, as deconvolved from variable-temperature UV-vis-NIR vs. calculated spectra of **$Ni^{II}(IB)Br_2$** and $Ni^{II}(IB)(O\text{-}DMA)Br_2$ at the TDDFT (TPSSh) level with CPCM solvation model (ε = 38).*

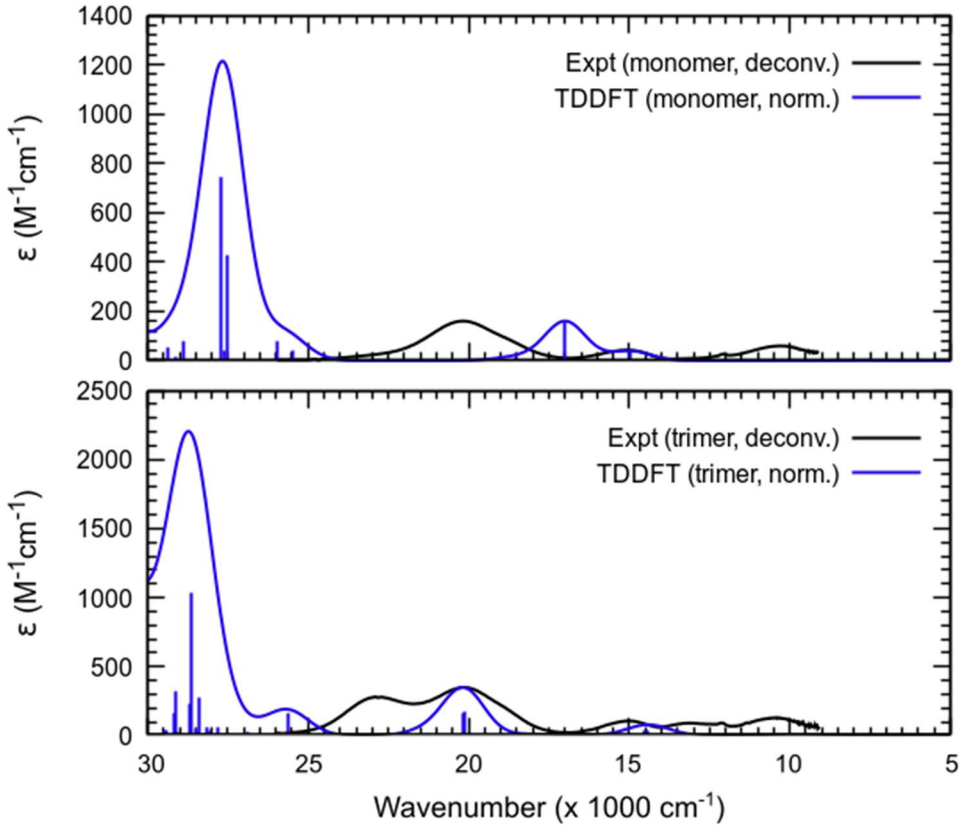

***Figure S132**: Comparison of UV-vis-NIR spectra of **Ni^{II}(IB)Cl$_2$** monomer and trimer, as deconvolved from variable-temperature UV-vis-NIR in **Figure 7** vs. calculated spectra of **Ni^{II}(IB)Cl$_2$** monomer and trimer at the TDDFT (TPSSh) level with CPCM solvation model (ε = 38).*

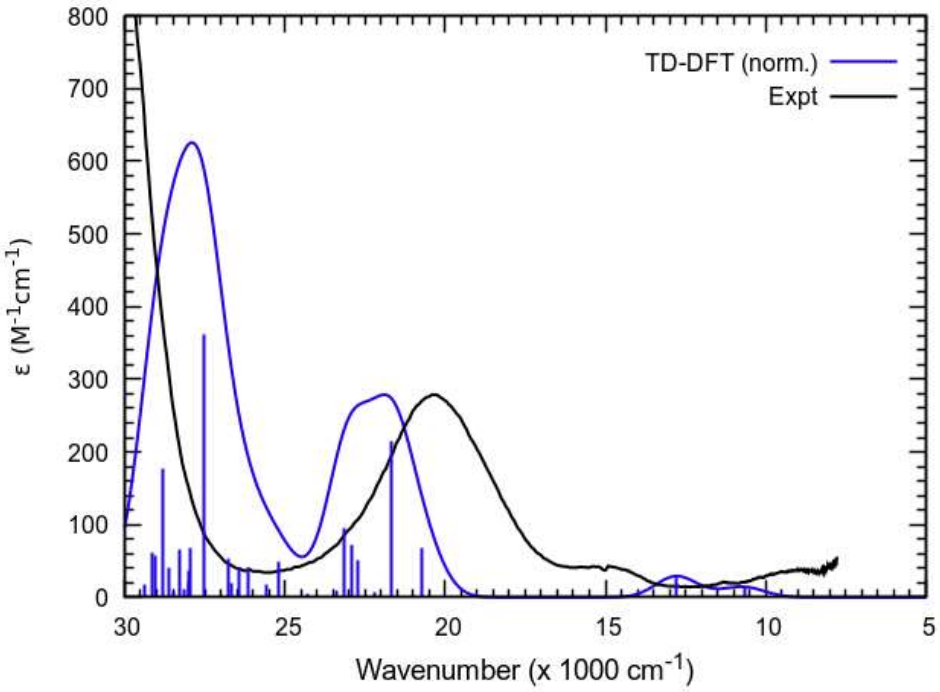

***Figure S133**: Comparison of experimental UV-vis-NIR spectrum of **Ni^{II}(IB)Cl$_2$** collected after five minutes of controlled potential electrolysis at −1.50 V vs. Fc$^{+/0}$ in DCM vs. calculated UV-vis-NIR spectrum of **Ni^{I}(IB)Cl** at the TDDFT (TPSSh/CPCM) level.*

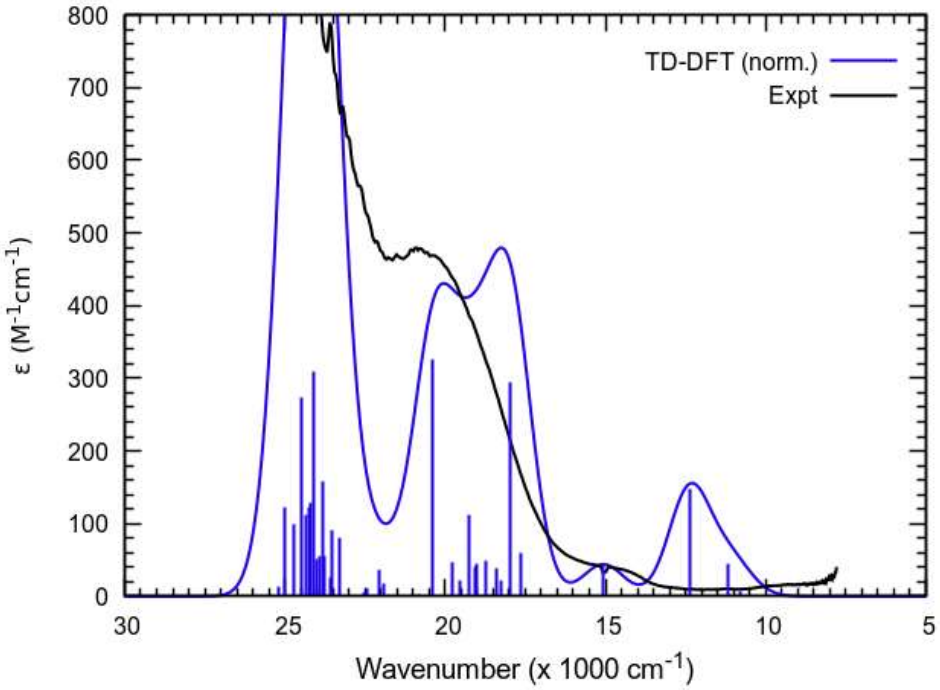

***Figure S134**: Comparison of experimental UV-vis-NIR spectrum of **$Ni^{II}(IB)Cl_2$** collected after five minutes of controlled potential electrolysis at –1.80 V vs. $Fc^{+/0}$ in DMA vs. calculated UV-vis-NIR spectrum of **$Ni^{I}(IB)(O\text{-}DMA)Cl$** at the TDDFT (TPSSh/CPCM) level.*

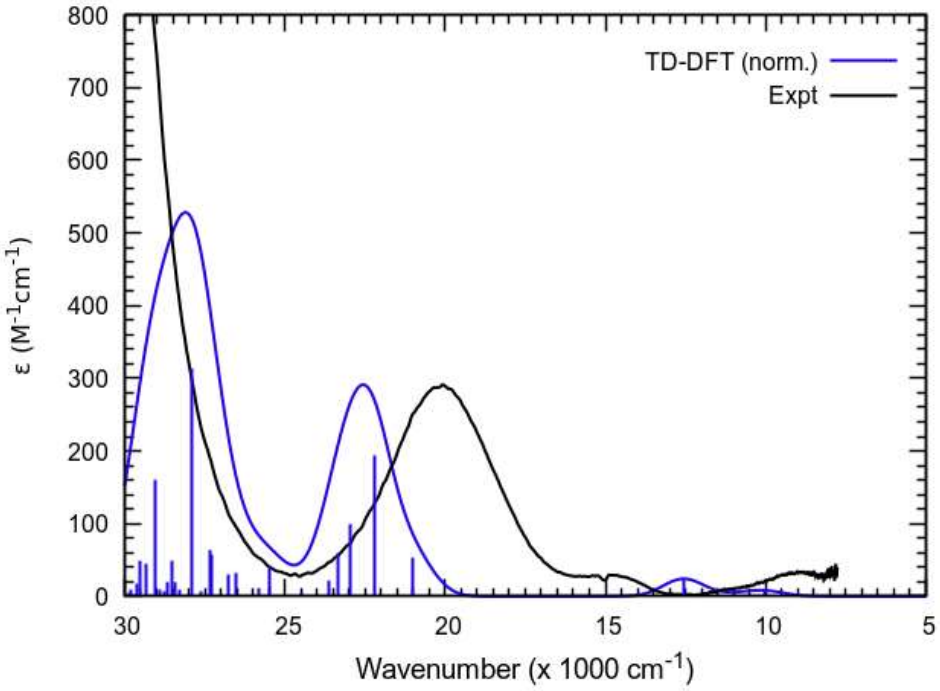

***Figure S135**: Comparison of experimental UV-vis-NIR spectrum of **$Ni^{II}(IB)Br_2$** collected after five minutes of controlled potential electrolysis at –1.50 V vs. $Fc^{+/0}$ in DCM vs. calculated UV-vis-NIR spectrum of **$Ni^{I}(IB)Br$** at the TDDFT (TPSSh/CPCM) level.*

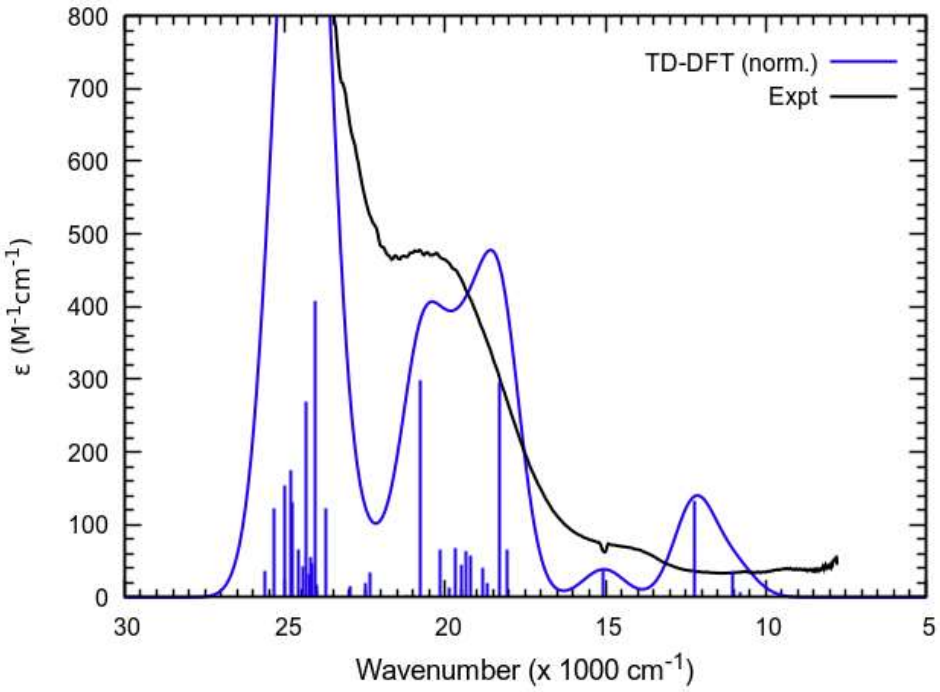

***Figure S136**: Comparison of experimental UV-vis-NIR spectrum of **Ni^{II}(IB)Br$_2$** collected after four minutes of controlled potential electrolysis at –1.60 V vs. Fc$^{+/0}$ in DMA vs. calculated UV-vis-NIR spectrum of **Ni^{I}(IB)(O-DMA)Br** at the TDDFT (TPSSh/CPCM) level.*

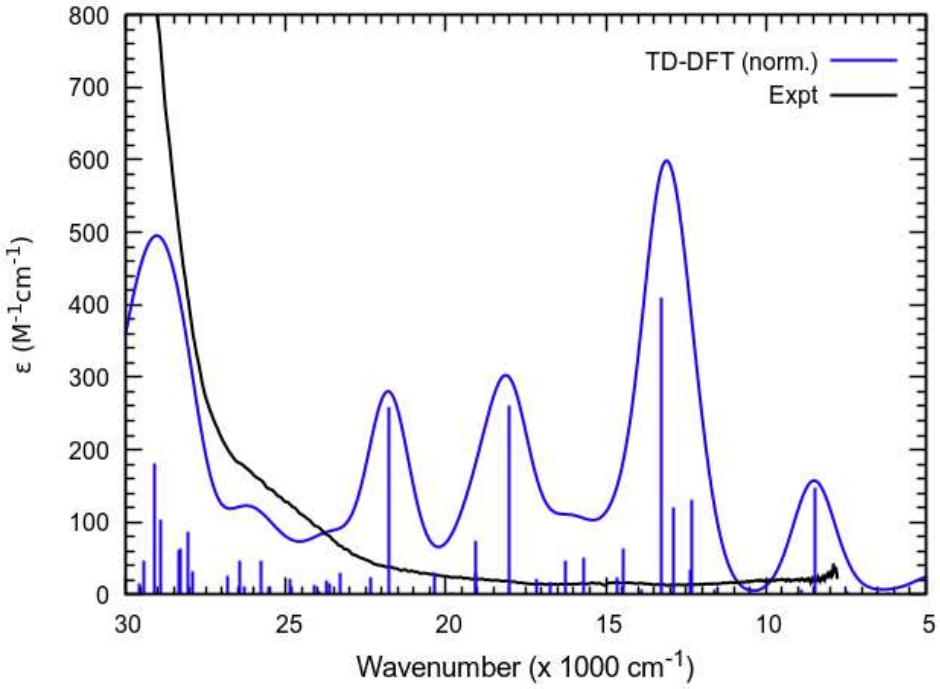

***Figure S137**: Comparison of experimental UV-vis-NIR spectrum of **$Ni^{II}(IB)Cl_2$** collected after five minutes of controlled potential electrolysis at 1.50 V vs. $Fc^{+/0}$ in DCM vs. calculated UV-vis-NIR spectrum of **$Ni^{III}(IB)Cl_2$** at the TDDFT (TPSSh/CPCM) level.*

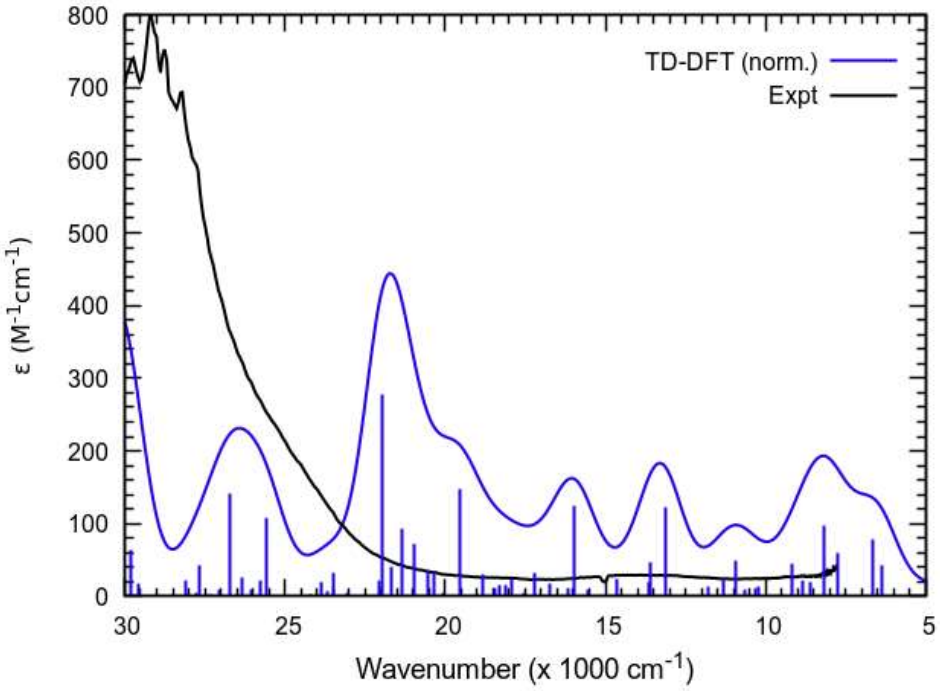

***Figure S138**: Comparison of experimental UV-vis-NIR spectrum of **$Ni^{II}(IB)Cl_2$** collected after four minutes of controlled potential electrolysis at 0.70 V vs. $Fc^{+/0}$ in DMA vs. calculated UV-vis-NIR spectrum of **$Ni^{III}(IB)(O\text{-}DMA)Cl_2$** at the TDDFT (TPSSh/CPCM) level.*

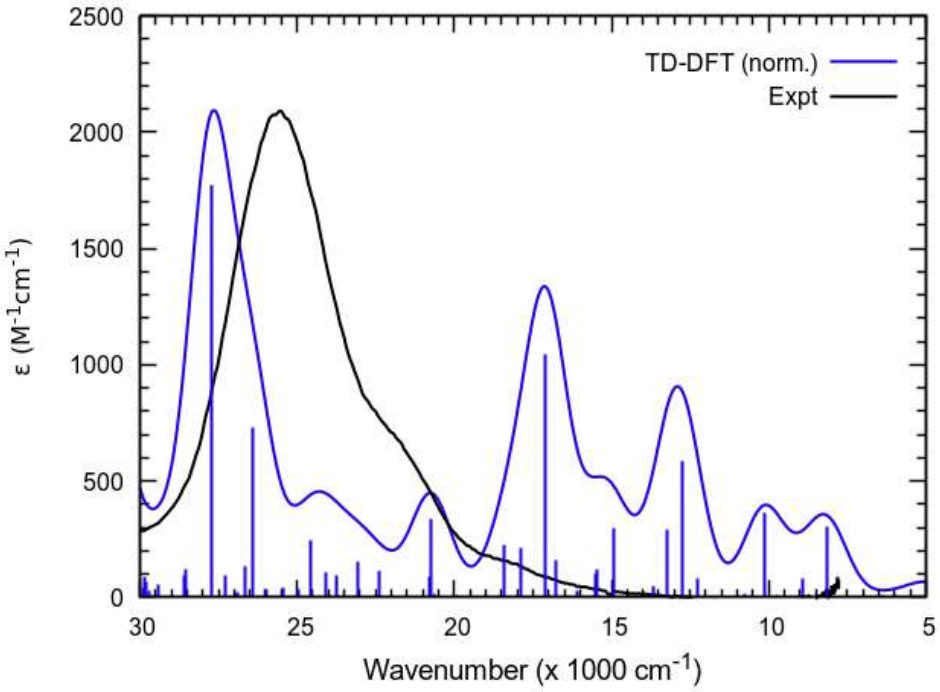

***Figure S139**: Comparison of experimental UV-vis-NIR spectrum of **Ni^{II}(IB)Br$_2$** collected after five minutes of controlled potential electrolysis at 1.20 V vs. Fc$^{+/0}$ in DCM vs. calculated UV-vis-NIR spectrum of **Ni^{III}(IB)Br$_2$** at the TDDFT (TPSSh/CPCM) level.*

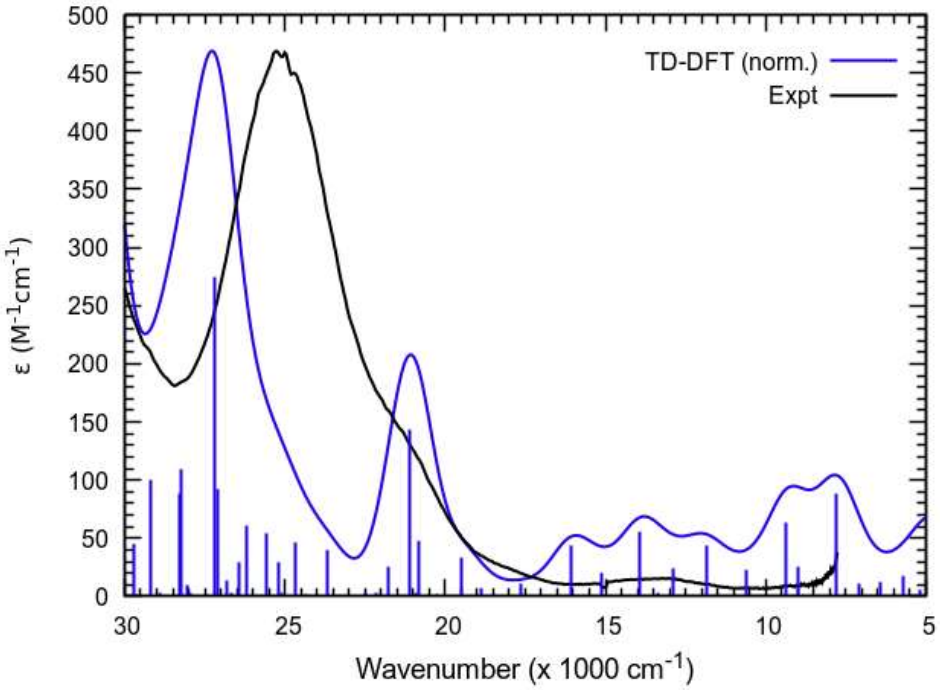

***Figure S140**: Comparison of experimental UV-vis-NIR spectrum of **Ni^{II}(IB)Br$_2$** collected after four minutes of controlled potential electrolysis at 0.24 V vs. Fc$^{+/0}$ in DMA vs. calculated UV-vis-NIR spectrum of **Ni^{III}(IB)(O-DMA)Br$_2$** at the TDDFT (TPSSh/CPCM) level.*

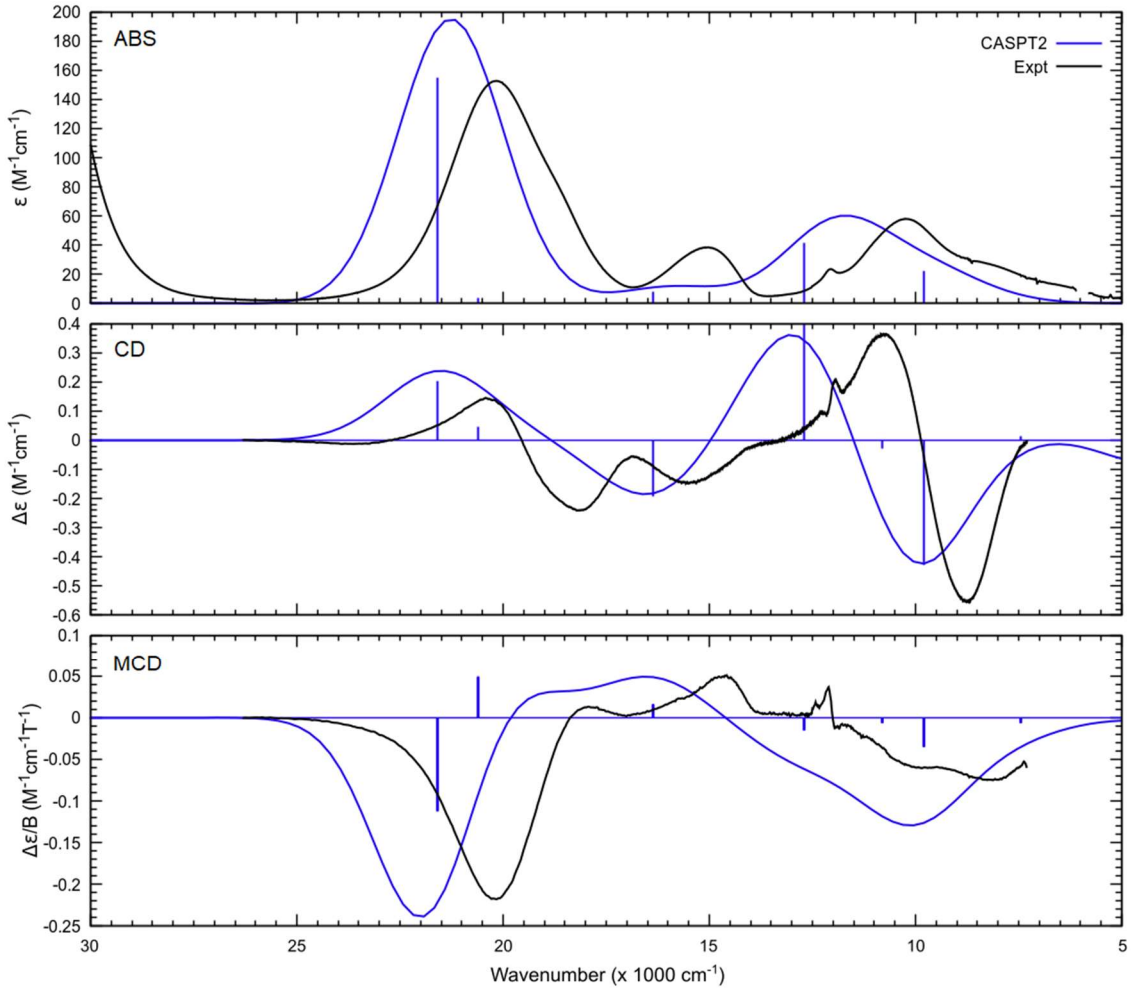

***Figure S141**: Comparison of the experimental UV-vis-NIR (ABS), circular dichroism* (CD), and magnetic circular dichroism (MCD) of NiII(IB)Cl2 vs. calculated spectra at the MS-CASPT2 level with 22e,12o active space (cf. Figure S91) with PCM solvation model (ε = 38).

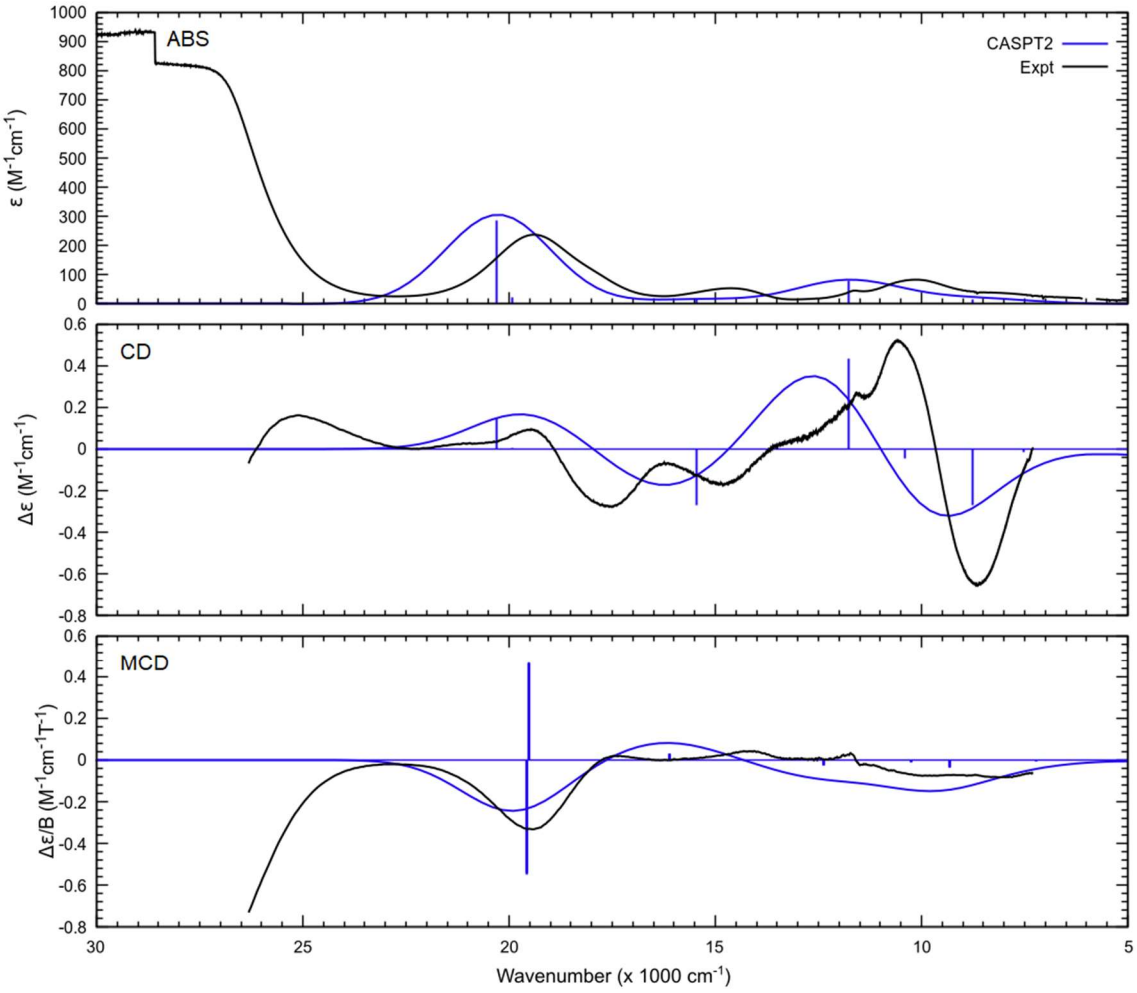

***Figure S142**: Comparison of the experimental UV-vis-NIR (ABS), circular dichroism (CD), and magnetic circular dichroism (MCD) of **Ni^{II}(IB)Br_2** vs. calculated spectra at the MS-CASPT2 level with 22e,12o active space (cf. Figure S91) with PCM solvation model (ε = 38).*

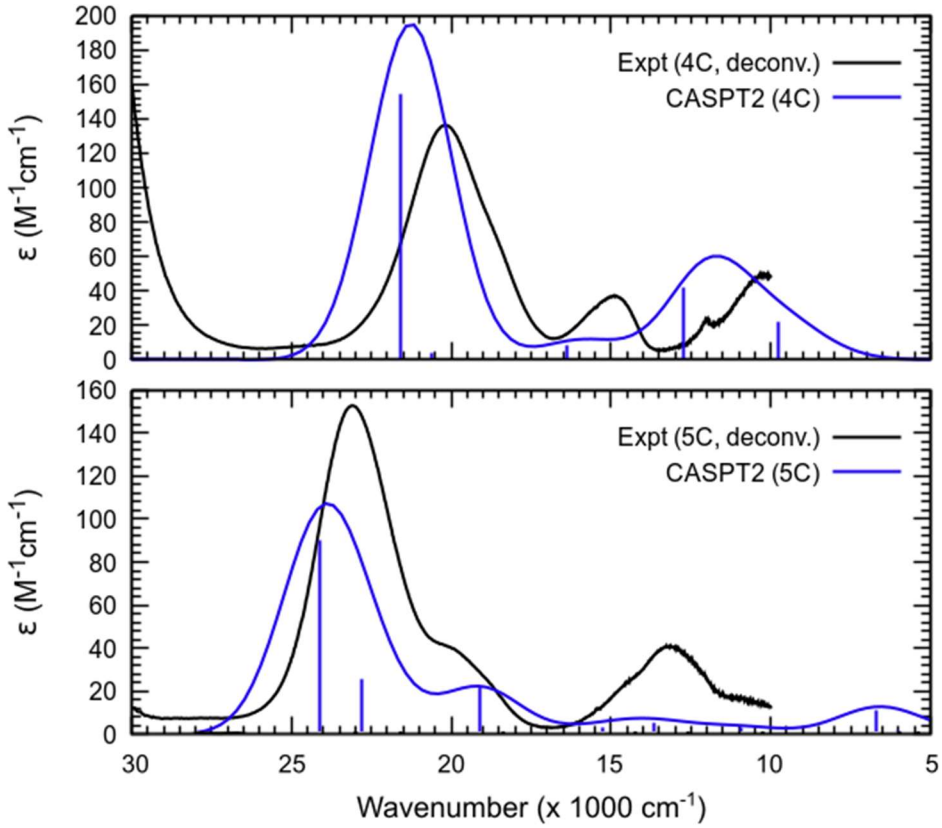

***Figure S143**: Comparison of UV-vis-NIR spectra of four-coordinate (4C) **$Ni^{II}(IB)Cl_2$** and five-coordinate (5C) $Ni^{II}(IB)(DMA)Cl_2$, as deconvolved from variable-temperature UV-vis-NIR spectra in **Figure 7** in the main text vs. calculated spectra of **$Ni^{II}(IB)Cl_2$** and $Ni^{II}(IB)(O\text{-}DMA)Cl_2$ at the MS-CASPT2 level with 22e,12o active space (cf. Figure S91) with PCM solvation model (ε = 38).*

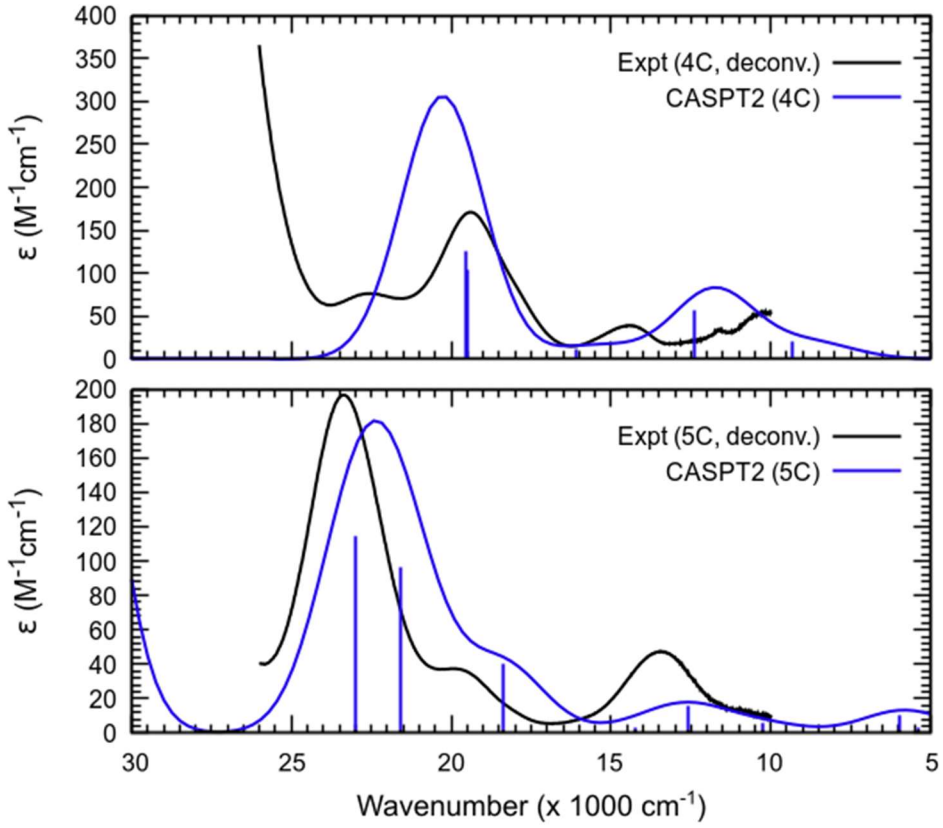

***Figure S144**: Comparison of UV-vis-NIR spectra of four-coordinate (4C) **$Ni^{II}(IB)Br_2$** and five-coordinate (5C) $Ni^{II}(IB)(DMA)Br_2$, as deconvolved from variable-temperature UV-vis-NIR spectra vs. calculated spectra of **$Ni^{II}(IB)Br_2$** and $Ni^{II}(IB)(O\text{-}DMA)Br_2$ at the MS-CASPT2 level with 22e,12o active space (cf. Figure S91) with PCM solvation model (ε = 38).*

S.8.4. Additional Tables

***Table S10**: Calculated electronic transitions for **$Ni^{II}(IB)Cl_2$** at the TDDFT (TPSSh) level in the gas phase.*

Transition	Energy (eV)	Energy (cm^{-1})	Energy ($kcal.mol^{-1}$)	Oscillator Strength
1	0.97	7854	22.5	0.0000886
2	1.21	9746	27.9	0.0000010
3	1.71	13795	39.4	0.0000004
4	1.83	14721	42.1	0.0008692
5	1.97	15883	45.4	0.0034545
6	2.36	19030	54.4	0.0003510

***Table S11**: Calculated electronic transitions for **$Ni^{II}(IB)Cl_2$** at the TDDFT (TPSSh) level with CPCM solvation model (ε = 38).*

Transition	Energy (eV)	Energy (cm^{-1})	Energy ($kcal.mol^{-1}$)	Oscillator Strength
1	0.95	7629	21.8	0.0000112
2	1.25	10056	28.8	0.0000052
3	1.78	14393	41.1	0.0000114
4	1.86	14991	42.9	0.0012049
5	2.12	17116	48.9	0.0046184
6	2.29	18462	52.8	0.0004352

***Table S12**: Calculated electronic transitions for **$Ni^{II}(IB)Br_2$** at the TDDFT (TPSSh) level in the gas phase.*

Transition	Energy (eV)	Energy (cm^{-1})	Energy ($kcal.mol^{-1}$)	Oscillator Strength
1	0.92	7423	21.2	0.0000991
2	1.17	9443	27.0	0.0000183
3	1.63	13183	37.7	0.0000467
4	1.81	14569	41.7	0.0009624

5	1.92	15485	44.3	0.0032813
6	2.22	17943	51.3	0.0006201

***Table S13**: Calculated electronic transitions for **$Ni^{II}(IB)Br_2$** at the TDDFT (TPSSh) level with CPCM solvation model (ε = 38).*

Transition	Energy (eV)	Energy (cm^{-1})	Energy ($kcal.mol^{-1}$)	Oscillator Strength
1	0.90	7242	20.7	0.0000853
2	1.21	9730	27.8	0.0000262
3	1.73	13924	39.8	0.0001327
4	1.86	14972	42.8	0.0010470
5	2.09	16834	48.1	0.0053356
6	2.17	17529	50.1	0.0014775

***Table S14**: Calculated electronic transitions for $Ni^{II}(IB)(O\text{-}DMA)Cl_2$ at the TDDFT (TPSSh) level with CPCM solvation model (ε = 38).*

Transition	Energy (eV)	Energy (cm^{-1})	Energy ($kcal.mol^{-1}$)	Oscillator Strength
1	1.37	11067	31.6	0.0000380
2	1.63	13109	37.5	0.0001836
3	1.75	14100	40.3	0.0012619
4	2.14	17242	49.3	0.0001261
5	2.50	20197	57.7	0.0009458
6	2.64	21286	60.9	0.0036666

***Table S15**: Calculated electronic transitions for $Ni^{II}(IB)(O\text{-}DMA)Br_2$ at the TDDFT (TPSSh) level with CPCM solvation model (ε = 38).*

Transition	Energy (eV)	Energy (cm^{-1})	Energy ($kcal.mol^{-1}$)	Oscillator Strength
1	1.41	11365	32.5	0.0000307
2	1.60	12885	36.8	0.0003500
3	1.70	13690	39.1	0.0012969

4	2.08	16766	47.9	0.0001541
5	2.37	19099	54.6	0.0019739
6	2.50	20181	57.7	0.0036730

***Table S16**: Calculated electronic transitions for **$Ni^{II}(IB)Cl_2$** trimer at the TDDFT (TPSSh) level with CPCM solvation model (ε = 38).*

Transition	Energy (eV)	Energy (cm^{-1})	Energy ($kcal.mol^{-1}$)	Oscillator Strength
1	1.21	9746	27.9	0.0000724
2	1.24	9985	28.5	0.0000660
3	1.72	13901	39.7	0.0000486
4	1.73	13963	39.9	0.0001179
5	1.74	13999	40.0	0.0001099
6	1.74	14072	40.2	0.0000733
7	1.79	14445	41.3	0.0009064
8	1.80	14515	41.5	0.0008827
9	2.05	16497	47.2	0.0001656
10	2.24	18069	51.7	0.0000526
11	2.24	18075	51.7	0.0002236
12	2.50	20132	57.6	0.0045479
13	2.50	20187	57.7	0.0040941
14	2.52	20297	58.0	0.0001275
15	2.63	21184	60.6	0.0001433
16	2.64	21259	60.8	0.0004167
17	2.65	21361	61.1	0.0001756
18	2.66	21422	61.2	0.0002617

***Table S17**: Calculated electronic transitions for **$Ni^{II}(IB)Br_2$** trimer at the TDDFT (TPSSh) level with CPCM solvation model (ε = 38).*

Transition	Energy (eV)	Energy (cm^{-1})	Energy ($kcal.mol^{-1}$)	Oscillator Strength
1	1.18	9478	27.1	0.0000722

2	1.19	9567	27.4	0.0000716
3	1.64	13229	37.8	0.0002195
4	1.66	13348	38.2	0.0002605
5	1.67	13433	38.4	0.0001369
6	1.68	13560	38.8	0.0000610
7	1.74	14022	40.1	0.0009517
8	1.75	14094	40.3	0.0009310
9	1.98	15958	45.6	0.0001217
10	2.22	17893	51.2	0.0001162
11	2.22	17919	51.2	0.0003179
12	2.40	19353	55.3	0.0030564
13	2.41	19404	55.5	0.0065833
14	2.42	19492	55.7	0.0016736
15	2.51	20257	57.9	0.0019291
16	2.52	20294	58.0	0.0008290
17	2.54	20463	58.5	0.0001849
18	2.55	20547	58.7	0.0002717

***Table S18**: Calculated electronic transitions for **Ni^{II}(IB)Cl_2** at the MS-CASPT2 level with 22e,12o active space (cf. Figure S91) in the gas phase.*

Transition	Energy (eV)	Energy (cm^{-1})	Energy (kcal.mol^{-1})	Oscillator Strength	Assignment from CI vector
1	0.31	2519	7.2	0.0000111	$^3B_1(F) \rightarrow {}^3A_2(F)$
2	0.40	3198	9.1	0.0000026	$^3B_1(F) \rightarrow {}^3B_2(F)$
3	0.95	7698	22.0	0.0000127	$^3B_1(F) \rightarrow {}^3B_2$
4	1.19	9584	27.4	0.0002858	$^3B_1(F) \rightarrow {}^3A_1$
5	1.37	11014	31.5	0.0000022	$^3B_1(F) \rightarrow {}^3B_1$
6	1.48	11896	34.0	0.0007678	$^3B_1(F) \rightarrow {}^3A_2$
7	1.97	15903	45.5	0.0001611	$^3B_1(F) \rightarrow {}^3B_2(P)$
8	2.62	21148	60.5	0.0000661	$^3B_1(F) \rightarrow {}^3B_1(P)$

9	2.64	21267	60.8	0.0026258	$^3B_1(F) \rightarrow {}^3A_2(P)$

***Table S19**: Calculated electronic transitions for **$Ni^{II}(IB)Br_2$** at the MS-CASPT2 level with 22e,12o active space (cf. Figure S91) in the gas phase.*

Transition	Energy (eV)	Energy (cm^{-1})	Energy (kcal.mol^{-1})	Oscillator Strength	Assignment from CI vector
1	0.29	2347	6.7	0.0000201	$^3B_1(F) \rightarrow {}^3A_2(F)$
2	0.36	2897	8.3	0.0000030	$^3B_1(F) \rightarrow {}^3B_2(F)$
3	0.93	7513	21.5	0.0000254	$^3B_1(F) \rightarrow {}^3B_2$
4	1.09	8755	25.0	0.0002450	$^3B_1(F) \rightarrow {}^3A_1$
5	1.29	10392	29.7	0.0000199	$^3B_1(F) \rightarrow {}^3B_1$
6	1.46	11779	33.7	0.0011246	$^3B_1(F) \rightarrow {}^3A_2$
7	1.92	15464	44.2	0.0002214	$^3B_1(F) \rightarrow {}^3B_2(P)$
8	2.47	19914	56.9	0.0002996	$^3B_1(F) \rightarrow {}^3B_1(P)$
9	2.52	20296	58.0	0.0039389	$^3B_1(F) \rightarrow {}^3A_2(P)$

***Table S20**: Calculated electronic transitions for $Ni^{II}(IB)(O\text{-}DMA)Cl_2$ at the MS-CASPT2 level with 22e,12o active space (cf. Figure S91) in the gas phase.*

Transition	Energy (eV)	Energy (cm^{-1})	Energy (kcal.mol^{-1})	Oscillator Strength	Assignment from CI vector
1	0.62	5037	14.4	0.0000128	$^3B_1(F) \rightarrow {}^3A_2(F)$
2	0.75	6028	17.2	0.0000218	$^3B_1(F) \rightarrow {}^3B_2(F)$
3	0.83	6705	19.2	0.0001529	$^3B_1(F) \rightarrow {}^3A_1$
4	1.36	10946	31.3	0.0000486	$^3B_1(F) \rightarrow {}^3A_2$
5	1.69	13646	39.0	0.0000757	$^3B_1(F) \rightarrow {}^3B_1$
6	1.89	15254	43.6	0.0000459	$^3B_1(F) \rightarrow {}^3B_2$
7	2.37	19121	54.7	0.0003030	$^3B_1(F) \rightarrow {}^3B_2(P)$
8	2.83	22819	65.2	0.0003569	$^3B_1(F) \rightarrow {}^3B_1(P)$
9	2.99	24093	68.9	0.0012445	$^3B_1(F) \rightarrow {}^3A_2(P)$

***Table S21**: Calculated electronic transitions for Ni^{II}(IB)(O-DMA)Br_2 at the MS-CASPT2 level with 22e,12o active space (cf. Figure S91) in the gas phase.*

Transition	Energy (eV)	Energy (cm^{-1})	Energy (kcal.mol^{-1})	Oscillator Strength	Assignment from CI vector
1	0.66	5327	15.2	0.0000056	$^3B_1(F) \rightarrow {}^3B_2(F)$
2	0.67	5384	15.4	0.0000415	$^3B_1(F) \rightarrow {}^3A_2(F)$
3	0.74	5949	17.0	0.0001407	$^3B_1(F) \rightarrow {}^3A_1$
4	1.27	10267	29.4	0.0000762	$^3B_1(F) \rightarrow {}^3B_2$
5	1.56	12604	36.0	0.0002137	$^3B_1(F) \rightarrow {}^3B_1$
6	1.76	14221	40.7	0.0000444	$^3B_1(F) \rightarrow {}^3B_2(P)$
7	2.28	18389	52.6	0.0005522	$^3B_1(F) \rightarrow {}^3A_2$
8	2.68	21581	61.7	0.0013306	$^3B_1(F) \rightarrow {}^3B_1(P)$
9	2.85	22989	65.7	0.0015792	$^3B_1(F) \rightarrow {}^3A_2(P)$

***Table S22**: Calculated electronic transitions for **Ni^{II}(IB)Cl_2** at the MS-CASPT2 level with 22e,12o active space (cf. Figure S91) with PCM solvation model (ε = 38).*

Transition	Energy (eV)	Energy (cm^{-1})	Energy (kcal.mol^{-1})	Oscillator Strength	Assignment from CI vector
1	0.25	2009	5.7	0.0000077	$^3B_1(F) \rightarrow {}^3A_2(F)$
2	0.41	3318	9.5	0.0000029	$^3B_1(F) \rightarrow {}^3B_2(F)$
3	0.92	7443	21.3	0.0000187	$^3B_1(F) \rightarrow {}^3B_1/{}^3B_2$
4	1.21	9786	28.0	0.0003087	$^3B_1(F) \rightarrow {}^3A_1$
5	1.34	10810	30.9	0.0000043	$^3B_1(F) \rightarrow {}^3B_1/{}^3B_2$
6	1.58	12709	36.3	0.0005755	$^3B_1(F) \rightarrow {}^3A_2$
7	2.03	16354	46.8	0.0001158	$^3B_1(F) \rightarrow {}^3B_1(P)/{}^3B_2(P)$
8	2.56	20607	58.9	0.0000561	$^3B_1(F) \rightarrow {}^3B_1(P)/{}^3B_2(P)$
9	2.68	21586	61.7	0.0021345	$^3B_1(F) \rightarrow {}^3A_2(P)$

***Table S23**: Calculated electronic transitions for **Ni^{II}(IB)Br_2** at the MS-CASPT2 level with 22e,12o active space (cf. Figure S91) with PCM solvation model (ε = 38).*

Transitio n	Energy (eV)	Energy (cm^{-1})	Energy ($kcal.mol^{-1}$)	Oscillator Strength	Assignment from CI vector
1	0.23	1824	5.2	0.0000192	$^3B_1(F) \rightarrow {}^3A_2(F)$
2	0.37	2974	8.5	0.0000031	$^3B_1(F) \rightarrow {}^3B_2(F)$
3	0.90	7229	20.7	0.0000244	$^3B_1(F) \rightarrow {}^3B_1/{}^3B_2$
4	1.16	9322	26.7	0.0002802	$^3B_1(F) \rightarrow {}^3A_1$
5	1.27	10244	29.3	0.0000139	$^3B_1(F) \rightarrow {}^3B_1/{}^3B_2$
6	1.54	12382	35.4	0.0007781	$^3B_1(F) \rightarrow {}^3A_2$
7	2.00	16112	46.1	0.0001711	$^3B_1(F) \rightarrow {}^3B_1(P)/{}^3B_2(P)$
8	2.42	19514	55.8	0.0014311	$^3B_1(F) \rightarrow {}^3B_1(P)/{}^3B_2(P)$
9	2.43	19561	55.9	0.0017455	$^3B_1(F) \rightarrow {}^3A_2(P)$

***Table S24**: Calculated electronic transitions for **Ni^{II}(IB)Cl_2** at the CASSCF level with 8e,5o active space (cf. Figure S91) in the gas phase. Active Space Orbitals (in order for CI vector notation below): $3d_{xy}$(Ni), $3d_{x2-y2}$(Ni), $3d_{z2}$(Ni), $3d_{yz}$(Ni), $3d_{xz}$(Ni). Starred CI vectors refer to the determinants that are already present in the particular state with the flipped alpha/beta orbitals.*

State	Multiplicity	Energy (eV)	Energy (cm^{-1})	Energy ($kcal.mol^{-1}$)	CI Vector	Contribution
1	3	0	0	0	12221	14.8%
					21221	68.8%
2	3	0.28	2285	6.5	12221	11.5%
					22121	45.4%
					22211	20.7%
3	3	0.43	3489	10.0	21122	13.3%
					21221	11.5%
					22211	52.3%
4	3	0.71	5740	16.4	12221	10.2%
					21122	12.7%
					21212	19.1%
					22112	24.5%
5	3	0.77	6218	17.8	11222	48.0%
					12122	17.3%
					21122	24.6%
6	3	0.90	7284	20.8	12122	50.9%
					12212	31.5%
7	3	1.05	8470	24.2	12122	11.0%
					12212	22.0%
					21122	11.2%
					21212	30.7%
					22112	21.8%
8	1	2.11	17002	48.6	20222	16.8%
					22220	57.7%
9	1	2.12	17122	49	21221	29.1%

					21221*	29.1%
10	1	2.35	18967	54.2	22121	19.4%
					22121*	19.4%
11	1	2.50	20173	57.7	22211	19.9%
					22211*	19.9%
12	1	2.69	21689	62.0	11222	10.8%
					11222*	10.8%
					21212	11.8%
					21212*	11.8%
					22022	23.3%
13	3	2.71	21871	62.5	12221	27.4%
					21122	31.4%
14	3	3.02	24338	69.6	11222	24.1%
					12212	34.2%
					21212	24.4%
15	1	3.29	26503	75.8	20222	23.5%
					21122	14.8%
					21122*	14.8%
					22220	11.1%
16	1	3.33	26869	76.8	20222	11.3%
					21122	13.2%
					21122*	13.2%
17	1	3.44	27777	79.4	11222	11.7%
					11222*	11.7%
					21212	15.8%
					21212*	15.8%
18	1	3.46	27897	79.8	12221	15.5%
					12221*	15.5%
19	1	3.62	29166	83.4	12221*	19.0%
					12221*	19.0%

					22202	14.4%
20	1	3.75	30285	86.6	22112	10.8%
					22112*	10.8%
21	1	3.89	31379	89.7	22022	36.5%
					22202	11.2%
22	1	4.00	32286	92.3	02222	32.0%
					22202	21.9%
23	1	4.05	32690	93.5	12212	19.4%
					12212*	19.4%
					22112	13.3%
					22112*	13.3%

***Table S25**: Calculated electronic transitions for **Ni^{II}(IB)Cl_2** at the MS-CASPT2 level with 8e,5o active space (cf. Figure S91) in the gas phase. Active Space Orbitals (in order for CI vector notation below): $3d_{xy}$(Ni), $3d_{x2-y2}$(Ni), $3d_{z2}$(Ni), $3d_{yz}$(Ni), $3d_{xz}$(Ni). Starred CI vectors refer to the determinants that are already present in the particular state with the flipped alpha/beta orbitals.*

State	Multiplicity	Energy (eV)	Energy (cm^{-1})	Energy ($kcal.mol^{-1}$)	CI Vector	Contribution
1	3	0	0	0	12221	14.8%
					21221	68.8%
2	3	0.29	2311	6.6	12221	11.5%
					22121	45.4%
					22211	20.7%
3	3	0.46	3715	10.6	21122	13.3%
					21221	11.5%
					22211	52.3%
4	3	0.90	7278	20.8	12221	10.2%
					21122	12.7%
					21212	19.1%
					22112	24.5%
5	3	1.07	8608	24.6	11222	48.0%
					12122	17.3%
					21122	24.6%
6	3	1.24	9972	28.5	12122	50.9%
					12212	31.5%
7	3	1.41	11363	32.5	12122	11.0%
					12212	22.0%
					21122	11.2%
					21212	30.7%
					22112	21.8%
8	1	1.70	13722	39.2	21221	29.1%
					21221*	29.1%
9	1	1.72	13860	39.6	20222	16.8%

					22220	57.7%
10	1	1.96	15800	45.2	22121	19.4%
					22121*	19.4%
11	1	2.16	17455	49.9	22211	19.9%
					22211*	19.9%
12	3	2.28	18378	52.5	12221	27.4%
					21122	31.4%
13	1	2.44	19651	56.2	11222	10.8%
					11222*	10.8%
					21212	11.8%
					21212*	11.8%
					22022	23.3%
14	3	2.76	22241	63.6	11222	24.1%
					12212	34.2%
					21212	24.4%
15	3	2.80	22597	64.6	12221	25.8%
					22112	37.4%
					22121	16.5%
16	1	2.84	22867	65.4	20222	23.5%
					21122	14.8%
					21122*	14.8%
					22220	11.1%
17	1	2.92	23513	67.2	20222	11.3%
					21122	13.2%
					21122*	13.2%
18	1	3.16	25464	72.8	11222	11.7%
					11222*	11.7%
					21212	15.8%
					21212*	15.8%
19	1	3.24	26114	74.7	12221	15.5%

					12221*	15.5%
20	1	3.31	26733	76.4	12221	19.0%
					12221*	19.0%
					22202	14.4%
21	1	3.46	27920	79.8	22112	10.8%
					22112*	10.8%
22	1	3.85	31036	88.7	22022	36.5%
					22202	11.2%
23	1	4.04	32606	93.2	02222	32.0%
					22202	21.9%
24	1	4.08	32901	94.1	12212	19.4%
					12212*	19.4%
					22112	13.3%
					22112*	13.3%

***Table S26**: Calculated electronic transitions for **Ni^{II}(IB)Cl_2** at the CASSCF level with 20e,11o active space (cf. Figure S91) in the gas phase. Active Space Orbitals (in order for CI vector notation below): 3p(Cl), $3d_{xy}$(Ni), 3p(Cl), $3d_{z2}$(Ni), $3d_{yz}$(Ni), 3p(Cl), 3p(Cl), 3p(Cl), 3p(Cl), $3d_{x2-y2}$(Ni), $3d_{xz}$(Ni). Starred CI vectors refer to the determinants that are already present in the particular state with the flipped alpha/beta orbitals.*

State	Multiplicity	Energy (eV)	Energy (cm^{-1})	Energy ($kcal.mol^{-1}$)	CI Vector	Contribution
1	3	0	0	0	22222222211	95.1%
2	3	0.34	2715	7.8	21222222212	15.4%
					22221222221	80.5%
3	3	0.49	3990	11.4	21222222221	54.6%
					22221222212	38.6%
4	3	0.75	6047	17.3	21221222222	22.1%
					22211222222	21.7%
					22212222221	27.1%
					22221222212	19.4%
5	3	0.83	6684	19.1	22212222212	91.7%
6	3	1.03	8271	23.6	21221222222	61.2%
					22211222222	25.2%
7	3	1.15	9310	26.6	21212222222	57.7%
					21222222212	33.7%
8	1	1.76	14173	40.5	22222222202	39.6%
					22222222220	41.3%
9	1	1.78	14354	41.0	22222222211	39.8%
					22222222211*	39.8%
10	1	2.01	16236	46.4	22221222221	31.4%
					22221222221*	31.4%
					22222222202	11.3%
11	1	2.20	17770	50.8	21222222221	14.1%
					21222222221*	14.1%
					22221222212	25.1%
					22221222212*	25.1%

12	3	2.33	18758	53.6	21222222221	26.4%
					22211222222	21.5%
					22212222221	12.8%
					22221222212	33.3%
13	1	2.36	19003	54.3	22212222212	13.9%
					22212222212*	13.9%
					22220222222	41.3%
					22222222202	10.1%
14	3	2.73	21999	62.9	21212222222	39.6%
					21222222212	41.8%
15	1	2.74	22126	63.3	20222222222	13.0%
					22212222212	16.8%
					22212222212*	16.8%
					22222222202	13.0%
					22222222220	14.1%
16	1	2.77	22352	63.9	21222222221	17.4%
					21222222221*	17.4%
					22221222212	16.7%
					22221222212*	16.7%
17	1	2.84	22941	65.6	21222222212	37.3%
					21222222212*	37.3%
18	1	2.99	24096	68.9	21221222222	25.9%
					21221222222*	25.9%
19	3	2.99	24117	69.0	21221222222	12.4%
					22211222222	24.1%
					22212222221	52.6%
20	1	3.29	26541	75.9	20222222222	24.1%
					22212222212	10.7%
					22212222212*	10.7%
					22220222222	20.4%

21	1	3.32	26745	76.5	21221222222	13.6%
					21221222222*	13.6%
					21222222221	10.3%
					21222222221*	10.3%
					22212222221	13.7%
					22212222221*	13.7%
22	1	3.70	29826	85.3	22211222222	20.8%
					22211222222*	20.8%
					22212222221	18.4%
					22212222221*	18.4%
23	1	3.81	30748	87.9	21212222222	35.0%
					21212222222*	35.0%
24	1	3.90	31430	89.9	20222222222	24.0%
					22202222222	44.0%

***Table S27**: Calculated electronic transitions for **Ni^{II}(IB)Cl_2** at the MS-CASPT2 level with 20e,11o active space (cf. Figure S91) in the gas phase. Active Space Orbitals (in order for CI vector notation below): 3p(Cl), $3d_{xy}$(Ni), 3p(Cl), $3d_{z2}$(Ni), $3d_{yz}$(Ni), 3p(Cl), 3p(Cl), 3p(Cl), 3p(Cl), $3d_{x2-y2}$(Ni), $3d_{xz}$(Ni). Starred CI vectors refer to the determinants that are already present in the particular state with the flipped alpha/beta orbitals.*

State	Multiplicity	Energy (eV)	Energy (cm^{-1})	Energy ($kcal.mol^{-1}$)	CI Vector	Contribution
1	3	0	0	0	22222222211	95.1%
2	3	0.28	2226	6.4	21222222212	15.4%
					22221222221	80.5%
3	3	0.39	3110	8.9	21222222221	54.6%
					22221222212	38.6%
4	3	0.91	7365	21.1	21221222222	22.1%
					22211222222	21.7%
					22212222221	27.1%
					22221222212	19.4%
5	3	1.11	8930	25.5	22212222212	91.7%
6	3	1.32	10615	30.4	21221222222	61.2%
					22211222222	25.2%
7	1	1.32	10618	30.4	22222222211	39.8%
					22222222211*	39.8%
8	1	1.38	11126	31.8	22222222202	39.6%
					22222222220	41.3%
9	3	1.40	11286	32.3	21212222222	57.7%
					21222222212	33.7%
10	1	1.58	12724	36.4	22221222221	31.4%
					22221222221*	31.4%
					22222222202	11.3%
11	1	1.90	15329	43.8	21222222221	14.1%
					21222222221*	14.1%
					22221222212	25.1%
					22221222212*	25.1%

12	3	1.97	15867	45.4	21222222221	26.4%
					22211222222	21.5%
					22212222221	12.8%
					22221222212	33.3%
13	1	2.07	16696	47.7	22212222212	13.9%
					22212222212*	13.9%
					22220222222	41.3%
					22222222202	10.1%
14	1	2.28	18427	52.7	20222222222	13.0%
					22212222212	16.8%
					22212222212*	16.8%
					22222222202	13.0%
					22222222220	14.1%
15	1	2.37	19136	54.7	21222222221	17.4%
					21222222221*	17.4%
					22221222212	16.7%
					22221222212*	16.7%
16	1	2.47	19930	57.0	21222222212	37.3%
					21222222212*	37.3%
17	3	2.59	20886	59.7	21212222222	39.6%
					21222222212	41.8%
18	3	2.68	21578	61.7	21221222222	12.4%
					22211222222	24.1%
					22212222221	52.6%
19	1	2.68	21615	61.8	21221222222	25.9%
					21221222222*	25.9%
20	1	2.93	23600	67.5	20222222222	24.1%
					22212222212	10.7%
					22212222212*	10.7%
					22220222222	20.4%

21	1	3.00	24194	69.2	21221222222	13.6%
					21221222222*	13.6%
					21222222221	10.3%
					21222222221*	10.3%
					22212222221	13.7%
					22212222221*	13.7%
22	1	3.67	29584	84.6	22211222222	20.8%
					22211222222*	20.8%
					22212222221	18.4%
					22212222221*	18.4%
23	1	3.81	30739	87.9	20222222222	24.0%
					22202222222	44.0%
24	1	3.84	30939	88.5	21212222222	35.0%
					21212222222*	35.0%

***Table S28**: Calculated electronic transitions for **Ni^{II}(IB)Cl_2** at the CASSCF level with 22e,12o active space (cf. Figure S91) in the gas phase. Active Space Orbitals (in order for CI vector notation below): $3d_{z2}$(Ni), σ-bonding(IB), 3p(Cl), 3p(Cl), 3p(Cl), 3p(Cl), 3p(Cl), 3p(Cl), $3d_{xy}$(Ni), $3d_{yz}$(Ni), $3d_{x2-y2}$(Ni), $3d_{xz}$(Ni). Starred CI vectors refer to the determinants that are already present in the particular state with the flipped alpha/beta orbitals.*

State	Multiplicity	Energy (eV)	Energy (cm^{-1})	Energy ($kcal.mol^{-1}$)	CI Vector	Contribution
1	3	0	0	0	222222222211	95.2%
2	3	0.36	2927	8.4	222222221212	14.8%
					222222222121	81.6%
3	3	0.54	4359	12.5	222222221221	58.4%
					222222222112	37.3%
4	3	0.82	6647	19.0	122222222122	24.8%
					122222222221	19.9%
					222222221122	30.5%
					222222222112	18.6%
5	3	0.91	7369	21.1	122222222212	94.9%
6	3	1.11	8979	25.7	122222222122	25.3%
					222222221122	49.1%
					222222221221	12.4%
7	3	1.25	10063	28.8	122222221222	58.9%
					222222221212	33.4%
8	1	1.66	13412	38.3	222222222202	33.9%
					222222222220	43.9%
9	1	1.71	13770	39.4	222222222211	40.6%
					222222222211*	40.6%
10	1	1.96	15821	45.2	222222222121	29.9%
					222222222121*	29.9%
					222222222202	10.3%
11	1	2.19	17686	50.6	222222221221	15.0%
					222222221221*	15.0%
					222222222112	22.5%

					222222222112*	22.5%
12	3	2.32	18714	53.5	122222222122	27.5%
					122222222221	12.6%
					222222221221	22.4%
					222222222112	29.4%
13	1	2.36	19047	54.5	222222222022	41.2%
					222222222202	14.4%
14	1	2.70	21752	62.2	122222222212	19.3%
					122222222212*	19.3%
					222222220222	15.4%
					222222222202	12.6%
					222222222220	17.0%
15	1	2.73	22012	62.9	222222221221	20.8%
					222222221221*	20.8%
					222222222112	16.8%
					222222222112*	16.8%
16	3	2.77	22317	63.8	122222221222	38.5%
					222222221212	45.5%
17	1	2.84	22880	65.4	222222221212*	34.5%
					222222221212*	34.5%
18	3	2.95	23789	68.0	122222222122	18.1%
					122222222221	59.2%
					222222221122	13.7%
19	1	2.98	24022	68.7	222222221122	24.9%
					222222221122*	24.9%
20	1	3.25	26195	74.9	122222222212	10.5%
					122222222212*	10.5%
					222222220222	11.8%
					222222222022	24.3%
21	1	3.26	26333	75.3	122222222221	13.7%

					122222222221*	13.7%
					222222221122	14.7%
					222222221122*	14.7%
22	1	3.65	29428	84.1	122222222122	22.2%
					122222222122*	22.2%
					122222222221	21.3%
					122222222221*	21.3%
23	1	3.84	30986	88.6	122222221222	28.4%
					122222221222*	28.4%
					222222220222	17.2%
24	1	3.90	31440	89.9	022222222222	29.9%
					122222221222	12.9%
					122222221222*	12.9%
					222222220222	21.5%

***Table S29**: Calculated electronic transitions for **Ni^{II}(IB)Cl_2** at the MS-CASPT2 level with 22e,12o active space (cf. Figure S91) in the gas phase. Active Space Orbitals (in order for CI vector notation below): $3d_{z2}$(Ni), σ-bonding(IB), 3p(Cl), 3p(Cl), 3p(Cl), 3p(Cl), 3p(Cl), 3p(Cl), $3d_{xy}$(Ni), $3d_{yz}$(Ni), $3d_{x2-y2}$(Ni), $3d_{xz}$(Ni). Starred CI vectors refer to the determinants that are already present in the particular state with the flipped alpha/beta orbitals.*

State	Multiplicity	Energy (eV)	Energy (cm^{-1})	Energy ($kcal.mol^{-1}$)	CI Vector	Contribution
1	3	0.00	0	0.0	222222222211	95.2%
2	3	0.31	2519	7.2	222222221212	14.8%
					222222222121	81.6%
3	3	0.40	3198	9.1	222222221221	58.4%
					222222222112	37.3%
4	3	0.95	7698	22.0	122222222122	24.8%
					122222222221	19.9%
					222222221122	30.5%
					222222222112	18.6%
5	3	1.19	9584	27.4	122222222212	94.9%
6	1	1.33	10705	30.6	222222222211	40.6%
					222222222211*	40.6%
7	1	1.34	10782	30.8	222222222202	33.9%
					222222222220	43.9%
8	3	1.37	11014	31.5	122222222122	25.3%
					222222221122	49.1%
					222222221221	12.4%
9	3	1.47	11896	34.0	122222221222	58.9%
					222222221212	33.4%
10	1	1.60	12913	36.9	222222222121	29.9%
					222222222121*	29.9%
					222222222202	10.3%
11	1	1.92	15489	44.3	222222221221	15.0%
					222222221221*	15.0%
					222222222112	22.5%

					222222222112*	22.5%
12	3	1.97	15903	45.5	122222222122	27.5%
					122222222221	12.6%
					222222221221	22.4%
					222222222112	29.4%
13	1	2.11	16996	48.6	222222222022	41.2%
					222222222202	14.4%
14	1	2.31	18650	53.3	122222222212	19.3%
					122222222212*	19.3%
					222222220222	15.4%
					222222222202	12.6%
					222222222220	17.0%
15	1	2.35	18973	54.2	222222221221	20.8%
					222222221221*	20.8%
					222222222112	16.8%
					222222222112*	16.8%
16	1	2.54	20503	58.6	222222221212	34.5%
					222222221212*	34.5%
17	3	2.62	21148	60.5	122222222122	18.1%
					122222222221	59.2%
					222222221122	13.7%
18	3	2.64	21267	60.8	122222221222	38.5%
					222222221212	45.5%
19	1	2.73	21980	62.8	222222221122	24.9%
					222222221122*	24.9%
20	1	2.88	23216	66.4	122222222212	10.5%
					122222222212*	10.5%
					222222220222	11.8%
					222222222022	24.3%
21	1	2.96	23867	68.2	122222222221	13.7%

					122222222221*	13.7%
					222222221122	14.7%
					222222221122*	14.7%
22	1	3.51	28319	81.0	122222222122	22.2%
					122222222122*	22.2%
					122222222221	21.3%
					122222222221*	21.3%
23	1	3.82	30811	88.1	022222222222	29.9%
					122222221222	12.9%
					122222221222*	12.9%
					222222220222	21.5%
24	1	3.85	31076	88.9	122222221222	28.4%
					122222221222*	28.4%
					222222220222	17.2%

***Table S30**: Calculated electronic transitions for **Ni^{II}(IB)Br_2** at the CASSCF level with 8e,5o active space (cf. Figure S91) in the gas phase. Active Space Orbitals (in order for CI vector notation below): $3d_{xy}$(Ni), $3d_{z2}$(Ni), $3d_{yz}$(Ni), $3d_{x2-y2}$(Ni), $3d_{xz}$(Ni). Starred CI vectors refer to the determinants that are already present in the particular state with the flipped alpha/beta orbitals.*

State	Multiplicity	Energy (eV)	Energy (cm^{-1})	Energy ($kcal.mol^{-1}$)	CI Vector	Contribution
1	3	0	0	0	21221	28.6%
					22121	30.7%
					22211	38.3%
2	3	0.27	2196	6.3	12212	10.6%
					21221	13.1%
					22121	58.9%
					22211	10.1%
3	3	0.41	3328	9.5	12221	73.2%
					21122	10.2%
					22112	11.8%
4	3	0.72	5785	16.5	12122	24.9%
					21221	14.1%
					22112	37.3%
					22211	11.3%
5	3	0.77	6194	17.7	21122	12.1%
					21212	73.7%
					22112	10.2%
6	3	0.87	7057	20.2	12122	31.1%
					21212	17.5%
					22112	32.2%
7	3	1.03	8287	23.7	11222	81.1%
8	1	2.08	16807	48.1	22220	59.3%
9	1	2.12	17133	49.0	21221	11.7%
					21221*	11.7%
					22121	14.5%

					22121*	14.5%
					22211	15.6%
					22211*	15.6%
10	1	2.35	18932	54.1	22121	24.0%
					22121*	24.0%
11	1	2.48	20002	57.2	12221	27.1%
					12221*	27.1%
12	1	2.69	21687	62.0	02222	14.3%
					20222	20.9%
					22022	14.0%
					22112	14.7%
					22112*	14.7%
					22202	18.4%
13	3	2.74	22076	63.1	12221	18.5%
					21122	36.8%
					21221	19.9%
14	3	2.97	23995	68.6	12212	26.3%
					21122	23.2%
					22211	29.0%
15	1	3.32	26765	76.5	21122	16.9%
					21122*	16.9%
					22220	12.8%
16	1	3.37	27191	77.7	12221	11.1%
					12221*	11.1%
					20222	10.7%
					22022	28.9%
17	1	3.44	27738	79.3	21221	21.9%
					21221*	21.9%
					22211	12.0%
					22211*	12.0%

18	1	3.48	28030	80.1	11222	17.6%
					11222*	17.6%
					12122	14.9%
					12122*	14.9%
19	1	3.58	28855	82.5	12122	18.4%
					12122*	18.4%
					22211	13.6%
					22211*	13.6%
20	1	3.74	30163	86.2	20222	17.3%
					22022	17.1%
21	1	3.83	30865	88.2	20222	12.3%
					21122	17.9%
					21122*	17.9%
22	1	3.95	31849	91.1	02222	42.0%
					22202	27.5%
23	1	3.99	32147	91.9	12212	25.8%
					12212*	25.8%

***Table S31**: Calculated electronic transitions for **Ni^{II}(IB)Br_2** at the MS-CASPT2 level with 8e,5o active space (cf. Figure S91) in the gas phase. Active Space Orbitals (in order for CI vector notation below): $3d_{xy}$(Ni), $3d_{z2}$(Ni), $3d_{yz}$(Ni), $3d_{x2-y2}$(Ni), $3d_{xz}$(Ni). Starred CI vectors refer to the determinants that are already present in the particular state with the flipped alpha/beta orbitals.*

State	Multiplicity	Energy (eV)	Energy (cm^{-1})	Energy ($kcal.mol^{-1}$)	CI Vector	Contribution
1	3	0	0	0	21221	28.6%
					22121	30.7%
					22211	38.3%
2	3	0.28	2250	6.4	12212	10.6%
					21221	13.1%
					22121	58.9%
					22211	10.1%
3	3	0.46	3741	10.7	12221	73.2%
					21122	10.2%
					22112	11.8%
4	3	0.90	7246	20.7	12122	24.9%
					21221	14.1%
					22112	37.3%
					22211	11.3%
5	3	1.05	8490	24.3	21122	12.1%
					21212	73.7%
					22112	10.2%
6	3	1.20	9717	27.8	12122	31.1%
					21212	17.5%
					22112	32.2%
7	3	1.41	11353	32.5	11222	81.1%
8	1	1.69	13632	39.0	21221	11.7%
					21221*	11.7%
					22121	14.5%
					22121*	14.5%

					22211	15.6%
					22211*	15.6%
9	1	1.69	13654	39.0	22220	59.3%
10	1	1.96	15826	45.2	22121	24.0%
					22121*	24.0%
11	1	2.14	17297	49.5	12221	27.1%
					12221*	27.1%
12	3	2.32	18688	53.4	12221	18.5%
					21122	36.8%
					21221	19.9%
13	1	2.45	19725	56.4	2222	14.3%
					20222	20.9%
					22022	14.0%
					22112	14.7%
					22112*	14.7%
					22202	18.4%
14	3	2.68	21600	61.8	12212	26.3%
					21122	23.2%
					22211	29.0%
15	3	2.73	22027	63.0	12122	25.6%
					12212	45.7%
					21122	11.9%
					21221	10.6%
16	1	2.86	23089	66.0	21122	16.9%
					21122*	16.9%
					22220	12.8%
17	1	2.96	23864	68.2	12221	11.1%
					12221*	11.1%
					20222	10.7%
					22022	28.9%

18	1	3.21	25883	74.0	11222	17.6%
					11222*	17.6%
					12122	14.9%
					12122*	14.9%
19	1	3.25	26223	75.0	21221	21.9%
					21221*	21.9%
					22211	12.0%
					22211*	12.0%
20	1	3.30	26590	76.0	12122	18.4%
					12122*	18.4%
					22211	13.6%
					22211*	13.6%
21	1	3.49	28114	80.4	20222	17.3%
					22022	17.1%
22	1	3.76	30312	86.7	20222	12.3%
					21122	17.9%
					21122*	17.9%
23	1	3.98	32092	91.8	02222	42.0%
					22202	27.5%
24	1	4.00	32278	92.3	12212	25.8%
					12212*	25.8%

***Table S32**: Calculated electronic transitions for **Ni^{II}(IB)Br_2** at the CASSCF level with 20e,11o active space (cf. Figure S91) in the gas phase. Active Space Orbitals (in order for CI vector notation below): 4p(Br), 4p(Br), 4p(Br), 4p(Br), 4p(Br), 4p(Br), $3d_{z2}$ (Ni), $3d_{x2-y2}$(Ni), $3d_{yz}$(Ni), $3d_{xy}$ (Ni), $3d_{xz}$(Ni). Starred CI vectors refer to the determinants that are already present in the particular state with the flipped alpha/beta orbitals.*

State	Multiplicity	Energy (eV)	Energy (cm^{-1})	Energy ($kcal.mol^{-1}$)	CI Vector	Contribution
1	3	0	0	0	22222221221	91.0%
2	3	0.33	2680	7.7	22222221212	11.5%
					22222222121	77.2%
3	3	0.51	4117	11.8	22222221122	33.8%
					22222222211	53.7%
4	3	0.78	6313	18.0	22222212122	27.7%
					22222212221	20.0%
					22222221122	25.9%
					22222222112	18.3%
5	3	0.85	6893	19.7	22222211222	85.1%
6	3	1.03	8279	23.7	22222212122	20.7%
					22222222112	59.9%
7	3	1.18	9518	27.2	22222212212	61.1%
					22222221212	31.3%
8	1	1.67	13471	38.5	22222220222	13.4%
					22222221221	20.1%
					22222221221*	20.1%
					22222222220	18.9%
9	1	1.71	13771	39.4	22222220222	20.5%
					22222221221	16.6%
					22222221221*	16.6%
					22222222220	26.9%
10	1	1.95	15742	45.0	22222222121	27.3%
					22222222121*	27.3%
11	1	2.15	17361	49.6	22222221122	22.4%

					22222221122*	22.4%
					22222222211	13.2%
					22222222211*	13.2%
12	3	2.27	18344	52.4	22222212122	26.1%
					22222212221	10.6%
					22222221122	29.5%
					22222222211	24.1%
13	1	2.30	18529	53.0	22222211222	11.2%
					22222211222*	11.2%
					22222220222	14.1%
					22222222022	40.4%
14	1	2.63	21199	60.6	22222211222	10.5%
					22222211222*	10.5%
					22222222220	13.6%
15	3	2.67	21511	61.5	22222212212	36.6%
					22222221212	44.6%
16	1	2.68	21641	61.9	22222222211	12.5%
					22222222211*	12.5%
17	1	2.75	22206	63.5	22222221212	31.3%
					22222221212*	31.3%
18	3	2.88	23192	66.3	22222212122	21.2%
					22222212221	52.5%
					22222222112	13.8%
19	1	2.90	23360	66.8	22222222112*	22.1%
					22222222112*	22.1%
20	1	3.15	25389	72.6	22222222022	20.2%
					22222222202	17.5%
21	1	3.18	25648	73.3	22222222112	13.0%
					22222222112*	13.0%
22	1	3.56	28691	82.0	22222212122	18.4%

					22222212122*	18.4%
					22222212221	19.4%
					22222212221*	19.4%
23	1	3.69	29798	85.2	22222212212	35.8%
					22222212212*	35.8%
24	1	3.76	30366	86.8	22222202222	35.0%
					22222222202	29.1%

***Table S33**: Calculated electronic transitions for **Ni^{II}(IB)Br_2** at the MS-CASPT2 level with 20e,11o active space (cf. Figure S91) in the gas phase. Active Space Orbitals (in order for CI vector notation below): 4p(Br), 4p(Br), 4p(Br), 4p(Br), 4p(Br), 4p(Br), $3d_{z2}$ (Ni), $3d_{x2-y2}$(Ni), $3d_{yz}$(Ni), $3d_{xy}$ (Ni), $3d_{xz}$(Ni). Starred CI vectors refer to the determinants that are already present in the particular state with the flipped alpha/beta orbitals.*

State	Multiplicity	Energy (eV)	Energy (cm^{-1})	Energy ($kcal.mol^{-1}$)	CI Vector	Contribution
1	3	0	0	0	22222221221	91.0%
2	3	0.26	2079	5.9	22222221212	11.5%
					22222222121	77.2%
3	3	0.39	3167	9.1	22222221122	33.8%
					22222222211	53.7%
4	3	0.91	7349	21.0	22222212122	27.7%
					22222212221	20.0%
					22222221122	25.9%
					22222222112	18.3%
5	3	1.06	8560	24.5	22222211222	85.1%
6	1	1.24	10028	28.7	22222220222	13.4%
					22222221221	20.1%
					22222221221*	20.1%
					22222222220	18.9%
7	1	1.24	10030	28.7	22222220222	20.5%
					22222221221	16.6%
					22222221221*	16.6%
					22222222220	26.9%
8	3	1.25	10053	28.7	22222212122	20.7%
					22222222112	59.9%
9	3	1.39	11201	32.0	22222212212	61.1%
					22222221212	31.3%
10	1	1.51	12143	34.7	22222222121	27.3%
					22222222121*	27.3%
11	1	1.82	14704	42.0	22222221122	22.4%

					22222221122*	22.4%
					22222222211	13.2%
					22222222211*	13.2%
12	3	1.94	15617	44.7	22222212122	26.1%
					22222212221	10.6%
					22222221122	29.5%
					22222222211	24.1%
13	1	1.99	16012	45.8	22222211222	11.2%
					22222211222*	11.2%
					22222220222	14.1%
					22222222022	40.4%
14	1	2.17	17532	50.1	22222211222	10.5%
					22222211222*	10.5%
					22222222220	13.6%
15	1	2.24	18059	51.6	22222222211	12.5%
					22222222211*	12.5%
16	1	2.34	18847	53.9	22222221212	31.3%
					22222221212*	31.3%
17	3	2.48	19978	57.1	22222212212	36.6%
					22222221212	44.6%
18	3	2.52	20307	58.1	22222212122	21.2%
					22222212221	52.5%
					22222222112	13.8%
19	1	2.54	20509	58.6	22222222112	22.1%
					22222222112*	22.1%
20	1	2.68	21649	61.9	22222222022	20.2%
					22222222202	17.5%
21	1	2.81	22697	64.9	22222222112	13.0%
					22222222112*	13.0%
22	1	3.34	26947	77.0	22222212122	18.4%

					22222212122*	18.4%
					22222212221	19.4%
					22222212221*	19.4%
23	1	3.53	28470	81.4	22222202222	35.0%
					22222222202	29.1%
24	1	3.57	28790	82.3	22222212212	35.8%
					22222212212*	35.8%
25	1	4.30	34683	99.2	21222222221	40.8%
					21222222221*	40.8%
26	1	4.32	34858	99.7	12222222221	30.8%
					12222222221*	30.8%

***Table S34**: Calculated electronic transitions for **Ni^{II}(IB)Br_2** at the CASSCF level with 22e,12o active space (cf. Figure S91) in the gas phase. Active Space Orbitals (in order for CI vector notation below): 4p(Br), $3d_{z2}$ (Ni), $3d_{yz}$(Ni), 4p(Br), $3d_{xy}$(Ni), 4p(Br), 4p(Br), 4p(Br), 4p(Br), σ-bonding(IB), $3d_{x2-y2}$(Ni), $3d_{xz}$(Ni). Starred CI vectors refer to the determinants that are already present in the particular state with the flipped alpha/beta orbitals.*

State	Multiplicity	Energy (eV)	Energy (cm^{-1})	Energy ($kcal.mol^{-1}$)	CI Vector	Contribution
1	3	0	0	0	222222222211	94.90%
2	3	0.36	2905	8.3	221222222221	83.60%
					222212222212	12.00%
3	3	0.56	4481	12.8	221222222212	29.70%
					222212222221	61.30%
4	3	0.86	6945	19.9	211222222222	19.40%
					212222222212	11.90%
					212222222221	15.90%
					221212222222	25.00%
					221222222212	21.80%
5	3	0.95	7636	21.8	212222222212	85.10%
6	3	1.12	9006	25.7	211222222222	27.10%
					221212222222	42.80%
					222212222221	13.10%
7	3	1.28	10305	29.5	212212222222	57.80%
					222212222212	28.40%
8	1	1.57	12703	36.3	222222222202	23.40%
					222222222220	36.70%
9	1	1.63	13161	37.6	222222222211	33.60%
					222222222211*	33.60%
10	1	1.89	15250	43.6	221222222221	28.80%
					221222222221*	28.80%
					222222222202	11.00%
11	1	2.14	17221	49.2	221222222212	23.00%
					221222222212*	23.00%

					222212222221	14.50%
					222212222221*	14.50%
12	3	2.26	18259	52.2	211222222222	30.90%
					212222222221	10.90%
					221222222212	27.20%
					222212222221	17.70%
13	1	2.28	18403	52.6	220222222222	36.30%
					222222222202	19.70%
14	1	2.57	20736	59.3	212222222212	16.30%
					212222222212*	16.30%
					222222222202	12.80%
					222222222220	12.20%
15	1	2.63	21178	60.6	221222222212	15.10%
					221222222212*	15.10%
					222212222221	11.80%
					222212222221*	11.80%
16	3	2.69	21733	62.1	212212222222	38.10%
					222212222212	42.90%
17	1	2.74	22116	63.2	222212222212	34.90%
					222212222212*	34.90%
18	3	2.83	22834	65.3	211222222222	12.90%
					212222222221	57.90%
					221212222222	14.60%
19	1	2.88	23193	66.3	221212222222	20.70%
					221212222222*	20.70%
20	1	3.08	24831	71.0	220222222222	21.50%
21	1	3.11	25108	71.8	212222222221	11.70%
					212222222221*	11.70%
					221212222222	14.40%
					221212222222*	14.40%

22	1	3.47	27986	80.0	211222222222	17.30%
					211222222222*	17.30%
					212222222221	22.50%
					212222222221*	22.50%
23	1	3.72	29966	85.7	202222222222	12.00%
					212212222222	22.00%
					212212222222*	22.00%
					222202222222	22.00%
24	1	3.75	30246	86.5	202222222222	17.60%
					212212222222	16.70%
					212212222222*	16.70%
					222202222222	21.20%

***Table S35**: Calculated electronic transitions for **Ni^{II}(IB)Br_2** at the MS-CASPT2 level with 22e,12o active space (cf. Figure S91) in the gas phase. Active Space Orbitals (in order for CI vector notation below): 4p(Br), $3d_{z2}$ (Ni), $3d_{yz}$(Ni), 4p(Br), $3d_{xy}$(Ni), 4p(Br), 4p(Br), 4p(Br), 4p(Br), σ-bonding(IB), $3d_{x2-y2}$(Ni), $3d_{xz}$(Ni). Starred CI vectors refer to the determinants that are already present in the particular state with the flipped alpha/beta orbitals.*

State	Multiplicity	Energy (eV)	Energy (cm^{-1})	Energy ($kcal.mol^{-1}$)	CI Vector	Contribution
1	3	0	0	0	222222222211	94.9%
2	3	0.29	2347	6.7	221222222221	83.6%
					222212222212	12.0%
3	3	0.36	2897	8.3	221222222212	29.7%
					222212222221	61.3%
4	3	0.93	7513	21.5	211222222222	19.4%
					212222222212	11.9%
					212222222221	15.9%
					221212222222	25.0%
					221222222212	21.8%
5	3	1.09	8755	25.0	212222222212	85.1%
6	1	1.22	9827	28.1	222222222202	23.4%
					222222222220	36.7%
7	1	1.27	10214	29.2	222222222211	33.6%
					222222222211*	33.6%
8	3	1.29	10392	29.7	211222222222	27.1%
					221212222222	42.8%
					222212222221	13.1%
9	3	1.46	11780	33.7	212212222222	57.8%
					222212222212	28.4%
10	1	1.52	12242	35.0	221222222221	28.8%
					221222222221*	28.8%
					222222222202	11.0%
11	1	1.84	14840	42.4	221222222212	23.0%
					221222222212*	23.0%

					222212222221	14.5%
					222212222221*	14.5%
12	3	1.92	15465	44.2	211222222222	30.9%
					212222222221	10.9%
					221222222212	27.2%
					222212222221	17.7%
13	1	2.01	16196	46.3	220222222222	36.3%
					222222222202	19.7%
14	1	2.20	17759	50.8	212222222212	16.3%
					212222222212*	16.3%
					222222222202	12.8%
					222222222220	12.2%
15	1	2.23	18016	51.5	221222222212	15.1%
					221222222212*	15.1%
					222212222221	11.8%
					222212222221*	11.8%
16	1	2.41	19410	55.5	222212222212	34.9%
					222212222212*	34.9%
17	3	2.47	19914	56.9	211222222222	12.9%
					212222222221	57.9%
					221212222222	14.6%
18	3	2.52	20296	58.0	212212222222	38.1%
					222212222212	42.9%
19	1	2.56	20674	59.1	221212222222	20.7%
					221212222222*	20.7%
20	1	2.68	21577	61.7	220222222222	21.5%
21	1	2.77	22347	63.9	212222222221	11.7%
					212222222221*	11.7%
					221212222222	14.4%
					221212222222*	14.4%

22	1	3.20	25784	73.7	211222222222	17.3%
					211222222222*	17.3%
					212222222221	22.5%
					212222222221*	22.5%
23	1	3.47	27961	79.9	202222222222	17.6%
					212212222222	16.7%
					212212222222*	16.7%
					222202222222	21.2%
24	1	3.50	28265	80.8	202222222222	12.0%
					212212222222	22.0%
					212212222222*	22.0%
					222202222222	22.0%

***Table S36**: Calculated electronic transitions for **Ni^{II}(IB)Cl_2** at the CASSCF level with 22e,12o active space (cf. Figure S91) with the PCM solvation model (ε = 38). Active Space Orbitals (in order for CI vector notation below): $3d_{z2}$(Ni), σ-bonding(IB), 3p(Cl), 3p(Cl), 3p(Cl), 3p(Cl), 3p(Cl), 3p(Cl), $3d_{xy}$(Ni), $3d_{yz}$(Ni), $3d_{x2-y2}$(Ni), $3d_{xz}$(Ni). Starred CI vectors refer to the determinants that are already present in the particular state with the flipped alpha/beta orbitals.*

State	Multiplicity	Energy (eV)	Energy (cm^{-1})	Energy ($kcal.mol^{-1}$)	CI Vector	Contribution
1	3	0	0	0	222222222211	96.2%
2	3	0.35	2792	8.0	222222222121	85.6%
3	3	0.54	4376	12.5	122222222221	14.3%
					222222221221	55.3%
					222222222112	28.7%
4	3	0.85	6816	19.5	222222221122	45.7%
					222222221221	18.6%
					222222222112	27.7%
5	3	0.94	7618	21.8	122222222212	68.9%
					222222221212	29.7%
6	3	1.12	9061	25.9	122222222122	70.4%
					222222222112	11.3%
7	3	1.30	10448	29.9	122222221222	71.1%
					122222222212	11.1%
					222222221212	14.1%
8	1	1.67	13439	38.4	222222222202	24.7%
					222222222220	58.4%
9	1	1.76	14216	40.6	222222222211	42.8%
					222222222211*	42.8%
10	1	2.01	16236	46.4	222222222121	35.9%
					222222222121*	35.9%
11	1	2.27	18273	52.2	222222221221	20.8%
					222222221221*	20.8%
					222222222112	20.1%

					222222222112*	20.1%
12	3	2.42	19515	55.8	122222222122	25.3%
					122222222221	40.7%
					222222222112	26.7%
13	1	2.48	19980	57.1	222222222022	39.6%
					222222222202	25.1%
14	1	2.81	22646	64.7	122222222212	15.6%
					122222222212*	15.6%
					222222222202	17.5%
					222222222220	13.3%
15	3	2.85	22957	65.6	122222221222	27.7%
					122222222212	14.5%
					222222221212	45.5%
16	1	2.86	23058	65.9	222222221221	13.8%
					222222221221*	13.8%
					222222222112	25.5%
					222222222112*	25.5%
17	3	2.91	23474	67.1	122222222221	24.7%
					222222221122	41.8%
					222222221221	21.8%
18	1	3.03	24471	70.0	022222222222	12.3%
					122222222212	17.9%
					122222222212*	17.9%
					222222221212	16.9%
					222222221212*	16.9%
19	1	3.08	24824	71.0	122222222122	18.7%
					122222222122*	18.7%
					122222222221	25.1%
					122222222221*	25.1%
20	1	3.31	26704	76.4	122222222221	12.5%

					122222222221*	12.5%
					222222221122	19.5%
					222222221122*	19.5%
21	1	3.38	27243	77.9	022222222222	17.9%
					222222221212	12.4%
					222222221212*	12.4%
					222222222022	33.0%
22	1	3.65	29423	84.1	122222222122	14.1%
					122222222122*	14.1%
					222222221122	20.7%
					222222221122*	20.7%
					222222221221	10.4%
					222222221221*	10.4%
23	1	3.91	31553	90.2	022222222222	19.8%
					122222221222	15.1%
					122222221222*	15.1%
					222222220222	32.1%
24	1	3.95	31888	91.2	022222222222	10.6%
					122222221222	24.5%
					122222221222*	24.5%
					222222220222	19.0%

***Table S37**: Calculated electronic transitions for **Ni^{II}(IB)Cl_2** at the MS-CASPT2 level with 22e,12o active space (cf. Figure S91) with the PCM solvation model (ε = 38). Active Space Orbitals (in order for CI vector notation below): $3d_{z2}$(Ni), σ-bonding(IB), 3p(Cl), 3p(Cl), 3p(Cl), 3p(Cl), 3p(Cl), 3p(Cl), $3d_{xy}$(Ni), $3d_{yz}$(Ni), $3d_{x2-y2}$(Ni), $3d_{xz}$(Ni). Starred CI vectors refer to the determinants that are already present in the particular state with the flipped alpha/beta orbitals.*

State	Multiplicity	Energy (eV)	Energy (cm^{-1})	Energy ($kcal.mol^{-1}$)	CI Vector	Contribution
1	3	0	0	0	222222222211	96.2%
2	3	0.25	2009	5.7	222222222121	85.6%
3	3	0.41	3318	9.5	122222222221	14.3%
					222222221221	55.3%
					222222222112	28.7%
4	3	0.92	7443	21.3	222222221122	45.7%
					222222221221	18.6%
					222222222112	27.7%
5	3	1.21	9786	28.0	122222222212	68.9%
					222222221212	29.7%
6	1	1.27	10276	29.4	222222222202	24.7%
					222222222220	58.4%
7	3	1.34	10810	30.9	122222222122	70.4%
					222222222112	11.3%
8	1	1.39	11201	32.0	222222222211	42.8%
					222222222211*	42.8%
9	3	1.58	12709	36.3	122222221222	71.1%
					122222222212	11.1%
					222222221212	14.1%
10	1	1.62	13091	37.4	222222222121	35.9%
					222222222121*	35.9%
11	1	1.94	15665	44.8	222222221221	20.8%
					222222221221*	20.8%
					222222222112	20.1%

					222222222112*	20.1%
12	3	2.03	16355	46.8	122222222122	25.3%
					122222222221	40.7%
					222222222112	26.7%
13	1	2.23	17988	51.4	222222222022	39.6%
					222222222202	25.1%
14	1	2.43	19610	56.1	122222222212	15.6%
					122222222212*	15.6%
					222222222202	17.5%
					222222222220	13.3%
15	1	2.47	19909	56.9	222222221221	13.8%
					222222221221*	13.8%
					222222222112	25.5%
					222222222112*	25.5%
16	3	2.55	20607	58.9	122222222221	24.7%
					222222221122	41.8%
					222222221221	21.8%
17	3	2.68	21586	61.7	122222221222	27.7%
					122222222212	14.5%
					222222221212	45.5%
18	1	2.80	22596	64.6	122222222122	18.7%
					122222222122*	18.7%
					122222222221	25.1%
					122222222221*	25.1%
19	1	2.81	22642	64.7	022222222222	12.3%
					122222222212	17.9%
					122222222212*	17.9%
					222222221212	16.9%
					222222221212*	16.9%
20	1	3.02	24323	69.5	122222222221	12.5%

					122222222221*	12.5%
					222222221122	19.5%
					222222221122*	19.5%
21	1	3.03	24426	69.8	022222222222	17.9%
					222222221212	12.4%
					222222221212*	12.4%
					222222222022	33.0%
22	1	3.51	28274	80.8	122222222122	14.1%
					122222222122*	14.1%
					222222221122	20.7%
					222222221122*	20.7%
					222222221221	10.4%
					222222221221*	10.4%
23	1	3.98	32106	91.8	022222222222	10.6%
					122222221222	24.5%
					122222221222*	24.5%
					222222220222	19.0%
24	1	4.03	32493	92.9	022222222222	19.8%
					122222221222	15.1%
					122222221222*	15.1%
					222222220222	32.1%

***Table S38**: Calculated electronic transitions for **Ni^{II}(IB)Br_2** at the CASSCF level with 22e,12o active space (cf. Figure S91) with the PCM solvation model (ε = 38). Active Space Orbitals (in order for CI vector notation below): 4p(Br), $3d_{xy}$(Ni), $3d_{yz}$(Ni), 4p(Br), $3d_{z2}$(Ni), 4p(Br), 4p(Br), 4p(Br), 4p(Br), σ-bonding(IB), $3d_{x2-y2}$(Ni), $3d_{xz}$(Ni). Starred CI vectors refer to the determinants that are already present in the particular state with the flipped alpha/beta orbitals.*

State	Multiplicity	Energy (eV)	Energy (cm^{-1})	Energy ($kcal.mol^{-1}$)	CI Vector	Contribution
1	3	0.00	0	0.0	221222222221	12.1%
					222222222211	82.7%
2	3	0.34	2764	7.9	212222222212	10.2%
					221222222221	76.5%
3	3	0.55	4419	12.6	212222222221	70.5%
					221222222212	23.1%
4	3	0.88	7127	20.4	211222222222	21.9%
					221212222222	10.2%
					221222222212	28.7%
					222212222212	14.2%
					222212222221	19.5%
5	3	0.98	7891	22.6	221212222222	19.3%
					222212222212	74.0%
6	3	1.13	9092	26.0	211222222222	35.7%
					212222222212	11.2%
					221212222222	22.6%
					221222222212	14.1%
7	3	1.32	10662	30.5	212212222222	72.5%
					212222222212	15.1%
8	1	1.59	12834	36.7	222222222202	16.4%
					222222222220	57.1%
9	1	1.70	13751	39.3	222222222211	35.4%
					222222222211*	35.4%
10	1	1.96	15807	45.2	221222222221	31.7%

					221222222221*	31.7%
11	1	2.23	17972	51.4	212222222221	23.3%
					212222222221*	23.3%
					222222222202	10.4%
12	3	2.40	19321	55.2	212222222221	16.0%
					221212222222	24.5%
					221222222212	24.0%
					222212222221	19.3%
13	1	2.44	19662	56.2	220222222222	17.0%
					221222222212	18.8%
					221222222212*	18.8%
					222222222202	12.1%
14	1	2.72	21953	62.8	222212222212	19.4%
					222212222212*	19.4%
					222222222202	19.7%
					222222222220	10.3%
15	3	2.78	22433	64.1	211222222222	22.1%
					212212222222	19.4%
					212222222212	22.0%
					222212222221	16.0%
16	1	2.80	22573	64.5	212222222221	11.6%
					212222222221*	11.6%
					220222222222	15.1%
					221222222212	12.9%
					221222222212*	12.9%
17	3	2.84	22911	65.5	212222222212	32.7%
					221212222222	11.9%
					222212222221	29.9%
18	1	2.98	24018	68.7	212222222212	30.4%
					212222222212*	30.4%

19	1	3.00	24223	69.3	222212222221	24.5%
					222212222221*	24.5%
20	1	3.21	25919	74.1	211222222222	27.9%
					211222222222*	27.9%
21	1	3.27	26397	75.5	220222222222	25.5%
					222202222222	13.2%
22	1	3.53	28445	81.3	221212222222	25.8%
					221212222222*	25.8%
23	1	3.84	30991	88.6	202222222222	33.5%
					212212222222	13.7%
					212212222222*	13.7%
					222202222222	18.4%
24	1	3.88	31256	89.4	202222222222	11.7%
					212212222222	24.8%
					212212222222*	24.8%
					222202222222	14.6%

***Table S39**: Calculated electronic transitions for **Ni^{II}(IB)Br_2** at the MS-CASPT2 level with 22e,12o active space (cf. Figure S91) with the PCM solvation model (ε = 38). Active Space Orbitals (in order for CI vector notation below): 4p(Br), $3d_{xy}$(Ni), $3d_{yz}$(Ni), 4p(Br), $3d_{z2}$(Ni), 4p(Br), 4p(Br), 4p(Br), 4p(Br), σ-bonding(IB), $3d_{x2-y2}$(Ni), $3d_{xz}$(Ni). Starred CI vectors refer to the determinants that are already present in the particular state with the flipped alpha/beta orbitals.*

State	Multiplicity	Energy (eV)	Energy (cm^{-1})	Energy ($kcal.mol^{-1}$)	CI Vector	Contribution
1	3	0	0	0	221222222221	12.1%
					222222222211	82.7%
2	3	0.23	1824	5.2	212222222212	10.2%
					221222222221	76.5%
3	3	0.37	2974	8.5	212222222221	70.5%
					221222222212	23.1%
4	3	0.90	7229	20.7	211222222222	21.9%
					221212222222	10.2%
					221222222212	28.7%
					222212222212	14.2%
					222212222221	19.5%
5	3	1.16	9322	26.7	221212222222	19.3%
					222212222212	74.0%
6	1	1.17	9428	27.0	222222222202	16.4%
					222222222220	57.1%
7	3	1.27	10244	29.3	211222222222	35.7%
					212222222212	11.2%
					221212222222	22.6%
					221222222212	14.1%
8	1	1.34	10828	31.0	222222222211	35.4%
					222222222211*	35.4%
9	3	1.54	12382	35.4	212212222222	72.5%
					212222222212	15.1%
10	1	1.55	12504	35.8	221222222221	31.7%

					221222222221*	31.7%
11	1	1.85	14932	42.7	212222222221	23.3%
					212222222221*	23.3%
					222222222202	10.4%
12	3	2.00	16112	46.1	212222222221	16.0%
					221212222222	24.5%
					221222222212	24.0%
					222212222221	19.3%
13	1	2.17	17475	50.0	220222222222	17.0%
					221222222212	18.8%
					221222222212*	18.8%
					222222222202	12.1%
14	1	2.31	18654	53.3	222212222212	19.4%
					222212222212*	19.4%
					222222222202	19.7%
					222222222220	10.3%
15	1	2.38	19223	55.0	212222222221	11.6%
					212222222221*	11.6%
					220222222222	15.1%
					221222222212	12.9%
					221222222212*	12.9%
16	3	2.42	19514	55.8	212222222212	32.7%
					221212222222	11.9%
					222212222221	29.9%
17	3	2.43	19561	55.9	211222222222	22.1%
					212212222222	19.4%
					212222222212	22.0%
					222212222221	16.0%
18	1	2.67	21572	61.7	222212222221*	24.5%
					222212222221*	24.5%

19	1	2.68	21602	61.8	212222222212	30.4%
					212222222212*	30.4%
20	1	2.88	23206	66.3	211222222222	27.9%
					211222222222*	27.9%
21	1	2.88	23248	66.5	220222222222	25.5%
					222202222222	13.2%
22	1	3.28	26468	75.7	221212222222	25.8%
					221212222222*	25.8%
23	1	3.77	30417	87.0	202222222222	11.7%
					212212222222	24.8%
					212212222222*	24.8%
					222202222222	14.6%
24	1	3.83	30905	88.4	202222222222	33.5%
					212212222222	13.7%
					212212222222*	13.7%
					222202222222	18.4%

***Table S40**: Calculated electronic transitions for **Ni^{II}(IB)(O-DMA)Cl_2** at the CASSCF levelwith 22e,12o active space (cf. Figure S91) in the gas phase. Active Space Orbitals (in order for CI vector notation below): $3d_{z2}$(Ni), σ-bonding(IB), 3p(Cl), $3d_{xy}$(Ni), 3p(Cl), 3p(Cl), 3p(Cl), 3p(Cl), $3d_{yz}$(Ni), 3p(Cl), $3d_{x2-y2}$(Ni), $3d_{xz}$(Ni). Starred CI vectors refer to the determinants that are already present in the particular state with the flipped alpha/beta orbitals.*

State	Multiplicity	Energy (eV)	Energy (cm^{-1})	Energy ($kcal.mol^{-1}$)	CI Vector	Contribution
1	3	0.00	0	0.0	222222222211	97.2%
2	3	0.47	3779	10.8	222122222221	17.0%
					222222221221	75.4%
3	3	0.71	5746	16.4	122222222212	12.5%
					122222222221	12.1%
					222122222221	42.1%
4	3	0.81	6530	18.7	122222222212	41.2%
					122222222221	23.0%
					222122222212	10.7%
					222122222221	13.7%
5	3	1.15	9253	26.5	122122222222	19.7%
					122222222212	12.1%
					222122222212	45.1%
6	3	1.30	10472	29.9	122122222222	21.7%
					122222222212	18.0%
					122222222221	10.2%
					222122221222	40.7%
7	1	1.38	11098	31.7	222222222211	12.7%
					222222222211*	12.7%
					222222222220	54.4%
8	3	1.41	11407	32.6	122122222222	15.1%
					122222221222	55.3%
					222222221212	15.2%
9	1	1.74	14033	40.1	222222222202	18.2%
					222222222211	26.3%

					222222222211*	26.3%
					222222222220	16.4%
10	1	2.20	17724	50.7	222222221221	32.3%
					222222221221*	32.3%
11	1	2.35	18936	54.1	222122222221	21.8%
					222122222221*	21.8%
12	1	2.49	20107	57.5	122222222221	12.3%
					122222222221*	12.3%
					222122222221	16.7%
					222122222221*	16.7%
13	3	2.55	20561	58.8	122222221222	20.4%
					122222222221	13.9%
					222122222221	14.2%
					222222221212	24.1%
14	1	2.87	23165	66.2	222122222212	31.1%
					222122222212*	31.1%
15	3	2.95	23774	68.0	122222221222	11.7%
					122222222221	32.9%
					222122221222	27.2%
16	1	2.98	24028	68.7	222022222222	12.2%
					222222222202	45.8%
17	3	3.16	25516	73.0	122122222222	35.3%
					222122222212	16.0%
					222222221212	38.1%
18	1	3.25	26250	75.1	122222222212	16.6%
					122222222212*	16.6%
					122222222221	16.4%
					122222222221*	16.4%
19	1	3.46	27932	79.9	222222221212	28.0%
					222222221212*	28.0%

20	1	3.64	29386	84.0	022222222222	11.0%
					122122222222	14.3%
					122122222222*	14.3%
					222222220222	27.8%
21	1	3.69	29771	85.1	022222222222	13.9%
					222022222222	19.6%
					222122221222	11.7%
					222122221222*	11.7%
22	1	3.85	31022	88.7	222022222222	16.0%
					222222220222	19.3%
23	1	3.97	32008	91.5	022222222222	31.5%
					222022222222	10.5%
					222122221222	12.2%
					222122221222*	12.2%
24	1	4.02	32385	92.6	122122222222	15.5%
					122122222222*	15.5%
					122222221222	19.7%
					122222221222*	19.7%

***Table S41**: Calculated electronic transitions for **Ni^{II}(IB)(O-DMA)Cl_2** at the MS-CASPT2 level with 22e,12o active space (cf. Figure S91) in the gas phase. Active Space Orbitals (in order for CI vector notation below): $3d_{z2}$(Ni), σ-bonding(IB), 3p(Cl), $3d_{xy}$(Ni), 3p(Cl), 3p(Cl), 3p(Cl), 3p(Cl), $3d_{yz}$(Ni), 3p(Cl), $3d_{x2-y2}$(Ni), $3d_{xz}$(Ni). Starred CI vectors refer to the determinants that are already present in the particular state with the flipped alpha/beta orbitals.*

State	Multiplicity	Energy (eV)	Energy (cm^{-1})	Energy ($kcal.mol^{-1}$)	CI Vector	Contribution
1	3	0.00	0	0.0	222222222211	97.2%
2	3	0.62	5037	14.4	222122222221	17.0%
					222222221221	75.4%
3	3	0.75	6028	17.2	122222222212	12.5%
					122222222221	12.1%
					222122222221	42.1%
4	3	0.83	6705	19.2	122222222212	41.2%
					122222222221	23.0%
					222122222212	10.7%
					222122222221	13.7%
5	1	0.97	7849	22.4	222222222211	12.7%
					222222222211*	12.7%
					222222222220	54.4%
6	3	1.36	10946	31.3	122122222222	19.7%
					122222222212	12.1%
					222122222212	45.1%
7	1	1.40	11258	32.2	222222222202	18.2%
					222222222211	26.3%
					222222222211*	26.3%
					222222222220	16.4%
8	3	1.69	13646	39.0	122122222222	21.7%
					122222222212	18.0%
					122222222221	10.2%
					222122221222	40.7%
9	3	1.89	15254	43.6	122122222222	15.1%

					122222221222	55.3%
					222222221212	15.2%
10	1	1.97	15903	45.5	222222221221	32.3%
					222222221221*	32.3%
11	1	2.20	17749	50.7	222122222221	21.8%
					222122222221*	21.8%
12	1	2.31	18662	53.4	122222222221	12.3%
					122222222221*	12.3%
					222122222221	16.7%
					222122222221*	16.7%
13	3	2.37	19121	54.7	122222221222	20.4%
					122222222221	13.9%
					222122222221	14.2%
					222222221212	24.1%
14	1	2.63	21223	60.7	222022222222	12.2%
					222222222202	45.8%
15	1	2.73	22054	63.1	222122222212	31.1%
					222122222212*	31.1%
16	3	2.83	22819	65.2	122222221222	11.7%
					122222222221	32.9%
					222122221222	27.2%
17	3	2.99	24093	68.9	122122222222	35.3%
					222122222212	16.0%
					222222221212	38.1%
18	1	3.24	26150	74.8	122222222212	16.6%
					122222222212*	16.6%
					122222222221	16.4%
					122222222221*	16.4%
19	1	3.36	27077	77.4	222222221212	28.0%
					222222221212*	28.0%

20	1	3.64	29352	83.9	022222222222	13.9%
					222022222222	19.6%
					222122221222	11.7%
					222122221222*	11.7%
21	1	3.82	30786	88.0	022222222222	11.0%
					122122222222	14.3%
					122122222222*	14.3%
					222222220222	27.8%
22	1	4.05	32697	93.5	222022222222	16.0%
					222222220222	19.3%
23	1	4.13	33320	95.3	122122222222	15.5%
					122122222222*	15.5%
					122222221222	19.7%
					122222221222*	19.7%
24	1	4.20	33887	96.9	022222222222	31.5%
					222022222222	10.5%
					222122221222	12.2%
					222122221222*	12.2%

***Table S42**: Calculated electronic transitions for **Ni^{II}(IB)(O-DMA)Br_2** at the CASSCF level with 22e,12o active space (cf. Figure S91) in the gas phase. Active Space Orbitals (in order for CI vector notation below): $3d_{z2}$(Ni), σ-bonding(IB), 4p(Br), 4p(Br), 4p(Br), 4p(Br), 4p(Br), $3d_{yz}$(Ni), 4p(Br), $3d_{xy}$(Ni), $3d_{xz}$(Ni), $3d_{x2-y2}$(Ni). Starred CI vectors refer to the determinants that are already present in the particular state with the flipped alpha/beta orbitals.*

State	Multiplicity	Energy (eV)	Energy (cm^{-1})	Energy ($kcal.mol^{-1}$)	CI Vector	Contribution
1	3	0	0	0	222222222211	96.9%
2	3	0.53	4297	12.3	222222222112	73.1%
					222222222121	16.2%
3	3	0.75	6027	17.2	122222222221	27.1%
					222222212212	48.2%
4	3	0.81	6529	18.7	122222222221	44.6%
					222222212212	31.2%
					222222212221	11.6%
5	3	1.14	9203	26.3	122222222122	23.1%
					122222222221	11.2%
					222222212221	34.4%
6	1	1.31	10570	30.2	222222222202	22.8%
					222222222211	29.2%
					222222222211*	29.2%
7	3	1.32	10684	30.5	122222222212	17.8%
					222222212122	53.7%
8	3	1.45	11658	33.3	122222212222	57.8%
					122222222122	17.4%
					222222212221	10.9%
9	1	1.62	13066	37.4	222222222202	34.9%
					222222222220	41.6%
10	1	2.15	17313	49.5	222222222112	19.0%
					222222222112*	19.0%
11	1	2.27	18309	52.3	122222222221	17.0%
					122222222221*	17.0%

12	1	2.42	19518	55.8	222222212212	29.3%
					222222212212*	29.3%
13	3	2.45	19731	56.4	122222222122	21.4%
					122222222212	14.8%
					222222212221	28.0%
14	1	2.70	21816	62.4	222222212221	33.3%
					222222212221*	33.3%
15	1	2.75	22157	63.3	222222222202	20.6%
					222222222220	25.5%
16	3	2.86	23063	65.9	122222222212	37.0%
					222222212122	33.4%
17	3	3.08	24869	71.1	122222212222	19.1%
					122222222122	19.9%
					222222222121	38.6%
18	1	3.16	25468	72.8	122222222212	26.4%
					122222222212*	26.4%
19	1	3.22	25981	74.3	222222222121	20.8%
					222222222121*	20.8%
20	1	3.52	28428	81.3	022222222222	13.9%
					122222212222	14.9%
					122222212222*	14.9%
					222222202222	11.8%
					222222212122	10.7%
					222222212122*	10.7%
21	1	3.58	28902	82.6	222222202222	29.7%
22	3	3.58	28908	82.7	222212222212	47.7%
					222212222221	34.8%
23	1	3.71	29960	85.7	122222212222	11.3%
					122222212222*	11.3%
					222222212122	13.0%

					222222212122*	13.0%
24	1	3.74	30162	86.2	222212222212	29.9%
					222212222212*	29.9%
25	1	3.87	31230	89.3	022222222222	17.8%
					122222222122	12.9%
					122222222122*	12.9%
					222222222022	13.0%
26	1	3.91	31566	90.3	122222222122	17.3%
					122222222122*	17.3%
					222222222022	17.0%
27	3	3.93	31722	90.7	222212222212	43.7%
					222212222221	42.2%
28	1	4.01	32376	92.6	222212222212	11.7%
					222212222212*	11.7%
					222212222221	30.8%
					222212222221*	30.8%
29	3	4.11	33131	94.7	222122222212	63.5%
					222122222221	24.8%
30	1	4.14	33432	95.6	222122222212	25.3%
					222122222212*	25.3%
					222122222221	13.1%
					222122222221*	13.1%
31	3	4.20	33838	96.7	222212222221	15.2%
					222221222212	28.4%
					222221222221	28.1%
					222222221212	15.6%
32	3	4.34	34977	100.0	222212212222	57.9%

***Table S43**: Calculated electronic transitions for **Ni^{II}(IB)(O-DMA)Br_2** at the MS-CASPT2 level with 22e,12o active space (cf. Figure S91) in the gas phase. Active Space Orbitals (in order for CI vector notation below): $3d_{z2}$(Ni), σ-bonding(IB), 4p(Br), 4p(Br), 4p(Br), 4p(Br), 4p(Br), $3d_{yz}$(Ni), 4p(Br), $3d_{xy}$(Ni), $3d_{xz}$(Ni), $3d_{x2-y2}$(Ni). Starred CI vectors refer to the determinants that are already present in the particular state with the flipped alpha/beta orbitals.*

State	Multiplicity	Energy (eV)	Energy (cm^{-1})	Energy ($kcal.mol^{-1}$)	CI Vector	Contribution
1	3	0	0	0	222222222211	96.9%
2	3	0.66	5327	15.2	222222222112	73.1%
					222222222121	16.2%
3	3	0.67	5384	15.4	122222222221	27.1%
					222222212212	48.2%
4	3	0.74	5949	17.0	122222222221	44.6%
					222222212212	31.2%
					222222212221	11.6%
5	1	0.95	7681	22.0	222222222202	22.8%
					222222222211	29.2%
					222222222211*	29.2%
6	3	1.27	10267	29.4	122222222122	23.1%
					122222222221	11.2%
					222222212221	34.4%
7	1	1.28	10329	29.5	222222222202	34.9%
					222222222220	41.6%
8	3	1.56	12604	36.0	122222222212	17.8%
					222222212122	53.7%
9	3	1.76	14221	40.7	122222212222	57.8%
					122222222122	17.4%
					222222212221	10.9%
10	1	1.90	15301	43.7	222222222112	19.0%
					222222222112*	19.0%
11	1	2.10	16899	48.3	122222222221	17.0%
					122222222221*	17.0%

12	1	2.22	17876	51.1	222222212212	29.3%
					222222212212*	29.3%
13	3	2.28	18389	52.6	122222222122	21.4%
					122222222212	14.8%
					222222212221	28.0%
14	1	2.33	18791	53.7	222222222202	20.6%
					222222222220	25.5%
15	1	2.49	20055	57.3	222222212221	33.3%
					222222212221*	33.3%
16	3	2.68	21581	61.7	122222222212	37.0%
					222222212122	33.4%
17	3	2.85	22989	65.7	122222212222	19.1%
					122222222122	19.9%
					222222222121	38.6%
18	1	3.00	24230	69.3	222222222121	20.8%
					222222222121*	20.8%
19	1	3.02	24327	69.6	122222222212	26.4%
					122222222212*	26.4%
20	1	3.27	26380	75.4	122222212222	11.3%
					122222212222*	11.3%
					222222212122	13.0%
					222222212122*	13.0%
21	1	3.42	27553	78.8	022222222222	13.9%
					122222212222	14.9%
					122222212222*	14.9%
					222222202222	11.8%
					222222212122	10.7%
					222222212122*	10.7%
22	1	3.46	27869	79.7	222222202222	29.7%
23	1	3.64	29368	84.0	222212222212	29.9%

					222212222212*	29.9%
24	1	3.73	30084	86.0	122222222122	17.3%
					122222222122*	17.3%
					222222222022	17.0%
25	1	3.78	30500	87.2	022222222222	17.8%
					122222222122	12.9%
					122222222122*	12.9%
					222222222022	13.0%
26	3	3.96	31915	91.3	222212222212	47.7%
					222212222221	34.8%
27	1	4.16	33525	95.9	222212222212	11.7%
					222212222212*	11.7%
					222212222221	30.8%
					222212222221*	30.8%
28	3	4.22	34056	97.4	222212222212	43.7%
					222212222221	42.2%

2.6.9 References

(1) Hofstra, J. L. Development and Mechanistic Studies of Ni-Catalyzed Asymmetric Reductive Cross-Coupling Reactions.Ph.D Dissertation, California Institute of Technology, Pasadena, CA.**2019**

(2) Hofstra, J. L.; Cherney, A. H.; Ordner, C. M.; Reisman, S. E. Synthesis of Enantioenriched Allylic Silanes via Nickel-Catalyzed Reductive Cross-Coupling. *J. Am. Chem. Soc.* **2018**, *140* (1), 139–142. https://doi.org/10.1021/jacs.7b11707.

(3) Wang, Y.; Rogers, E. I.; Compton, R. G. The Measurement of the Diffusion Coefficients of Ferrocene and Ferrocenium and Their Temperature Dependence in Acetonitrile Using Double Potential Step Microdisk Electrode

Chronoamperometry. *Journal of Electroanalytical Chemistry* **2010**, *648* (1), 15–19. https://doi.org/10.1016/j.jelechem.2010.07.006.

(4) Bard, A. J.; Faulkner, L. R. *Electrochemical Methods: Fundamentals and Applications*, 2nd ed.; Wiley: New York, 2001.

(5) Gerloch, M.; Hanton, L. R.; Manning, M. R. Tetrahedral Complexes of Nickel(II): Electronic Spectra, γ and π Bonding, Andthe Electroneutrality Principle. *Inorganica Chimica Acta* **1981**, *48*, 205–214. https://doi.org/10.1016/S0020-1693(00)90092-6.

(6) Koester, V. J.; Dunn, T. M. Electronic Spectrum of the Tetrachloronickelate(II) Complex at 2.2.Deg.K. *Inorg. Chem.* **1975**, *14* (8), 1811–1817. https://doi.org/10.1021/ic50150a014.

(7) Fereday, R. J.; Hathaway, B. J.; Dudley, R. J. Polarised Single-Crystal Electronic Spectrum of Dichlorobis(Triphenylphosphine)Nickel(II). *J. Chem. Soc. A* **1970**, No. 0, 571–574. https://doi.org/10.1039/J19700000571.

(8) Lever, A. B. P. *Inorganic Electronic Spectroscopy*, 2nd ed.; Elsevier, 1984.

(9) Davies, J. E.; Gerloch, M.; Phillips, D. J. Phosphine π-Acceptor Properties in Dihalogenobis(Triphenylphosphine)-Nickel(II) and -Cobalt(II). *J. Chem. Soc., Dalton Trans.* **1979**, No. 11, 1836–1842. https://doi.org/10.1039/DT9790001836.

(10) Goodgame, D. M. L.; Goodgame, M.; Cotton, F. A. Electronic Spectra of Some Tetrahedral Nickel(II) Complexes. *J. Am. Chem. Soc.* **1961**, *83* (20), 4161–4167. https://doi.org/10.1021/ja01481a014.

(11) Espinoza, E. M.; Clark, J. A.; Soliman, J.; Derr, J. B.; Morales, M.; Vullev, V. I. Practical Aspects of Cyclic Voltammetry: How to Estimate Reduction Potentials

When Irreversibility Prevails. *J. Electrochem. Soc.* **2019**, *166* (5), H3175–H3187. https://doi.org/10.1149/2.0241905jes.

(12) Bard, A. J.; Faulkner, L. R.; White, H. S. *Electrochemical Methods: Fundamentals and Applications*, 3rd ed.; John Wiley & Sons, Inc.: Hoboken, NJ, USA, 2022.

(13) Wang, J.; Tian, Y.; Zhao, Y.; Zhuo, K. A Volumetric and Viscosity Study for the Mixtures of 1-n-Butyl-3-Methylimidazolium Tetrafluoroborate Ionic Liquid with Acetonitrile, Dichloromethane, 2-Butanone and N, N – Dimethylformamide. *Green Chem.* **2003**, *5* (5), 618–622. https://doi.org/10.1039/B303735E.

(14) Grande, M. del C.; García, M.; Marschoff, C. M. Density and Viscosity of Anhydrous Mixtures of Dimethylsulfoxide with Acetonitrile in the Range (298.15 to 318.15) K. *J. Chem. Eng. Data* **2009**, *54* (2), 652–658. https://doi.org/10.1021/je8001909.

(15) Pal, A.; Kumar, A. Excess Molar Volumes and Kinematic Viscosities for Binary Mixtures of Dipropylene Glycol Monobutyl Ether and Dipropylene Glycol Tert-Butyl Ether with 2-Pyrrolidinone, N-Methyl-2-Pyrrolidinone, N,N-Dimethylformamide, and N,N-Dimethylacetamide at 298.15 K. *J. Chem. Eng. Data* **2005**, *50* (3), 856–862. https://doi.org/10.1021/je049657g.

(16) Tang, T.; Jones, E.; Wild, T.; Hazra, A.; Minteer, S. D.; Sigman, M. S. Investigating Oxidative Addition Mechanisms of Allylic Electrophiles with Low-Valent Ni/Co Catalysts Using Electroanalytical and Data Science Techniques. *J. Am. Chem. Soc.* **2022**, *144* (43), 20056–20066. https://doi.org/10.1021/jacs.2c09120.

(17) Ju, L.; Lin, Q.; LiBretto, N. J.; Wagner, C. L.; Hu, C. T.; Miller, J. T.; Diao, T. Reactivity of (Bi-Oxazoline)Organonickel Complexes and Revision of a Catalytic Mechanism. *J. Am. Chem. Soc.* **2021**, *143* (36), 14458–14463. https://doi.org/10.1021/jacs.1c07139.

(18) Zhou, Y.-Y.; Uyeda, C. Reductive Cyclopropanations Catalyzed by Dinuclear Nickel Complexes. *Angewandte Chemie International Edition* **2016**, *55* (9), 3171–3175. https://doi.org/10.1002/anie.201511271.

(19) Turro, R. F.; Wahlman, J. L. H.; Tong, Z. J.; Chen, X.; Yang, M.; Chen, E. P.; Hong, X.; Hadt, R. G.; Yang, Y.-F.; Houk, K. N.; Reisman, S. E. Mechanistic Investigation of Ni-Catalyzed Reductive Cross-Coupling of Alkenyl and Benzyl Electrophiles. *Submitted and Uploaded to ChemRxiv* **2023**.

(20) Sheldrick, G. M. Phase Annealing in SHELX-90: Direct Methods for Larger Structures. *Acta Crystallogr A Found Crystallogr* **1990**, *46* (6), 467–473. https://doi.org/10.1107/S0108767390000277.

(21) Sheldrick, G. M. Crystal Structure Refinement with It SHELXL. *Acta Crystallographica Section C* **2015**, *71* (1), 3–8. https://doi.org/10.1107/S2053229614024218.

(22) Müller, P. Practical Suggestions for Better Crystal Structures. *Crystallography Reviews* **2009**, *15* (1), 57–83. https://doi.org/10.1080/08893110802547240.

(23) Neese, F. The ORCA Program System. *WIREs Comput Mol Sci* **2012**, *2* (1), 73–78. https://doi.org/10.1002/wcms.81.

(24) Weigend, F.; Ahlrichs, R. Balanced Basis Sets of Split Valence, Triple Zeta Valence and Quadruple Zeta Valence Quality for H to Rn: Design and Assessment

of Accuracy. *Phys. Chem. Chem. Phys.* **2005**, *7* (18), 3297. https://doi.org/10.1039/b508541a.

(25) Grimme, S.; Antony, J.; Ehrlich, S.; Krieg, H. A Consistent and Accurate Ab Initio Parametrization of Density Functional Dispersion Correction (DFT-D) for the 94 Elements H-Pu. *The Journal of Chemical Physics* **2010**, *132* (15), 154104. https://doi.org/10.1063/1.3382344.

(26) Grimme, S.; Ehrlich, S.; Goerigk, L. Effect of the Damping Function in Dispersion Corrected Density Functional Theory. *J. Comput. Chem.* **2011**, *32* (7), 1456–1465. https://doi.org/10.1002/jcc.21759.

(27) Barone, V.; Cossi, M. Quantum Calculation of Molecular Energies and Energy Gradients in Solution by a Conductor Solvent Model. *J. Phys. Chem. A* **1998**, *102* (11), 1995–2001. https://doi.org/10.1021/jp9716997.

(28) Klamt, A.; Schüürmann, G. COSMO: A New Approach to Dielectric Screening in Solvents with Explicit Expressions for the Screening Energy and Its Gradient. *J. Chem. Soc., Perkin Trans. 2* **1993**, No. 5, 799–805. https://doi.org/10.1039/P29930000799.

(29) Eichkorn, K.; Treutler, O.; Öhm, H.; Häser, M.; Ahlrichs, R. Auxiliary Basis Sets to Approximate Coulomb Potentials. *Chemical Physics Letters* **1995**, *240* (4), 283–290. https://doi.org/10.1016/0009-2614(95)00621-A.

(30) Tao, J.; Perdew, J. P.; Staroverov, V. N.; Scuseria, G. E. Climbing the Density Functional Ladder: Nonempirical Meta–Generalized Gradient Approximation Designed for Molecules and Solids. *Phys. Rev. Lett.* **2003**, *91* (14), 146401. https://doi.org/10.1103/PhysRevLett.91.146401.

(31) Staroverov, V. N.; Scuseria, G. E.; Tao, J.; Perdew, J. P. Comparative Assessment of a New Nonempirical Density Functional: Molecules and Hydrogen-Bonded Complexes. *The Journal of Chemical Physics* **2003**, *119* (23), 12129–12137. https://doi.org/10.1063/1.1626543.

(32) Roos, B. O.; Taylor, P. R.; Sigbahn, P. E. M. A Complete Active Space SCF Method (CASSCF) Using a Density Matrix Formulated Super-CI Approach. *Chemical Physics* **1980**, *48* (2), 157–173. https://doi.org/10.1016/0301-0104(80)80045-0.

(33) Siegbahn, P. E. M.; Almlöf, J.; Heiberg, A.; Roos, B. O. The Complete Active Space SCF (CASSCF) Method in a Newton–Raphson Formulation with Application to the HNO Molecule. *The Journal of Chemical Physics* **1981**, *74* (4), 2384–2396. https://doi.org/10.1063/1.441359.

(34) Andersson, K. Different Forms of the Zeroth-Order Hamiltonian in Second-Order Perturbation Theory with a Complete Active Space Self-Consistent Field Reference Function. *Theoretica chimica acta* **1995**, *91* (1), 31–46. https://doi.org/10.1007/BF01113860.

(35) Andersson, Kerstin.; Malmqvist, P. Aake.; Roos, B. O.; Sadlej, A. J.; Wolinski, Krzysztof. Second-Order Perturbation Theory with a CASSCF Reference Function. *J. Phys. Chem.* **1990**, *94* (14), 5483–5488. https://doi.org/10.1021/j100377a012.

(36) Andersson, K.; Malmqvist, P.; Roos, B. O. Second-order Perturbation Theory with a Complete Active Space Self-consistent Field Reference Function. *The Journal of Chemical Physics* **1992**, *96* (2), 1218–1226. https://doi.org/10.1063/1.462209.

(37) Finley, J.; Malmqvist, P.-Å.; Roos, B. O.; Serrano-Andrés, L. The Multi-State CASPT2 Method. *Chemical Physics Letters* **1998**, *288* (2), 299–306. https://doi.org/10.1016/S0009-2614(98)00252-8.

(38) Widmark, P.-O.; Malmqvist, P.-Å.; Roos, B. O. Density Matrix Averaged Atomic Natural Orbital (ANO) Basis Sets for Correlated Molecular Wave Functions. *Theoretica chimica acta* **1990**, *77* (5), 291–306. https://doi.org/10.1007/BF01120130.

(39) Roos, B. O.; Lindh, R.; Malmqvist, P.-Å.; Veryazov, V.; Widmark, P.-O. New Relativistic ANO Basis Sets for Transition Metal Atoms. *J. Phys. Chem. A* **2005**, *109* (29), 6575–6579. https://doi.org/10.1021/jp0581126.

(40) Douglas, M.; Kroll, N. M. Quantum Electrodynamical Corrections to the Fine Structure of Helium. *Annals of Physics* **1974**, *82* (1), 89–155. https://doi.org/10.1016/0003-4916(74)90333-9.

(41) Hess, B. A. Relativistic Electronic-Structure Calculations Employing a Two-Component No-Pair Formalism with External-Field Projection Operators. *Phys. Rev. A* **1986**, *33* (6), 3742–3748. https://doi.org/10.1103/PhysRevA.33.3742.

(42) Jansen, G.; Hess, B. A. Revision of the Douglas-Kroll Transformation. *Phys. Rev. A* **1989**, *39* (11), 6016–6017. https://doi.org/10.1103/PhysRevA.39.6016.

(43) Sigel, H.; Martin, R. B. Coordinating Properties of the Amide Bond. Stability and Structure of Metal Ion Complexes of Peptides and Related Ligands. *Chem. Rev.* **1982**, *82* (4), 385–426. https://doi.org/10.1021/cr00050a003.

(44) Bursch, M.; Mewes, J.-M.; Hansen, A.; Grimme, S. Best-Practice DFT Protocols for Basic Molecular Computational Chemistry**. *Angewandte Chemie* **2022**, *134* (42), e202205735. https://doi.org/10.1002/ange.202205735.

2.7 Notes and References

(1) Semmelhack, M. F.; Helquist, P. M.; Jones, L. D. Synthesis with Zerovalent Nickel. Coupling of Aryl Halides with Bis(1,5-Cyclooctadiene)Nickel(0). *J. Am. Chem. Soc.* **1971**, *93* (22), 5908–5910. https://doi.org/10.1021/ja00751a062.

(2) Poremba, K. E.; Dibrell, S. E.; Reisman, S. E. Nickel-Catalyzed Enantioselective Reductive Cross-Coupling Reactions. *ACS Catal.* **2020**, *10* (15), 8237–8246. https://doi.org/10.1021/acscatal.0c01842.

(3) Durandetti, M.; Nédélec, J.-Y.; Périchon, J. Nickel-Catalyzed Direct Electrochemical Cross-Coupling between Aryl Halides and Activated Alkyl Halides. *J. Org. Chem.* **1996**, *61* (5), 1748–1755. https://doi.org/10.1021/jo9518314.

(4) Durandetti, M.; Gosmini, C.; Périchon, J. Ni-Catalyzed Activation of α-Chloroesters: A Simple Method for the Synthesis of α-Arylesters and β-Hydroxyesters. *Tetrahedron* **2007**, *63* (5), 1146–1153. https://doi.org/10.1016/j.tet.2006.11.055.

(5) Cherney, A. H.; Kadunce, N. T.; Reisman, S. E. Catalytic Asymmetric Reductive Acyl Cross-Coupling: Synthesis of Enantioenriched Acyclic α,α-Disubstituted Ketones. *J. Am. Chem. Soc.* **2013**, *135* (20), 7442–7445. https://doi.org/10.1021/ja402922w.

(6) Hofstra, J. L.; Cherney, A. H.; Ordner, C. M.; Reisman, S. E. Synthesis of Enantioenriched Allylic Silanes via Nickel-Catalyzed Reductive Cross-Coupling. *J. Am. Chem. Soc.* **2018**, *140* (1), 139–142. https://doi.org/10.1021/jacs.7b11707.

(7) Cherney, A. H.; Reisman, S. E. Nickel-Catalyzed Asymmetric Reductive Cross-Coupling Between Vinyl and Benzyl Electrophiles. *J. Am. Chem. Soc.* **2014**, *136* (41), 14365–14368. https://doi.org/10.1021/ja508067c.

(8) DeLano, T. J.; Reisman, S. E. Enantioselective Electroreductive Coupling of Alkenyl and Benzyl Halides via Nickel Catalysis. *ACS Catal.* **2019**, *9* (8), 6751–6754. https://doi.org/10.1021/acscatal.9b01785.

(9) Cagan, D. A.; Bím, D.; Silva, B.; Kazmierczak, N. P.; McNicholas, B. J.; Hadt, R. G. Elucidating the Mechanism of Excited-State Bond Homolysis in Nickel–Bipyridine Photoredox Catalysts. *J. Am. Chem. Soc.* **2022**, *144* (14), 6516–6531. https://doi.org/10.1021/jacs.2c01356.

(10) Cagan, D. A.; Bîm, D.; McNicholas, B. J.; Kazmierczak, N. P.; Oyala, P. H.; Hadt, R. G. Photogenerated Ni(I)–Bipyridine Halide Complexes: Structure-Function Relationships for Competitive C(sp^2)–Cl Oxidative Addition and Dimerization Reactivity Pathways. *Inorg. Chem.* **2023**, *62*, 9538–9551.

(11) Gao, Y.; Hill, D. E.; Hao, W.; McNicholas, B. J.; Vantourout, J. C.; Hadt, R. G.; Reisman, S. E.; Blackmond, D. G.; Baran, P. S. Electrochemical Nozaki–Hiyama–Kishi Coupling: Scope, Applications, and Mechanism. *J. Am. Chem. Soc.* **2021**, *143* (25), 9478–9488. https://doi.org/10.1021/jacs.1c03007.

(12) Daifuku, S. L.; Al-Afyouni, M. H.; Snyder, B. E. R.; Kneebone, J. L.; Neidig, M. L. A Combined Mössbauer, Magnetic Circular Dichroism, and Density Functional Theory Approach for Iron Cross-Coupling Catalysis: Electronic Structure, In Situ Formation, and Reactivity of Iron-Mesityl-Bisphosphines. *J. Am. Chem. Soc.* **2014**, *136* (25), 9132–9143. https://doi.org/10.1021/ja503596m.

(13) Day, C. S.; Somerville, R. J.; Martin, R. Deciphering the Dichotomy Exerted by Zn(Ii) in the Catalytic sp^2 C–O Bond Functionalization of Aryl Esters at the Molecular Level. *Nature Catalysis* **2021**, *4* (2), 124–133. https://doi.org/10.1038/s41929-020-00560-3.

(14) Jensen, A. E.; Knochel, P. Nickel-Catalyzed Cross-Coupling between Functionalized Primary or Secondary Alkylzinc Halides and Primary Alkyl Halides. *J. Org. Chem.* **2002**, *67* (1), 79–85. https://doi.org/10.1021/jo0105787.

(15) Dorval, C.; Gosmini, C. Low-Valent Cobalt Complexes in C–X Coupling and Related Reactions. In *Cobalt Catalysis in Organic Synthesis*; 2020; pp 163–205. https://doi.org/10.1002/9783527814855.ch5.

(16) Cahiez, G.; Marquais, S. Highly Chemo- and Stereoselective Fe-Catalyzed Alkenylation of Organomanganese Reagents. *Tetrahedron Letters* **1996**, *37* (11), 1773–1776. https://doi.org/10.1016/0040-4039(96)00116-5.

(17) Cahiez, G.; Marquais, S. Copper-Catalyzed Alkylation of Organomanganese Chloride Reagents. *Synlett* **2002**, *1993* (01), 45–47.

(18) Cahiez, G.; Avedissian, H. Cobalt-Catalyzed Alkenylation of Organomagnesium Reagents. *Tetrahedron Letters* **1998**, *39* (34), 6159–6162. https://doi.org/10.1016/S0040-4039(98)01266-0.

(19) Yanagi, T.; Somerville, R. J.; Nogi, K.; Martin, R.; Yorimitsu, H. Ni-Catalyzed Carboxylation of C(Sp2)–S Bonds with CO_2: Evidence for the Multifaceted Role of Zn. *ACS Catal.* **2020**, *10* (3), 2117–2123. https://doi.org/10.1021/acscatal.9b05141.

(20) Ju, L.; Lin, Q.; LiBretto, N. J.; Wagner, C. L.; Hu, C. T.; Miller, J. T.; Diao, T. Reactivity of (Bi-Oxazoline)Organonickel Complexes and Revision of a Catalytic

Mechanism. *J. Am. Chem. Soc.* **2021**, *143* (36), 14458–14463. https://doi.org/10.1021/jacs.1c07139.

(21) Xu, J.; Li, Z.; Xu, Y.; Shu, X.; Huo, H. Stereodivergent Synthesis of Both Z- and E-Alkenes by Photoinduced, Ni-Catalyzed Enantioselective C(sp^3)–H Alkenylation. *ACS Catal.* **2021**, *11* (21), 13567–13574. https://doi.org/10.1021/acscatal.1c04314.

(22) Lu, Q.; Guan, H.; Wang, Y.-E.; Xiong, D.; Lin, T.; Xue, F.; Mao, J. Nickel/Photoredox-Catalyzed Enantioselective Reductive Cross-Coupling between Vinyl Bromides and Benzyl Chlorides. *J. Org. Chem.* **2022**, *87* (12), 8048–8058. https://doi.org/10.1021/acs.joc.2c00707.

(23) Liu, J.; Gong, H.; Zhu, S. Nickel-Catalyzed, Regio- and Enantioselective Benzylic Alkenylation of Olefins with Alkenyl Bromide. *Angewandte Chemie International Edition* **2021**, *60* (8), 4060–4064. https://doi.org/10.1002/anie.202012614.

(24) Zhu, Z.; Lin, L.; Xiao, J.; Shi, Z. Nickel-Catalyzed Stereo- and Enantioselective Cross-Coupling of Gem-Difluoroalkenes with Carbon Electrophiles by C−F Bond Activation. *Angewandte Chemie International Edition* **2022**, *61* (6), e202113209. https://doi.org/10.1002/anie.202113209.

(25) Hu, X.; Cheng-Sánchez, I.; Cuesta-Galisteo, S.; Nevado, C. Nickel-Catalyzed Enantioselective Electrochemical Reductive Cross-Coupling of Aryl Aziridines with Alkenyl Bromides. *J. Am. Chem. Soc.* **2023**. https://doi.org/10.1021/jacs.2c12869.

(26) Jiang, Y.; Yang, K.; Wei, Y.; Wang, Q.; Li, S.-J.; Lan, Y.; Koh, M. J. Catalytic Multicomponent Synthesis of C-Acyl Glycosides by Consecutive Cross-

Electrophile Couplings. *Angewandte Chemie International Edition* **2022**, *61* (46), e202211043. https://doi.org/10.1002/anie.202211043.

(27) Geng, J.; Sun, D.; Song, Y.; Tong, W.; Wu, F. Ni-Catalyzed Asymmetric Reductive Alkenylation of α-Chlorosulfones with Vinyl Bromides. *Org. Lett.* **2022**, *24* (9), 1807–1811. https://doi.org/10.1021/acs.orglett.2c00217.

(28) Duan, M.; Wang, Y.; Zhu, S. Nickel-Catalyzed Asymmetric 1,2-Alkynylboration of Vinylarenes. *Tetrahedron Letters* **2023**, *114*, 154247. https://doi.org/10.1016/j.tetlet.2022.154247.

(29) Sun, D.; Ma, G.; Zhao, X.; Lei, C.; Gong, H. Nickel-Catalyzed Asymmetric Reductive Arylation of α-Chlorosulfones with Aryl Halides. *Chem. Sci.* **2021**, *12* (14), 5253–5258. https://doi.org/10.1039/D1SC00283J.

(30) Ye, Y.; Liu, J.; Xu, B.; Jiang, S.; Bai, R.; Li, S.; Xie, T.; Ye, X.-Y. Nickel-Catalyzed Enantioselective 1,2-Vinylboration of Styrenes. *Chem. Sci.* **2021**, *12* (39), 13209–13215. https://doi.org/10.1039/D1SC04071E.

(31) Lin, Q.; Spielvogel, E. H.; Diao, T. Carbon-Centered Radical Capture at Nickel(II) Complexes: Spectroscopic Evidence, Rates, and Selectivity. *Chem* **2023**, *9* (5), 1295–1308. https://doi.org/10.1016/j.chempr.2023.02.010.

(32) Laurence, C.; Gal, J. F. *Lewis Basicity and Affinity Scales: Data and Measurements*; Wiley, New York, 2010.

(33) Classification of Solvents. In *Solvents and Solvent Effects in Organic Chemistry*; 2010; pp 65–106. https://doi.org/10.1002/9783527632220.ch3.

(34) Best, S. P.; Clark, R. J. H. The Identification of an Electronic Raman Transition for the Hexa-Aquavanadium(III) Ion. A Direct Spectroscopic Determination of the

Trigonal Field Splitting of the 3T1g Ground Term. *Chemical Physics Letters* **1985**, *122* (4), 401–405. https://doi.org/10.1016/0009-2614(85)80245-1.

(35) Pescitelli, G.; Lüdeke, S.; Chamayou, A.-C.; Marolt, M.; Justus, V.; Górecki, M.; Arrico, L.; Di Bari, L.; Islam, M. A.; Gruber, I.; Enamullah, M.; Janiak, C. Broad-Range Spectral Analysis for Chiral Metal Coordination Compounds: (Chiro)Optical Superspectrum of Cobalt(II) Complexes. *Inorg. Chem.* **2018**, *57* (21), 13397–13408. https://doi.org/10.1021/acs.inorgchem.8b01932.

(36) Lu, R.; Yang, T.; Chen, X.; Fan, W.; Chen, P.; Lin, Z.; Liu, G. Enantioselective Copper-Catalyzed Radical Cyanation of Propargylic C–H Bonds: Easy Access to Chiral Allenyl Nitriles. *J. Am. Chem. Soc.* **2021**, *143* (36), 14451–14457. https://doi.org/10.1021/jacs.1c07190.

(37) Hofstra, J. L. Development and Mechanistic Studies of Ni-Catalyzed Asymmetric Reductive Cross-Coupling Reactions, California Institute of Technology, 2019. https://resolver.caltech.edu/CaltechTHESIS:06012019-034543690.

(38) Kazmierczak, N. P.; Chew, J. A.; Vander Griend, D. A. Bootstrap Methods for Quantifying the Uncertainty of Binding Constants in the Hard Modeling of Spectrophotometric Titration Data. *Analytica Chimica Acta* **2022**, *1227*, 339834. https://doi.org/10.1016/j.aca.2022.339834.

(39) Vander Griend, D. A.; Bediako, D. K.; DeVries, M. J.; DeJong, N. A.; Heeringa, L. P. Detailed Spectroscopic, Thermodynamic, and Kinetic Characterization of Nickel(II) Complexes with 2,2'-Bipyridine and 1,10-Phenanthroline Attained via Equilibrium-Restricted Factor Analysis. *Inorg. Chem.* **2008**, *47* (2), 656–662. https://doi.org/10.1021/ic700553d.

(40) Espinoza, E. M.; Clark, J. A.; Soliman, J.; Derr, J. B.; Morales, M.; Vullev, V. I. Practical Aspects of Cyclic Voltammetry: How to Estimate Reduction Potentials When Irreversibility Prevails. *J. Electrochem. Soc.* **2019**, *166* (5), H3175–H3187. https://doi.org/10.1149/2.0241905jes.

(41) Tang, T.; Jones, E.; Wild, T.; Hazra, A.; Minteer, S. D.; Sigman, M. S. Investigating Oxidative Addition Mechanisms of Allylic Electrophiles with Low-Valent Ni/Co Catalysts Using Electroanalytical and Data Science Techniques. *J. Am. Chem. Soc.* **2022**, *144* (43), 20056–20066. https://doi.org/10.1021/jacs.2c09120.

(42) Bard, A. J.; Faulkner, L. R.; White, H. S. *Electrochemical Methods: Fundamentals and Applications*, 3rd ed.; John Wiley & Sons, Inc.: Hoboken, NJ, USA, 2022.

(43) Zhou, Y.-Y.; Uyeda, C. Reductive Cyclopropanations Catalyzed by Dinuclear Nickel Complexes. *Angewandte Chemie International Edition* **2016**, *55* (9), 3171–3175. https://doi.org/10.1002/anie.201511271.

(44) Turro, R. F.; Wahlman, J. L. H.; Tong, Z. J.; Chen, X.; Yang, M.; Chen, E. P.; Hong, X.; Hadt, R. G.; Yang, Y.-F.; Houk, K. N.; Reisman, S. E. Mechanistic Investigation of Ni-Catalyzed Reductive Cross-Coupling of Alkenyl and Benzyl Electrophiles. *J. Am. Chem. Soc.* **2023**, *145* (27), 14705–14715. https://doi.org/10.1021/jacs.3c02649.

(45) Li, G.; Brady, M. D.; Meyer, G. J. Visible Light Driven Bromide Oxidation and Ligand Substitution Photochemistry of a Ru Diimine Complex. *J. Am. Chem. Soc.* **2018**, *140* (16), 5447–5456. https://doi.org/10.1021/jacs.8b00944.

(46) Harding, M. J.; Mason, S. F.; Robbins, D. J.; Thomson, A. J. Magnetic Circular Dichroism Spectra of Some Nickel(II) Complexes. Part I. The Temperature

Dependence of the Spectrum of the Nickel(II) Hexaquo-Ion. *J. Chem. Soc. A* **1971**, No. 0, 3047–3058. https://doi.org/10.1039/J19710003047.

(47) Burkholder, C.; Dolbier, W. R.; Médebielle, M. Tetrakis(Dimethylamino)Ethylene as a Useful Reductant of Some Bromodifluoromethyl Heterocycles. Application to the Synthesis of New Gem-Difluorinated Heteroarylated Compounds. *J. Org. Chem.* **1998**, *63* (16), 5385–5394. https://doi.org/10.1021/jo980201+.

(48) Gaur, J. N.; Goswami, N. K. Kinetics of the Reduction of Mn^{2+} at the Dropping Mercury Electrode in Non-Aqueous Media. *Electrochimica Acta* **1967**, *12* (11), 1489–1493. https://doi.org/10.1016/0013-4686(67)80064-1.

(49) Lin, Q.; Diao, T. Mechanism of Ni-Catalyzed Reductive 1,2-Dicarbofunctionalization of Alkenes. *J. Am. Chem. Soc.* **2019**, *141* (44), 17937–17948. https://doi.org/10.1021/jacs.9b10026.

(50) Anxolabéhère-Mallart, E.; Glaser, T.; Frank, P.; Aliverti, A.; Zanetti, G.; Hedman, B.; Hodgson, K. O.; Solomon, E. I. Sulfur K-Edge X-Ray Absorption Spectroscopy of 2Fe−2S Ferredoxin: Covalency of the Oxidized and Reduced 2Fe Forms and Comparison to Model Complexes. *J. Am. Chem. Soc.* **2001**, *123* (23), 5444–5452. https://doi.org/10.1021/ja010472t.

(51) Dey, A.; Jenney, F. E.; Adams, M. W. W.; Babini, E.; Takahashi, Y.; Fukuyama, K.; Hodgson, K. O.; Hedman, B.; Solomon, E. I. Solvent Tuning of Electrochemical Potentials in the Active Sites of HiPIP Versus Ferredoxin. *Science* **2007**, *318* (5855), 1464–1468. https://doi.org/10.1126/science.1147753.

(52) Dey, A.; Okamura, T.; Ueyama, N.; Hedman, B.; Hodgson, K. O.; Solomon, E. I. Sulfur K-Edge XAS and DFT Calculations on P450 Model Complexes: Effects of

Hydrogen Bonding on Electronic Structure and Redox Potentials. *J. Am. Chem. Soc.* **2005**, *127* (34), 12046–12053. https://doi.org/10.1021/ja0519031.

(53) Hadt, R. G.; Sun, N.; Marshall, N. M.; Hodgson, K. O.; Hedman, B.; Lu, Y.; Solomon, E. I. Spectroscopic and DFT Studies of Second-Sphere Variants of the Type 1 Copper Site in Azurin: Covalent and Nonlocal Electrostatic Contributions to Reduction Potentials. *J. Am. Chem. Soc.* **2012**, *134* (40), 16701–16716. https://doi.org/10.1021/ja306438n.

(54) Suzuki, N.; Hofstra, J. L.; Poremba, K. E.; Reisman, S. E. Nickel-Catalyzed Enantioselective Cross-Coupling of N-Hydroxyphthalimide Esters with Vinyl Bromides. *Org. Lett.* **2017**, *19* (8), 2150–2153. https://doi.org/10.1021/acs.orglett.7b00793.

(55) Arias-Rotondo, D. M.; McCusker, J. K. The Photophysics of Photoredox Catalysis: A Roadmap for Catalyst Design. *Chem. Soc. Rev.* **2016**, *45* (21), 5803–5820. https://doi.org/10.1039/C6CS00526H.

(56) Fillman, K. L.; Przyojski, J. A.; Al-Afyouni, M. H.; Tonzetich, Z. J.; Neidig, M. L. A Combined Magnetic Circular Dichroism and Density Functional Theory Approach for the Elucidation of Electronic Structure and Bonding in Three- and Four-Coordinate Iron(II)–N-Heterocyclic Carbene Complexes. *Chem. Sci.* **2015**, *6* (2), 1178–1188. https://doi.org/10.1039/C4SC02791D.

(57) Kawamata, Y.; Vantourout, J. C.; Hickey, D. P.; Bai, P.; Chen, L.; Hou, Q.; Qiao, W.; Barman, K.; Edwards, M. A.; Garrido-Castro, A. F.; deGruyter, J. N.; Nakamura, H.; Knouse, K.; Qin, C.; Clay, K. J.; Bao, D.; Li, C.; Starr, J. T.; Garcia-Irizarry, C.; Sach, N.; White, H. S.; Neurock, M.; Minteer, S. D.; Baran, P. S.

Electrochemically Driven, Ni-Catalyzed Aryl Amination: Scope, Mechanism, and Applications. *J. Am. Chem. Soc.* **2019**, *141* (15), 6392–6402. https://doi.org/10.1021/jacs.9b01886.

(58) Cherney, A. H. Development of Nickel-Catalyzed Asymmetric Reductive Cross-Coupling of Benzylic Electrophiles, California Institute of Technology, 2015. https://resolver.caltech.edu/CaltechTHESIS:06012015-102412340.

(59) Venanzi, L. M. 140. Tetrahedral Nickel(II) Complexes and the Factors Determining Their Formation. Part I. Bistriphenylphosphine Nickel(II) Compounds. *J. Chem. Soc.* **1958**, No. 0, 719–724. https://doi.org/10.1039/JR9580000719.

(60) Garton, G.; Henn, D. E.; Powell, H. M.; Venanzi, L. M. 682. Tetrahedral Nickel(II) Complexes and the Factors Determining Their Formation. Part V. The Tetrahedral Co-Ordination of Nickel in Dichlorobistriphenylphosphinenickel. *J. Chem. Soc.* **1963**, No. 0, 3625–3629. https://doi.org/10.1039/JR9630003625.

(61) Cotton, F. A.; Goodgame, D. M. L. New Tetrahedral Complexes of Nickel(II). *J. Am. Chem. Soc.* **1960**, *82* (22), 5771–5774. https://doi.org/10.1021/ja01507a001.

(62) Venanzi, L. M. Tetrahedral Complexes of Nickel (II) and the Factors Determining Their Formation. *Journal of Inorganic and Nuclear Chemistry* **1958**, *8*, 137–142. https://doi.org/10.1016/0022-1902(58)80175-X.

(63) Cotton, F. A.; Faut, O. D.; Goodgame, D. M. L. Preparation, Spectra and Electronic Structures of Tetrahedral Nickel(II) Complexes Containing Triphenylphosphine and Halide Ions as Ligands. *J. Am. Chem. Soc.* **1961**, *83* (2), 344–351. https://doi.org/10.1021/ja01463a021.

(64) Davies, J. E.; Gerloch, M.; Phillips, D. J. Phosphine π-Acceptor Properties in Dihalogenobis(Triphenylphosphine)-Nickel(II) and -Cobalt(II). *J. Chem. Soc., Dalton Trans.* **1979**, No. 11, 1836–1842. https://doi.org/10.1039/DT9790001836.

(65) Gerloch, M.; Hanton, L. R.; Manning, M. R. Tetrahedral Complexes of Nickel(II): Electronic Spectra, γ and π Bonding, and the Electroneutrality Principle. *Inorganica Chimica Acta* **1981**, *48*, 205–214. https://doi.org/10.1016/S0020-1693(00)90092-6.

(66) Koester, V. J.; Dunn, T. M. Electronic Spectrum of the Tetrachloronickelate(II) Complex at 2.2.Deg.K. *Inorg. Chem.* **1975**, *14* (8), 1811–1817. https://doi.org/10.1021/ic50150a014.

(67) Lever, A. B. P. *Inorganic Electronic Spectroscopy*, 2nd ed.; Elsevier, 1984.

(68) Gerloch, M.; Manning, M. R. Structural and Ligand Field Parameters of Some Trigonally Distorted Tetrahedral Cobalt(II) and Nickel(II) Complexes. *Inorg. Chem.* **1981**, *20* (4), 1051–1056. https://doi.org/10.1021/ic50218a020.

(69) Sigel, H.; Martin, R. B. Coordinating Properties of the Amide Bond. Stability and Structure of Metal Ion Complexes of Peptides and Related Ligands. *Chem. Rev.* **1982**, *82* (4), 385–426. https://doi.org/10.1021/cr00050a003.

(70) Connelly, N. G.; Geiger, W. E. Chemical Redox Agents for Organometallic Chemistry. *Chem. Rev.* **1996**, *96* (2), 877–910. https://doi.org/10.1021/cr940053x.

(71) Okamoto, K.; Shida, N.; Morizumi, H.; Kitano, Y.; Chiba, K. Oxidation Potential Gap (ΔEox): The Hidden Parameter in Redox Chemistry. *Angewandte Chemie International Edition* **2022**, *61* (30), e202206064. https://doi.org/10.1002/anie.202206064.

Chapter 3

Mechanistic Investigation of Ni-Catalyzed Reductive Cross-Coupling of Alkenyl and Benzyl Electrophiles[*]

3.1 Introduction

Ni-catalyzed reductive cross-couplings (RCCs) of organic electrophiles have emerged as useful reactions for $C(sp^2)$–$C(sp^3)$ bond formation.[1] These reactions provide direct access to cross-coupled products from readily available organic electrophiles, such as halides, precluding the need to pre-generate an organometallic coupling partner. The use of a metal powder (Mn^0, Zn^0) or an organic electron donor such as tetrakis(dimethylamino)ethylene (TDAE)[2] provides reducing equivalents to render the system catalytic in Ni. Ni-catalyzed RCC reactions can also be driven electrochemically using either sacrificial anodes or paired electrolysis systems.[3] A key challenge in the development of these reactions is achieving selectivity for the cross-coupled product over possible homo-coupling products; this requires a catalyst that oxidatively adds each electrophile in sequence, or a catalyst system with mechanistically distinct modes of activating each coupling partner. Despite this challenge,

[*] This chapter is reproduced from a published manuscript.

several different Ni catalysis systems have been developed that afford high selectivity for cross-coupled products.[1,4,5]

Our lab has developed several Ni-catalyzed asymmetric reductive alkenylation (ARA) reactions (**Figure 1**), which leverage the intermediacy of C(sp^3) radicals to enable stereoconvergent, enantioselective bond formation.[6,7,8] In 2014, we reported an ARA between benzylic chlorides and alkenyl bromides using cyclopropyl-containing IndaBOX ligand **L1** and Mn^0 as the terminal reductant (**Figure 1a**).[6] We subsequently developed a related ARA that uses the same ligand (**L1**), but employs redox-active *N*-hydroxyphthalimide (NHP) esters as the C(sp^3) coupling partner.[7] In this case, TDAE was used as the reductant, and trimethylsilyl bromide (TMSBr) was identified as a key additive (**Figure 1b**). In addition to chiral ligand **L1** being optimal for both reactions, the use of DMA as solvent and NaI as an additive was shared between the two transformations. Given their similarities, we identified this pair of transformations as well suited for investigating the mechanism of Ni-catalyzed RCCs and how the mechanism might change depending on the C(sp^3) coupling partner.

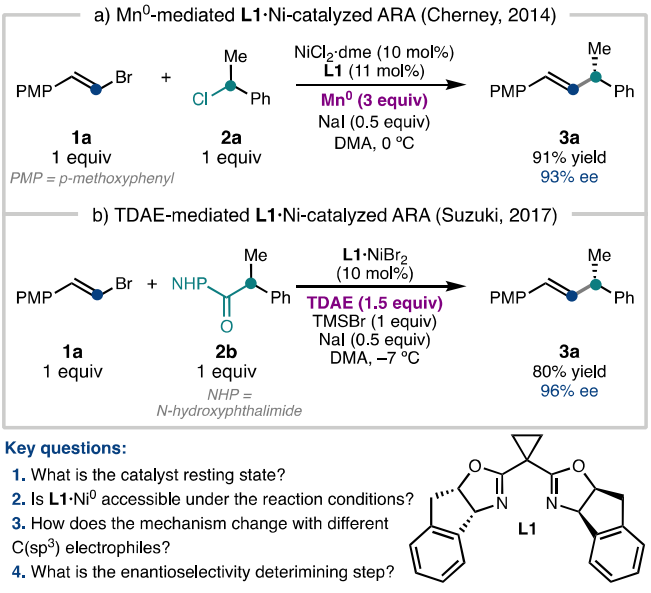

Figure 1. *Ni-catalyzed asymmetric reductive cross-coupling between alkenyl and benzylic electrophiles.*

Since many RCCs use heterogenous terminal reductants, the mechanisms of these reactions have been difficult to elucidate. Nonetheless, insightful studies of reductive arylation have been disclosed by the groups of Weix[9], Diao[10]; these systems have primarily focused on reactions in which catalytically relevant Ni^{II}(aryl)X complexes can be isolated and characterized. Diao has also recently investigated bi(oxazoline)[10a,b] and pyridine-oxazoline[10c] ligands in reductive arylation; however, mechanistic studies of reductive alkenylation and of Ni-catalysts supported by chiral bis(oxazolines) such as **L1** are lacking.[11] Here, we report our mechanistic investigations of two **L1**·Ni-catalyzed ARA reactions. In this study we sought to: (1) determine the kinetic driving forces and resting state for the homogenous reaction of alkenyl bromide **1a** with NHP ester **2b**; (2) investigate the redox properties of the **L1**·$Ni^{II}X_2$ precatalysts and determine whether **L1**·Ni^0 is accessible using common reductants; (3) interrogate the mechanism of electrophile activation for both **2a** and **2b**; (4) use computational methods to understand the enantioselectivity determining step. These studies have revealed that chloride **2a** and NHP ester **2b** are activated through distinct mechanisms and provide insights that can guide the optimization of reaction conditions for Ni-catalyzed RCC reactions.

3.2 Results and Discussion

3.2.1 Reaction Kinetics of TDAE-mediated RCC

Since the TDAE-driven **L1**·Ni-catalyzed ARA[7] is homogeneous and does not suffer from an induction period, we initiated our mechanistic investigation by determining the kinetic orders in **1a**, **2b**, and Ni under standard reaction conditions (**Figure 2a**). For this, we employed Variable Time Normalization Analysis[12] (VTNA) to analyze the results of different excess experiments (**Figure 2b–d**). These experiments revealed a 1st order rate dependence on the concentration of NHP ester **2b** (**Figure 2c**). The rate dependence on [**1a]** appears to be 0th order at concentrations similar to the standard conditions (0.1 and 0.2 M **1a**, **Figure 2b**); however, a fractional inverse rate dependence is observed at higher concentrations of **1a** (**Figure 2b**, S27). Moreover, at higher [**1a]**, minor amounts of dienyl homodimer is observed; the slight inverse rate dependence is proposed to derive from this off-cycle pathway. We note that inverse order in C(sp^2) electrophile has been observed previously by Weix for a related (bpy)Ni-catalyzed RCC of aryl and alkyl halides.[9a] Interestingly, there is an apparent 0th order rate dependence on **L1**·$NiBr_2$ at loadings similar to the optimized conditions (5 and 10 mol %, **Figure 2d**); however, a positive rate dependence develops at low catalyst loadings (<1 mol %). The observation that the catalyst loading does not influence the rate of product formation has not been previously reported for Ni-catalyzed RCC reactions.[9b,10a]

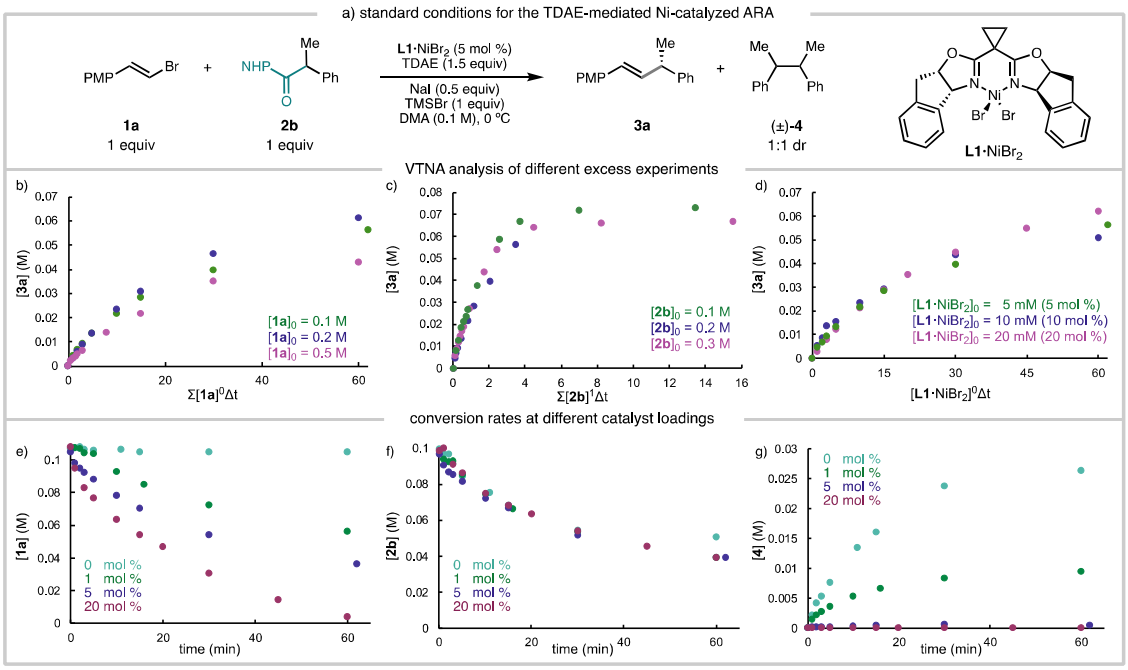

***Figure 2**. a) Standard conditions for different excess experiments on TDAE-mediated ARA. Different excess VTNA experiments varying initial concentrations of: b) alkenyl bromide **1a**, c) NHP ester **2b**, d) catalyst **L1**·$NiBr_2$. Impact of [**L1**·$NiBr_2$] on rate of conversion of e) alkenyl bromide **1a**, f) NHP ester **2b**, and g) byproduct **4**. Concentrations determined vs. dodecane internal standard using GC-FID.*

To further investigate this unusual rate dependence, the concentration of **1a**, **2b**, and homodimer **4** were monitored over time, at different concentrations of Ni (**Figure 2e-g**). The conversion of alkenyl bromide **1a** shows a clear rate dependence on the concentration of Ni (**Figure 2e**). In contrast, the rate of conversion of NHP ester **2b** is independent of [Ni]: even in experiments where **L1**·$Ni^{II}Br_2$ is omitted, **2b** is consumed at the same rate as when using 20 mol % Ni (**Figure 2f**). Correspondingly, as the concentration of Ni decreases, the yield of cross-coupled product **3a** decreases and the yield of homocoupled product **4** (formed as a 1:1 diastereomeric mixture) increases (**Figure 2g**). These data are consistent with generation of a cage-escaped benzylic radical from **2b** by a non-Ni-catalyzed process. This represents a distinct mode of NHP ester activation for the **L1**·Ni-catalyzed RCC in comparison to the (bpy)Ni-mediated coupling of NHP esters reported by Weix[13] and Baran,[14] in which a (bpy)Ni^{I}–Ar is proposed to reduce the NHP ester by single electron transfer (SET). In a preprint article,

Rousseaux reported a similar finding, that the combination of Zn^0 and TMSCl initiates decarboxylation of an NHP ester as part of a Ni-catalyzed RCC process.[15]

3.2.2 Reduction of Ni(II) Pre-catalyst and Oxidative Addition of Alkenyl Bromide.

Given the kinetic data (*vide supra*), we sought to investigate the reduction of the Ni pre-catalyst and the ability of the resulting species to oxidatively add the alkenyl bromide. We first used cyclic voltammetry (CV) to determine the reduction potentials of **L1**·$Ni^{II}Br_2$ and **L1**·$Ni^{II}Cl_2$; these complexes (isolable as crystalline solids) catalyze the reductive alkenylations of both benzylic chlorides and NHP esters in comparable yields and slightly improved ee relative to in situ catalyst generation.[6,7] Electrochemically, **L1**·$Ni^{II}Cl_2$ and **L1**·$Ni^{II}Br_2$ exhibit irreversible reduction waves at $E_{p/2}$ = –1.47 V and –1.23 V vs. $Fc^{0/+}$, respectively (**Figure 3a**). These reduction events have a large peak separation with the corresponding oxidation events, suggesting that a chemical change, such as halide loss, occurs rapidly upon one electron reduction. More detailed electrochemical studies of these pre-catalysts, performed by Hadt and coworkers,[16] support a single-electron reduction event to give a **L1**·$Ni^{I}X$·DMA species. Notably, these studies suggest that reduction to **L1**·Ni^0 does not proceed within the solvent window of DMA.

To verify the ability of TDAE to reduce **L1**·$Ni^{II}Br_2$ to **L1**·$Ni^{I}Br$, a solution of **L1**·$Ni^{II}Br_2$ in DMA was treated with TDAE ($E_{1/2}$ = –1.1 V vs. $Fc^{0/+}$); the resulting solution was frozen and analyzed by electron paramagnetic resonance (EPR) spectroscopy. A strong signal at g=2.02 is assigned to the organic $TDAE^{+\bullet}$ radical,[17] and the weaker signal (g_1 = 2.07, g_2 = 2.08, g_3 = 2.330) is assigned to a reduced **L1**·$Ni^{I}Br$ species (**Figure 3b**, SI section 4.7.3). The same **L1**·$Ni^{I}Br$ signal is observed when **L1**·$Ni^{II}Br_2$ is reduced with $Ni(cod)_2$. When Zn^0 is used as the reductant, more pronounced changes are observed, which could potentially arise from the

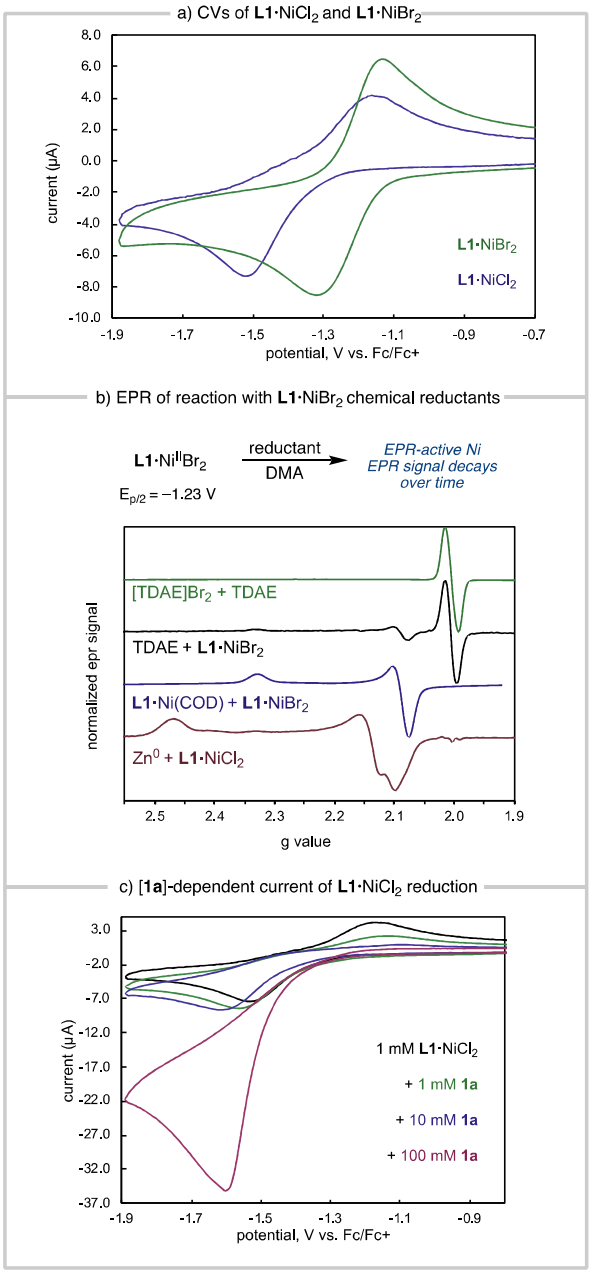

***Figure 3**. Reduction of precatalysts **L1**·NiX_2 used in ARA reactions and reactivity of reduced species with **1a**. (a) 1 mM **L1**·$NiBr_2$ and **L1**·$NiCl_2$, 0.1 M $TBAPF_6$ in DMA, v = 100mv/s, V vs $Fc^{0/+}$ (b) – 77 K X-band (9.4 GHz) perpendicular EPR spectra, for detailed instrument parameters and simulations see SI section 7,1. (c) 1 mM **L1**·$NiCl_2$ with sequential additions of **1a** (0 – 0.1 M), 0.1 M $TBAPF_6$ in DMA, v = 100 mv/s. V vs $Fc^{0/+}$.*

interaction between a **L1**·Ni^{I} species with the Zn^{II} formed upon oxidation (**Figure S69**).[18] We note that electrochemical and spectroscopic studies by Hadt and coworkers suggest that DMA can bind to both **L1**·Ni^{I} and **L1**·Ni^{II} redox states.[16] Given the strong variation of EPR signals

and speciation of **L1**·Ni^{I} species observed herein, no formal assignments of the EPR signals are provided. Nevertheless, these data support the presence of **L1**·$Ni^{I}X$ species forming from reduction under cross-coupling reaction conditions, and the nature of these species is clearly dependent on the reaction conditions.

A time course of the Zn^{0} reduction of **L1**·$NiCl_2$ revealed that the observed EPR signals decrease over time (Figure S72-S74) in concert with a change in the corresponding UV-vis-NIR spectra (Figure S75-S76), and the terminal EPR-silent mixture was catalytically inactive. Attempts to isolate **L1**·$Ni^{I}X$ complexes were unsuccessful; this might be due to the formation of **L1**·Ni^{I} oligomers in the absence of electrophiles **1** and **2**, or due to the difference in stability between DMA-bound and un-bound species.[10a,19,20]

To test whether the putative **L1**·$Ni^{I}Cl$ species formed upon reduction of **L1**·$Ni^{II}Cl_2$ can react with alkenyl bromide **1a**, a series of CV studies were performed in the presence of **1a** (Figure 3c). A concentration-dependent increase in current was observed as [**1a**] increased, which was accompanied by a loss of re-oxidation current. Taken together, these studies are consistent with reaction between **L1**·$Ni^{I}X$ and alkenyl bromide **1a**.

3.2.3 Catalyst Resting State

At this stage, we sought to determine the resting state of the Ni catalyst under the reaction conditions. If a Ni^{I} or Ni^{III} intermediate were the resting state, then it could be observable by EPR. The Ni-catalyzed reaction of **1a** and **2b** was performed using 2 mol % **L1**·$NiBr_2$ under otherwise standard conditions and aliquots were removed, filtered, and frozen in an EPR tube. No signal corresponding to a metal-based radical was observed by EPR; instead, a signal consistent with an organic radical was observed, which decreased in intensity over time (**Figure S77**). This species was assigned as the TDAE radical cation by comparison to an independently prepared sample (**Figure S67**) and previously reported spectra.[17] Although this does not rule out a Ni^{I} or Ni^{III} resting state, we sought to investigate other possibilities.

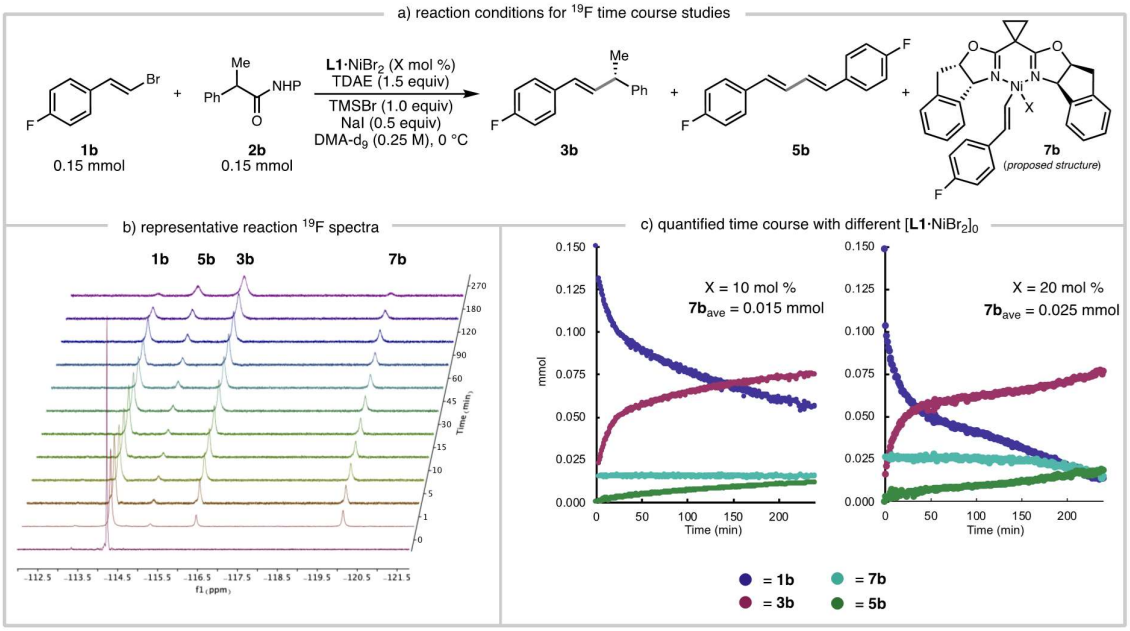

***Figure 4**. Reaction monitoring by ^{19}F NMR tracking the consumption of **1b** and the formation of **1b**-derived species. Reaction run at 0 ºC using C_6F_6 as an internal standard.*

Given the rapid reaction of **L1**·NiCl with alkenyl bromide **1a** (**Figure 3c**), and prior RCC mechanistic studies,[10b,10a] we hypothesized that the catalyst resting state likely resides after oxidative addition of the C(sp^2)-electrophile. To monitor the reaction by *in situ* ^{19}F NMR, ^{19}F-labeled alkenyl bromide **1b** was used and all alkenyl bromide-derived species were tracked over the course of the reaction (**Figure 4a**). Upon the addition of TDAE (0. 23 mmol, 1.5 equiv) to a solution of **1b** (0.15 mmol), **2b** (0.15 mmol), **L1**·$NiBr_2$ (0.015 mmol, 10 mol %), TMSBr (0.15 mmol), and NaI (0.075 mmol) in DMA-d_9, several new signals appeared that were assigned to product **3b** (δ =–116.5 ppm), homocoupled diene **5b** (δ =–115 ppm), and a new species (broad signal at δ =–120 ppm, **Figure 4b**).[21] This species persisted throughout the reaction, maintaining steady concentration corresponding to 15 μmol, or 10 mol %, which is the concentration of **L1**·$NiBr_2$ used in the reaction. When this experiment was repeated with 20 mol% **L1**·$NiBr_2$, the concentration of this species corresponded to 17 mol% (25 μmol) for the first 2.5 hours of catalysis and then decreased as the reaction approached the last few turnovers, eventually disappearing at the end of the reaction (**Figure 4c**). Although attempts to

isolate this species or prepare it independently have been unsuccessful due to its instability, we propose that this intermediate is the diamagnetic Ni^{II} oxidative addition complex **7b**.[22] We note that Diao and coworkers reported a dimagnetic (phen)Ni^{II}ArBr resting state, observable by ^{1}H NMR, for a Ni-catalyzed 1,2-dicarbofunctionalization reaction.[10b]

3.2.4 Mechanism of NHP Ester Activation

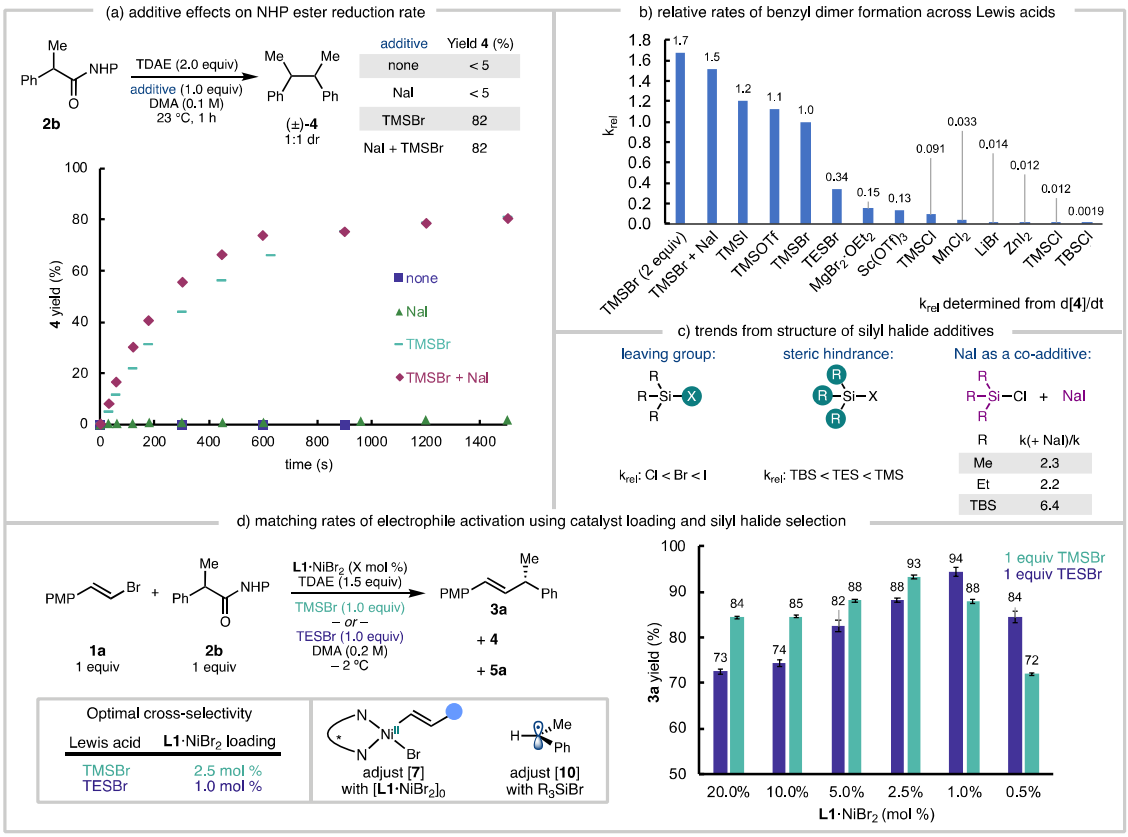

Figure 5*. Studies investigating the influence of Lewis acids on the rate of radical generation from TDAE reduction of* ***2b****. Yields and time course data analyzed by GC-FID with n-dodecane internal standard.*

Given that the kinetic studies revealed that the NHP ester **2b** is not reduced by Ni, we hypothesized that it is instead reduced by TDAE. To test this hypothesis, NHP ester **2b** was treated with TDAE in DMA and the formation of homodimer **4** was monitored as an indirect measurement of benzylic radical generation. In the absence of additional additives, the mixture of **2b** and TDAE results in minimal conversion to homodimer **4**, even at ambient temperature

(**Figure 5a**, purple). This can be rationalized by the difference in reduction potential of NHP ester **2b** ($E_{p/2}$ = –1.62 V vs. $Fc^{0/+}$), which is 0.5 V more cathodic than TDAE ($E_{1/2}$ = –1.11 V vs. $Fc^{0/+}$); the irreversible loss of CO_2 following SET does not appear to be sufficient to drive the thermodynamically unfavorable process. Similarly, the mixture of **2b**, TDAE, and NaI also fail to produce homodimer **4** (**Figure 5a**, green).

In contrast, when TDAE is added to a mixture of **2b** and TMSBr (1.0 equiv), **2b** is converted to **4** at a rate that is comparable to the rate of **2b** conversion in the catalytic reaction (**Figure 5a**, teal). We note that TMSBr is essential to form **3a** in high yields under standard reaction conditions (19% yield **3a** when TMSBr is excluded). The rate is increased further (k_{rel} = 1.5) when both TMSBr and NaI are present, presumably through the *in situ* generation of TMSI (**Figure 5a**, maroon). We propose that the silyl halide additive functions as a Lewis acid to lower the reduction potential[23] of the NHP ester and enable reduction by TDAE.

3.2.5 Altering Rate of Radical Generation Through Lewis Acid Selection

The observation that a Lewis acid gates NHP ester reduction inspired us to question whether the rate of radical generation could be tuned by using TDAE in combination with different Lewis acids, similar to Weix's work tuning rate of radical generation by using derivatized NHP esters.[24] To test this, we measured the rate of radical generation (as d[**4**]/dt) in the presence of a variety of Lewis acids (**Figure 5b**). The more sterically hindered triethylsilyl bromide (TESBr) results in a 3-fold decrease in the rate (k_{rel} = 0.34) of radical generation. Further investigation of different silyl halides revealed an intuitive trend in sterics (TBS<TES<TMS), with larger groups slowing down radical generation, as well as the leaving group identity (Cl<Br<OTf<I)[25], with the better leaving group accelerating radical generation (**Figure 5c**). As observed with TMSBr (**Figure 5a**, purple), addition of NaI as a co-additive to various R_3Si–Cl additives can increase the rate by more than 2-fold. Increasing the concentration of TMSBr increases the rate (k_{rel} = 1.68), presumably by driving the equilibrium

to increase the concentration of silylated NHP ester **8** (**Figure 6**). Additionally, non-silyl Lewis acids can also increase the rate of **2b** reduction by TDAE. We have quantified the ability of several common additives[26] to modulate the rate of radical generation, with rates spanning three orders of magnitude (**Figure5b**).

After demonstrating the rate of NHP ester activation can be tuned with different Lewis acid additives, we sought to investigate how the yield of product was effected by the silyl additive. Although the ARA reaction between **1a** and **2b** was initially reported using TMSBr, we observed that at lower catalyst loadings, increased amounts of benzyl dimer **4** is formed (**Figure 2g**). We hypothesized that slower rate of radical generation could improve the yield of **3a** at low catalyst loadings by better matching of the relative concentrations of the resting state species (**7**) and benzylic radical. Given that TESBr decreases the rate of benzylic radical formation by 3-fold, we performed a series of experiments varying the concentration of **L1**·$NiBr_2$ in the presence of either TMSBr or TESBr (**Figure 5d**). First, we note that for this well-performing substrate pair, high yields can be maintained using 1 mol% **L1**·$NiBr_2$. Second, we found that TMSBr performs better relative to TESBr when 20 mol% **L1**·$NiBr_2$ is used (higher concentration of resting state **7**) and performs worse than TESBr at 0.5 mol% **L1**·$NiBr_2$, when rapid release of benzyl radical would outpace radical capture by resting state **7** (**Figure 5d**). Using 0.5 mol% **L1**·$NiBr_2$, higher yield of **3a** was obtained with TESBr (84% yield) than with TMSBr (72% yield), which we propose results from slower release of the benzyl radical. Analysis of the product profiles for each bromosilane shows that the ratio of cross-coupled to homocoupled products reaches a maxima at 2.5 mol % Ni for TMSBr (k_{rel} = 1.0) and 1 mol % Ni for TESBr (k_{rel} = 0.34) (**Figure S78** and **S79**), which is consistent with the trends observed in yield. Using these conditions (1 mol % **L1**·$NiBr_2$ and 1.0 equiv TESBr), the reactioncan be performed on gram scale to give product **3a** in 81% yield and 94% ee (SI Section 4.8.2). We propose that monitoring the conversion of starting materials as well as the yield of product and

alkyl homodimer at different [Ni] can help chemists identifying the optimal combination of catalyst loading and silyl additive for new substrate combinations.

Taken together, a mechanism for the TDAE mediated Ni-catalyzed RCC is proposed in **Figure 6**. Upon reduction of the Ni precatalyst, the resulting **L1**·$Ni^{I}Br$ (**6-Br**) rapidly reacts with alkenyl bromide to give Ni^{III} species **9** which can be reduced to furnish resting state species **7**. Given Hadt and coworker's studies,[16] it is possible that DMA is coordinated to **6** during oxidative addition. While the reductant in this oxidative addition-reduction sequence is not known, we propose that the oxidative addition step is fast and reversible since we can observe the formation of halide scrambling products **1a-I** and **1a-Cl** (when a Cl^- source is present).[7,27] The Ni^{II} complex **7** can then intercept NHP ester-derived radical **10** to give Ni^{III} complex **11** which can undergo reductive elimination to give product **3**. NHP ester **2b** is activated by TMSBr followed by reduction with TDAE in the turnover-limiting step. This reduced species undergoes N–O homolysis and subsequent decarboxylation to give **10** (**Figure 6**).

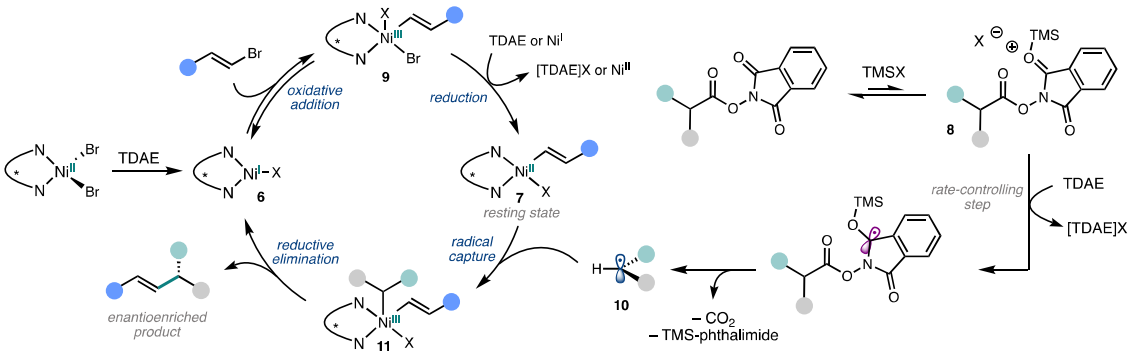

***Scheme 6**. Proposed mechanism for the TDAE-mediated Ni-catalyzed coupling between NHP esters and alkenyl bromides under standard conditions (see **Figure 2a**).*

3.2.6 Reaction Kinetics of the Mn-mediated Ni-catalyzed RCC

Kinetic studies of the heterogenous metal-powder conditions (**Figure 1a**) proved more challenging than the homogenous TDAE-mediated reaction. We observe long induction periods (up to 90 minutes) and reaction times of 6 hours using previously reported conditions.[6]

The induction period and reaction times can be shortened to 30 and 100 min, respectively, by pre-activating the Mn^0 with HCl. Use of Zn^0 powder further improved the reaction times (5–10 minute induction period and 45 minute reaction times, **Figure S16**) and provided product in comparable yield and with only slightly lower enantioselectivity as Mn^0 (Zn: 91% yield, 90% ee; Mn: 96% yield, 96% ee). Both Mn^0 and Zn^0 gave reactions with linear rates of product formation, indicative of mass transport-limited reduction; however, Zn^0 displayed a less significant stir rate dependence that saturated >1000 rpm (**Figure S15**). Use of 6 equiv Zn^0 slightly increased the reaction rate by a factor of 1.1, similar to observations by Weix[9b] and Diao[10a] in related arylation reactions **(Figure S17**). These modified reaction conditions (Figure 7a) enabled the collection of reproducible kinetic data allowing us to kinetically observe the next slowest step after mass transported-limited heterogeneous reduction.[9a,28]

Kinetics experiments reveal a first-order rate dependence on [**L1**·$NiCl_2$], unlike the TDAE system, across catalyst loadings ranging from 5 mol % to 20 mol % (**Figure 7b**). The reaction exhibits a negative first-order rate dependence on [**1a**]$_0$. A similar inverse dependence on the $C(sp)^2$ partner has been observed by Weix.[9b] The rate dependence on [**2a**]$_0$ is more complex: a fractional positive rate dependence was observed at 1.0 and 2.0 equivalents of **2a**, but the rate decreases again when >2.0 equiv **2a** is employed (**Figure 7b**). Notably, as [**2a**]$_0$ increases, the ee of **3a** decreases. Taken together, these data might indicate that there are competing mechanisms that depend on the concentration of [**2a**]$_0$. One possibility is that when [**2a**]>>[**1a**], the reaction of **L1**·Ni^IX with **2a** begins to compete with the reaction between **L1**·Ni^IX and **1a**, therefore reversing the order of oxidative addition of the electrophiles to Ni.

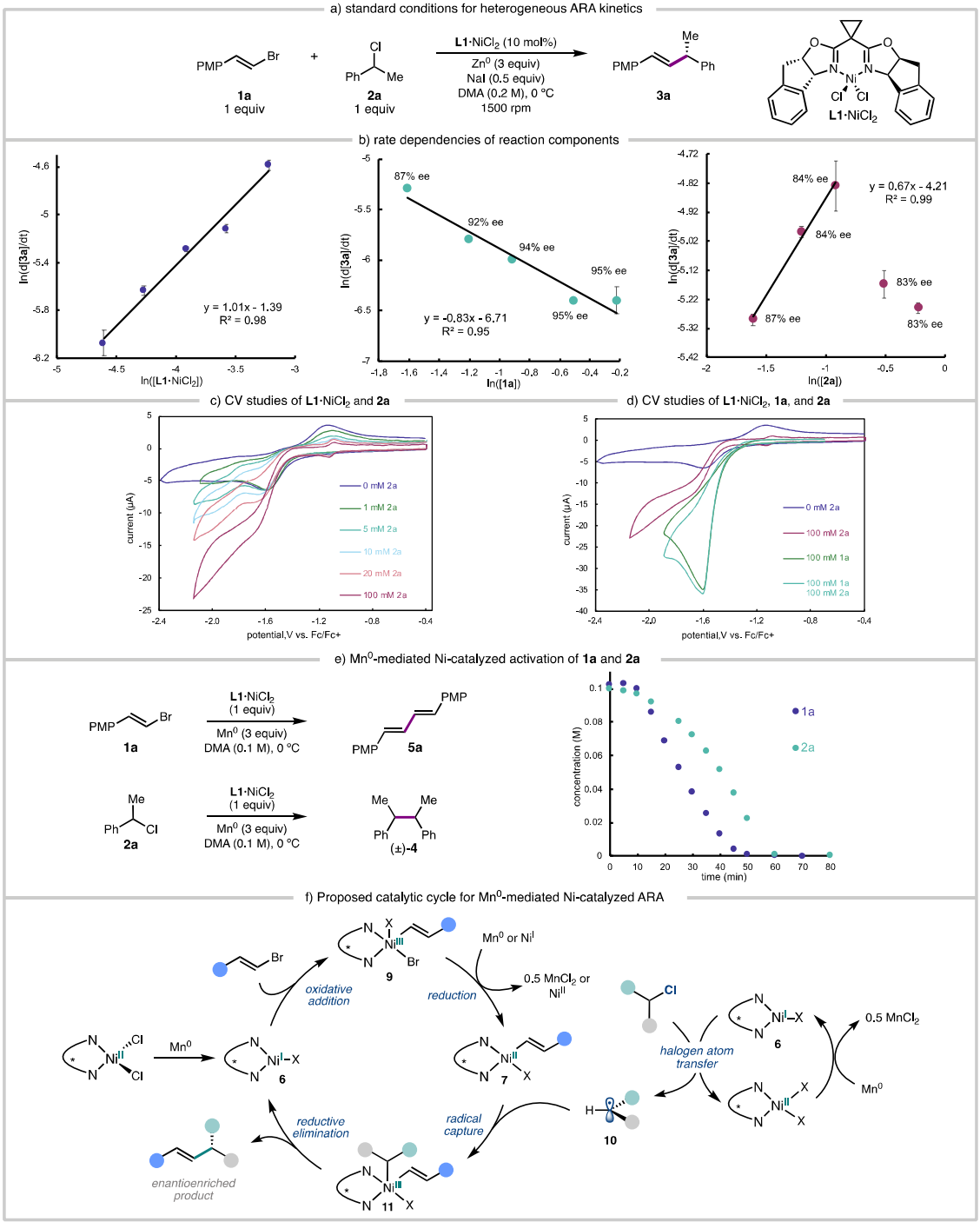

Scheme 7*. a) Standard conditions used the Zn-mediated ARA kinetics experiments. b) Kinetics experiments varying initial concentrations of* ***1a****, benzyl chloride* ***2a****, and catalyst* ***L1****·NiCl₂. c) CV studies of sequential addition of* ***2a*** *(0 – 0.1M) to 1 mM* ***L1****·NiCl₂. d) CV studies* ***L1****·NiCl₂ reacting with either* ***1a****,* ***2a*** *or both* ***1a*** *and* ***2a*** *(0.1 M TBAPF₆ in DMA, v = 100 mv/s. V vs Fc0/+). e) Mn-mediated stoichiometric reactions of* ***L1****·NiCl₂ with* ***1a*** *and with* ***2a****. f) Proposed mechanism for the Mn-mediated Ni-catalyzed coupling between benzyl chlorides and alkenyl bromides. Concentrations determined by GC-FID vs. dodecane internal standard.*

3.2.7 Reaction Kinetics of the Mn-mediated Ni-catalyzed RCC

To interrogate the role of Ni in the activation of benzylic chloride **2a**, a DMA solution of **2a** was treated with Mn^0 (3.0 equiv) and NaI (0.5 equiv) and the formation of homodimer **4** was monitored (see SI, section 4.3). No conversion of **2a** or formation of **4** was observed at 0 or 23 °C, even with extended reaction times. In contrast, when **2a** was subjected to identical conditions but **L1**·$Ni^{II}Cl_2$ (10 mol %; standard reaction conditions minus **1a**) was added, **2a** was cleanly converted to homodimer **4** over 60 min (**Figure 7e**). These findings suggest that **L1**·$Ni^{I}X$ can activate **2a**.

CV studies were also performed to investigate the reaction of in situ generated **L1**·$Ni^{I}Cl$ with **1a** and **2a**. CVs were acquired for **L1**·$Ni^{II}Cl_2$ (1.0 mM) in the presence of varying concentrations of **1a** (1 – 100 mM), which showed a concentration-dependent current with cathodic shifting of the onset potential and loss of the anodic return wave (**Figures 7c**). This current likely results from the reaction of the reduced **L1**·Ni complex reacting with **2a**, presumably corresponding to the catalytic homocoupling to give **4**. The same studies were performed in the presence of alkenyl bromide **1a**, which also showed a concentration-dependent current (**Figure 3c**). In the presence of 100 mM **1a** and **2a**, regardless of the order of addition, a catalytic current consistent with the reaction with **1a** is observed (**Figure 7d**).

This is consistent with the Mn-mediated Ni-catalyzed homodimerization reactions of **1a** and **2a**, in which the conversion of **1a** is faster than the conversion of **2a** under otherwise identical conditions (**Figure 7e**). Taken together with the CV studies, these data qualitatively suggests that the reductively generated **L1**·$Ni^{I}Cl$ reacts faster with **1a** and is consistent with previous RCC studies investigating the relative rates of Ni(I) complexes with aryl and alkyl electrophiles.[9b,10a,12]

Based on our experimental studies, a proposed mechanism for the Mn-mediated Ni-catalyzed ARA is shown in **Figure 7f**. Upon reduction of precatalyst **L1**·$Ni^{II}Cl_2$ the resulting

complex **6** reacts with alkenyl bromide **1** in an oxidative addition-reduction step to give **L1**·Ni(II) complex **7**. This could proceed by a bimolecular oxidative addition as proposed by Diao,[10a] or by reduction of the transiently formed Ni(III) species by Mn^0. Ni-catalyzed halogen atom transfer (XAT)[29] from the benzylic chloride gives rise to a cage-escaped radical **10** that can be captured by **7** to yield product **3** following reductive elimination. We again note that both **6** and **7** are in equilibrium with DMA-bound complexes,[14] and DMA coordination might facilitate the oxidative addition of **1** or XAT from **2a.**

The mechanism shown in **Figure 7f** is consistent with our observation that **L1**·$Ni^{I}X$ (**6**) can react with both **1a** and **2a**, but that **1a** reacts with **6** more rapidly. This mechanism is also consistent with the observed inverse dependence on [**1a**]$_0$: complex **6** is partitioned between two processes. When **1a** reacts with **6**, it effectively reduces the concentration of **6** available to react with **2a**. If benzylic radical generation by reaction of **6** with **2a** is the rate-controlling step (the studies in **Figure 7e** show that reaction of **6** with **2a** is slower than with **1a**), then increased [**1a**] would be expected to decrease the rate of reaction between **6** and **2a**, and therefore the overall rate of product formation. We note that we cannot rule out the possibility that **7** is reduced and that the corresponding **L1**·Ni^{I}(alkenyl) species – which is calculated to be a stronger reductant[16] – mediates the XAT; however, we would not expect a significant inverse rate dependence on **1a** for such a process. In addition, recent studies by Diao and coworkers have suggested that similar (biox)Ni^{II}(aryl)X complexes are unlikely to be reduced by Mn^0.[10b]

3.2.8 Computational Investigation into the Origin of Enantioselectivity

To explore the origins of enantioinduction, the structures and relative Gibbs free energies of the competing transition states for addition of radical **10** to resting state complex **7** were computed (**Figure 8a**). The free energy difference between **TS1-*S*** and **TS1-*R*** is computed to be 3.0 kcal/mol, which slightly overestimates the enantioselectivity for the reaction. In both transition states, the smallest substituent of the approaching benzyl radical

(**10**), hydrogen, is pointing towards the sterically bulky part of the ligand (highlighted in blue in **Figure 8a**). This allows the largest substituent, the phenyl group, to project away from this region of the ligand in the favored transition state **TS1-*S***. In the disfavored transition state **TS1-*R***, the phenyl group is proximal to the bulky region of the ligand. This results in an almost perfectly staggered approach of the benzyl radical with respect to the Ni ligands in **TS2-*S***, while steric repulsion from the ligand forces the benzyl radical to adopt a more eclipsed conformation in **TS1-*R***.[30] Subsequent reductive elimination for **11-*S*** is facile with a computed barrier of 0.9 kcal/mol (**Figure 8b**) for the major pathway. This is in contrast to previously reported computational results for a related Ni-photoredox coupling, which proposed a reversible radical addition and enantiodetermining reductive elimination;[31] however, this mechanism is consistent with recently published experimental results that measure a rapid reductive elimination from a Ni^{III} complex that is analogous to **11**.[32] These calculations suggest the facial selectivity of the enantiodetermining radical addition is influenced by the steric environment of BOX ligand **L1**.

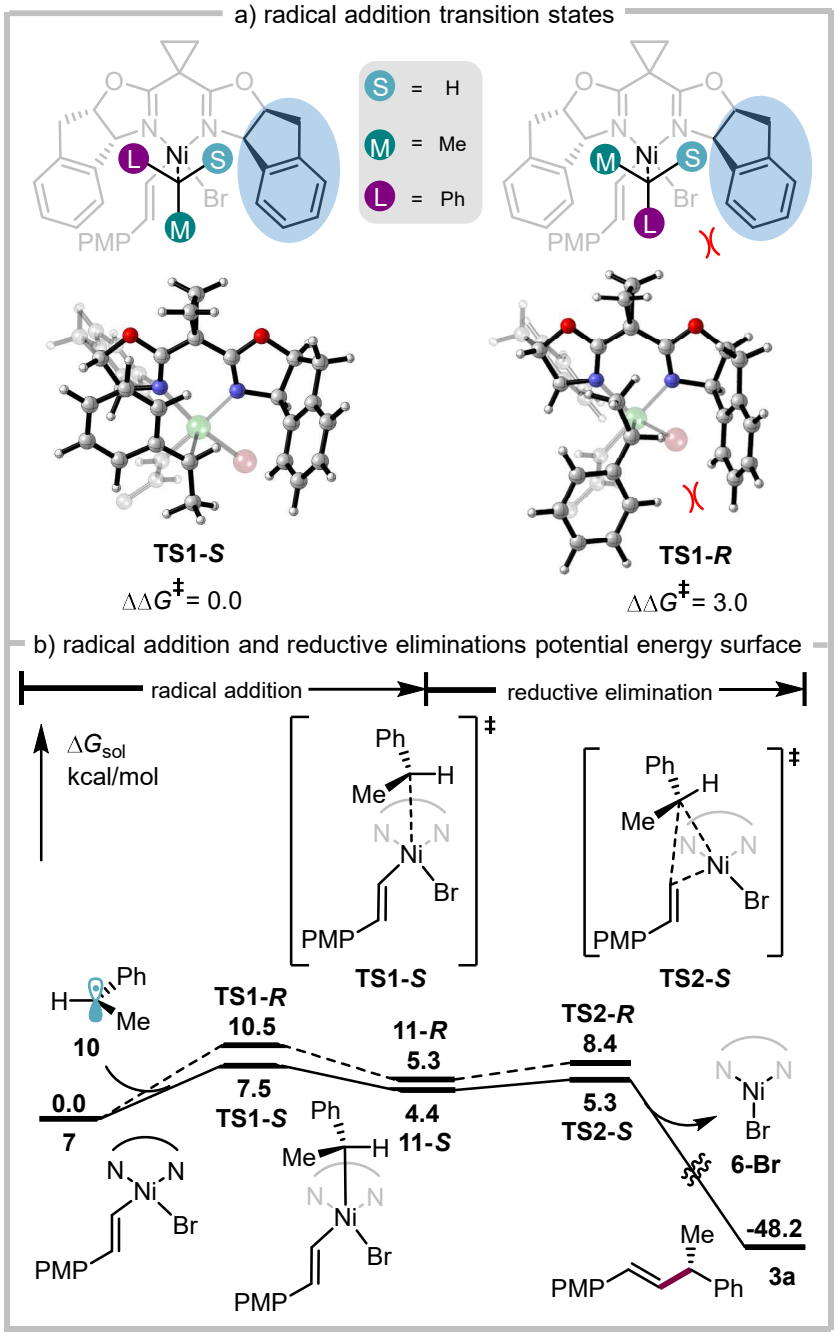

Scheme 8. *Calculated potential energy surface of enantiodetermining radical capture step and subsequent reductive elimination.*

3.3 Conclusion

In summary, we have investigated two Ni-catalyzed asymmetric RCC reactions to determine how changing the reductant and C(sp^3) electrophile influences the reaction mechanism. These reactions proceed through a $Ni^{I/III}$ cycle with fast activation of the alkenyl bromide electrophile by a Ni^{I} species. Both reactions have a rate-determining activation of the C(sp^3) electrophile to furnish a cage escaped benzyl radical. We have demonstrated that Ni is not required for NHP ester activation; instead, the combination of TDAE and TMSBr results in reductive decarboxylation to give the benzylic radical. The radical can then be intercepted by a Ni^{II}–alkenyl resting state that we were able to detect spectroscopically. In the case of the Mn^0-mediated ARA with benzylic chlorides, we propose that **L1**·Ni^{I}X generates the benzylic radical by an XAT process. This is a subtle distinction from the mechanism proposed by Diao for the (biox)Ni-catalyzed RCC between aryl halides and benzylic chlorides,[10b] which did not suggest an explicit role for Ni in generating the radical from the benzylic halide.

The fact that reduction of NHP esters by TDAE is Lewis acid-mediated, rate controlling, and independent of the alkenyl bromide activation has significant implications for the development of other Csp^3-Csp^n RCCs. This mechanistic regime allows for independent tuning of the rates of electrophile activation where d[Csp^3]/dt can be tuned with additives and d[Csp^2]/dt through catalyst design. It is our hope that these findings aid in the adoption of C(sp^2)–X reductive couplings with NHP ester fragments in more complex settings by providing a framework to guide reaction optimization.

3.4 Experimental Sections

3.4.1 Experimental Details

Materials and Methods

Unless otherwise stated, reactions were performed under a N_2 atmosphere using freshly dried solvents. All reagents were purchased from commercial suppliers (Sigma Aldrich, Combi- Blocks, TCI, Enamine, Strem) and used without further purification unless mentioned otherwise. Tetrahydrofuran (THF), acetonitrile (MeCN), and methylene chloride (CH_2Cl_2) were dried by passing through activated alumina columns. Anhydrous dimethylacetamide (DMA) was purchased from Aldrich and stored in a N_2-filled glovebox. $NiCl_2$·dme was purchased from Strem and stored in the glovebox. Manganese powder (~325 mesh, 99.3%) was purchased from Alfa Aesar. Zinc dust (97.5%) was purchased from Strem. NaI (anhydrous, 99%) was purchased from Strem and stored in a N_2-filed glovebox. Flash column chromatography was performed as described by Still et al. using silica gel (230-400 mesh, Silicycle).[33] Purified compounds were dried on a high vacuum line (0.2 torr) to remove trace solvent. ^{1}H and ^{13}C NMR spectra were recorded on a Bruker Avance III HD with Prodigy cryoprobe (at 400 MHz and 101 MHz, respectively), a Varian 400 MR (at 400 MHz and 101 MHz, respectively), or a Varian Inova 500 (at 500 MHz and 126 MHz, respectively). ^{1}H and ^{19}F NMR spectra were also recorded on a Varian Inova 300 (at 300 MHz and 282 MHz, respectively). NMR data is reported relative to internal $CHCl_3$ (^{1}H, δ = 7.26) and $CDCl_3$ (^{13}C, δ = 77.0) or C_6F_6 (^{19}F -164.9 ppm). HRMS were acquired from the Caltech Center for Catalysis and Chemical Synthesis Facility using electrospray ionization (ESI-TOF). Analytical chiral SFC was performed with a Mettler SFC supercritical CO_2 analytical chromatography system with Chiralcel AD-H, OD-H, AS-H, OB-H, and OJ-H columns (4.6 mm x 25 cm). Analytical achiral GC was performed with an Agilent 6850 GC utilizing an HP-1 capillary column (methyl

siloxane, 30.0 m x 320 µm x 0.25 µm, Agilent) column with a splitless injection and a helium flow of 7.3 mL/min. The temperature program began at 50 °C and was held for 2 min, increased to 250 °C at 25 °C/min and then held at 250 °C for 3 min. X-band perpendicular mode EPR spectra were recorded on a Bruker EMX spectrometer at 77 K using a LN_2 immersion dewar. Parallel mode EPR were recorded at 5K using a LHe cryostat. EPR spectra were simulated with Easyspin (version 5.2.35)[34]. Electronic absorption spectra were obtained using CARY 300 spectrophotometer. Electroanalytical experiments were conducted in the Beckman Resource Laser Resource Center at the California Institute of Technology using a Bio-Logic SP300 potentiostat/galvanostat. Cyclic voltammetry experiments we conducted with a glassy carbon disk working electrode, a platinum wire counter electrode, and a silver wire reference electrode containing a 10 mM $AgNO_3$ solution with 0.1 M $TBAPF_6$ in MeCN.

3.4.2 Synthetic Procedures

Substrate and Catalyst Synthesis

Substrates

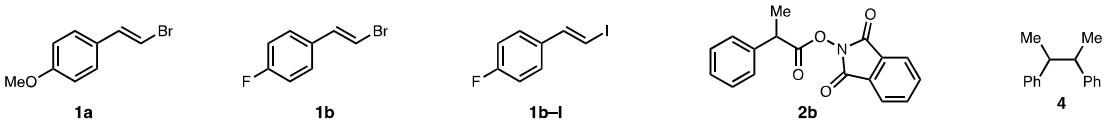

Catalysts

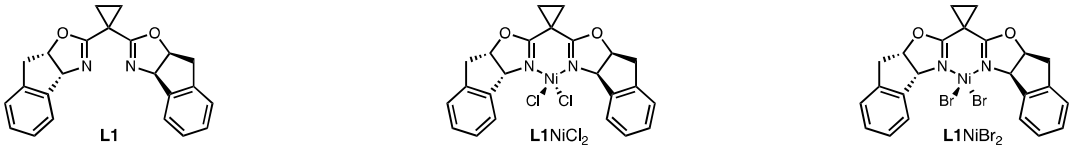

Figure S1. *Substrates and catalysts used for mechanistic studies.*

Catalysts:(3a*R*,3a'*R*,8a*S*,8a'*S*)-2,2'-(Cyclopropane-1,1-diyl)bis(3a,8a-dihydro-8*H*-indeno[1,2-*d*]-oxazole) **(L1)** was synthesized according to our previously published procedure.[35] Complexation with $NiBr_2$ or $NiCl_2$ were prepared according to previously reported synthesis of **L1**$NiCl_2$[36] and **L1**$NiBr_2$.[37] Complexes were recrystallized once by vapor diffusion of pentane

in a saturated DCM solution for use in catalytic reactions and 3 times for use in electroanalytical experiments.

Substrates: Coupling partners **1a**, **1b** and **2b** were synthesized according to the procedure described in the initial disclosure.[37]

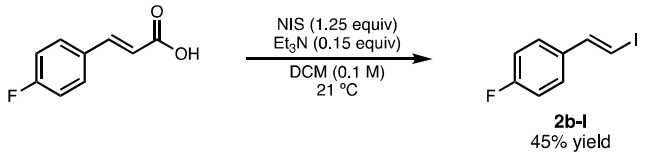

2b-I
45% yield

(*E*)-1-fluoro-4-(2-iodovinyl)benzene (**2b-I**): To a 250 mL oven-dried round bottom flask with a stir bar was added (*E*)-4-fluorocinnamic acid (831.6mg, 5.0 mmol, 1 equiv). The acid was then suspended in 50 mL (0.1 M) DCM then triethylamine (105 µL, 0.75 mmol, 0.15 equiv) was added and the reaction was stirred under N_2. To the stirring solution was then added *N*-iodosuccinimide (1.41 g, 6.25 mmol, 1.25 equiv) in one portion. After 12 minutes, the reaction solution had turned red and then deep black after 20 minutes. After 1h the starting material was consumed by TLC and the reaction mixture was concentrated *in vacuo*. Residue was taken up in 30 mL EtOAc and washed with 25 mL sat. $Na_2S_2O_3$ solution. The aqueous layer was then extracted two more times and combined organics were dried over $MgSO_4$, filtered through celite, rinsed with EtOAc then concentrated in vacuo to give a brown solid. The crude was then purified by filtration through SiO_2 with pentane to give alkenyl iodide **2b-I** (558 mg, 2.3 mmol, 45% yield). *Note:* we observed significant discoloration and decomposition upon prolonged exposure to light so storage at -20 ºC in the darkness under Ar is essential to prevent decomposition.

3.4.3 Kinetics and Time Course Experiments

Methods of GC-FID Quantification: For each reaction component and product, authentic samples were isolated to determine response factors for GC-FID analysis. Three standards were made for each analyte to normalize the GC-FID area counts and convert the obtained data into

reaction concentration (M) values. The analyte and dodecane standard were each added to a 20 mL vial and massed on a balance. The mixture was dissolved in 10 mL of EtOAc and transferred to a GC vial for analysis. The density of dodecane (0.75 g/mL) was also used to convert the area values to concentration.

3.4.3.1 Heterogeneous Reaction Kinetics

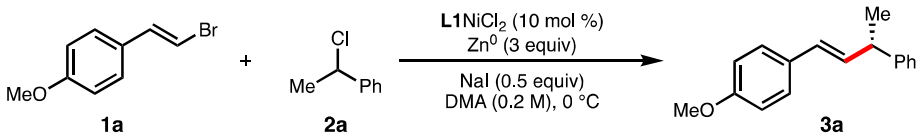

General Procedure 1 (Zn^0 powder): A 10 mL round bottom flask with a small magnetic stirring rod was charged with the sodium iodide (22.5 mg, 0.15 mmol, 0.5 equiv) and zinc powder (58.8 mg, 0.9 mmol, 3 equiv). The flask was sealed with a rubber septum, purged with N_2, and cooled to 0 °C by being placed in an ice water bath. The alkenyl bromide **1a** (85.2 mg, 0.4 mmol) and **L**·$NiCl_2$ complex (19.4 mg, 0.04 mmol) were added to a 2 mL volumetric flask, sealed with a rubber septum, and purged with N_2. The benzyl chloride **2a** (53 μL, 0.4 mmol) and dodecane (48 μL) as an internal standard were added via syringe to the volumetric flask. Then anhydrous DMA was added to the volumetric flask until it reached the 2 mL line. A small stir bar was added to the volumetric flask and the solution was stirred until all of the **L**·$NiCl_2$ complex was dissolved. The solution was taken up into a 2 mL syringe to ensure homogeneity, and then 1.5 mL of the solution was added to the round bottom flask. The reaction was stirred under a positive N_2 flow by using an IKA stir plate set to a stirring speed of 1500 rpm. At appropriate time points, approximately 50 μL of the solution was removed by syringe (syringe and needle were pre-flushed with N_2), loaded onto a short silica plug (1 cm) in a glass pipette packed with cotton. The crude mixture was flushed through the silica plug with 2 mL of 10% EtOAc/hexane directly into GC vials and analyzed by GC-FID.

All data runs obtained from the GC-FID instrument were appropriately integrated for the product and the dodecane standard. The integrated data points were further processed by normalizing each product area value by its corresponding standard area value. The normalized areas were then converted to concentration by using calculated response factors obtained from preparing known mixtures of the standard and purified reaction product. Each reaction was analyzed and graphed to show the product concentration (M) as a function of reaction time (min). All data points were plotted with black markers (•) as shown below, while only the data points included in the linear fit are shown with red markers (•). The best-fit linear regression line is also shown and the y=mx+b equation is given. Each reaction was run in duplicates as indicated by Trial 1 and Trial 2.

Standard Reaction Conditions

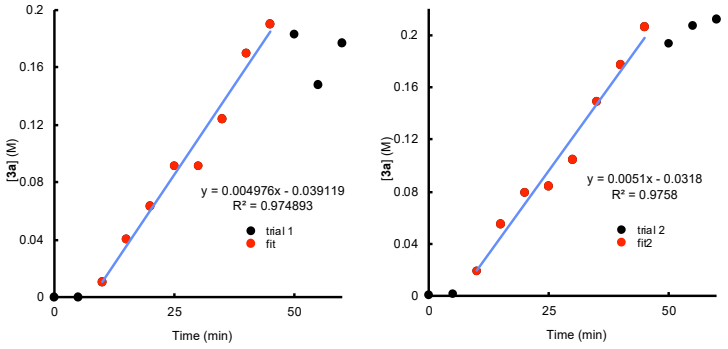

***Figure S2**: Results of standard reaction conditions runs with linear fit regions highlighted: [**1a**]$_0$ = 0.2M, [**2a**]$_0$ = 0.2M, [**L1**·NiCl$_2$] = 0.02M.*

Effect of Changing [L1·NiCl$_2$]

The general procedure 1 was followed except varying the amounts of **L1**NiCl$_2$ were used to give final loadings of 5%, 7%, 14%, and 20%.

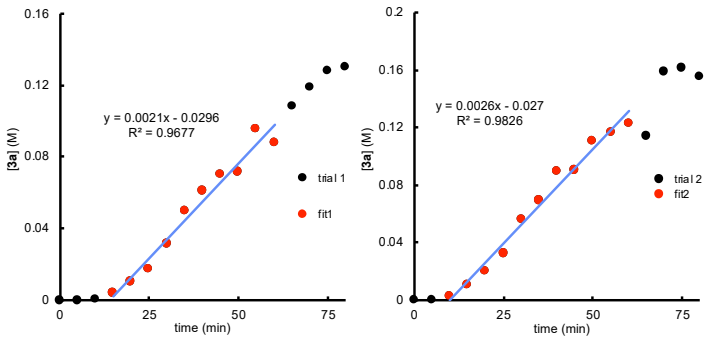

***Figure S3**: Kinetics runs with linear fit regions highlighted: [**1a**]$_0$ = 0.2M, [**2a**]$_0$ = 0.2M, [**L1**·NiCl$_2$] = 0.01M.*

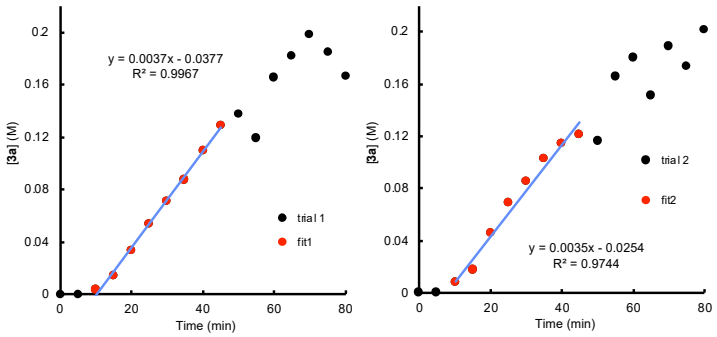

***Figure S4**: Kinetics runs with linear fit regions highlighted: [**1a**]$_0$ = 0.2M, [**2a**]$_0$ = 0.2M, [**L1**·NiCl$_2$] = 0.014M.*

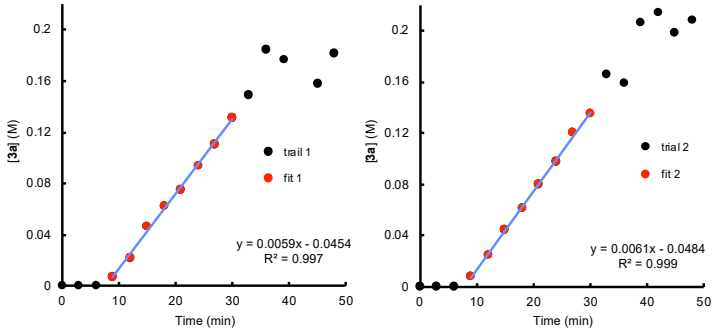

***Figure S5**: Kinetics runs with linear fit regions highlighted: [**1a**]$_0$ = 0.2M, [**2a**]$_0$ = 0.2M, [**L1**·NiCl$_2$] = 0.028M.*

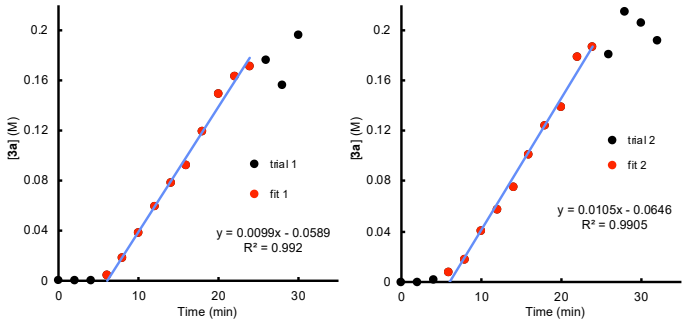

***Figure S6**: Kinetics runs with linear fit regions highlighted: [**1a**]$_0$ = 0.2M, [**2a**]$_0$ = 0.2M, [**L1**·NiCl$_2$] = 0.04M.*

Effect of Changing Alkenyl Bromide 1a Equivalents

The general procedure 1 was followed except varying the amounts of **1a** were used to give final amounts of 1.5, 2, 3, and 4 equivalents.

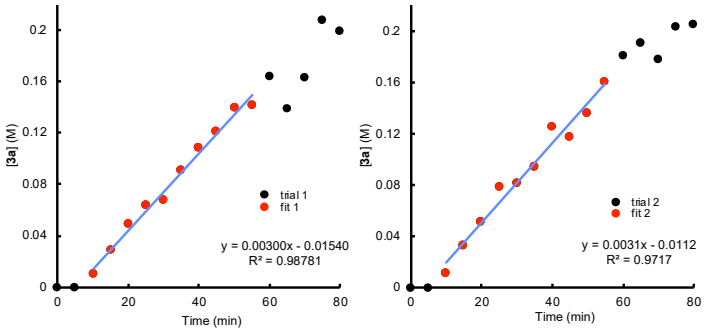

***Figure S7**: Kinetics runs with linear fit regions highlighted: [**1a**]$_0$ = 0.3M, [**2a**]$_0$ = 0.2M, [**L1**·NiCl$_2$] = 0.02M*

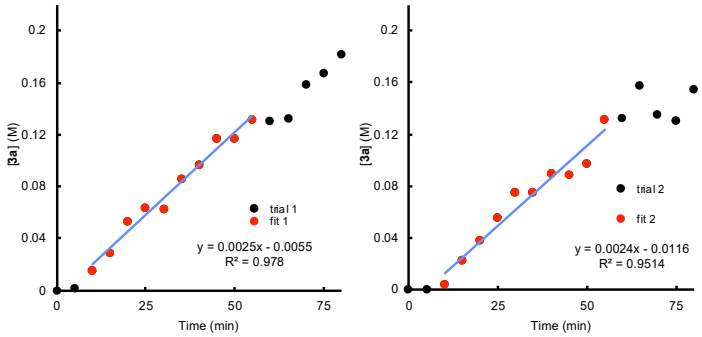

***Figure S8**: Kinetics runs with linear fit regions highlighted: [**1a**]$_0$ = 0.4M, [**2a**]$_0$ = 0.2M, [**L1**·NiCl$_2$] = 0.02M.*

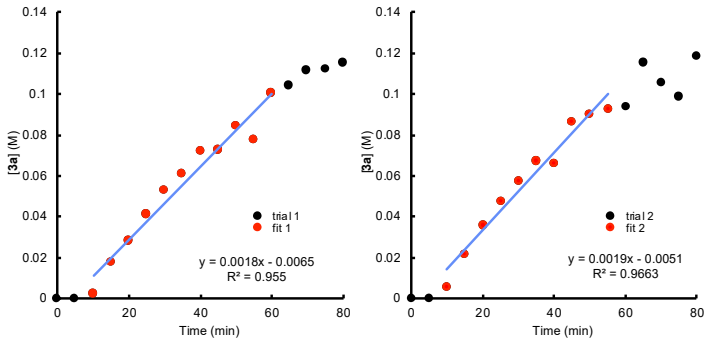

***Figure S9**: Kinetics runs with linear fit regions highlighted: [**1a**]$_0$ = 0.6M, [**2a**]$_0$ = 0.2M, [**L1**·NiCl$_2$] = 0.02M.*

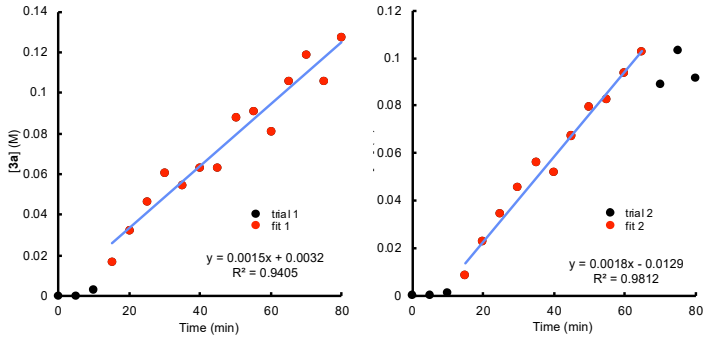

***Figure S10**: Kinetics runs with linear fit regions highlighted: [**1a**]$_0$ = 0.8M, [**2a**]$_0$ = 0.2M, [**L1**·NiCl$_2$] = 0.02M.*

Effect of Changing Benzyl Chloride 2a Equivalents

The general procedure 1 was followed except varying the amounts of **2a** were used to give final amounts of 1.5, 2, 3, and 4 equivalents.

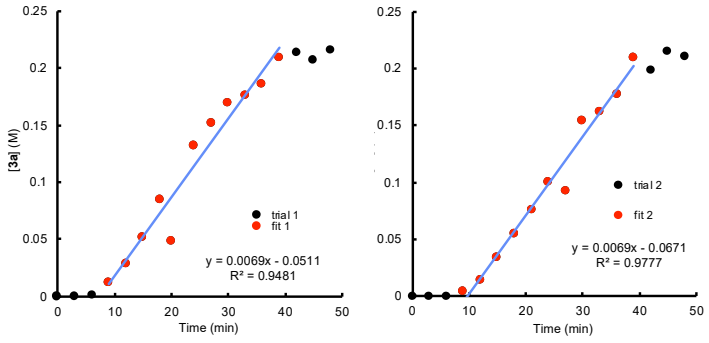

***Figure S11**: Kinetics runs with linear fit regions highlighted: [**1a**]$_0$ = 0.2M, [**2a**]$_0$ = 0.3M,*

*[**L1**·$NiCl_2$] = 0.02M.*

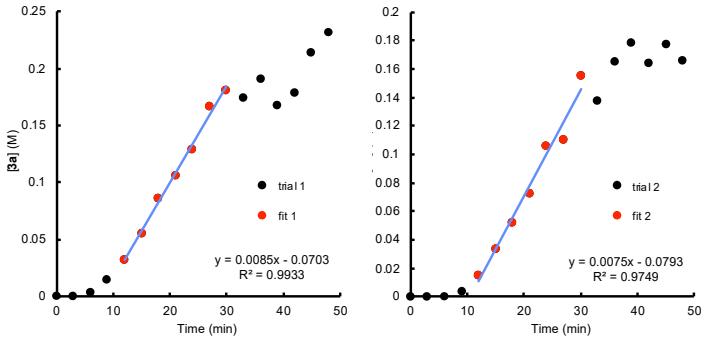

***Figure S12**: Kinetics runs with linear fit regions highlighted: [**1a**]$_0$ = 0.2M, [**2a**]$_0$ = 0.4M, [**L1**·$NiCl_2$] = 0.02M.*

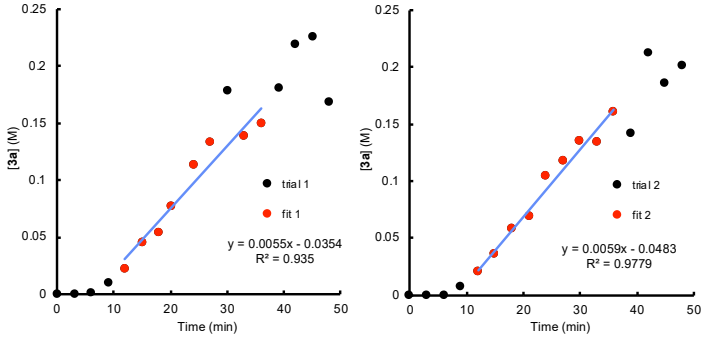

***Figure S13**: Kinetics runs with linear fit regions highlighted: [**1a**]$_0$ = 0.2M, [**2a**]$_0$ = 0.6M, [**L1**·$NiCl_2$] = 0.02M.*

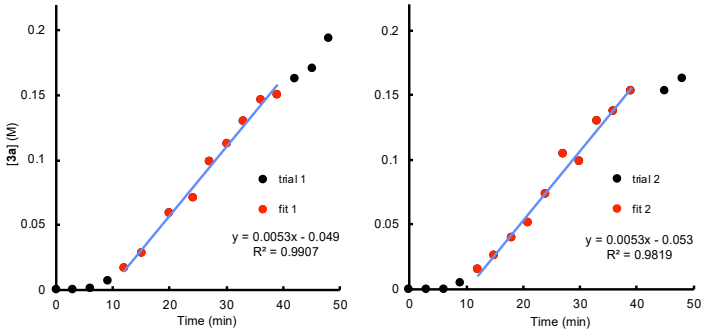

***Figure S14**: Kinetics runs with linear fit regions highlighted: [**1a**]$_0$ = 0.2M, [**2a**]$_0$ = 0.8M, [**L1**·$NiCl_2$] = 0.02M.*

Tabulated Summary of Heterogeneous Kinetics Data:

$[Ni]_0$ (M)	Trial 1 Rate (M/min)	Trial 2 Rate (M/min)	Average Rate (M/min)	Standard deviation	**3a** ee at End of Trial 1	**3a** ee at End of Trial 2
0.02	0.0050	0.0051	0.0050	0.0001	93	93
0.01	0.0025	0.0021	0.0023	0.0003	87	88
0.014	0.0035	0.0037	0.0036	0.0001	89	89
0.028	0.0061	0.0059	0.0060	0.0002	86	85
0.04	0.0099	0.011	0.010	0.0004	85	85

Table S1*: Reaction rate data for each trial at different Ni loadings.*

$[$**1a**$]_0$ (M)	Trial 1 Rate (M/min)	Trial 2 Rate (M/min)	Average Rate (M/min)	Standard deviation	**3a** ee at End of Trial 1	**3a** ee at End of Trial 2
0.2	0.0050	0.0051	0.0050	0.0001	93	93
0.3	0.0030	0.0031	0.0030	0.0001	93	91
0.4	0.0025	0.0025	0.0025	0.0001	94	94
0.6	0.0016	0.0017	0.0017	0.00003	95	95
0.8	0.0018	0.0015	0.017	0.0002	95	95

Table S2*: Reaction rate data for each trial at different initial concentrations of* ***1a****.*

$[$**2a**$]_0$ (M)	Trial 1 Rate (M/min)	Trial 2 Rate (M/min)	Average Rate (M/min)	Standard deviation	**3a** ee at End of Trial 1	**3a** ee at End of Trial 2
0.2	0.0050	0.0051	0.0050	0.0001	93	93
0.3	0.0069	0.0067	0.0068	0.0001	83	84
0.4	0.0075	0.0085	0.0080	0.0007	84	83
0.6	0.0055	0.0059	0.0057	0.0003	82	83

0.8	0.0052	0.0053	0.0053	0.0001	83	83

***Table S3**: Reaction rate data for each trial at different initial concentrations of **2a**.*

Impact of Stir Rate

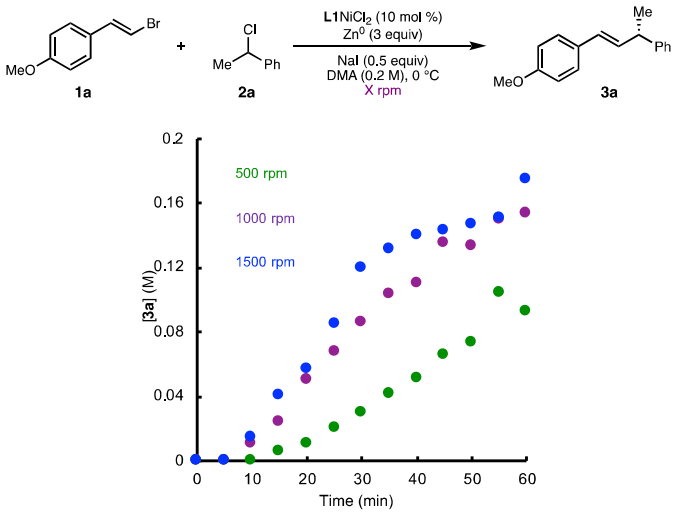

***Figure S15**: Rate of **3a** formation at different stir rates (average of 2 runs shown). There is a a significant rate dependence on stirring from 500 rpm to 1000 rpm and a smaller difference between 1000 rpm and 1500 rpm. The stir rate dependence is smaller at high stir rates and kinetic runs measured runs at 1500 rpm are reproducible.*

Mn^0 vs. Zn^0 Profile:

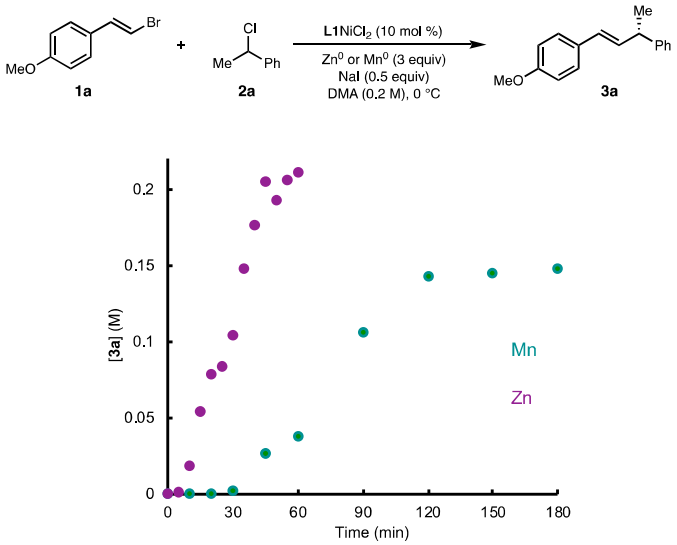

***Figure S16**: Representative profile of **3a** formation with Zn^0 and Mn^0 stirring at 1500 rpm.*

Excess Zn^0 Profile

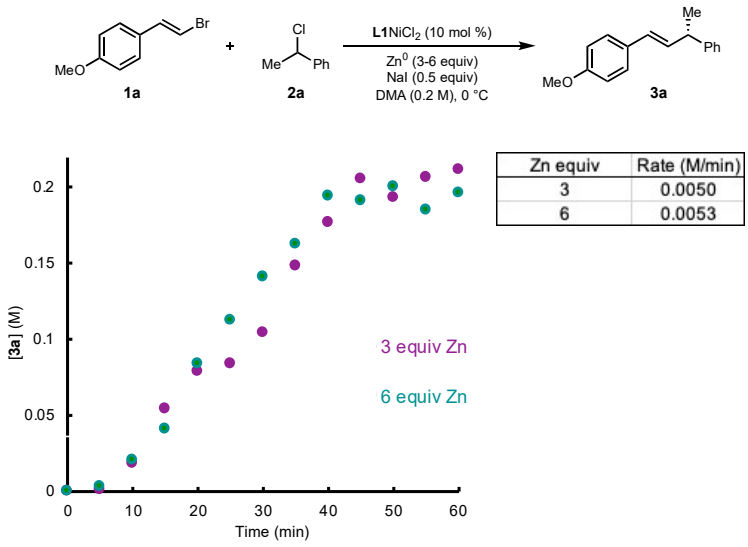

***Figure S17**: Rate of **3a** formation with 3 equiv and 6 equiv of Zn^0 stirring at 1500 rpm shown as average of two runs for each loading.*

3.4.3.2 Homogenous Reaction Kinetics

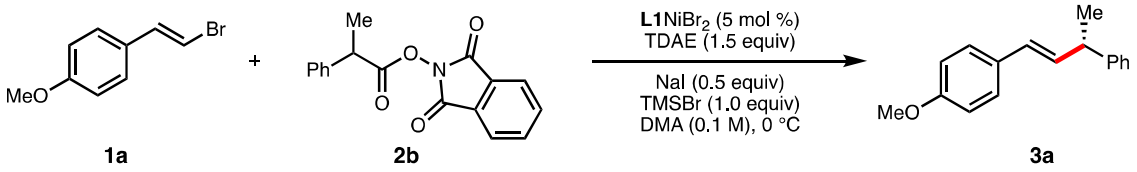

General Procedure 2: To a 2mL volumetric flask was added (*E*)-1-(2-bromovinyl)-4-methoxybenzene (65.6 mg, 0.308 mmol, 1.0 equiv), 1,3-dioxoisoindolin-2-yl 2-phenylpropanoate (90.9 mg, 0.308 mmol, 1.0 equiv) and **L1**$NiBr_2$ (8.8 mg, 0.0154 mmol, 5 mol%) on the bench. The volumetric flask was then placed under argon and sealed with a septa. In a N_2-filled glovebox was then added sodium iodide (23.1 mg, 0.154 mmol, 0.5 equiv) to the volumetric flask which was then filled to volume with DMA (0.154 M). A stir bar was then added and the solution was stirred for 15 minutes. In a 1mL volumetric flask was added *N,N'*-

tetrakis(dimethylamino)ethylene (TDAE, 100μL, 0.43 mmol, 1.5 equiv) and then filled to volume with DMA (0.43 M) in the glovebox and sealed with a rubber septum and tape. Then 1.3mL of the homogeneous solution in the 2 mL volumetric flask was then added to a 10mL oven-dried round bottom flask with a 2 dram stir bar. The flask was then sealed with a rubber septum and electrical tape. To the 10mL round bottom flask was added 15μL of dodecane as the internal standard followed by TMSBr (26.4 μL, 0.2 mmol, 1.0 equiv). The round bottom flask was then quickly removed from the glovebox and placed in an ice bath under N_2 and stirred. A ~50 μL aliquot were removed by an N_2-purged 1mL syringe for a t = 0 timepoint. Once cooled, TMSBr (26.4 μL, 0.2 mmol, 1.0 equiv) was added via syringe and the reaction was stirred for 30 seconds before 0.7 mL of the cooled TDAE solution was added initiating the reaction. ~50 μL aliquots were removed by an N_2-purged 1mL syringe and quenched into a 1-dram vial containing EtOAc and 1M $HCl_{(aq)}$. The vial was then capped and shaken then the organic layer was removed and pushed through a $MgSO_4$ plug into a GC vial for analysis. All samples were analyzed directly by GC-FID. Each experiment was run in duplicate with representative profiles shown below.

Standard Reaction Conditions

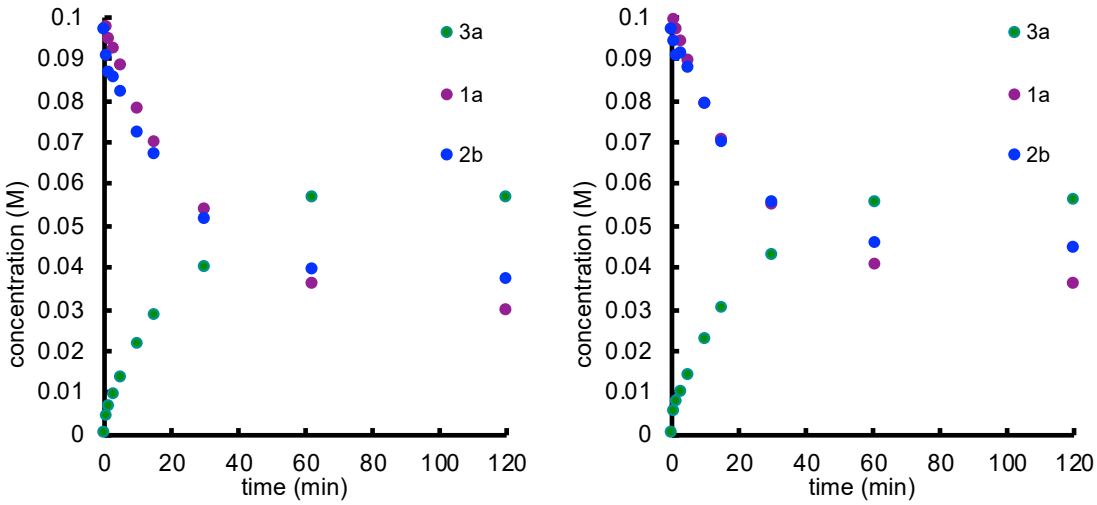

Figure S18: *Results of standard reaction conditions under general procedure 2: [1a]0 = 0.1M, [2b]0 = 0.1M, [L1·NiBr2] = 0.005 M.*

Reaction Profiles for Experiments Varying [L1NiBr$_2$]$_0$

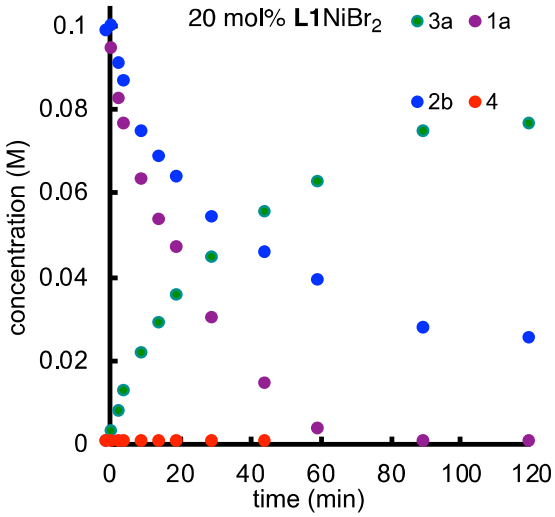

Figure S19*: Profile of reaction under general procedure 2: [**1a**]$_0$ = 0.1M, [**2b**]$_0$ = 0.1M, [**L1**·NiBr$_2$] = 0.02 M.*

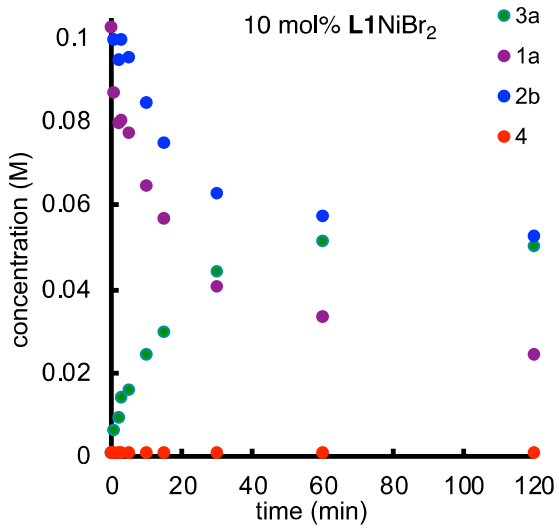

***Figure S20**: Profile of reaction under general procedure 2: [**1a**]$_0$ = 0.1M, [**2b**]$_0$ = 0.1M, [**L1**·NiBr$_2$] = 0.01 M.*

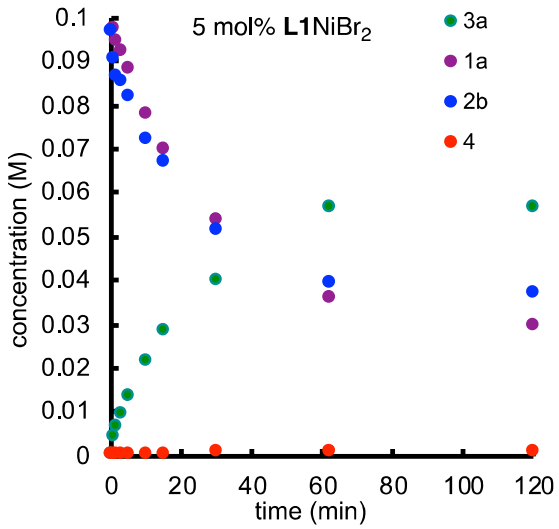

***Figure S21**: Profile of reaction under general procedure 2: [**1a**]$_0$ = 0.1M, [**2b**]$_0$ = 0.1M, [**L1**·NiBr$_2$] = 0.005 M.*

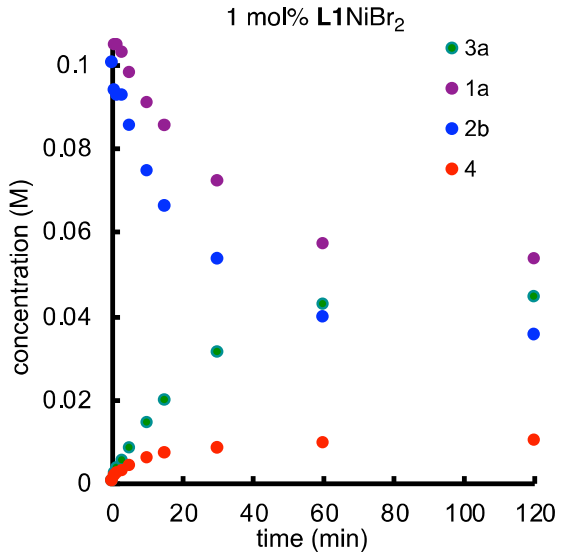

***Figure S22**: Profile of reaction under general procedure 2: [**1a**]$_0$ = 0.1M, [**2b**]$_0$ = 0.1M, [**L1**·NiBr$_2$] = 0.001 M.*

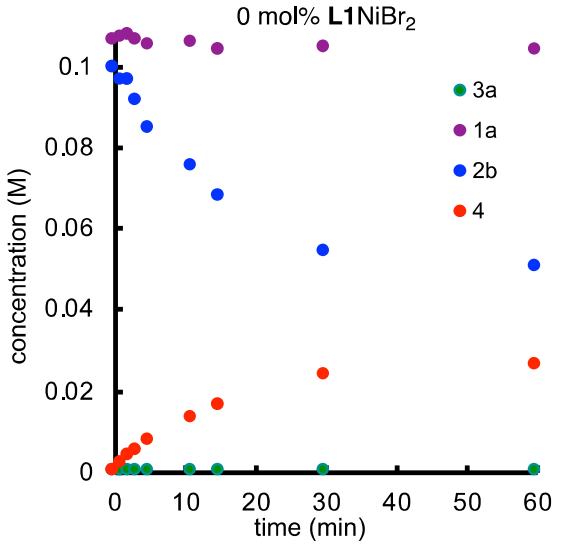

***Figure S23**: Profile of reaction under general procedure 2: [**1a**]$_0$ = 0.1M, [**2b**]$_0$ = 0.1M, [**L1**·NiBr$_2$] = 0 M.*

Reaction Profiles for Experiments Varying [1a]$_0$

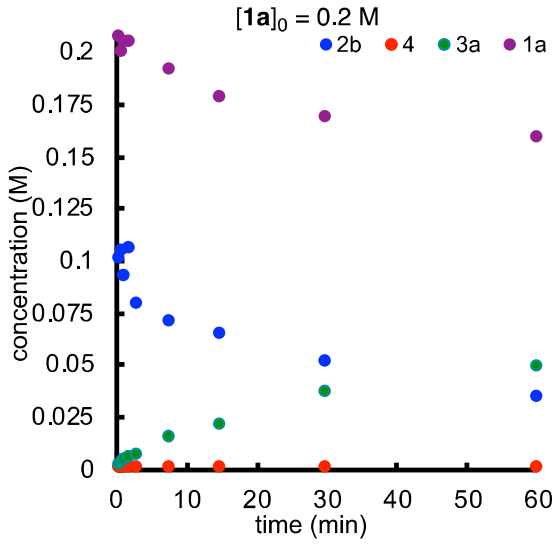

***Figure S24**: Profile of reaction under general procedure 2: [**1a**]$_0$ = 0.2M, [**2b**]$_0$ = 0.1M, [**L1**·NiBr$_2$] = 0.005 M.*

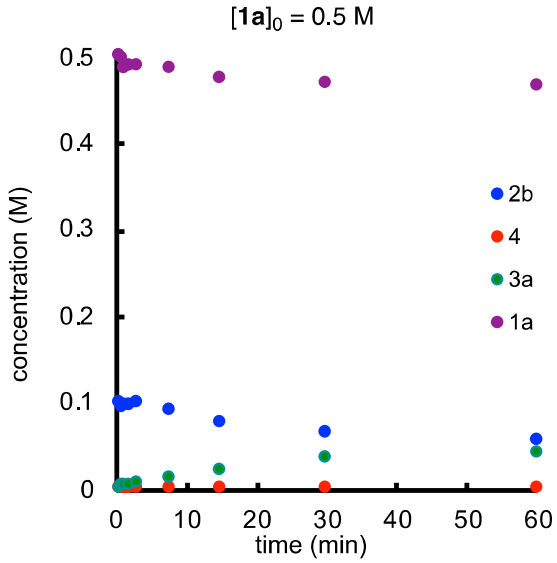

***Figure S25**: Profile of reaction under general procedure 2: [**1a**]$_0$ = 0.5M, [**2b**]$_0$ = 0.1M, [**L1**·NiBr$_2$] = 0.005 M.*

Reaction Profiles for Experiments Varying [2b]$_0$

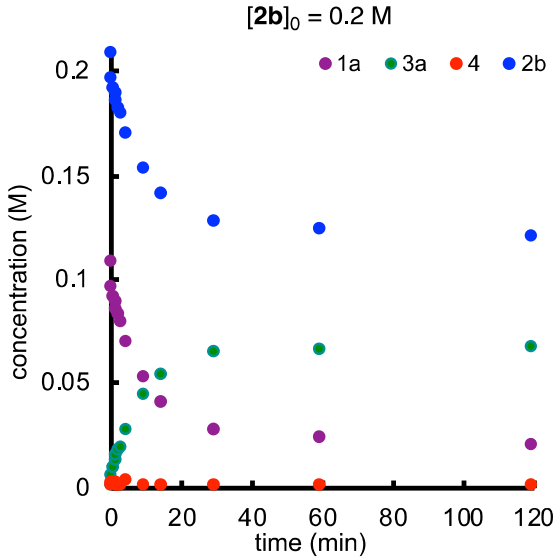

***Figure S26**: Profile of reaction under general procedure 2: [**1a**]$_0$ = 0.1M, [**2b**]$_0$ = 0.2M, [**L1**·NiBr$_2$] = 0.005 M.*

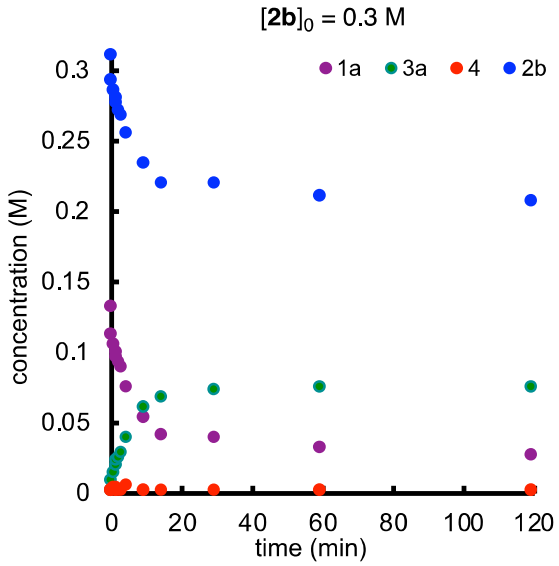

***Figure S26**: Profile of reaction under general procedure 2: [**1a**]$_0$ = 0.1M, [**2b**]$_0$ = 0.3M, [**L1**·NiBr$_2$] = 0.005 M.*

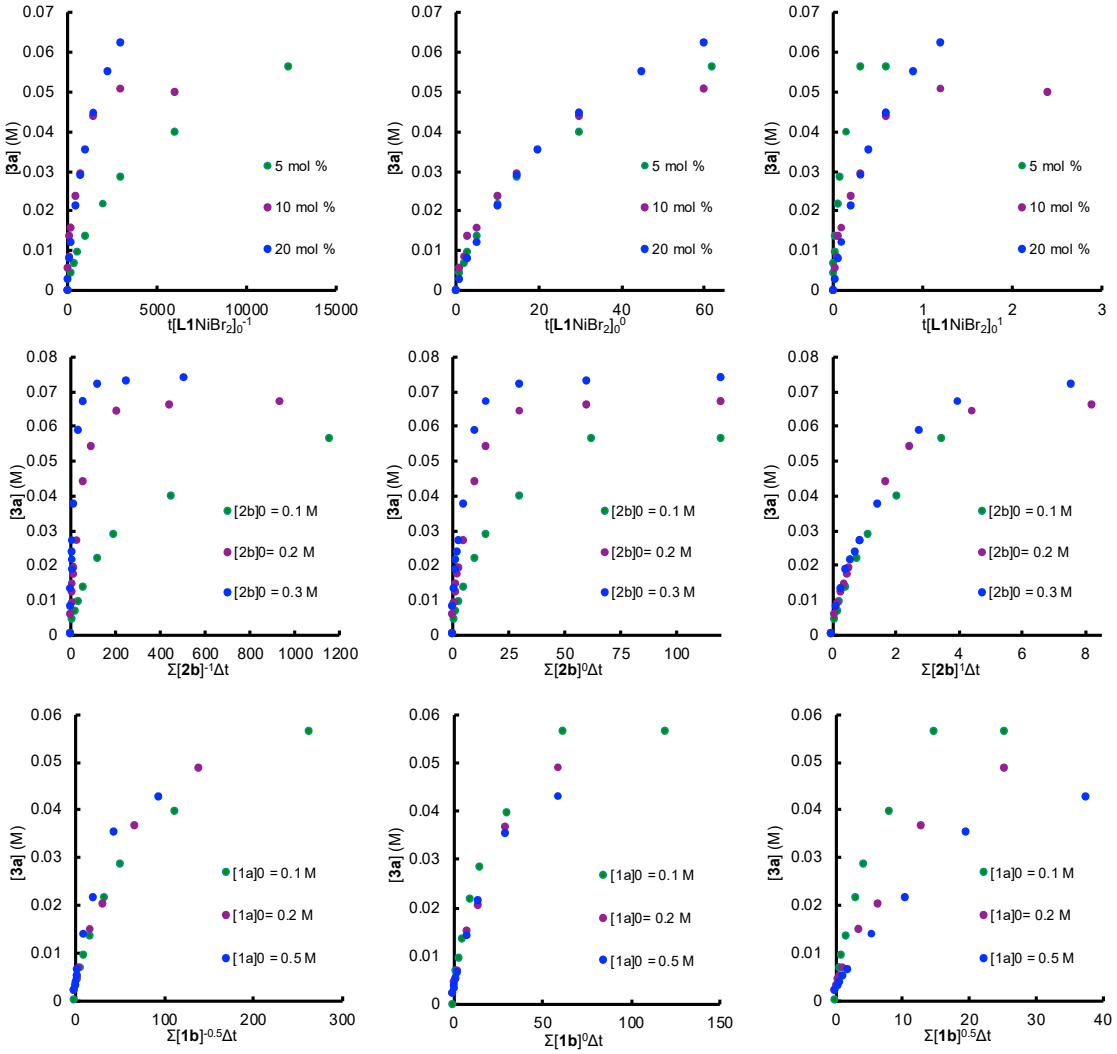

***Figure S27**: Grid of reactions analyzed by Variable Time Normalization Analysis (VTNA) showing the coefficients that result in the best profile overlay next to coefficients that show poor overlay.*

3.4.4 Mechanism of Substrate Activation

3.4.4.1 Additive Effects of NHP Ester Reduction Rate

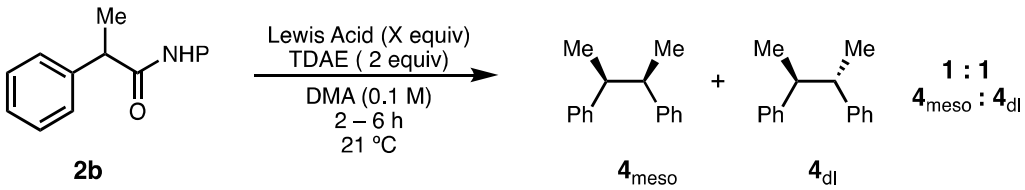

General Procedure 3: To an oven-dried 10 mL round bottom flask with a stir bar was added 1,3-dioxoisoindolin-2-yl 2-phenylpropanoate **2b** (59.1 mg, 0.20 mmol, 1.0 equiv). The flask was then brought into a N_2-filled glovebox where NaI (if applicable), DMA (2.0 mL, 0.1 M) and *n*-dodecane (target: 20 μL, 0.088 mmol, 0.44 eqiuv, actual mass was recorded for each experiment) internal standard was added. The solution was stirred until homogenous and then the respective Lewis acid (0.2 mmol, 1 equiv) was added and the flask was sealed with a septa and electrical tape. The flask was removed from the glovebox and placed under N_2 and stirred. A ~50 μL aliquot of the solution was removed with a N_2-purged syringe then quenched into a 1-dram vial containing EtOAc and 1M $HCl_{(aq)}$ and the organic layer was passed through a $MgSO_4$ plug into a GC vial then further diluted with EtOAc for the appropriate concentration for GC analysis. To the stirring solution was then added *N,N'*-tetrakis(dimethylamino)ethylene (93.1 μL, 0.40 mmol, 2.0 equiv) to start the reaction (t = 0). The reaction was then aliquoted with the same procedure previously described at regular intervals.

Data Analysis: The calculated concentrations of **2b**, meso-**4** and dl-**4** were calculated from the analyte:standard integral ratios measured by GC-FID at each timepoint. The measured response for each component was used to calculate the amount of analyte which was then converted to concentration corresponding to 2 mL reaction volume. In all cases, diastereomers of **4** were produced in a 1:1 ratio and summed to determine the total amount of product produced ($[\mathbf{4}]_{meso} + [\mathbf{4}]_{dl} = [\mathbf{4}]_{tot}$, noted as [**4**] throughout the remainder of the text). Due to the fact that the formation of **4** from the diffusion-limited termination of two **2b**-derived radicals is much faster than the reactions leading to the generation of the radical species it is reasonable to treat the rate of radical generation as the rate of [**4**] formation.

The relative rate of **2b**-derived radical formation was determined from the [**4**] vs. time profiles for each Lewis acid additive. The rates were determined in a similar method as described by Weix and coworkers[38] using equation **1** to linearize the data.

$$\frac{1}{(1-f)} = mt \quad \textbf{(1)}$$

Where f is the fraction of [**4**]$_t$ over the theoretical yield of [**4**]. The rate was then extracted from the slope determined from least-squares linear regression. To calculate the relative rate (k_{rel}) the absolute rate obtained from experiments employing 1 equivalent of TMSBr was used as a baseline according to equation **2** due to its use in the optimized catalytic reaction.

$$k_{rel} = \frac{k_{Lewis\ acid}}{k_{TMSBr}} \quad \textbf{(2)}$$

Representative Concentration Profiles and Rate Determination:

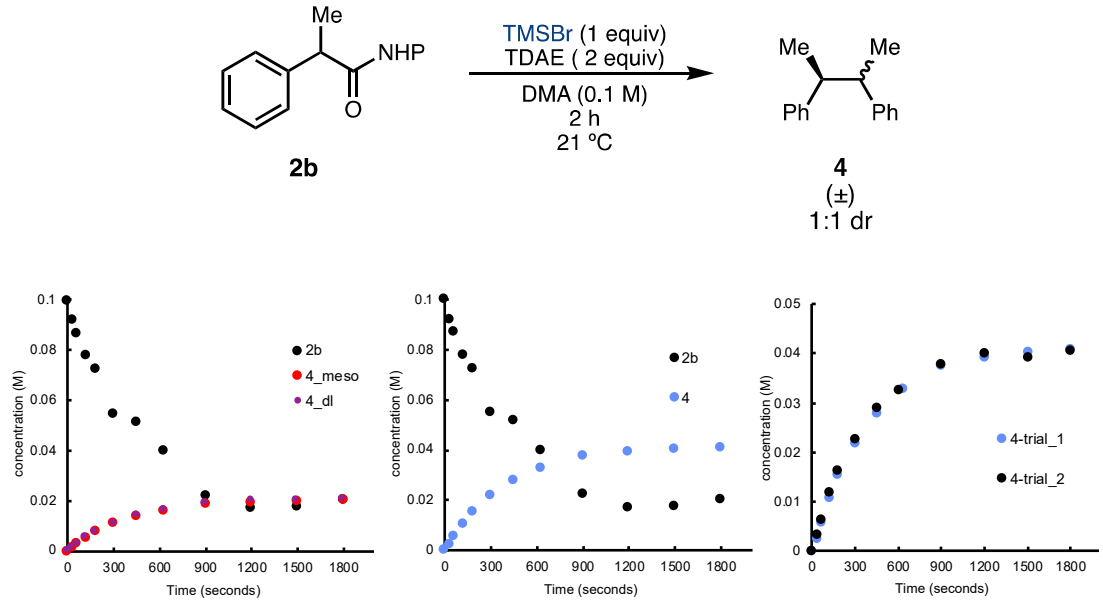

***Figure S28**: Representative reaction profile for **2b** activation kinetics. The profile is shown with all quantified species (left) and with the sum of **4** diastereomers (middle). Runs were run in duplicate to ensure reproducibility (right).*

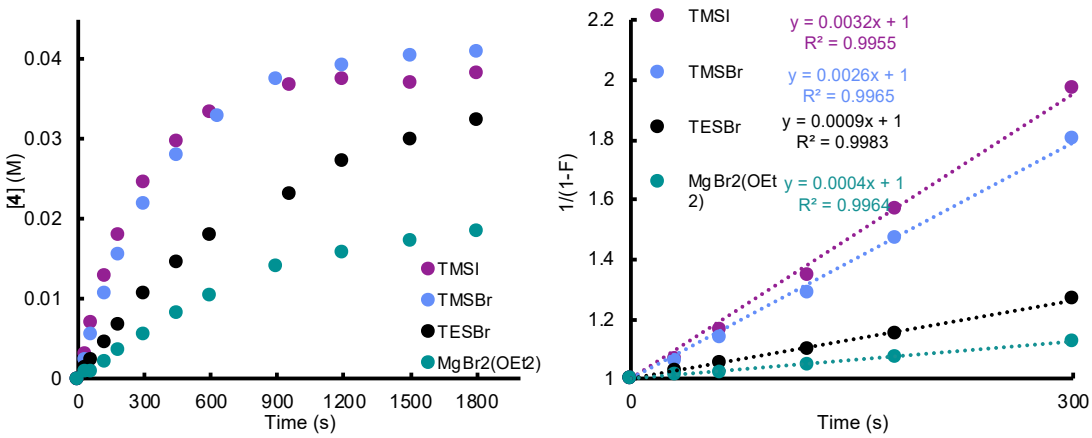

***Figure S28**: Comparative reaction profiles for different Lewis acids (left) and the corresponding linearized data with equation **1** (right).*

Tabulated Rate Data:

Lewis Acid	TMSBr	1 equiv
k	0.002625	
krel	1.000	
Time (s)	**[4] (M)**	**1/(1-F)**
0	0.000	1.00
30	0.002	1.05
60	0.006	1.13
120	0.011	1.27
180	0.016	1.45
300	0.022	1.78
450	0.028	2.27
630	0.033	2.91
900	0.038	4.04
1200	0.039	4.70
1500	0.040	5.20
1800	0.041	5.59
2700	0.041	5.62
3600	0.041	5.88
5400	0.039	4.61
7202	0.043	6.88

***Table S4**: Reaction data and linearization by general procedure 3. $[TMSBr]_0$ = 0.1 M.*

Lewis Acid	TMSI	1 equiv
k	0.00317	
krel	1.210	
Time (s)	**[4] (M)**	**1/(1-F)**
0	0.000	1.00
30	0.003	1.07
60	0.007	1.17
120	0.013	1.35
180	0.018	1.57
300	0.025	1.97
450	0.030	2.48
600	0.033	3.02
960	0.037	3.83
1200	0.038	4.03
1500	0.037	3.85
1800	0.038	4.25
2700	0.038	4.27
3600	0.038	4.15
5400	0.039	4.42

***Table S5**: Reaction data and linearization by general procedure 3. $[TMSI]_0$ = 0.1 M.*

Lewis Acid	TMSOTf	1 equiv
k	0.00296	
krel	1.128	
Time (s)	**[4] (M)**	**1/(1-F)**
0	0.000	1.00
30	0.003	1.07
60	0.007	1.16
120	0.013	1.36
180	0.018	1.55
300	0.023	1.88
450	0.028	2.24
600	0.030	2.52
960	0.033	2.91
1200	0.033	2.97
1500	0.034	3.08
1800	0.034	3.16
2700	0.035	3.24
3600	0.034	3.22
5400	0.034	3.19

***Table S5**: Reaction data and linearization by general procedure 3. $[TMSOTf]_0 = 0.1$ M.*

Lewis Acid	TESBr	1 equiv
k	0.00088	
krel	0.335	
Time (s)	**[4] (M)**	**1/(1-F)**
0	0.000	1.00
30	0.002	1.03
60	0.002	1.05
120	0.005	1.10
180	0.007	1.15
300	0.011	1.27
450	0.015	1.41
600	0.018	1.56
960	0.023	1.87
1200	0.027	2.21
1500	0.030	2.51
1800	0.032	2.84
2700	0.036	3.53
3600	0.037	3.85
5400	0.038	4.05

***Table S6**: Reaction data and linearization by general procedure 3. $[TESBr]_0 = 0.1$ M.*

Lewis Acid	TMSBr	2 equiv
k	0.0044	
krel	1.676	
Time (s)	**[4] (M)**	**1/(1-F)**
0	0.000	1.00
30	0.005	1.11
60	0.010	1.24
120	0.016	1.47
180	0.021	1.75
300	0.029	2.38
450	0.035	3.39
600	0.039	4.73
900	0.045	10.23
1200	0.048	32.81
1500	0.051	-70.94

***Table S7**: Reaction data and linearization by general procedure 3. $[TMSBr]_0 = 0.2$ M.*

Lewis Acid	TMSCl	1 equiv
k	0.00024	
krel	0.091	
Time (s)	**[4] (M)**	**1/(1-F)**
0	0.000	1.00
30	0.001	1.02
60	0.001	1.02
120	0.002	1.04
180	0.002	1.05
300	0.004	1.08
450	0.005	1.12
600	0.007	1.15
900	0.010	1.24
1200	0.013	1.34
1500	0.015	1.44
1800	0.017	1.53
2700	0.023	1.84
3600	0.026	2.06
5400	0.031	2.59

***Table S8**: Reaction data and linearization by general procedure 3. $[TMSCl]_0 = 0.1$ M.*

Lewis Acid	TESCl	1 equiv
k	0.000031	
krel	0.012	
Time (s)	**[4] (M)**	**1/(1-F)**
0	0.000	1.00
30	0.000	1.00
60	0.000	1.00
120	0.000	1.01
180	0.000	1.01
300	0.000	1.01
450	0.001	1.01
600	0.001	1.02
960	0.001	1.02
1200	0.001	1.03
1500	0.001	1.03
1800	0.002	1.03
2700	0.002	1.05
3600	0.003	1.07
5400	0.005	1.12

Table S9: Reaction data and linearization by general procedure 3. $[TESCl]_0 = 0.1$ M.

Lewis Acid	TBSCl	1 equiv
k	0.0000049	
krel	0.002	
Time (s)	**[4] (M)**	**1/(1-F)**
0	0.000	1.00
300	0.000	1.00
600	0.000	1.00
900	0.000	1.00
1800	0.000	1.01
2700	0.000	1.01
3600	0.001	1.01
5400	0.001	1.02
7200	0.001	1.03
9000	0.002	1.03
10860	0.002	1.05
12600	0.002	1.05
14400	0.003	1.07
18000	0.004	1.10

***Table S10**: Reaction data and linearization by general procedure 3. $[TBSCl]_0$ = 0.1 M.*

Lewis Acid	MnCl2	1 equiv
k	0.000094	
krel	0.036	
Time (s)	**[4] (M)**	**1/(1-F)**
0	0.000	1.00
30	0.000	1.01
60	0.001	1.01
120	0.001	1.02
180	0.001	1.02
300	0.002	1.03
450	0.002	1.05
600	0.003	1.07
900	0.004	1.10
1200	0.006	1.13
1500	0.007	1.15
1800	0.007	1.18
2700	0.010	1.26
3600	0.013	1.35
5400	0.016	1.49

***Table S11**: Reaction data and linearization by general procedure 3. $[MnCl_2]_0$ = 0.1 M.*

Lewis Acid	MgBr2(OEt2)	1 equiv
k	0.00044	
krel	0.147	
Time (s)	**[4] (M)**	**1/(1-F)**
0	0.000	1.00
30	0.001	1.02
60	0.001	1.02
120	0.002	1.05
180	0.004	1.08
300	0.006	1.13
450	0.008	1.20
600	0.011	1.27
900	0.014	1.39
1200	0.016	1.47
1500	0.017	1.53
1800	0.019	1.59
2700	0.019	1.59
3600	0.019	1.64
6300	0.020	1.67
9000	0.021	1.70

***Table S12**: Reaction data and linearization by general procedure 3. $[MgBr_2 \cdot OEt_2]_0 = 0.1$ M.*

Lewis Acid	Sc(OTf)3	1 equiv
k	0.00038	
krel	0.127	
Time (s)	**[4] (M)**	**1/(1-F)**
0	0.000	1.00
30	0.001	1.02
60	0.002	1.03
120	0.003	1.06
180	0.004	1.08
300	0.006	1.14
450	0.008	1.20
600	0.010	1.25
900	0.013	1.36
1200	0.016	1.47
1500	0.018	1.57
1800	0.021	1.72
2700	0.026	2.07
3600	0.030	2.51
5400	0.036	3.70

***Table S13**: Reaction data and linearization by general procedure 3. $[Sc(OTf)_3]_0 = 0.1$ M.*

Lewis Acid	LiBr	1 equiv
k	0.000043	
krel	0.014	
Time (s)	**[4] (M)**	**1/(1-F)**
0	0.000	1.00
30	0.000	1.01
60	0.000	1.01
120	0.000	1.01
180	0.000	1.01
300	0.001	1.01
450	0.001	1.02
600	0.001	1.02
900	0.002	1.04
1200	0.002	1.05
1500	0.003	1.06
1800	0.003	1.07
2700	0.005	1.12
3600	0.007	1.15
5400	0.010	1.26
7200	0.013	1.35

***Table S14**: Reaction data and linearization by general procedure 3. $[LiBr]_0$ = 0.1 M.*

Lewis Acid	ZnI2	1 equiv
k	0.000037	
krel	0.012	
Time (s)	**[4] (M)**	**1/(1-F)**
0	0.000	1.00
30	0.001	1.01
60	0.001	1.02
120	0.001	1.02
180	0.002	1.03
300	0.002	1.04
450	0.002	1.05
600	0.003	1.06
900	0.003	1.07
1200	0.004	1.08
1500	0.004	1.09
1800	0.004	1.10
2700	0.005	1.12
3600	0.006	1.14
5400	0.007	1.17
7200	0.008	1.19

***Table S15**: Reaction data and linearization by general procedure 3. $[ZnI_2]_0$ = 0.1 M.*

Lewis Acid	TMSBr, NaI	1 equiv, 0.5 equiv
k	0.0046	
krel	1.533	
Time (s)	**[4] (M)**	**1/(1-F)**
0	0.000	1.00
30	0.004	1.09
60	0.008	1.20
120	0.015	1.43
180	0.020	1.69
300	0.028	2.24
450	0.033	2.96
600	0.037	3.79
900	0.038	4.01
1200	0.039	4.68
1500	0.040	5.11
1800	0.040	4.98
2700	0.041	5.60
3600	0.041	5.76
5400	0.042	6.07

***Table S16**: Reaction data and linearization by general procedure 3. $[TMSBr]_0$ = 0.1 M, $[NaI]_0$ = 0.05 M.*

Lewis Acid	TMSCl, NaI	1 equiv, 1 equiv
k	0.000549	
krel	0.209	
Time (s)	**[4] (M)**	**1/(1-F)**
0	0.000	1.00
30	0.001	1.02
60	0.002	1.04
120	0.003	1.07
180	0.004	1.10
300	0.007	1.16
450	0.009	1.23
600	0.012	1.31
960	0.015	1.43
1200	0.018	1.58
1500	0.021	1.72
1800	0.022	1.76
2700	0.026	2.07
3600	0.028	2.28
5400	0.031	2.65
7200	0.034	3.10

***Table S17**: Reaction data and linearization by general procedure 3. $[TMSCl]_0$ = 0.1 M, $[NaI]_0$ = 0.1 M.*

Lewis Acid	TESCl, NaI	1 equiv, 1 equiv
k	0.000068	
krel	0.026	
Time (s)	**[4] (M)**	**1/(1-F)**
0	0.000	1.00
30	0.000	1.00
60	0.000	1.01
120	0.001	1.01
180	0.001	1.02
300	0.001	1.02
450	0.002	1.03
600	0.002	1.04
1200	0.003	1.06
1500	0.003	1.06
1800	0.003	1.07
2700	0.004	1.09
3600	0.006	1.13
5400	0.008	1.18
7200	0.010	1.25

***Table S18**: Reaction data and linearization by general procedure 3. $[TESCl]_0$ = 0.1 M, $[NaI]_0$ = 0.1 M.*

Lewis Acid	TBSCl, NaI	1 equiv, 1 equiv
k	0.000032	
krel	0.012	
Time (s)	**[4] (M)**	**1/(1-F)**
0	0.000	1.00
30	0.000	1.00
60	0.000	1.00
120	0.000	1.01
180	0.000	1.01
300	0.000	1.01
450	0.001	1.01
600	0.001	1.01
900	0.001	1.02
1200	0.001	1.02
1500	0.001	1.02
1800	0.001	1.03
2700	0.002	1.03
3600	0.002	1.04
5400	0.003	1.06
7200	0.003	1.07

***Table S19:** Reaction data and linearization by general procedure 3. [TBSCl]0 = 0.1 M, [NaI]0 = 0.1 M.*

3.4.4.2 Comparison of 1a and 2a Activation Rates by L1NiCl₂

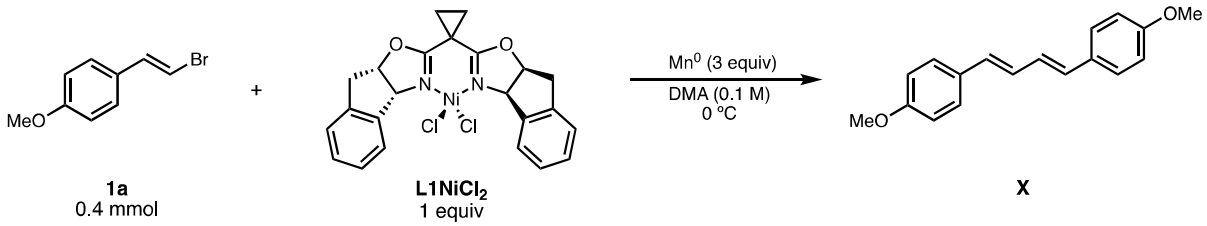

1a
0.4 mmol

L1NiCl₂
1 equiv

X

Reaction of L1·NiCl₂ with 1a: To an oven-dried 10 mL round bottom flask with a stir bar was added (*E*)-1-(2-bromovinyl)-4-methoxybenzene **1a** (85.2 mg, 0.40 mmol, 1 equiv) and Mn^0 powder (65.9 mg, 1.2 mmol, 3 equiv). In a 2-dram oven-dried vial with a stir bar was added **L1**$NiCl_2$ (1.1 times the needed amount, 213.4 mg, 0.44 mmol, 1.1 equiv). The flask and vial were then brought into a N_2-filled glovebox where 4.4 mL of DMA was added to the vial and the contents were stirred until homogenous to make a 0.1 M stock solution of **L1**·$NiCl_2$. To the flask was then added *n*-dodecane (target: 40 μL, 0.176 mmol, 0.44 eqiuv, actual mass was recorded for each experiment) internal standard was added followed by 4 mL of the **L1**·$NiCl_2$ stock solution. The flask was then sealed with a septa and electrical tape then removed from the glovebox where it was placed under N_2 and submerged in an ice bath. A ~50 μL aliquot of the solution was removed with a N_2-purged syringe then pushed through a SiO_2 plug and eluted with 10% EtOAc:hexanes into a GC vial then further diluted with EtOAc. Once cooled, the solution was then stirred at 1500 rpm to start the reaction (t = 0). The reaction was then aliquoted with the same procedure previously described at regular intervals.

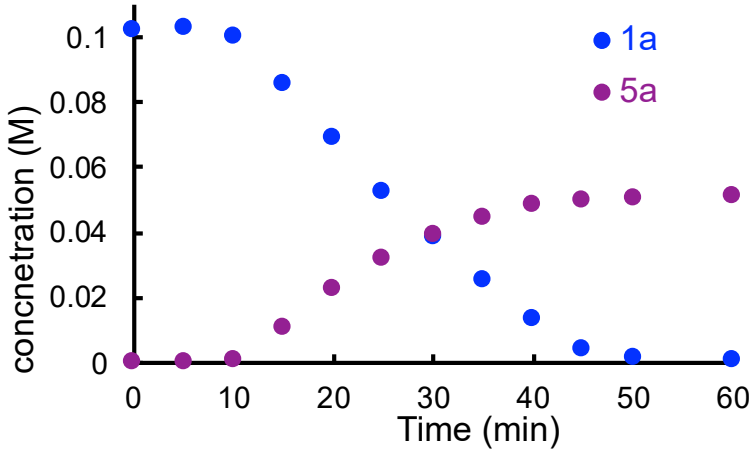

Reaction:	**1a** with **L1**NiCl2	
Time (min)	[1**a**] (M)	[**5a**] (M)
0	0.1025	0.0000
5	0.1030	0.0000
10	0.1003	0.0007
15	0.0859	0.0108
20	0.0689	0.0227
25	0.0528	0.0322
30	0.0388	0.0396
35	0.0255	0.0450
40	0.0134	0.0487
45	0.0043	0.0497
50	0.0014	0.0506
60	0.0007	0.0510

***Figure S29**: Reaction profile and tabulated data of stoichiometric reaction between **L1**·$NiCl_2$ and **1a**.*

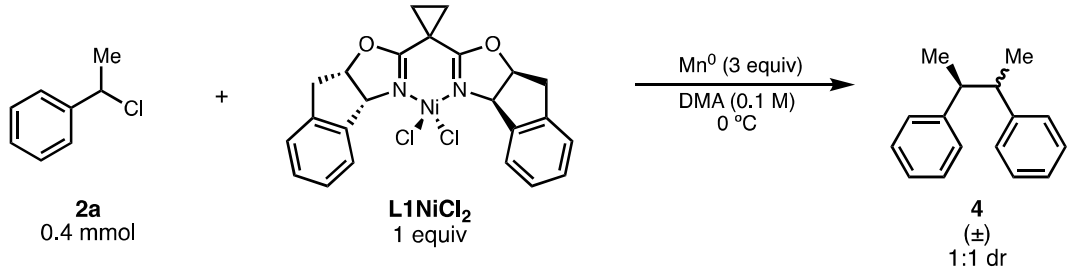

Reaction of L1·$NiCl_2$ with 2a: To an oven-dried 10 mL round bottom flask with a stir bar was added Mn^0 powder (65.9 mg, 1.2 mmol, 3 equiv). In a 2-dram oven-dried vial with a stir bar was added **L1**·$NiCl_2$ (1.1 times the needed amount, 213.4 mg, 0.44 mmol, 1.1 equiv). The flask and vial were then brought into a N_2-filled glovebox where 4.4 mL of DMA was added to the vial and the contents were stirred until homogenous to make a 0.1 M stock solution of **L1**$NiCl_2$. To the flask was added (1-Chloroethyl)benzene **2a** (53.1 µL, 0.40 mmol, 1 equiv) and *n*-dodecane (target: 40 µL, 0.176 mmol, 0.44 equiv, actual mass was recorded for each experiment) internal standard. The **L1**·$NiCl_2$ (4 mL) stock solution was then added to the flask before it was sealed with a septa and electrical tape then removed from the glovebox where it was placed under N_2 and submerged in an ice bath. A

~50 µL aliquot of the solution was removed with a N_2-purged syringe then pushed through a SiO_2 plug and eluted with 10% EtOAc:hexanes into a GC vial then further diluted with EtOAc. Once cooled, the solution was then stirred at 1500 rpm to start the reaction (t = 0). The reaction was then aliquoted with the same procedure previously described at regular intervals.

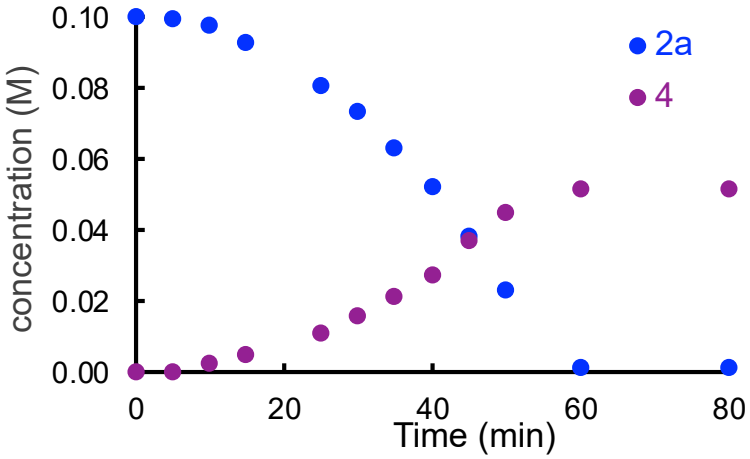

Reaction:	**2a** with **L1**NiCl2	
Time (min)	[**2a**] (M)	[**4**] (M)
0	0.0998	0.0000
5	0.0987	0.0000
10	0.0971	0.0021
15	0.0921	0.0046
25	0.0804	0.0108
30	0.0728	0.0153
35	0.0628	0.0210
40	0.0516	0.0272
45	0.0381	0.0367
50	0.0228	0.0446
60	0.0013	0.0511
80	0.0008	0.0513

***Figure S30**: Reaction profile and tabulated data of stoichiometric reaction between **L1**·$NiCl_2$ and **2a**.*

Overlaid Reaction Profiles and Simulated Profiles

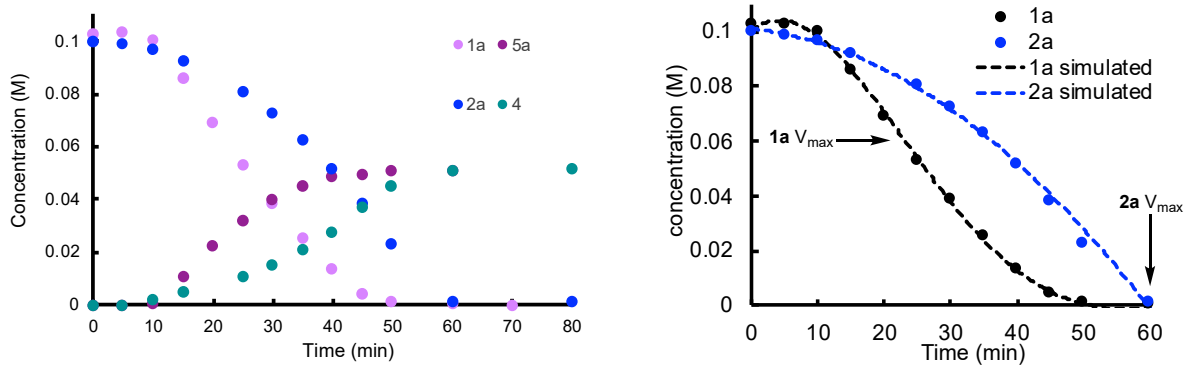

***Figure S31**: Left: Overlaid reaction profiles from the stoichiometric reaction of **L1**·$NiCl_2$ with **1a** and **2a** to compare the relative rates of electrophile activation. Right: Simulated reaction profiles to get relative rates.*

Estimating k_{rel} for 1a and 2a Activation

To estimate the relative rates of **1a** and **2a** activation the concentration profiles were fitted with an appropriate n^{th}-order polynomial. The simulated profile from these equations (Figure S31, right) were then derived with the power rule to obtain an expression for d[**1a**]/dt and d[**2a**]/dt. Comparing the rates at 15% conversion gives a **1a**:**2a** k_{rel} = 4.1 whereas comparison of the maximum rates (V_{max}) gives a **1a**:**2a** k_{rel} = 1.3. These values are reasonable based on the reaction kinetic data that shows **1a** activation is faster yet **2a** is competitive at higher concentrations of **2a**.

3.4.4.3 Catalyst-Mediated 1a Activation Control Experiments

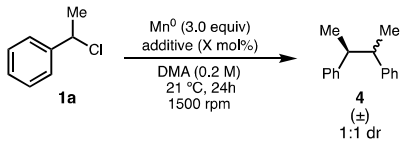

additive	4 yield %
NA	ND
NaI (50 mol%)	< 5
$MnCl_2$ (10 mol%)	ND
L1$NiCl_2$ (10 mol%)	82
$NiCl_2$·dme (10 mol%)	63
L1 (10 mol%)	ND

Procedure for Control Experiments: To an oven dried 1 dram vial with a stir bar was added Mn^0 powder (8.2 mg, 0.15 mmol, 3 equiv). The vial was then brought into a N_2-filled glovebox where (1-chloroethyl)benzene **2a** (6.6 µL, 0.050 mmol, 1 equiv), *n*-dodecane internal standard, and the respective additive (if applicable) was added. DMA (0.25 mL, 0.2 M) was then added to the vial before it was sealed with a teflon-lined cap and removed from the glovebox. The reactions were allowed to stir at ambient temperature for 24h at 1500 rpm. Upon completion the crude reaction mixture was filtered through SiO_2 plug and eluted with 10% EtOAc:hexanes into a GC vial then further diluted with EtOAc, then analyzed by GC-FID. Reaction were run in duplicate and no other **2a**-derived byproducts (other than **4**) were detected.

These control experiments show that Ni is required for **2a** activation meaning a reductant-mediated activation pathway, like **2b**, is unlikely.

3.4.5 Cyclic Voltammetry Experiments

General Details: Cyclic voltammograms were obtained in a N_2-filled glovebox using a standard three electrode cell consisting of a freshly polished (0.3 μm then 0.05 μm alumina) glassy carbon working electrode, platinum counter electrode, and a silver wire non-aqueous reference electrode containg a 10 mM $AgNO_3$, 0.1 M $TBAPF_6$, MeCN filling solution. Data were collected using a Biologic SP-300 potentiostat and analyzed in EC-Lab. All cyclic voltammograms were measured in DMA with 0.1 M $TBAPF_6$ or 0.1 M $TBAClO_4$ supporting electrolyte and then referenced to freshly sublimed ferrocene (Fc). $TBAPF_6$ was recrystallized from boiling absolute ethanol and stored in a N_2-filled gloveox. The reduction potentials are reported versus the reduction potential of the Fc/Fc^+ peak. Ohmic drop compensation was done with all samples before each scan using positive-feedback iR-compensation at 85% of uncompensated resistance (R_u) measured from potentio electrochemical impedence spectroscopy (PEIS). The first scan is shown in the following section and the main text unless otherwise specified.

3.4.5.1 CVs of L1NiX2 complexes, 2b, and TDAE

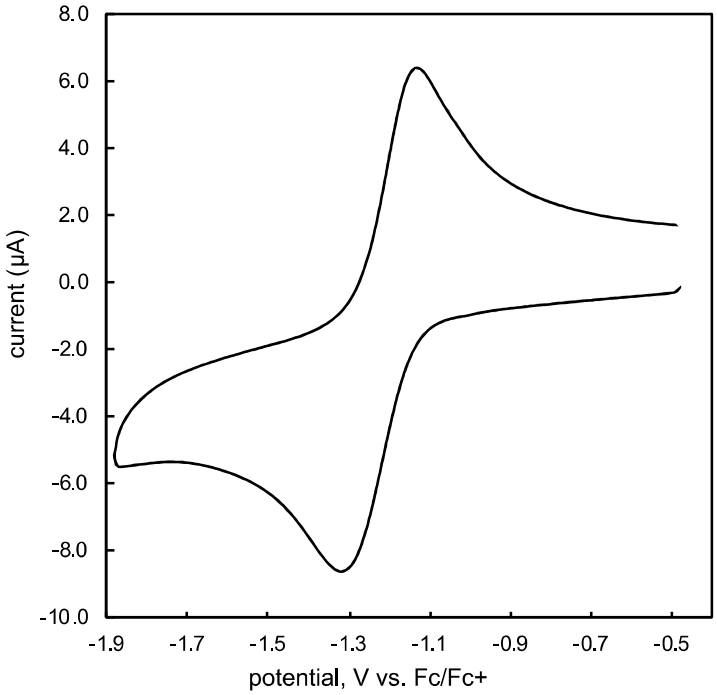

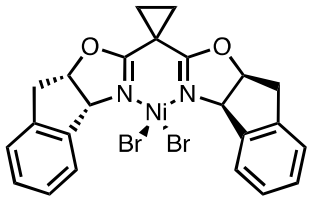

Analyte	**L1**NiBr2
Epc (Fc/Fc+)	– 1.32 V
Epc/2 (Fc/Fc+)	– 1.23 V
Epa (Fc/Fc+)	– 1.05 V

Figure S32*: Voltammogram of 1 mM L1·NiBr2 in DMA with 0.1 M TBAPF6 supporting electrolyte, v = 100 mV/s.*

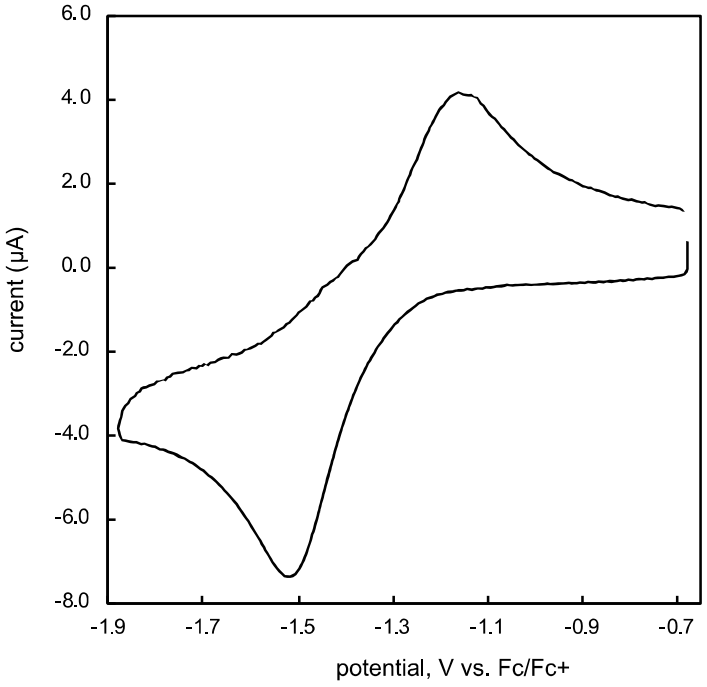

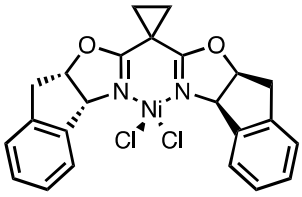

Analyte	**L1**NiCl2
Epc (Fc/Fc+)	– 1.52 V
Epc/2 (Fc/Fc+)	– 1.47 V
Epa (Fc/Fc+)	– 1.17 V

***Figure S33**: Voltammogram of 1 mM L1·NiCl2 in DMA with 0.1 M TBAPF6 supporting electrolyte, v = 100 mV/s.*

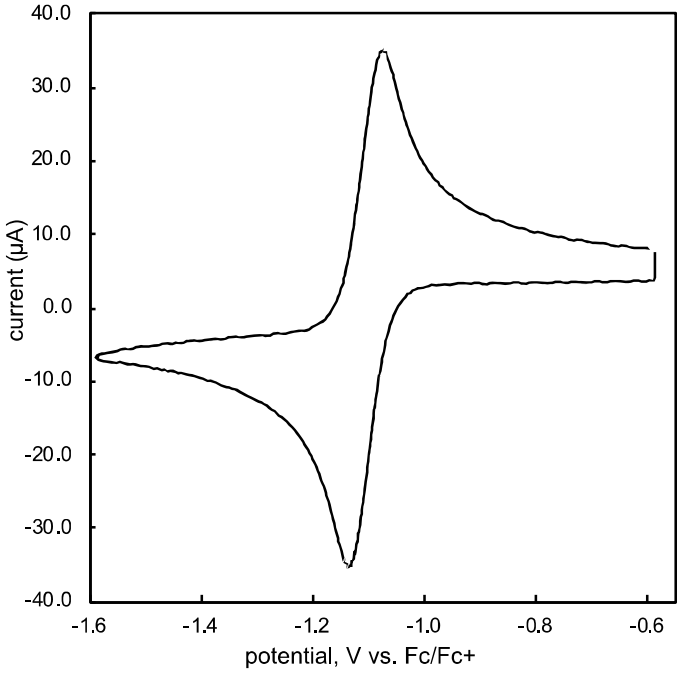

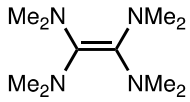

Analyte:	TDAE
E1/2(Fc/Fc+)	-1.11 V

***Figure S34**: Voltammogram of 1 mM TDAE in DMA with 0.1 M $TBAPF_6$ supporting electrolyte, v = 100 mV/s.*

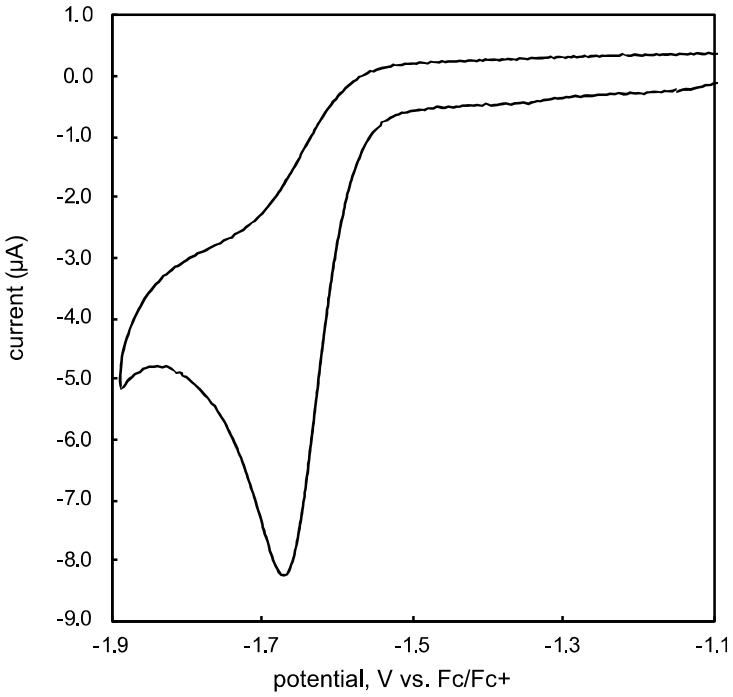

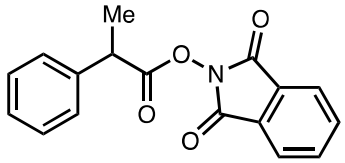

Analyte:	**2b**
Ep (Fc/Fc+)	-1.67 V
Ep/2 (Fc/Fc+)	-1.61 V

***Figure S35**: Voltammogram of 1 mM **2b** in DMA with 0.1 M $TBAPF_6$ supporting electrolyte, v = 100 mV/s.*

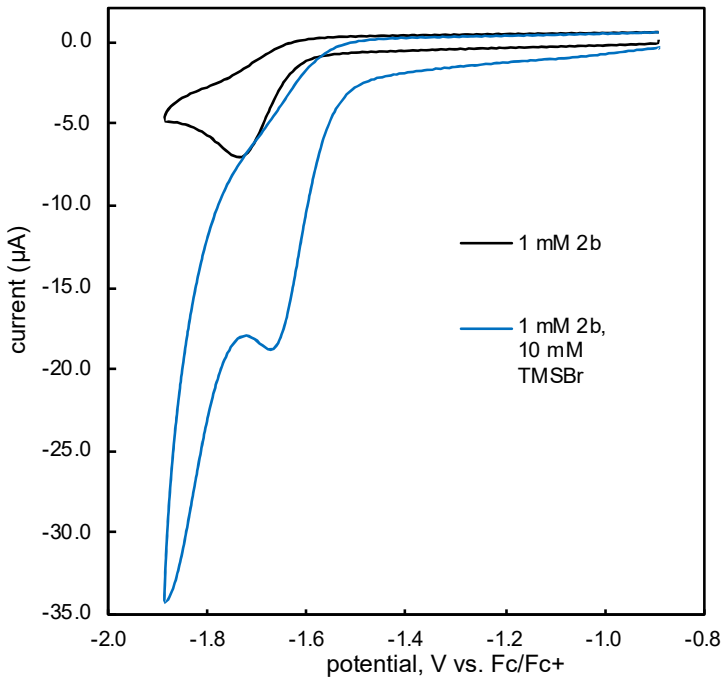

Figure S36: *Effect of TMSBr on* ***2b*** *reduction. 1 mM* ***2b*** *and 10 mM TMSBr in DMA with 0.1 M $TBAClO_4$ supporting electrolyte, v = 100 mV/s.*

3.4.5.2 Substrate Titration and Catalytic Current Comparison

Procedure for Substrate Titration for Current response of L1·$NiCl_2$: For these experiments CVs were taken of 1 mM **L1**·$NiCl_2$ followed by the addition of an appropriate amount of **1a** or **2a** was added for subsequent scans. At the end of each titration the substrate that was not previously titrated in was then added in equimolar amounts.

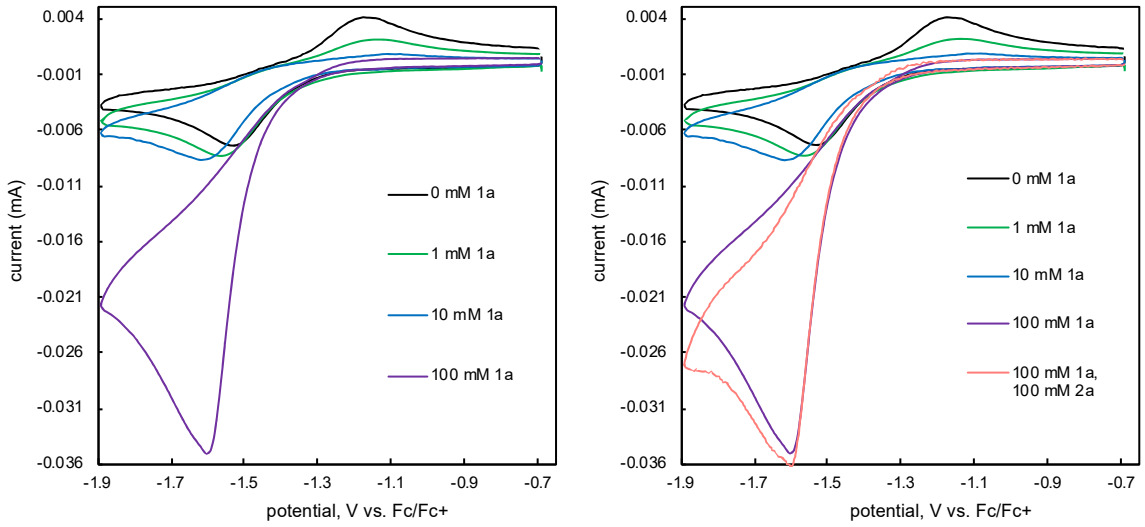

Figure S37: *CV of 1 mM* ***L1***·$NiCl_2$ *with increasing concentrations of* ***1a*** *(left) and subsequent addition of 100 mM* ***2a*** *(right). CVs run in DMA with0.1 M $TBAPF_6$ supporting electrolyte, v = 100 mV/s.*

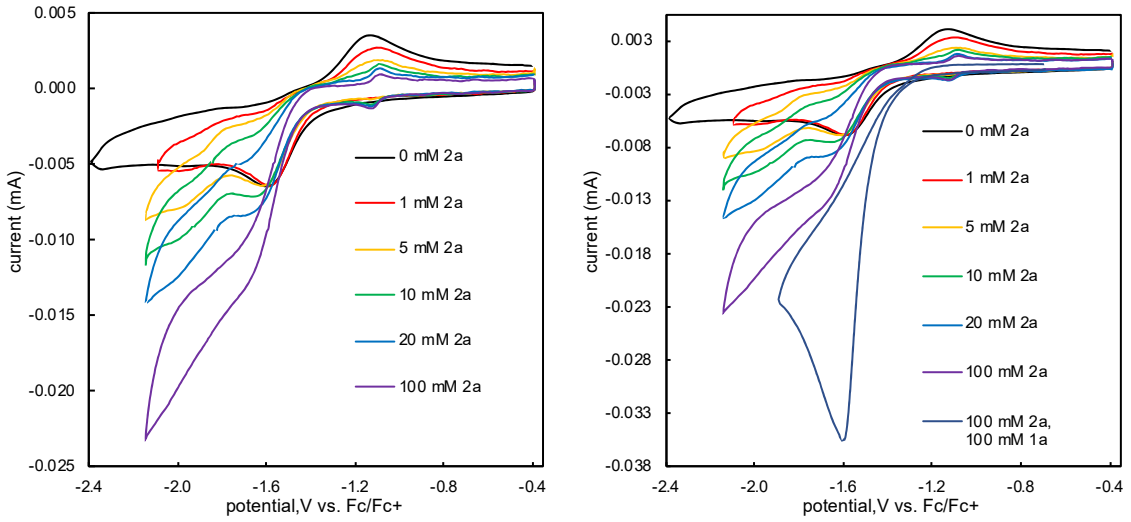

Figure S38: *CV of 1 mM **L1**·$NiCl_2$ with increasing concentrations of **2a** (left) and subsequent addition of 100 mM **1a** (right). CVs run in DMA with 0.1 M $TBAPF_6$ supporting electrolyte, v = 100 mV/s.*

3.4.6 NMR Reaction Monitoring

3.4.6.1 ^{19}F NMR Reaction Monitoring

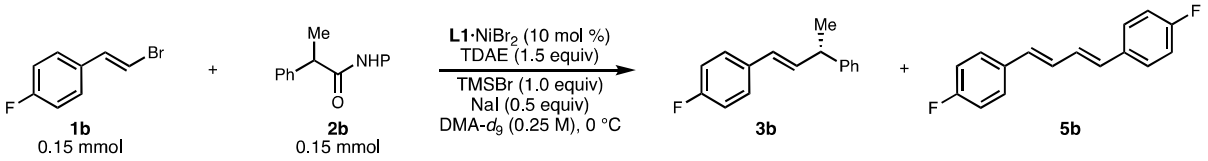

General procedure for ^{19}F Reaction Monitoring: In a N_2-filled glovebox (*E*)-1-(2-bromovinyl)-4-fluorobenzene **1b** (30.2 mg, 0.15 mmol, 1 equiv), 1,3-dioxoisoindolin-2-yl 2-phenylpropanoate **2b** (44.3 mg, 0.15 mmol, 1 equiv), **L1**$NiBr_2$ (8.6 mg, 0.015 mmol, 0.1 equiv), NaI (11.2 mg, 0.075 mmol, 0.5 equiv), and hexafluorobenzene internal standard were added to a dry 1 dram vial with a stir bar. The contents were then dissolved in 0.3 mL of DMA-d^9 then transferred to a dry J-young NMR tube. The vial was rinsed with 0.3 mL of DMA (0.6 mL final volume, 0.25 M final concentration) to ensure quantitative transfer. The NMR tube was then sealed and removed from the glovebox where it was then cooled

to 0 ºC in the NMR instrument (air bath cooling to 0 ºC). The sample was locked/shimmed and an initial quantitative ^{19}F NMR measurement was taken in order to determine starting concentration. The tube was then removed from the instrument, submerged in an ice bath, fitted with a septa, and Ar balloon. The tube was opened then TMSBr (19.8 uL, 0.15 mmol, 1 equiv) was added via syringe and the tube was agitated to ensure adequate mixing. After 30 seconds TDAE (52.3 μL, 0.225 mmol, 1.5 equiv) was added to start the reaction and the tube was immediately sealed, placed back in the NMR instrument, and qNMR (single scan, 27s interscan delay) scans (measured 3 minute delay from TDAE addition to completion of first measurement). Measurements were taken every 30 seconds for the first 3 hours of the reaction and then every minute for the next 3 hours (6 hours total). At the end of the reaction the product was isolated to determine ee of **3b** as 93% by SFC analysis (OJ-H, 7% IPA:CO_2, t_{major} = 7.07 min, t_{minor}=5.86 min).[37]

Modifications to General Procedure for 20 mol % Catalyst Loadings: For this experiment more **L1**$NiBr_2$ (17.2 mg, 0.030 mmol, 0.2 equiv) added to 1 dram vial. The delay between TDAE addition and the first scan was shortened to one minute instead of three minutes. Scan taken every one minute for the entire experiment and the reaction was monitored for 5 hours total.

Representative Spectra (full window):

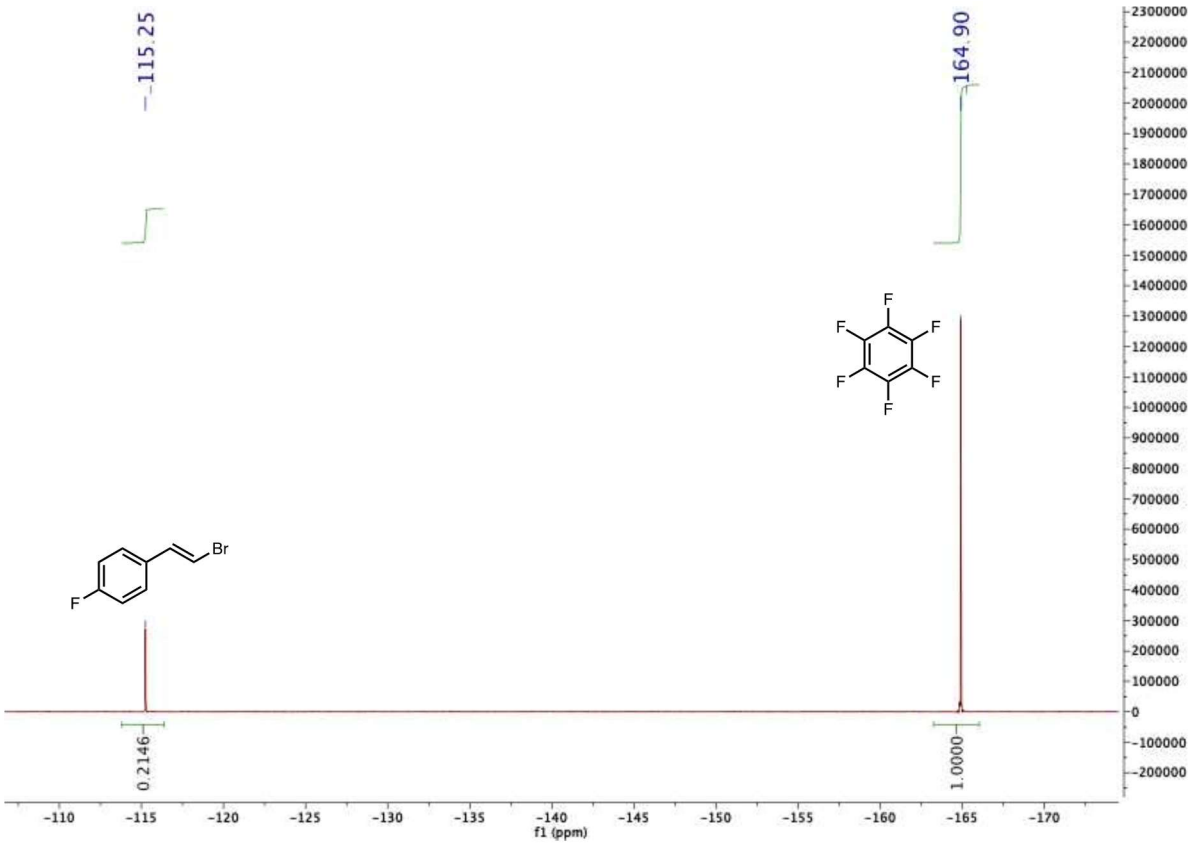

Figure S39: *^{19}F NMR full window view of reaction mixture before TDAE is added.*

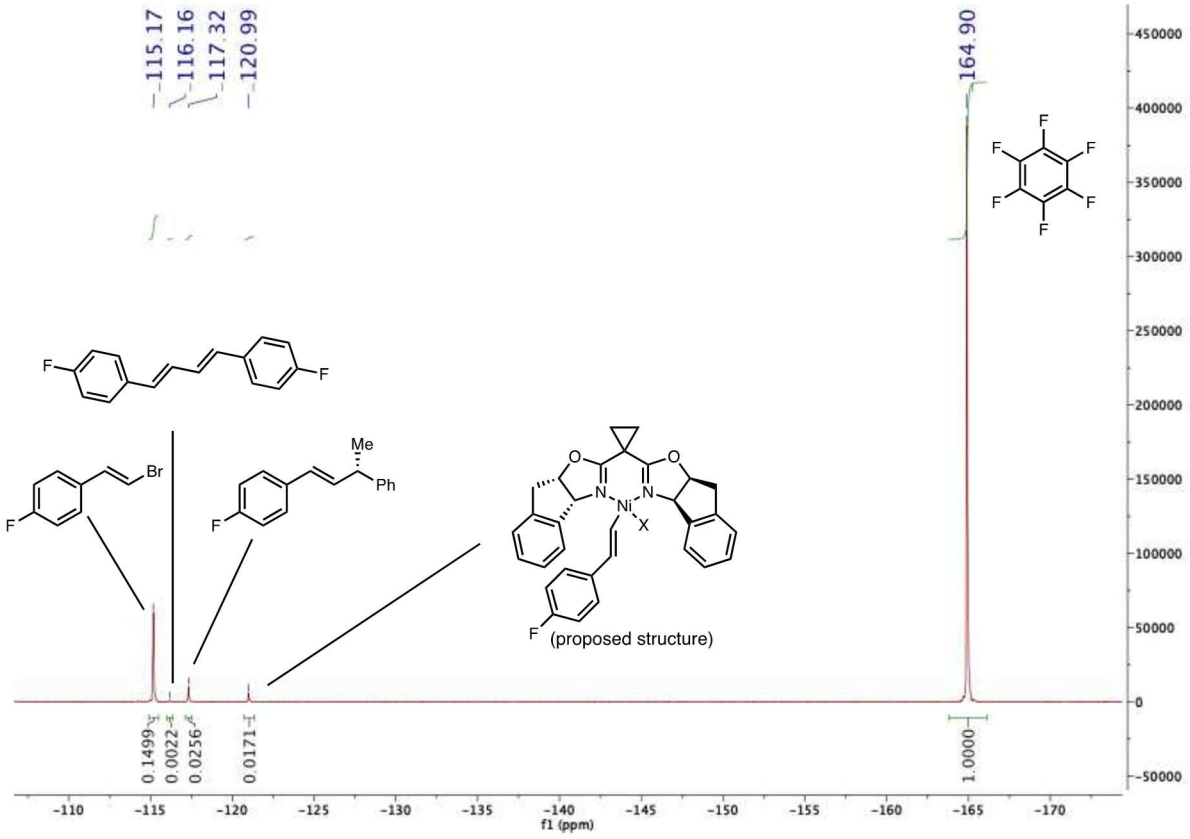

Figure S40: *^{19}F NMR full window view of reaction mixture 3 minutes after TDAE was added.*

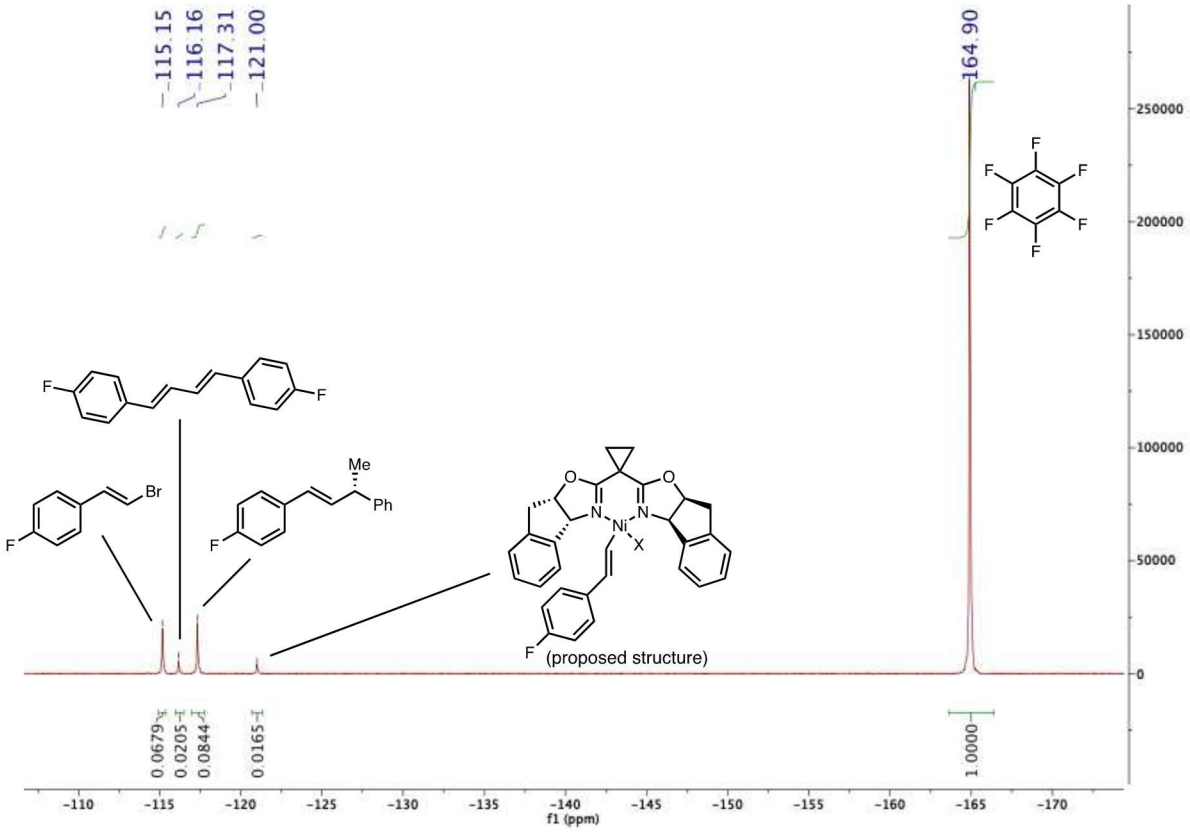

Figure S41: *^{19}F NMR full window view of reaction mixture 3 hours after TDAE was added.*

Independently prepared, C_6F_6-referenced (C_6F_6 = -164.9 ppm) NMR characterization in $CDCl_3$ of possible **1b**-derived species. This includes species like 4-fluorostyrene and **1b-I** that were not observed in the reaction mixture. It is noteworthy that while the absolute chemical shifts of independently prepared species in $CDCl_3$ are different than those observed in the reaction mixture in DMA-d_9 (Figure S39-41), the relative shifts are the same (Table S20).

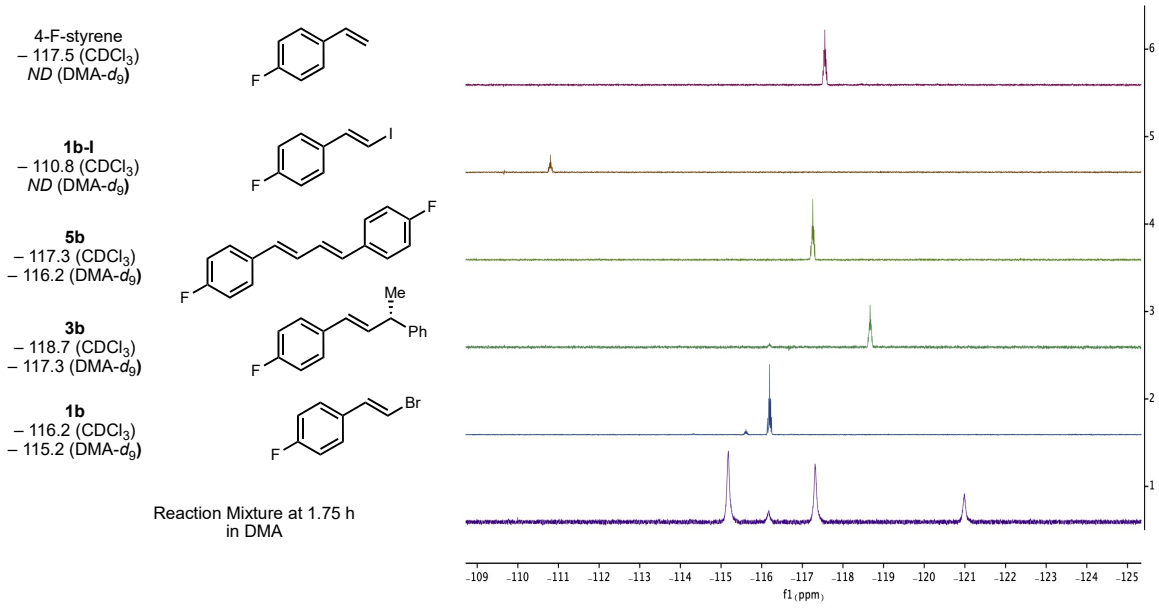

Figure S42: *^{19}F chemical shifts for reaction components and potential byproducts. No species corresponds to observed intermediate that is previously assigned to resting state species. Reported shifts are referenced such that C_6F_6 =-164.9 ppm.*

	4-F-styrene	**1b-I**	**5b**	**3b**	**1b**	Resting State
CDCl3 (ppm)	-117.5	-110.8	-117.3	-118.7	-116.2	ND
DMA-d9 (ppm)	ND	ND	-116.2	-117.3	-115.2	-120.99
Δ to **1b** ppm (CDCl3)	-1.3	5.4	-1.1	-2.5	0	–
Δ to 1b ppm (DMA-d9)	–	–	-1	-2.1	0	-5.79

Table S20: *Tabulated ^{19}F NMR shifts in $CDCl_3$ and DMA-d_9 as well as the relative shifts compared to **1b**.*

Δ to C_6F_6 (DMA)	**1b**	**5b**	**7b**
Observed	51.00	50.00	45.00
DFT Predicted	47.00	46.00	37.00

Table S21: *Comparison between observed and DFT predicted ^{19}F chemical shifts.*

Processed Reaction Data:

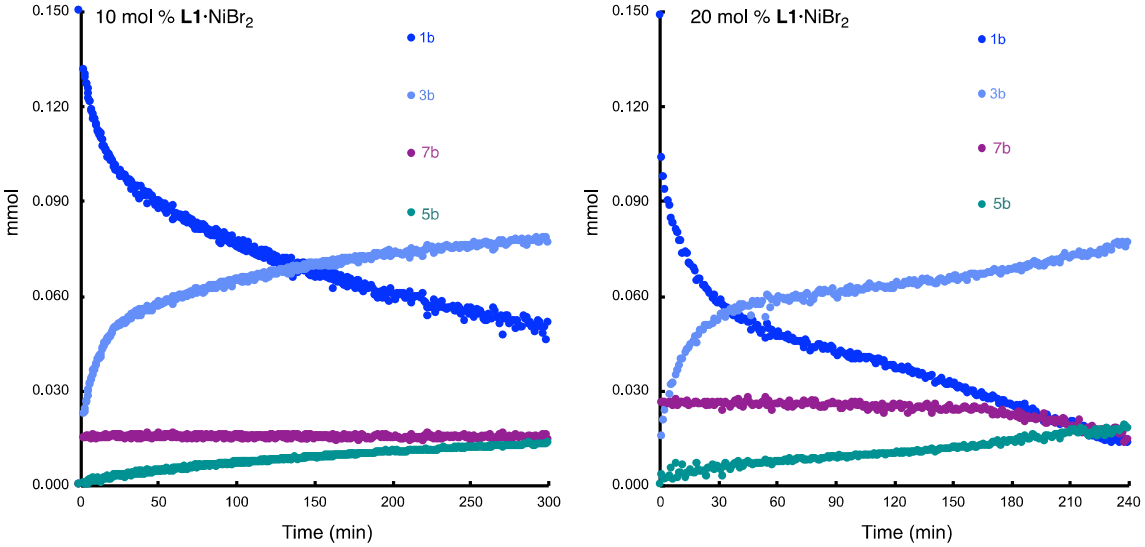

Figure S43: *Quantified amount of each species for ^{19}F time courses shown in main text.*

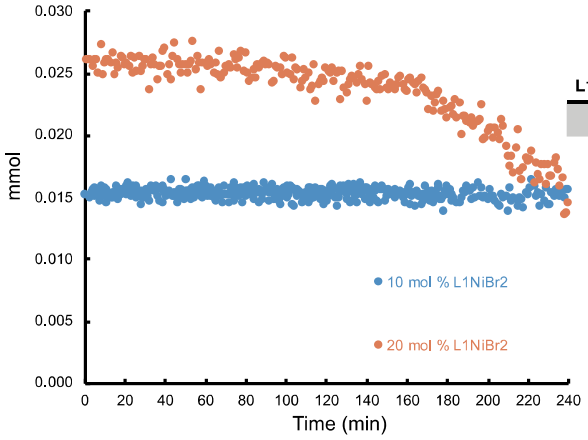

L1$NiBr_2$ loading	Avg **L1**$NiBr_2$ (mmol/mol %)	Std Dev (mmol)	Period Used for Avg
10 mol %	0.015 / 10.1	0.0005	3 min – 5 h
20 mol %	0.025 / 16.9	0.0008	1 min – 2 h

Figure S44: *Comparison of resting state concentration for experiments starting with 10 mol % and 20 mol % **L1**·$NiBr_2$. Table showing calculation of average amount of the proposed resting state species.*

3.4.6.2 Room Temperature ^{19}F NMR

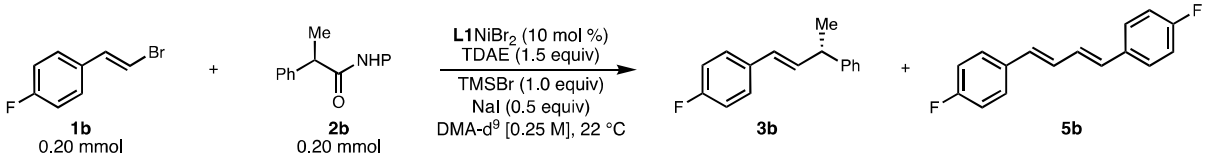

Ambient Temperature NMR Reaction: In a N_2-filled glovebox (*E*)-1-(2-bromovinyl)-4-fluorobenzene **1b** (40.2 mg, 0.20 mmol, 1 equiv), 1,3-dioxoisoindolin-2-yl 2-phenylpropanoate **2b** (59.1 mg, 0.2 mmol, 1 equiv), **L1**·$NiBr_2$ (11.5 mg, 0.020 mmol, 0.1 equiv), NaI (15.0 mg, 0.10 mmol, 0.5 equiv), and hexafluorobenzene internal standard were added to a dry 1 dram vial with a stir bar. The contents were then dissolved in 0.4 mL of DMA-d_9 then transferred to a dry J-young NMR tube. The vial was rinsed with 0.4 mL of DMA (0.6 mL final volume, 0.25 M final concentration) to ensure quantitative transfer. The NMR tube was then sealed and removed from the glovebox. The sample was locked/shimmed and an initial quantitative ^{19}F NMR measurement was taken in order to determine starting concentration. The tube was then removed from the instrument, fit with a septa, and Ar balloon. To the tube was then added TMSBr (26.4 µL, 0.20 mmol, 1 equiv) was added via syringe and the tube was agitated to ensure adequate mixing. After 30 seconds TDAE (69.8 µL, 0.30 mmol, 1.5 equiv) was added to start the reaction and the tube was immediately sealed, placed back in the NMR instrument and monitored at 22 ºC.

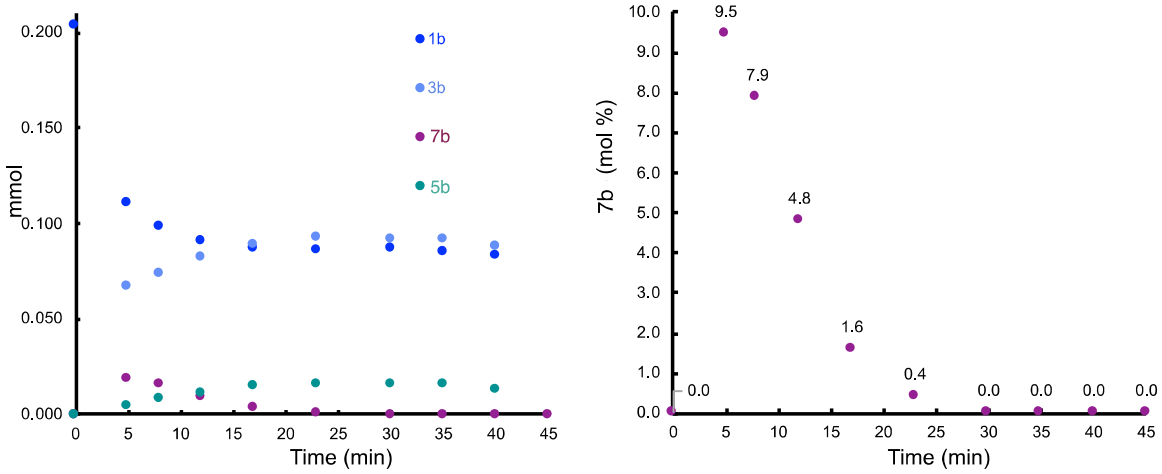

Figure S45: *Concentration of **1b**-derived species over the course of the reaction (left). Concentration of putative resting state species **7b** during the time course (right).*

3.4.7 Electron Paramagnetic Resonance (EPR) Experiments

3.4.7.1 Generation of Ni(I) from Chemical Reduction of L1NiX$_2$

Reduction of L1·NiBr$_2$ by TDAE: To an oven-dried 20 mL was added **L1**·NiBr$_2$ (5.7 mg, 0.010 mmol, 1 equiv). The vial was brought into a N_2-filled glovebox and the solid was dissolved in 10 mL of anhydrous DMA. To this vial TDAE (2.33 uL, 0.010 mmol, 1 equiv) was added. The reaction was stirred for 2 h, after which an aliquot was removed by a syringe, filtered, and transferred to an oven-dried EPR tube. The tube was sealed, removed from the glovebox, and then frozen in LN_2 for analysis by EPR at 77 K.

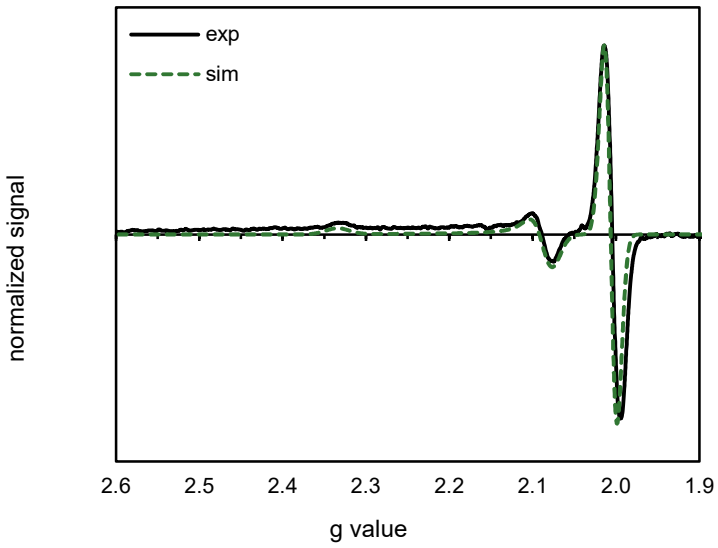

Figure S46: *Observed and simulated spectra of reduction of **L1**·NiBr$_2$ by TDAE. The EPR spectra were collected at 9.371 GHz with a micropower of 2 mW, a modulation amplitude of 4 G, and a conversion time of 40.96 ms. The spectrum shown here was averaged over 4 scans. Nickel signals were simulated with g = [2.078, 2.089, 2.335] with a linewidth of 4 mT. TDAE$^{\bullet+}$ signals were simulated with g_{iso} = 2.0069 with a linewidth of 3 mT. The two species exist in a 1:0.78 ratio.*

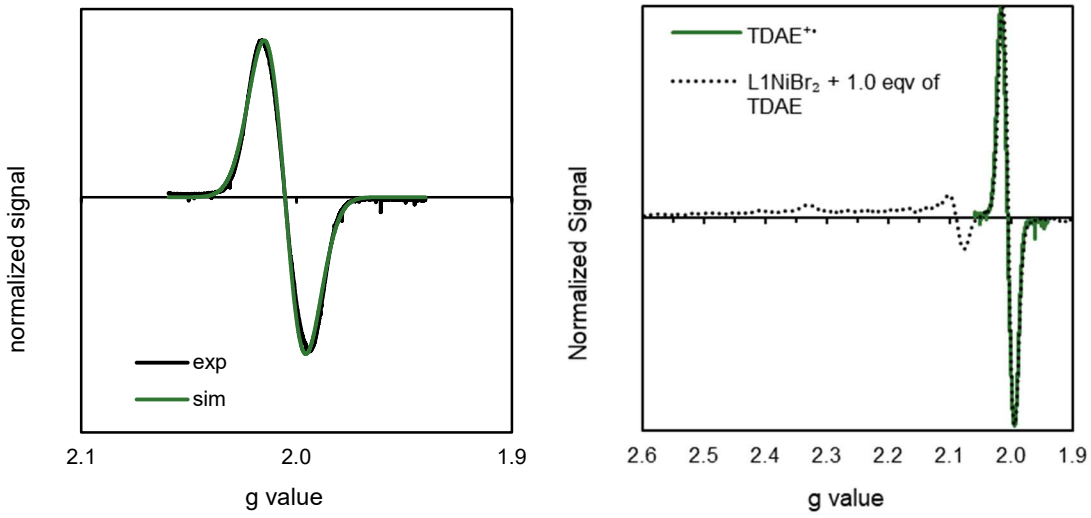

Figure S47: *Observed and simulated spectra of [TDAE]Br (left). Overlay of independent [TDAE]Br and* ***L1****·NiBr$_2$ from Figure S46 (right). The EPR spectra were collected at 9.370 GHz with a micropower of 2 mW, a modulation amplitude of 4 G, and a conversion time of 40.96 ms. The spectrum shown here was averaged over 4 scans. The isotropic signal was simulated with g_{iso} = 2.006 with a linewidth of 3.8 mT prepared by mixing TDAE and isolated*

Reduction of L1·NiBr$_2$ by L1·Ni(cod): In a N_2-filled glovebox Ni(cod)$_2$ (8.3 mg, 0.030 mmol, 1 equiv) and **L1** (10.7 mg, 0.030 mmol, 1 equiv) were added to an oven-dried 20 mL scintillation and dissolved in 7.5 mL of anhydrous DMA. The reaction was stirred for 1.5 h for and then **L1**·NiBr$_2$ (17.2 mg, 0.030 mmol, 1 equiv) was added. After 1 min of stirring, a 300 uL aliquot was removed by a syringe and transferred to an oven-dried EPR tube. The tube was sealed, removed from the glovebox, and then frozen in LN_2 for analysis by EPR at 77 K.

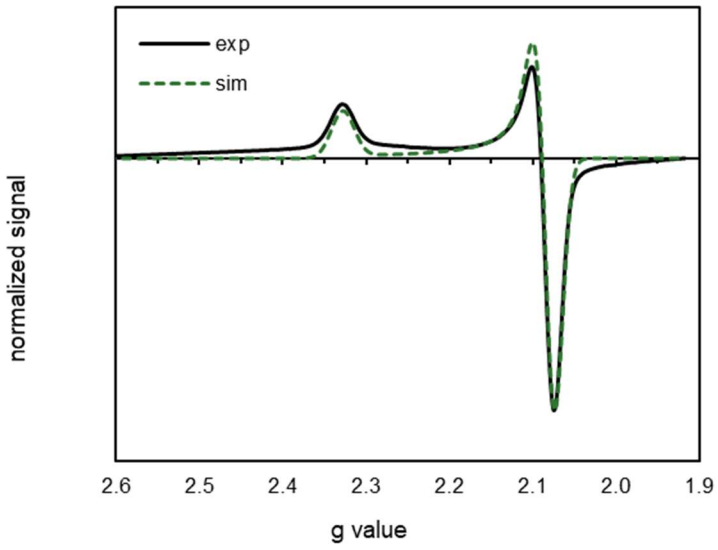

Figure S48: *Observed and simulated spectra of reduction of* ***L1***·$NiBr_2$ *by* ***L1***·*Ni(cod). The EPR spectra were collected at 9.392 GHz with a micropower of 2.0 mW, a modulation amplitude of 4 G, and a conversion time of 4 ms. The spectrum shown here was averaged over 9 scans. Nickel signals were simulated with g = [2.075, 2.085, 2.328] with a linewidth of 4 mT.*

Reduction of L1·$NiCl_2$ by Zn: For preparation procedure see S7.3

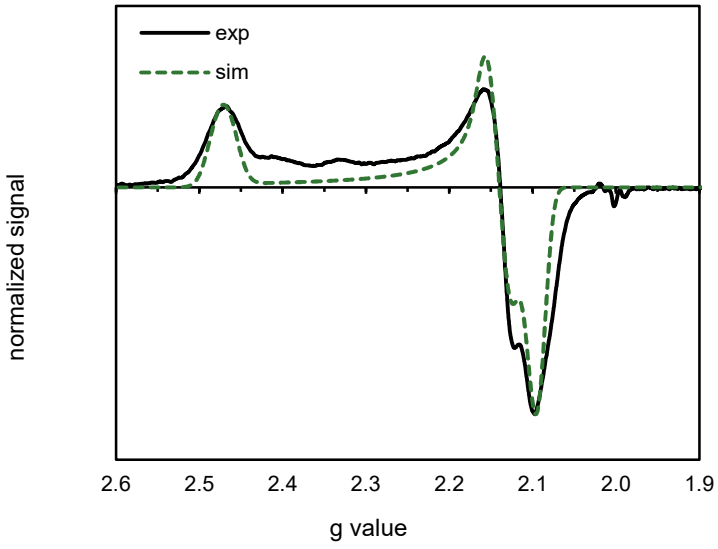

Figure S49: *Observed and simulated spectra of reduction of* ***L1***·$NiCl_2$ *by Zn at 2.75 h. The EPR spectra were collected at 9.368 GHz with a micropower 2.0 mW, a modulation amplitude of 4 G, and a conversion time of 40.96 ms. The spectrum shown here was averaged over 9 scans. The nickel signals were simulated with g = [2.095, 2.141, 2.471]*

with a nitrogen superhyperfine tensor A = [30, 40, 40] MHz and a linewidth of 4 mT.

3.4.7.2 Reaction of L1Ni(cod) with 1a

reagent mixture	solvent	time	Ni species 1				Ni species 2			
			g1	g2	g3	weight	g1	g2	g3	weight
1 equiv **L1**Ni(cod) + **1a**	DMA	1 min	2.078	2.085	2.330	100%	unobserved			
2 equiv **L1**Ni(cod) + **1a**	DMA	1 min	2.078	2.085	2.330	100%	unobserved			

Table S22: Summary of EPR data of **L1**Ni·(cod) and **1a** reaction.

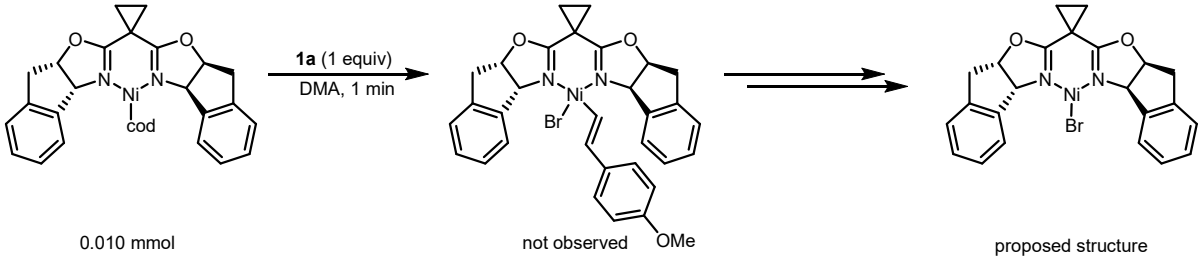

Oxidative addition of 1a by L1·Ni(cod): In a N_2-filled glovebox $Ni(cod)_2$ (2.8 mg, 0.010 mmol, 1 equiv) and **L1** (3.7 mg, 0.010 mmol, 1 equiv) were added to an oven-dried 2-dram vial. The mixture was dissolved in DMA and stirred for 24 h at 30 °C, after which **1a** (2.1 mg, 0.100 mmol, 1 equiv) was added . In a separate vial, 21.4 mg of **1a** was dissolved in 100 uL of anhydrous DMA; 10 uL (0.010 mol, 1 equiv) or 5 uL (0.005 mol, 0.5 equiv) of this 1M stock solution was added **L1**·Ni(cod). The reaction was stirred for 1 min after which an aliquot was removed and transferred to an oven-dried EPR tube. The tube was sealed, removed from the glovebox, and then frozen in LN_2 for analysis by EPR at 77 K.

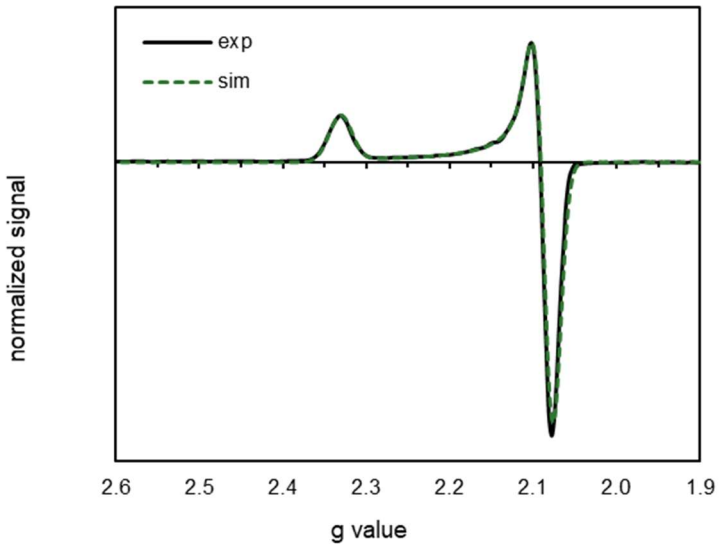

Figure S50: *Truncated observed and simulated spectra of the stoichiometric mixture of* ***L1****·Ni(cod) (1.0 equivalent) and* ***1a*** *(1.0 equivalent). The EPR spectrum was collected at 9.511 GHz with a micropower of 6.4 mW, a modulation amplitude of 4 G, and a conversion time of 40.96 ms. No additional signals were observed for g values between 2.60 and 6.80 that would suggest S ≠ ½ species were present. The nickel signals were simulated with g = [2.078, 2.085, 2.330] with a linewidth of 4 mT.*

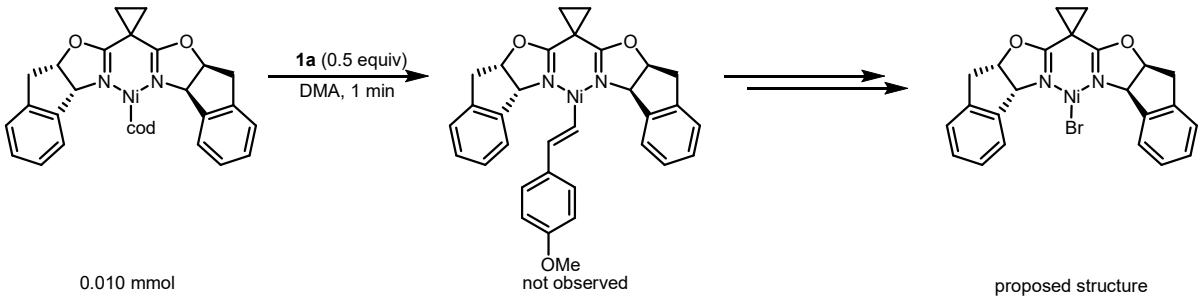

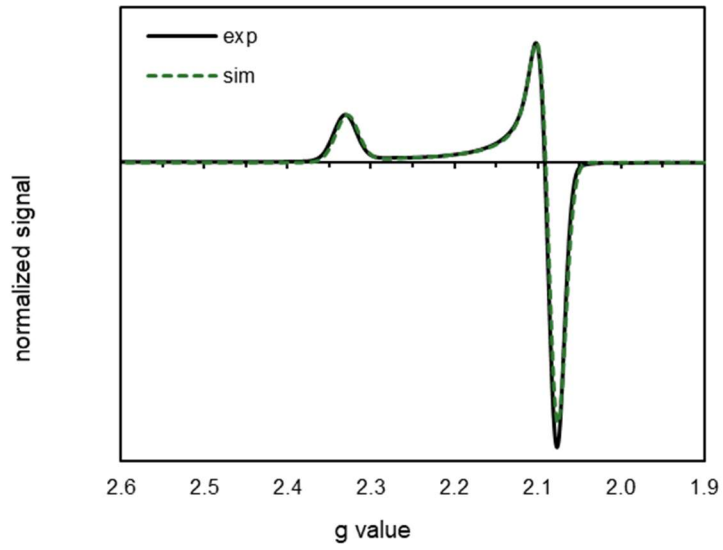

Figure S51: *Truncated observed and simulated spectra of the stoichiometric mixture of* ***L1****Ni(cod) (2.0 equivalent) and* ***1a*** *(1.0 equivalent). The EPR spectrum was collected at 9.510 GHz with a micropower of 6.4 mW, a modulation amplitude of 4 G, and a conversion time of 40.96 ms. No additional signals were observed for g values between 2.60 and 6.79 that would suggest S ≠ ½ species were present. The nickel signals were simulated with g = [2.078, 2.085, 2.328] with a linewidth of 4 mT.*

3.4.7.3 Time Course Reduction of L1 $NiCl_2$ with Zn^0

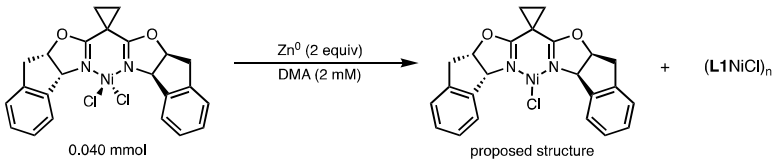

Reduction Reaction and Sample Preparation Procedure: To an oven-dried 50 mL round bottom flask was added Zn^0 powder (5.2 mg, 0.080 mmol, 2 equiv) and **L1**·$NiCl_2$ (19.4 mg, 0.040 mmol, 1 equiv). The flask was then brought into a N_2-filled glovebox where DMA (20 mL, 2 mM) was added. Before the reaction was stirred, a 2 mL aliquot was removed by a syringe fit with a 0.45 μm filter and added to a 10 mm pathlength optical cell and an oven-dried EPR tube. The tube was then removed from the glovebox and frozen

in LN_2 for analysis by perpendicular mode EPR at 77 K and parallel mode EPR at 5 K. The optical cell was sealed and removed from the glovebox for analysis by optical spectroscopy. The reaction mixture was then stirred at 1000 rpm to start the reaction and aliquots (same procedure as before) were removed at regular intervals: 0.5 h, 1 h, 1.5 h, 2.75 h, 5 h, 8 h, and 30 h.

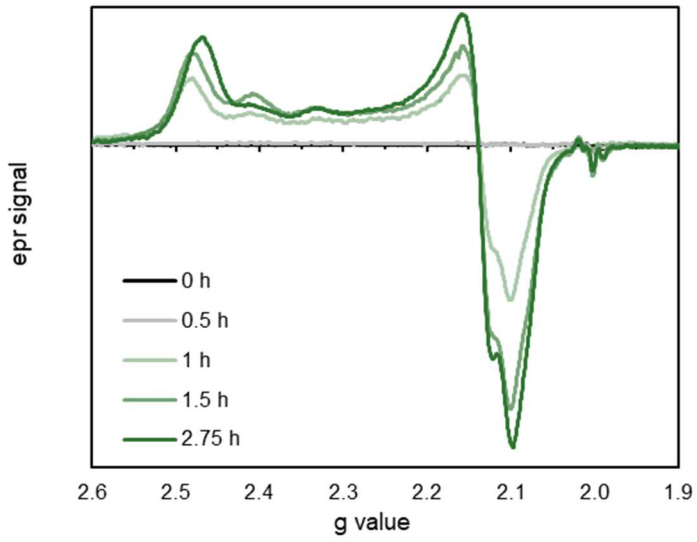

Figure S52: *Observed perpendicular mode EPR spectra during the first 2.75 h of reaction. The EPR spectra were taken at 9.368 GHz (0 h), 9.364 GHz (0.5 h), 9.375 GHz (1 h), 9.368 GHz (1.5 h), and 9.368 GHz (2.75 h). Spectrum at each timepoint was averaged over 9 scans. The spectra were collected at microwave power of 2.0 mW with a modulation amplitude of 4 G and conversion time of 40.96 ms.*

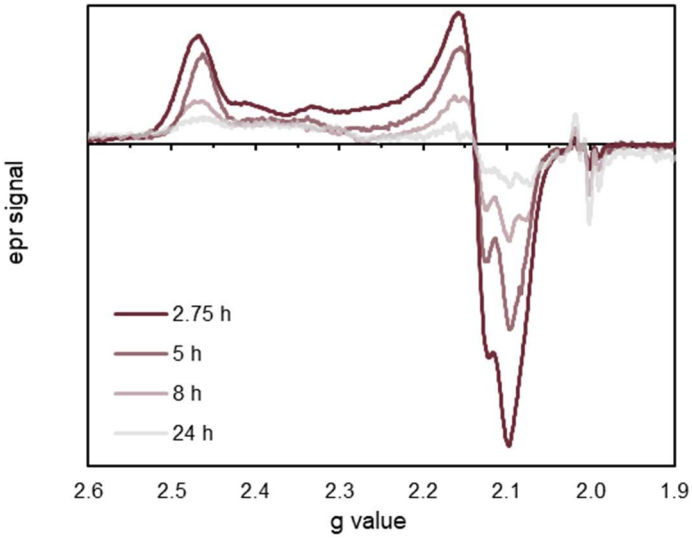

Figure S53: *Observed perpendicular mode EPR spectra after 2.75 h of the reaction. The EPR spectra were taken at 9.368 GHz (2.75 h), 9.369 GHz(5 h), 9.367 GHz(8 h), and 9.367 GHz (24 h), Spectrum at each timepoint was averaged over 9 scans. The spectra were collected at microwave power of 2.0 mW with a modulation amplitude of 4 G and conversion time of 40.96 ms.*

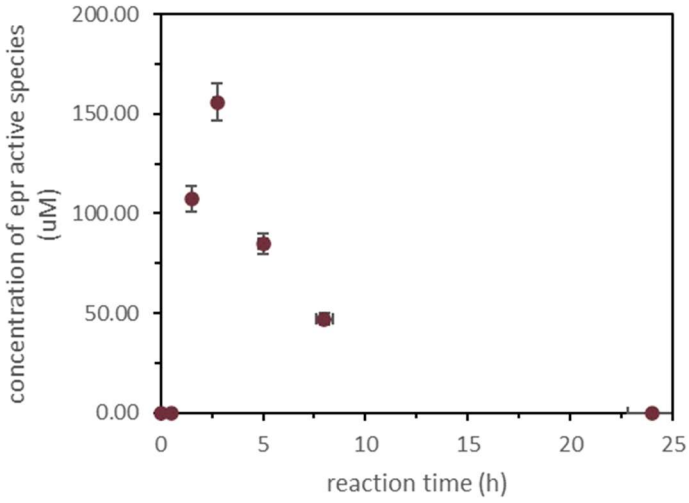

Figure S54: *Concentration of EPR active species quantified with an external calibration curve.*[39] *The integrated EPR intensity at each timepoint were halved to account for the microwave power difference between the calibration curve (0.5 mW) and the experimental condition (2.0 mW). A 6% error bar is shown in accordance with the error analysis.*

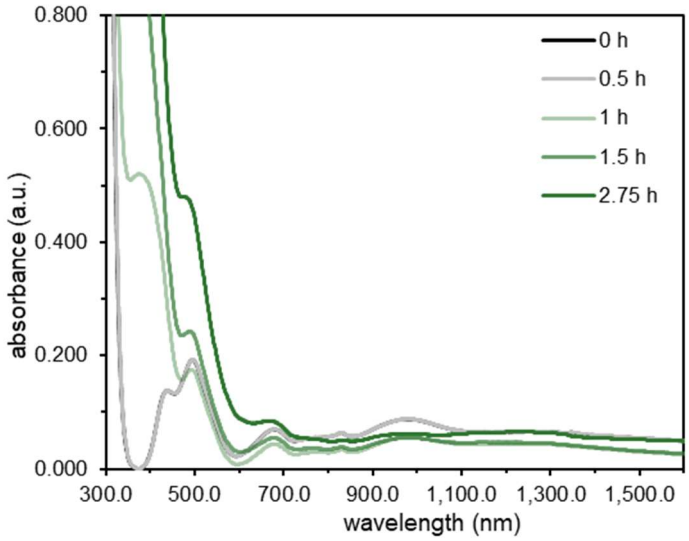

Figure S55: *Corresponding optical spectra during the first 2.75 h of the reaction.*

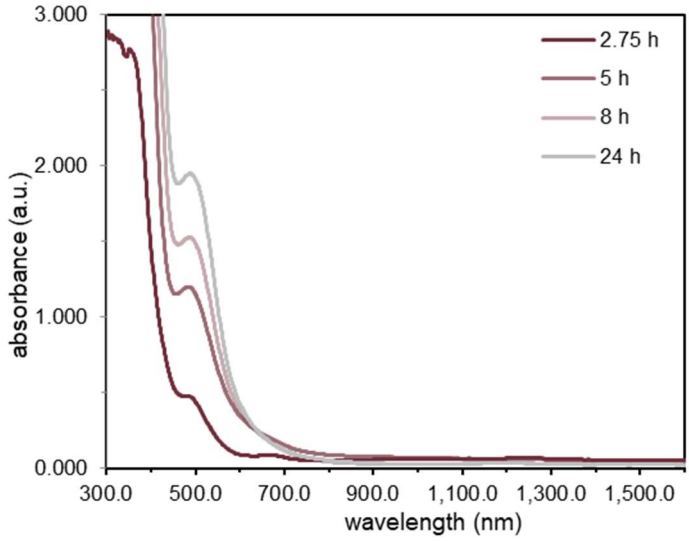

Figure S56: *Corresponding optical spectra after the first 2.75 h of the reaction*

3.4.7.4 Reaction Monitoring with EPR

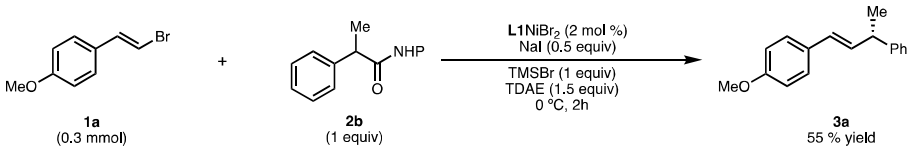

Cross-Coupling Reaction and Sample Preparation Procedure: In a dry 20 mL scintillation vial with a stir bar was added (*E*)-1-(2-bromovinyl)-4-methoxybenzene **1a** (63.9 mg, 0.30 mmol, 1 equiv) 1,3-dioxoisoindolin-2-yl 2-phenylpropanoate **2b** (88.6 mg, 0.30 mmol, 1 equiv), **L1**·$NiBr_2$ (3.5 mg, 6.0 μmol, 0.02 equiv), and NaI (22.5 mg, 0.15 mmol, 0.5 equiv). The vial was then placed under Ar, sealed and brought into a N_2-filled glovebox. The contents of the vial were dissolved in DMA (3.0 mL, 0.1 M) and cooled to 0 ºC in a cold well. Once cooled, TMSBr (39.6 μL, 0.30 mmol, 1 equiv) was added and the reaction was stirred for 5 min before TDAE (105 μL, 0.45 mmol, 1.5 equiv) was added to start the reaction. After 5 minutes, a ~0.4 mL aliquot was removed by syringe fitted with a 0.45 μm filter and transferred to an oven-dried EPR tube. The tube was then rapidly removed from the glove box and frozen in LN_2 for EPR analysis. The same procedure was done at 15 min and 90 min. After the final aliquot was removed, the reaction was quenched with 0.5 mL 1M HCl, further diluted with 3 mL H_2O then extracted three times with 5 mL of Et_2O. The combined organics were then washed with 3 mL 1M LiCl, dried over $MgSO_4$, then filtered and concentrated. The crude mixture was then diluted with 10 mL EtOAc and analyzed by GC-FID to confirm the presence of product **3a** (55% yield).

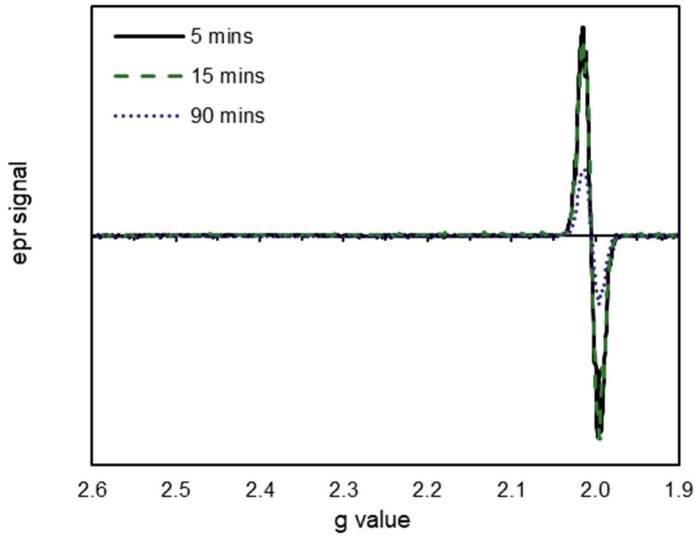

Figure S57: *EPR spectra over the course of the reaction. The EPR spectra were taken at 9.360 GHz (5 mins), 9.360 GHz (15 mins), and 9.362GHz (90 mins). Spectrum at each timepoint was averaged over 4 scans. The spectra were collected at a modulation amplitude of 4 G and conversion time of 40.96 ms. The spectra were taken at 0.5 mW (shown here), 2.0 mW, and 8.0 mW, which showed EPR no oversaturation occurred for a microwave power below 2.0 mW.*

3.4.8 Catalyst Loading Experiments (Figure 5d)

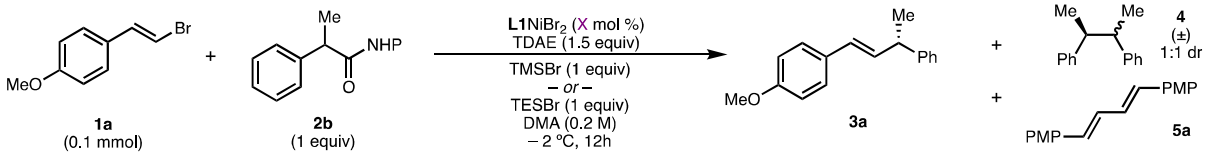

Changing Lewis Acid at Different Catalyst Loadings Cross-Coupling Procedure: In a N_2-filled glovebox to an oven-dried 20 mL scintillation vial was added **1a**, **2b**, *n*-dodecane internal standard and dry DMA to make a 0.4 M stock solution of substrates. In an oven-dried 1-dram vial with a stir bar was added **L1**$NiBr_2$ complex followed by dry DMA to make a 0.08 M catalyst stock solution. Stock solutions of substrates and catalyst were added to oven-dried 1 dram vials with a stir bar then diluted with dry DMA (final reaction concentration 0.2 M). This was done such that there was 6 different catalyst loadings: 20,

10, 5, 2.5, 1.0, 0.5 mol% and done in triplicate for each loading (total 18 reactions for each Lewis acid). Each reaction was then cooled to –2 ºC and stirred at 200 rpm. *Note: Julabo LH45 chiller was set to 0 ºC however we measured a reaction temperature of –2 ºC for these experiments.* Once cooled, either TMSBr (13.2 μL, 0.10 mmol, 1 equiv) or TESBr (17.2 μL, 0.10 mmol, 1 equiv) was added to each reaction and they were allowed to stir for 10 minutes before TDAE (35 μL, 0.15 mmol, 1.5 equiv) was added to start the reaction. Each reaction was allowed to stir for 12 hours at –2 ºC. Upon completion the reactions were diluted with EtOAc and quenched with 1M HCl. An aliquot of the organic layer was extracted and filtered through MgSO4 then further diluted for GC analysis. For one sample reaction of each Lewis acid/catalyst loading combination the remaining crude was purified by preparative-TLC for chiral SFC analysis to determine ee.

Data analysis: Reaction yields and conversions were determined by GC-FID analysis against *n*-dodecane internal standard. In Figure 5d, Figure S66, and Figure S67 the average of three runs is displayed with the error bars representing the standard deviation of the three runs. Yields of homocoupled products **4** and **5a** are not based on their theoretical yields (0.05 mmol) but instead of the reaction product's theoretical yield (0.10 mmol) to allow for facile comparison of relative mass balance across reactions.

Raw Data:

run #	Ni mol %	**3a** yield (%)	**4** yield (%)	**5** yield (%)
1	20	84	3	0
2	20	84	3	0
3	20	85	3	0
1	10	85	4	0
2	10	84	5	0

3	10	85	4	0
1	5.0	87	4	0
2	5.0	88	4	0
3	5.0	88	4	0
1	2.5	93	3	0
2	2.5	93	3	0
3	2.5	94	3	0
1	1.0	87	5	1
2	1.0	88	5	0
3	1.0	89	5	0
1	0.5	72	14	0
2	0.5	72	14	0
3	0.5	71	14	0

***Table S23**: Raw data on reactions using TMSBr as a Lewis acid at varying catalyst concentrations.*

run #	Ni mol %	**3a** yield (%)	**4** yield (%)	**5** yield (%)
1	20	73	8	13
2	20	74	8	15
3	20	71	8	13
1	10	75	8	12
2	10	75	9	13
3	10	73	9	10
1	5.0	80	7	9
2	5.0	83	7	1
3	5.0	85	7	11
1	2.5	87	5	8
2	2.5	88	5	11

3	2.5	89	5	9
1	1.0	92	3	11
2	1.0	95	3	9
3	1.0	96	3	8
1	0.5	82	9	8
2	0.5	87	3	9
3	0.5	84	9	8

***Table S24**: Raw data on reactions using TESBr as a Lewis acid at varying catalyst concentrations.*

	Ni mol %	**3a** avg yield ± STDEV	**4** avg yield ± STDEV	**5a** avg yield ± STDEV	**3a** ee (%)
	20	84 ± 0.4	3 ± 0	0 ± 0	96
	10	85 ± 0.6	4 ± 0.2	1 ± 0	95
TMSBr	5	88 ± 0.6	4 ± 0	2 ± 0	93
	2.5	93 ± 0.8	3 ± 0	3 ± 0	88
	1	88 ± 0.8	5 ± 0	4 ± 0	82
	0.5	72 ± 0.6	14 ± 0.2	5 ± 0	76
	20	73 ± 1.2	8 ± 0	14 ± 1.2	95
	10	74 ± 1.4	9 ± 0.2	12 ± 1.2	94
TESBr	5	82 ± 2.4	7 ± 0	7 ± 5.4	93
	2.5	88 ± 0.8	5 ± 0	9 ± 1.2	90
	1	94 ± 2.0	3 ± 0	9 ± 1.4	85
	0.5	84 ± 2.6	7 ± 3.6	58± 0.6	78

***Table S25**: Averaged yield data with standard deviation for each catalyst loading and Lewis Acid. Yields determined by GC-FID analysis versus dodecane internal standard.*

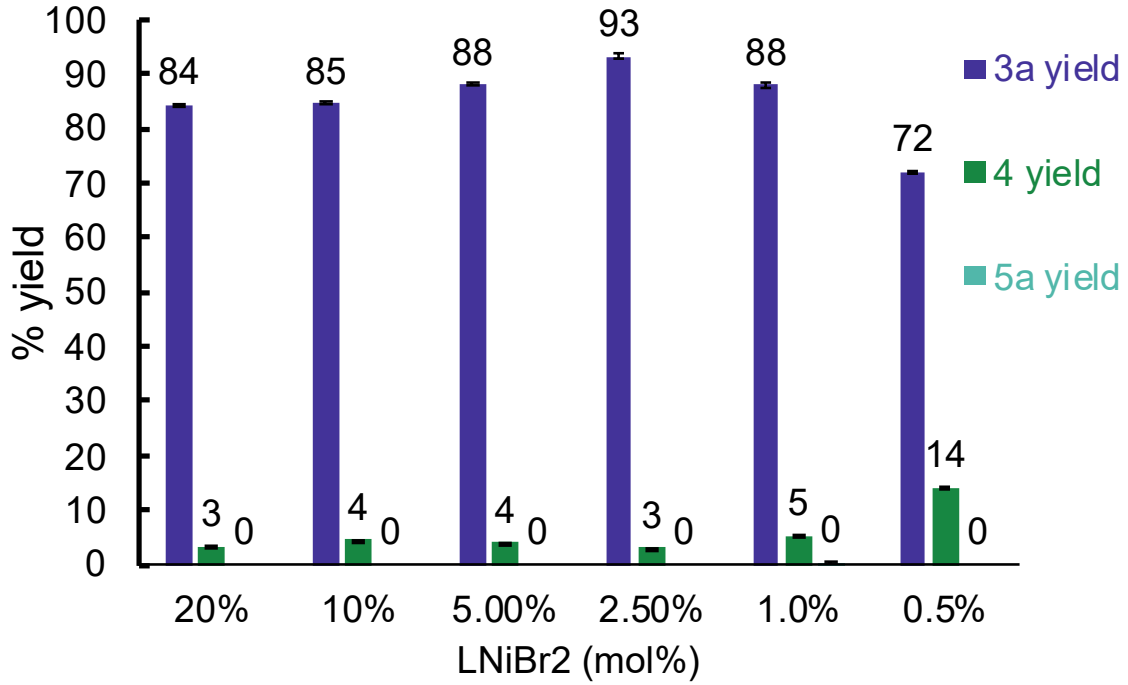

***Figure S58**: TMSBr reaction data in graphical form similar to main text (Figure 5d).*

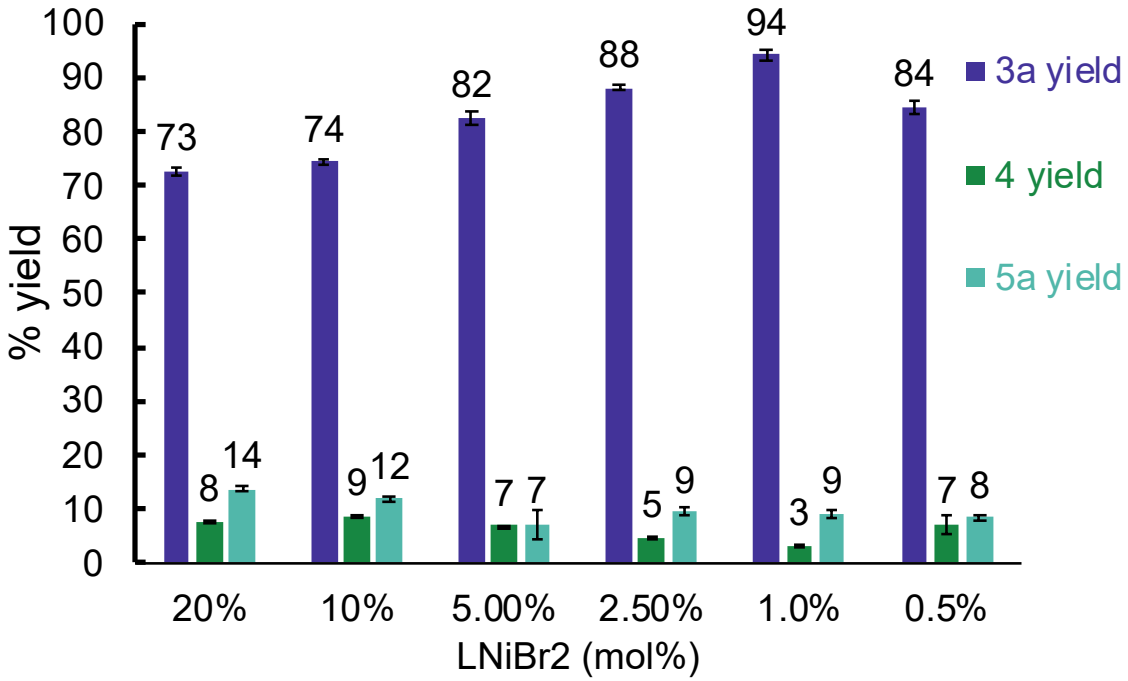

***Figure S59**: TESBr reaction data in graphical form similar to main text (Figure 5d).*

3.4.9 Computational Data

Unless otherwise noted, all calculations were carried out with the Gaussian 16 package.[40] Geometry optimization and energy calculations were performed with B3LYP-D3.[41] The LANL2DZ basis set[42] with ECP was used for Ni, and the 6-31G(d) basis set[43] was used for other atoms. Frequency analysis was conducted at the same level of theory to verify that the stationary points are minima or saddle points. To ensure that the correct unrestricted wave functions were obtained, a stability test was carried out with the Gaussian keyword *stable = opt*. Single point energies were calculated at the M06[44]/6-311+G(d,p)-SDD[45] level using SMD solvation model[46] (solvent = DMA). Computed structures were visualized using CYLview.[47]

^{19}F Chemical shifts were carried out with ORCA 4.2.1 package.[48] Geometry optimizations and frequency calculations were performed with BP86. Chemical shifts calculation were performed with TPSSh and accelerated with RIJCOSX approximation using SMD solvation model (solvent = DMA). All atoms were described with def2-TZVPP basis set.

3.4.9.1 DFT-Computed Gibbs Free Energy Barriers for Radical Addition and Reductive Elimination Transition States

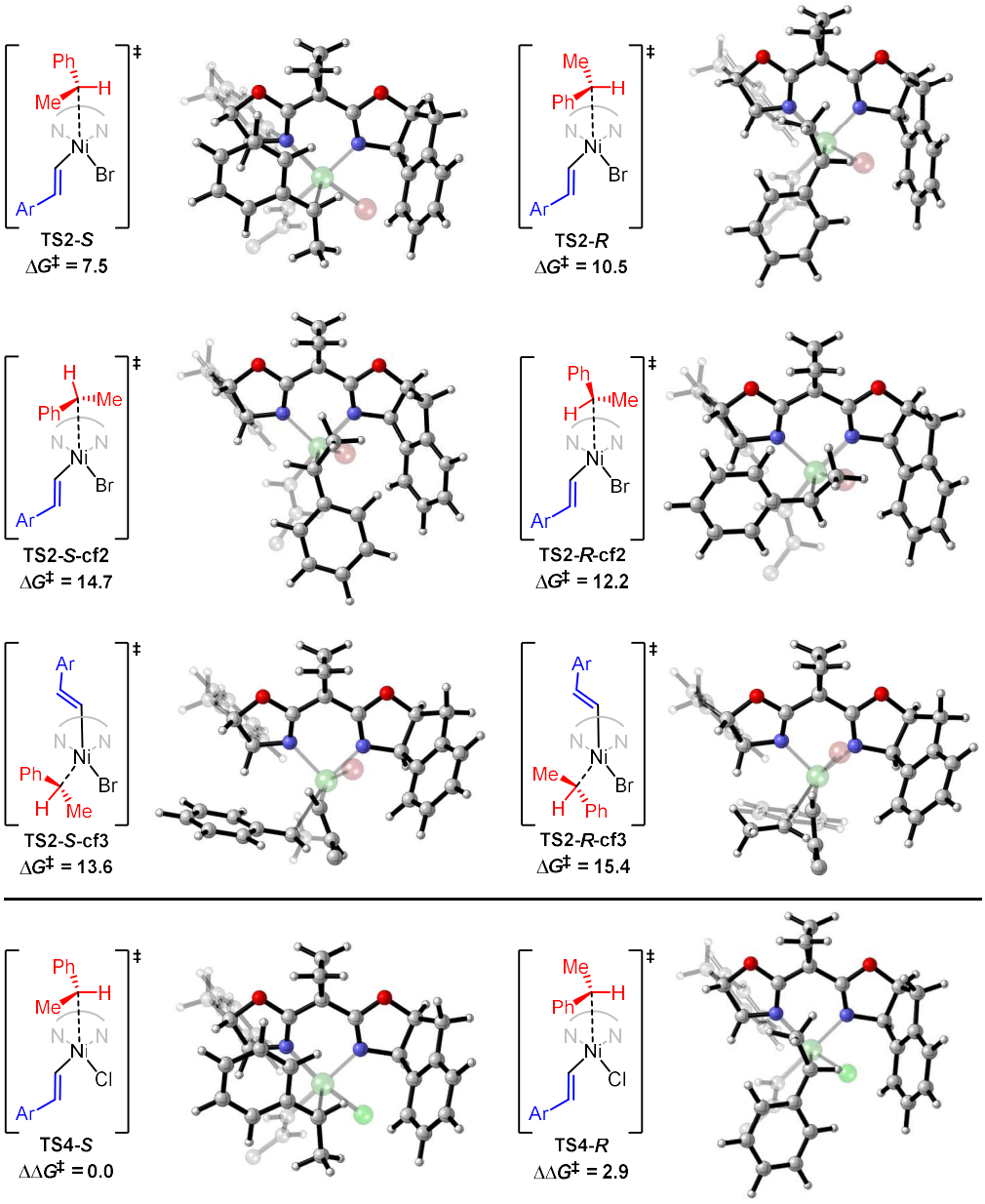

Figure S60. *DFT-computed Gibbs free energy barriers for radical addition transition states. Energies in kcal/mol, only the α-carbon of aryl group (p-OMe-Ph) is shown for simplicity.*

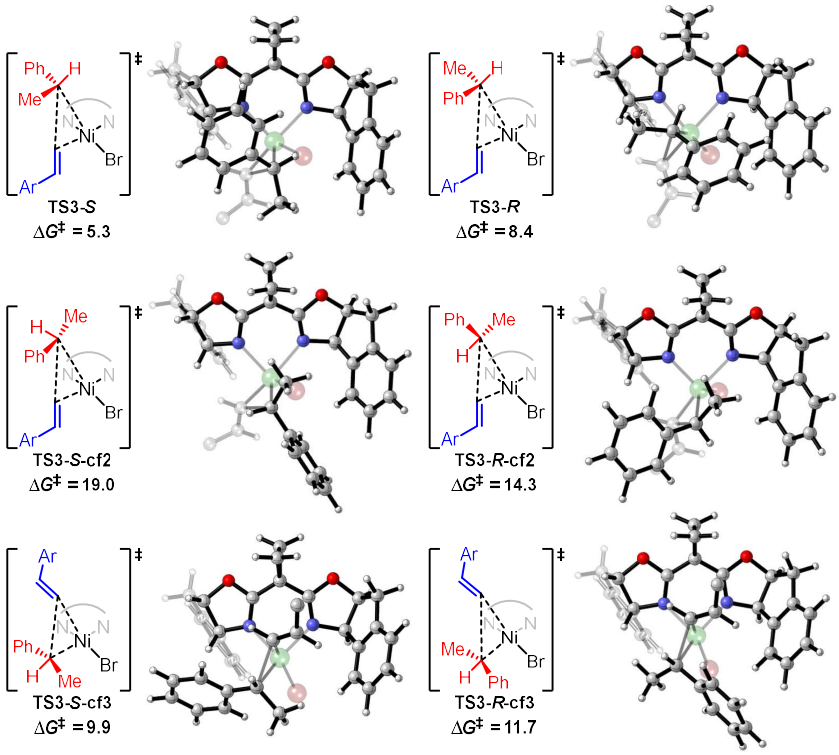

Figure S61. *DFT-computed Gibbs free energy barriers for reductive elimination transition states. Energies in kcal/mol, only the α-carbon of aryl group (p-OMe-Ph) is shown for simplicity.*

3.4.9.2 Table of Energies

structures	*ZPE*	*TCH*	*TCG*	*E*	*H*	*G*	Imaginary Frequency
1a	0.157103	0.168714	0.118363	-2994.814718	-2994.813774	-2994.864125	—
10	0.143410	0.151702	0.111157	-310.086145	-310.085200	-310.125745	—
3a	0.305310	0.322803	0.258415	-733.546167	-733.545222	-733.609611	—
6-Br	0.387446	0.412098	0.330548	-3888.876796	-3888.875852	-3888.957402	—
9	0.545058	0.582077	0.471467	-6883.698127	-6883.697183	-6883.807793	—
7	0.544906	0.579268	0.475840	-4312.265954	-4312.265010	-4312.368438	—
11	0.693066	0.735906	0.613379	-4622.384353	-4622.383409	-4622.505936	—
L1·NiBr$_2$	0.389305	0.415738	0.330948	-6460.314111	-6460.313167	-6460.397957	—
L1·NiCl$_2$	0.390313	0.416097	0.334385	-2237.879255	-2237.878311	-2237.960023	—
TS1	0.544407	0.580802	0.470800	-6883.686941	-6883.685997	-6883.795998	77.97*i*
TS2-*S*	0.691161	0.733509	0.612775	-4622.377688	-4622.376744	-4622.497478	86.29*i*

TS2-*S*-cf2	0.690994	0.733306	0.613450	-4622.366077	-4622.365133	-4622.484988	99.49*i*
TS2-*S*-cf3	0.689948	0.732831	0.609722	-4622.368744	-4622.367800	-4622.490909	43.26*i*
TS2-*R*	0.690489	0.733056	0.610999	-4622.369068	-4622.368124	-4622.490181	93.39*i*
TS2-*R*-cf2	0.691202	0.733535	0.613484	-4622.373867	-4622.372923	-4622.492974	122.69*i*
TS2-*R*-cf3	0.690101	0.732833	0.611372	-4622.363507	-4622.362563	-4622.484024	29.39*i*
TS3-*S*	0.692081	0.734347	0.612426	-4622.378747	-4622.377802	-4622.499724	228.06*i*
TS3-*S*-cf2	0.693128	0.735204	0.613722	-4622.360576	-4622.359631	-4622.481113	188.10*i*
TS3-*S*-cf3	0.692833	0.734938	0.616204	-4622.384026	-4622.383082	-4622.501816	163.77*i*
TS3-*R*	0.692106	0.734445	0.612125	-4622.370255	-4622.369311	-4622.491631	250.12*i*
TS3-*R*-cf2	0.693082	0.735002	0.614428	-4622.367556	-4622.366612	-4622.487187	213.19*i*
TS3-*R*-cf3	0.692876	0.734861	0.616167	-4622.379267	-4622.378323	-4622.497017	195.93*i*
TS4-*S*	0.691521	0.733615	0.613914	-2511.159973	-2511.159029	-2511.278730	91.24*i*
TS4-*R*	0.690833	0.733155	0.611956	-2511.150744	-2511.149799	-2511.270998	102.88*i*

Table S26. *Zero-point correction (ZPE), thermal correction to enthalpy (TCH), thermal correction to Gibbs free energy (TCG), energies (E), enthalpies (H), and Gibbs free energies (G) (in Hartree) of the structures calculated at the M06/6-311+G(d,p)-SDD-SMD(DMA)//B3LYP-D3/6-31G*-LANL2DZ level of theory.*

3.4.9.3 Cartesian Coordinates for Calculated Species

1a

Br	3.88090800	-0.05446600	-0.00003200
C	2.04318100	0.44922200	0.00055600
C	1.05264300	-0.45014700	-0.00077900
H	1.91071500	1.52387800	0.00210800
H	1.32134700	-1.50469200	-0.00207000
C	-0.38593400	-0.16251700	-0.00053200
C	-1.29087000	-1.23408600	-0.00023400
C	-0.92482900	1.14221900	-0.00060600
C	-2.67281500	-1.03722800	0.00012800
H	-0.90780400	-2.25189200	-0.00022900
C	-2.29264800	1.35456200	-0.00024800
H	-0.26441000	2.00430200	-0.00106700
C	-3.18250600	0.26592200	0.00014900
H	-3.33165300	-1.89772700	0.00037100
H	-2.70717900	2.35770000	-0.00033600
O	-4.50597500	0.58767300	0.00046800
C	-5.45497000	-0.46821100	0.00085400
H	-6.43595400	0.01042300	0.00109800
H	-5.35854200	-1.09783700	-0.89418800
H	-5.35801300	-1.09766100	0.89596200

10

C	1.83322100	-0.65199900	0.00004500
H	2.08025400	-1.71111700	0.00002500
C	0.46218600	-0.30019600	0.00000800
C	-0.54340000	-1.31146300	-0.00004900
C	0.02037200	1.05542000	0.00002500
C	-1.89146700	-0.98836800	-0.00008600
H	-0.23452900	-2.35444100	-0.00006300
C	-1.33233400	1.36765200	-0.00001200
H	0.75473700	1.85543900	0.00006800
C	-2.30004300	0.35380700	-0.00006800
H	-2.63543400	-1.78104500	-0.00012900
H	-1.64206100	2.40984800	0.00000200
H	-3.35692000	0.60491000	-0.00009600
C	2.95955100	0.33474300	0.00010600
H	2.92767900	0.99432600	0.88074100
H	3.92999900	-0.16984900	0.00014200
H	2.92775500	0.99434700	-0.88051600

3a

C	-0.89419600	1.51166900	-0.25111200
C	-0.15813300	0.39239600	-0.18067500
H	-0.39834100	2.48271600	-0.27730500
H	-0.67988500	-0.56313700	-0.16658600
C	1.30641100	0.29100500	-0.12049800
C	1.90139600	-0.97895400	-0.09917500
C	2.17066300	1.40603900	-0.07970400
C	3.28615800	-1.15298300	-0.04467500
H	1.26489100	-1.86058800	-0.12772600
C	3.54627000	1.25264500	-0.02497100
H	1.75879600	2.41092300	-0.08770300
C	4.11939100	-0.03019900	-0.00767100
H	3.69536400	-2.15666900	-0.03153000
H	4.20849300	2.11234000	0.00722700
O	5.48282900	-0.06751800	0.04718400
C	6.11699800	-1.33581400	0.06792300
H	7.18939400	-1.13548200	0.11138700
H	5.82198500	-1.92183900	0.94946400
H	5.89322300	-1.91542500	-0.83845200
C	-3.76795400	-1.61797800	1.24498500
C	-3.09639200	-0.40683900	1.08072400
C	-3.12430200	0.27252900	-0.14728000
C	-3.83962100	-0.30001600	-1.20522200
C	-4.51513700	-1.51275800	-1.04629100
C	-4.48253500	-2.17559600	0.18098000
H	-3.73292100	-2.12811700	2.20427700
H	-2.53161600	0.01210800	1.90912000
H	-3.86867400	0.21005400	-2.16565900
H	-5.06563600	-1.93737500	-1.88189200
H	-5.00711600	-3.11878800	0.30870500
C	-2.40640000	1.60109200	-0.32528000
H	-2.65336600	1.97333900	-1.33257200
C	-2.92710700	2.66358000	0.67098300
H	-2.70693900	2.37690400	1.70482300
H	-2.45217700	3.63420100	0.48451900
H	-4.01117200	2.78605500	0.57418800

6-Br

C	-0.36197700	-3.82183400	0.64792100
C	0.00000000	-2.47192800	-0.00001700
C	0.36197200	-3.82181600	-0.64799500
H	0.18960700	-4.06808200	1.54864200
H	-1.41774200	-4.06938300	0.65315900
H	-0.18961400	-4.06803400	-1.54872400
H	1.41773600	-4.06936800	-0.65324100
C	-1.10716600	-1.70895600	-0.61880500
C	-3.06015700	-1.54459400	-1.76366800
C	-2.53247600	-0.14513900	-1.32829900
H	-3.01912600	-1.73277600	-2.83888600
H	-2.37605000	0.55621300	-2.15238100
C	1.10716800	-1.70897900	0.61879400
C	3.06017000	-1.54465700	1.76364500
C	2.53248400	-0.14518800	1.32833100
H	3.01915100	-1.73287600	2.83885700
H	2.37606300	0.55613500	2.15244000
O	-2.10340100	-2.46199700	-1.14717300
O	2.10340700	-2.46203800	1.14712900
N	-1.22318600	-0.43422100	-0.70416200
N	1.22319200	-0.43424600	0.70418900
C	-4.46409300	-1.72539100	-1.15867200
C	4.46410100	-1.72543000	1.15862800
C	-3.54941100	0.33992800	-0.31837500
C	-3.48867700	1.49828700	0.45643100
C	-4.60775700	-0.56504900	-0.19674200
C	-4.51932700	1.73749600	1.36871600
H	-2.64978600	2.18386500	0.36262900
C	-5.63598400	-0.32103700	0.71362800
C	-5.58356300	0.83571300	1.49640300
H	-4.49123300	2.63128600	1.98564800
H	-6.46422000	-1.01821700	0.81551500
H	-6.37708300	1.03668000	2.21147900
H	-5.22433100	-1.68760200	-1.94973800
H	-4.55216900	-2.70631900	-0.67813200
C	3.54940800	0.33991900	0.31841600
C	3.48866000	1.49830400	-0.45635000
C	4.60775600	-0.56505100	0.19674100
C	4.51930200	1.73755000	-1.36863500
H	2.64976400	2.18387300	-0.36252200
C	5.63597300	-0.32100200	-0.71362900
C	5.58354100	0.83577600	-1.49636200
H	4.49119700	2.63136000	-1.98553800
H	6.46421000	-1.01817500	-0.81554900
H	6.37705400	1.03677100	-2.21143800
H	5.22434700	-1.68767000	1.94968900
H	4.55217300	-2.70633900	0.67805000
Ni	0.00001800	0.98322500	0.00002100
Br	-0.00000700	3.30195300	-0.00002900

9

C	0.20675000	-2.54672700	3.05661000
C	0.03498500	-1.58269300	1.87478600

C	1.19881500	-2.59681300	1.95455000
H	0.49681700	-2.08791500	3.99491300
H	-0.53276200	-3.33647300	3.12341000
H	1.15151600	-3.41383200	1.24289500
H	2.18238300	-2.16494000	2.10339200
C	-1.02381500	-1.88678400	0.88607300
C	-2.39906900	-3.30249000	-0.23413400
C	-2.52780200	-1.84666600	-0.77356500
H	-1.94855800	-4.00772800	-0.93569000
H	-2.27520000	-1.72498300	-1.82946800
C	0.39108200	-0.16529000	2.09780700
C	1.61222800	1.47096700	3.04715000
C	0.61588700	2.06680800	2.01173600
H	1.51882700	1.88684600	4.05026800
H	-0.20560100	2.65989000	2.42130500
O	-1.44839600	-3.16904600	0.87296800
O	1.22156200	0.06828800	3.14127300
N	-1.52886800	-1.09422700	0.01645900
N	0.02388000	0.84961900	1.41041100
C	-3.78662500	-3.74120000	0.27310900
C	3.03277600	1.62805700	2.44868000
C	-3.94785300	-1.44736400	-0.45393200
C	-4.54915500	-0.21142200	-0.68368000
C	-4.63897500	-2.49450200	0.16188100
C	-5.87288400	-0.03575500	-0.27509200
H	-3.98994500	0.59831800	-1.13912700
C	-5.96260800	-2.31747500	0.56360500
C	-6.57318500	-1.07942900	0.34257500
H	-6.35636400	0.92430500	-0.43015400
H	-6.51133900	-3.12545000	1.04167100
H	-7.60262700	-0.92561900	0.65570200
H	-4.17874300	-4.55679000	-0.34780800
H	-3.71251500	-4.12758500	1.29622500
C	1.48661700	2.83756100	1.05038700
C	1.07592300	3.67256600	0.01147900
C	2.83987900	2.57987500	1.28819700
C	2.05449200	4.23853100	-0.81063000
H	0.01718700	3.84637600	-0.15953700
C	3.81485300	3.15802500	0.47559400
C	3.41245700	3.98228900	-0.58069000
H	1.75755200	4.88249400	-1.63333300
H	4.87015500	2.96486800	0.65237600
H	4.16202600	4.43189300	-1.22636000
H	3.75170700	1.99769700	3.18823000
H	3.39722700	0.65175700	2.10364100
Ni	-0.92707600	0.83769700	-0.40361100
C	0.83294900	0.37386400	-1.23372600
C	1.36680000	-0.84896800	-1.26035100
H	1.36873700	1.30987700	-1.36783000
H	0.69918200	-1.70847900	-1.25223700
C	2.79813400	-1.17381100	-1.18318900
C	3.20396200	-2.51663100	-1.18074700
C	3.80213800	-0.19179000	-1.03335800
C	4.54430300	-2.88656200	-1.04412500
H	2.45386300	-3.29677800	-1.29386700

C	5.13421400	-0.54335000	-0.89371900
H	3.53290300	0.85912500	-1.01500600
C	5.52095200	-1.89516200	-0.89761100
H	4.80906100	-3.93766700	-1.05440700
H	5.90493400	0.21273800	-0.77831600
O	6.85661100	-2.12784700	-0.74797000
C	7.30923700	-3.47240100	-0.76347400
H	8.39296400	-3.42633900	-0.64070000
H	6.87577200	-4.05496200	0.06142100
H	7.07274400	-3.96747300	-1.71530300
Br	-1.32480800	0.84804800	-2.78048400
Br	-2.49495900	2.56254800	0.39800900

7

C	-3.45641300	3.36847900	-0.98383400
C	-2.66854600	2.04467700	-1.00132200
C	-3.53683000	2.50615100	-2.18818400
H	-4.30326500	3.38899400	-0.30678800
H	-2.85835700	4.27160800	-1.02792200
H	-2.98697800	2.80395000	-3.07468200
H	-4.43920700	1.92925900	-2.35828100
C	-1.20617000	2.13914900	-1.15655300
C	0.68871900	3.11618700	-1.93015500
C	0.99951800	1.99017500	-0.91734500
H	0.90072700	2.87416100	-2.97495400
H	1.73024400	1.25570500	-1.25560600
C	-3.18988600	0.93986300	-0.17270400
C	-4.85197600	-0.19178200	0.86671700
C	-3.49898100	-0.94150700	0.97129300
H	-5.19273100	0.27843000	1.79271000
H	-3.19176300	-1.21613900	1.98086600
O	-0.76827000	3.23463800	-1.81353300
O	-4.53586500	0.89705500	-0.06265500
N	-0.31176000	1.32645900	-0.71209000
N	-2.51442500	0.02584900	0.42316000
C	1.36886600	4.39452300	-1.42567600
C	-5.87072400	-1.14659200	0.23234900
C	1.44608500	2.74305500	0.32116100
C	1.61854400	2.24676400	1.61277600
C	1.63440600	4.09959200	0.03517500
C	2.00526900	3.13511600	2.61959000
H	1.43627600	1.19938800	1.82532800
C	2.02233400	4.98330700	1.04101700
C	2.20996600	4.49088200	2.33578700
H	2.14197000	2.76883500	3.63322700
H	2.16900100	6.03897300	0.82581300
H	2.50870600	5.16900700	3.13084200
H	2.30132200	4.55945700	-1.98193400
H	0.73428300	5.27176300	-1.59281600
C	-3.68524300	-2.13743600	0.05516500
C	-2.72381500	-3.05549000	-0.36784300
C	-5.00971700	-2.22524900	-0.38778500
C	-3.11084300	-4.06542300	-1.25254200
H	-1.70382800	-2.97994500	-0.00614400
C	-5.39374800	-3.23510900	-1.26914000

C	-4.43411200	-4.15446000	-1.70168700
H	-2.37536800	-4.78897300	-1.59350200
H	-6.42176300	-3.30627100	-1.61647300
H	-4.71837500	-4.94528700	-2.39103200
H	-6.52877500	-1.55687200	1.00996600
H	-6.51006600	-0.61959700	-0.48457700
Ni	-0.50635000	-0.30348800	0.37724300
C	1.21759400	-0.85976400	-0.14389600
C	2.36331000	-1.05674100	0.52538300
H	1.21232300	-0.98116700	-1.23799800
H	2.34159100	-0.97215500	1.61168800
C	3.68756900	-1.38278500	-0.03341400
C	4.77353900	-1.57263100	0.83417500
C	3.94746000	-1.50339200	-1.41538900
C	6.05765200	-1.87079800	0.37084200
H	4.61030500	-1.48841300	1.90633700
C	5.21449300	-1.79923300	-1.89371100
H	3.13807800	-1.36609600	-2.12728500
C	6.28459400	-1.98595000	-1.00402000
H	6.86073800	-2.00966600	1.08598200
H	5.40797700	-1.89336400	-2.95824300
O	7.49343300	-2.27094700	-1.58046000
C	8.60330300	-2.48026700	-0.72594200
H	9.45168400	-2.69609900	-1.37910300
H	8.82825100	-1.58771100	-0.12474400
H	8.44144700	-3.33210200	-0.05028200
Br	-0.50214400	-1.74640000	2.22145000

11

C	4.00627100	3.10774600	-0.42997400
C	3.06837500	1.96969500	0.01765400
C	4.15037600	2.55854000	0.94114300
H	4.74434800	2.84057200	-1.17742200
H	3.53272900	4.07521300	-0.55267000
H	3.77753800	3.14072800	1.77610400
H	4.99176600	1.90680100	1.15087100
C	1.66789000	2.35000700	0.30527900
C	0.10029800	3.75994300	1.13717900
C	-0.53839300	2.50240200	0.49004700
H	0.05338300	3.77848000	2.22825100
H	-1.20425400	1.96133200	1.16359700
C	3.33469200	0.63008000	-0.55254300
C	4.72640800	-0.97971200	-1.29225000
C	3.24752800	-1.40728500	-1.46991500
H	5.31432300	-1.00672400	-2.20991200
H	2.87750000	-1.42542000	-2.49794200
O	1.51331000	3.60688800	0.78885500
O	4.63421900	0.41637200	-0.89497300
N	0.61316200	1.64368100	0.15391800
N	2.51035100	-0.32556400	-0.76796600
C	-0.50604300	4.99286200	0.44903800
C	5.31534500	-1.87242800	-0.16936300
C	-1.22369300	3.03146500	-0.75070500
C	-1.78126300	2.29376400	-1.79426800
C	-1.18063900	4.42894800	-0.78480000

C	-2.32288700	2.98935000	-2.87799700
H	-1.76256400	1.20869900	-1.77613300
C	-1.72540500	5.11922800	-1.86701000
C	-2.29991400	4.38927500	-2.91190900
H	-2.75450300	2.43487100	-3.70645000
H	-1.69716800	6.20573100	-1.90399500
H	-2.72329400	4.91445400	-3.76427200
H	-1.22890000	5.47536900	1.12047600
H	0.26761800	5.73588800	0.22520000
C	3.15611500	-2.74374200	-0.78491700
C	2.09825500	-3.64928000	-0.82643600
C	4.31062500	-2.99953800	-0.03756800
C	2.20649000	-4.82900000	-0.08472000
H	1.21462600	-3.41922800	-1.41603700
C	4.41609000	-4.17745100	0.70042900
C	3.35371800	-5.08767400	0.67502200
H	1.39390400	-5.54997600	-0.09754900
H	5.30844600	-4.39086500	1.28380800
H	3.42405000	-6.00974800	1.24592900
H	6.32338100	-2.22755600	-0.41050500
H	5.39592200	-1.28739000	0.75622300
Ni	0.37394900	-0.51206900	-0.36861400
C	-1.47083400	-0.64491500	0.17951300
C	-2.44002300	-1.34902500	-0.41843200
H	-1.68423300	-0.04707100	1.06676400
H	-2.19063900	-1.92639600	-1.30655100
C	-3.85739000	-1.39096200	-0.01669500
C	-4.80051500	-1.96938400	-0.87891300
C	-4.33540300	-0.87892800	1.20821900
C	-6.15917200	-2.03229000	-0.56069100
H	-4.46386500	-2.37634900	-1.82963300
C	-5.67996000	-0.93147300	1.53997100
H	-3.63715900	-0.43844200	1.91477400
C	-6.60708800	-1.50776900	0.65633300
H	-6.84821200	-2.48742600	-1.26313600
H	-6.04455100	-0.53972200	2.48483200
O	-7.90679000	-1.51079500	1.08103200
C	-8.88488900	-2.08167900	0.22905600
H	-9.83800100	-1.97836200	0.75201000
H	-8.94165000	-1.55506900	-0.73395600
H	-8.68864400	-3.14681900	0.04191400
C	0.71852900	-1.43197500	1.56529900
H	1.73763300	-1.70412200	1.28227200
C	0.71604800	-0.35795100	2.57388800
C	1.88987900	0.39168000	2.80284500
C	-0.42907600	-0.00759300	3.32005700
C	1.91152400	1.46178300	3.69077400
H	2.78975400	0.12634600	2.25428000
C	-0.41228200	1.07143700	4.20518000
H	-1.33795300	-0.58990900	3.21209300
C	0.75268100	1.82009000	4.39028400
H	2.83368000	2.01632500	3.84613200
H	-1.31249000	1.32151200	4.76119600
H	0.76646000	2.65370900	5.08729400
C	-0.11050500	-2.67720100	1.82296800

H	-0.11115300	-3.32244100	0.94142400
H	0.32641700	-3.24542000	2.65885200
H	-1.15237700	-2.45879000	2.06445000
Br	0.05704200	-1.05193200	-2.80568000

L1·NiBr$_2$

C	0.35281100	-4.05239100	-0.65177700
C	-0.00013400	-2.70088800	0.00001300
C	-0.35326200	-4.05231400	0.65186400
H	-0.21169000	-4.29370300	-1.54590800
H	1.40866000	-4.29806600	-0.67366300
H	0.21120400	-4.29366300	1.54600700
H	-1.40914600	-4.29784200	0.67376300
C	1.10618800	-1.93484000	0.60579700
C	3.08896300	-1.75477500	1.69404700
C	2.54537800	-0.35989500	1.28288300
H	3.06155700	-1.95980700	2.76632300
H	2.42435000	0.35224900	2.09963700
C	-1.10635800	-1.93472200	-0.60579600
C	-3.08902800	-1.75444900	-1.69419300
C	-2.54538600	-0.35964000	-1.28287600
H	-3.06148000	-1.95943200	-2.76647500
H	-2.42432000	0.35258100	-2.09955700
O	2.12640500	-2.67546300	1.07689300
O	-2.12663700	-2.67523700	-1.07693100
N	1.20169600	-0.65967400	0.72599800
N	-1.20172900	-0.65954600	-0.72599400
C	4.47793200	-1.92368200	1.05843500
C	-4.47809300	-1.92327800	-1.05878300
C	3.50385000	0.10838900	0.20798400
C	3.40038500	1.24656700	-0.59231000
C	4.56102600	-0.79421500	0.05383800
C	4.37780900	1.46286200	-1.56675500
H	2.57687600	1.94162100	-0.46077800
C	5.53802000	-0.57207400	-0.91589400
C	5.43696900	0.56115600	-1.72801400
H	4.31078200	2.33923800	-2.20491400
H	6.36378200	-1.26826300	-1.04134900
H	6.18861900	0.74382000	-2.49142300
H	5.25424300	-1.83256200	1.82931600
H	4.58347600	-2.92005600	0.61476900
C	-3.50388000	0.10856900	-0.20795400
C	-3.40036300	1.24660500	0.59254000
C	-4.56115600	-0.79395600	-0.05402200
C	-4.37783100	1.46283000	1.56695600
H	-2.57678300	1.94160900	0.46118700
C	-5.53819400	-0.57188300	0.91568200
C	-5.43709000	0.56120200	1.72799600
H	-4.31076100	2.33909600	2.20526300
H	-6.36402900	-1.26801600	1.04096500
H	-6.18877700	0.74381800	2.49138000
H	-5.25429200	-1.83194800	-1.82975200
H	-4.58381600	-2.91970400	-0.61527500
Ni	0.00005300	0.77347900	0.00001300
Br	-0.60168700	2.35892200	-1.66454900

Br	0.60199600	2.35881200	1.66461900

L1·NiCl₂

C	0.36934700	3.67764800	0.64258800
C	0.00000100	2.32595500	0.00000000
C	-0.36934600	3.67764100	-0.64260100
H	-0.17237100	3.91868200	1.55077700
H	1.42551800	3.92296700	0.63776900
H	0.17237100	3.91866800	-1.55079200
H	-1.42551800	3.92295900	-0.63778400
C	1.09063800	1.55889300	-0.63047100
C	3.04198500	1.37425300	-1.77216800
C	2.52420300	-0.01632400	-1.31750100
H	2.97370800	1.56203300	-2.84586200
H	2.39777600	-0.75012700	-2.11317000
C	-1.09063600	1.55889700	0.63047700
C	-3.04198700	1.37426400	1.77216700
C	-2.52420400	-0.01631400	1.31750900
H	-2.97371400	1.56205000	2.84586000
H	-2.39778000	-0.75011300	2.11318300
O	2.09531600	2.29789400	-1.13382400
O	-2.09531400	2.29790200	1.13382200
N	1.18788800	0.28228600	-0.74021100
N	-1.18788900	0.28229100	0.74022000
C	4.44989400	1.56501900	-1.18871300
C	-4.44989300	1.56502700	1.18870500
C	3.51063200	-0.44384900	-0.24985100
C	3.43503000	-1.55628900	0.58899900
C	4.56515000	0.46973700	-0.15032000
C	4.43788000	-1.73471100	1.54536000
H	2.61538800	-2.26205000	0.49551000
C	5.56698100	0.28560300	0.80180900
C	5.49408000	-0.82146100	1.65198300
H	4.39445600	-2.59166900	2.21140600
H	6.39045800	0.99085500	0.88432000
H	6.26565400	-0.97493500	2.40182100
H	5.20011200	1.44661000	-1.98147600
H	4.56967100	2.57594200	-0.78328300
C	-3.51062700	-0.44384400	0.24985700
C	-3.43501700	-1.55628800	-0.58898700
C	-4.56514300	0.46974100	0.15031400
C	-4.43786000	-1.73471500	-1.54535500
H	-2.61537500	-2.26204700	-0.49549000
C	-5.56696800	0.28560300	-0.80182100
C	-5.49406000	-0.82146500	-1.65198900
H	-4.39443100	-2.59167400	-2.21139800
H	-6.39044400	0.99085500	-0.88434100
H	-6.26562700	-0.97494200	-2.40183300
H	-5.20011400	1.44661500	1.98146500
H	-4.56967300	2.57595000	0.78327400
Ni	-0.00000200	-1.14356200	0.00000300
Cl	-0.71978600	-2.66568700	1.48657600
Cl	0.71975700	-2.66569100	-1.48657800

TS1

C	-1.05584700	0.89662900	-3.79898300
C	-0.92083500	1.17557100	-2.29343800
C	-1.06769600	2.30559400	-3.32646300
H	-0.16620700	0.51693600	-4.28908200
H	-1.99528800	0.44884900	-4.10598300
H	-2.00856000	2.84351200	-3.30064600
H	-0.17975200	2.90975700	-3.48015400
C	-2.09530300	0.83643400	-1.46137000
C	-4.29566400	0.90548800	-0.94148600
C	-3.51430500	-0.02258700	0.02688400
H	-4.59199000	1.86533200	-0.51392300
H	-3.63456200	0.22184900	1.08420100
C	0.41473600	1.05373700	-1.67121800
C	2.66920900	0.85510800	-1.71649500
C	2.14510400	1.10600700	-0.28042400
H	2.98683100	-0.17258200	-1.91186600
H	2.49463200	0.37043000	0.44594000
O	-3.28871500	1.20140000	-1.96844900
O	1.46357000	1.08268800	-2.52378900
N	-2.09915500	0.19721600	-0.34813100
N	0.67950300	0.99420600	-0.41813200
C	-5.44190700	0.09126400	-1.55083300
C	3.72885000	1.92119100	-2.01636800
C	-3.99803800	-1.41188500	-0.34834300
C	-3.50273900	-2.64360700	0.07883900
C	-5.05237000	-1.34284600	-1.26646300
C	-4.07447500	-3.81104700	-0.43326900
H	-2.69797700	-2.68765900	0.80437500
C	-5.62274600	-2.50862700	-1.77612800
C	-5.12515800	-3.74506400	-1.35621100
H	-3.70012100	-4.77862100	-0.11001500
H	-6.44092900	-2.45778200	-2.49048300
H	-5.55868000	-4.66163200	-1.74753900
H	-6.38671300	0.35341000	-1.05667800
H	-5.56293400	0.31617000	-2.61610300
C	2.60104300	2.51909500	0.02464300
C	2.22385600	3.33003400	1.09353800
C	3.48199100	2.97826000	-0.96083800
C	2.76054300	4.61793600	1.16938500
H	1.48841300	2.98993300	1.81581200
C	4.01768500	4.26278800	-0.88054000
C	3.65324700	5.07902500	0.19418300
H	2.46940700	5.27051000	1.98761100
H	4.70094500	4.62772300	-1.64372300
H	4.05865700	6.08488700	0.26687600
H	4.73044300	1.48068300	-1.92230800
H	3.63604500	2.29146900	-3.04328800
Ni	-0.62992500	0.39158400	1.09701700
C	0.14520600	-1.46090200	1.05306000
C	1.40732100	-1.61682700	1.50717100
H	-0.31299900	-2.04962100	0.26152600
H	1.68174300	-1.10086300	2.42747200
C	2.49157700	-2.32559200	0.82522800
C	3.74667800	-2.44072900	1.44634600
C	2.36658500	-2.85002800	-0.48193600

C	4.82896100	-3.06044800	0.82009200
H	3.87940700	-2.03847100	2.44795200
C	3.43208400	-3.46857700	-1.11546300
H	1.42078100	-2.76087600	-1.00897100
C	4.67635700	-3.58135200	-0.47045400
H	5.77552200	-3.12906600	1.34371200
H	3.33380500	-3.87313600	-2.11815400
O	5.65806800	-4.20007800	-1.18629800
C	6.93347900	-4.35406700	-0.58259200
H	7.55201700	-4.87442800	-1.31620500
H	7.38965200	-3.38248300	-0.34759100
H	6.87577700	-4.95503500	0.33512900
Br	-1.44118600	-1.23197500	2.80236100
Br	-1.30366700	2.56382000	1.96385100

TS2-*S*

C	3.06533600	3.75139600	-0.25459700
C	2.43773300	2.38254800	0.08018700
C	3.34577300	3.13862400	1.06689800
H	3.84222100	3.73508700	-1.00992800
H	2.36947800	4.58111900	-0.30266600
H	2.84254900	3.53642500	1.94074400
H	4.32116600	2.69577400	1.23789300
C	0.98949600	2.38723100	0.34882200
C	-0.90790000	3.32868100	1.14922800
C	-1.20355200	2.05954800	0.31764600
H	-1.01878000	3.20317500	2.22812000
H	-1.83818800	1.33816600	0.82819300
C	3.01699600	1.19812400	-0.58757000
C	4.71129500	0.16140800	-1.67453800
C	3.49998200	-0.79599300	-1.47785700
H	4.88489600	0.46227000	-2.71024600
H	3.07288700	-1.19479400	-2.39845100
O	0.52167700	3.52713300	0.89863900
O	4.30538100	1.36373500	-0.95864400
N	0.13497500	1.46911400	0.07213000
N	2.46071500	0.06827000	-0.83920100
C	-1.71954400	4.47901300	0.54038100
C	5.94182600	-0.46804400	-1.00032700
C	-1.81501400	2.60062400	-0.95816300
C	-2.06009600	1.91699000	-2.14808600
C	-2.08142200	3.96888000	-0.83883600
C	-2.59813500	2.62800800	-3.22388600
H	-1.82825000	0.86058600	-2.22544100
C	-2.61980300	4.67550500	-1.91329000
C	-2.87849700	3.99502200	-3.10681700
H	-2.79664300	2.11477300	-4.16077900
H	-2.82906800	5.73923700	-1.82895300
H	-3.29487300	4.53427700	-3.95368700
H	-2.61429200	4.66205300	1.15040800
H	-1.14110900	5.40943500	0.53072400
C	4.04047400	-1.88375500	-0.57030500
C	3.37611200	-3.01122400	-0.08701500
C	5.38561300	-1.66010800	-0.25579000
C	4.05976700	-3.88257900	0.76377800

H	2.35079300	-3.19728000	-0.38330500
C	6.06861400	-2.53117300	0.59287900
C	5.39348000	-3.63875900	1.11226200
H	3.54949600	-4.75863800	1.15459900
H	7.11341300	-2.35751100	0.83923700
H	5.91280700	-4.32347200	1.77762700
H	6.67311400	-0.78228400	-1.75590000
H	6.44273400	0.26409600	-0.35662100
Ni	0.44699700	-0.43770500	-0.57422900
C	-1.34020500	-0.88513600	-0.08926900
C	-2.37633600	-1.35969400	-0.79547900
H	-1.50812900	-0.62470400	0.95860100
H	-2.21484800	-1.65504500	-1.83081300
C	-3.75781400	-1.53355200	-0.30880400
C	-4.72552000	-2.08282400	-1.16277400
C	-4.18447600	-1.16739000	0.98628500
C	-6.05207300	-2.27175300	-0.76606700
H	-4.43240400	-2.37656000	-2.16825500
C	-5.49578300	-1.34795200	1.39760200
H	-3.47324100	-0.73300000	1.68389900
C	-6.44479700	-1.90323100	0.52425000
H	-6.75881300	-2.70301700	-1.46618000
H	-5.81838800	-1.06543100	2.39544400
O	-7.71013800	-2.03640100	1.02945800
C	-8.70447200	-2.59637600	0.19038300
H	-9.62325400	-2.61462100	0.78063000
H	-8.86601900	-1.98803700	-0.71091500
H	-8.44975300	-3.62154800	-0.11369100
C	0.96679000	-1.54179300	1.75743500
H	1.98701400	-1.52659300	1.38724500
C	0.62295100	-0.48967300	2.66278100
C	1.54986900	0.56303300	2.90315300
C	-0.62920900	-0.40880200	3.33182800
C	1.24074800	1.62863500	3.73492800
H	2.51855300	0.51957200	2.41134200
C	-0.93846000	0.67044400	4.15425700
H	-1.35556900	-1.20472400	3.20600700
C	-0.01266400	1.70002100	4.36291900
H	1.97704600	2.40938300	3.90913800
H	-1.90633100	0.70466400	4.64852400
H	-0.25278200	2.53250400	5.01856300
C	0.26399300	-2.86369700	1.67067800
H	0.35700400	-3.28125500	0.66461400
H	0.70717600	-3.57850200	2.38380900
H	-0.80484800	-2.79535300	1.88649100
Br	0.56273400	-2.22066500	-2.18652600

TS2-*S*-cf2

C	-5.24604100	0.93263800	-1.09771400
C	-3.78020100	0.46035300	-1.07308800
C	-4.72742500	0.15407600	-2.24963500
H	-5.90476600	0.43784500	-0.39323900
H	-5.38939800	2.00062000	-1.21509500
H	-4.50794100	0.67868100	-3.17351100
H	-5.02398900	-0.88431700	-2.35061300

C	-2.74655500	1.49274900	-1.29434100
C	-1.98700200	3.42406000	-2.20753000
C	-0.96486100	2.81826100	-1.20851700
H	-1.70266200	3.34862100	-3.26044300
H	0.03323200	2.68154400	-1.62838100
C	-3.45812900	-0.65564400	-0.15661300
C	-3.95584800	-2.58543100	0.89349500
C	-2.56383100	-2.06153000	1.33506700
H	-4.65722600	-2.72712100	1.71631600
H	-2.51102600	-1.67969700	2.35673600
O	-3.15146000	2.55628200	-2.02782300
O	-4.48810900	-1.50756000	0.07301600
N	-1.53755500	1.49752100	-0.86628200
N	-2.34852700	-0.89515100	0.43738200
C	-2.29907900	4.85454200	-1.74476600
C	-3.71530200	-3.88040700	0.08024000
C	-0.99473400	3.77315600	-0.03206800
C	-0.40792700	3.60279400	1.22151300
C	-1.76991900	4.89979400	-0.32721500
C	-0.60415400	4.59756500	2.18260700
H	0.15652200	2.70512100	1.45229500
C	-1.95947700	5.89195900	0.63363600
C	-1.36958100	5.73318900	1.89111600
H	-0.16606000	4.47731500	3.16917200
H	-2.56087000	6.77063600	0.41295500
H	-1.51413000	6.49578700	2.65203700
H	-1.78308600	5.57546900	-2.39295200
H	-3.37165200	5.06429800	-1.82287900
C	-1.63701400	-3.22968500	1.11404200
C	-0.32240600	-3.37122400	1.55443700
C	-2.29174100	-4.26218300	0.43149700
C	0.33339800	-4.58010100	1.30880200
H	0.16271500	-2.55238700	2.07634500
C	-1.63083300	-5.46401400	0.17928500
C	-0.31473600	-5.61749800	0.62868500
H	1.35947900	-4.70970400	1.63921900
H	-2.13241000	-6.27485600	-0.34340400
H	0.20868400	-6.55261500	0.44675600
H	-4.44056000	-4.66386700	0.32549000
H	-3.82651700	-3.66274500	-0.99024600
Ni	-0.57037800	0.09954800	0.34237500
C	1.19758600	0.77276100	0.08725800
C	2.29005800	0.49311700	0.81753900
H	1.34097700	1.32648500	-0.84872600
H	2.16264300	-0.06577100	1.74245300
C	3.68876100	0.77871900	0.45664600
C	4.72233100	0.11693400	1.13625400
C	4.06738100	1.64744600	-0.58872200
C	6.06653300	0.27757500	0.79072700
H	4.46646400	-0.55885700	1.94895800
C	5.39590500	1.81982100	-0.94714600
H	3.30220700	2.20003800	-1.12725200
C	6.41049900	1.13107300	-0.26287700
H	6.82529300	-0.26400500	1.34449200
H	5.68159500	2.49075000	-1.75189700

O	7.68691800	1.36894400	-0.69721200
C	8.74819700	0.70512800	-0.03467800
H	9.66530500	1.03134600	-0.53002100
H	8.79619600	0.97591900	1.02958500
H	8.66069100	-0.38751700	-0.11963100
C	0.02816900	-1.10197600	-1.99384200
H	0.16064700	-0.07561300	-2.32286600
C	1.23175600	-1.87556800	-1.83920300
C	2.50292300	-1.25761600	-1.95384800
C	1.20378100	-3.26829100	-1.58674900
C	3.67706700	-1.97925900	-1.79379100
H	2.55788800	-0.19373500	-2.15525100
C	2.38227300	-3.99083100	-1.43611600
H	0.25316500	-3.77895600	-1.48118200
C	3.62487900	-3.35413400	-1.53162100
H	4.63222900	-1.46575800	-1.85857900
H	2.33047900	-5.05709900	-1.23090100
H	4.54247300	-3.92228100	-1.40350700
C	-1.26706300	-1.75529500	-2.38832200
H	-2.06450400	-1.01734700	-2.49361900
H	-1.15810800	-2.26936900	-3.35697800
H	-1.59331200	-2.50707600	-1.66326800
Br	-0.44406200	0.11836600	2.80762700

TS2-*S*-cf3

C	-0.47501300	2.80575700	3.30454100
C	-0.91695400	2.30951000	1.91624500
C	-1.67712900	3.41112500	2.67567000
H	-0.61024400	2.10347700	4.11993700
H	0.44560300	3.37997800	3.32015500
H	-1.59936900	4.40606100	2.25314900
H	-2.65391400	3.12822000	3.05175500
C	-0.06998900	2.72342100	0.77504700
C	0.96474700	4.28006000	-0.49971100
C	1.27756800	2.84038900	-0.99239300
H	0.27193000	4.83662200	-1.13485400
H	1.02455900	2.66503100	-2.04073700
C	-1.60267300	1.00403500	1.83219500
C	-2.85384100	-0.67757300	2.69557100
C	-2.66246100	-0.82548600	1.16991900
H	-2.26255700	-1.36870200	3.30234700
H	-2.30112200	-1.80473600	0.86803200
O	0.26562000	4.03419900	0.76312200
O	-2.31380200	0.66269700	2.93519900
N	0.39620500	1.98574700	-0.16097800
N	-1.65885000	0.20273300	0.83144800
C	2.29793000	4.99243100	-0.23850800
C	-4.36105700	-0.72438000	2.97740900
C	2.74952200	2.66870500	-0.66665800
C	3.51999100	1.51158000	-0.75572400
C	3.30765900	3.86638300	-0.20588000
C	4.85776700	1.55627900	-0.35721700
H	3.07449600	0.58488600	-1.09092100
C	4.64576200	3.91554300	0.18410600
C	5.41685900	2.75155600	0.11079700

H	5.45586500	0.65005600	-0.40177800
H	5.08274300	4.84365900	0.54515300
H	6.45803600	2.77564800	0.42216100
H	2.51020000	5.69618700	-1.05429700
H	2.25490200	5.57750700	0.68685900
C	-4.02804700	-0.48532300	0.60918600
C	-4.36323900	-0.19793700	-0.71238300
C	-4.98323300	-0.43032100	1.62852400
C	-5.69301400	0.11018000	-1.00868400
H	-3.59734900	-0.16207700	-1.48013800
C	-6.31143000	-0.12717600	1.33040600
C	-6.66179100	0.13471300	0.00272400
H	-5.97284900	0.34671600	-2.03153200
H	-7.06062600	-0.08201100	2.11725600
H	-7.69214900	0.37777400	-0.24355300
H	-4.63263300	-1.72489200	3.34003100
H	-4.64241300	-0.00964800	3.75859600
Ni	-0.43574700	0.13162200	-0.87840800
C	1.01519800	-0.96171900	-0.10574800
C	2.04267300	-1.55781600	-0.73849400
H	1.08599800	-0.87082900	0.98616300
H	2.02095000	-1.62319100	-1.83192500
C	3.30171100	-2.06014300	-0.15285600
C	4.40947000	-2.29128700	-0.98127800
C	3.47755000	-2.28007300	1.22896200
C	5.64727600	-2.70041800	-0.47553000
H	4.30862500	-2.13483400	-2.05347700
C	4.69504400	-2.69143000	1.74810300
H	2.63940900	-2.12598700	1.90267900
C	5.79557200	-2.90077600	0.90085500
H	6.47385700	-2.86011500	-1.15876900
H	4.82606800	-2.86218700	2.81248500
O	6.95042700	-3.29973900	1.51595100
C	8.09042500	-3.52921400	0.70660600
H	8.88821400	-3.83347200	1.38742200
H	7.91470300	-4.33011000	-0.02542300
H	8.39880500	-2.61958000	0.17185900
C	-1.03792700	-2.22098700	-2.20683500
H	0.04302000	-2.27980200	-2.19687400
C	-1.71452400	-3.03305200	-1.22790200
C	-3.11634700	-3.24115700	-1.25635500
C	-0.97686400	-3.66936900	-0.19176800
C	-3.74802900	-4.01123400	-0.28423800
H	-3.71289300	-2.77234000	-2.03052200
C	-1.61287700	-4.44456000	0.76839600
H	0.09515400	-3.51032100	-0.14714500
C	-3.00571700	-4.61388200	0.73658000
H	-4.82702800	-4.13561600	-0.31873700
H	-1.02567800	-4.91938500	1.55049200
H	-3.50239100	-5.21473700	1.49369900
C	-1.67313000	-1.85503000	-3.51482600
H	-1.82654100	-2.76770300	-4.11535800
H	-2.64517800	-1.36835500	-3.39782000
H	-1.04290800	-1.16617700	-4.07804600
Br	-1.53281300	1.39671500	-2.66981400

TS2-*R*

C	4.22818600	2.95283600	1.33414200
C	3.18356600	1.83386900	1.16632000
C	4.10022600	1.93023200	2.40160700
H	5.07893700	2.89766400	0.66480300
H	3.82535500	3.94320900	1.51214100
H	3.60416200	2.20321200	3.32702500
H	4.86238600	1.16238400	2.47959900
C	1.77025100	2.21715000	1.34853600
C	0.11011700	3.47711000	2.24200700
C	-0.41614800	2.54064400	1.12569800
H	-0.16215500	3.18544500	3.25996600
H	-1.27687800	1.93439100	1.40867100
C	3.49150800	0.77343100	0.17975100
C	4.93449400	-0.58545600	-0.89311200
C	3.47790700	-0.84540200	-1.37080100
H	5.62177100	-0.30810000	-1.69291400
H	3.25789500	-0.54356700	-2.39652100
O	1.56199400	3.30125300	2.13029500
O	4.81611300	0.57575500	-0.02482100
N	0.73657800	1.65885700	0.83299700
N	2.67228000	0.03861900	-0.47876200
C	-0.28571700	4.91117200	1.86837500
C	5.39312200	-1.83634700	-0.10543400
C	-0.70272700	3.48572200	-0.02532200
C	-0.97249000	3.15932200	-1.35400500
C	-0.60495100	4.81774300	0.39145000
C	-1.16281400	4.20186000	-2.26460100
H	-1.00363000	2.12333900	-1.67264500
C	-0.79959500	5.85488700	-0.51944800
C	-1.08251100	5.53726400	-1.85116500
H	-1.36596300	3.96896300	-3.30606200
H	-0.72454500	6.89263900	-0.20340200
H	-1.23144800	6.33543600	-2.57379900
H	-1.16319500	5.21540600	2.45476500
H	0.51901200	5.61618500	2.10438400
C	3.26929600	-2.32335300	-1.13831600
C	2.20105500	-3.11743300	-1.55822600
C	4.32682600	-2.86790800	-0.40232700
C	2.19214700	-4.46753900	-1.19878300
H	1.39258300	-2.67481000	-2.13125200
C	4.31576900	-4.21613100	-0.04584700
C	3.23669500	-5.01137600	-0.44166400
H	1.36478300	-5.09966900	-1.50898300
H	5.13444400	-4.64494800	0.52696700
H	3.21393500	-6.06268300	-0.16740200
H	6.39207300	-2.16756300	-0.41130400
H	5.45139800	-1.59514100	0.96366900
Ni	0.60934800	0.05817200	-0.42880600
C	-1.26167500	-0.14690900	-0.10097900
C	-2.30371300	-0.26818400	-0.93807100
H	-1.45843900	-0.17467300	0.97684300
H	-2.11876000	-0.22913000	-2.00981100
C	-3.71622900	-0.45603400	-0.56020800

C	-4.71807700	-0.32025600	-1.53241900
C	-4.13104800	-0.79107200	0.74594100
C	-6.07359800	-0.48741600	-1.23479700
H	-4.43151900	-0.07317900	-2.55243700
C	-5.47048800	-0.96335500	1.05828600
H	-3.38703700	-0.94706500	1.51952100
C	-6.45672600	-0.80942500	0.07101600
H	-6.80902200	-0.36785300	-2.02264900
H	-5.78361800	-1.23278900	2.06286500
O	-7.74855400	-1.00341700	0.48551600
C	-8.77977700	-0.87281500	-0.47553600
H	-9.71489600	-1.06644500	0.05488000
H	-8.81114300	0.13889800	-0.90479500
H	-8.67034700	-1.60084200	-1.29210200
C	0.88829200	-1.80576800	1.50093000
C	-0.37012000	-2.44243300	1.75272300
C	-1.08484900	-2.26467100	2.96391900
C	-0.95457200	-3.27636200	0.76343700
C	-2.30006700	-2.90993500	3.18178100
H	-0.67330000	-1.62885600	3.74232200
C	-2.16997700	-3.90583200	0.98144600
H	-0.44032400	-3.39050200	-0.18582300
C	-2.85072300	-3.73342600	2.19559900
H	-2.82491300	-2.76483300	4.12287200
H	-2.60319900	-4.52581600	0.20140200
H	-3.80739800	-4.22071100	2.35989900
C	1.62165000	-1.05690700	2.57420500
H	1.05265700	-0.19133100	2.93714000
H	1.81814500	-1.69938800	3.44725100
H	2.58358700	-0.69295700	2.20896000
H	1.47579600	-2.20432600	0.68354400
Br	0.49764500	-0.21368200	-2.86300700

TS2-*R*-cf2

C	4.61806900	2.25812300	0.60197100
C	3.37474000	1.35362400	0.64547200
C	4.29028600	1.55676400	1.86886400
H	5.44315100	1.88693400	0.00490800
H	4.41891800	3.32128300	0.53226300
H	3.85892600	2.13038000	2.68246400
H	4.88486800	0.69611100	2.15601400
C	2.05899600	2.02838300	0.67508300
C	0.68984600	3.75653800	1.20908500
C	-0.05381500	2.66422000	0.39603400
H	0.38796300	3.81603300	2.25498200
H	-0.93675300	2.28253700	0.91035600
C	3.46816500	0.05391000	-0.05514600
C	4.62186600	-1.72761000	-0.84650200
C	3.10916500	-1.84143100	-1.19080400
H	5.27264500	-1.64899100	-1.71859400
H	2.87001600	-1.80945500	-2.25507300
O	2.07253900	3.27406100	1.20366000
O	4.72152900	-0.45018600	-0.14762200
N	0.93544500	1.57407900	0.26011200
N	2.51551400	-0.62810000	-0.57145400

C	0.56148300	5.08104800	0.43954500
C	4.98595400	-2.91163700	0.07805700
C	-0.34392100	3.32173500	-0.93700200
C	-0.84236800	2.72537500	-2.09574100
C	0.02679100	4.67051900	-0.91626000
C	-0.98611000	3.51596600	-3.23862000
H	-1.07740900	1.66569200	-2.11962800
C	-0.12241500	5.45711100	-2.05785600
C	-0.63468700	4.87114800	-3.21899200
H	-1.36378400	3.06709900	-4.15281600
H	0.16242500	6.50657500	-2.04935000
H	-0.75077500	5.47140600	-4.11769200
H	-0.13327900	5.75106400	0.96307000
H	1.52680100	5.59747700	0.39026200
C	2.65934500	-3.11805700	-0.52467600
C	1.38197600	-3.67852900	-0.54102500
C	3.69683300	-3.69415100	0.21430000
C	1.15048200	-4.82762800	0.21864400
H	0.59602800	-3.21165400	-1.12667500
C	3.46430500	-4.84563000	0.96673800
C	2.18288700	-5.40455900	0.96928600
H	0.16119600	-5.27683500	0.22658200
H	4.26320200	-5.29992700	1.54778900
H	1.98761800	-6.29760200	1.55704300
H	5.78994800	-3.51832300	-0.35582900
H	5.35451400	-2.53511000	1.03985500
Ni	0.50392500	-0.26841200	-0.58224000
C	-1.39415800	-0.17808200	-0.41733900
C	-2.29751800	-1.09707200	-0.79584600
H	-1.74718000	0.68600700	0.14846000
H	-1.95679300	-1.95601700	-1.37243900
C	-3.73975200	-1.09323200	-0.49147600
C	-4.51997900	-2.21156300	-0.82307800
C	-4.40250700	-0.01969300	0.14397200
C	-5.88545300	-2.28244900	-0.53578300
H	-4.04510100	-3.05418800	-1.32098500
C	-5.75652700	-0.07285300	0.43721800
H	-3.84391600	0.87236200	0.40975000
C	-6.51276200	-1.20754500	0.10240300
H	-6.44066600	-3.17132700	-0.81374000
H	-6.26135800	0.75804600	0.92132400
O	-7.83865800	-1.15769700	0.43765300
C	-8.65030600	-2.27053500	0.10684700
H	-9.65660000	-2.02426100	0.45256300
H	-8.67392100	-2.44829600	-0.97761300
H	-8.30953500	-3.18655200	0.61015300
C	0.25062300	-1.10137500	1.94414400
C	-0.48815300	-0.07298100	2.63343100
C	0.15497900	0.94275700	3.38612900
C	-1.90626200	-0.04586000	2.59081300
C	-0.57573500	1.93430300	4.03365400
H	1.23818400	0.95268800	3.45754000
C	-2.63176500	0.95239800	3.23201700
H	-2.43019400	-0.81768600	2.03871900
C	-1.97378100	1.95617300	3.95281200

H	-0.05393100	2.69536700	4.60985100
H	-3.71666000	0.94223600	3.16853300
H	-2.54078600	2.73429100	4.45635000
C	1.64870400	-1.44437500	2.37497900
H	2.33135000	-0.58990400	2.31643900
H	1.65008100	-1.77365600	3.42690400
H	2.06438800	-2.24862800	1.77109900
H	-0.33284800	-1.90584700	1.50794100
Br	0.34383600	-1.00613000	-2.91029500

TS2-*R*-cf3

C	-0.39683000	4.14318800	2.26550300
C	-0.78091500	2.98313200	1.33267000
C	-1.71213200	4.18486200	1.57599000
H	-0.37001900	3.90835100	3.32371900
H	0.39652400	4.78695900	1.90093500
H	-1.84023600	4.85211400	0.73126000
H	-2.60572100	3.97051800	2.15238200
C	-0.06979300	2.91798100	0.03741100
C	0.72092400	3.83054300	-1.87658400
C	1.08255800	2.32239800	-1.77055100
H	-0.05688700	4.05837400	-2.60804300
H	0.72242700	1.72320100	-2.61079100
C	-1.20771800	1.70897200	1.94754900
C	-1.94680000	0.44661200	3.68114700
C	-1.92642300	-0.35010400	2.35224100
H	-1.15470600	0.18505300	4.38782500
H	-1.37581400	-1.29114200	2.40546000
O	0.14560200	4.11264600	-0.55909400
O	-1.66286300	1.80683200	3.22125300
N	0.37392000	1.87387700	-0.55354200
N	-1.25088200	0.54944100	1.40261200
C	2.02633400	4.61495000	-2.07226800
C	-3.36398400	0.34121900	4.26341600
C	2.58838100	2.32243000	-1.59858000
C	3.41813800	1.24057300	-1.30754100
C	3.10887900	3.61463600	-1.72804000
C	4.78584600	1.46994300	-1.13632900
H	3.00192600	0.24690900	-1.18621500
C	4.47508500	3.84216000	-1.56360300
C	5.31033300	2.76208200	-1.26363600
H	5.43779400	0.63758500	-0.88729400
H	4.88494200	4.84470800	-1.66146700
H	6.37564500	2.92789200	-1.12534000
H	2.10817300	4.94971300	-3.11479700
H	2.04003200	5.51354100	-1.44548200
C	-3.39414100	-0.51543300	2.01621600
C	-3.94736900	-0.91427200	0.80213700
C	-4.20042800	-0.12575000	3.09053600
C	-5.33854000	-0.97345200	0.69201500
H	-3.31722900	-1.12128700	-0.05427100
C	-5.58899100	-0.18211800	2.97824000
C	-6.15236600	-0.61952800	1.77481200
H	-5.78214200	-1.28426800	-0.24948500
H	-6.22550800	0.12017500	3.80637800

H	-7.23365100	-0.66534100	1.67431600
H	-3.37125800	-0.38521800	5.08709800
H	-3.69007000	1.30093500	4.67919700
Ni	-0.44571300	-0.10150200	-0.41657600
C	1.21958500	-0.85395800	0.35949800
C	2.03015900	-1.88034100	0.03954700
H	1.61439900	-0.14369500	1.09862100
H	1.68696600	-2.63337300	-0.67641600
C	3.40269300	-2.13623400	0.52196100
C	4.01924000	-3.36837900	0.25904100
C	4.16664800	-1.17382200	1.21587700
C	5.32262200	-3.65500100	0.67278500
H	3.46362600	-4.13049600	-0.28387700
C	5.46302800	-1.43894200	1.63152000
H	3.74111200	-0.19401600	1.40941500
C	6.05386700	-2.68489500	1.36657700
H	5.75084300	-4.62507400	0.44659600
H	6.04914600	-0.69223700	2.15908400
O	7.33613900	-2.84170900	1.81705600
C	7.98386900	-4.07644700	1.56556200
H	8.98147100	-3.98858200	2.00114400
H	7.45569100	-4.91635600	2.03865300
H	8.07588000	-4.27519300	0.48838300
C	-1.13227000	-2.76119200	-0.84380000
C	-2.23205400	-2.94461900	-1.74655400
C	-3.48212800	-3.46899200	-1.32767600
C	-2.08275100	-2.62492000	-3.12075800
C	-4.51933600	-3.65802100	-2.23376100
H	-3.63573900	-3.72489100	-0.28471400
C	-3.11796900	-2.82456000	-4.02248100
H	-1.14425100	-2.19575100	-3.45639800
C	-4.34500100	-3.33862600	-3.58558100
H	-5.46735400	-4.06297300	-1.88849400
H	-2.97806300	-2.56559100	-5.06832300
H	-5.15789000	-3.48742900	-4.29119600
C	-1.13460900	-3.33844800	0.54209000
H	-0.23945100	-3.03099600	1.08454000
H	-2.01838100	-3.03171800	1.11378700
H	-1.15755900	-4.43991500	0.50251600
H	-0.16642400	-2.59456400	-1.30825900
Br	-2.03898400	0.56242800	-2.14637500

TS3-*S*

C	3.69301300	3.47518800	-0.64044600
C	2.87608200	2.25666700	-0.17715000
C	3.92036200	2.94410700	0.72701600
H	4.43656200	3.27539700	-1.40339000
H	3.13306400	4.39676300	-0.75072200
H	3.51486200	3.48957400	1.57189700
H	4.82198000	2.37165600	0.91641400
C	1.45774900	2.49811700	0.16155300
C	-0.19782200	3.78491000	1.02321800
C	-0.73611800	2.42898700	0.49739800
H	-0.19403500	3.87388400	2.11195800
H	-1.26959600	1.86585300	1.26365500

C	3.25586800	0.94044400	-0.73613700
C	4.78422300	-0.52787400	-1.51229000
C	3.35974000	-1.15431800	-1.50721500
H	5.25528700	-0.49973600	-2.49548600
H	2.93117000	-1.36118900	-2.49015000
O	1.20101500	3.75145500	0.60763900
O	4.55551700	0.85508800	-1.12218100
N	0.47562100	1.67761900	0.10248900
N	2.52177600	-0.09744700	-0.88128300
C	-0.96701000	4.90318800	0.29980900
C	5.62889000	-1.28380400	-0.45721800
C	-1.58860300	2.79807900	-0.69582600
C	-2.17483900	1.93858700	-1.62485000
C	-1.69215000	4.18723200	-0.82118900
C	-2.89000200	2.49917900	-2.68584600
H	-2.05641000	0.86300500	-1.53653500
C	-2.40870600	4.74273800	-1.88065000
C	-3.00873900	3.88890200	-2.81085000
H	-3.34940800	1.84773300	-3.42369900
H	-2.49507500	5.82149100	-1.98718600
H	-3.56639400	4.30904500	-3.64383700
H	-1.66980100	5.38357500	0.99325700
H	-0.28108100	5.68259900	-0.05073300
C	3.49787000	-2.39400700	-0.65732800
C	2.55069200	-3.39721400	-0.45393200
C	4.75389000	-2.44848200	-0.04481900
C	2.87091500	-4.45234700	0.40420000
H	1.58905000	-3.33620300	-0.95520500
C	5.07262500	-3.50450000	0.80862100
C	4.11978800	-4.50232000	1.03538700
H	2.14435800	-5.24050700	0.58090700
H	6.04766700	-3.55660900	1.28717600
H	4.35576300	-5.32973300	1.69947500
H	6.58988200	-1.61358800	-0.86897500
H	5.85648300	-0.61339800	0.38120700
Ni	0.42576000	-0.37968900	-0.47077600
C	-1.27355900	-0.77182900	0.38256000
C	-2.17501400	-1.65809200	-0.08327500
H	-1.60953400	0.00650800	1.06209400
H	-1.83287500	-2.44363500	-0.75318900
C	-3.61979700	-1.62129300	0.16580100
C	-4.47489600	-2.40903400	-0.62223700
C	-4.22055200	-0.82454700	1.16598300
C	-5.85975900	-2.40649900	-0.44667700
H	-4.04381200	-3.03327800	-1.40127700
C	-5.59317900	-0.81021300	1.35276100
H	-3.59706800	-0.21535500	1.81475200
C	-6.42851900	-1.60004600	0.54549700
H	-6.47622200	-3.03032000	-1.08396400
H	-6.05153000	-0.20036000	2.12546600
O	-7.76582900	-1.51305500	0.81439500
C	-8.65554000	-2.29021100	0.03105200
H	-9.65749100	-2.07125700	0.40607000
H	-8.60039900	-2.02080800	-1.03297500
H	-8.45639400	-3.36582400	0.13753800

C	0.48889000	-1.39203200	1.45009400
H	1.49064700	-1.55089700	1.04096500
C	0.55803400	-0.36160700	2.52330000
C	1.71927700	0.42047300	2.66771800
C	-0.51852800	-0.09739600	3.39023400
C	1.79408700	1.44464200	3.60801800
H	2.56106300	0.22613600	2.00850700
C	-0.44964600	0.93221800	4.33132400
H	-1.41946500	-0.69993100	3.32367900
C	0.70198600	1.71548200	4.43995900
H	2.70509100	2.03203200	3.69510200
H	-1.29822800	1.11971600	4.98452600
H	0.75581600	2.51402900	5.17517200
C	-0.06050700	-2.76299600	1.82618000
H	-0.15124900	-3.38671100	0.93307800
H	0.63863300	-3.25577600	2.51691300
H	-1.04422100	-2.71641400	2.29845600
Br	0.13717800	-1.58531800	-2.63128400

TS3-*S*-cf2

C	-2.89739700	4.22721900	-1.47020700
C	-2.20981200	2.89088400	-1.17188100
C	-3.01969300	3.13035500	-2.46483400
H	-3.75603200	4.46049800	-0.85300000
H	-2.23774500	5.05614600	-1.69585300
H	-2.44138700	3.18603400	-3.38205900
H	-3.95751800	2.58843100	-2.53598900
C	-0.73637200	2.84988600	-1.30260700
C	1.26192000	3.72151800	-1.92966900
C	1.43185600	2.41222500	-1.11350900
H	1.50400100	3.63716300	-2.99240400
H	2.05028600	1.66450800	-1.61186900
C	-2.83676200	2.01614700	-0.14575000
C	-4.57168800	1.46317700	1.19924400
C	-3.38913200	0.45827300	1.35751200
H	-4.80127100	2.03092800	2.10261800
H	-2.92078600	0.43383100	2.34357500
O	-0.17719200	3.95804500	-1.84554200
O	-4.07600200	2.42357600	0.22572800
N	0.05050300	1.90012700	-0.95414500
N	-2.36549600	0.95718400	0.39599000
C	2.04043500	4.82875800	-1.20017900
C	-5.78754600	0.69136000	0.63905400
C	2.01914000	2.87164800	0.20406900
C	2.20669900	2.11728600	1.36143200
C	2.33076000	4.23430600	0.16189700
C	2.72611000	2.75671400	2.48948100
H	1.92341600	1.07061500	1.39790500
C	2.85435300	4.86746100	1.28843400
C	3.05067500	4.11836800	2.45250100
H	2.86575900	2.18950100	3.40513900
H	3.09963600	5.92660400	1.26624000
H	3.45177000	4.60100900	3.33997900
H	2.96516700	5.05622400	-1.74704500
H	1.45531400	5.75426900	-1.16105100

C	-3.98161700	-0.87068500	0.95341200
C	-3.35917300	-2.11501200	0.98328800
C	-5.29123500	-0.72904600	0.48457600
C	-4.04421300	-3.22299400	0.48016000
H	-2.35711900	-2.19945600	1.38214400
C	-5.98279900	-1.83702400	-0.00469700
C	-5.34510100	-3.08201000	-0.01707800
H	-3.55175200	-4.19064100	0.46314000
H	-7.00225900	-1.73736800	-0.37019100
H	-5.86951800	-3.94989500	-0.40870700
H	-6.63931400	0.74698500	1.32831700
H	-6.11392400	1.14289800	-0.30552100
Ni	-0.39367400	-0.02339300	0.03594900
C	1.23964400	-0.77853200	-0.68959600
C	2.10209600	-1.52012700	0.03201000
H	1.61113000	-0.24898900	-1.56455900
H	1.74414200	-2.03257200	0.91882800
C	3.54944300	-1.59267500	-0.20006500
C	4.39357000	-1.98885700	0.84988500
C	4.15998300	-1.26863600	-1.43088200
C	5.78067200	-2.04325100	0.70550400
H	3.95231400	-2.24984500	1.80882000
C	5.53593200	-1.31693900	-1.59048100
H	3.54105600	-0.99708400	-2.28179300
C	6.36143200	-1.70071300	-0.52114000
H	6.38984200	-2.35068700	1.54787100
H	6.00330900	-1.07590600	-2.54048400
O	7.70231200	-1.71595200	-0.78462600
C	8.58241800	-2.10871800	0.25504200
H	9.58896600	-2.05174700	-0.16453500
H	8.51282300	-1.43605800	1.12131900
H	8.38584400	-3.13819700	0.58559900
C	-0.54069500	-1.50446700	-1.57300400
H	0.16019300	-1.46196700	-2.40846700
C	-0.71253300	-2.95930700	-1.18811500
C	-1.06919800	-3.86676800	-2.20141000
C	-0.53320500	-3.46093000	0.10543300
C	-1.26274000	-5.22031100	-1.92736400
H	-1.19420000	-3.50970000	-3.22146700
C	-0.72308000	-4.81660600	0.38462900
H	-0.26751600	-2.78159600	0.90624500
C	-1.09312100	-5.70319300	-0.62721700
H	-1.54013700	-5.89822700	-2.73088600
H	-0.58048200	-5.17384400	1.40138100
H	-1.23969600	-6.75807800	-0.40981400
C	-1.84614600	-0.86747500	-2.10495600
H	-1.69563000	0.18052300	-2.38450900
H	-2.15452900	-1.40839700	-3.01217300
H	-2.66378200	-0.93059600	-1.38780500
Br	-0.25568000	-0.60870500	2.48313100

TS3-*S*-cf3

C	1.60857000	-2.54903300	1.37114900
C	0.45608400	-1.58616000	1.73603300
C	0.92419800	-2.69686000	2.68052600

H	1.39308400	-3.25793300	0.57879500
H	2.59555800	-2.10101300	1.32391400
H	1.43953300	-2.36367100	3.57377200
H	0.23480600	-3.52211700	2.81399800
C	0.84843900	-0.19497600	2.06413500
C	2.11495300	1.34816100	3.11904800
C	1.11042400	2.02252300	2.12996200
H	1.98589300	1.64637100	4.16034700
H	0.34693000	2.65230700	2.59502400
C	-0.82874700	-1.78209800	1.02153600
C	-2.52079900	-3.06716500	0.23160000
C	-2.74840700	-1.56535900	-0.08143500
H	-2.24566200	-3.67713000	-0.63334700
H	-2.93456300	-1.36100900	-1.13283400
O	1.77557800	-0.06607900	3.04881300
O	-1.34984600	-3.03018200	1.10846800
N	0.43043400	0.87276600	1.50354000
N	-1.48158100	-0.92305900	0.32670500
C	3.54341800	1.60966400	2.58521400
C	-3.75393200	-3.57872100	0.99076500
C	1.98903100	2.78958000	1.16722000
C	1.58452900	3.61896800	0.12119500
C	3.34263300	2.54398700	1.41295700
C	2.56416500	4.18922100	-0.69684300
H	0.52693200	3.79343900	-0.05257900
C	4.31917300	3.12546900	0.60331000
C	3.92182100	3.94288300	-0.45941900
H	2.26699300	4.83181600	-1.52110000
H	5.37480500	2.94305600	0.79101600
H	4.67360100	4.39446300	-1.10119500
H	4.19200100	2.04169700	3.35642100
H	3.99745800	0.66011800	2.27506300
C	-3.91607700	-1.18392000	0.80300000
C	-4.42212200	0.09220300	1.04322400
C	-4.46931500	-2.31331400	1.41466300
C	-5.51027700	0.22010400	1.91019400
H	-3.95305900	0.96497900	0.59953100
C	-5.55747400	-2.18243000	2.27697100
C	-6.07604400	-0.90719200	2.51919900
H	-5.91424300	1.20699600	2.11895100
H	-5.99297200	-3.05529100	2.75774700
H	-6.92140500	-0.78960800	3.19241000
H	-4.37570300	-4.18823500	0.32151500
H	-3.45979700	-4.22051300	1.82873700
Ni	-0.60763200	0.90738200	-0.43140800
C	0.75665700	-0.11212200	-1.37031700
C	2.06214200	0.20656700	-1.29386200
H	0.44153900	-1.13633400	-1.57876300
H	2.34412900	1.23946600	-1.09828800
C	3.16677200	-0.76356400	-1.28685200
C	4.39369300	-0.41232100	-0.70032000
C	3.04760000	-2.07930400	-1.78528500
C	5.44663700	-1.32336400	-0.57772500
H	4.52334400	0.59894300	-0.32468400
C	4.08317200	-2.99422800	-1.67229700

H	2.12750400	-2.38372400	-2.27664000
C	5.29290500	-2.62833500	-1.05910500
H	6.37268100	-1.00322500	-0.11319200
H	3.98869600	-4.00361800	-2.06136000
O	6.24436800	-3.60754400	-0.99311000
C	7.49245400	-3.28591300	-0.40344500
H	8.09480800	-4.19502200	-0.45700900
H	8.00349800	-2.48041900	-0.94922300
H	7.37968800	-2.98848100	0.64878200
C	-0.62444500	0.98065600	-2.69355300
H	0.10413900	0.45654400	-3.30561700
C	-1.95964500	0.36373000	-2.91852400
C	-3.17126100	0.98607900	-2.55725900
C	-2.02547400	-0.90869900	-3.52157900
C	-4.39181900	0.35262100	-2.78310100
H	-3.14412200	1.94508400	-2.05254700
C	-3.24829100	-1.54142700	-3.74780300
H	-1.10168700	-1.40160000	-3.81762000
C	-4.44050900	-0.91355400	-3.37624900
H	-5.31137900	0.84635700	-2.48081600
H	-3.27017400	-2.52141200	-4.21842600
H	-5.39543100	-1.40328900	-3.54651500
C	-0.43061000	2.47816000	-2.88724500
H	-0.54848000	2.72445500	-3.95315500
H	-1.13123600	3.07842300	-2.30603900
H	0.58436600	2.76127400	-2.58680700
Br	-2.00361500	2.85830100	0.30308500

TS3-*R*

C	4.83539800	-0.06231100	1.96008100
C	3.42062200	-0.08523600	1.37450400
C	3.75071000	-0.69697900	2.75256000
H	5.55674300	-0.70154300	1.46516500
H	5.19929100	0.90961500	2.27162000
H	3.34909600	-0.16807600	3.61103100
H	3.70560600	-1.78036200	2.80809000
C	2.67159200	1.19678900	1.36864300
C	2.23540200	3.28681300	2.13504700
C	1.33770700	2.91643100	0.92095300
H	1.71828600	3.32121600	3.09753200
H	0.26757200	3.03479000	1.10777000
C	3.15207300	-1.03188000	0.25989400
C	3.67326500	-2.73899900	-1.11892100
C	2.31015400	-2.10070400	-1.51119800
H	4.42201000	-2.71347200	-1.91123300
H	2.30482700	-1.53486900	-2.44683000
O	3.15787800	2.15196700	2.19867600
O	4.17084000	-1.87158100	-0.05615000
N	1.63145900	1.49130500	0.68058500
N	2.07608300	-1.12379000	-0.42435600
C	2.98431100	4.58125700	1.78256900
C	3.37588700	-4.17382700	-0.61909600
C	1.84463500	3.80671900	-0.19337700
C	1.50398700	3.75275300	-1.54395000
C	2.78391500	4.72375400	0.28857100

C	2.11891200	4.65616100	-2.41459700
H	0.81493100	2.99840700	-1.91409600
C	3.39328100	5.62488200	-0.58380800
C	3.05170600	5.58635800	-1.93876500
H	1.87555300	4.62703900	-3.47293900
H	4.12551400	6.34156400	-0.21963900
H	3.52170100	6.28040000	-2.63076500
H	2.54727000	5.42570300	2.33192400
H	4.03649500	4.51565100	2.08097900
C	1.34258000	-3.25512200	-1.53441900
C	0.02288300	-3.24892800	-1.98335500
C	1.94343600	-4.42089800	-1.04824900
C	-0.69617400	-4.44592200	-1.94327900
H	-0.41584200	-2.32820200	-2.35803600
C	1.22501000	-5.61596300	-1.01695200
C	-0.09861200	-5.61983900	-1.46965400
H	-1.72661100	-4.46586400	-2.28643700
H	1.68529400	-6.53197000	-0.65404200
H	-0.66901900	-6.54487100	-1.45143900
H	4.07610500	-4.90638800	-1.03596200
H	3.48846100	-4.21130600	0.47244300
Ni	0.27450100	0.06457800	-0.23961900
C	-1.44634600	0.67227100	0.38217800
C	-2.60835800	0.09474800	0.02235800
H	-1.42958000	1.69473600	0.76332200
H	-2.58824200	-0.96102300	-0.24730300
C	-3.93541600	0.71335300	-0.02553400
C	-5.06961300	-0.10004700	-0.17888300
C	-4.15126000	2.10372300	0.09109500
C	-6.36336600	0.42506500	-0.19913300
H	-4.93631300	-1.17541800	-0.27374000
C	-5.42839500	2.64037200	0.07433300
H	-3.29954700	2.77241200	0.17871700
C	-6.54911400	1.80561900	-0.06917400
H	-7.20685000	-0.24591100	-0.31677700
H	-5.59156700	3.71060000	0.15804300
O	-7.76190200	2.43807700	-0.07502700
C	-8.92472300	1.64683800	-0.24479900
H	-9.76752000	2.34118300	-0.22947700
H	-8.91469200	1.11099600	-1.20438800
H	-9.04279700	0.91751700	0.56925500
C	-0.36751400	-0.53696300	1.84984500
C	-1.07281300	-1.84490000	1.90449200
C	-2.40893200	-1.96567600	2.32882900
C	-0.38572400	-3.01883400	1.55088900
C	-3.02676300	-3.21361400	2.40229900
H	-2.97272700	-1.07641100	2.58928200
C	-0.99859400	-4.26762900	1.62994000
H	0.63881900	-2.94402700	1.19798100
C	-2.32485600	-4.37093300	2.05573200
H	-4.06043500	-3.28093000	2.73237000
H	-0.44158800	-5.15413900	1.34514300
H	-2.80726100	-5.34311200	2.11546500
C	-0.67607200	0.45426800	2.96469400
H	-1.72929200	0.74528500	2.99840900

H	-0.41951600	0.00946400	3.93688500
H	-0.08188800	1.36572800	2.84493600
H	0.70992300	-0.72205600	1.85322900
Br	0.14901400	0.43718100	-2.69357000

TS3-*R*-cf2

C	4.43857400	2.96426800	0.15677300
C	3.37114100	1.87788600	0.37296000
C	4.39798100	2.25552700	1.46056500
H	5.22419700	2.70916400	-0.54490900
H	4.06877600	3.98177200	0.10838100
H	3.99643800	2.77779200	2.32268300
H	5.15359400	1.50567300	1.66898100
C	1.98151900	2.34334300	0.58561100
C	0.45378300	3.87631500	1.27157900
C	-0.22378000	2.63294600	0.63725400
H	0.32593200	3.96163300	2.35378200
H	-0.95454400	2.16115700	1.29651000
C	3.58335600	0.59080000	-0.33179500
C	4.90160400	-1.01478300	-1.22279300
C	3.39437500	-1.35255500	-1.41956400
H	5.46244200	-0.91419200	-2.15274600
H	3.03499900	-1.34154300	-2.45103100
O	1.87414000	3.61629900	1.04045800
O	4.88385800	0.30712100	-0.60824300
N	0.89232200	1.69276300	0.40055900
N	2.70070200	-0.25342500	-0.70497900
C	-0.01827700	5.11301100	0.48944900
C	5.49587400	-2.07893900	-0.26797100
C	-0.81316000	3.14800400	-0.65805900
C	-1.37774000	2.40497500	-1.69484100
C	-0.67271800	4.53675400	-0.74895000
C	-1.82140800	3.08646500	-2.83073900
H	-1.43314300	1.32191400	-1.64570000
C	-1.12128200	5.21335100	-1.88244100
C	-1.69949400	4.47828800	-2.92166900
H	-2.25124600	2.52367700	-3.65408800
H	-1.01653700	6.29276100	-1.96232200
H	-2.04750000	4.99237300	-3.81383200
H	-0.73192500	5.68726800	1.09499000
H	0.82394300	5.77892400	0.27055200
C	3.21253200	-2.69084300	-0.74625400
C	2.05843500	-3.47431000	-0.71191400
C	4.37162700	-3.07312500	-0.06483000
C	2.07528100	-4.64952800	0.04323500
H	1.17616000	-3.15399200	-1.25877900
C	4.38658100	-4.24965200	0.68465000
C	3.22874000	-5.03134800	0.74024000
H	1.18679300	-5.27371700	0.08705100
H	5.28264600	-4.55637100	1.21888600
H	3.22721700	-5.94806900	1.32415200
H	6.38846400	-2.54904900	-0.69767700
H	5.80813800	-1.60196000	0.66924900
Ni	0.58434700	-0.27805000	-0.35984400
C	-1.22083300	-0.54730800	0.30921300

C	-2.05372500	-1.50483300	-0.15440100
H	-1.64671600	0.34776600	0.75671500
H	-1.61869500	-2.39843100	-0.59889400
C	-3.51224000	-1.41175600	-0.19900200
C	-4.23830400	-2.22655900	-1.08450900
C	-4.25212700	-0.53771200	0.62974800
C	-5.62974800	-2.17208800	-1.16842400
H	-3.69614600	-2.90803100	-1.73567000
C	-5.63479900	-0.47371500	0.55693700
H	-3.73349400	0.07645400	1.35943300
C	-6.33791000	-1.28702800	-0.34605000
H	-6.14411800	-2.81579500	-1.87299900
H	-6.20238600	0.19288700	1.19928500
O	-7.69812500	-1.14604100	-0.33597200
C	-8.45757000	-1.93852400	-1.23225900
H	-9.50191300	-1.66633800	-1.06516100
H	-8.19335400	-1.73375700	-2.27921000
H	-8.32803100	-3.01218000	-1.03546200
C	0.13812400	-1.23442500	1.72532600
C	-0.72379000	-0.65805200	2.80860800
C	-0.39373300	0.55573100	3.43688500
C	-1.90375100	-1.30589700	3.21323800
C	-1.21511800	1.10391600	4.42351000
H	0.51069500	1.08013000	3.14419700
C	-2.72040500	-0.76641200	4.20545000
H	-2.19276300	-2.22792900	2.71704600
C	-2.38343200	0.44612700	4.81395400
H	-0.93838100	2.04574600	4.89181200
H	-3.62812300	-1.28885100	4.49559900
H	-3.02322700	0.87177700	5.58214700
C	1.63385500	-1.14848500	2.08596600
H	2.02259100	-0.12789500	2.08838500
H	1.76349500	-1.55237000	3.10179500
H	2.24334800	-1.74146100	1.40717900
H	-0.11552600	-2.27493700	1.52977100
Br	0.21479500	-0.98657100	-2.75061600

TS3-*R*-cf3

C	0.67802800	-3.36424500	0.30548600
C	-0.45266800	-2.44665000	0.82329600
C	-0.28022500	-3.88784100	1.31137200
H	0.58820200	-3.68251700	-0.72756200
H	1.68177000	-3.08418800	0.60791300
H	0.05309900	-3.99525300	2.33692400
H	-1.03961500	-4.58939500	0.98678000
C	-0.04226100	-1.35572100	1.73933700
C	1.02847400	-0.53305200	3.55100400
C	0.37018200	0.61113300	2.71458000
H	0.64544300	-0.62168900	4.56864700
H	-0.42654900	1.16349300	3.22017500
C	-1.56734800	-2.16201100	-0.11069900
C	-3.14829800	-2.78624800	-1.61148100
C	-3.20170800	-1.26275000	-1.31468400
H	-2.74762600	-3.05158200	-2.59403800
H	-3.16281400	-0.63874800	-2.20995400

O	0.62679300	-1.74807600	2.85318600
O	-2.18194600	-3.25740900	-0.62231500
N	-0.23005400	-0.10467700	1.57204500
N	-2.00061000	-1.01531700	-0.49296500
C	2.56125100	-0.33587200	3.49262000
C	-4.54210900	-3.36556500	-1.32927700
C	1.52733800	1.49408700	2.30757500
C	1.47383200	2.68096500	1.57749900
C	2.74736500	0.95062500	2.71883800
C	2.67362900	3.31445800	1.24351600
H	0.51724300	3.08583500	1.26131200
C	3.94394700	1.59181000	2.39635300
C	3.89923600	2.77237100	1.64797600
H	2.64783800	4.22358900	0.65334000
H	4.89784300	1.17837300	2.71630200
H	4.82517300	3.27460900	1.38012500
H	2.99745000	-0.28182000	4.49739100
H	3.02281100	-1.19288600	2.98656300
C	-4.48964900	-1.09266500	-0.53500600
C	-4.92903100	0.04111500	0.14630000
C	-5.22943300	-2.27971900	-0.52928100
C	-6.14570200	-0.02967500	0.82973400
H	-4.31798400	0.93876500	0.18069300
C	-6.44384600	-2.34548700	0.15267900
C	-6.89878700	-1.21047700	0.82987800
H	-6.50346600	0.83967200	1.37440600
H	-7.02456400	-3.26476500	0.16447400
H	-7.84180800	-1.24860700	1.36910300
H	-5.06245600	-3.56163400	-2.27635500
H	-4.46769200	-4.32198200	-0.80012400
Ni	-0.81363800	0.82244300	-0.30445500
C	0.56866000	0.01088100	-1.38804700
C	1.85613000	0.08275200	-1.00429600
H	0.20906700	-0.82334800	-1.99268100
H	2.18302500	0.94165200	-0.42129000
C	2.84390000	-0.99192900	-1.16986300
C	3.92364500	-1.08142500	-0.27610400
C	2.73617300	-1.99967600	-2.15249200
C	4.83854100	-2.13691400	-0.32308100
H	4.04147700	-0.31102100	0.48120200
C	3.63748900	-3.05185700	-2.21316100
H	1.93536900	-1.94774900	-2.88530300
C	4.69488100	-3.13646300	-1.29241500
H	5.65269400	-2.16403600	0.39265800
H	3.55520500	-3.82221100	-2.97405300
O	5.52063100	-4.21652700	-1.43532100
C	6.61865300	-4.33860800	-0.54741100
H	7.14038100	-5.25313900	-0.83661100
H	7.30710700	-3.48633100	-0.63385600
H	6.28826100	-4.42597000	0.49737500
C	-0.35258600	1.75059200	-2.31844200
H	0.09851600	1.17612400	-3.12570100
Br	-2.20814600	2.51441200	0.88022800
C	0.48380800	2.96056000	-2.06102500
C	1.82004400	2.98102000	-2.50439500

C	-0.02564300	4.11865900	-1.44668100
C	2.61316600	4.11747800	-2.35805400
H	2.23401800	2.09220500	-2.97248300
C	0.76755200	5.25729100	-1.30279500
H	-1.03684900	4.11690200	-1.05824400
C	2.08738500	5.26735700	-1.76273300
H	3.63936600	4.10771400	-2.71676500
H	0.34833100	6.14163400	-0.82967000
H	2.69947800	6.15949600	-1.65627200
C	-1.82012300	1.98835600	-2.69192200
H	-1.85601300	2.60690100	-3.60203600
H	-2.31254600	1.03876300	-2.92192700
H	-2.39475400	2.48641500	-1.90980800

TS4-*S*

C	3.23208300	3.56651500	-0.17821100
C	2.55391200	2.20444100	0.07091700
C	3.51707700	2.84573900	1.08674200
H	3.98959300	3.57442900	-0.95313900
H	2.57258900	4.42613900	-0.14592700
H	3.05250600	3.19710200	2.00103200
H	4.47586200	2.35053700	1.19817400
C	1.11377100	2.24595700	0.38011200
C	-0.71817100	3.20386400	1.30393600
C	-1.09123600	2.00074700	0.40711500
H	-0.79969400	3.01482900	2.37595600
H	-1.72930900	1.27068400	0.90054000
C	3.06518200	1.04870000	-0.69427900
C	4.66968200	0.02202600	-1.91729100
C	3.43259300	-0.90272600	-1.72229800
H	4.80580900	0.38580700	-2.93836800
H	2.95499100	-1.23593900	-2.64382500
O	0.70893600	3.36358700	1.01776000
O	4.34442400	1.18830900	-1.10469400
N	0.21487000	1.38084500	0.07243100
N	2.45476800	-0.04007100	-0.99375300
C	-1.50207400	4.42061900	0.79630200
C	5.90451400	-0.69422700	-1.34678500
C	-1.73461600	2.64154600	-0.80555100
C	-2.06259100	2.04116500	-2.02019700
C	-1.93972200	4.00923100	-0.59366300
C	-2.61770200	2.83633400	-3.02612600
H	-1.88337400	0.98193500	-2.16772200
C	-2.49513500	4.80004800	-1.59856200
C	-2.83416300	4.20392400	-2.81673100
H	-2.88079500	2.38837800	-3.98043500
H	-2.65699100	5.86382100	-1.44165900
H	-3.26490800	4.80923400	-3.61008000
H	-2.36368000	4.60448100	1.45203600
H	-0.88417400	5.32515700	0.81655300
C	3.96863200	-2.05511900	-0.89514600
C	3.27947800	-3.17638300	-0.43267900
C	5.33501800	-1.90043800	-0.63560600
C	3.96494500	-4.11490500	0.34199500
H	2.23407200	-3.30441600	-0.68591600

C	6.01952100	-2.83882000	0.13664600
C	5.32294400	-3.94264200	0.63529800
H	3.43697400	-4.98767000	0.71637200
H	7.08098500	-2.71918800	0.34027800
H	5.84331300	-4.67958600	1.24143400
H	6.57823700	-0.99754700	-2.15839000
H	6.47274900	-0.02046900	-0.69533900
Ni	0.44027400	-0.49214000	-0.69145900
C	-1.35322000	-0.91633000	-0.21843700
C	-2.36855400	-1.37681600	-0.96268000
H	-1.53956800	-0.68850300	0.83398800
H	-2.17617100	-1.63860200	-2.00184000
C	-3.75998400	-1.57751300	-0.51671800
C	-4.70841100	-2.07799800	-1.42084900
C	-4.21420700	-1.28694300	0.78805400
C	-6.04305900	-2.28862400	-1.06413100
H	-4.39343300	-2.31452300	-2.43475900
C	-5.53379000	-1.49004800	1.16024100
H	-3.51774400	-0.89510200	1.52468700
C	-6.46359500	-1.99364800	0.23626400
H	-6.73418700	-2.67951800	-1.80249400
H	-5.87762200	-1.26608900	2.16581500
O	-7.73934400	-2.15483200	0.70589600
C	-8.71530600	-2.66469300	-0.18503700
H	-9.64665700	-2.71538600	0.38321800
H	-8.85725500	-2.00568100	-1.05341100
H	-8.45420500	-3.67118200	-0.54160500
C	0.94402300	-1.73548000	1.55048900
H	1.96024300	-1.73528800	1.16805400
C	0.65416500	-0.73047400	2.52700400
C	1.62530000	0.26729900	2.82041600
C	-0.58353200	-0.64627100	3.22144200
C	1.37209600	1.28469500	3.72823600
H	2.58407700	0.22008600	2.30974400
C	-0.83628000	0.38463000	4.12167600
H	-1.34324300	-1.40238500	3.05368600
C	0.13319500	1.36042500	4.38374000
H	2.14142800	2.02310300	3.94065400
H	-1.79422700	0.42232600	4.63471300
H	-0.06293000	2.15391200	5.09962500
C	0.19776500	-3.02887900	1.40754300
H	0.26571900	-3.39825400	0.38110300
H	0.62499300	-3.79140100	2.07995300
H	-0.86582200	-2.93708900	1.63995500
Cl	0.51419300	-2.14139600	-2.26255300

TS4-*R*

C	4.04933100	3.12538100	1.27529700
C	3.06849300	1.95975600	1.05542800
C	3.97254100	2.05562000	2.30067500
H	4.90526300	3.14363200	0.61092700
H	3.59313500	4.08443400	1.49116600
H	3.45822500	2.26281100	3.23331400
H	4.77414900	1.32648000	2.35327700
C	1.63589200	2.26096300	1.23724400

C	-0.09550500	3.43748400	2.11060000
C	-0.56063800	2.47560500	0.98961000
H	-0.36883700	3.13619200	3.12532900
H	-1.39677900	1.83097400	1.25987200
C	3.43702200	0.95398700	0.03153900
C	4.96489000	-0.18572300	-1.18220900
C	3.51832000	-0.64131300	-1.54156700
H	5.51435200	0.24808700	-2.01883700
H	3.19334400	-0.40563900	-2.55624800
O	1.36428600	3.33015600	2.01956100
O	4.76455400	0.88863400	-0.22054900
N	0.63672900	1.64993500	0.71247500
N	2.66546100	0.16088800	-0.61677700
C	-0.55236100	4.85081400	1.72618900
C	5.69422100	-1.38366300	-0.53319400
C	-0.87090700	3.40320600	-0.16906400
C	-1.09958600	3.06073800	-1.50152400
C	-0.84146300	4.73937600	0.24413500
C	-1.32123900	4.09021200	-2.41995000
H	-1.08471000	2.02173600	-1.81241500
C	-1.06626900	5.76351900	-0.67460900
C	-1.30963800	5.42919700	-2.01002200
H	-1.49680600	3.84593100	-3.46385900
H	-1.04448400	6.80466500	-0.36168600
H	-1.48199800	6.21740000	-2.73830500
H	-1.45324100	5.11441200	2.29648000
H	0.21393300	5.59368500	1.97354600
C	3.51911700	-2.12893400	-1.26498700
C	2.51451300	-3.05627700	-1.54783100
C	4.71719900	-2.53038000	-0.66546600
C	2.71136200	-4.38952800	-1.18068000
H	1.60006200	-2.72638700	-2.02986000
C	4.91290200	-3.86289200	-0.30211300
C	3.89776200	-4.78929900	-0.55413900
H	1.93387800	-5.12120000	-1.38194200
H	5.84309400	-4.17875400	0.16412800
H	4.03604600	-5.82981300	-0.27249400
H	6.64414600	-1.59541000	-1.03818100
H	5.93559900	-1.14898300	0.51092800
Ni	0.59428100	0.04388500	-0.53437800
C	-1.26358700	-0.23003600	-0.19873100
C	-2.29302900	-0.35155700	-1.04972600
H	-1.46475600	-0.28733800	0.87669600
H	-2.09740600	-0.28710800	-2.11858700
C	-3.70465300	-0.57052200	-0.68387800
C	-4.71294500	-0.35053100	-1.63338300
C	-4.10903900	-1.01772500	0.59157700
C	-6.06662800	-0.53847800	-1.33953300
H	-4.43367900	-0.01853300	-2.63107900
C	-5.44685200	-1.21152200	0.89924100
H	-3.35794600	-1.24590300	1.34009600
C	-6.44032300	-0.96925300	-0.06258300
H	-6.80802900	-0.35066600	-2.10823800
H	-5.75278600	-1.56810500	1.87856600
O	-7.72973700	-1.19360800	0.34456300

C	-8.76762800	-0.98349400	-0.59481100
H	-9.69914800	-1.21976100	-0.07542700
H	-8.80115200	0.06026800	-0.93886200
H	-8.66495500	-1.64160300	-1.46953200
C	0.94623400	-1.79843300	1.32873700
C	-0.26221600	-2.54276400	1.53836500
C	-1.00842000	-2.46014100	2.74020600
C	-0.76345600	-3.38671700	0.51319200
C	-2.17499000	-3.20207200	2.91403700
H	-0.65990800	-1.82136000	3.54644700
C	-1.93124400	-4.11295300	0.68728900
H	-0.23051600	-3.42573400	-0.43181400
C	-2.64477200	-4.03174500	1.89213400
H	-2.72503400	-3.12787100	3.84904000
H	-2.30183900	-4.73818800	-0.12044700
H	-3.56383100	-4.59574000	2.02280000
C	1.59031600	-1.01557900	2.43498700
H	0.93761200	-0.21684900	2.81001100
H	1.83337500	-1.66079800	3.29448100
H	2.51915000	-0.55403200	2.09481700
H	1.59073000	-2.14468000	0.53059100
Cl	0.49161100	-0.53365900	-2.76197000

C_6F_6 (ORCA)

C	-2.08035480745116	-0.00000002082751	-1.58571637452826
C	-3.23769074609703	-0.35506623649578	-0.88678634286898
C	-0.92301885233540	0.35506620501065	-0.88678633289870
F	-4.34757496386184	-0.69560642286598	-1.55705193271356
F	0.18686535087026	0.69560647574205	-1.55705190979329
C	-3.23769072197718	-0.35506626792560	0.51107006734975
C	-0.92301888078694	0.35506626628939	0.51107007660397
F	-4.34757492081340	-0.69560645694073	1.18133567640156
F	0.18686527613664	0.69560653123027	1.18133569163507
C	-2.08035478998591	-0.00000002292387	1.21000011999390
F	-2.08035478968096	-0.00000002759632	2.55054875632649
F	-2.08035483801706	-0.00000002269656	-2.92626500750795

1b

C	-0.60660232044200	-0.64433995736758	-3.38005900922667
H	-1.60460746635295	-0.65333316008541	-2.93305121239365
C	0.45328983433487	-0.63003599455311	-2.55907618308245
H	1.49371646233862	-0.61917515448373	-2.87727047533960
C	-0.57195750470224	-0.64861128117865	-4.84562063603251
C	0.61998802181281	-0.64566072383544	-5.60004674907194
C	-1.79395229994265	-0.65623905033384	-5.54712355152329
C	0.59517064787864	-0.64949435993566	-6.99133310043017
C	-1.83877360137507	-0.66018199574130	-6.94122267777344
C	-0.63805521806712	-0.65660166165618	-7.64189706791389
H	1.58733125793119	-0.64084111737458	-5.09619226931526
H	-2.72959761049744	-0.65893299398530	-4.98438732683538
H	1.51428622431806	-0.64739411187043	-7.57720370736237
H	-2.78463544871623	-0.66600376119840	-7.48253959334636
F	-0.66382938969596	-0.66046915172425	-8.99889893159037
Br	0.28753780217748	-0.62612448467614	-0.66915781976260

5b

C	-4.11532733969400	-1.12491356946914	-6.01429941298077
H	-5.16322602983630	-1.18831310673920	-5.69956900909472
C	-3.16762685914312	-1.13905534301137	-5.03808195186337
H	-2.10787415739093	-1.07707981623321	-5.30788545720844
C	-3.91045792977807	-1.03391764636984	-7.45326825019406
C	-2.63517196350950	-0.94763086729187	-8.05638453755352
C	-5.03578889837609	-1.03059708961062	-8.30621104514578
C	-2.48924585320593	-0.86218979261019	-9.43718523379085
C	-4.90926778262523	-0.94565654158294	-9.69165106403804
C	-3.63208872736911	-0.86244512329972	-10.23619868915133
H	-1.73841991553155	-0.94745158212351	-7.43570092957264
H	-6.03294651870383	-1.09641924344777	-7.86583450438134
H	-1.50595499406426	-0.79571102427353	-9.90305274209395
H	-5.78036122167198	-0.94331164978294	-10.34674289253264
F	-3.49132406175592	-0.77912663157127	-11.58447816915054
C	-2.51469059029440	-1.24576756800706	-2.66099915450661
H	-1.46687926140760	-1.18133021087182	-2.97581356345228
C	-3.46240715910281	-1.23201887654516	-3.63721103848032
H	-4.52215243116646	-1.29415602968902	-3.36740962017595
C	-2.71942537499200	-1.33692986135368	-1.22203428823827
C	-3.99440254918885	-1.42969757739758	-0.61920347627904
C	-1.59432007195093	-1.33379279785311	-0.36880889762441
C	-4.14025890510305	-1.51467685159697	0.76162695209982
C	-1.72077805437147	-1.41813833281390	1.01667612550167
C	-2.99765036725211	-1.50753157476434	1.56095297035080
H	-4.89091017520987	-1.43587163754732	-1.24020875430780
H	-0.59740181833295	-1.26311777973175	-0.80897429389443
H	-5.12328860004276	-1.58630054772655	1.22728282564892
H	-0.84986377820378	-1.41537981423140	1.67200496308725
F	-3.13833900772507	-1.59044516645319	2.90926760902267

7b low spin (ORCA)

Ni	-0.00448447947817	0.00164020935805	0.00239302745841
Br	1.48051895103094	-1.06498553032033	-1.42227277162176
O	-2.14618384754168	2.70992481822853	2.28296153762120
O	2.37980000208120	1.45487800242610	3.14553552778769
N	-1.22320307906186	1.24516125844987	0.82001397365091
N	1.38187625645077	0.45142569725855	1.37268370607038
C	-2.50473685992759	1.69215636182839	0.20028167496512
H	-3.02703521838075	0.81954243180769	-0.21284803429169
C	-2.31414275829491	2.79291707793566	-0.82891167485076
C	-1.51232164190342	2.78354092305962	-1.97151518676158
H	-0.91049815291267	1.90705015537969	-2.21296422085385
C	-1.48667183784918	3.92329934054902	-2.78164286180547
H	-0.86400414733098	3.93421369639543	-3.67748163198082
C	-2.24859325449193	5.05089471093451	-2.45132495367893
H	-2.21699304159929	5.93275922013676	-3.09340087627570
C	-3.04370247594705	5.05993212985855	-1.30037856197006
H	-3.62841865175398	5.94527500807122	-1.04169202149398
C	-3.07032191595432	3.92462134312011	-0.48855181182245
C	-3.84960356218091	3.69579574776801	0.78758163630582
H	-4.92295813349767	3.54333522451468	0.58491826850845
H	-3.77594304049303	4.52241849465255	1.50957617890282
C	-3.24782198837848	2.40494676146387	1.34996429789153

H	-3.96181548987140	1.77984856842228	1.90421276940742
C	-1.09373624482642	1.93610966048983	1.91190877407963
C	0.08827487863875	2.02707353287255	2.78263295351118
C	0.30730255664132	3.36135515193982	3.52746537385254
H	1.34653079630200	3.67037733750601	3.61840043281037
H	-0.41234425523186	4.14546701019410	3.30285053411278
C	-0.14793530388374	2.18122249430214	4.30349516773825
H	-1.18964241399308	2.13532039477542	4.61554073715783
H	0.56860777104095	1.66629142186091	4.94026945293758
C	1.28394818055181	1.27319317310105	2.36563742651106
C	3.48191174327627	0.72368410573533	2.48920495801151
H	4.12422097702651	1.48580470131008	2.02662190639825
C	4.20274200542984	-0.17332887910662	3.49859326451102
H	5.27190389476995	-0.23974757835717	3.23630663075593
H	4.15016485558222	0.24321584348415	4.51544988063502
C	3.51466753766513	-1.51073413328666	3.34409244178004
C	3.63740994066102	-2.64517637862000	4.14876463050819
H	4.27231145295736	-2.63258666009796	5.03739448769345
C	2.93467878923394	-3.80286202606502	3.79970833654877
H	3.02093633812608	-4.69635418451876	4.42049587820722
C	2.12461490652130	-3.82420395829027	2.65754694487539
H	1.58689261393112	-4.73596305778894	2.39252422867949
C	1.99959201633266	-2.68990406879442	1.84907993232279
H	1.38061955905140	-2.70181397824566	0.95098959516874
C	2.69685644850178	-1.53271201153393	2.20372943294103
C	2.72663367802005	-0.18761704582790	1.49388927054575
H	3.16825451112758	-0.25449746077197	0.49010899285342
C	-1.40149009875006	-0.78861801427904	-0.96238725294244
H	-2.03510631596574	-1.28764677439133	-0.20524543892123
C	-1.75652521743068	-0.86523505167258	-2.25838195017227
H	-1.10501207355006	-0.40857308973478	-3.01166561912331
C	-2.95112365620622	-1.51914280490975	-2.81650139221344
C	-3.85728499891261	-2.28306114369508	-2.04982337266299
C	-3.22151252707195	-1.39017338112351	-4.19468295364675
C	-4.97922286924958	-2.87842821603045	-2.62231397369321
C	-4.33992211595134	-1.97850977092046	-4.78764052083420
C	-5.20574311712741	-2.71388056534712	-3.98709027461802
H	-3.67377801332535	-2.42693252758972	-0.98369370994579
H	-2.53258188490982	-0.81230109787859	-4.81459548781304
H	-5.67387381635059	-3.47346317041941	-2.02849829659437
H	-4.54200225250226	-1.87474016712144	-5.85400827132554
F	-6.30308490686389	-3.29527128245169	-4.55036414280337

3.5 Notes and References

1. For reviews see: (a) Everson, D. A.; Weix, D. J. Cross-Electrophile Coupling: Principles of Reactivity and Selectivity. *J.*Wang, X.; Dai, Y.; Gong,J. Cross-Electrophile Coupling. In Nickel Catalysis in Organic Synthesis; John Wiley & Sons, Ltd, **2020**; pp 183–222. (g) Poremba, K. E.; Dibrell, S. E.; Reisman, S. E. Nickel-Catalyzed Enantioselective Reductive Cross-Coupling Reactions. *ACS Catal*. **2020**, 10, 8237–8246.

[2]. Charboneau, D. J.; Hazari, N.; Huang, H.; Uehling, M. R.; Zultanski, S. L. Homogeneous Organic Electron Donors in Nickel-Catalyzed Reductive Transformations. *J. Org. Chem*. **2022**, 87, 7589–7609.

[3] . Zhou, Z.; Xu, S.; Zhang, J.; Kong, W. Nickel-Catalyzed Enantioselective Electroreductive Cross-Couplings. *Org. Chem. Front*. **2020**, 7, 3262–3265.

[4]. Diccianni, J. B.; Diao, T. Mechanisms of Nickel-Catalyzed Cross-Coupling Reactions. *TRECHEM* **2019**, 1, 830–844.

[5]. For examples using(a) Zhang, P.; Le, C. "Chip"; MacMillan, D. W. C. Silyl Radical Activation of Alkyl Halides in Metallaphotoredox Catalysis: A Unique Pathway for Cross-Electrophile Coupling. *J. Am. Chem. Soc*. **2016**, 138, 8084–8087. (b) Duan, Z.; Li, W.; Lei, A. Nickel-Catalyzed Reductive Cross-Coupling of Aryl Bromides with Alkyl Bromides: Et_3N as the Terminal Reductant. *Org. Lett*. **2016**, 18, 4012–4015. (c) Yi, J.; Badir, S. O.; Kammer, L. M.; Ribagorda, M.; Molander, G. A. Deaminative Reductive Arylation Enabled by Nickel/Photoredox Dual Catalysis. *Org. Lett*. **2019**, 21, 3346–3351. For Examples using electrochemistry: (d) Perkins, R. J.; Pedro, D. J.; Hansen, E. C.

Electrochemical Nickel Catalysis for sp^2-sp^3 Cross-Electrophile Coupling Reactions of Unactivated Alkyl Halides. *Org. Lett*. **2017**, 19, 3755–3758. (e) Truesdell, B. L.; Hamby, T. B.; Sevov, C. S. General C(sp^2)–C(sp^3) Cross-Electrophile Coupling Reactions Enabled by Overcharge Protection of Homogeneous Electrocatalysts. *J. Am. Chem. Soc*. **2020**, 142, 5884–5893. (f) Kumar, G. S.; Peshkov, A.; Brzozowska, A.; Nikolaienko, P.; Zhu, C.; Rueping, M. Nickel-Catalyzed Chain-Walking Cross-Electrophile Coupling of Alkyl and Aryl Halides and Olefin Hydroarylation Enabled by Electrochemical Reduction. *Angew. Chem. Int. Ed.* **2020**, 59, 6513–6519. For examples using metal powder: (g) Durandetti, M.; Gosmini, C.; Périchon, J. Ni-Catalyzed Activation of α-Chloroesters: A Simple Method for the Synthesis of α-Arylesters and β-Hydroxyesters. *Tetrahedron* **2007**, 63, 1146–1153. (h) Nimmagadda, S. K.; Korapati, S.; Dasgupta, D.; Malik, N. A.; Vinodini, A.; Gangu, A. S.; Kalidindi, S.; Maity, P.; Bondigela, S. S.; Venu, A.; Gallagher, W. P.; Aytar, S.; González-Bobes, F.; Vaidyanathan, R. Development and Execution of an Ni(II)-Catalyzed Reductive Cross-Coupling of Substituted 2-Chloropyridine and Ethyl3-Chloropropanoate. *Org. Process Res. Dev*. **2020**, *24*, 1141–1148.

[6]. Cherney, A. H.; Reisman, S. E. Nickel-Catalyzed Asymmetric Reductive Cross-Coupling Between Vinyl and Benzyl Electrophiles. *J. Am. Chem. Soc*. **2014**, *136*, 14365–14368.

[7]. Suzuki, N.; Hofstra, J. L.; Poremba, K. E.; Reisman, S. E. Nickel-Catalyzed Enantioselective Cross-Coupling of N-Hydroxyphthalimide Esters with Vinyl Bromides. *Org. Lett*. **2017**, *19*, 2150–2153.

[8]. (a) Hofstra, J. L.; Cherney, A. H.; Ordner, C. M.; Reisman, S. E. Synthesis of Enantioenriched Allylic Silanes via Nickel-Catalyzed Reductive Cross-Coupling. *J. Am.*

Chem. Soc. **2018**, *140*, 139–142. (b) DeLano, T. J.; Reisman, S. E. Enantioselective Electroreductive Coupling of Alkenyl and Benzyl Halides via Nickel Catalysis. *ACS Catal*. **2019**, *9*, 6751–6754.

[9]. (a) Everson, D. A.; Jones, B. A.; Weix, D. J. Replacing Conventional Carbon Nucleophiles with Electrophiles: Nickel-Catalyzed Reductive Alkylation of Aryl Bromides and Chlorides. *J. Am. Chem. Soc*. **2012**, *134*, 6146–6159. (b) Biswas, S.; Weix, D. J. Mechanism and Selectivity in Nickel-Catalyzed Cross-Electrophile Coupling of Aryl Halides with Alkyl Halides. *J. Am. Chem. Soc*. **2013**, 135, 16192–16197. (c) Wotal, A. C.; Ribson, R. D.; Weix, D. J. Stoichiometric Reactions of Acylnickel(II) Complexes with Electrophiles and the Catalytic Synthesis of Ketones. *Organometallics* **2014**, *33*, 5874–5881.

[10]. (a) Lin, Q.; Diao, T. Mechanism of Ni-Catalyzed Reductive 1,2-Dicarbofunctionalization of Alkenes. *J. Am. Chem. Soc*. **2019**, *141*, 17937–17948. (b) Ju, L.; Lin, Q.; LiBretto, N. J.; Wagner, C. L.; Hu, C. T.; Miller, J. T.; Diao, T. Reactivity of (Bi-Oxazoline)Organonickel Complexes and Revision of a Catalytic Mechanism. *J. Am. Chem. Soc*. **2021**, *143*, 14458–14463. (c) Wagner, C. L.; Herrera, G.; Lin, Q.; Hu, C. T.; Diao, T. Redox Activity of Pyridine-Oxazoline Ligands in the Stabilization of Low-Valent Organonickel Radical Complexes. *J. Am. Chem. Soc*. **2021**, *143*, 5295–5300.

[11]. Just before the submission of this manuscript, an investigation of an electrochemically driven Ni-catalyzed enantioselective reductive alkenylation using a **L1**·Ni catalyst was reported. Hu, X.; Cheng-Sánchez, I.; Cuesta-Galisteo, S.; Nevado, C. Nickel-Catalyzed

Enantioselective Electrochemical Reductive Cross-Coupling of Aryl Aziridines with Alkenyl Bromides. *J. Am. Chem. Soc.* **2023**. https://doi.org/10.1021/jacs.2c12869.

[12]. Burés, J. Variable Time Normalization Analysis: General Graphical Elucidation of Reaction Orders from Concentration Profiles. *Angew. Chem. Int. Ed.* **2016**, *55*, 16084–16087.

[13]. Huihui, K. M. M.; Caputo, J. A.; Melchor, Z.; Olivares, A. M.; Spiewak, A. M.; Johnson, K. A.; DiBenedetto, T. A.; Kim, S.; Ackerman, L. K. G.; Weix, D. J. Decarboxylative Cross-Electrophile Coupling of N-Hydroxyphthalimide Esters with Aryl Iodides. *J. Am. Chem. Soc*. **2016**, *138*, 5016–5019.

[14]. Cornella, J.; Edwards, J. T.; Qin, T.; Kawamura, S.; Wang, J.; Pan, C.-M.; Gianatassio, R.; Schmidt, M.; Eastgate, M. D.; Baran, P. S. Practical Ni-Catalyzed Aryl–Alkyl Cross-Coupling of Secondary Redox-Active Esters. *J. Am. Chem. Soc*. **2016**, *138*, 2174–2177.

[15]. Rousseaux and coworkers have also reported the rate-enhancing effect of TMSCl of NHP ester reduction using Zn^0 reductant in a preprint article: Michel, N.; Edjoc, R.; Fagbola, E.; Hughes, J.; Campeau, L.-C.; Rousseaux, S. Nickel-Catalyzed Reductive Arylation of Redox Active Esters for the Synthesis of α-Aryl Nitriles – Role of a Chlorosilane Additive. *ChemRxiv* April 20, 2021 (DOI: 10.26434/chemrxiv.14450007.v2).

[16]. McNicholas, B. J.; Tong, Z. J.; Bím, D.; Turro, R. F.; Kazmierczak, N. P.; Chalupský, Reisman, S. E.; Hadt, R. G.* Electronic structures of nickel(II)bis(indanyloxazoline)-

dihalide catalysts: Understanding ligand field contributions that promote C(sp^2)–C(sp^3) cross-coupling. **2023**, *Submitted.*

[17]. Kuwata, Keiji.; Geske, D. H. The Cation Radical of Tetrakis(Dimethylamino)Ethylene. *J. Am. Chem. Soc*. **1964**, 86, 2101–2105.

[18]. For an example of Zn^{II} salts effecting Ni^{I} speciation, see: Diccianni, J. B.; Hu, C. T.; Diao, T. Insertion of CO_2 Mediated by a (Xantphos)Ni^{I}–Alkyl Species. *Angew. Chem. Int. Ed.* **2019**, *58*, 13865–13868.

[19]. (a) Sun, R.; Qin, Y.; Ruccolo, S.; Schnedermann, C.; Costentin, C.; Daniel G. Nocera. Elucidation of a Redox-Mediated Reaction Cycle for Nickel-Catalyzed Cross Coupling. *J. Am. Chem. Soc*. **2019**, *141*, 89–93. (b) Mohadjer Beromi, M.; Brudvig, G. W.; Hazari, N.; Lant, H. M. C.; Mercado, B. Q. Synthesis and Reactivity of Paramagnetic Nickel Polypyridyl Complexes Relevant to C(Sp2)–C(Sp3)Coupling Reactions. *Angew. Chem. Int. Ed.* **2019**, *58,* 6094–6098.

[20]. (a) Ting, S. I.; Williams, W. L.; Doyle, A. G. Oxidative Addition of Aryl Halides to a Ni(I)-Bipyridine Complex. *J. Am. Chem. Soc*. **2022**, 144, 5575–5582. (b) Till, N. A.; Oh, S.; MacMillan, D. W. C.; Bird, M. J. The Application of Pulse Radiolysis to the Study of Ni(I) Intermediates in Ni-Catalyzed Cross-Coupling Reactions. *J. Am. Chem. Soc*. **2021**, 143, 9332–9337.

[21]. Under the conditions of the NMR experiment, approximately 8% and 12% yield of diene **5b** is formed when 10 mol % and 20 mol % L1$NiBr_2$ is used, respectively. Under standard reaction conditions, < 5% yield of the diene is typically observed.

[22]. The calculated ^{19}F NMR chemical shift (Table S23) for **7b** was found to be –115.2 ppm.

[23]. CV measurements of **2b** in the presence of TMSBr display a more anodic onset potential for reduction and an increase in current consistent with a more facile reduction (Figure S45).

[24]. Salgueiro, D. C.; Chi, B. K.; Guzei, I. A.; García-Reynaga, P.; Weix, D. J. Control of Redox-Active Ester Reactivity Enables a General Cross-Electrophile Approach to Access Arylated Strained Rings. *Angew. Chem. Int. Ed.* **2022**, 61, e202205673.

[25]. We observe a counterion effect with triflate salts where the rate of activation is slower than would be expected compared to iodide salts. We attribute this difference to the remarkable solubility of $TDAE(OTf)_2$ salts in DMA. For all halides, $[TDAE]X_2$ salts precipitate out of the reaction mixture which likely acts as an additional driving force for reduction.

[26]. Metal additives chosen in this study have been used in reductive NHP ester reactions previously reported in the literature. Although the role of these additives in these selected examples is not known, they are likely non-innocent in the NHP ester reduction process as demonstrated in this study. For examples with Li+ salts: (a) Huang, L.; Olivares, A. M.; Weix, D. J. Reductive Decarboxylative Alkynylation of N-Hydroxyphthalimide Esters with Bromoalkynes. *Angew. Chem.* **2017**, 129, 12063–12067. (b) Qin, T.; Malins, L. R.; Edwards, J. T.; Merchant, R. R.; Novak, A. J. E.; Zhong, J. Z.; Mills, R. B.; Yan, M.; Yuan, C.; Eastgate, M. D.; Baran, P. S. Nickel-Catalyzed Barton Decarboxylation and Giese Reactions: A Practical Take on Classic Transforms. *Angew. Chem. Int. Ed.* **2017**, 56, 260–265. Examples with Mg^{2+} salts: (c) Zhang, J.-J.; Yang, J.-C.; Guo, L.-N.; Duan, X.-H. Visible-Light-Mediated Dual Decarboxylative Coupling of Redox-Active Esters with α,β-

Unsaturated Carboxylic Acids. *Chem. Eur. J.* **2017**, 23, 10259–10263. (d) Lu, X.; Xiao, B.; Liu, L.; Fu, Y. Formation of C(Sp3)–C(Sp3) Bonds through Nickel-Catalyzed Decarboxylative Olefin Hydroalkylation Reactions. *Chem. Eur. J* **2016**, 22, 11161–11164.

[27]. Hofstra, J. L.; Poremba, K. E.; Shimozono, A. M.; Reisman, S. E. Nickel-Catalyzed Conversion of Enol Triflates into Alkenyl Halides. *Angew. Chem. Int. Ed.* **2019**, 58, 14901–14905.

[28]. Amatore, C.; Jutand, A. Rates and Mechanism of Biphenyl Synthesis Catalyzed by Electrogenerated Coordinatively Unsaturated Nickel Complexes. *Organometallics* **1988**, *7*, 2203–2214.

[29]. (a) Lin, Q.; Fu, Y.; Liu, P.; Diao, T. Monovalent Nickel-Mediated Radical Formation: a Concerted Halogen-Atom Dissociation Pathway Determined by Electroanalytical Studies. *J. Am. Chem. Soc.* **2021**, *143*, 14196–14206. (b) Diccianni, J. B.; Katigbak, J.; Hu, C.; Diao, T. Mechanistic Characterization of (Xantphos)Ni(I)-Mediated Alkyl Bromide Activation: Oxidative Addition, Electron Transfer, or Halogen-Atom Abstraction. *J. Am. Chem. Soc.* **2019**, *141*, 1788–1796.

[30]. The benzyl radical addition to intermediate **L1**·Ni^{II}(alkenyl)Cl was also studied. The TS4-R is 2.9 kcal/mol lower than the TS4-S (Figure S80). This indicates that the influence of the halide ligand on the enantioselectivity is minimal.

[31] Gutierrez, O.; Tellis, J. C.; Primer, D. N.; Molander, G. A.; Kozlowski, M. C. Nickel-Catalyzed Cross-Coupling of Photoredox-Generated Radicals: Uncovering a General

Manifold for Stereoconvergence in Nickel-Catalyzed Cross-Couplings. *J. Am. Chem. Soc.* **2015**, *137*, 4896–4899.

[32] Lin, Q.; Spielvogel, E. H.; Diao, T. Carbon-Centered Radical Capture at Nickel(II) Complexes: Spectroscopic Evidence, Rates, and Selectivity. *Chem* **2023**,

[33] W. C. Still, M. Kahn, A. Mitra, *J. Org. Chem.* **1978**, *43*, 2923–2925.

[34] Stoll, S.; Schweiger, A. Easyspin, a comprehensive software package for spectral simulation and analysis in EPR. *J. Magn. Reson.* **2006**, *178*, 42–45.

[35] L. Hofstra, J. Synthesis of Chiral Bisoxazoline Ligands: (3aR,3a'R,8aS,8a'S)-2,2'-(Cyclopropane-1,1-Diyl)Bis(3a,8a-Dihydro-8H-Indeno[1,2-d]Oxazole). *Org. Synth.* **2020**, *97*, 172–188.

[36] Hofstra, J. L.; Cherney, A. H.; Ordner, C. M.; Reisman, S. E. Synthesis of Enantioenriched Allylic Silanes via Nickel-Catalyzed Reductive Cross-Coupling. *J. Am. Chem. Soc.* **2018**, *140* (1), 139–142.

[37] Suzuki, N.; Hofstra, J. L.; Poremba, K. E.; Reisman, S. E. Nickel-Catalyzed Enantioselective Cross-Coupling of N-Hydroxyphthalimide Esters with Vinyl Bromides. *Org. Lett.* **2017**, *19* (8), 2150–2153.

[38] Everson, D. A.; Jones, B. A.; Weix, D. J. Replacing Conventional Carbon Nucleophiles with Electrophiles: Nickel-Catalyzed Reductive Alkylation of Aryl Bromides and Chlorides. *J. Am. Chem. Soc.* **2012**, *134* (14), 6146–6159.

[39] Jette, C.I.; Tong, Z.J.; Hadt, R.G.; Stoltz, B.M. Copper-catalyzed enantoselective allylic alkylation with a butyrolactone-derived silyl ketene acetal. *Angew. Chem. Int. Ed.* **2019**, *59*, 2033–2038.

[40] Frisch, M. J.; Trucks, G. W.; Schlegel, H. B.; Scuseria, G. E.; Robb, M. A.; Cheeseman, J. R.; Scalmani, G.; Barone, V.; Petersson, G. A.; Nakatsuji, H.; Li, X.; Caricato, M.; Marenich, A. V.; Bloino, J.; Janesko, B. G.; Gomperts, R.; Mennucci, B.; Hratchian, H. P.; Ortiz, J. V.; Izmaylov, A. F.; Sonnenberg, J. L.; Williams-Young, D.; Ding, F.; Lipparini, F.; Egidi, F.; Goings, J.; Peng, B.; Petrone, A.; Henderson, T.; Ranasinghe, D.; Zakrzewski, V. G.; Gao, J.; Rega, N.; Zheng, G.; Liang, W.; Hada, M.; Ehara, M.; Toyota, K.; Fukuda, R.; Hasegawa, J.; Ishida, M.; Nakajima, T.; Honda, Y.; Kitao, O.; Nakai, H.; Vreven, T.; Throssell, K.; Montgomery, J. A., Jr.; Peralta, J. E.; Ogliaro, F.; Bearpark, M. J.; Heyd, J. J.; Brothers, E. N.; Kudin, K. N.; Staroverov, V. N.; Keith, T. A.; Kobayashi, R.; Normand, J.; Raghavachari, K.; Rendell, A. P.; Burant, J. C.; Iyengar, S. S.; Tomasi, J.; Cossi, M.; Millam, J. M.; Klene, M.; Adamo, C.; Cammi, R.; Ochterski, J. W.; Martin, R. L.; Morokuma, K.; Farkas, O.; Foresman, J. B.; Fox, D. J. Gaussian 16, Revision C.01; Gaussian, Inc.: Wallingford, CT, 2019.

[41] (a) Grimme, S.; Antony, J.; Ehrlich, S.; Krieg, H. A Consistent and Accurate Ab Initio Parametrization of Density Functional Dispersion Correction (DFT-D) for the 94 Elements H-Pu. *J. Chem. Phys.* **2010**, *132*, 154104. (b) Grimme, S.; Ehrlich, S.; Goerigk, L. Effect of the Damping Function in Dispersion Corrected Density Functional Theory. *J. Comput. Chem.* **2011**, *32*, 1456. (c) Witte, J.; Mardirossian, N.; Neaton, J. B.; Head-Gordon, M. Assessing DFT-D3 Damping Functions Across Widely Used Density Functionals: Can We Do Better? *J. Chem. Theory Comput.* **2017**, *13*, 2043.

[42] (a) Hay, P. J.; Wadt, W. R. Ab Initio Effective Core Potentials for Molecular Calculations. Potentials for K to Au Including the Outermost Core Orbitals. *J. Chem. Phys.*

1985, *82*, 299. (b) Ehlers, A. W.; Böhme, M.; Dapprich, S.; Gobbi, A.; Höllwarth, A.; Jonas, V.; Köhler, K. F.; Stegmann, R.; Veldkamp, A.; Frenking, G. A Set of f-Polarization Functions for Pseudo-Potential Basis Sets of the Transition Metals Sc-Cu, Y-Ag and La-Au. *Chem. Phys. Lett.* **1993**, *208*, 111. (c) Roy, L. E.; Hay, P. J.; Martin, R. L. Revised Basis Sets for the LANL Effective Core Potentials. *J. Chem. Theory Comput.* **2008**, *4*, 1029.

[43] (a) Ditchfield, R.; Hehre, W. J.; Pople, J. A. Self-Consistent Molecular-Orbital Methods. IX. An Extended Gaussian-Type Basis for Molecular-Orbital Studies of Organic Molecules. *J. Chem. Phys.* **1971**, *54*, 724. (b) Hehre, W. J.; Ditchfield, R.; Pople, J. A. Self-Consistent Molecular Orbital Methods. XII. Further Extensions of Gaussian-Type Basis Sets for Use in Molecular Orbital Studies of Organic Molecules. *J. Chem. Phys.* **1972**, *56*, 2257. (c) Hariharan, P. C.; Pople, J. A. The Influence of Polarization Functions on Molecular Orbital Hydrogenation Energies. *Theoret. Chim. Acta.* **1973**, *28*, 213.

[44] (a) Zhao, Y.; Truhlar, D. G. The M06 Suite of Density Functionals for Main Group Thermochemistry, Thermochemical Kinetics, Noncovalent Interactions, Excited States, and Transition Elements: Two New Functionals and Systematic Testing of Four M06-class Functionals and 12 other Functionals. *Theor. Chem. Acc*. **2008**, *120*, 215. (b) Zhao, Y.; Truhlar, D. G. Density Functionals with Broad Applicability in Chemistry. *Acc. Chem. Res*. **2008**, *41*, 157.

[45] Dolg, M.; Wedig, U.; Stoll, H.; Preuss, H. Energy-Adjusted Ab Initio Pseudopotentials for the First Row Transition Elements. *J. Chem. Phys.* **1987**, *86*, 866.

[46] Marenich, A. V.; Cramer, C. J.; Truhlar, D. G. Universal Solvation Model Based on Solute Electron Density and on a Continuum Model of the Solvent Defined by the Bulk Dielectric Constant and Atomic Surface Tensions. J. *Phys. Chem. B* **2009**, *113*, 6378.

[47] Legault, C. Y. CYLview, 1.0b; Université de Sherbrooke: Canada, 2009. http://www.cylview.org.

[48] Neese, F.; Wennnmohs, F.; Becker, U.; Riplinger, C.; The ORCA quantum chemistry program package. *J. Chem. Phys.* **2020**, *152*, 224108

Chapter 4

Mechanistic Studies of Ni-Catalyzed Acylation of Benzylic Chlorides[†]

4.1 Introduction

Ni-mediated cross-coupling via C–O bond activation of commercially available synthons can be an efficient approach to access densely functionalized products[1,2] that can be further valorized[3]. Motivated by the synthesis of the natural product (–)-isodocarpin as well as pharmaceutical candidates such as MLC1 inhibitor AMG–176[4] (**Scheme 1A**), our lab has built on prior findings[5–7] (**Scheme 1B&C**) and developed an enantioselective and diastereoselective Ni-catalyzed reductive acylation of benzylic chlorides using *meso*-anhydrides as the C(sp^2) electrophile (**Scheme 1D**). Although this new acylation reaction conceptually differs from the mechanistically characterized Ni-catalyzed reductive alkenylation reaction[6] only in the identity C(sp^2) electrophile (**Scheme 1B**), a drastic evolution of reaction conditions was necessary to achieve high cross-coupling selectivity.

[†] The result of this chapter is related to a published manuscript.

Otherwise, bibenzyl formation manifests as the dominant deleterious pathway. These notable condition changes include a) the modification to the BOX ligand backbone with a pendant heteroarene, b) the inclusion of reaction additive BF_3•Et_2O, and c) the use of DMA in stoichiometric quantity in lieu of solvent quantity.

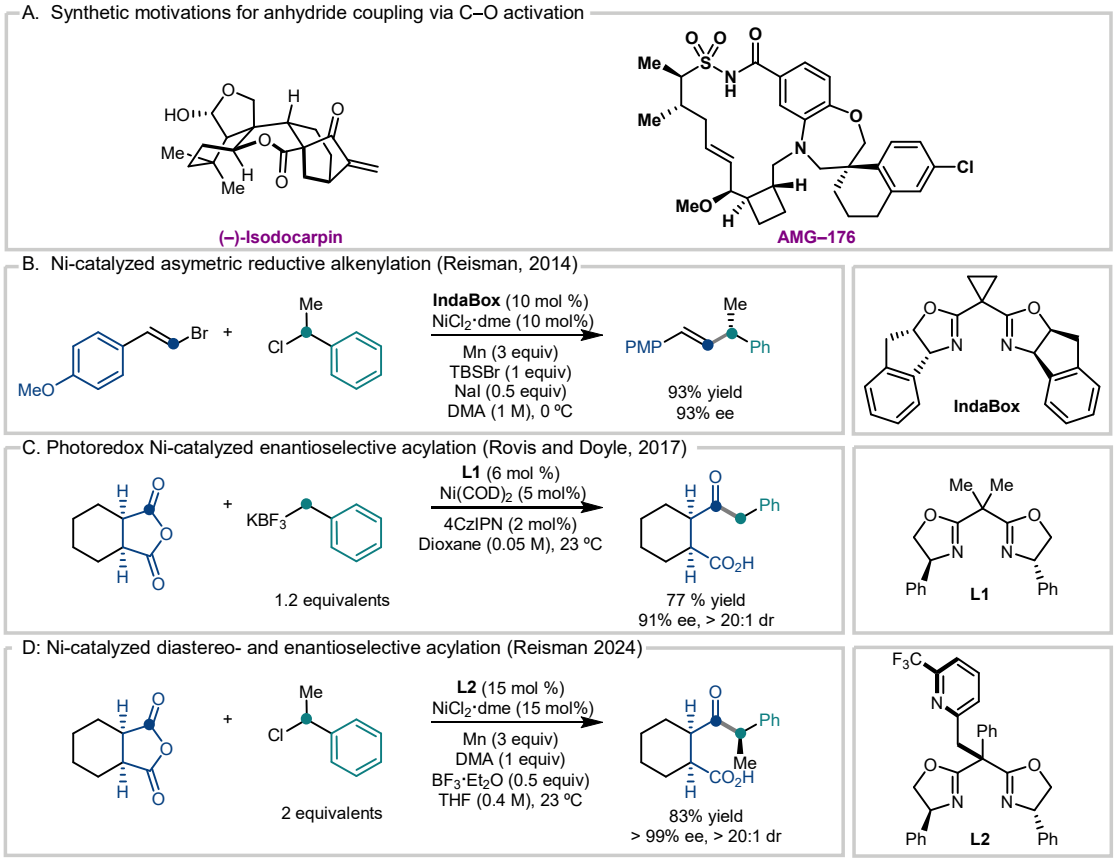

Scheme 1. *Motivation for and prior-arts on Ni-catalyzed acylation of benzylic electrophile.*

Mechanistically, the activation of anhydrides by nickel under reductive conditions remains comparatively understudied. To the best of our knowledge, one relevant example exists wherein the combination of nickel and photoredox catalysts effect the acylation of benzylic KBF_3 salt with *meso*-anhydrides[7]. In their report, Stache et al. proposed a preliminary $Ni^{0/I/II/III}$ cycle based on stoichiometric studies with $Ni(COD)_2$ as a surrogate

for the putative Ni(0) intermediate generated by the photoredox co-catalyst. Since then, numerous studies[8–11] have recognized Ni(I) as competent nucleophilic species for

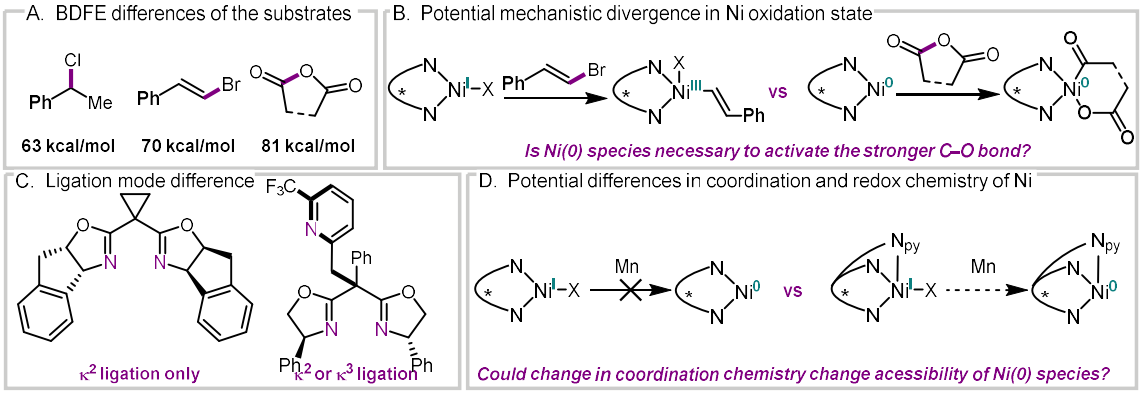

Scheme 2. *Possible mechanistic divergence in C(sp^2) electrophile activation pathway.*

activating aryl halide or alkenyl halide C(sp^2) electrophiles. These subsequent findings cast doubts on the necessity of accessing Ni(0) intermediates, particularly with non-redox active bis-oxazoline(Box) ligands. Nevertheless, since the C–O bond of anhydride is 11 kcal/mol stronger[12] than the C–X bonds of the aryl halide and alkenyl halides that had been examined mechanistically thus far, zerovalent Ni species could be necessary to effect C–O bond activation[13,14] (**Scheme 2**). Consequently, the accessibility of Ni(0) and its catalytic intermediacy for substrate activation under reductive conditions remains an important consideration for precise engineering of the redox chemistry between a given substrate pair for selective cross-coupling. Conversely, mechanistic elucidations of reduced Ni intermediates and the elementary transformation they engage with the anhydride may reveal important design principles on how to tailor existing reactions to tolerate less activated substrates.

In this regard, a particular feature of the optimized acylation reaction that drew our attention was the stringent reliance on decorated BOX ligands with a pendent heteroarene

(**Scheme 2C**). Our optimization campaign showed that such a ligand modification improved diastereoselectivity and suppressed bibenzyl formation. Because this ligand archetype may engage in a κ^3 coordination mode, Ni species with distinct coordination environments may be present in this reaction. Subsequently, these alternative Ni species with disparate redox chemistry (**Scheme 3D**) may undergo distinct elementary transformations to effect the cleavage of the C–O bond (**Scheme 3D**), thereby modifying both the thermodynamics and kinetics of the key catalytic step. In particular, kinetic modification can be important in tuning the overall synergy among the elementary transformations and determining the product outcome[11,14]. Given these considerations, our mechanistic studies endeavored to address interrelated questions about structure, reactivity, and catalytic kinetics. More importantly, given our goal of discerning transferable design principles, our research approach sought to assess whether spectroscopic observation could correlate or explain reactivity differences. To this end, we shall focus on the spectroscopic characterization of reaction intermediates generated under both optimized conditions and unoptimized conditions to elucidate variation in catalytic performance.

Having laid out the goal and approach of our mechanistic study, we now overview features of the acylation reaction and survey relevant prior findings to articulate particular questions we aim to address in terms of structure, reactivity, and catalytic implications.

4.2 Background

4.2.1 *Features of Optimized Reaction*

Based on the optimized conditions for the alkenylation reaction, the initial optimization effort revealed that the combination of **L1** ligand and Lewis acid BF_3•Et_2O facilitated the formation of the desired acylation product **3**, albeit at low yield and diastereoselectivity. Subsequent backbone modification to the ligand could

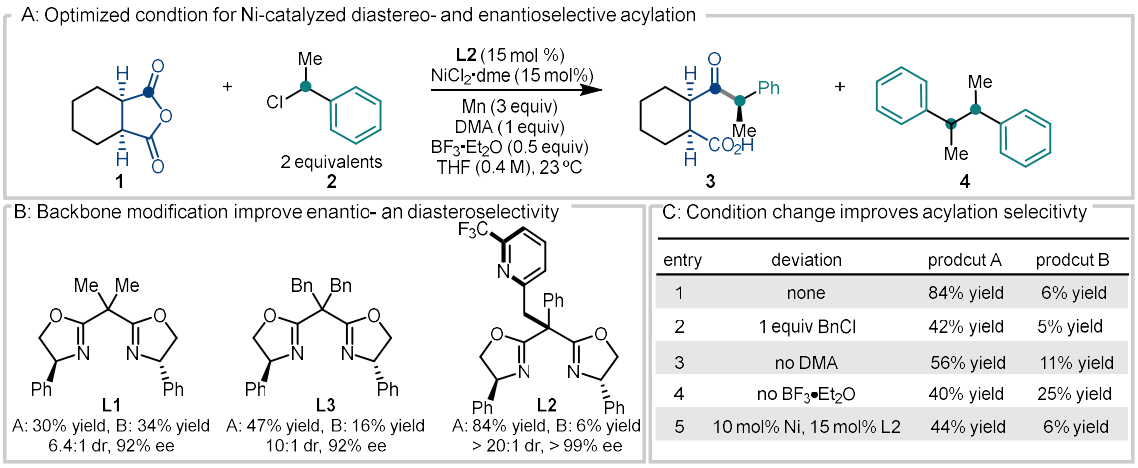

Scheme 3. *Ligand optimization and modifications to the reaction condition.*

improve the diastereoselectivity (**L3**), but low cross-coupling selectivity persisted, leading to the formation of the undesired bibenzyl side-product **4**. Thus, much of the remaining optimization campaigns centered on improving the selectivity for cross-coupling.

Extended experimentations showed that using two equivalents of benzylic chloride (**Scheme 3C**, entry 2), DMA as a solvent additive (entry 3), BF_3•Et_2O as Lewis acid additive (entry 4) as well as increasing catalyst loading (entry 5) all boosted the yield of cross-coupling products. Based on these modifications, an extensive ligand optimization campaign identified ligand **L2** with a 2-(6-CF_3-picoline) moiety as the optimal ligand,

furnishing the desired product in 84% yield. While the resulting optimized reaction undoubtedly broadened the applicability of Ni cross-electrophile coupling reactions to new substrate classes, the requisite ligand modification raised questions about the relationship between ligand structure and catalytic reactivity.

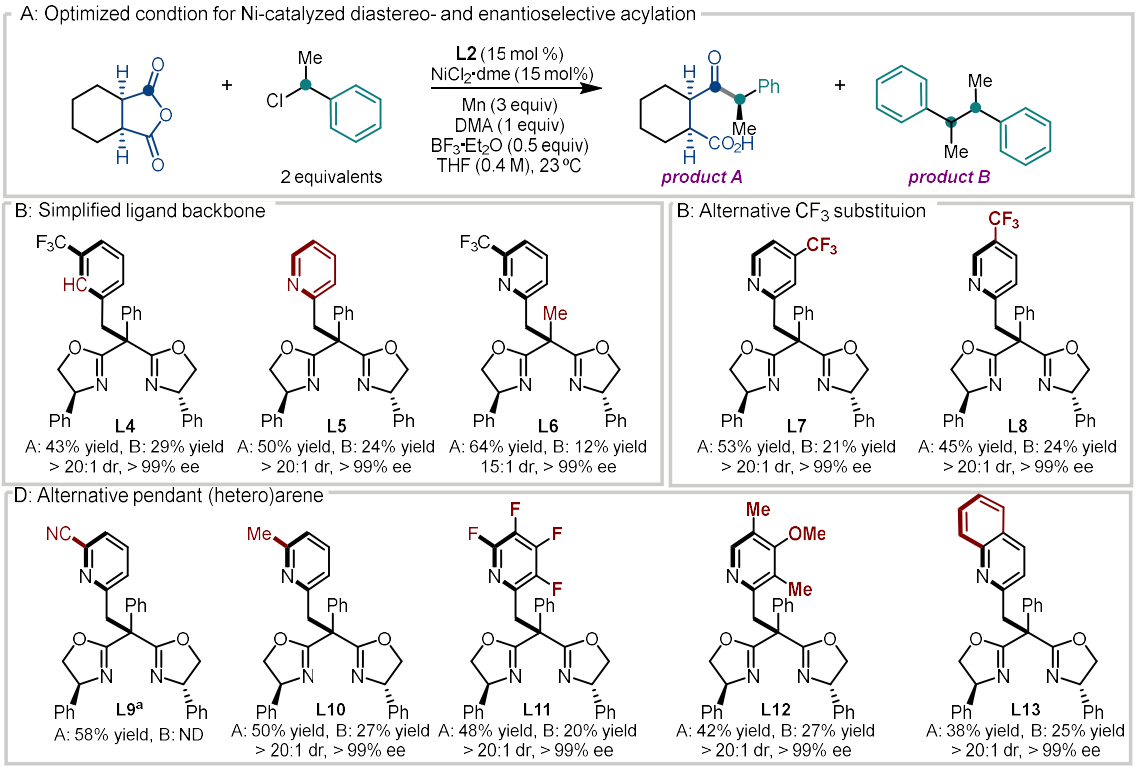

Scheme 4. *Structural deviation from the optimized ligand. a. reaction is done at 10 mol% Ni and 15% ligand loading instead. Bibenzyl formation, ee, and dr were not determined.*

A series of additional ligands were evaluated to perform the structural-reactivity study. The results revealed a perplexing picture: None of the structural modifications alone sufficed in promoting cross-coupling reactivity. For instance, the elimination of pyridine nitrogen as the third potential binding site (**Scheme 4**, **L4**) resulted in a drop in yield from 84% to 43%. Removing the *ortho* CF_3 substitution (**L5**) or changing its position (**L7** and **L8**) also decreased the acylation yield. Modifying the electronic of the pyridine ring with

a cyano (**L9**) or methyl group (**L10**) while retaining the steric hindrance of the *ortho* substitution caused the yield to drop to 58% and 50%, respectively. All alternative pendant heteroaromatic rings examined exhibited inferior cross-coupling reactivity (**L11**–**L13**). Even the 6-CF_3-picoline alone, the central motif identified during the optimization campaign, failed to retain high cross-selectivity when the backbone phenyl group was simplified to a methyl group (**L6**). The reaction yield dropped from 84% to 64%, with a minor decrease in diastereoselectivity.

As these structural deviations failed to identify alternative ligands that can sustain comparable reactivity, the reaction's stringent requirement for all structural modifications of **L2** to be intact precluded us from unambiguously articulating the ligand design rationale for further tailoring the reaction condition to elaborate substrates. Therefore, given the high cross-coupling-, enantio-, and diastereoselectivity achieved by the final optimized reaction, rationalizing these systematic modifications would invariably elevate the impact of and broaden the applicability of this reaction. Consequently, such a goal entailed addressing how these changes in reaction conditions and ligand decoration affect the catalytic mechanism and the kinetic synergy among its elementary steps.

4.2.2 *Prior Mechanistic Findings and the Proposed Catalytic Cycle*

Our prior mechanistic investigation of Ni-mediated reductive alkenylation of benzyl electrophiles in DMA solvent provides the foundational understanding of the elementary steps in which Ni catalysts may engage[15]. In prior chapters, we have established that the BOX ligand acts as a redox innocent spectator and that metal-based reduction of Ni(I) to Ni(0) is inaccessible due to the destabilization of Ni(I) RAMO. Consequently, Ni

catalysts with bidentate BOX ligands undergo the $Ni^{I/II/III}$ cycle and activate substrates at the Ni(I) oxidation state. Additionally, the reducing strength of the Ni intermediate is dependent on the identity of the co-ligands, such as halide, alkenyl, or coordinated solvent. For Ni(I)X species, the coordination of solvents can significantly destabilize the SOMO of Ni(I) species; this ligand field destabilization is thought to accelerate the oxidation of alkenyl bromide C(sp^2) electrophile.

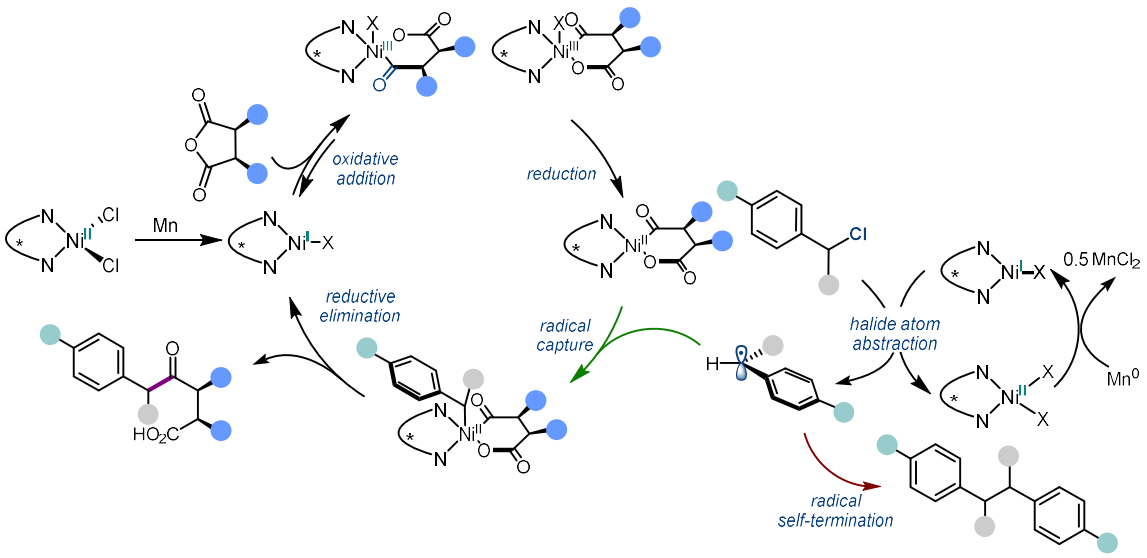

Scheme 5. *Proposed catalytic cycle.*

Building on these prior understandings[15,16], we propose that the same $Ni^{I/II/III}$ mechanistic cycle may be operative for the acylation of benzylic electrophiles (**Scheme 5**). Under this mechanism, the oxidative addition of the anhydride **1** and the halogen atom abstraction from benzyl chloride **2** compete for the related, if not identical, Ni(I) species. Thus, effective catalysis requires the activation of two electrophiles to proceed synergistically. Otherwise, if the requisite intermediates for radical addition are not sufficiently present, the acyl Ni(II) species may degrade[14], or the benzylic radical may self-

terminate bi-molecularly. Indeed, to the latter possibility, the observation that the bibenzyl **4** forms in a 1:1 diastereomers ratio suggests homo-coupling of the cage-escaped benzyl radical as the competing pathway[16]. Consequently, bibenzyl formation could be indicative of mismatched substrate activation rates.

Based on this interpretation, whether benzyl radicals undergo acylation or homodimerization depends on the generation rate of benzyl radical, the activation rate of anhydride, and the rate of irreversible consumption of benzyl radical by nickel (e.g., the sequence of radical addition and reductive elimination). When these rates are mistuned, bimolecular bibenzyl formation siphons away any unutilized radical intermediates. From this view, we can envision two ways by which reaction modification addresses this problem: I) Alternative elementary transformations, such as oxidative addition by Ni(0) species, whose thermodynamic driving force or reaction kinetics synergize better with the rest of elementary transformations, serve as the dominant pathway for productive cross-coupling. II) Reaction additives and pendent heteroarenes tune the rates of proposed steps to improve the catalytic synergy of the proposed $Ni^{I/II/III}$ cycle.

Adjudicating these two possibilities requires elucidating the coordination chemistry of Ni species and its implication to reactivity. As such, cognizant of the influence of co-ligand on the redox chemistry of nickel[15], we shall endeavor to clarify the coordination geometry of the Ni(II) precatalysts and their reduced intermediates. To this point, we now survey relevant literature reports of alternative coordinate geometries of Ni catalysts wherein the ligand provides a permanent or hemilabile third coordination site.

4.2.3 *Structural Inquiry of Ligand Ligation Mode: Prior Research on the Coordination Chemistry of Ni Catalysts*

The presence of pyridine in the optimized ligand suggests that the ligand may temporarily or permanently adopt a κ^3-binding mode to influence the redox chemistry of the nickel species. The decorated **L2** ligand is distinguished from the typical tridentate ligand by its lack of symmetry element. To this point, to the best of our knowledge, the C_1 symmetric tris oxazoline ligand reported by Zhou and coworkers[17] is the sole relevant example of a tridentate oxazoline ligand used for Ni catalysis (**Scheme 6**). In their report of a Ni-mediated asymmetric ring-opening of cyclopropane reaction, the authors found that changing from a C_2 symmetric BOX ligand to a C_1 symmetric BOX ligand improved the ring-opening yield from 22% to 66%. The reaction yield and the enantioselectivity of this reaction could be further boosted with a C_1 symmetric tris oxazoline ligand (**Scheme 6A**). Crystallography of the ligated $Ni(ClO_4)_2$ precatalyst showed that the tris oxazoline ligand adopted a κ^3 ligation mode (**Scheme 6B**), resulting in an octahedral nickel species. And this six-coordinate geometry was purportedly maintained throughout the redox-neutral reaction sequence and provided the facial bias for asymmetric induction. Conversely, it may be inferred from the poor reactivity with C_2 symmetric ligand that four-coordinate geometry may be ineffective at catalysis.

Given Zhou's precedent, the C_1 symmetric **L2** ligand may cause the Ni(II) center to adopt 5- or 6-coordinate geometry. Unlike Zhou's reaction, however, where the Ni(II) catalyst does not undergo oxidation state changes, deviation from the proposed tetragonal Ni(II) geometry would likely alter the ligand field splitting and impact the reduction

chemistry of the nickel catalyst. Therefore, structural characterization of Ni(II) precatalyst with decorated ligands would be the priority for mechanistic investigation.

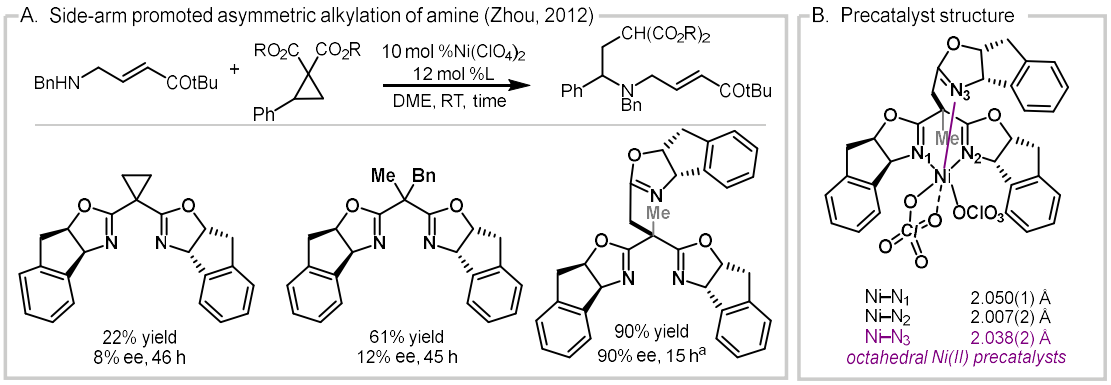

Scheme 6. *κ^3 ligation of C1 symmetric tris(Ox) ligand effect asymmetric alkylation reaction. a. at 25 h, the reaction furnishes the product at 72% yield with 91% ee.*

4.2.4 *Inquiry of Elementary Reactivity: Prior Research on Hemilabile Ligand Enabled Ni Redox Chemistry*

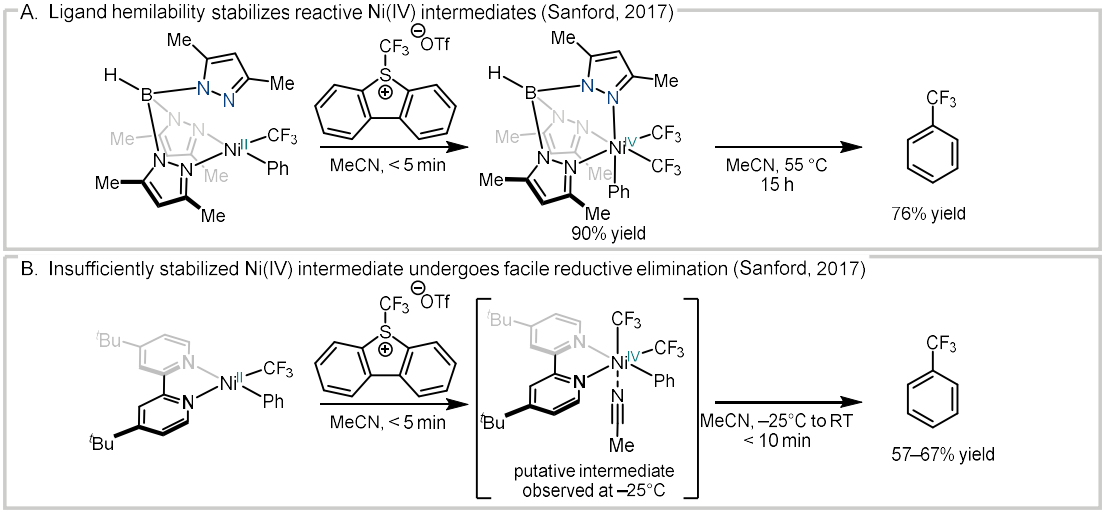

Scheme 7. *Hemilabile ligand stabilizes Ni(IV) species and tunes the rate of reductive elimination.*

Another possibility is the temporary ligation of the pendant pyridine to nickel. While this ligand hemilability may be much harder to characterize, the works by Sanfords[18]

reveal that they could have important implications for reactivity by stabilizing unusual oxidation states (**Scheme 7A**). For a Ni-mediated trifluoromethylation of arenes, **t**ris**p**yrazolylborate (**Tp**) ligand was found to adopt a κ^2 coordination mode to **Tp**Ni(II)(Aryl)(CF_3) and **Tp**Ni(II)$(CF)_2$ complexes. Upon treatment of a second electrophile, these complexes underwent a net oxidative addition generating six-coordinate TpNi(IV)(Aryl)$(CF3)_2$ complex, wherein the **Tp** ligand changed to a κ^3-coordination mode[18]. The isolated Ni(IV) complex could undergo reductive elimination to furnish aryl-CF_3 products upon heating at 50°C for 15 h. When the same chemistry was repeated with the bipyridyl (**bpy**) ligand, which lacked a third hemilabile site, the analogous bpyNi(IV)Aryl(MeCN)$(CF3)_2$ species was transient and converted to the product within 10 minutes.

While it is unlikely that high valent Ni(IV) species would be present under reductive conditions, Sanford's studies demonstrate that the hemilability of the ligand could stabilize reactive Ni intermediates and alter the rates of elementary reactions. For the system of interest, it is possible that pyridine may ligate to Ni(I) or Ni(0) centers, thereby facilitating the reduction of Ni(I) intermediate to Ni(0) species. This would enable an alternative anhydride activation pathway via a $Ni^{0/II}$ oxidative addition (**Scheme 8A**). Similarly, pyridine may ligate to Ni(III) species generated after oxidative addition by Ni(I) intermediates or radical addition, thereby providing rate modulation. Alternatively, reports by Hazari[19], Nocera[20], and Doyle[21] have consistently revealed the propensity of coordinatively unsaturated monomeric Ni(I) species to oligomerize to higher-order aggregates. Our mechanistic studies show that higher-order aggregates, generated by prolonged stirring between Ni(II) precatalysts and reductants, may be inactive for

catalysis[16]. Therefore, the inclusion of a hemilabile pyridine, as well as the steric congestion it introduces, may help protect reactive Ni(I) centers against deactivation (**Scheme 8B**), thereby tuning the rates of Ni(I)-mediated substrate activation.

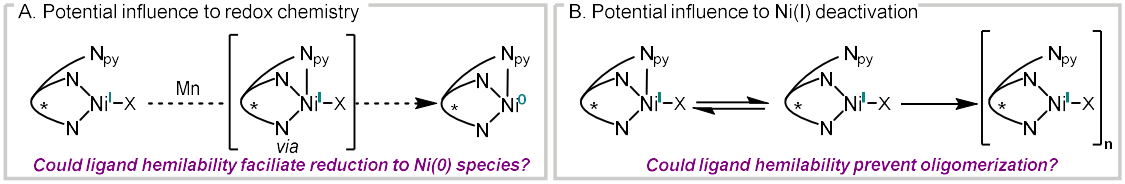

Scheme 8. *Potential influence of ligand hemilability to the reactivity and stability of Ni(I) species.*

These hypotheses motivate us to extend our structural interrogations beyond the Ni(II) precatalysts to reduced Ni intermediates, which necessitated combining *in situ* spectroscopy and computational chemistry to detect these elusive species. Importantly, as the stabilization of Ni intermediates is intertwined with the rates of their elementary chemistry, kinetic information could provide valuable hints for the role of ligand and reaction modification. Considering this, we now survey the kinetic framework that the cumulative work of this thesis hypothesizes to be operative for Ni-mediated reductive coupling chemistry and its implications for tuning the rates of elementary transformations for effective catalysis.

4.2.5 *Inquiry of Catalytic Kinetics: Kinetics Framework for Relative Activation Rates of Electrophiles*

The preceding discussion of prior literature and mechanistic findings motivate the kinetics question of how the identity of elementary transformation and the rates at which they proceed could benefit effective catalysis. While this vast question is tied to the networks of elementary reactions during catalysis, focusing on the reactivity of the benzyl

radicals simplifies our mechanistic consideration.

Namely, upon generation, the caged benzyl radical may undergo radical addition to organonickel to furnish a cross-coupling product or undergo self-termination via bibenzyl formation (**Scheme 9A**). The former process, though desired, is unfavorable on the thermodynamic ground since radical addition steps tend to be thermally uphill in energy[22,23]. Moreover, the resulting Ni–C bond could be 36.3–49.4 kcal/mol weaker than the C–C bond[24] that would otherwise form from bibenzyl formation. Thermodynamic considerations alone cannot account for cross-coupling product formation without considering the kinetics of the elementary steps involved.

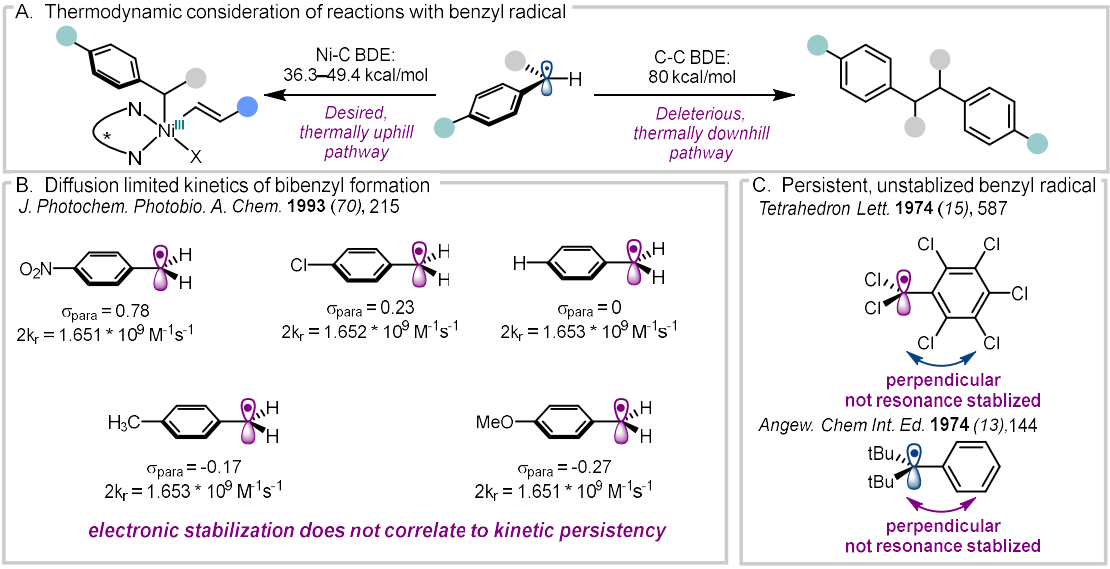

Scheme 9. *Thermodynamics and kinetics of the homodimerization of benzylic radicals.*

Kinetically, the rate of bibenzyl formation has been extensively studied and measured. Irrespective of the substitution[25,26] to the benzylic radicals and the polarity of the solvent[25–27], bimolecular bibenzyl formation proceeds with a rate on the order of 10^9 $M^{-1}s^{-1}$ (**Scheme 9B**). This rate constant can be satisfactorily predicted by Von

Smoluchowski equation[25], indicating that the measured rates are diffusion-limited. Recognizing its brief lifetime appears at odds with its stabilized electronic structures, Griller and Ingold categorize benzylic radicals as stabilized, transient radicals[28]. The independence of kinetic persistency from electronic stabilization has been demonstrated explicitly with examples of unstabilized, persistent benzyl radicals[29,30] (**Scheme 9C**).

Owing to their rapid dimerization process, reactions involving transient radicals must be conducted under specific conditions. For example, to evaluate absolute radical addition rates with radical clock experiments, the reaction condition must be adjusted such that the steady-state concentration of radical is around 10^{-4}–10^{-6} M so that radical dimerization becomes negligible[31]. Furthermore, the reaction partner of the radical is often employed in pseudo-first-order excess to bias the radical addition process of interest[31,32]. It is unlikely that typical conditions of Ni-mediated XEC reactions, which employ substrate at 0.1–1 M concentration with 10–20 mol% of catalyst loading[33], would satisfy these concentration requirements, as evidenced by the bibenzyl formation.

Kinetic persistent radical effects[34] offer an alternative kinetic paradigm in which transient radicals can be selectively captured by a long-lived species. In the titular case, the model posits that if the coupling partner of the transient radical is slow to dimerize, i.e., a persistent radical, then, during the initialization period of the reaction, the concentration of the persistent radical steadily increases while the concentration of the transient radical remains low (See ref 34, Figure 2 and the discussion therein). Once the resting state concentration of persistent radicals is sufficiently high, cross-coupling of transient and persistent radicals becomes kinetically favored over homo-coupling of the transient radicals. As this kinetic effect is agnostic to specific chemical interactions, transition metal

species, too, can serve as the persistent coupling partner. Indeed, the emergent radical sorting strategy, which converts a transient radical intermediate into a persistent metaloradical species[35], resoundingly demonstrates the utility of the kinetic radical effect to achieve even cross-selective triple radical coupling[36].

An important implication of the persistent radical effect is that the highest possible cross-selectivity depends on the relative rate of radical generation and the decay rate of the persistent species[34]. Namely, for a given set of the persistent radical dimerization rate and the cross-radical coupling rate, the highest cross-coupling selectivity arises when the transient and persistent radicals are generated at comparable rates (see Ref 34, Figure 3 and the discussion therein). The highest possible cross-selectivity increases if the degradation rate of persistent species is slowed or, equivalently, if the cross-coupling rate is increased. Thus, the persistent radical effect describes achieving rate-matching kinetics as an important factor for selective cross-coupling of transient radicals. Conceptually, the intricate dependency of cross-selectivity on various rates can be summarily simplified into the following: Matching the generation rate of transient radical with the rate of its conversion by its persistent reaction partner would maximize cross-selectivity.

Mechanistic studies from Chapter 3 revealed signs that this persistent radical effect is present for the optimized alkenylation reaction where the reaction resting state alkenyl nickel serves as the persistent species. Under the homogenous reaction condition, the generation rate of the radical can be tuned by the steric bulk of the Lewis acid additive[16]. Additionally, because the turnover limiting step is the radical addition, the effective consumption rate of radical could be varied by nickel loading (See Chapter 3, **Scheme 5D**). When nickel loading is reduced to 1 mol% from the optimization condition, a decrease in

cross-coupling product was observed. Consistent with the rate-matching kinetic predicted by persistent radical, however, reducing the rate of radical generation by employing the sterically encumbered TESBr restores cross-selectivity.

Although these results are insufficient to establish a causal relationship between persistent radical effect and effective catalysis for mechanistically ambiguous scenarios, the paradigm of rate-matching kinetics, as a working hypothesis, nevertheless generates useful suggestions on how catalytic synergy may improve if the persistent radical effect is operative. Unlike alkenylation chemistry, acylation chemistry of interest requires the activation of a stronger C–O bond, suggesting that the generation of the persistent species, the Ni(II) oxidative addition complex, may be sluggish (**Scheme 10A**). Furthermore, comparing the corresponding products, the C–O bond formed under acylation chemistry is also weaker than the C–C bond forged under alkenylation chemistry; this similarly suggests reductive elimination may be sluggish as well (**Scheme 10B**). Taken together, the effective consumption of benzylic radical for acylation chemistry is anticipated to be slower than alkenylation under an identical condition (**Scheme 10C**). Should persistent radical effect *cause* effective catalysis, conditions that improve cross-coupling yield should have endeavored to accelerate the anhydride activation rate or slow the benzyl radical generation rate. These two predictions provide an important link between structure modifications and reaction kinetics to help discern catalytically important modification. For this reason, we analyze the evolution of ligands and reaction conditions in terms of the relative kinetics of substrate activation.

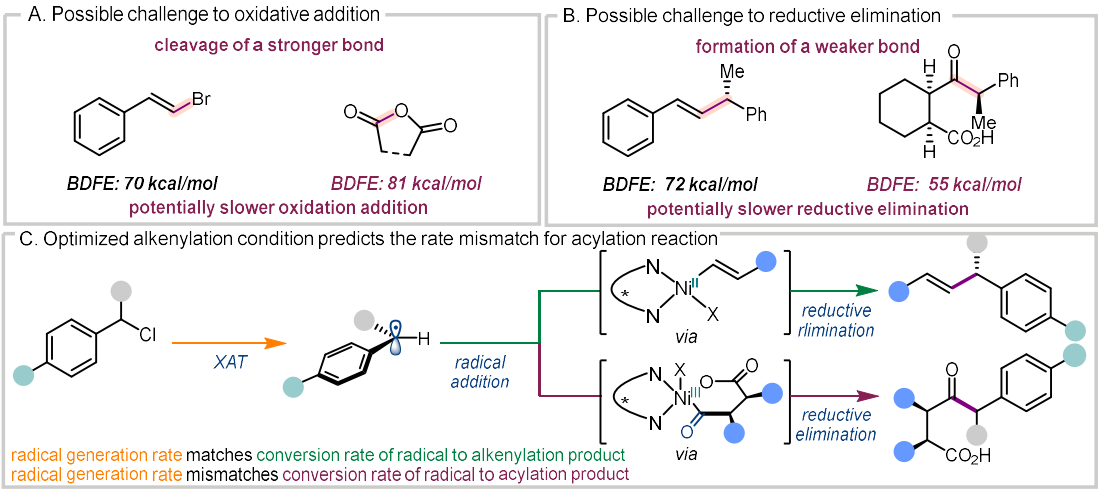

Scheme 10. *Thermodynamics and kinetics of the homodimerization of benzyl radicals.* The BDFEs were obtained from NREL ALFABET database[12], and machine-learned values were used for comparison.

4.2.6 *Summary of Research Methodology and Specific Inquiries*

A $Ni^{I/II/III}$ cycle is proposed based on the existing mechanistic study on the alkenylation chemistry catalyzed by nickel species bearing **IndaBox** ligand. Owing to the similarity between bidentate ligand **L1** and **IndaBox**, the poor acylation reactivity when **L1** is used suggests that the proposed mechanism is likely operative but kinetically uncompetitive in comparison to deleterious bibenzyl formation. Thus, either an alternative mechanism serves as the dominant reaction pathway (hypothesis A), or the evolution of the ligand and the reaction conditions tune the kinetics of the proposed reaction pathway (hypothesis B). In this regard, both hypotheses draw attention to the possible role of the pendant pyridine in catalytically optimal ligand **L2**. Specifically, the pendant pyridine may permanently or temporarily adopt a κ^3 ligation mode to enable, for example, the generation of stabilized Ni(0) species and the oxidative addition of anhydride by the Ni(0) species. It is also possible that ligand decoration modulates the redox property of Ni(I) species and

stereoelectronically protects the reactive monomeric Ni(I) species from oligomerization, a putative deactivation pathway. In other words, the ligand decoration may serve to tune the rates of the proposed reaction steps. Given these considerations, section 4.3 describes the effort to characterize the coordination behavior of the ligand experimentally and computationally. Section 4.4 details the redox property of isolated Ni(II) precatalysts and assesses the reactivity of Ni(I) species towards anhydrides. Finally, building on these findings, section 4.5 leverages cyclic voltammetry to provide semiquantitative kinetic information about the rate of substrate activation, thereby distinguishing the possible dominant reaction pathway under catalysis. From these interrelated investigations of structure, reactivity, and kinetics of the catalytic species, we hoped to answer how the evolution of ligands and reaction conditions improve the overall catalytic performance.

4.3 Structural Investigation of the Ligand Binding Mode

4.3.1 *Ligand Binding Mode to Ni(II) Precatalyst*

Because permanent coordination changes may signal reactivity differences, we first sought to elucidate the geometry of Ni(II) precatalysts to address whether the inclusion of the pendant heteroaromatic moiety induces changes in coordination geometry. Initial attempts to access a well-defined **L2**$NiCl_2$ precatalyst that was pertinent to the optimization condition were unsuccessful due to the spontaneous formation of the high-order aggregates[15,37,38]. Using $NiBr_2$•dme as the nickel precursor ameliorated the speciation issues and furnished a single product whose pink coloration was consistent with four-coordinate **L2**$NiBr_2$ precatalysts (**Scheme 11A**). From this product, well-defined single crystals of **L2**$NiBr_2$ (**Scheme 11B**) could be accessed upon further solvent

optimization (Section 4.8.1). This modified synthesis and purification procedure extended to alternative decorated ligand **L12** to access related precatalysts(**Scheme 11B**). The resulting precatalyst structures, along with relevant literature precedents[17,37,39,40], allowed us to compare structural differences and discern structure-reactivity correlation.

The bond metrics of nickel dihalide precatalysts bearing **IndaBox**(entry 1–2), **L1**(entry 3), **L2** (entry 4), and **L12** (entry 5–6) were tabulated in **Scheme 11C**. The catalytic performance of the ligands was included to correlate structural differences with reactivity. In all cases, the pyridine-containing ligands (entries 4–5) adopted a κ^2 coordination mode to a tetragonal Ni(II) center. The Ni–N_{ox} distances observed for these new precatalysts with pyridine-containing ligands were highly similar to those with

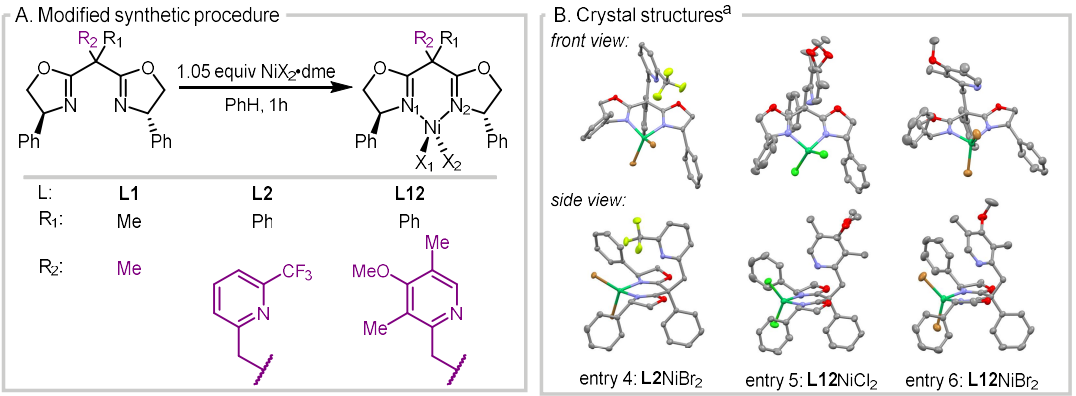

C. Bond metrics comparison

entry	ligand	halide	Ni–N_1	Ni–N_2	Ni–N_{py}	Ni–X_1	Ni–X_2	∠N_1-Ni–N_2	acylation yield[b]
1	**IndaBox**	Cl	1.987(1) Å	1.971(1) Å	-	2.2330(6) Å	2.2254(6) Å	90.52(5)°	0%
2	**IndaBox**	Br	1.974(5) Å	1.981(5) Å	-	2.3749(9) Å	2.358(1) Å	90.8(2)°	0%
3	**L1**	Br	1.9807(9) Å	1.9788(9)Å	-	2.3740(3) Å	2.3376(3)	90.64(3)°	30%
4	**L2**	Br	1.978(2) Å	1.981(1) Å	4.325(2) Å	2.3524(9) Å	2.3833(9) Å	88.87(8)°	84%
5	**L12**	Cl	1.983(4) Å	1.993(3) Å	3.824(4) Å	2.218(1) Å	2.233(1) Å	90.2(1)°	42%
6	**L12**	Br	1.983(2) Å	1.970(2) Å	4.079(2) Å	2.3461(7) Å	2.3634(5) Å	90.75(6)°	42%

Scheme 11. *Crystal structures of the precatalysts and bond metric comparison. a. crystal structures shown at 50% ellipsoid. b. acylation yields of* ***3*** *under the in situ complexation condition with $NiCl_2$•dme as the nickel source were reported.*

the non-pyridine-containing variates that showed no (entry 1) or inferior catalytic reactivity (entry 2–3). Other bond metrics were also comparable, except for a reduced bite angle observed for **L2** (entry 4). For ligands with pendant pyridine (entry 4–6), the pyridine nitrogen pointed toward the nickel center, suggesting the presence of a stereoelectronic effect. However, in stark contrast to the observation by Zhou and coworkers[17] (**Scheme 6B**) where the axial and equatorial Ni–N_{ox} distances were highly comparable, the Ni–N_{py} distance observed was significantly longer than the Ni–N_{ox} distances for all three precatalysts. With a Ni–N_{py} distance of 4.325(2) Å for **L2**$NiBr_2$ (entry 5), the interaction between the nickel center and pyridine nitrogen fell under the range of non-covalent interaction[41,42] instead of direct coordination.

The extent of this putative interaction between the nickel center and the pyridine could be further probed with the modified **L12** ligand, where the positioning of the pyridine needs to minimize the possible steric clash between the nickel center and the substitution. Thus, steric due to the tri-substitution pattern may bias the interaction between pyridine nitrogen and nickel center. Nevertheless, neither **L12**$NiCl_2$ (entry 5) nor **L12**$NiBr_2$ suggested the presence of a Ni–N_{py} bond. These results suggest that pendant pyridine does not directly coordinate with the meal center but may fine-tune the electronic or steric of the metal catalyst with possible non-covalent interaction.

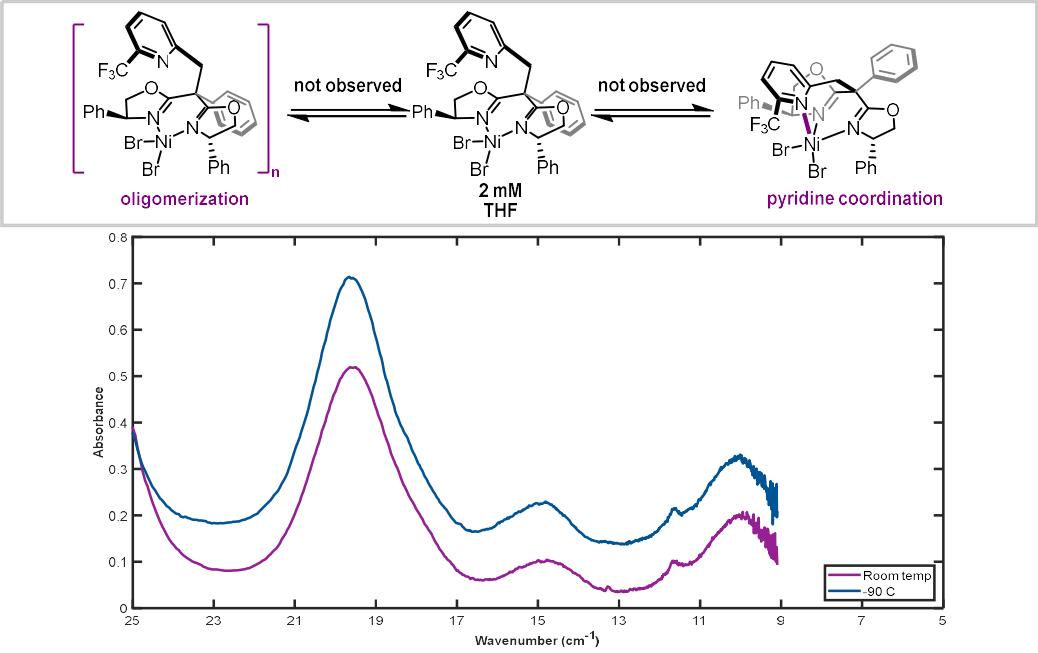

Scheme 12. *Variable Temperature Optical Spectra of* ***L2****NiBr*$_2$.

To ascertain whether these solid-state structures reflected the solution-phase behavior during catalysis, variable temperature UV-Vis-NIR spectroscopy was sought. Based on spectroscopic observation of temperature-dependent DMA coordination to Ni(II)[15], we anticipated that an LMCT band near 400 nm (25000 cm^{-1}) might emerge if pyridine ligates in solution. At room temperature, the absorption spectrum of crystalized **L2**NiBr$_2$ in THF showed weakly absorbing bands, and the position and shape of these bands were similar to the d-d transitions of **IndaBox**NiX$_2$ complexes[15] (**Scheme 12**). Perturbation to speciation equilibria by way of temperature variation revealed no new band –90 °C. While an isosbestic point may exist near 400 nm, the increase in absorption intensity across the entire spectroscopic region precluded us from unambiguously attributing these spectroscopic changes to a second species. Because findings from Chapter 2 show the low temperature (–90 °C) and low concentration (ca 2 mM) should favor the

formation of the monomeric four-coordinate species, the similarity between the two spectra suggests the major Ni(II) species is likely those observed in the solid phase.

Taken together, structural investigation in the solid phase and solution phase reveals a consistent picture that the ligand adopts a κ^2 ligation mode. Nevertheless, these results cannot rule out the existence of minor reactive nickel species with κ^3 ligations. As such, we attempt to characterize reduced nickel species to gain a broader picture of the ligation mode for downstream catalytic intermediates.

4.3.2 *Ligand Binding Mode to Ni(I) Intermediates*

The reduction of nickel dihalides precatalysts is proposed to eliminate a halide anion to furnish three-coordinate Ni(I) species. Because these 15-electron Ni(I) intermediates are coordinatively unsaturated, oligomerization[15,19–21] and solvent ligation[15] to form electronically stable four coordinate species have been directly or indirectly observed. The inclusion of pendant pyridine may serve to provide an intramolecular pathway to stabilize these Ni(I) species, either enabling its further reduction to Ni(0) species or protecting it from deactivation pathways.

Structural elucidation of Ni(I) species remains a challenge in literature owing to speciation challenges and thermal instability. Monomeric Ni(I) structures are particularly rare, and their reported isolations are aided by the use of tridentate ligands[43], sterically bulky ligands[44,45], or stabilizing agent[21]. Only a handful of structures of Ni(I) species bearing bidentate nitrogen ligands exist, namely ones from Fu[40,46], Hazari[44], and Doyle[21]. Storage of the resulting species at reduced temperatures may be necessary to isolate suitable single crystals[40].

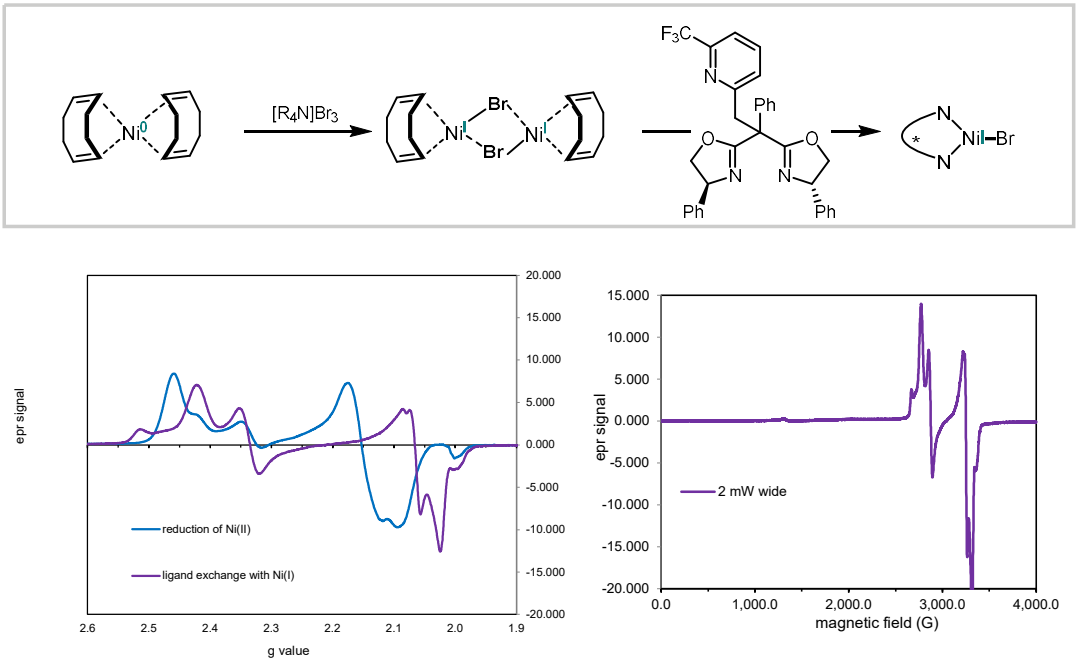

Scheme 13. *Synthesis and EPR Characterization of* ***L2****NiBr.*

Anticipating the challenge that may be posed by the oligomerization of Ni(I) species in solution, we postulated that limiting solution-phase handling during the synthesis and the isolation of Ni(I) species could facilitate structural elucidation of Ni(I) intermediates and the ligand coordination mode. The synthetic procedure[21] reported by the Doyle lab with a well-defined $[Ni(I)(COD)X]_2$ synthon appeared well suited for this goal. In collaboration with the Doyle Lab, a ligand exchange reaction between $[Ni(I)(COD)X]_2$ and **L2** resulted in an isolable yellow powder (**Scheme 13**). The EPR spectrum of this species in 2-MeTHF indicated the presence of rhombic monomeric Ni(I)

species that differed from the EPR spectra of Ni(I) species generated through the reduction of Ni(II) precatalyst (vide infra). Assuming a molecular formula of **L2**NiBr, the maximal concentration of Ni(I) species was determined to be 2.12 mM, accounting for 19% of total

Ni species in a 10.8 mM solution. Thus, additional species may be present. Indeed, an expanded scan window revealed the presence of an additional signal at 1300 mT, suggesting the presence of dimeric Ni(I) species based on similar observations[9,44].

To further minimize solution handling, we opted to utilize microcrystal electron diffraction to assess the structure of this yellow in collaboration with the Nelson Lab. To our delight, a weak diffraction pattern was observed, and an orthorhombic unit cell with lengths of 11.6 (±1.4) Å, 13.5 (±1.4) Å and 29.1 (±1.4) Å was determined. This observed unit cell was distinct from the triclinic unit cell of the **L2**$NiBr_2$ precatalyst (P1, a=8.5963(17) Å, b=9.804(3) Å, 10.307(2) Å). Unfortunately, the microcrystal was too small for full data collection, and the diffraction pattern eventually disappeared after several hours. Repurification of the yellow crystals failed to regenerate microcrystals. Thus, we were unable to assess the structure of Ni(I) species from these attempts. Further optimization of the synthetic procedure and sample preparation is needed to maximize the yield of monomeric species as well as the size of microcrystals. Exploration of solvent systems and concentration could be fruitful.

4.3.3 *Conformational Analysis of Ligand Binding Mode*

As experimental investigations failed to provide positive evidence for pyridine ligation, we next sought to use conformer searches at the DFTB[47] and DFT levels of theory to exhaustively evaluate the viability of pyridine ligation to Ni(II) or Ni(I) centers. Such an evaluation of conformer ensembles had revealed the influence of the steric of conformationally flexible monophosphine on the speciation of ligated nickel catalysts and their reactivity for Suzuki coupling[48]. Similarly, we anticipated that adopting this workflow

could elucidate the role of ligand decoration.

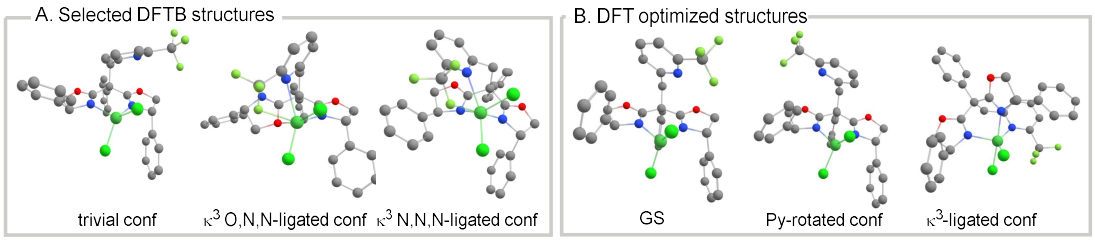

C. Bond metrics comparison

entry	name	Ni–N_1	Ni–N_2	Ni–N_{py}	Ni–Cl_1	Ni–Cl_2	∠N_1-Ni–N_2	∠N_1-Ni–N_3	∠N_2-Ni–N_3
1	GS	1.96 Å	1.96 Å	4.30 Å	2.22 Å	2.24 Å	91°	-	-°
2	Py-rotated conf	1.95 Å	1.95 Å	5.00 Å	2.22 Å	2.24 Å	91°	-	-
3	κ^3-ligated conf	2.04 Å	2.00 Å	2.33 Å	2.32 Å	2.30 (3)	86°	78°	111°

Scheme 14. *Representative conformer ensemble of* ***L2****Ni(II)*Cl_2.

Mirroring our experimental investigations, we first focus on the conformers of the **L2**$NiCl_2$ precatalyst. At the DFTB level of theory, 433 conformers were identified within the 6 kcal/mol energy threshold. Among them, most of the conformers were trivial to the present inquiry as they differed from the GS conformer only in the positions and the orientations of the phenyl groups on the oxazoline units. Given the large size of the ensemble, only the 20 lowest-energy conformers and/or structurally distinct high-energy conformers were further refined at the DFT level, revealing a tetragonal Ni species with a κ^2-ligation mode as the ground state (GS) conformer (**Scheme 14A**). Similar to solid-state structures, the GS geometry showed an unligated pyridine oriented at the metal center. The Ni–N_{py} distance of 4.30 Å and the Ni–N_{ox} distances of 1.95 Å and 1.95 Å well agreed with a solid structure of analogous **L2**$NiBr_2$. Of the 20 lowest energy conformers, only one conformer was structurally distinct from the GS conformer(**Scheme 14A&B**). This conformer oriented its pyridine nitrogen away from the metal center and was found to be 0.6 kcal/mol higher in energy than the GS conformer at DFTB level of theory. This small

energy difference fell within the expected strength of non-covalent interaction.

The first conformer that indicated Ni–N_{py} bond of 2.60 Å was the 6.4 kcal/mol higher in the GS conformation (**Scheme 14A**, κ^3-O,N,N conf). At 7.8 kcal/mol above the GS, a second instance of Ni–N_{py} ligation with a bond distance of 2.36 Å was identified (**Scheme 14A**, κ^3-N,N,N conf). Structural refinement at the DFT level of theory revealed a five-coordinate Ni species with a distorted trigonal bipyramidal geometry. Given the large difference between this pyridine-ligated conformer and the GS conformer, pyridine-bound nickel species would be minimally thermally occupied. As such, spectroscopic techniques applied to mixtures at equilibrium were unlikely to identify this species. Consequently, if these high-energy κ^3-ligated nickel species were of catalytic importance, they must exhibit a significantly enhanced reactivity profile, such as its intermediacy may be inferred from kinetic information from *in situ* spectroscopies.

Extending the conformer search to **L2**Ni(I)Cl revealed 9 conformers within a 6 kcal/mol threshold and 116 conformers within a 15 kcal/mol threshold at the DFTB level of theory. All 20 lowest energy conformers showed additional interaction between the ligand and nickel (e.g., arene interaction, agnostic interaction, or pyridine ligation), resulting in four- or five-coordinate geometries. These interactions, however, were found

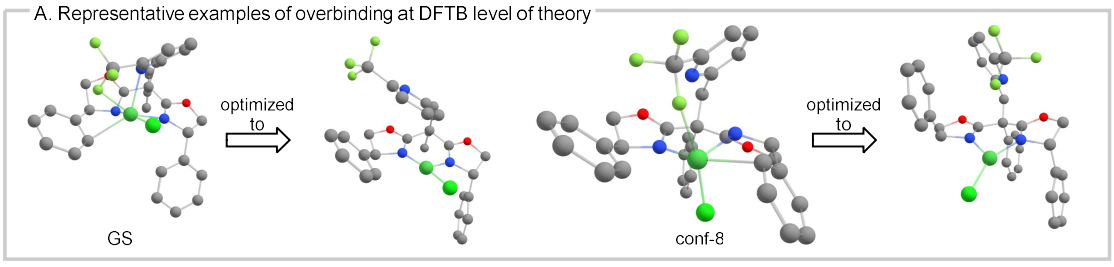

Scheme 15. *Representative conformer ensemble of* ***L2****Ni(I)Cl*.

to be an artifact of the tight binding theory: When these structures were refined at DFT level, all 20 lowest energy conformers optimized to a three-coordinate Ni(I) species with a κ^2 ligand (**Scheme 15**). No pyridine ligation was observed. The propensity of DFTB to overbind and generate fictitious interaction called for refinement of geometries at an intermediate level of theory where optimization of conformer ensemble is possible.

4.3.4 *Summary of Findings: Direct Ligation is Unlikely*

In summary, structural investigations of Ni(II) precatalysts and Ni(I) intermediates failed to support pyridine ligation as an explanation for its beneficial role in catalytic reactivity. The bond metrics of the pyridine-containing ligand **L2** were highly comparable to those of the undecorated variates **IndaBox** and **L1**, which results in similar ligand field splitting as evident in absorption spectra. Although the computational evaluation of the conformer ensemble indicated that κ^3 ligation mode to Ni(II) center was possible, its high energy indicated the corresponding five-coordinate **L2**$NiCl_2$ species would be minimally thermally occupied. Therefore, the catalytic relevance of this species must be assessed with kinetic data. Instead, we reported signs of non-covalent interaction between the pendant heteroarenes and nickel, which may modulate the electronic and the steric of the nickel catalysts. The observed preference for the decorated ligands to adopt a κ^2 ligation mode was consistent with our assessment that the proposed mechanism may be operative but kinetically ineffective without additional tuning conferred by the pendant pyridine. Alternatively, it remained possible that the temporary ligation of pyridine moiety may facilitate disparate elementary transformation. Key to evaluating these two competing hypotheses would be the elucidation of the dominant mode of reactivity. Motivated by this

line of inquiry, we next discuss our research spectroscopic investigations of the redox reactivity of Ni catalysts and the stability of the reduced intermediates.

4.4 Reactivity and Stability of Reduced Ni Intermediates

Because ligand decoration and modification of reaction conditions appeared to influence bibenzyl formation, we aimed to address how these changes affected the reactivity and stability of the nickel intermediate that was responsible for radical generation with the ensuing spectroscopic investigations. Namely, we sough to clarify whether ligand decoration may facilitate the generation of Ni(0) species or, alternatively, if Ni(I) species could activate anhydrides. Cyclic voltammetry was applied to characterize the redox chemistry of Ni(II) precatalysts and their reduced intermediates to this point. Electron paramagnetic resonance (EPR) spectroscopy was leveraged to elucidate the stability of the Ni(I) species and its reactivity towards the anhydride substrate. Building on insights from these two flavors of spectroscopic techniques, in situ IR spectroscopy was applied to monitor the catalytic reactions to provide support for anhydride activation.

4.4.1 *Redox Chemistry of Ni(II) Precatalysts*

Cyclic voltammograms of **L1**$NiBr_2$ and **L2**$NiBr_2$ in THF indicated that the pendant pyridine could weakly modulate the reduction potentials of the precatalyst (**Scheme 16**). Similar to the cyclic voltammograms of the **IndaBox**NiX_2 precatalysts[15], only a broad redox couple was observed within the solvent window for both **L1**$NiBr_2$ and **L2**$NiBr_2$. This redox feature may be assigned as a one-electron electrochemical reduction of Ni(II) followed by a concerted process of halide dissociation and solvent coordination[15]. Because this concerted chemical step rendered the electron transfer step irreversible, broadening the separation between the cathodic peak and the anodic peaks, half-wave potential $E_{1/2}$ insufficiently described the redox differences between the precatalysts: Whereas the $E_{1/2}$

suggested **L2**$NiBr_2$ to be 70 mV easier to reduce than **L1**$NiBr_2$, the cathodic peak E_c suggested the **L2**$NiBr_2$ is 30 mV harder to reduce. This electrochemical irreversibility could also cause the cyclic voltammograms to be highly sensitive to the electrochemical setup and the purity of the analyte, particularly for

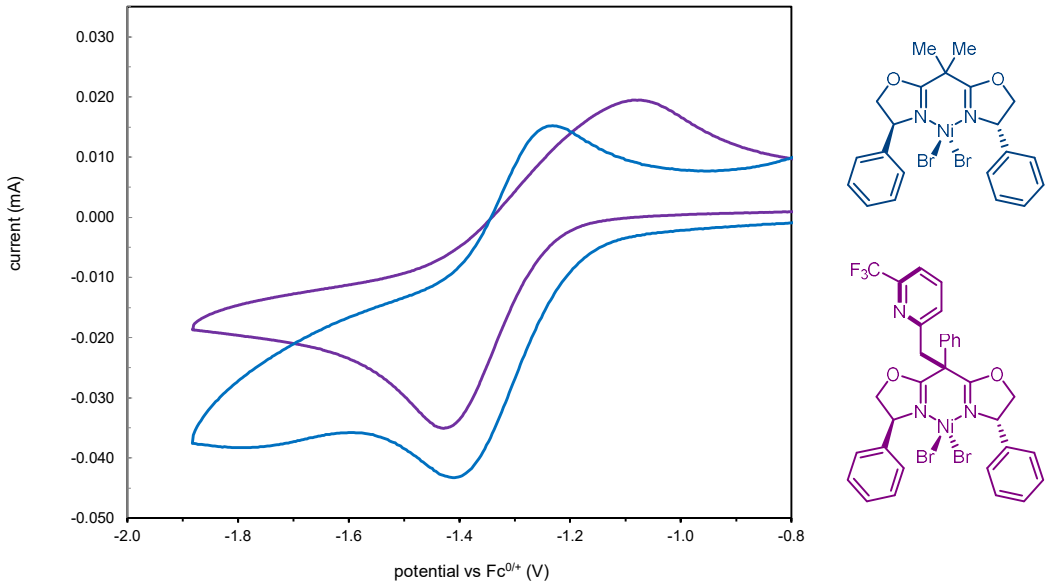

Scheme 16. *Cyclic Voltammogram of Precatalysts (4 mM, 0.2 M TBAPF6 in THF using Ag/Ag+ reference electrode, Pt wire counter electrode, and glassy carbon working electrode).*

L2$NiBr_2$ (See Section 4.8.5). Nevertheless, these qualitatively comparable $Ni^{2/1+}$ couples were consistent with our structural findings that the coordination mode and the bond metrics were highly comparable among the precatalysts with **IndaBox**, **L1**, or **L2**. More importantly, Ni(0) species appeared inaccessible, irrespective of the inclusion of the pendant pyridine.

Owing to the confounding contribution of halide dissociation and solvent coordination to cyclic voltammograms, computational predictions of $Ni^{2/1+}$ reduction

couple were sought to clarify the subtle electronic modulation of nickel by ligand. For **L1**$NiCl_2$ and **L2**$NiCl_2$, the calculated reduction potentials were –1.62 V and –1.61 V vs Fc/Fc.[15] Provided that dichloride precatalyst was found to be 0.21–0.27 V harder to reduce than the dibromide precatalyst, these calculated reduction potentials were in good qualitative agreement with experimental values. Experimental and computational evaluation of redox potentials of Ni(II) provided a consistent picture that pendent heteroarene can fine-tune the redox property of Ni(II) without direct ligation.

A. Predicted $Ni^{2/1+}$ couple and buried volume

entry	ligand	$Ni^{2/1+}$ couple	$\%V_{bur}$[a]	acylation yield[b]
1	L3	–1.47 V	60.0%	47%
2	L4	–1.58 V	55.9%	43%
3	L2	–1.61 V	56.5%	84%
4	L7	–1.61 V	54.5%	53%
5	L1	–1.62 V	48.3%	30%
6	L10	–1.67 V	57.4%	50%
7	L5	–1.68 V	54.1%	50%

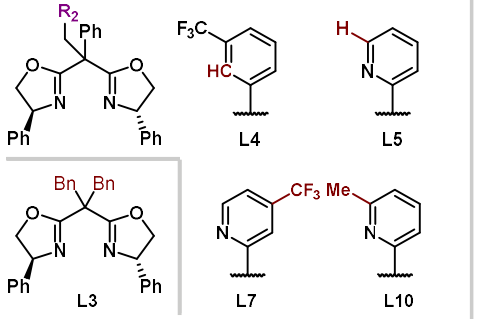

D. Bivariate linear regression model

$$\%\ \text{yield} = -92\ (\pm 102) \times Ni^{2/1+} + 3.1\ (\pm 1.9) \times \%\text{Vbur} - 264\ (\pm 230)$$

$R^2 = 0.385$, Standard Error = 15

B. Correlation between redox potential and cross-coupling yield

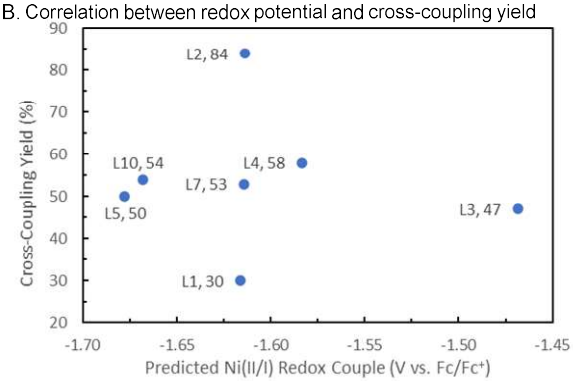

C. Correlation between % buried volume and cross-coupling yield

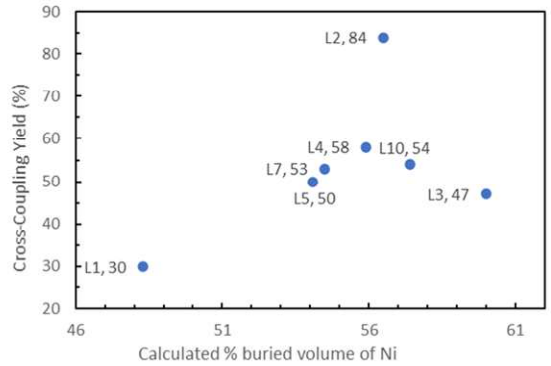

Scheme 17. *Predicted reduction potentials of the Ni2/1+ couple and their correlation with reactivity. a. %V_{bur} evaluated at r=4.5 Å. b. acylation yields under the in situ complexation condition with NiCl2•dme as the nickel source were reported.*

To verify whether this modulation of redox potential impacted reactivity, the redox potential of an expanded set of precatalysts was evaluated computationally (**Scheme 3&4**, **L1**–**L5**, **L7**, and **L10**). The results, shown in **Scheme 17A**, indicated that backbone

modification could lead to an up to 210 mV difference in reduction potential. The strength of this modulation was on par with the variation solvent coordination and halide identity could provide. However, plotting the cross-coupling yield against the reduction potential indicated that the cross-coupling yield did not linearly correlate with the reduction potential (**Scheme 17B**). Intriguingly, for precatalysts with comparable reduction potentials (entry 4–6), the cross-coupling yield appeared to improve with an increase of ligand steric, as measured by the buried volume ($\%V_{bur}$) of the ligand, and there appeared to be a small window for an optimal buried volume (**Sheme 17C**). Although bivariate linear regression showed the reduction potential and the buried volumes could not satisfactorily explain cross-coupling yield (**Scheme 17D**), these computational data support the assessment in the preceding section that both the electronics and steric modulation of the precatalyst by the ligand may be important for reactivity.

4.4.2 *Stability of Reduced Ni(I) Intermediates*

Concerning the observed ligand steric's influence on reactivity, we hypothesized that the increased steric profile from the ligand helped protect the reduced Ni(I) species against oligomerization of Ni(I) species, a possible deactivation pathway. This hypothesis stemmed from the observation in Chapter 3 that a prolonged stirring between **IndaBox**$NiCl_2$ causes the EPR signals that range in g value from 1.8 to 2.5 to gradually disappear over 30 hours, resulting in an unreactive nickel species for alkenylation of benzyl chloride. Given the challenges of accessing well-defined Ni(I) species, this previous experiment suggested that EPR spectroscopy may elucidate the lifetime of Ni(I) species that the in situ reduction of Ni(II) precatalyst would generate. Therefore, provided that

chemical reduction was fast and negligibly contributed to the observed decay rate, the observed decay process would reflect the intrinsic stability of EPR-observable monomeric Ni(I) species. In this view, heterogenous reductants were unsuited for this purpose due to their mass-transported limited reduction process[8]. The use of an alternative homogenous reductant that mimics the reduction strength of Mn was necessary.

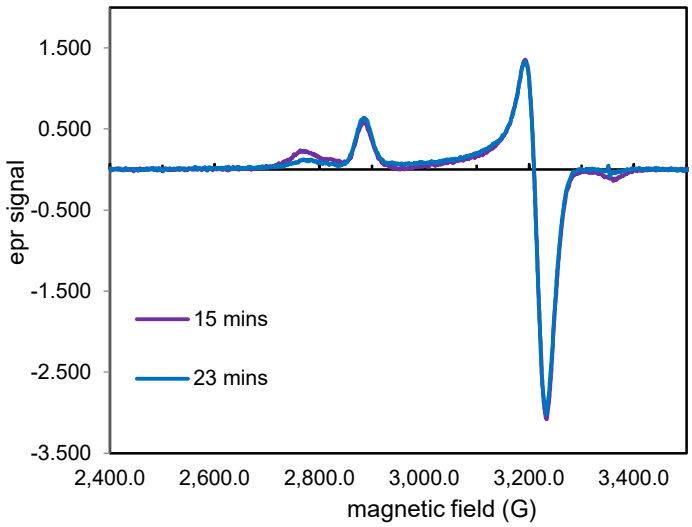

Scheme 18. *Decay of* ***L1****Ni(I) species. X band (9.39 GHz) EPR spectra were collected at 0.5 mW microwave power. For additional spectra, see section 4.8.*

Noting that the measured reduction potential of decamethylcoboltacene $Co(Cp^*)_2$ (–1.91 V vs. Fc/Fc^+ in MeCN)[49] was similar to the estimated reduction potential range of $Mn^{2+/0}$ couple[50], we tested this one-electron reductant for the in situ generation of Ni(I) species. To our delight, $Co(Cp^*)_2$ could effect the reduction of the model system **IndaBox**$NiBr_2$ 15 minutes of stirring, and the quantified EPR concentration of observed monomeric Ni(I) decayed exponentially afterward (See Section 4.8.3). Controlling other relevant experimental parameters such as stir rate, we move to measure the decay process of Ni(I) species bearing various ligands over a 30-minute interval after the admixture of

Ni(II) precatalyst and $Co(Cp^*)_2$ reductant.

With the experimental protocol established, we conducted a series of EPR experiments under identical conditions for **L1**$NiBr_2$ and **L2**$NiBr_2$ to probe the effects of pendant pyridine to the stability of Ni(I) species. Admixture of **L1**NiBr2 with Co(Cp*) revealed the presence of at least two Ni(I) species (**Scheme 18**). The major species appeared to be **L1**Ni(I)Br which had been isolated and characterized with EPR spectroscopy previously[40]. Unlike the reduction of **IndaBox**$NiBr_2$, the concentration reached its maximum of 0.17 (±0.07) mM only after 19 minutes of stirring (**Scheme 20B**, yellow trace). A rapid decay ensued over the next 16 minutes, and after the 35-minute time-point, the observed EPR signal fell below the quantification limit. No signal was observable at the 40- and 45-minute time-points. Over the course of the reaction, the extended scan window showed no sign of EPR active higher-order species. Using the time-points between 19 and 35 minutes of reaction time, an exponential decay could be fitted as $C(t) = 2.11 * e^{-0.113*t}$($R^2 = 0.88$) (**Scheme 20C** entry 2).

In comparison, the decay behavior of in situ generated of EPR observable **L2**Ni(I) species was much slower, consistent with the hypothesis that ligand decoration could improve the stability of the Ni(I) species(**Scheme 19** and **Scheme 20B** blue trace). The maximum concentration of Ni(I) species of 1.34 mM at 15 minutes was nearly eight times greater, and the concentration at 21 minutes was six times greater. The decay constant of 0.018 min^{-1} from the exponential fit ($R^2 = 0.8667$) was also approximately six times smaller (**Scheme 20C** entry 3), showing a similar picture of a delayed decay. While the rhombic signals expected from the C_1 symmetric ligand precluded simulations of these signals, we presumed the major species in this reaction was *likely* **L2**Ni(I)Br because only the short-

lived, minor species in the reduction of **L1**$NiBr_2$ contained the negative signal near 3400 G or g = 2.00. To this point, for the reduction of **L2**$NiBr_2$, the negative signal also belonged to a short-lived minor species, as evidenced by the signal change at 2850 G (g = 2.33) relative to 2700 G (g = 2.46). It should be cautioned that the observed EPR signals were distinct from the signals of the isolated solid during the attempted structural elucidation of Ni(I) by MicroED (vide supra). Thus, synthetic pathways could influence Ni(I) speciation. Further experiments are needed for the definitive structural assignment of the EPR active species herein.

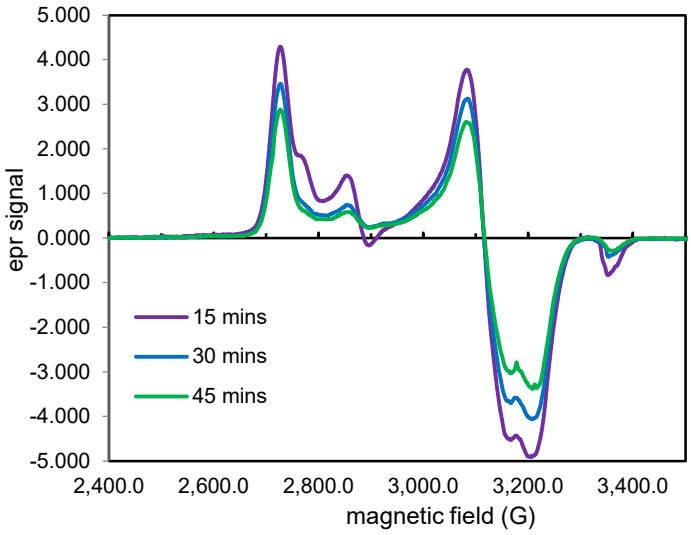

Scheme 19. *Decay of* ***L2****Ni(I) species. X band (3.90 GHz) EPR spectra were collected at 0.5 mW microwave power. For additional spectra, see section 4.8.*

Encouraged by these observed lifetime differences, we next examined the effect of 10 equivalents of DMA to provide a better approximation of the reaction condition. Surprisingly, while the maximum concentration of the observed Ni(I) of 1.24 mM was similar, the overall decay process appeared more sluggish (the spectra were presented in Section 4.8). For example, the concentration of 1.12 (±0.07) mM at the 30-minute time-

point with DMA was three-error greater or 1.27 times greater than the concentration of 0.88 (±0.07) mM at the same time-point without DMA. This slowed decay process appeared reproducible from a second set of experiments, and, from the combined set of data, an excellent exponential decay of $C(t) = 1.80 * e^{-0.015*t}$ could be fitted (**Scheme 20B** green trace, **Scheme 20C** entry 4). The exponential constant equally showed decay was 1.25 times slower with DMA present.

Alternatively, because the electrochemical irreversibility of these precatalysts implied that rapid solvent coordination occurred in concert with electrochemical reduction and that solvent dissociation was slow in comparison to electrochemical re-oxidation, we wondered if the observed decay could be fitted with a zero-order kinetic where the decay is interrupted by a rapid pre-equilibrium. Indeed, a linear fit of $C(t) = 1.72 - 0.02 * t$ could be obtained with a coefficient of determination of $R^2 = 0.9047$. This alternative interpretation warrants additional qEPR kinetic measurements as well as possible 2D-EPR studies to detect the intermediacy of DMA-bound Ni(I) species.

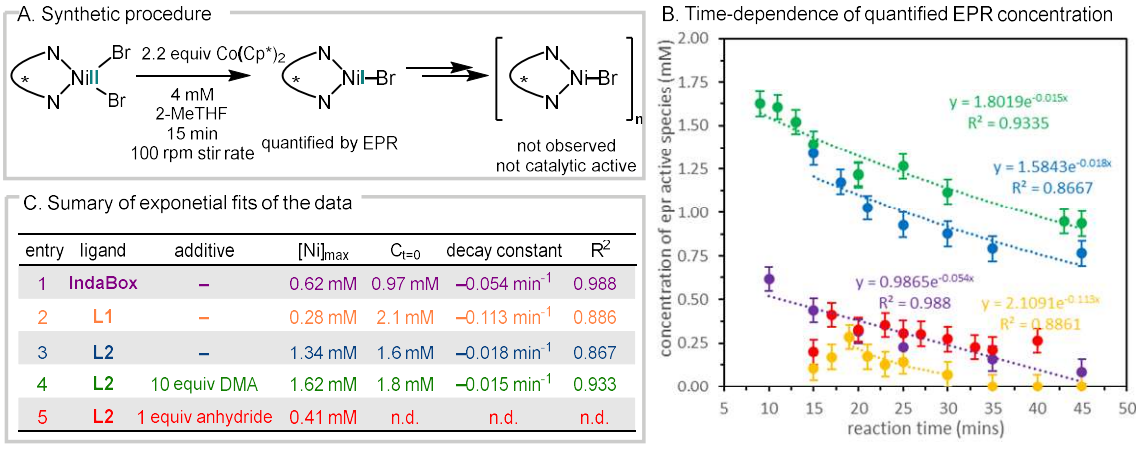

C. Sumary of exponetial fits of the data

entry	ligand	additive	$[Ni]_{max}$	$C_{t=0}$	decay constant	R^2
1	IndaBox	–	0.62 mM	0.97 mM	–0.054 min^{-1}	0.988
2	L1	–	0.28 mM	2.1 mM	–0.113 min^{-1}	0.886
3	L2	–	1.34 mM	1.6 mM	–0.018 min^{-1}	0.867
4	L2	10 equiv DMA	1.62 mM	1.8 mM	–0.015 min^{-1}	0.933
5	L2	1 equiv anhydride	0.41 mM	n.d.	n.d.	n.d.

Scheme 20. *Comparison of EPR decays.*

Summarized in **Scheme 20**, quantitative EPR spectra support that ligand steric

helps protect monomeric Ni(I) species against oligomerization, a possible deactivation pathway. When the steric is reduced (entry 1 and entry 2), a decrease in lifetime is observed; conversely, when the steric is increased (entry 2 and entry 3), the lifetime is prolonged. The solvent additive also appears to impact the lifetime of the observed EPR species, and the presence of 10 equivalents of DMA further increases the lifetime of the observed Ni(I) species.

Because changes to the ligand and solvent additives impact cross-coupling yield, these observed changes in Ni(I) lifetime likely relate to the changes in reactivity. Since, in all cases, we observe Ni(I) intermediates despite the presence of one additional electron equivalent of a reductant, the delayed decay of Ni(I) with the decorated ligand, along with the experimentally determined reduction potential, does not support the interpretation that a temperate ligation of decorated pyridine to Ni(I) facilitates the generation of Ni(0) species. Instead, these observations favor the interpretation that the reactivity of the proposed Ni(I) intermediates is fine-tuned to improve catalytic efficiency. In other words, Ni(I) species should be able to activate anhydride, and ligand decoration should impact the substrate activation rate.

4.4.3 *Reactivity of Reduced Ni(I) Intermediates for Anhydride Activation*

To verify that Ni(I) species can activate anhydride as proposed, we quantified the concentration of EPR observable monomeric Ni(I) species generated by admixture of $Co(Cp^*)_2$ and **L2**$NiBr_2$ when a stoichiometric amount of the anhydride **1** was present (Scheme 20B red trace; the spectra were presented in Section 4.8). In the presence of anhydride, the maximum Ni(I) concentration dropped 0.41(±0.07) mM at 17 minute time-

point. Within an experimental error of 0.07 mM, the observed Ni species reached a relatively steady concentration of 0.30 mM.

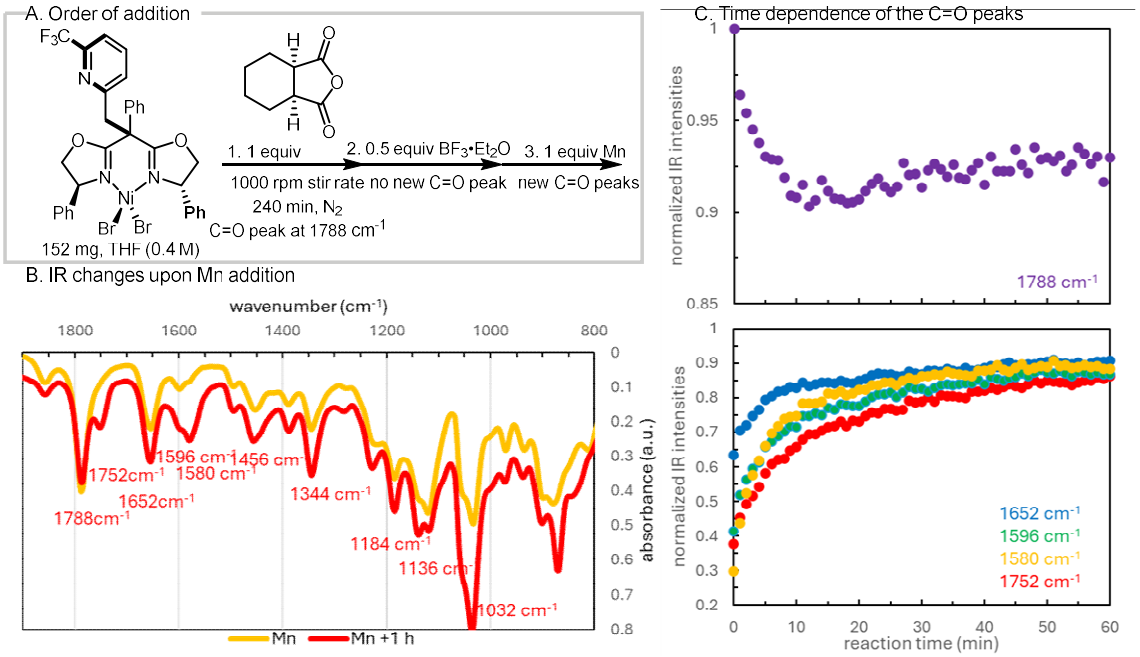

Scheme 21. *In situ IR monitoring of activation of anhydride by* ***L2****NiBr₂ (Orange, addition of Mn dust, Red 60 mins after the addition of Mn).*

To gain additional support, we opted to use ReactIR to monitor the consumption of anhydride *in situ*. Mixing a stoichiometric amount of precatalyst, anhydride, and BF_3•Et_2O, appreciable changes to C=O stretches and new IR peaks emerged only when Mn dust was added (**Scheme 21A&B** and Section 4.8.4). Monitoring the C=O stretch of anhydride at 1788 cm^{-1} revealed that the IR intensity quickly dropped within 10 minutes (**Scheme 21C**). Concurrent with this consumption of free anhydride, a new IR peak at 1652 cm^{-1} emerged at a qualitatively comparable rate(**Scheme 21D**). This new IR peak closely resembled the reported C=O stretch of the Ni acyl carboxylate complexes generated via the oxidative addition of anhydride by LNi(0) anhydride complexes (1655 cm^{-1} for L=bpy and 1622 cm^{-}

^{1} for L=TMEDA)[51], indicating that a similar oxidative addition nickel complex may be generated within 10 minutes.

Stirring over the next 60 minutes showed the emergence of new peaks at 1752 cm^{-1}, 1596 $cm^{-1,}$ and 1580 cm^{-1} and partial restoration of free anhydride C=O intensity (**Scheme 21C**). These continued spectroscopic changes suggested the presence of additional reactivity. The overall IR spectra likely resulted from a mixture of multiple nickel-containing species. Given these ambiguities, the time dependency of the C=O peaks of the free anhydride **1** appeared most useful for assessing the rate of anhydride activation.

Despite the difference in concentration of Ni species and the identity of the reductant, EPR and *in situ* IR consistently indicated that **L2**Ni(I) mediated anhydride activation was facile. To interrogate whether ligand influenced anhydride, we extended

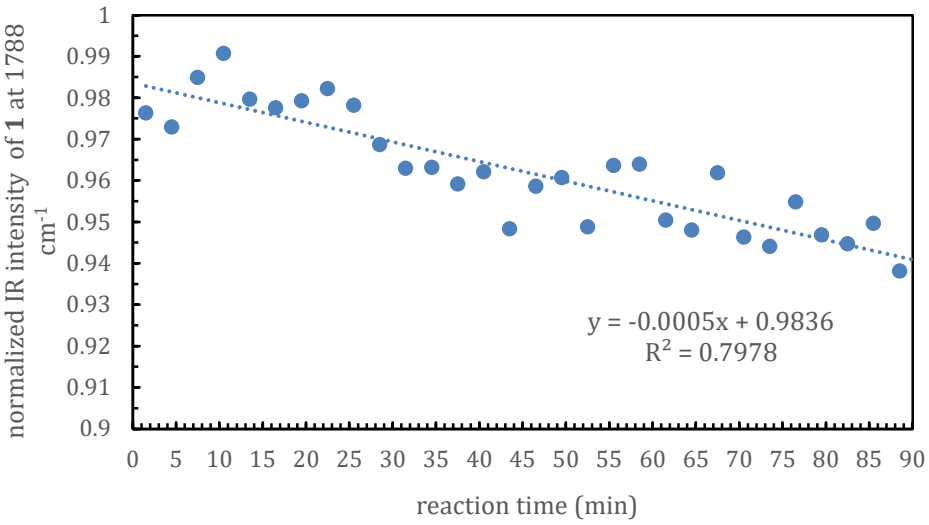

Scheme 22. *Consumption of the anhydride **1** the reduced **L1**NiBr₂.*

this approach to study the activation of anhydride by **L1**Ni species. Gratifyingly, as indicated by the differences in catalytic reactivity, the activation rate of anhydride **1** by reduced **L1**Ni species appeared qualitatively different. Instead of plateauing to 90%

intensity within 10 minutes, the normalized IR intensities of the free anhydride **1** at 1788 cm^{-1} steadily decreased over 90 minutes but never reached 90% of its intensity (**Scheme 22**). This qualitative difference in anhydride consumption from *in situ* IR suggested that anhydride activation by **L2**Ni(I) species was faster than **L1**Ni(I) species. This conclusion was consistent with the EPR observation that the **L2** ligand preserved a higher concentration of the observed Ni(I) species, the proposed intermediates for the activation of the anhydride **1**.

4.4.4 *Attempted Synthesis of Oxidative Addition Complex*

To aid the IR assignment, we sought to access the putative oxidative addition complex independently. Heating the free ligand and $Ni(COD)_2$ at 60 °C for 10 minutes

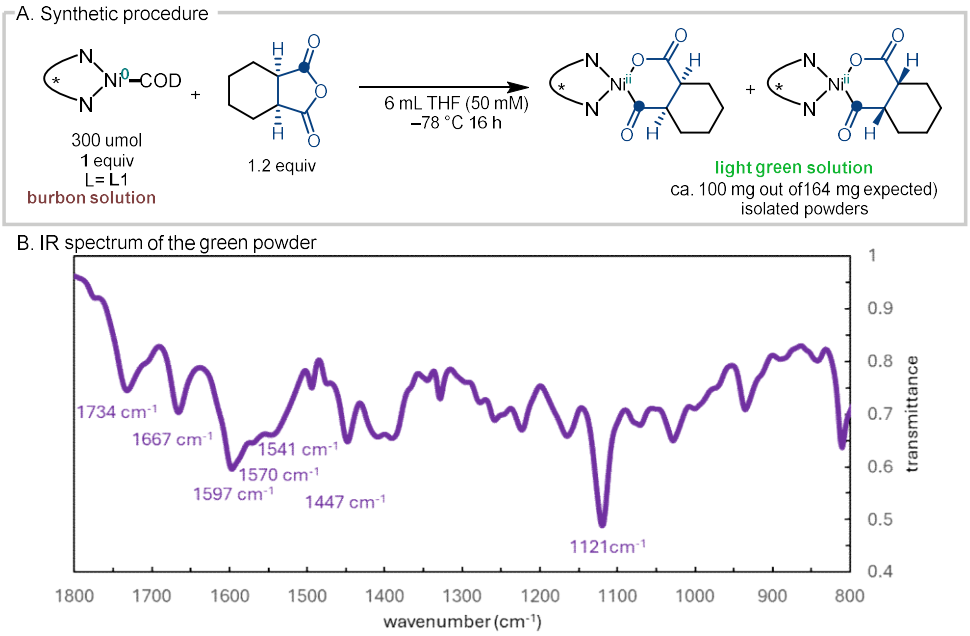

Scheme 23. *Preliminary synthesis of the putative oxidative addition complex.*

resulted in a bourbon solution. indicative of a ligated Ni(0) species. Then, 1.2 equivalent of anhydride was added upon cooling this reaction mixture to –78 °C. No color change was

observed initially, which was consistent with Stache's observation of this exact reaction at room temperature at a reduced concentration[7]. However, continued stirring at –78 °C over 16–24 h resulted in the formation of a weakly absorbing green solution (**Scheme 23A**)‡. Upon removal of solvent at –78 °C and trituration with pentane, a green solid could be isolated with a putative 64% yield by mass. Characterization of this green solid by IR revealed multiple peaks in the C=O region, namely at 1734 cm^{-1}, 1667 cm^{-1}, and 1597 cm^{-1} (**Scheme 23B**). Although the green solid appeared crystalline, preliminary crystallization efforts had been unsuccessful. While the product appeared stable in solid form, storage in solution, as in the case of crystallization by liquid diffusion, eventually caused discoloration and furnished white precipitants. These preliminary results indicated that further synthetic and purification modification may be fruitful. MicroED may be suitable for structural determination should crystallization prove challenging.

4.4.5 *Summary of Findings: Ligand Modification Tunes Ni(I)-Mediated Anhydride*

In this section, we endeavor to adjudicate the two competing hypotheses concerning the activation pathway of anhydride and the role of ligand decoration in it. The collective spectroscopic results favor the hypothesis that pendant pyridine fine-tunes the rate of substrate activation rather than enabling new modes of reactivity: Cyclic voltammetry shows that Ni(0) species is inaccessible, and computationally evaluated reduction potential of Ni(II) precatalysts show redox properties insufficiently describe reactivity trend alone.

‡ It should be noted that qualitative comparison of these observations to the react IR data was not possible, as this synthetic procedure excluded BF_3•Et_2O, and the concentration was 8 times more dilute.

EPR spectroscopy reveals that the increased steric from the ligand helps preserve monomeric Ni(I) species instead of aiding its reduction to Ni(0). The quenching of EPR signals when anhydride is present lends support that Ni(I) is competent at activating anhydride, which was qualitatively corroborated with *in situ* IR of the stoichiometric reaction. Importantly, *in situ* IR indicates a qualitative difference in the rate of anhydride activation between **L1** and **L2**. These findings indicate that accelerating the anhydride activation by increasing the effective concentration of reactive Ni(I) species and/or increasing the intrinsic elementary rate constant for anhydride activation is beneficial to catalysis. The concentration bias, in particular, satisfactorily explains why increasing nickel loading improves acylation yield (**Scheme 3C**, entry 5).

4.5 Kinetic Analysis of Substrate Activations

In the preceding sections, the results from the series of experiments we performed appeared inconsistent with κ^3-ligation to Ni(II) or Ni(I) species. The pendant pyridine also didn't appear to facilitate reduction to Ni(0) species. These findings indicated that the pendant pyridine of **L2** and the modifications to the reaction conditions improved the overall kinetic synergy of the proposed catalytic cycle by tuning the rate of elementary steps involved. As such, illuminating what kinetic regime can cause high cross-selectivity became an important question to address to provide mechanistic explanations for the necessity of reaction modifications and elucidate transferable design strategies for next-generation chemistry.

Concerning this hypothesis on the causal relationship between rate-matching kinetics and optimized reactivity, we reason that accelerating the generation rate of Ni oxidative addition complex would help favor the acylation of benzyl radical over the homodimerization of benzyl radical. The qualitative observation from *in situ* IR experiments supports our hypothesis that re-establishing rate-matching kinetics restores high cross-coupling selectivity due to persistent radical effect. To this point, we describe our preliminary effort to use electrochemistry to extract kinetic rates, after a brief introduction of the background of our approach.

4.5.1 *Overview of Electrochemical Rate Determination*

Quantitative rate determination via electrochemistry has been successfully applied to Ni(I) mediated oxidative addition of aryl iodides to elucidate the influence of supporting ligands on reactivity[52]. In comparison to the method of initial rates, which would require

several experiments at various concentrations to extract the rate constant, the electrochemical approach enables the determination of the rate constant with a single set of electrochemical experiments that can be completed within several hours using only milligrams of the analyte. This efficiency is highly desirable for our interests in evaluating the kinetic interplay of reaction components and lends itself well to data science for data-driven reaction development.

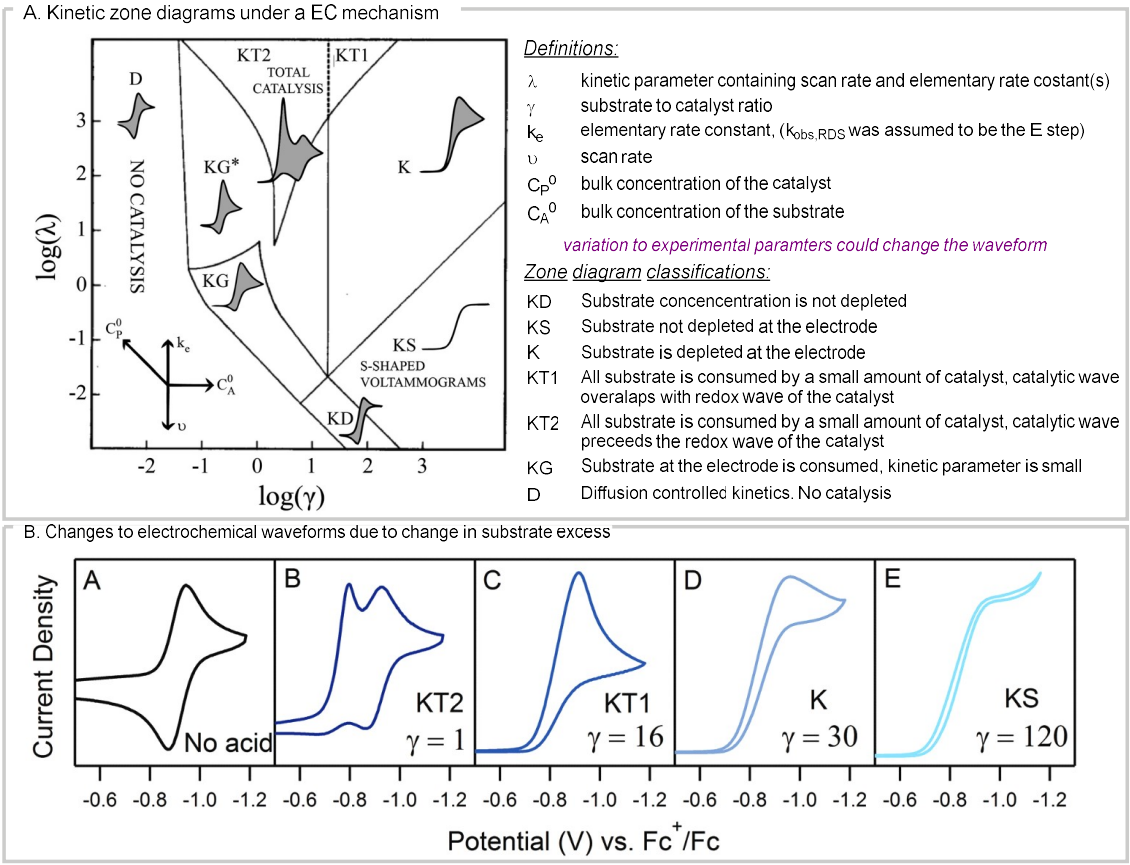

Scheme 24. *Excerpts from the review article of electrochemical zone diagrams and electrochemical rate extraction by Dempsey and coworkers[53].*

Experimentally, the aforementioned electrochemical rate determination approach assumes the chemical system of interest follows an EC mechanism[53]: An **e**lectron transfer step at the electrode junction is followed by the **c**hemical consumption of the reduced

species by way of oxidative addition of the substrate. Under the additional assumption that the system of interest is electrochemically reversible, i.e., in the absence of substrate, no side reactivity siphons away the reduced intermediate at electrochemical timescale, the difference between cathodic and anodic peaks reflect the number of reduced species consumed by the chemical step during the time interval between initial reduction and re-oxidation, from which reaction rate can be calculated. Owing to this need for a measurable anodic peak, this approach is limited to the specific kinetic regime where catalytic active species are partially consumed (**Scheme 24A**, e.g., the partial catalysis regime KG under zone diagram classification[54]). Depending on the underlying electrochemical mechanism (e.g., if it is EC) and the rate constants of elementary steps, partial catalysis is not always observed. Thus, in cases where an electrocatalytic current is observed, the substrate-to-catalyst excess ratio (γ) or other experimental factors must be significantly altered from the catalytic condition to shift the kinetic regime to partial catalysis and restore the anodic current (**Scheme 24B**). Moreover, this approach may break down if the EC mechanism is not obeyed.

Pioneering work from Savéant[55–57] and Bards[58] show that electrochemical rate can be determined for broader sets of kinetic regimes and electrochemical mechanisms by solving the differential equations about the analyte concentration at the electrode junction under either steady-state or pre-equilibrium assumption. Although this method requires numerically solving the differential equations to extract rate constant for most kinetic regimes, the rate expression greatly simplifies under KS regime[54] (**Scheme 24A**; for detailed discussions about zone diagrams, see Ref 59, 55, or 60) where the catalytic current adopts a characteristic S-shape with a plateauing current, illustrating that the observed rate

relates to the substrate-to-catalyst excess ratio (γ), normalized cathodic peak current ψ_{cat}, and the composite kinetic parameter of the rate-limiting step λ, which contains both the chemical rate constant and concentration of reactants (C) and electrochemical scan rate(ν):

$$\lim_{\frac{\lambda_1}{\gamma}\to 0} \psi_{cat} = \psi_{KS} = \sqrt{\gamma\lambda_{RDS}} \tag{1}$$

$$\psi = \frac{i_c}{i_p} * 0.4463 \tag{2}$$

i_c is the catalytic cathodic current and i_p is the cathodic peak of the catalyst in the absence of substrate. For the simplest case of $E_{RDS}C$ mechanism where the electrochemical reduction is the rate-determining step (e.g., reduced nickel catalyzed substrate activation) the composite kinetic parameter has the form:

$$\lambda_1 = \frac{RT}{F}\left(\frac{c^{\circ}_{ox} * k_1}{v}\right) \tag{3}$$

where $C_{ox}°$ is the bulk concentration of the oxidized species (e.g., the concentration of the Ni(II). Upon substitution of equation 2 and 3 to equation 1 and rearrangement, equation 1 becomes[59]

$$i_c = \frac{i_p}{0.4463}\sqrt{\frac{RT}{F}\frac{c^{\circ}_{substrate} * k_1}{v}} \tag{4}$$

or, upon rearrangement

$$k_1 = \frac{v}{c^{\circ}_{substrate}}\frac{F}{RT}\left(0.4463 * \frac{i_c}{i_p}\right)^2 \tag{5}$$

Equation 5 shows that the observed rate constant can be extracted from the catalytic current for a given scan rate and excess ratio. Discussed in Section 4.8.5, we further reasoned that if the catalytic current is a strictly increasing function of the kinetic parameter λ, which

appears to be satisfied when the excess ratio is greater than 10, plugging in the observed catalytic peak current in any intermediate kinetic regime before the limiting behavior of KS current (i.e., a non-S shaped catalytic current is observed), then the rate constant calculated from the expression will be the upper limit of the actual rate constant. Using the estimation from equation 5 allows us to bypass solving the different equations to quickly evaluate the applicability and the utility of this approach as a proof of principle.

4.5.2 *Kinetics of Benzyl chloride Activation*

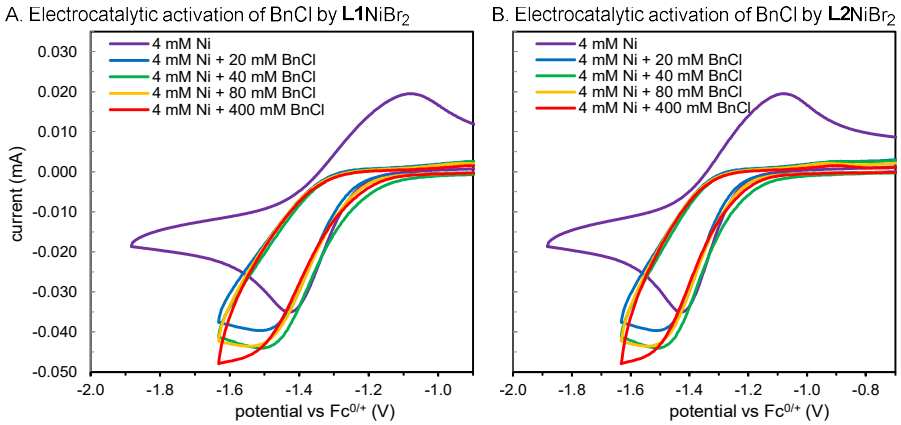

Scheme 25. *Electrocatalytic activation of benzyl chloride (4 mM, 0.2 M $TBAPF_6$ in THF using Ag/Ag^+ reference electrode, Pt wire counter electrode, and glassy carbon working electrode, 100 mV/s scan rate).*

We first turn our attention to the activation of the benzyl chloride **2** because we expect the regeneration of NI (II) after Ni(I) mediated XAT from benzyl chloride could result in an electrocatalytic current. The cyclic voltammograms of 0.4 mM **L1**$NiBr_2$ and **L2**$NiBr_2$ were shown in **Scheme 25**, along with those obtained in the presence of various excess of the benzyl chloride **2**. In both cases, an excess factor of five resulted in the complete disappearance of the anodic peak, indicating the depletion of Ni(I) species, likely by the XAT reaction between Ni(I) and the substrate. The non-S-shaped waveform and the

increase in current suggest electrocatalyst operates under an intermediate kinetic regime between KT1 and KS. Increasing the excess ratio causes the catalytic current to increase in accordance with the expected behavior of the EC mechanism; however, at a sufficiently high excess ratio (i.e., = 100), the catalytic current plateaus, suggesting the RDS has changed to a later step. Assuming the reaction between Ni(I) and benzyl chloride is the rate0determing step, we estimate the upper limit of the observed rate constant for benzyl chloride activation by **L1**$NiBr_2$ to be 0.135 $M^{-1}s^{-1}$ (i_c/i_p =1.33; $C_{substrate}$=40 mM), 0.0677 $M^{-1}s^{-1}$(i_c/i_p =1.33; $C_{substrate}$=80 mM), or 0.0135 $M^{-1}s^{-1}$ (i_c/i_p =1.33; $C_{substrate}$=400 mM). In comparison, for **L2**$NiBr_2$, the observed rate constant for 0.117 $M^{-1}s^{-1}$ (i_c/i_p =1.24; $C_{substrate}$=40 mM), 0.0589 $M^{-1}s^{-1}$ (i_c/i_p =1.24; $C_{substrate}$=80 mM), and 0.0123 $M^{-1}s^{-1}$ (i_c/i_p =1.27; $C_{substrate}$=400 mM), In lieu of estimation, graphically solving for the observed rate constant with the working graph[60] for γ=10 determines the observed rate constant to be approximately 0.005 $M^{-1}s^{-1}$ for both precatalysts. Because graphically solved rate constant catalysts fall under the estimated upper bound, the estimations appeared robust. It is important to address that, given the poor electrochemical behavior of the precatalysts, these rate analyses were preliminary in nature. Specifically, the evaluation of the electrochemical mechanism is necessary, and the validity of the electrochemical rates should be verified with independent kinetic measurement. Nevertheless, from these results, the inclusion of the pendant pyridine did not appear to significantly modulate the activation rate of benzyl chlorides.

Alarmed by the small quantified rate and the peculiar electrochemical waveforms, we sought to verify that these observations were not due to electrochemical artifacts. We suspected the solvent choice likely had a nontrivial impact. Previously, we had observed

that, for the electrocatalytic activation of the benzyl chloride **2** by **Inda**BoxNiCl$_2$ in DMA, the electrocatalytic current was large and increased as substrate excess increased.[15] The estimated rate of benzyl chloride activation of 31 $M^{-1}s^{-1}$ was also much faster (Section 4.8.5). To verify this apparent influence of solvent on rates, we repeated the GS kinetic experiment from Chapter 3 to monitor benzyl chloride activation catalyzed by **IndaBox**NiCl$_2$ and Mn dust. Shockingly, unlike the previous observation that benzyl chloride was fully consumed within 100 minutes in DMA, no consumption of benzyl chloride was observed in THF for 16 hours. Intriguingly, the inclusion of one equivalent of DMA restored the reactivity of benzyl chloride activation. Consistent with the electrochemical observations, the solvent appeared to exert a significant influence on benzyl chloride activation.

As the observed electrochemical waveform did not appear to originate from the poor electrochemical behaviors of the precatalysts, the small values of estimated rate constants, the weakness of the catalytic current, and the waveform's dependency on the excess ratio were particularly concerning. These observations suggested the presence of at least one additional chemical step, such as an ECC mechanism. This downstream step cannot be the irreversible bibenzyl formation as the rate constant of these reactions is orders of magnitude greater. The ambiguity of this additional step questions the validity of describing electrocatalytic Ni-mediated XAT as an $EC_{XAT,\ RDS}$ mechanism, iterating the caution that evaluation of the electrochemical mechanism is necessary.

Surveying literature for potential explanations, we found Savéant showed[57] that the weak catalytic current and the insensitivity to substrate concentration *may* be explained by an EC_1C_{RDS} mechanism. Namely, if the first chemical step reached pre-equilibrium, then

the expression for catalytic current would no longer depend on the substrate concentration. Instead, the current would depend only on the excess and kinetic parameter (λ_1 λ_3/ λ_2) [57,58,61]

$$\frac{\lambda_1\lambda_3}{\lambda_2} = \frac{RT}{F}\left(\frac{k_1 k_3}{k_2\ v}\right)$$

Emperically, the Savéant noted that pre-equilibrium constant described by k_1/k_2 was often small, and as a result, the current ratio is i_p/i_c is often small and close to unity[57]. Our observations echoed Savéant's statement. Therefore, the experimental protocol[57] described by Savéant to discern this EC_1C_{RDS} mechanism could be fruitful for quantitative electrochemical rate extraction.

To complete the discussion about the possibility of an EC_1C_{RDS} mechanism, we searched for possible explanations. Given the importance of the solvent, one potential hypothesis is that the first chemical step is the concerted halide dissociation from Ni(I) and solvent coordination[15], and the second chemical step was the halogen atom abstraction. The coordination step of the solvent modulates the extent of the pre-equilibrium. Alternatively, a series of related works by Savéant[62–66] shows that the mechanism of mediated benzyl halide activation is much more enhanced than proposed. In addition to the proposed one-step XAT pathway, a stepwise mechanism is also possible[62] (**Scheme 25**): First, an electron transfer from NI(I) to benzyl chloride occurs to generate a radical anion. From this radical anion, the heterolytic extrusion of halide anion ensues to generate a benzyl radical. For systems that can undergo both concerted and stepwise mechanisms, the stepwise mechanism, induced by the addition of water, is consistently slower than the concerted mechanisms[65]. Of the various factors[62,63] , the solvent stabilization of the radical anion intermediate or halide anion and solvent's influence on the driving force of the

electron transfer step all influence whether benzyl halide proceeds in a stepwise or concerted fashion[64,65]. It is known that the activation of unsubstituted benzyl chloride undergoes a concerted mechanism in DMF[62]. Thus, it is possible that the solvent change to THF favors the slower stepwise pathway. Although outside the scope of this work, similar electrochemical studies of XAT reaction in nonpolar solvents could be fruitful.

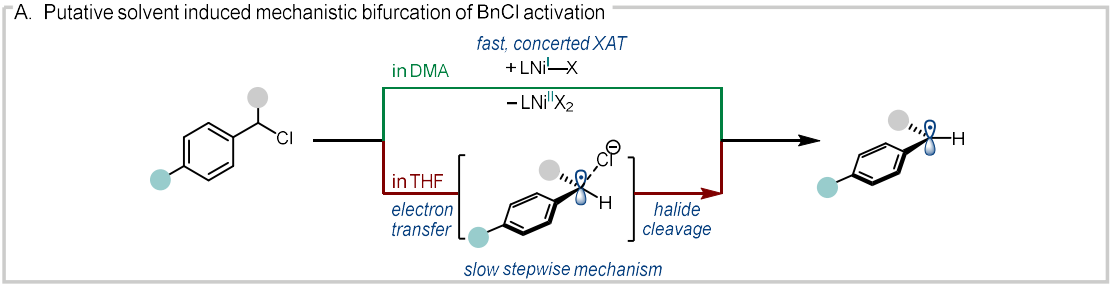

Scheme 26. *Possibility of solvent-induced mechanistic bifurcation of electrochemical activation of benzyl chloride.*

4.5.3 *Kinetics of Anhydride Activation*

Turning our attention to the activation of the anhydride **1** by Ni(I) species, we anticipated that the current behavior might be more complex. For example, due to the lack of a known turnover mechanism that can regenerate Ni(II) precatalyst after initial oxidative addition near the electrode surface, the observation of electrocatalytic current may be challenging. From a mechanistic perspective, we also recognized that the determination of the electrochemical rate of anhydride activation by the Ni intermediate alone was unlikely to be reflective of activation kinetics during catalysis, as the Lewis acid additive BF3•Et_2O could influence the activation rate and electrochemical current behavior. These two reasons motivated us to focus on identifying the necessary components to effect electrocatalytic currents under chemical kinetic control.

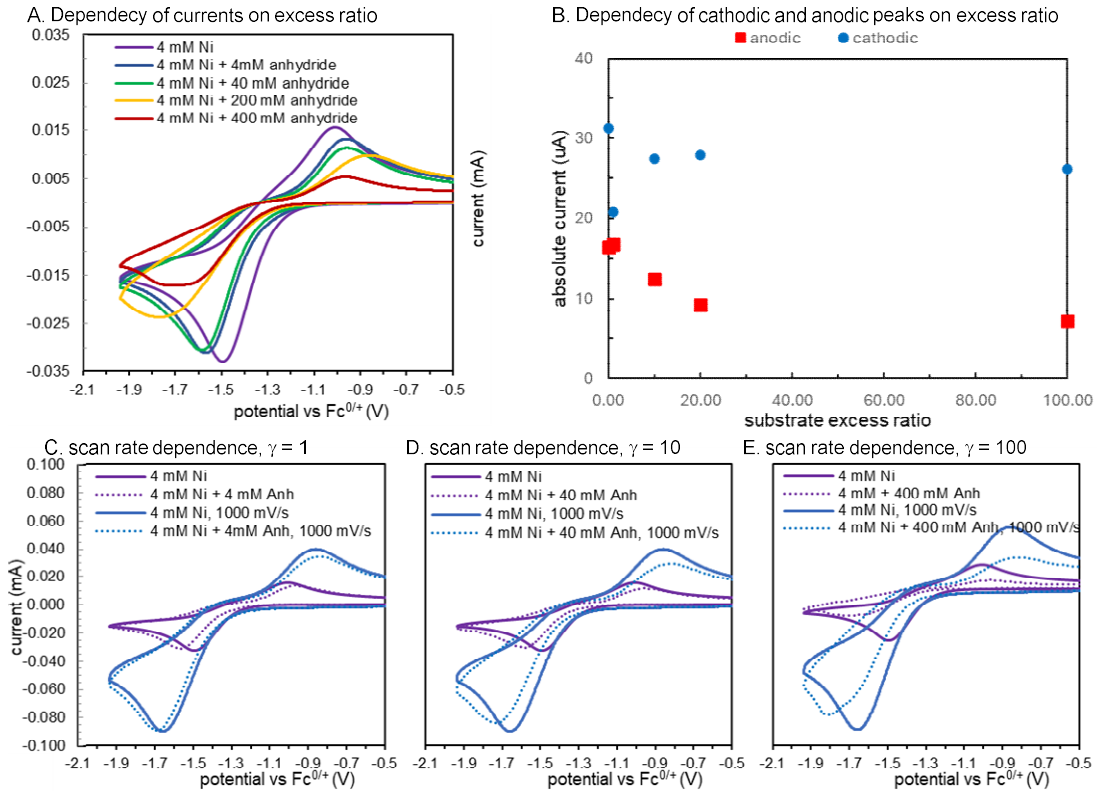

Scheme 27. *Currents of electrochemical Ni-mediated anhydride activation (4 mM, 0.2 M TBAPF6 in THF using Ag/Ag+ reference electrode, Pt wire counter electrode, and glassy carbon working electrode).*

The cyclic voltammograms of 4 mM **L2**$NiBr_2$ collected in THF were collected in the presence of various excess anhydride **1** (**Scheme 27A**). Intriguingly, the addition of one equivalent of anhydride initially resulted in a suppression of the cathodic and the anodic peak as well as an increase in the peak-to-peak separation. Increasing the excess ratio showed a partial restoration of the cathodic peak, but the anodic peak continued to decrease in intensity (**Scheme 27B**), suggesting a partial depletion of reduced species at the electrode surface by either diffusion or chemical transformation. Even with an excess factor of 100, both cathodic peaks and anodic peaks can be seen. Although the suppression of the cathodic current suggested that an EC mechanism may not be

assumed, the decrease in the anodic current, even at high scan rates, suggested that a reaction between the reduced **L2**Ni(I) species and anhydride slowly occurred.

Turning our attention to the role of BF_3•Et_2O, we are surprised to find that Lewis acid activation of anhydride **1** by BF_3•Et_2O may not be as significant to catalysis as we anticipated. Admixture of a 1:1 stoichiometric ratio of BF_3•Et_2O and anhydride at 4 mM in THF showed a cathodic peak at ca. –2.4 V vs. Fc/Fc^+ in THF (**Scheme 28A**, black dotted trace), which is outside of the accessible region of Mn dust reductant[50] or nickel.

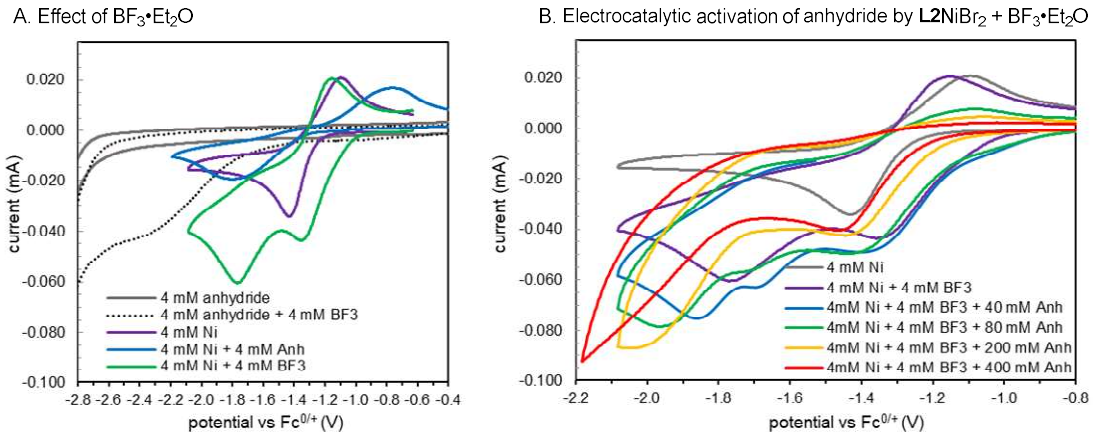

Scheme 28. Effect of BF3•Et2O on the Ni-mediated electrocatalytic activation of anhydride (4 mM, 0.2 M TBAPF6 in THF using Ag/Ag+ reference electrode, Pt wire counter electrode, and glassy carbon working electrode).

This result was also echoed by in situ IR spectroscopy, which did not reveal redshifted carbonyl peaks (Section 4.8.4). Unexpectedly, the 1:1 stoichiometric mixture of BF_3•Et_2O and $LNiBr_2$ precatalyst shows an additional unexpected cathodic peak –1.76 V vs. Fc/Fc+, which remains partially accessible by Mn (**Scheme 27A**, green trace). This second irreversible redox feature did not appear to be the second reduction of the Ni(I) species to Ni(0) species. Namely, if the Ni(I) species was irreversibly consumed by the

second redox event at –1.76 V, then the re-oxidation current of the Ni(I) species around –1.10V should decrease.

This unexpected Ni species significantly impacted the anhydride activation pathway (**Scheme 28B**). When various excess of anhydride was added to the 1:1 stoichiometric mixture of BF_3•Et_2O and $LNiBr_2$ precatalyst, catalytic currents emerged around the second redox peak. The catalytic current showed an EC-like behavior as it increased when more anhydride was added. Equally, the anodic peak eventually disappeared at an excess ratio of 50, indicating the depletion of any reduced Ni(I) species. Given the EC-like current behavior, a crude estimation of the rate may be made by subtracting a baseline current of 0.040 mA from the second cathodic peak current. With the i_c/i_p ratio of 1.92 (γ=20) or 2.34 (γ=50), the upper limit of the anhydride activation rate constant was estimated to be 17.6 $M^{-1}s^{-1}$ (γ=20) or 10.5 $M^{-1}s^{-1}$ (γ=50), respectively. These values were at least 4 times smaller than the estimated alkenyl bromide activation rate of 88 $M^{-1}s^{-1}$ (γ=100) in DMA, which may be attributed to the solvent effect described previously and/or the increased bond strength of the C–O of anhydride in comparison to C–Br of the alkenyl bromide.

Since the more reducing species clearly accelerates anhydride activation, its important role under catalysis warrants discussion of its possible identity to aid future investigation. In hypothesis A, we propose a BF_3•Py moiety is formed in situ (**Scheme 29A**). Experimentally, the ligation of BF_3 to heteroaromatic cycles such as pyridine anodically shifts the reduction of heteroarene such that, for example, irreversible first reduction of the pyridine electrochemically at 1.36 V vs Li/Li^{+}[67] (–1.95 V vs SCE or –2.35 V vs Fc/Fc^{+}). For the pyridine-containing ligand **L2**, its *ortho* CF_3 substitution likely

further favors the pyridine reduction. Thus, it may be proposed that the second reduction generates either a formal Ni(I) species or a formal Ni(0) species where the pendant pyridine is reduced. This redox non-innocent of the pyridine moiety could help activate anhydride in tandem with the metal center. Cyclic voltammetry of a 1:1 mixture of the free ligand and BF_3•Et_2O could clarify the accessibility of the pyridine radical anion under reaction conditions. Hypothesis A predicts that the second redox peak would disappear if the ligands without pendant heteroarenes, such as **L1,** were used. It also follows that BF_3•Et_2O would not improve acylation yield as effectively if ligands without pendant heteroarenes are used.

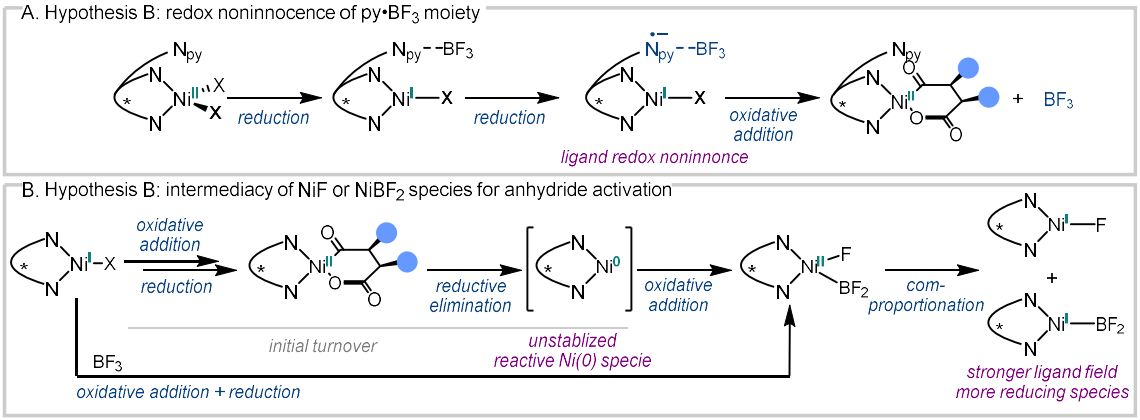

Scheme 29. *Two mechanistic hypotheses on the role of BF_3•Et_2O behind the observed acceleration of Ni-catalyzed anhydride activation.*

Alternatively, cognizant that an unstabilized Ni(0) species could be generated by way of reductive elimination from the oxidative addition complex, hypothesis B posits that BF_3 may not be a stable species under reductive conditions when anhydride is present (**Scheme 29B**). To this point, literature precedents indicate that Pt(0)$(PR_3)_2$ species[68] and Ni(0)$(PPh)_4$ [69] could effect B–F cleavage to generate divalent metal boride fluoride complexes. As both boride[70] and fluoride are stronger ligands than chloride or bromide, the reduction of the putative Ni(II)(BF_2)F species would be cathodically shifted.

Consequently, hypothesis B explains that the increased reducing strength of either a Ni(I) boride or Ni(I) fluoride species causes accelerated anhydride activation. Under this hypothesis, the second redox wave would be present irrespective of the ligand utilized. Isolation and characterization of Ni(II) boride fluoride species would also help clarify its intermediacy.

In summary, as anticipated by the lack of a turnover mechanism to regenerate Ni(II) precatalyst, the electrochemical current is not guaranteed to reflect the rate of anhydride activation without elucidation of the underlying electrochemical mechanism. When one equivalent BF_3•Et_2O is present, a second, unexpected redox active species significantly accelerates the activation of anhydrides such that the electrochemical becomes EC-like. The correlation between improved acylation yields and accelerated anhydride activation due to the addition of BF_3•Et_2O is consistent with the prediction from the persistent radical effect. Namely, accelerating anhydride activation improves the conversion rate of benzyl chloride to product, which helps re-establish the rate-matching kinetics. To this point, it is worth noting that although the role of solvent difference cannot be ruled out, the greater than the four-fold difference between the anhydride activation rate (17 $M^{-1}s^{-1}$) and the alkenyl bromide activation rate (88 $M^{-1}s^{-1}$) agrees that oxidative cleavage of the stronger C–O may be more sluggish than the C–Br bond.

4.5.4 *Summary of Finding: Tuning the Relative Rate of Electrophile Activation*

In summary, we show that cyclic voltammetry can provide qualitatively correct kinetic information about substrate activation. Extraction of the rate constant requires the

determination of the electrochemical mechanisms to ensure electrochemical current is limited by the substrate activation step. Then, the quantitative rate constant can be extracted graphically interpolated or numerically solved from the catalytic current for a given scan rate and the excess ratio between the substrate and the catalyst.

Semiquantitative estimation of substrate activation rates reveals deacceleration of benzyl chloride activation with solvent change and acceleration of anhydride activation with the BF_3•Et_2O additive correlate with improved cross-selectivity for the acylation product **3** over homo-coupling product **4**. These trends are consistent with the prediction from persistent radical effect under the assumption that the conversion of benzyl radical to acylation product by nickel catalyst may be slower than alkenylation due to the bond strength of the strong C–O bond of the anhydride and the weak C–C bond of the acylation product. The evolution of reaction conditions appears to rectify the mismatched kinetics systematically, thereby providing proof that rate-matching kinetics *cause* high cross-selectivity. Furthermore, this electrochemical rate evaluation of a multi-component mixture reveals hidden interactions that could be otherwise missed under a hypothesis-driven structure-reactivity investigation.

4.6 Discussions

4.6.1 *Proposed Catalytic Mechanism*

Based on the collection of findings from structural elucidation, spectroscopic reactivities studies, and electrochemical kinetics analysis, we sustain the proposed $Ni^{I/II/III}$ mechanistic cycle as both the operative and the dominant reaction pathway (**Scheme 29A**). The evolution of the reaction conditions and ligands systematically remedy the mismatched kinetics introduced by the change in C(sp^2) electrophile (**Scheme 29B**, i to

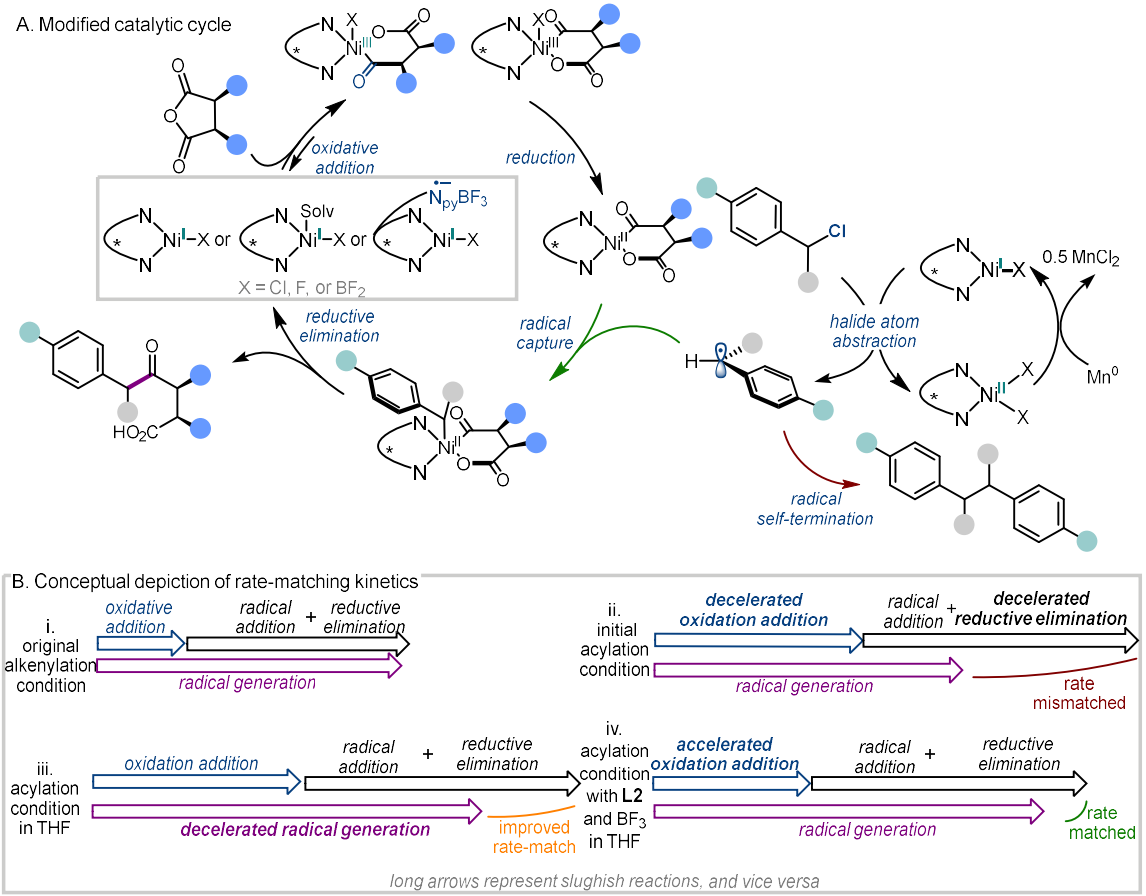

Scheme 30. *Summary of mechanistic findings and modified proposed mechanistic cycle.*

ii). Solvent change from DMA to THF endeavors to decelerate radical generation (**Scheme 28B**, ii to iii). Ligand decoration stereoelectronically modulates the reducing strength and

the lifetime of the Ni(I) intermediate and, in doing so, modulates the rate of anhydride activation. Specifically, the use of the ligand **L2** in tandem with the BF_3•Et_2O additive accelerates the activation of anhydride (**Scheme 29B**, iii to iv) either via *in situ* generation of alternative Ni(I) species or via ligand non-innocence. The evolution of the substrate activation kinetics provides support that persistent radical effect and its rate-matching kinetics *cause* high cross-selectivity.

In terms of fundamental chemistry, results from this chapter draw attention to the speciation and identity of Ni(I) species within a multi-component mixture. Solvent, additive, or reductant can significantly impact the spectroscopic behaviors, reactivity, and stability of the Ni(I) species. Given the importance of Ni(I) species in substrate activation, the interplays between these components can be otherwise missed under a hypothesis-driven structural and reactivity interrogation of catalytic intermediate in isolation. For the same reason, investigations that focus exclusively on the optimal system could also bias mechanistic interpretation. Although unambiguous mechanistic elucidation of chemical interactions among multiple reaction components is inherently more challenging due to the increased combinatorial possibilities, this chapter shows that kinetic data could valuably inform hypothesis formulation.

Indeed, although this chapter starts with hypotheses surrounding the ligation mode of the decorated ligand, we do not observe any spectroscopic indications that high energy κ^3 ligation mode could be beneficial. Instead, we observe the unexpected interaction between the BF_3•Et_2O additive and the reduced **L2**Ni species. These results encourage future mechanistic studies to elucidate this interaction. Similarly, we note that the choice

of solvent could alter the mechanism of electrochemical substrate activation. Although we do not have sufficient evidence to prove this is the case, our observations and literature nevertheless caution against making mechanistic inferences from CV data that are collected in solvents that are different from reaction conditions.

4.6.2 *Implication to Data-Driven Experimentation: Rapid Determination of Substrate Activation Rate*

As a proof of concept, we show that electrochemical substrate activation may be used to interrogate the kinetic of substrate activation under catalytic reductive conditions. From the current dependency on scan rate and the concentration of analytes, both mechanistic information about the rate-limiting step of the reaction as well as the observed rate constant, can be extracted. Specifically, we show that the estimated rate constants are qualitatively in agreement with spectroscopic or experimental GS kinetic observations. These preliminary results encourage similar studies in the future and numerically solve for the observed rate constants. Additionally, it is worthwhile to highlight that the electrochemical approach adopted herein should be broadly applicable to a broad range of electrochemical waveforms, thus complementing the existing rate measurement that requires both cathodic and anodic peaks present.

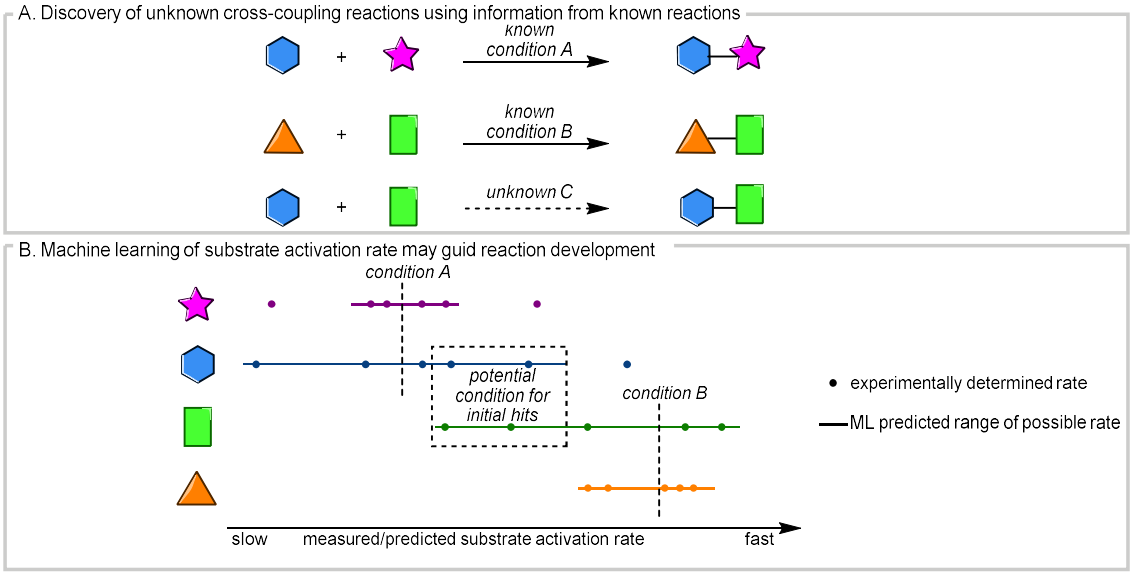

Scheme 31. *Prediction of reaction condition for development of new reaction using machine-learned substrate activation rate.*

Provided that the electrochemical experiments are appropriately designed, e.g., controlling the excess factor while varying scan rate and concentration, quantitative kinetic information surrounding substrate activation may be generated rapidly within a few hours. This efficient workflow lends itself elegantly to data-driven optimization, where machine intelligence may be leveraged to recognize the features that influence the substrate activation rates, thereby generating predictions of relevant reaction conditions *in silico*. While comparatively rarer in the context of organic catalysis, machine learning of the kinetics of competing elementary reactions has been highly successful in predicting useful synthetic intermediate that undergoes the desired reactivity for natural product syntheses[71,72]. To this point, given that we have identified effecting a rate-matched kinetic regime as a target for reaction optimization, we propose the following workflow to leverage machine intelligence to develop new Ni XEC reactions: For a reaction of interest C, there likely exists precedences where each of the reaction partners has been utilized for other cross-coupling chemistry such as reaction A and B (**Scheme 31A**). The range of substrate

activation rate as a function of reaction conditions can be experimentally probed with electrochemistry. From here, machine learning helps sample chemical space *in silico* and assess the tunability of substrate activation. Once this process has been repeated for both substrates of interest, possible reaction conditions where the activation of both substrates proceed at a comparable rate might emerge from the machine learning model, thereby guiding the discovery of initial reaction hits. Importantly, because the proposed machine learning workflow models on experimental conditions' influence on elementary kinetics instead of the yield of a specific product, the resulting models can be easily extended for future chemistry.

4.7 Concluding Remarks

This chapter details the structural, spectroscopic, and electrochemical investigation of Ni-catalyzed acylation of benzylic chloride. After structural elucidation of ligand ligation mode, reactivity assessment of redox chemistry of Ni(I), and the kinetic rate estimation of substrate activation, we sustained the initially proposed $Ni^{I/II/III}$ cycle. The evolution of the ligand and the reaction conditions appear to modulate the rate of anhydride activation of benzyl chloride activation to establish rate-matching kinetics to favor acylation over homodimerization of benzylic radicals. The systematic comparisons between the unoptimal and optimal catalysts support that the rate-matching kinetics, as described by persistent radical effect, *cause* optimal reactivity, thereby providing a qualitative target for reaction optimization with data science.

Mechanistically, our data-driven approach based on qualitative and quantitative data allowed us to identify two underappreciated interactions. Namely, the solvent choice seemed to qualitatively bifurcate the rate of Ni(I) mediated XAT from benzyl to generate benzyl radical. The presence of BF_3 additive appeared to generate a second reduced Ni species that activates anhydride. Thus, further mechanistic investigations in these two areas may reveal hitherto underappreciated chemical interactions that may be leveraged for future catalyst design.

Importantly, this chapter shows that qualitatively accurate rate constant can be extracted from electrochemical catalytic current, provided that important variables such as excess ratio are controlled. If the underlying electrochemically mechanism is known, numerically or graphically solving for the exact rate constant is also possible. While the

accuracy of the electrochemically extracted rate constants must be affirmed by additional means such as pseudo-first order kinetic experiments, this cyclic voltammetry-based approach may enable rapid determination of substrate activations within a few hours to enable recognition of structure-kinetics relationship by machine intelligence. Specifically, within the context of rate-matching kinetics, machine-learned chemical rates could help predict reaction conditions for reaction development and elevate the mechanistic understanding of nickel-catalyzed cross-electrophile coupling reactions.

4.8 Experimental Details and Supplementary Information

4.8.1 *Supplementary Information on Synthesis and Isolation of Precatalysts*

Preparation of Precatalyst

Under an N_2 atmosphere, 144 mg of $NiBr_2$(dme) (1.01 equivalent, 466 mol), 250 mg of ligand (1.0 equivalent, 462 mmol), and a stir bar were added to a 2-dram vial. Then, 4.62 mL of PhH was added to dissolve the mixture to afford a 0.1 M solution. The vial was capped and stirred at 1000 rpm for one hour to afford a heterogenous pink solution with pink precipitate, indicative of a precatalyst formation. Then, the heterogeneous mixture was directly transferred to a flame-dried 250 mL round bottom flask, and additional anhydrous PhH was added the 2-dram vial to aid a quantitative transfer. The volatile was then removed *in vacuo,* after which a minimal amount of anhydrous THF (ca. 60 mL) was added to the round bottom flask while stirring such that all pink solids dissolved but the residual orange $NiBr_2$(dme) solids remained visibly undissolved. Then, the pink solution was filtered, and the volatile was removed *in vacuo*, resulting pink solid. This solid was rinsed with pentane thrice and dried *in vacuo* to afford the pink precatalyst at 78% yield.

Crystallization of the precatalyst at an analytical scale was accomplished via liquid diffusion between a mixed solvent system (1:3 PhH and THF) and antisolvent in a 1:1 volume ratio using the technique reported by Orvig[73]. Specifically, 250 μL PhH and 750 μL of THF were mixed in a flame-dried 1-dram vial. To this vial, the precatalyst was added as solids to the solution until saturation under an N_2 atmosphere. The saturated

solution was then transferred and filtered with a 1 mL syringe capped with a syringe filter. Separately, 1 mL of anhydrous Et_2O was added to a second flame-dried 1 dram vial. Then, the saturated THF solution was slowly injected into the bottom of the Et_2O layer, thereby displacing the Et_2O layer to generate a well-defined liquid-liquid boundary. The crystallization vessel was then capped and stored under ambient temperature for 24–72 hours, during which the crystal formation occurred. The crystal structure of **L2**$NiBr_2$ can be accessed from the Cambridge Crystallographic Data Centre with the deposit number 2415579.

The synthetic procedure can be extended to $NiCl_2$(dme) as a synthon to afford the corresponding dichloronickel(II) precatalyst. However, we note that precatalysts with the pyridine-containing ligand showed complex speciation behavior such that a molecular structure of **L**$NiCl_2$ may not be assumed. As an example, during the synthesis of **L2**$NiCl_2$, the pink solution would change to dark blue at high concentrations after the solvent had been partially removed in *vacuo,* resulting in the isolation of the blue solid. Dissolving this blue solid in THF eventually regenerated the pink coloration characteristic of **L2**$NiCl_2$. Similarly, crystallization from the dark purple DCM solution by way of vapor diffusion or liquid diffusion consistently led to rapid precipitation of brown powders, which likely was the trimeric species observed previously. The brown precipitate eventually underwent a second speciation change to a blue or a green powder upon further storage in the crystallization setup. While dissolving these solids at low concentrations invariably regenerates monomeric **L2**$NiCl_2$ species, indicated by characteristic pink coloration, we were unable to isolate **L2**$NiCl_2$ as a solid.

Optimization of Solvent Systems for Crystallization

To overcome the issues in speciation and poor crystallinity observed for the precatalysts of interest, we opted to examine the effect of solvent and antisolvent systematically to identify conditions that were conducive to controlled crystal formation. We hypothesized that the outcome of crystallization depended on the saturation concentration, which may be tuned by the choice of solvent or solvent mixture. To control for the hidden effects, all crystallization was set up in a caped 1-dram vial with 1 mL of antisolvent and 1 mL of the saturated solution. The saturated solution was obtained by adding the precatalyst as a solid to the solvent system in a separate vial until pecks of solid remained undissolved. This solution was then filtered with a 1 mL syringe capped with a solvent filter and slowly injected into the bottom of the vial that contained 1 mL of antisolvent, thereby creating a well-defined solvent antisolvent boundary by displacing the antisolvent. In particular, Et_2O was chosen as the antisolvent, as initial attempts with pentane as the antisolvent all resulted in powder formation irrespective of the solvent.

The optimization campaign commenced with **L12**$NiBr_2$ because we believed the tri-substitution pattern should constrict the rotational flexibility of the picoline moiety and impart crystallinity. Based on the initial observations that using THF as solvent caused precipitation and PhH caused no precipitation, we examined a mixture of THF and PhH in various ratios as the solvent system. Experimentally, the requisite amount of THF and PhH were measured via a 1mL syringe and premixed in 1 dram vial prior to the addition of the solid. Consistent with our hypothesis that saturation concentration could influence the outcome of crystallization, mixing PhH and THF in 1:1 or 1:3 ratios both afforded single crystals. Similarly, using an alternative ethereal solvent tetrahydropyran (THP) could also afford single crystals, from which the solid structure was determined by

X-ray diffraction. This approach of modifying the solvent system for liquid diffusion extended to the conformationally more flexible **L2**$NiBr_2$ to generate single crystals. Specifically, the single crystals obtained under a 1:3 ratio of PhH and THF were subjected to XRD analysis. The crystal structure of **L12**$NiBr_2$ can be accessed from the Cambridge Crystallographic Data Centre with the deposit number 2415581.

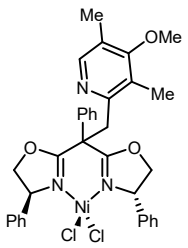

solvent	antisolvent	results
3:1 Et_2O:PhH	Et_2O	did not dissolve
1:1 Et_2O:PhH	Et_2O	no precipitation
1:5 Et_2O:PhH	Et_2O	no precipitation
1:3 Et_2O:PhH	Et_2O	no precipitation
Dioxane	Et_2O	no precipitation
THP	Et_2O	no precipitation

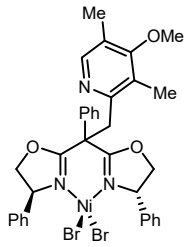

solvent	antisolvent	results
3:1 PhH:THF	Et_2O	salts
1:1 PhH:THF	Et_2O	single crystals
1:3 PhH:THF	Et_2O	single crystals
Dioxane	Et_2O	cloudy solution
THP	Et_2O	single crystals

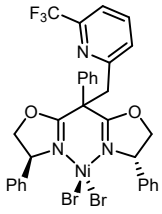

solvent	antisolvent	results
3:1 Et_2O:PhH	Et_2O	solvent evaporation
1:1 Et_2O:PhH	Et_2O	no precipitation
1:3 Et_2O:PhH	Et_2O	no precipitation
3:1 PhH:THF	Et_2O	salts
1:1 PhH:THF	Et_2O	single crystals
1:3 PhH:THF	Et_2O	single crystals
Dioxane	Et_2O	cloudy solution
THP	Et_2O	fine needle crystal

Figure S32.*Crystallization attempts with liquid diffusion.*

Unfortunately, liquid diffusion with various solvent systems was ineffective at generating single crystals of **L2**$NiCl_2$ or **L12**$NiCl_2$ due to their speciation issues. However, noting that THP appeared to be a competent alternative to THF, we examined its viability as a solvent for vapor diffusion with ethereal antisolvent of varying degrees of volatility. Experimentally, a 1-dram vial containing 1 mL of saturated solution was

inserted into a 20 mL scintillation vial. Then, approximately 4 mL of antisolvent was added to the scintillation vial. The vial was capped and stored for 24–72 hours, during which the vial was occasionally inspected for crystal formations. In all cases, we observed the formation of blue powders. However, to our delight, methyl tert-butyl ether (MTBE), with a boiling point of 55.2 °C, afforded fine crystals in addition to the blue powder for structural analysis by XRD. The crystal structure of **L12**$NiCl_2$ can be accessed from the Cambridge Crystallographic Data Centre with the deposit number 2415580.While we were unable to extend this protocol to provide crystals of **L2**$NiCl_2$ under the identical condition, these observations nevertheless encouraged that vapor diffusion setup with an appropriate saturation concentration and antisolvent volatility may be fruitful at overcoming speciation issues associated with dichloronickel(II) precatalysts.

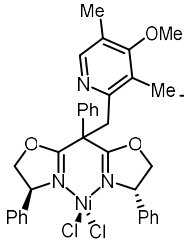

solvent	antisolvent	results
Dioxane	MTBE	powder
Dioxane	Et_2O	powder
THP	MTBE	powder
THP	Et_2O	powder + single crystals

Figure S33. Crystallization attempts with vapor diffusion. Image: pink single crystals were isolated among blue powders.

4.8.2 *Supplementary Information to Computational Evaluation of Conformer Ensemble and Redox Potential*

Computational Details

Conformer search was achieved with CREST[74] program at the GFN2-xTB level of theory with the default setting. Depending on the results, 20 conformers with the lowest energies were further refined using the Orca 5.1.2[75] program at the BP86-D3BJ level of theory. The nickel atom was described with a def2-TZVPP basis set, and all other atoms were described with a def2-TZVP basis set. An implicit PCM solvation was included to model the solvation effect of THF on the geometry, per recommendation by Grimme and coworkers. All calculations were accelerated with the resolution of identity approximation, evaluated at the finest grid (defgrid3), and converged to the TightSCF threshold. Frequency calculations verified that the converged geometries resided at the local minima of the potential energy surface.

Reduction potential was calculated by finding the difference in standard Gibbs Free energy between the oxidized and reduced species of interest in electron volt (i.e., adiabatic ionization potential). This process was repeated for Fc^+ and Fc. Thus, the differences between the ionization potential (in eV) correspond to the predicted reduction potential in V vs Fc/Fc^+ for a one-electron process. Per discussion in the previous chapter, single-point calculation with hybrid density functional was necessary to generate accurate predictions, and TPSSh-D3BJ/def2-TZVPP(Ni)+def2-TZVP level of theory was employed in conjunction with CPCM solvation of THF for electronic energy valuation. In other words, the Gibbs energies at 298.15 K were calculated from the electronic energies at TPSSh-D3BJ/def2-TZVPP(Ni)+def2-TZVP level of theory and the thermal corrections calculated at BP86-D3BJ/def2-TZVPP(Ni)+def2-TZVP level of theory.

The buried volumes of the Ni(II) complexes were determined with DFT-optimized geometries using the ChimeraX programs. To include the steric influence from the pendant

(hetero)arene, the buried volumes of the nickel center were evaluated at a radius of 4.5 Å.

Coordinates of DFT Optimized Structure

L1Ni(II)Cl_2				[**L1**Ni(I)Cl_2]$^-$			
28	-0.426386000	1.424881000	-2.039174000	28	-0.719278000	1.525138000	-1.662153000
7	1.002073000	0.373750000	-1.200893000	7	0.859746000	0.406316000	-1.417637000
7	-1.680387000	-0.050464000	-1.764809000	7	-1.819567000	-0.083319000	-1.633700000
6	2.306301000	0.955787000	-0.790752000	6	2.188734000	1.018416000	-1.171255000
6	3.104057000	-0.299377000	-0.352333000	6	3.111170000	-0.212437000	-0.992999000
1	3.379441000	-0.286526000	0.708311000	1	3.737779000	-0.169441000	-0.095159000
1	3.983709000	-0.492205000	-0.975440000	1	3.728874000	-0.407240000	-1.880023000
8	2.172770000	-1.421363000	-0.547837000	8	2.187177000	-1.337602000	-0.840286000
6	1.030506000	-0.902579000	-1.032239000	6	0.952675000	-0.859843000	-1.181703000
6	-0.036613000	-1.913965000	-1.392013000	6	-0.131402000	-1.909836000	-1.210374000
6	-1.405146000	-1.278318000	-1.495001000	6	-1.478797000	-1.325578000	-1.556571000
8	-2.449565000	-2.117256000	-1.378814000	8	-2.455973000	-2.252707000	-1.787196000
6	-3.666881000	-1.316092000	-1.595774000	6	-3.700595000	-1.498133000	-1.949290000
1	-4.243280000	-1.346785000	-0.664862000	1	-4.327759000	-1.698402000	-1.070563000
1	-4.228118000	-1.790090000	-2.408347000	1	-4.194171000	-1.859468000	-2.858616000
6	-3.150455000	0.100483000	-1.940650000	6	-3.247206000	-0.018978000	-2.032335000
6	-0.052333000	-3.063113000	-0.362897000	6	-0.232055000	-2.555643000	0.200528000
1	0.931551000	-3.543231000	-0.334063000	1	0.724742000	-3.021373000	0.466030000
1	-0.799400000	-3.807787000	-0.657653000	1	-1.014493000	-3.324603000	0.196618000
1	-0.439883000	-3.201024000	-3.107404000	1	-0.512573000	-3.782750000	-2.264792000
1	-0.296916000	-2.692096000	0.641181000	1	-0.480718000	-1.796058000	0.953534000
6	0.311965000	-2.458752000	-2.811220000	6	0.244085000	-2.989437000	-2.259258000
1	0.326778000	-1.640660000	-3.543021000	1	0.304129000	-2.548746000	-3.263539000
1	1.297124000	-2.940758000	-2.781895000	1	1.216884000	-3.425866000	-2.003741000
1	2.757084000	1.420722000	-1.678849000	1	2.462950000	1.606719000	-2.056383000
6	2.121479000	2.004630000	0.280421000	6	2.143273000	1.939535000	0.028833000
6	1.480088000	1.682208000	1.484258000	6	1.348290000	1.639548000	1.143436000
1	1.114486000	0.666798000	1.652202000	1	0.714291000	0.751989000	1.131215000
6	1.284763000	2.658488000	2.460892000	6	1.341329000	2.485444000	2.254799000

1	0.776905000	2.401839000	3.391766000	1	0.708954000	2.248009000	3.111889000
6	1.730621000	3.967479000	2.242852000	6	2.128675000	3.642051000	2.263412000
1	1.573011000	4.732091000	3.004923000	1	2.115322000	4.307801000	3.127919000
6	2.371511000	4.293417000	1.045060000	6	2.921907000	3.947871000	1.153352000
1	2.715952000	5.313235000	0.867563000	1	3.528549000	4.855036000	1.146621000
6	2.564278000	3.313359000	0.066685000	6	2.925492000	3.100210000	0.041635000
1	3.051539000	3.567126000	-0.877012000	1	3.526347000	3.349442000	-0.835644000
1	-3.501717000	0.846059000	-1.215385000	1	-3.775612000	0.607995000	-1.302630000
6	-3.436562000	0.593332000	-3.341254000	6	-3.389769000	0.605449000	-3.402900000
6	-3.218371000	-0.234589000	-4.450986000	6	-2.475121000	0.316092000	-4.425129000
1	-2.882177000	-1.264183000	-4.310995000	1	-1.626405000	-0.338493000	-4.221330000
6	-3.406782000	0.256067000	-5.743362000	6	-2.627962000	0.883697000	-5.691635000
1	-3.228905000	-0.393230000	-6.601794000	1	-1.902606000	0.661463000	-6.476045000
6	-3.812114000	1.581368000	-5.938093000	6	-3.696984000	1.749176000	-5.949790000
1	-3.953619000	1.966064000	-6.949145000	1	-3.809999000	2.201083000	-6.936589000
6	-4.029868000	2.411390000	-4.835326000	6	-4.611297000	2.042871000	-4.933915000
1	-4.341575000	3.446621000	-4.981143000	1	-5.439931000	2.727255000	-5.123512000
6	-3.841469000	1.917623000	-3.541389000	6	-4.455279000	1.473336000	-3.666413000
1	-3.990894000	2.567036000	-2.677035000	1	-5.153880000	1.720432000	-2.864277000
17	-1.318500000	3.036349000	-0.793155000	17	-2.273323000	2.913741000	-0.543874000
17	0.317674000	1.392385000	-4.147977000	17	0.299126000	3.125983000	-3.072444000
L2Ni(II)Cl_2				[**L2**Ni(I)Cl_2]$^-$			
28	-0.030712000	-0.052546000	-0.085250000	28	-0.279742000	0.197207000	-0.081637000
7	1.359273000	-1.422652000	0.028083000	7	1.210862000	-1.067374000	-0.097488000
7	-1.417932000	-1.414440000	0.120631000	7	-1.509882000	-1.274244000	0.180299000
6	2.804350000	-1.076636000	-0.047536000	6	2.642908000	-0.656117000	-0.090139000
6	3.478242000	-2.463122000	0.078199000	6	3.355246000	-1.928346000	-0.583082000
1	3.954134000	-2.617535000	1.054548000	1	4.255279000	-2.202175000	-0.024700000
1	4.177785000	-2.687355000	-0.732463000	1	3.570879000	-1.893196000	-1.659502000
8	2.365958000	-3.424068000	-0.018219000	8	2.370272000	-2.992858000	-0.367867000
6	1.230918000	-2.701052000	0.016379000	6	1.181130000	-2.352837000	-0.181641000
6	-0.037465000	-3.524589000	0.020299000	6	-0.001842000	-3.280242000	-0.056173000
6	-1.291639000	-2.692695000	0.187111000	6	-1.288483000	-2.545506000	0.235876000

8	-2.420558000	-3.408387000	0.319102000	8	-2.365350000	-3.358146000	0.437412000
6	-3.517486000	-2.438716000	0.463525000	6	-3.479611000	-2.450862000	0.734889000
1	-3.885933000	-2.519475000	1.492115000	1	-3.617986000	-2.444539000	1.824412000
1	-4.298584000	-2.719771000	-0.250466000	1	-4.371626000	-2.844760000	0.236698000
6	-2.866101000	-1.068033000	0.169914000	6	-3.000307000	-1.093152000	0.208136000
6	0.066610000	-4.543735000	1.196482000	6	0.315827000	-4.276023000	1.108982000
1	0.877543000	-5.247270000	0.980203000	1	1.146204000	-4.923003000	0.804396000
1	-0.877403000	-5.099712000	1.256817000	1	-0.572813000	-4.892486000	1.291053000
6	0.329477000	-3.830360000	2.498152000	6	0.677431000	-3.507997000	2.352716000
7	-0.655149000	-3.032603000	2.949244000	7	-0.335473000	-2.906477000	2.999565000
6	-0.438698000	-2.334819000	4.067786000	6	-0.037002000	-2.135553000	4.054094000
6	-1.615544000	-1.513053000	4.566440000	6	-1.243741000	-1.516873000	4.731375000
9	-2.416698000	-1.078094000	3.569017000	9	-2.040561000	-0.854275000	3.855663000
9	-2.400344000	-2.258383000	5.406714000	9	-2.023970000	-2.471871000	5.324657000
9	-1.209732000	-0.425773000	5.273265000	9	-0.893161000	-0.635063000	5.705110000
6	0.745097000	-2.384019000	4.805512000	6	1.254083000	-1.916973000	4.527934000
1	0.870194000	-1.787689000	5.707622000	1	1.438248000	-1.265794000	5.379343000
6	1.756657000	-3.226341000	4.343530000	6	2.300938000	-2.557403000	3.862087000
1	2.700247000	-3.301236000	4.884295000	1	3.330598000	-2.407765000	4.185487000
6	1.549558000	-3.958365000	3.175001000	6	2.011170000	-3.362927000	2.765500000
1	2.324501000	-4.614944000	2.779967000	1	2.805167000	-3.862371000	2.211586000
6	-0.161473000	-4.187966000	-1.371329000	6	-0.226657000	-3.972122000	-1.417551000
6	-0.161211000	-3.349449000	-2.496511000	6	-0.348805000	-3.150553000	-2.548787000
1	-0.057590000	-2.267580000	-2.378280000	1	-0.255506000	-2.067322000	-2.441243000
6	-0.300299000	-3.891958000	-3.773926000	6	-0.601751000	-3.708620000	-3.801421000
1	-0.299484000	-3.231000000	-4.641599000	1	-0.698317000	-3.058588000	-4.672079000
6	-0.442210000	-5.273843000	-3.937613000	6	-0.738936000	-5.094806000	-3.936284000
1	-0.551944000	-5.699196000	-4.936103000	1	-0.938509000	-5.533535000	-4.915086000
6	-0.444132000	-6.107720000	-2.816790000	6	-0.621070000	-5.914344000	-2.810984000
1	-0.555928000	-7.186261000	-2.935879000	1	-0.728746000	-6.995919000	-2.907213000
6	-0.305230000	-5.568073000	-1.533723000	6	-0.367686000	-5.355705000	-1.553074000
1	-0.314246000	-6.233372000	-0.671452000	1	-0.285973000	-6.008153000	-0.684323000
1	2.976568000	-0.633468000	-1.039177000	1	2.746897000	0.167069000	-0.813557000
6	3.170424000	-0.073531000	1.018548000	6	3.046896000	-0.157751000	1.292520000

6	2.966868000	-0.376269000	2.371086000	6	2.113329000	0.488125000	2.115357000
1	2.556212000	-1.346183000	2.654113000	1	1.077790000	0.594658000	1.773155000
6	3.255311000	0.566341000	3.356438000	6	2.484125000	0.980123000	3.367115000
1	3.082110000	0.323982000	4.406001000	1	1.736401000	1.473154000	3.990568000
6	3.750027000	1.825321000	2.996357000	6	3.797029000	0.832591000	3.824034000
1	3.970048000	2.566739000	3.765835000	1	4.085712000	1.209157000	4.806766000
6	3.951844000	2.133989000	1.648518000	6	4.737793000	0.198780000	3.007857000
1	4.329597000	3.116568000	1.362272000	1	5.768286000	0.080380000	3.347453000
6	3.660069000	1.186778000	0.662042000	6	4.365897000	-0.285915000	1.749787000
1	3.799558000	1.430034000	-0.393175000	1	5.122613000	-0.763263000	1.125071000
1	-3.017427000	-0.366939000	1.000257000	1	-3.229405000	-0.269961000	0.894948000
6	-3.257911000	-0.404527000	-1.129920000	6	-3.430111000	-0.735002000	-1.198507000
6	-3.280804000	-1.135349000	-2.326207000	6	-3.585389000	-1.721960000	-2.183346000
1	-3.061688000	-2.205154000	-2.321376000	1	-3.456625000	-2.775321000	-1.929258000
6	-3.561071000	-0.497264000	-3.534629000	6	-3.881740000	-1.366507000	-3.501349000
1	-3.569907000	-1.071742000	-4.462021000	1	-3.993045000	-2.143641000	-4.259388000
6	-3.820770000	0.877951000	-3.557824000	6	-4.025179000	-0.019311000	-3.849583000
1	-4.034951000	1.377147000	-4.503975000	1	-4.252348000	0.258640000	-4.880182000
6	-3.800368000	1.610358000	-2.368017000	6	-3.870599000	0.969415000	-2.872441000
1	-3.997830000	2.683184000	-2.381197000	1	-3.972762000	2.022814000	-3.138588000
6	-3.518175000	0.969531000	-1.158244000	6	-3.571954000	0.612830000	-1.554870000
1	-3.482440000	1.539788000	-0.227902000	1	-3.414514000	1.378229000	-0.792380000
17	-0.362958000	1.238288000	1.686375000	17	-1.477119000	1.791577000	1.202943000
17	0.286433000	0.462935000	-2.243480000	17	0.690870000	1.655377000	-1.647606000
L3Ni(II)Cl_2				[**L3**Ni(I)Cl_2]$^-$			
28	-0.135078000	1.396670000	-0.823498000	28	-0.008298000	1.377669000	-0.259266000
7	1.131550000	-0.026915000	-0.391218000	7	1.448345000	0.099574000	-0.224601000
7	-1.634866000	0.163363000	-0.557492000	7	-1.281408000	-0.085562000	-0.327558000
6	2.594407000	0.221446000	-0.272940000	6	2.863048000	0.531981000	-0.105428000
6	3.161507000	-1.211273000	-0.116695000	6	3.630808000	-0.805421000	0.052389000
1	3.657436000	-1.377196000	0.846283000	1	4.022209000	-0.945028000	1.069084000
1	3.813189000	-1.511904000	-0.943764000	1	4.428625000	-0.945677000	-0.685303000
8	1.979041000	-2.086103000	-0.151248000	8	2.620533000	-1.839458000	-0.176711000

6	0.905953000	-1.289891000	-0.292899000	6	1.420914000	-1.189173000	-0.250220000
6	-0.406992000	-2.026650000	-0.354468000	6	0.231592000	-2.103892000	-0.345711000
6	-1.602503000	-1.107711000	-0.363520000	6	-1.073786000	-1.357620000	-0.378600000
8	-2.790652000	-1.720896000	-0.193447000	8	-2.171491000	-2.164406000	-0.486243000
6	-3.815573000	-0.664574000	-0.171347000	6	-3.319018000	-1.271246000	-0.649900000
1	-4.216300000	-0.628981000	0.848022000	1	-4.081983000	-1.566786000	0.078733000
1	-4.602628000	-0.959797000	-0.871160000	1	-3.696923000	-1.402205000	-1.672841000
6	-3.057120000	0.621773000	-0.551010000	6	-2.744956000	0.148888000	-0.411700000
6	-0.486182000	-2.995042000	0.871497000	6	0.254652000	-3.065548000	0.896710000
1	0.214623000	-3.817864000	0.685320000	1	1.084112000	-3.770765000	0.756403000
1	-1.498342000	-3.419836000	0.892308000	1	-0.682752000	-3.638335000	0.880705000
6	-0.425697000	-2.854125000	-1.701034000	6	0.335473000	-2.964081000	-1.656931000
1	-1.404038000	-3.348650000	-1.765544000	1	-0.387399000	-3.785991000	-1.573294000
1	0.346230000	-3.628614000	-1.606579000	1	1.343346000	-3.401048000	-1.678465000
1	2.926045000	0.687463000	-1.210173000	1	3.126188000	1.050030000	-1.038825000
6	2.880405000	1.152661000	0.880441000	6	3.060096000	1.479768000	1.052204000
6	2.504017000	0.795736000	2.181501000	6	2.331330000	1.313340000	2.236682000
1	2.007663000	-0.158531000	2.365915000	1	1.591502000	0.516665000	2.307043000
6	2.737817000	1.665661000	3.245314000	6	2.533017000	2.175352000	3.315780000
1	2.432478000	1.381099000	4.253218000	1	1.948995000	2.041689000	4.227727000
6	3.347521000	2.904637000	3.015874000	6	3.468043000	3.212082000	3.222226000
1	3.524622000	3.589103000	3.846900000	1	3.619589000	3.891651000	4.062583000
6	3.721406000	3.266346000	1.718664000	6	4.199980000	3.380924000	2.042447000
1	4.190161000	4.233926000	1.533285000	1	4.923521000	4.193590000	1.958170000
6	3.486912000	2.391501000	0.653445000	6	3.993233000	2.518382000	0.961440000
1	3.759526000	2.676634000	-0.364269000	1	4.544676000	2.663894000	0.030027000
1	-3.141062000	1.376872000	0.242721000	1	-3.066686000	0.564177000	0.554043000
6	-3.372977000	1.274523000	-1.883336000	6	-3.096603000	1.127071000	-1.505527000
6	-4.039133000	0.616193000	-2.922757000	6	-4.179164000	1.999336000	-1.346981000
1	-4.418490000	-0.397257000	-2.788105000	1	-4.735560000	1.998197000	-0.407203000
6	-4.222069000	1.246553000	-4.157100000	6	-4.531182000	2.884097000	-2.370852000
1	-4.744098000	0.721450000	-4.958285000	1	-5.371923000	3.566347000	-2.233940000
6	-3.728757000	2.536998000	-4.368555000	6	-3.796215000	2.905111000	-3.560733000
1	-3.864180000	3.023270000	-5.335620000	1	-4.062456000	3.602835000	-4.356535000

6	-3.064774000	3.202297000	-3.333668000	6	-2.711580000	2.035972000	-3.721222000
1	-2.678021000	4.210568000	-3.486620000	1	-2.124373000	2.052816000	-4.640713000
6	-2.898324000	2.577443000	-2.096808000	6	-2.364937000	1.150585000	-2.699265000
1	-2.392146000	3.102984000	-1.283442000	1	-1.510442000	0.485916000	-2.820625000
6	-0.163099000	-1.978621000	-2.898374000	6	0.060599000	-2.161499000	-2.904162000
6	1.147186000	-1.787562000	-3.363792000	6	0.969075000	-1.193177000	-3.361781000
6	-1.203404000	-1.262904000	-3.507169000	6	-1.138987000	-2.338481000	-3.609702000
6	1.412661000	-0.887864000	-4.398132000	6	0.679993000	-0.416501000	-4.486072000
6	-0.941195000	-0.356737000	-4.536150000	6	-1.424494000	-1.574820000	-4.744675000
6	0.368997000	-0.163313000	-4.981490000	6	-0.516412000	-0.607789000	-5.184186000
1	1.965535000	-2.346153000	-2.905154000	1	1.912474000	-1.042234000	-2.835982000
1	-2.229382000	-1.409361000	-3.166805000	1	-1.857626000	-3.080882000	-3.257448000
1	2.437760000	-0.746428000	-4.743737000	1	1.390426000	0.343568000	-4.813998000
1	-1.762954000	0.206762000	-4.979442000	1	-2.364730000	-1.725529000	-5.277422000
1	0.576767000	0.553033000	-5.777268000	1	-0.742957000	0.000749000	-6.060697000
6	-0.140553000	-2.326590000	2.183119000	6	0.421990000	-2.326832000	2.201200000
6	-0.917507000	-1.283227000	2.711936000	6	-0.610443000	-1.531447000	2.724569000
6	1.003967000	-2.728588000	2.887700000	6	1.638408000	-2.385850000	2.897545000
6	-0.555602000	-0.655907000	3.905909000	6	-0.426558000	-0.806792000	3.904443000
6	1.360971000	-2.113768000	4.091130000	6	1.820997000	-1.674340000	4.086359000
6	0.582544000	-1.072053000	4.602772000	6	0.789107000	-0.878826000	4.591689000
1	-1.820077000	-0.953013000	2.197795000	1	-1.568760000	-1.476545000	2.206931000
1	1.623805000	-3.530087000	2.481624000	1	2.451418000	-2.993115000	2.495332000
1	-1.166091000	0.161546000	4.291533000	1	-1.235071000	-0.181151000	4.285170000
1	2.255323000	-2.442195000	4.622764000	1	2.776079000	-1.730774000	4.610963000
1	0.864467000	-0.582101000	5.535570000	1	0.933559000	-0.310521000	5.511513000
17	-0.567790000	2.617143000	1.030997000	17	-1.258105000	2.807324000	1.145790000
17	0.922337000	2.639483000	-2.318546000	17	1.057674000	2.960077000	-1.660657000
L4Ni(II)Cl_2				[**L4**Ni(II)Cl_2]$^-$			
28	-0.531291000	1.722830000	-1.978969000	28	-0.726060000	1.910770000	-1.860534000
7	0.880377000	0.377824000	-1.847704000	7	0.759161000	0.635981000	-1.944134000
7	-1.895796000	0.329613000	-1.850483000	7	-1.970757000	0.442215000	-1.729024000
6	2.319147000	0.755682000	-1.870101000	6	2.188176000	1.044094000	-1.935348000

6	3.018527000	-0.619592000	-1.757054000	6	2.915172000	-0.243982000	-2.376068000
1	3.473364000	-0.786121000	-0.772697000	1	3.773526000	-0.513994000	-1.752311000
1	3.742107000	-0.811639000	-2.554774000	1	3.203812000	-0.225395000	-3.435389000
8	1.929427000	-1.600851000	-1.902113000	8	1.908059000	-1.296017000	-2.215271000
6	0.779791000	-0.902708000	-1.879955000	6	0.722659000	-0.648137000	-2.042045000
6	-0.470054000	-1.751805000	-1.905419000	6	-0.467814000	-1.570802000	-1.959352000
6	-1.743234000	-0.944718000	-1.778358000	6	-1.761461000	-0.831684000	-1.720754000
8	-2.861462000	-1.681683000	-1.643284000	8	-2.854788000	-1.642191000	-1.586727000
6	-3.990829000	-0.736384000	-1.594016000	6	-3.982101000	-0.736788000	-1.331001000
1	-4.448452000	-0.830565000	-0.603262000	1	-4.208719000	-0.784450000	-0.257175000
1	-4.698849000	-1.034888000	-2.374352000	1	-4.835512000	-1.095956000	-1.915648000
6	-3.350541000	0.650904000	-1.833024000	6	-3.457801000	0.643014000	-1.750790000
6	-0.373435000	-2.769441000	-0.723185000	6	-0.203829000	-2.563761000	-0.776301000
1	0.407814000	-3.497830000	-0.968168000	1	0.620952000	-3.228638000	-1.059200000
1	-1.328687000	-3.305634000	-0.656350000	1	-1.106081000	-3.172172000	-0.633631000
6	-0.036719000	-2.094353000	0.585899000	6	0.148413000	-1.811159000	0.482855000
6	-0.945594000	-1.232566000	1.217166000	6	-0.839658000	-1.131670000	1.207760000
1	-1.937039000	-1.071543000	0.797873000	1	-1.884261000	-1.206527000	0.909235000
6	-0.594188000	-0.580943000	2.399966000	6	-0.491563000	-0.353255000	2.314129000
6	-1.575158000	0.327194000	3.091541000	6	-1.557422000	0.357786000	3.098825000
9	-2.675669000	0.592279000	2.340778000	9	-2.714871000	0.513687000	2.402658000
9	-2.026594000	-0.219375000	4.265506000	9	-1.888436000	-0.324752000	4.246052000
9	-1.017700000	1.526732000	3.423526000	9	-1.164854000	1.599563000	3.502588000
6	0.660122000	-0.790013000	2.986645000	6	0.841797000	-0.255666000	2.727777000
1	0.927971000	-0.277395000	3.910527000	1	1.107935000	0.363018000	3.583945000
6	1.560183000	-1.658990000	2.373043000	6	1.825306000	-0.943709000	2.020420000
1	2.540313000	-1.829261000	2.819083000	1	2.868894000	-0.861450000	2.324722000
6	1.215697000	-2.299852000	1.179405000	6	1.481206000	-1.710701000	0.905860000
1	1.930936000	-2.966417000	0.695351000	1	2.257874000	-2.227361000	0.340615000
6	-0.555923000	-2.416115000	-3.300242000	6	-0.638208000	-2.262248000	-3.329103000
6	-0.518927000	-1.578084000	-4.425347000	6	-0.740931000	-1.437627000	-4.460276000
1	-0.411611000	-0.496922000	-4.303783000	1	-0.673702000	-0.353376000	-4.344270000
6	-0.627097000	-2.119662000	-5.706153000	6	-0.938499000	-1.993852000	-5.723572000
1	-0.596510000	-1.459293000	-6.573700000	1	-1.019253000	-1.341461000	-6.594138000

6	-0.776852000	-3.500350000	-5.872999000	6	-1.038327000	-3.382278000	-5.869685000
1	-0.862696000	-3.925351000	-6.873959000	1	-1.193749000	-3.820029000	-6.856883000
6	-0.818331000	-4.333473000	-4.752336000	6	-0.939697000	-4.204917000	-4.744922000
1	-0.937725000	-5.410871000	-4.874311000	1	-1.018381000	-5.288159000	-4.850096000
6	-0.710214000	-3.794694000	-3.465962000	6	-0.742574000	-3.647721000	-3.476133000
1	-0.751349000	-4.458872000	-2.603829000	1	-0.674468000	-4.303091000	-2.608445000
1	2.513870000	1.228283000	-2.843737000	1	2.299663000	1.843687000	-2.683974000
6	2.622671000	1.739367000	-0.766500000	6	2.604829000	1.591007000	-0.577514000
6	2.387910000	1.392143000	0.570132000	6	1.664699000	2.106253000	0.322803000
1	2.005450000	0.400841000	0.816210000	1	0.600972000	2.079140000	0.064589000
6	2.611761000	2.316735000	1.588677000	6	2.070045000	2.649266000	1.543262000
1	2.414427000	2.038707000	2.625004000	1	1.318055000	3.042182000	2.229119000
6	3.071331000	3.601961000	1.278315000	6	3.423245000	2.678115000	1.889703000
1	3.240306000	4.329072000	2.073933000	1	3.739431000	3.095708000	2.847118000
6	3.303824000	3.954847000	-0.053772000	6	4.370576000	2.167981000	0.996135000
1	3.654660000	4.957677000	-0.301530000	1	5.431820000	2.188000000	1.250431000
6	3.077098000	3.025650000	-1.073930000	6	3.963421000	1.635130000	-0.230054000
1	3.240303000	3.302737000	-2.117352000	1	4.718857000	1.257236000	-0.922140000
1	-3.532538000	1.329620000	-0.989652000	1	-3.701138000	1.425137000	-1.021776000
6	-3.716520000	1.340061000	-3.126698000	6	-3.824446000	1.100012000	-3.145817000
6	-3.678328000	0.641514000	-4.341685000	6	-3.935136000	0.184873000	-4.203119000
1	-3.429299000	-0.421669000	-4.358110000	1	-3.817837000	-0.884353000	-4.018412000
6	-3.934300000	1.304954000	-5.541759000	6	-4.172148000	0.633252000	-5.504663000
1	-3.895173000	0.756277000	-6.483824000	1	-4.249950000	-0.087924000	-6.320006000
6	-4.230618000	2.672894000	-5.537409000	6	-4.300645000	2.002244000	-5.762550000
1	-4.425870000	3.192012000	-6.476880000	1	-4.481827000	2.352816000	-6.779988000
6	-4.270294000	3.373002000	-4.328758000	6	-4.190631000	2.919395000	-4.712330000
1	-4.496033000	4.440249000	-4.320547000	1	-4.281605000	3.989103000	-4.907766000
6	-4.011967000	2.707199000	-3.127250000	6	-3.950910000	2.469875000	-3.411296000
1	-4.022479000	3.252586000	-2.181568000	1	-3.829785000	3.178976000	-2.590089000
17	-0.988947000	2.908024000	-0.162069000	17	-1.942040000	3.388105000	-0.441611000
17	-0.150514000	2.307440000	-4.105633000	17	0.261307000	3.486621000	-3.285243000
L5Ni(II)Cl_2				[**L5**Ni(II)Cl_2]$^-$			

28	-0.010315000	0.033972000	-0.218475000	28	-0.076382000	0.078312000	0.010870000
7	1.396166000	-1.316391000	-0.055007000	7	1.285841000	-1.306452000	-0.123828000
7	-1.389160000	-1.329892000	0.002388000	7	-1.426627000	-1.293084000	0.228182000
6	2.840962000	-0.961049000	-0.083021000	6	2.727033000	-0.968233000	-0.193226000
6	3.524565000	-2.350304000	-0.045007000	6	3.422566000	-2.356856000	-0.192131000
1	4.121330000	-2.513351000	0.859694000	1	4.085625000	-2.503700000	0.669260000
1	4.116879000	-2.565694000	-0.940293000	1	3.956754000	-2.573490000	-1.125002000
8	2.412499000	-3.313392000	-0.012556000	8	2.325307000	-3.320458000	-0.075115000
6	1.275068000	-2.594982000	-0.010119000	6	1.175851000	-2.588068000	-0.042329000
6	0.012555000	-3.425183000	0.035613000	6	-0.081919000	-3.418314000	0.052806000
6	-1.241825000	-2.592835000	0.195589000	6	-1.319518000	-2.578118000	0.257747000
8	-2.359217000	-3.305013000	0.421674000	8	-2.473355000	-3.298691000	0.369995000
6	-3.469178000	-2.342187000	0.475203000	6	-3.521517000	-2.308897000	0.635136000
1	-3.848553000	-2.341210000	1.503218000	1	-3.740606000	-2.340318000	1.711141000
1	-4.240043000	-2.692811000	-0.219419000	1	-4.405915000	-2.596090000	0.056456000
6	-2.835217000	-0.990479000	0.069765000	6	-2.890269000	-0.973107000	0.215361000
6	0.146817000	-4.414557000	1.228503000	6	0.077602000	-4.413574000	1.246225000
1	0.938419000	-5.137667000	1.003844000	1	0.877808000	-5.124126000	1.010357000
1	-0.799402000	-4.963711000	1.329478000	1	-0.864396000	-4.965437000	1.359730000
6	0.459672000	-3.682992000	2.511296000	6	0.397655000	-3.673531000	2.519875000
7	-0.335025000	-2.637132000	2.807039000	7	-0.589294000	-2.913043000	3.036392000
6	-0.081886000	-1.937420000	3.922800000	6	-0.319051000	-2.183851000	4.131176000
1	-0.735804000	-1.082874000	4.113393000	1	-1.137120000	-1.565402000	4.510140000
6	0.956856000	-2.250741000	4.802093000	6	0.920990000	-2.187855000	4.772955000
1	1.120590000	-1.649290000	5.696044000	1	1.084313000	-1.572777000	5.657861000
6	1.778728000	-3.335883000	4.495232000	6	1.934620000	-2.989605000	4.246811000
1	2.609343000	-3.607403000	5.148051000	1	2.920669000	-3.018870000	4.712157000
6	1.532893000	-4.059738000	3.327010000	6	1.671213000	-3.738801000	3.100079000
1	2.165302000	-4.901631000	3.043479000	1	2.442602000	-4.360392000	2.645344000
6	-0.137738000	-4.121431000	-1.338201000	6	-0.276932000	-4.117735000	-1.312581000
6	-0.126634000	-3.316278000	-2.487343000	6	-0.338842000	-3.302435000	-2.453796000
1	0.006014000	-2.234891000	-2.400950000	1	-0.228474000	-2.220714000	-2.349307000
6	-0.295456000	-3.890077000	-3.747485000	6	-0.548564000	-3.864793000	-3.712340000
1	-0.285616000	-3.253897000	-4.633433000	1	-0.598417000	-3.219100000	-4.590246000

6	-0.479942000	-5.271108000	-3.870474000	6	-0.698867000	-5.250218000	-3.845009000
1	-0.613743000	-5.720871000	-4.855261000	1	-0.863407000	-5.692504000	-4.828726000
6	-0.493505000	-6.072447000	-2.726179000	6	-0.638498000	-6.063449000	-2.711004000
1	-0.638380000	-7.150163000	-2.813078000	1	-0.756149000	-7.144214000	-2.805025000
6	-0.323943000	-5.500983000	-1.460752000	6	-0.430114000	-5.500115000	-1.446509000
1	-0.342090000	-6.140631000	-0.579484000	1	-0.392671000	-6.148699000	-0.571995000
1	3.035338000	-0.442835000	-1.032250000	1	2.897261000	-0.428678000	-1.135017000
6	3.163871000	-0.039266000	1.068725000	6	3.137890000	-0.078198000	0.957161000
6	3.018574000	-0.482986000	2.389655000	6	2.492862000	-0.162371000	2.197054000
1	2.704368000	-1.508607000	2.591032000	1	1.653949000	-0.845709000	2.320484000
6	3.249538000	0.387381000	3.453875000	6	2.901029000	0.642787000	3.262318000
1	3.123645000	0.035022000	4.478557000	1	2.380951000	0.574501000	4.219068000
6	3.629661000	1.711610000	3.206067000	6	3.960291000	1.541568000	3.098319000
1	3.805290000	2.394507000	4.038569000	1	4.274147000	2.177168000	3.928026000
6	3.775985000	2.158938000	1.890368000	6	4.607529000	1.631033000	1.861475000
1	4.065695000	3.191752000	1.691722000	1	5.426900000	2.338280000	1.721956000
6	3.541130000	1.284880000	0.824703000	6	4.194608000	0.825774000	0.795676000
1	3.636302000	1.634227000	-0.205384000	1	4.683937000	0.910903000	-0.177141000
1	-2.970160000	-0.235096000	0.855319000	1	-3.067521000	-0.178605000	0.950337000
6	-3.271239000	-0.420988000	-1.260049000	6	-3.230499000	-0.478275000	-1.173515000
6	-3.272976000	-1.223531000	-2.409793000	6	-3.402169000	-1.373925000	-2.239266000
1	-3.002017000	-2.279211000	-2.342108000	1	-3.354662000	-2.450134000	-2.063733000
6	-3.596382000	-0.674420000	-3.650584000	6	-3.608880000	-0.898619000	-3.536363000
1	-3.588057000	-1.304198000	-4.541391000	1	-3.734074000	-1.605189000	-4.358631000
6	-3.921233000	0.683375000	-3.753166000	6	-3.646332000	0.478362000	-3.781454000
1	-4.169351000	1.113600000	-4.724574000	1	-3.802799000	0.849717000	-4.795630000
6	-3.921559000	1.487115000	-2.610174000	6	-3.476441000	1.376187000	-2.722727000
1	-4.168915000	2.546989000	-2.685509000	1	-3.495241000	2.451377000	-2.908086000
6	-3.595084000	0.935251000	-1.367789000	6	-3.267328000	0.899168000	-1.426103000
1	-3.574877000	1.562961000	-0.474598000	1	-3.098745000	1.591697000	-0.599286000
17	-0.389313000	1.298248000	1.572545000	17	-1.056436000	1.647136000	1.492029000
17	0.300579000	0.538742000	-2.377231000	17	0.881028000	1.559693000	-1.543430000
L7Ni(II)Cl_2				[**L7**Ni(II)Cl_2]$^-$			

28	-0.345972000	1.732329000	-0.697831000	28	-0.523844000	1.800882000	-0.456129000
7	1.003408000	0.327366000	-0.514276000	7	0.859198000	0.419027000	-0.553454000
7	-1.780490000	0.412108000	-0.594283000	7	-1.880732000	0.423063000	-0.404536000
6	2.460784000	0.630613000	-0.481371000	6	2.304089000	0.738968000	-0.492522000
6	3.092223000	-0.782080000	-0.427681000	6	2.981140000	-0.639595000	-0.696543000
1	3.631868000	-0.980156000	0.505440000	1	3.731845000	-0.878548000	0.064693000
1	3.725098000	-1.006411000	-1.292251000	1	3.402597000	-0.762046000	-1.702737000
8	1.946306000	-1.705599000	-0.471979000	8	1.884726000	-1.602215000	-0.560837000
6	0.836126000	-0.946513000	-0.504524000	6	0.738528000	-0.864137000	-0.549812000
6	-0.455513000	-1.732126000	-0.534159000	6	-0.522105000	-1.694817000	-0.549230000
6	-1.689279000	-0.860376000	-0.435253000	6	-1.772027000	-0.862494000	-0.402620000
8	-2.841185000	-1.538703000	-0.297310000	8	-2.927324000	-1.587867000	-0.383161000
6	-3.919787000	-0.538915000	-0.281362000	6	-3.995726000	-0.607430000	-0.166316000
1	-4.364792000	-0.558111000	0.719664000	1	-4.290296000	-0.668537000	0.890167000
1	-4.655057000	-0.839513000	-1.035455000	1	-4.835605000	-0.881232000	-0.813693000
6	-3.216046000	0.801644000	-0.598733000	6	-3.342135000	0.740406000	-0.505602000
6	-0.421592000	-2.731986000	0.658988000	6	-0.429411000	-2.707272000	0.638708000
1	0.357656000	-3.479765000	0.476923000	1	0.385069000	-3.413182000	0.441831000
1	-1.390487000	-3.247054000	0.707391000	1	-1.375998000	-3.259232000	0.695766000
6	-0.156926000	-2.009014000	1.956036000	6	-0.183863000	-1.971219000	1.928666000
7	-0.973958000	-0.976776000	2.240612000	7	-1.215599000	-1.254185000	2.420044000
6	-0.753395000	-0.272127000	3.356638000	6	-1.007859000	-0.520271000	3.523205000
1	-1.422658000	0.571317000	3.538428000	1	-1.858453000	0.062893000	3.883727000
6	0.276100000	-0.561844000	4.255736000	6	0.210722000	-0.472830000	4.202720000
1	0.419196000	0.043632000	5.148615000	1	0.326160000	0.142789000	5.092583000
6	1.115441000	-1.633612000	3.958138000	6	1.267272000	-1.227711000	3.695846000
6	2.251279000	-2.015516000	4.875484000	6	2.611158000	-1.255132000	4.376203000
6	0.905440000	-2.370140000	2.788980000	6	1.073738000	-1.986117000	2.540064000
1	1.559999000	-3.198892000	2.519956000	1	1.885129000	-2.570143000	2.107112000
6	-0.551928000	-2.413916000	-1.919251000	6	-0.631915000	-2.374312000	-1.932583000
6	-0.465350000	-1.597123000	-3.057112000	6	-0.622274000	-1.541336000	-3.062386000
1	-0.314204000	-0.519845000	-2.951377000	1	-0.519327000	-0.461431000	-2.934384000
6	-0.580888000	-2.154694000	-4.330348000	6	-0.752966000	-2.084135000	-4.340066000
1	-0.512445000	-1.510458000	-5.207802000	1	-0.747765000	-1.425201000	-5.209455000

6	-0.786650000	-3.530432000	-4.477422000	6	-0.894900000	-3.467160000	-4.502718000
1	-0.878585000	-3.967538000	-5.472616000	1	-0.997724000	-3.894301000	-5.501361000
6	-0.875269000	-4.342788000	-3.344399000	6	-0.905818000	-4.297752000	-3.379740000
1	-1.037272000	-5.416290000	-3.450586000	1	-1.017693000	-5.376748000	-3.497565000
6	-0.759620000	-3.787760000	-2.065587000	6	-0.776980000	-3.754153000	-2.096263000
1	-0.836493000	-4.435892000	-1.193675000	1	-0.794798000	-4.416313000	-1.231305000
1	2.709078000	1.146711000	-1.419163000	1	2.527022000	1.422239000	-1.324359000
6	2.767444000	1.536547000	0.687061000	6	2.679852000	1.426696000	0.805275000
6	2.598123000	1.078044000	1.999540000	6	1.767968000	1.593132000	1.852089000
9	1.980201000	-3.172687000	5.547908000	9	2.839909000	-2.466701000	4.973879000
9	3.406573000	-2.227833000	4.184711000	9	3.633877000	-1.064376000	3.496828000
9	2.511338000	-1.066183000	5.808625000	9	2.732506000	-0.313349000	5.344638000
1	2.285226000	0.048712000	2.179608000	1	0.742539000	1.239739000	1.731745000
6	2.806231000	1.935356000	3.078875000	6	2.154275000	2.238691000	3.030155000
1	2.665366000	1.570044000	4.096952000	1	1.427292000	2.369713000	3.832893000
6	3.187186000	3.263245000	2.853391000	6	3.459468000	2.712843000	3.179878000
1	3.345930000	3.936587000	3.696944000	1	3.759890000	3.215667000	4.100563000
6	3.357962000	3.726080000	1.545939000	6	4.379400000	2.542596000	2.138854000
1	3.649548000	4.761611000	1.365175000	1	5.400588000	2.913221000	2.243265000
6	3.146405000	2.864249000	0.465614000	6	3.988370000	1.908287000	0.957739000
1	3.261050000	3.225616000	-0.558286000	1	4.704653000	1.792685000	0.140516000
1	-3.369296000	1.533168000	0.205815000	1	-3.568573000	1.513867000	0.238068000
6	-3.551333000	1.435228000	-1.928704000	6	-3.592560000	1.273517000	-1.899020000
6	-3.524217000	0.674450000	-3.106165000	6	-3.676428000	0.408837000	-3.000444000
1	-3.306870000	-0.394931000	-3.064092000	1	-3.622681000	-0.671493000	-2.854120000
6	-3.748438000	1.282617000	-4.341393000	6	-3.803806000	0.921007000	-4.293547000
1	-3.717694000	0.685252000	-5.253756000	1	-3.861497000	0.238553000	-5.143215000
6	-4.002980000	2.657406000	-4.410316000	6	-3.849181000	2.304301000	-4.499080000
1	-4.173563000	3.133212000	-5.377150000	1	-3.944330000	2.704567000	-5.509824000
6	-4.032464000	3.419367000	-3.239433000	6	-3.767003000	3.171213000	-3.404770000
1	-4.225331000	4.492015000	-3.288222000	1	-3.793798000	4.251210000	-3.558489000
6	-3.805167000	2.808555000	-2.002678000	6	-3.637073000	2.657224000	-2.111857000
1	-3.807426000	3.402274000	-1.086350000	1	-3.539877000	3.326140000	-1.254734000
17	-0.776306000	2.926081000	1.130603000	17	-1.661404000	3.287133000	1.014625000

17	0.096631000	2.299020000	-2.815776000	17	0.610661000	3.370723000	-1.778203000
L10 Ni(II)Cl_2				[**L10**Ni(II)Cl_2]$^-$			
28	-0.586262000	1.773126000	-0.300506000	28	-0.670495000	1.897216000	-0.324088000
7	0.946076000	0.567981000	-0.453879000	7	0.829708000	0.641146000	-0.395256000
7	-1.793795000	0.247446000	-0.165981000	7	-1.901523000	0.413113000	-0.174605000
6	2.336230000	1.095126000	-0.471159000	6	2.254487000	1.065059000	-0.382470000
6	3.182303000	-0.199552000	-0.533254000	6	2.995994000	-0.215473000	-0.819065000
1	3.811938000	-0.350168000	0.351265000	1	3.859543000	-0.473141000	-0.197385000
1	3.777840000	-0.283344000	-1.447980000	1	3.281527000	-0.196582000	-1.879376000
8	2.193068000	-1.290607000	-0.552655000	8	2.002783000	-1.278769000	-0.651042000
6	0.979190000	-0.715740000	-0.480002000	6	0.808435000	-0.644314000	-0.484856000
6	-0.183048000	-1.680182000	-0.445697000	6	-0.372656000	-1.579520000	-0.399135000
6	-1.497076000	-1.005152000	-0.105374000	6	-1.670378000	-0.855522000	-0.130572000
8	-2.511671000	-1.854169000	0.127383000	8	-2.745275000	-1.679201000	0.036031000
6	-3.703879000	-1.028702000	0.372085000	6	-3.870972000	-0.787705000	0.329864000
1	-3.959172000	-1.136061000	1.432656000	1	-4.036301000	-0.812021000	1.415729000
1	-4.507801000	-1.419841000	-0.260195000	1	-4.749055000	-1.172706000	-0.199448000
6	-3.263786000	0.407178000	0.006697000	6	-3.390059000	0.589252000	-0.146137000
6	0.142032000	-2.772008000	0.611670000	6	-0.076733000	-2.583395000	0.763214000
1	0.983145000	-3.376876000	0.255734000	1	0.752454000	-3.236569000	0.468466000
1	-0.732339000	-3.430062000	0.710669000	1	-0.971944000	-3.197471000	0.926409000
6	0.474723000	-2.148690000	1.946345000	6	0.276689000	-1.815478000	2.012753000
7	-0.354643000	-1.175924000	2.358203000	7	-0.699878000	-1.040873000	2.518918000
6	-0.113256000	-0.540851000	3.520940000	6	-0.423760000	-0.227633000	3.556509000
6	-1.048631000	0.574953000	3.882550000	6	-1.525515000	0.691871000	3.997626000
1	-0.990737000	1.372688000	3.124814000	1	-1.689507000	1.464944000	3.226439000
1	-2.088353000	0.216738000	3.891925000	1	-2.469217000	0.140095000	4.111636000
1	-0.807726000	1.001220000	4.863873000	1	-1.280704000	1.191760000	4.943228000
6	0.976226000	-0.895367000	4.329947000	6	0.844036000	-0.207800000	4.155596000
1	1.149594000	-0.370237000	5.269623000	1	1.039040000	0.461891000	4.993061000
6	1.837003000	-1.907078000	3.905589000	6	1.847957000	-1.030435000	3.649743000
1	2.698871000	-2.188635000	4.512381000	1	2.845396000	-1.020829000	4.091716000
6	1.593691000	-2.542757000	2.687012000	6	1.568413000	-1.841825000	2.550120000

1	2.256609000	-3.322624000	2.311666000	1	2.335487000	-2.473206000	2.101830000
6	-0.374370000	-2.234842000	-1.878400000	6	-0.558623000	-2.251281000	-1.776436000
6	-0.525652000	-1.314206000	-2.926350000	6	-0.689248000	-1.412129000	-2.894026000
1	-0.484494000	-0.240354000	-2.727129000	1	-0.632100000	-0.328999000	-2.763125000
6	-0.742014000	-1.763828000	-4.229020000	6	-0.902811000	-1.952615000	-4.161589000
1	-0.860056000	-1.038336000	-5.034932000	1	-1.005955000	-1.288864000	-5.021177000
6	-0.811573000	-3.134901000	-4.495860000	6	-0.990779000	-3.339823000	-4.325997000
1	-0.982211000	-3.487672000	-5.513941000	1	-1.158848000	-3.765187000	-5.316573000
6	-0.662473000	-4.051671000	-3.452210000	6	-0.863844000	-4.177159000	-3.214974000
1	-0.716443000	-5.122898000	-3.651203000	1	-0.932937000	-5.259629000	-3.334302000
6	-0.445563000	-3.605238000	-2.144515000	6	-0.650468000	-3.635709000	-1.941974000
1	-0.337114000	-4.334803000	-1.343237000	1	-0.560455000	-4.301832000	-1.084489000
1	2.455638000	1.699566000	-1.380841000	1	2.360104000	1.864886000	-1.131766000
6	2.528457000	1.969073000	0.746675000	6	2.657651000	1.620259000	0.976490000
6	2.671000000	3.353074000	0.603621000	6	1.706934000	2.156486000	1.853657000
1	2.707738000	3.787709000	-0.397192000	1	0.647619000	2.135573000	1.575975000
6	2.741721000	4.174751000	1.732580000	6	2.095946000	2.714963000	3.072408000
1	2.846512000	5.253863000	1.612604000	1	1.335459000	3.126023000	3.738426000
6	2.663084000	3.614884000	3.010332000	6	3.443092000	2.737211000	3.442011000
1	2.707219000	4.256113000	3.891818000	1	3.746901000	3.166900000	4.398114000
6	2.519449000	2.230227000	3.157607000	6	4.400787000	2.204849000	2.572712000
1	2.448758000	1.787922000	4.152150000	1	5.457660000	2.219392000	2.845001000
6	2.453621000	1.411835000	2.030823000	6	4.010301000	1.657780000	1.347172000
1	2.323664000	0.335126000	2.154611000	1	4.774906000	1.264687000	0.674055000
1	-3.438247000	1.102411000	0.837926000	1	-3.620649000	1.384187000	0.573418000
6	-3.850944000	0.978259000	-1.263192000	6	-3.820489000	1.007497000	-1.534880000
6	-3.828581000	0.235819000	-2.452593000	6	-3.966335000	0.066784000	-2.565069000
1	-3.425581000	-0.778975000	-2.459805000	1	-3.827532000	-0.996128000	-2.360117000
6	-4.297554000	0.795842000	-3.641023000	6	-4.266766000	0.481504000	-3.864758000
1	-4.268266000	0.213938000	-4.563426000	1	-4.372294000	-0.259573000	-4.658917000
6	-4.795096000	2.104175000	-3.650875000	6	-4.423138000	1.842516000	-4.148561000
1	-5.156480000	2.544152000	-4.581555000	1	-4.654510000	2.166742000	-5.164586000
6	-4.822733000	2.846759000	-2.467417000	6	-4.276355000	2.785550000	-3.126109000
1	-5.204597000	3.868729000	-2.470626000	1	-4.388804000	3.849300000	-3.342166000

6	-4.350104000	2.284454000	-1.278044000	6	-3.973863000	2.369359000	-1.826905000
1	-4.347475000	2.868304000	-0.355759000	1	-3.826850000	3.099031000	-1.028050000
17	-1.332542000	3.288606000	1.133176000	17	-1.898244000	3.369624000	1.109599000
17	-0.527895000	2.480304000	-2.441203000	17	0.301730000	3.491942000	-1.738030000
Conformer of **L2**Ni(II)Cl_2: pyridine rotation				Conformer of **L2**Ni(II)Cl_2: κ^3 coordination			
28	0.343251000	1.035068000	-0.818641000	28	-0.108776000	-0.226416000	-1.638357000
7	0.182299000	-0.944153000	-0.361407000	7	0.106943000	-1.146549000	0.071764000
7	-1.652464000	1.090387000	-0.671216000	7	-1.428223000	0.985970000	-0.858940000
6	0.907789000	-2.120159000	-0.911252000	6	0.925730000	-2.376421000	0.210227000
6	-0.005638000	-3.284949000	-0.480636000	6	0.826645000	-2.656583000	1.726119000
1	0.521073000	-4.129716000	-0.027010000	1	1.718448000	-2.322861000	2.270916000
1	-0.657376000	-3.630963000	-1.292203000	1	0.581460000	-3.693383000	1.972801000
8	-0.882977000	-2.702358000	0.548862000	8	-0.291723000	-1.813196000	2.173963000
6	-0.732973000	-1.370709000	0.432860000	6	-0.531747000	-0.954205000	1.170724000
6	-1.677106000	-0.479405000	1.234149000	6	-1.543741000	0.116459000	1.502584000
6	-2.313708000	0.485237000	0.248099000	6	-1.842713000	1.049132000	0.354108000
8	-3.596832000	0.827594000	0.423241000	8	-2.691966000	2.047762000	0.656881000
6	-3.847866000	1.928289000	-0.528007000	6	-2.926184000	2.794444000	-0.588977000
1	-3.983388000	2.838429000	0.068129000	1	-2.610167000	3.828179000	-0.414357000
1	-4.763037000	1.682340000	-1.075770000	1	-4.001697000	2.752566000	-0.794335000
6	-2.580027000	1.969626000	-1.417770000	6	-2.069505000	2.067455000	-1.651535000
6	-0.882599000	0.487704000	2.218978000	6	-0.972720000	0.943771000	2.699727000
1	-1.275676000	0.343945000	3.228187000	1	-0.933685000	0.296942000	3.582439000
1	-1.115819000	1.521852000	1.936574000	1	-1.656134000	1.778773000	2.898377000
6	0.614403000	0.362959000	2.267137000	6	0.420318000	1.442566000	2.404019000
7	1.336399000	0.944772000	1.282821000	7	1.427470000	0.794293000	3.011999000
6	2.677690000	0.933612000	1.404075000	6	2.680518000	1.173033000	2.728338000
6	3.479189000	1.688929000	0.357381000	6	3.748903000	0.413084000	3.492434000
9	3.049580000	1.443916000	-0.904700000	9	3.620234000	-0.933911000	3.349937000
9	3.411871000	3.030890000	0.564899000	9	5.001798000	0.741058000	3.086756000
9	4.795677000	1.355927000	0.400359000	9	3.678279000	0.672875000	4.829471000
6	3.356240000	0.336915000	2.462403000	6	3.012893000	2.182298000	1.828924000
1	4.441798000	0.364966000	2.504380000	1	4.051139000	2.434203000	1.623486000

6	2.608861000	-0.297083000	3.450658000	6	1.961877000	2.857422000	1.205368000
1	3.102535000	-0.790896000	4.287115000	1	2.165312000	3.657594000	0.494467000
6	1.223631000	-0.276618000	3.351979000	6	0.653301000	2.495257000	1.505365000
1	0.602052000	-0.739248000	4.117553000	1	-0.181772000	3.025527000	1.049934000
6	-2.727233000	-1.361463000	1.919212000	6	-2.876498000	-0.597701000	1.802697000
6	-2.675438000	-1.686589000	3.276906000	6	-3.395575000	-1.436921000	0.805646000
1	-1.896033000	-1.287470000	3.923821000	1	-2.849403000	-1.576853000	-0.130933000
6	-3.619589000	-2.552525000	3.839405000	6	-4.608812000	-2.093855000	1.005435000
1	-3.560869000	-2.790017000	4.902300000	1	-5.003853000	-2.746722000	0.226325000
6	-4.624082000	-3.109728000	3.048694000	6	-5.312880000	-1.914414000	2.200752000
1	-5.362499000	-3.781210000	3.488633000	1	-6.262431000	-2.427271000	2.358964000
6	-4.671588000	-2.805437000	1.684316000	6	-4.796009000	-1.076734000	3.191555000
1	-5.444261000	-3.241708000	1.050035000	1	-5.340135000	-0.932252000	4.125773000
6	-3.728535000	-1.945393000	1.126829000	6	-3.578885000	-0.416619000	2.994985000
1	-3.770106000	-1.731727000	0.058202000	1	-3.190768000	0.235110000	3.776513000
1	0.934983000	-2.007025000	-2.002108000	1	0.424099000	-3.161137000	-0.376153000
6	2.323399000	-2.173968000	-0.377659000	6	2.334094000	-2.195867000	-0.294608000
6	2.602132000	-2.680425000	0.898336000	6	2.978459000	-3.247394000	-0.956032000
1	1.793391000	-3.037278000	1.538391000	1	2.439452000	-4.179113000	-1.139148000
6	3.915398000	-2.729200000	1.367130000	6	4.299887000	-3.103314000	-1.387076000
1	4.120401000	-3.125670000	2.362477000	1	4.795132000	-3.927151000	-1.902969000
6	4.963382000	-2.263181000	0.568252000	6	4.981585000	-1.902364000	-1.166212000
1	5.989730000	-2.299775000	0.936065000	1	6.011048000	-1.787465000	-1.508451000
6	4.690452000	-1.744165000	-0.699837000	6	4.335812000	-0.846181000	-0.515942000
1	5.502092000	-1.371048000	-1.325573000	1	4.855120000	0.099165000	-0.353133000
6	3.376213000	-1.701567000	-1.169736000	6	3.019118000	-0.994404000	-0.082011000
1	3.155735000	-1.292657000	-2.157194000	1	2.510731000	-0.164456000	0.406153000
1	-2.144714000	2.975756000	-1.450041000	1	-1.267762000	2.711938000	-2.036131000
6	-2.789907000	1.461944000	-2.825703000	6	-2.826097000	1.463605000	-2.810462000
6	-2.714504000	2.349213000	-3.903182000	6	-2.358460000	1.641376000	-4.115954000
1	-2.477350000	3.398451000	-3.716760000	1	-1.469126000	2.250507000	-4.287709000
6	-2.919080000	1.895252000	-5.209109000	6	-3.010993000	1.027668000	-5.188497000
1	-2.849067000	2.594037000	-6.044032000	1	-2.637509000	1.168347000	-6.203686000
6	-3.199275000	0.546783000	-5.444339000	6	-4.134389000	0.229797000	-4.958117000

1	-3.350852000	0.188544000	-6.463622000	1	-4.641829000	-0.254612000	-5.793519000
6	-3.276221000	-0.345080000	-4.368618000	6	-4.604646000	0.047874000	-3.652816000
1	-3.486606000	-1.400634000	-4.547583000	1	-5.476830000	-0.580577000	-3.467960000
6	-3.072030000	0.111314000	-3.066514000	6	-3.952646000	0.661963000	-2.583807000
1	-3.109397000	-0.595539000	-2.235113000	1	-4.314312000	0.498738000	-1.566525000
17	0.682740000	0.571227000	-3.047577000	17	1.378244000	1.280571000	-2.316382000
17	0.446432000	3.352488000	-0.898895000	17	-1.103299000	-1.931806000	-2.686133000
L2Ni(I)Cl, initial GS geometry from conformer search				**L2**Ni(I)Cl, final optimized geometry			
28	-0.375429000	1.470776000	-0.144718000	28	-0.333219000	1.440041000	-0.088914000
7	1.448482000	1.306423000	-0.747579000	7	1.485733000	1.278940000	-0.730371000
7	-0.146708000	-0.013938000	1.036450000	7	-0.109576000	-0.071862000	1.062089000
6	2.222350000	2.355073000	-1.475268000	6	2.258094000	2.337662000	-1.431166000
6	3.237474000	1.510641000	-2.271440000	6	3.415913000	1.535923000	-2.080524000
1	4.270225000	1.868873000	-2.202959000	1	4.410456000	1.911326000	-1.816494000
1	2.951695000	1.389584000	-3.325175000	1	3.315164000	1.444977000	-3.168497000
8	3.186915000	0.181414000	-1.648375000	8	3.293742000	0.183868000	-1.514123000
6	2.087504000	0.194083000	-0.848447000	6	2.146092000	0.174806000	-0.800032000
6	1.733087000	-1.126586000	-0.208187000	6	1.756507000	-1.165011000	-0.216981000
6	0.701685000	-0.975859000	0.889337000	6	0.731490000	-1.035402000	0.889135000
8	0.575496000	-2.043565000	1.710093000	8	0.612288000	-2.111829000	1.695412000
6	-0.703354000	-1.862502000	2.406196000	6	-0.630806000	-1.916678000	2.457477000
1	-0.547444000	-2.128223000	3.456522000	1	-0.419426000	-2.159645000	3.502782000
1	-1.414679000	-2.552937000	1.934699000	1	-1.363154000	-2.618296000	2.040008000
6	-1.055460000	-0.382832000	2.172149000	6	-0.993179000	-0.441330000	2.218718000
6	1.076227000	-2.054007000	-1.306695000	6	1.077260000	-2.021909000	-1.363970000
1	1.129258000	-3.090388000	-0.954458000	1	1.144579000	-3.077088000	-1.076658000
1	1.668367000	-1.955134000	-2.227610000	1	1.653667000	-1.867723000	-2.286515000
6	2.794816000	3.311508000	-0.454119000	6	2.694209000	3.406971000	-0.455848000
6	2.098903000	4.489290000	-0.157177000	6	2.461873000	4.756488000	-0.741774000
1	1.170514000	4.704859000	-0.690190000	1	1.943244000	5.026254000	-1.663801000
6	2.568418000	5.350822000	0.836228000	6	2.873261000	5.750876000	0.151043000
1	2.019739000	6.266390000	1.061232000	1	2.682852000	6.800100000	-0.079860000
6	3.732131000	5.039125000	1.544042000	6	3.517829000	5.399905000	1.340434000

1	4.099193000	5.713403000	2.319119000	1	3.834832000	6.174081000	2.040804000
6	4.423297000	3.857732000	1.259718000	6	3.750185000	4.050879000	1.633181000
1	5.329135000	3.606482000	1.813512000	1	4.248490000	3.770754000	2.562630000
6	3.954606000	2.996004000	0.266732000	6	3.339903000	3.060252000	0.739653000
1	4.492994000	2.067194000	0.064686000	1	3.515740000	2.009545000	0.979291000
1	1.518472000	2.888437000	-2.127454000	1	1.606928000	2.788490000	-2.190887000
6	-2.483387000	-0.048715000	1.804745000	6	-2.432031000	-0.113278000	1.888116000
6	-2.744997000	1.245197000	1.327576000	6	-2.720578000	1.202216000	1.491357000
1	-1.949372000	2.002436000	1.325348000	1	-1.929438000	1.961329000	1.514665000
6	-4.013336000	1.593415000	0.865059000	6	-4.006252000	1.562051000	1.086613000
1	-4.175457000	2.590188000	0.454830000	1	-4.200988000	2.582329000	0.754049000
6	-5.053282000	0.661906000	0.923257000	6	-5.034763000	0.614836000	1.112381000
1	-6.049327000	0.929970000	0.568069000	1	-6.042954000	0.891107000	0.800219000
6	-4.814788000	-0.611257000	1.444504000	6	-4.766295000	-0.684026000	1.549552000
1	-5.620965000	-1.343031000	1.497855000	1	-5.563694000	-1.426995000	1.582720000
6	-3.531913000	-0.968818000	1.871742000	6	-3.469070000	-1.048635000	1.927139000
1	-3.363274000	-1.978796000	2.243671000	1	-3.282140000	-2.072905000	2.247113000
1	-0.748973000	0.235850000	3.033322000	1	-0.671477000	0.181882000	3.069300000
17	-1.193965000	3.102198000	-1.344346000	17	-1.180136000	3.190209000	-1.129058000
6	-0.383777000	-1.740234000	-1.530757000	6	-0.381938000	-1.698804000	-1.556414000
7	-1.240811000	-2.656509000	-1.052497000	7	-1.240607000	-2.624888000	-1.098283000
6	-0.831471000	-0.534955000	-2.103359000	6	-0.829480000	-0.481821000	-2.106289000
6	-2.553515000	-2.405165000	-1.137266000	6	-2.554486000	-2.368097000	-1.173646000
6	-2.202795000	-0.271054000	-2.142968000	6	-2.201462000	-0.222768000	-2.149432000
6	-3.091772000	-1.223368000	-1.649465000	6	-3.093092000	-1.180014000	-1.667570000
1	-0.131047000	0.177452000	-2.533725000	1	-0.121693000	0.223783000	-2.536257000
1	-2.556123000	0.684009000	-2.530031000	1	-2.565499000	0.723542000	-2.547525000
1	-4.165716000	-1.052542000	-1.650193000	1	-4.167577000	-1.011153000	-1.679772000
6	-3.436461000	-3.547542000	-0.674961000	6	-3.436120000	-3.522054000	-0.746521000
9	-3.113948000	-3.980542000	0.578036000	9	-3.091270000	-4.024936000	0.472255000
9	-4.751667000	-3.201921000	-0.651044000	9	-4.748270000	-3.178974000	-0.683120000
9	-3.322456000	-4.624457000	-1.497978000	9	-3.343286000	-4.564920000	-1.627605000
6	3.030119000	-1.694048000	0.389792000	6	3.034305000	-1.811806000	0.342519000
6	3.614023000	-0.983095000	1.448446000	6	3.606003000	-1.238619000	1.488163000

6	3.663720000	-2.838248000	-0.095129000	6	3.666540000	-2.898132000	-0.265864000
6	4.807249000	-1.416989000	2.020959000	6	4.785588000	-1.751745000	2.025168000
6	4.862021000	-3.274475000	0.478940000	6	4.851458000	-3.413246000	0.271966000
6	5.435669000	-2.568724000	1.536616000	6	5.412765000	-2.845081000	1.417017000
1	3.126679000	-0.078822000	1.821283000	1	3.121061000	-0.382421000	1.963221000
1	3.235968000	-3.398825000	-0.924924000	1	3.252223000	-3.350807000	-1.165590000
1	5.247784000	-0.856600000	2.846538000	1	5.216062000	-1.298301000	2.919066000
1	5.347258000	-4.171750000	0.092883000	1	5.335333000	-4.262720000	-0.212073000
1	6.369402000	-2.912804000	1.982900000	1	6.335492000	-3.250027000	1.834764000
L2Ni(I)Cl, conf 8 from conformer search				**L2**Ni(I)Cl, final optimized geometry from conf 8			
28	-0.272272000	1.126165000	0.545692000	28	-0.248978000	1.329047000	1.414981000
7	0.923734000	0.583300000	-1.230013000	7	0.507397000	1.329404000	-0.328840000
7	-0.041780000	-0.910126000	1.196336000	7	-0.284602000	-0.583887000	1.429072000
6	1.596043000	1.720949000	-1.864760000	6	0.821678000	2.576430000	-1.101070000
6	3.082788000	1.310072000	-1.787918000	6	1.148692000	2.010236000	-2.489974000
1	3.600339000	1.821130000	-0.970590000	1	2.003510000	2.482753000	-2.985391000
1	3.626403000	1.439008000	-2.723920000	1	0.271486000	2.010638000	-3.150943000
8	3.040569000	-0.079536000	-1.467392000	8	1.499468000	0.612502000	-2.230082000
6	1.787344000	-0.331468000	-1.050004000	6	0.985480000	0.338007000	-1.002186000
6	1.528695000	-1.729813000	-0.554410000	6	1.251140000	-1.062668000	-0.495640000
6	0.413570000	-1.828424000	0.450865000	6	0.381114000	-1.401019000	0.689655000
8	-0.017808000	-3.080729000	0.700173000	8	0.316203000	-2.724952000	1.012184000
6	-1.047690000	-2.965372000	1.680766000	6	-0.416814000	-2.775714000	2.282071000
1	-0.895614000	-3.732360000	2.440138000	1	0.322480000	-2.935593000	3.079039000
1	-2.008674000	-3.116143000	1.176683000	1	-1.108625000	-3.623069000	2.235530000
6	-0.894408000	-1.523536000	2.212384000	6	-1.096450000	-1.400324000	2.385833000
6	1.160750000	-2.571695000	-1.798284000	6	0.977595000	-2.104016000	-1.610418000
1	0.844745000	-3.561812000	-1.465746000	1	1.343201000	-3.085616000	-1.287242000
1	2.022204000	-2.656945000	-2.460768000	1	1.540225000	-1.805831000	-2.507065000
6	1.190676000	2.996776000	-1.162430000	6	1.946362000	3.262948000	-0.358304000
6	-0.163829000	3.135059000	-0.821292000	6	1.628849000	4.132802000	0.693029000
1	-0.895453000	2.448354000	-1.247967000	1	0.583803000	4.365474000	0.904821000
6	-0.591612000	4.245417000	-0.103848000	6	2.636478000	4.665295000	1.498120000

1	-1.637399000	4.349957000	0.149070000	1	2.373416000	5.328824000	2.322352000
6	0.319724000	5.213977000	0.282757000	6	3.972323000	4.332477000	1.259177000
1	-0.007042000	6.063158000	0.864080000	1	4.760529000	4.747415000	1.889136000
6	1.646296000	5.096458000	-0.089158000	6	4.295533000	3.460687000	0.216220000
1	2.355859000	5.859341000	0.193982000	1	5.334958000	3.185357000	0.032783000
6	2.082126000	3.995155000	-0.809724000	6	3.286715000	2.923515000	-0.585167000
1	3.123831000	3.921505000	-1.082832000	1	3.550706000	2.214106000	-1.371052000
1	1.247250000	1.759242000	-2.910213000	1	-0.071485000	3.213328000	-1.121921000
6	-2.158723000	-0.736731000	2.458965000	6	-2.544944000	-1.321200000	1.950691000
6	-3.387115000	-1.347724000	2.666217000	6	-3.095966000	-2.236421000	1.046068000
1	-3.471663000	-2.423884000	2.657236000	1	-2.497268000	-3.064390000	0.661632000
6	-4.519263000	-0.581811000	2.890587000	6	-4.413751000	-2.088770000	0.607892000
1	-5.470878000	-1.069945000	3.041934000	1	-4.836209000	-2.814189000	-0.088552000
6	-4.436240000	0.798894000	2.918884000	6	-5.185235000	-1.013883000	1.054248000
1	-5.323181000	1.392064000	3.087062000	1	-6.211883000	-0.894970000	0.705374000
6	-3.208589000	1.415089000	2.740952000	6	-4.632688000	-0.087545000	1.942542000
1	-3.130831000	2.491648000	2.781427000	1	-5.222480000	0.764020000	2.283708000
6	-2.074262000	0.653350000	2.520190000	6	-3.320831000	-0.240564000	2.391816000
1	-1.096381000	1.150424000	2.421895000	1	-2.875511000	0.501482000	3.058378000
1	-0.308726000	-1.512181000	3.145875000	1	-0.983559000	-0.960325000	3.384602000
17	1.389271000	1.823210000	1.763571000	17	-0.899563000	2.437566000	3.126114000
6	0.029140000	-1.875078000	-2.491598000	6	-0.490938000	-2.188877000	-1.944127000
7	-0.970490000	-1.496235000	-1.709969000	7	-1.157648000	-1.027360000	-1.992862000
6	0.051267000	-1.552366000	-3.847077000	6	-1.129352000	-3.413954000	-2.183844000
6	-1.929520000	-0.741157000	-2.211939000	6	-2.462779000	-1.045263000	-2.273591000
6	-0.978741000	-0.793220000	-4.375324000	6	-2.485839000	-3.418400000	-2.500612000
6	-1.991853000	-0.345397000	-3.538273000	6	-3.180121000	-2.207744000	-2.547755000
1	0.869121000	-1.880371000	-4.470113000	1	-0.565784000	-4.345059000	-2.117240000
1	-0.983641000	-0.527176000	-5.421768000	1	-3.004638000	-4.357385000	-2.696481000
1	-2.791240000	0.282488000	-3.897039000	1	-4.242880000	-2.165395000	-2.775554000
6	-2.913417000	-0.254242000	-1.178395000	6	-3.121959000	0.324547000	-2.270762000
9	-3.963386000	0.390298000	-1.711063000	9	-2.570783000	1.132291000	-3.223984000
9	-3.410135000	-1.239922000	-0.425586000	9	-4.452804000	0.241663000	-2.540119000
9	-2.328041000	0.626980000	-0.336702000	9	-2.978307000	0.948457000	-1.084289000

6	2.755600000	-2.205596000	0.213149000	6	2.728520000	-1.036598000	-0.028300000
6	3.216499000	-1.387553000	1.240887000	6	3.062182000	-0.201319000	1.048631000
6	3.395124000	-3.407770000	-0.043865000	6	3.736642000	-1.757033000	-0.675445000
6	4.317510000	-1.764364000	1.987116000	6	4.384826000	-0.094230000	1.472986000
6	4.497057000	-3.780717000	0.709279000	6	5.062832000	-1.649521000	-0.245647000
6	4.962026000	-2.961737000	1.722261000	6	5.390601000	-0.819245000	0.827390000
1	2.709229000	-0.456549000	1.456181000	1	2.281032000	0.386247000	1.539791000
1	3.048196000	-4.065170000	-0.825879000	1	3.503487000	-2.402571000	-1.521189000
1	4.668231000	-1.119407000	2.778190000	1	4.627950000	0.569050000	2.303508000
1	4.991600000	-4.718144000	0.499814000	1	5.841274000	-2.217116000	-0.757454000
1	5.821909000	-3.257476000	2.305119000	1	6.426813000	-0.734967000	1.157587000

4.8.3 *Supplementary Information to EPR Studies*

Experimental Procedure

Continuous wave X-band EPR spectra were collected with a Bruker EMX spectrometer. All spectra were collected at 77K by inserting the quartz Norell EPR tube that contained the sample into a liquid N_2 immersion dewar. Unless otherwise noted, the EPR spectra were collected at 0.5 mW microwave power and 4G modulation amplitude. For quantitative EPR, additional spectra were collected at 2 mW and 8 mW to ensure EPR absorption fell under a linear response region. All reported spectra were averaged over four scans. A linear baseline subtraction was applied to the EPR spectra using SpinCount software (v 7.0.8508.34436). Selected spectra were simulated with EasySpin software (v 5.2.35).

A representative procedure for monitoring EPR is described. This procedure was designed to enable the collection of multiple aliquots for EPR analysis and to minimize the possible speciation change or disturbance to the reaction during sample preparation,

thereby improving the consistency of qEPR results: An N_2-filled glove box was set to active purging. Then, in this glovebox, 22.8 mg (1 equiv., 30 μmol) of **L2**$NiBr_2$, 7.5 mL of 2-MeTHF, and 1 dram stir bar were added to a 20 mL scintillation vial. The vial was placed at the center of a stir plate and stirred at 500 rpm until all solids had been dissolved. Separately, 21.7 mg (2.2 equiv., 66 μmol) of $Co(Cp^*)_2$ was measured with a weight paper that had been folded diagonally. A filter syringe was assembled by removing the plunger of a 1mL syringe and capping this syringe with a syringe filter and a long hypodermic needle.Additionally, seven 1 mL syringes capped with a long hypodermic needle were prepared for use. At this stage, the stir rate was changed to 100 rpm. Once a steady stir rate was attained, all of $Co(Cp^*)_2$ was directly added into the vial at once by tilting the folded weight paper above the center of the vial's opening without removing the vial from the center of the stir plate. Upon the addition of the reductant, the stopwatch was started. An immediate color change from pink to orange could be seen, and the solution became cloudy. Over the first 15 minutes, the cloudiness gradually subdued, and the color darkened to afford a transparent, dark red solution. As the first time point (15 minutes) approached, the small antechamber of the glovebox was filled and placed under a static status. A liquid N_2 dewar was filled and placed next to the opening of the small antechamber of the glovebox outside. Inside the glovebox, a prelabeled Norrel EPR tube was placed under a vertical position in a 125 mL Erlenmeyer flask. With the plunger removed, the filter syringe was inserted into the EPR tube. At the 15-minute time point, a 300 L aliquot was drawn from the bottle of the vial as close to the stir bar, using one of the seven syringes prepared. This aliquot was injected into the filter syringe through its top opening. Then, with the aid of the plunger, the aliquot was filtered to deliver approximately 200–250 μL of the filtrate

into the EPR tube. The EPR was sealed with a cap and immediately transferred out of the glovebox. Then, the EPR sample was slowly frozen by dipping the tip of the EPR tube into liquid N_2 for 15 seconds, after which the tube was fully immersed in liquid N_2. Then, in preparation for the next sample collection, the small antechamber was repeatedly partially refilled and evacuated until the next aliquot was drawn; for intervals less than 3 minutes, this may be accomplished by a second operator while the primary operator prepared the sample. This process was repeated 6 more times at 18-, 21-, 25-,30-, 35-, and 45-minute time-points. The EPR spectra were immediately collected for these samples.

Error Analysis

For analysis of the error associated with the quantified concentration, we considered the experimental error in mass, volume, and EPR signals. To start, we estimated an error of 0.5 mg s associated with measuring approximately 20 mg of materials. Similarly, an error of 0.2 mL was estimated for measuring 7.5 mL of 2MeTHF to afford a 4 mM solution. Propagating the errors accordingly, the uncertainty in concentration adds to a 2.2% relative error:

$$\frac{\sqrt{\left(\frac{0.5}{20}\right)^2 + \left(\frac{0.2}{7.5}\right)^2}}{7.5}$$

For an error associated with the signal, we considered the effect of baseline correction. In an ideal situation, the subtracting baseline contribution would generate a sigmoidal-like curve for double-integrated EPR intensity. However, in practice, we noted that a linear baseline correction was insufficient and, thus, introduced error to double integrated intensity depending on whether the baseline correction was applied to the EPR spectrum or the absorption spectrum (e.g., after first integration). To demonstrate this, the

baseline corrected EPR spectrum generated from the reduction of **L2**$NiBr_2$ by $Co(Cp^*)_2$ in 2-MeTHF after 15 minutes of stirring was shown. Integrating this baseline-corrected EPR spectrum resulted in an absorption spectrum with a non-zero baseline at highfield (purple trace) (e.g., for magnetic field > 3300 G); this non-zero baseline contributed to additional EPR double integrated signals. integral of the EPR spectrum) and the integrated intensity (double integral of the EPR spectrum). If a second baseline correction was applied to the absorption spectrum, then double integrated intensity showed the expected sigmoidal behavior with a plateauing intensity signal around 3300 G. However, doing so would result in unphysical negative absorption indeed at the low field region (C, blue trace). Thus, depending on whether a baseline correction was applied to the absorption spectrum, the value of double integrated intensity could show a difference up to $0.3*10^5$. As the "true value" likely existed between these two extremes, the uncertainty can be described as ± $0.15*10^5$. Then, propagating the errors yielded an absolute error of 0.06 mM with the calibration curve of

$$C\ (in\ mM) = \frac{x - 6 * 10^3}{1.54 * 10^5}$$

$$\frac{1.5 * 10^4 - 6 * 10^3}{1.54 * 10^5} = 0.058\ mM$$

$$C = \frac{x - 6 * 10^3}{1.54 * 10^5}$$

The combined error associated with a quantified concentration of Ni species C_{quant} would add in quadrature:

$$\sqrt{(C_{quant} * 0.022)^2 + 0.06^2}$$

For a typical quantified concentration of 1–2 mM, the absolute error ranges from 0.065 mM to 0.075 mM. Thus, an error of ±0.07 mM is ascribed for all points.

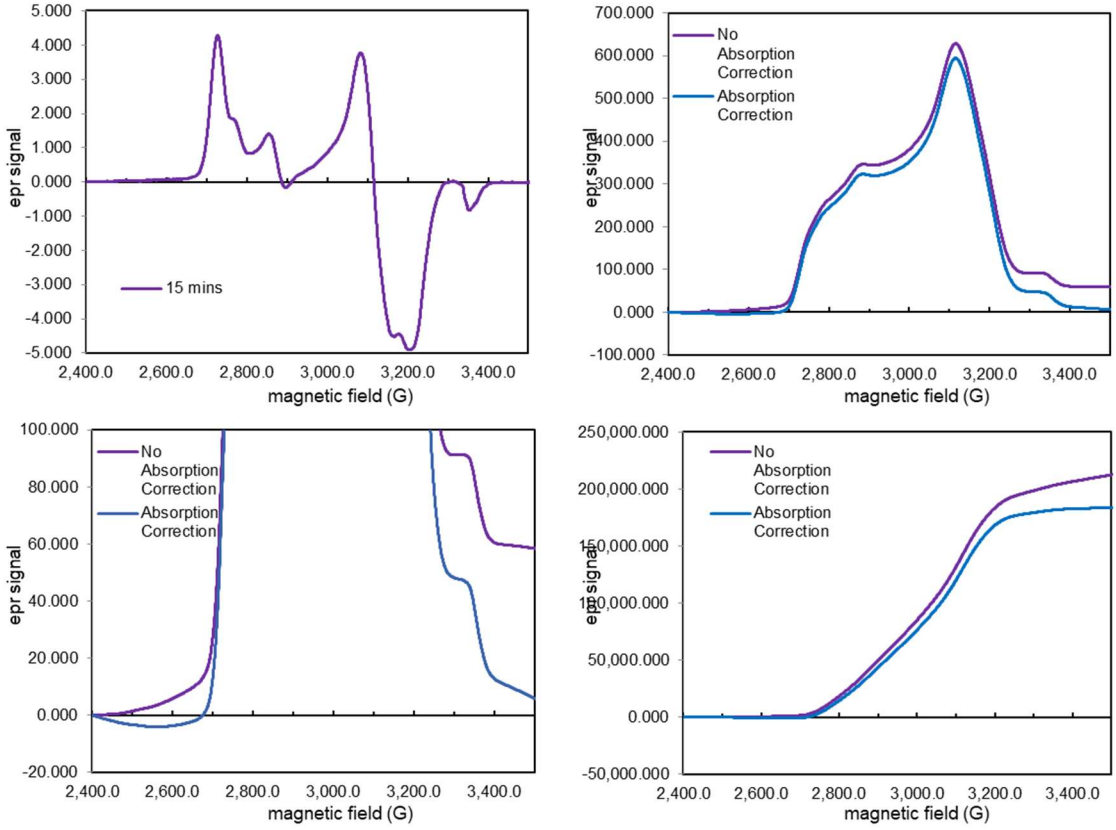

Figure S34. *Influence of baseline correction to EPR double integrated intensity. Purple: applying baseline correction to the EPR spectrum. Blue: applying baseline correction to the absorption spectra.*

EPR Decay of the IndaBoxNiBr$_2$

To test the applicability of Co(Cp*)$_2$ as a reductant to study the decay of Ni(I) species, 2.2 equivalents of Co(Cp*)$_2$ were added to a 4 mM solution of **IndaBox**NiBr$_2$. The addition of the reductant caused the dark purple solution to change to an opaque orangish heterogenous mixture rapidly. After 10–15 minutes of stirring, a strongly absorbing dark red solution could be formed, suggesting that initial reduction may be complete. Starting

at 15 minutes, qEPR spectra of the reaction aliquots revealed that the concentration of monomeric Ni(I) species steadily decreased over the next 30 minutes. This concentration change over time could be fitted with an exponential decay with an R^2 of 0.988, suggesting a first-order decay kinetics with respect to the monomeric EPR active species.

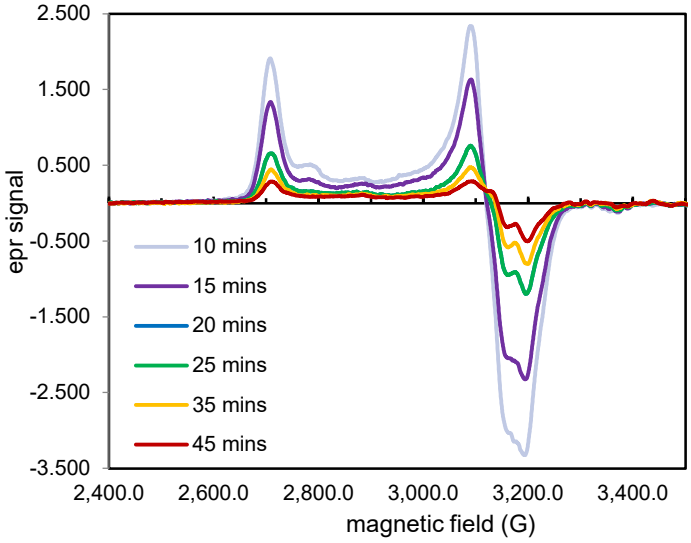

Figure S35. *Decay of* ***IndaBox****Ni(I) species. X band (9.31 GHz) EPR spectra were collected at 0.5 mW microwave power. The double-integrated intensities were 1.01*10^5, 7.32*10^4, 5.54*10^4, 4.13*10^4,3.06*10^4, and 1.92*10^4 at 10, 15, 20, 25, 35, and 45 minutes, respectively.*

Additional EPR Spectra

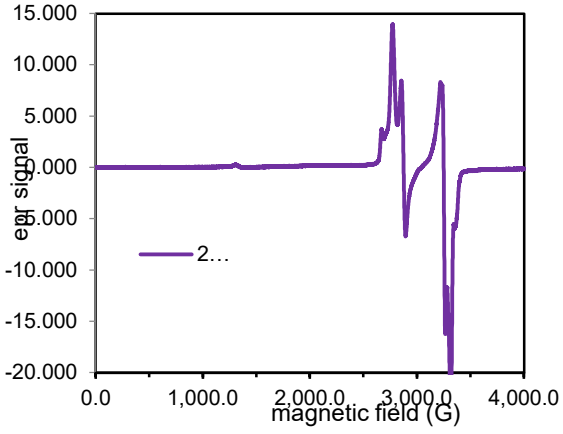

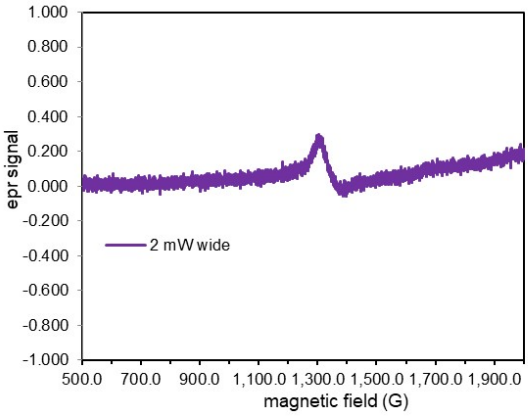

Figure S36. *Expanded scan of the isolated* ***L2****Ni(I) species. X band (9.39 GHz) EPR spectra were collected at 2 mW microwave power. Left: full scan. Right: oligomeric species.*

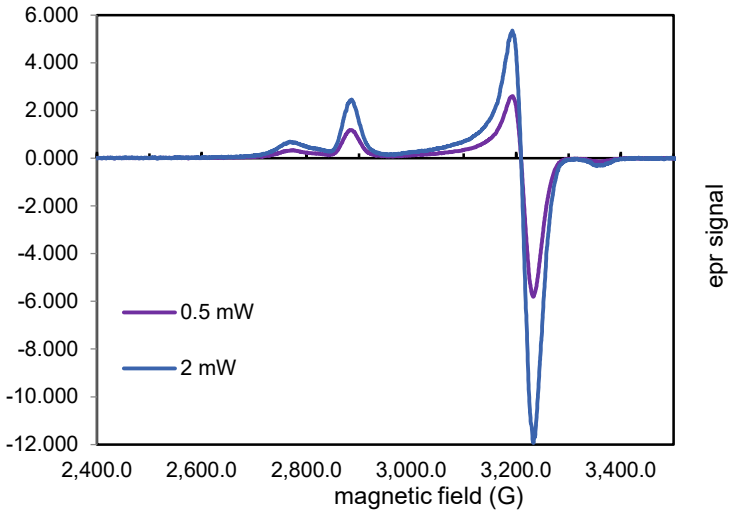

Figure S37. *Power dependency of the X band (9.39 GHz) EPR spectra of the reduced* ***L1****Ni(I) species at 19 minutes. The double-integrated intensities were 4.98*10^4 and 9.00*10^4 for spectra collected at 0.5 and 2 mW microwave power, respectively.*

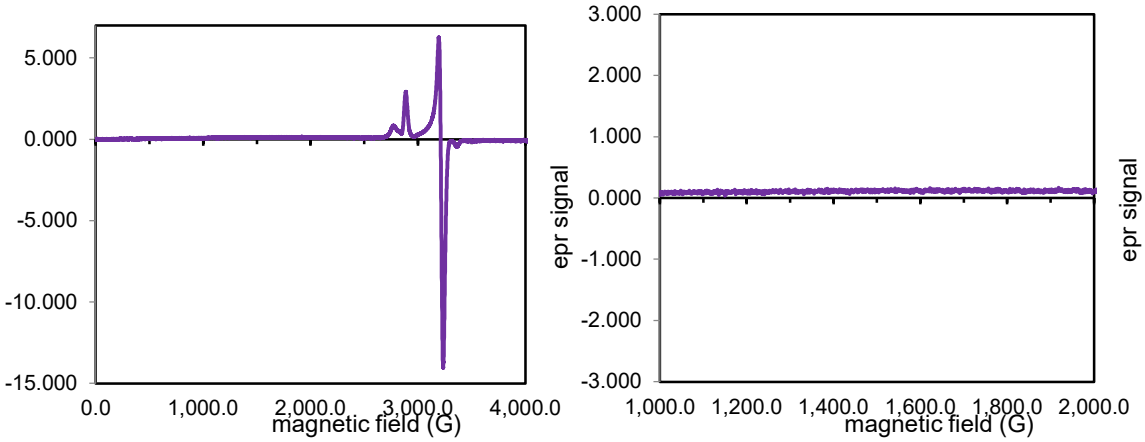

Figure S38. *Expanded scan for the reduced* ***L1****Ni(I) species at 19 minutes. X band (9.39 GHz) EPR spectra were collected at 2 mW microwave power. Left: full scan. Right: spectroscopic region of oligomeric species.*

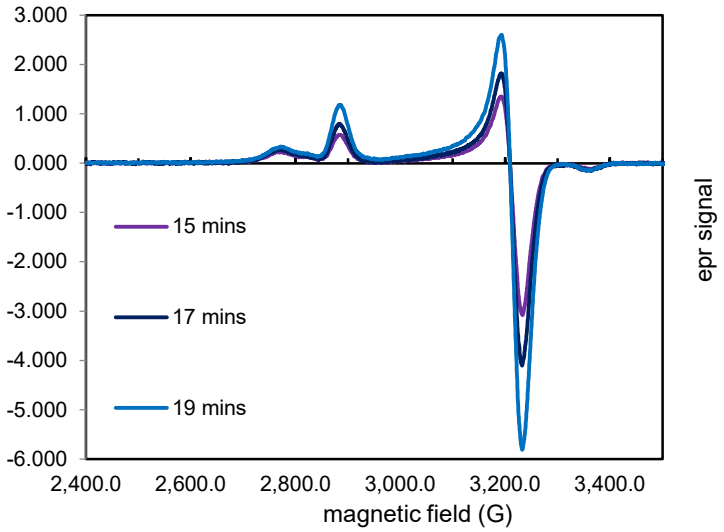

Figure S39. *Initial concentration increase of* ***L1****Ni(I) species. X band (9.39 GHz) EPR spectra were collected at 0.5 mW microwave power. The double-integrated intensities were 2.25*10^4, 3.22*10^4, and 4.98*10^4, 15, 17, and 19 minutes, respectively.*

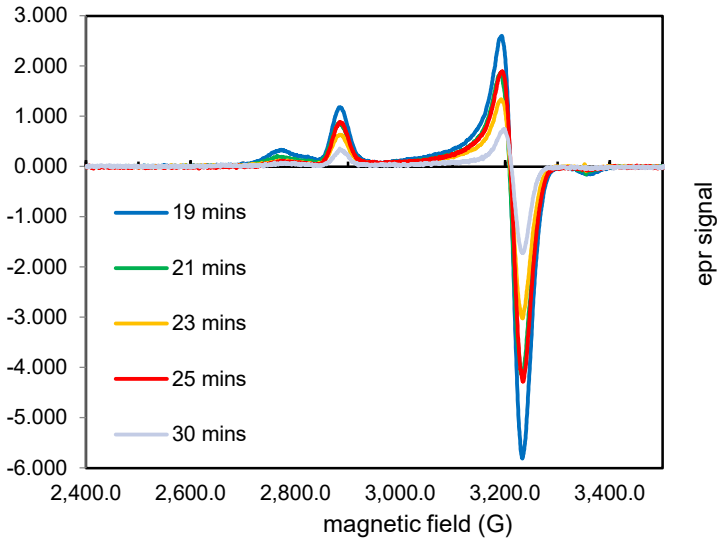

Figure S40. *Decay of* ***L1****Ni(I) species. X band (9.39 GHz) EPR spectra were collected at 0.5 mW microwave power. The double-integrated intensities were 4.98*10^4, 3.26*10^4, 2.59*10^4, 2.78*10^4, and 2.59*10^4 at 19, 21, 23, 25, and 30 minutes, respectively.*

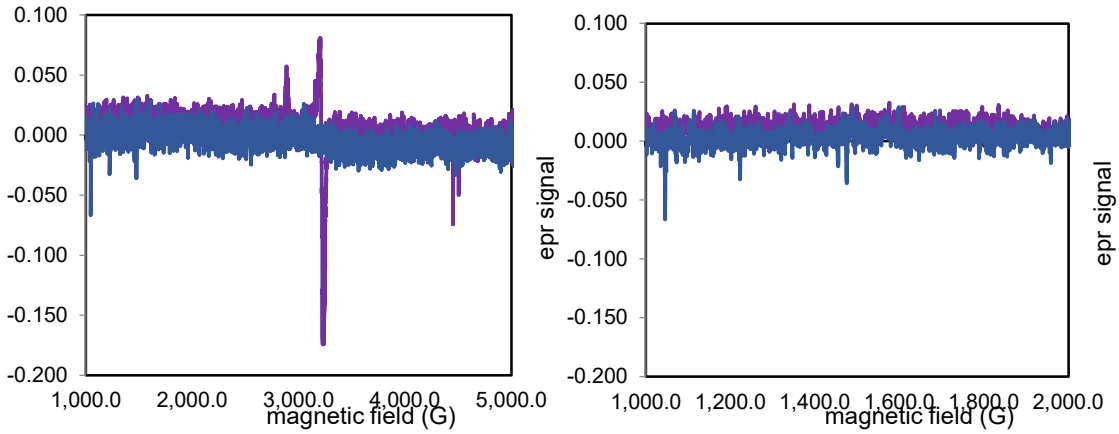

Figure S41. *Decay of **L1**Ni(I) species spectra at 35 and 45 minutes. X band (9.39 GHz) EPR spectra were collected at 2 mW microwave power. Right: Spectroscopic region of oligomeric species.*

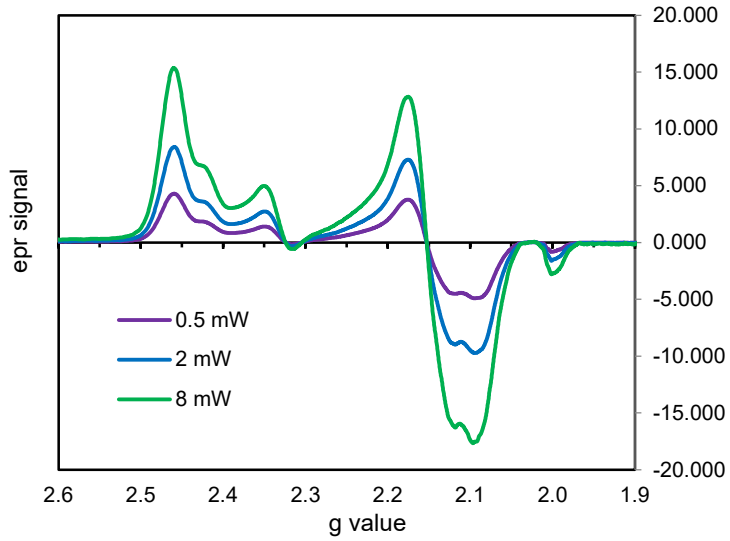

Figure S42. *Power dependency of the X band (9.39 GHz) EPR spectra of the reduced **L2**Ni(I) species at 15 minutes. The double-integrated intensities were $2.13*10^5$, $4.15*10^5$, and $7.59*10^5$ for spectra collected at 0.5, 2, and 8 mW microwave power, respectively.*

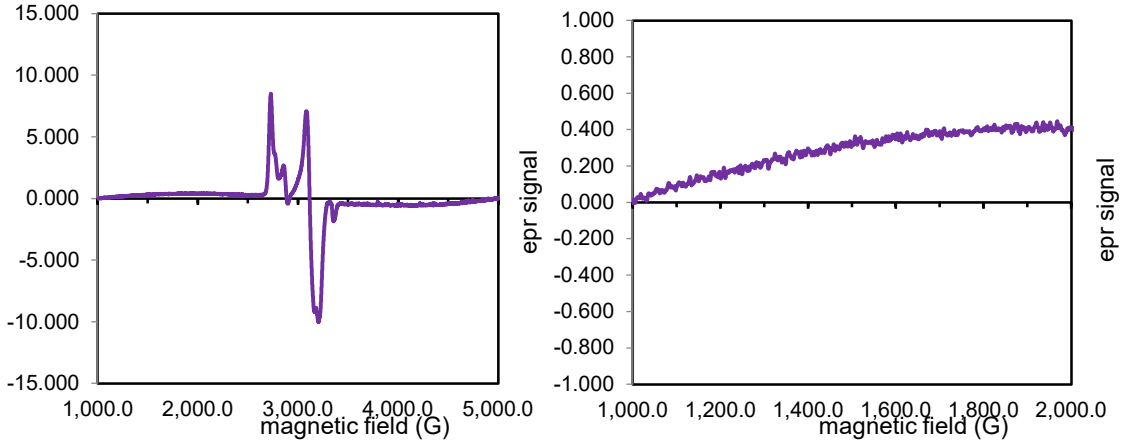

Figure S43. *Expanded scan for the reduced* ***L2****Ni(I) species at 15 minutes. X band (9.39 GHz) EPR spectra were collected at 2 mW microwave power. Left: full scan. Right: spectroscopic region of oligomeric species.*

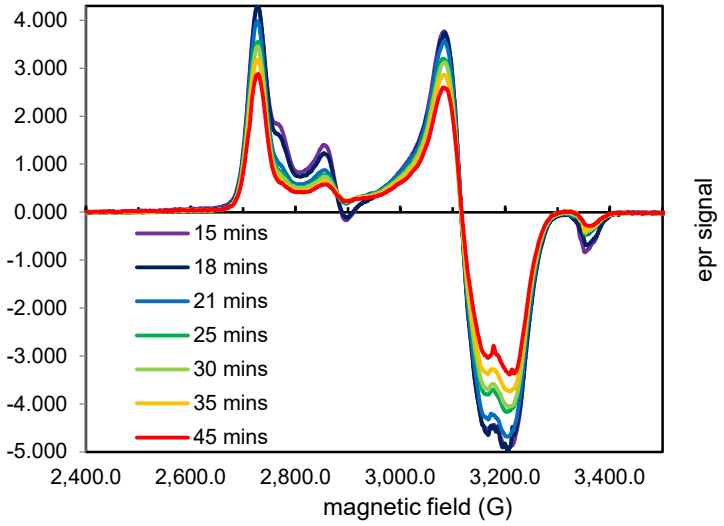

Figure S44. *Decay of* ***L2****Ni(I) species. X band (9.39 GHz) EPR spectra were collected at 0.5 mW microwave power. The double-integrated intensities were 2.13*10^5, 1.87*10^5, 1.64*10^5, 1.49*10^5, 1.41*10^5, 1.28*10^5, and 1.24*10^5 at 15, 18, 21, 25, 23, 35, and 45 minutes, respectively.*

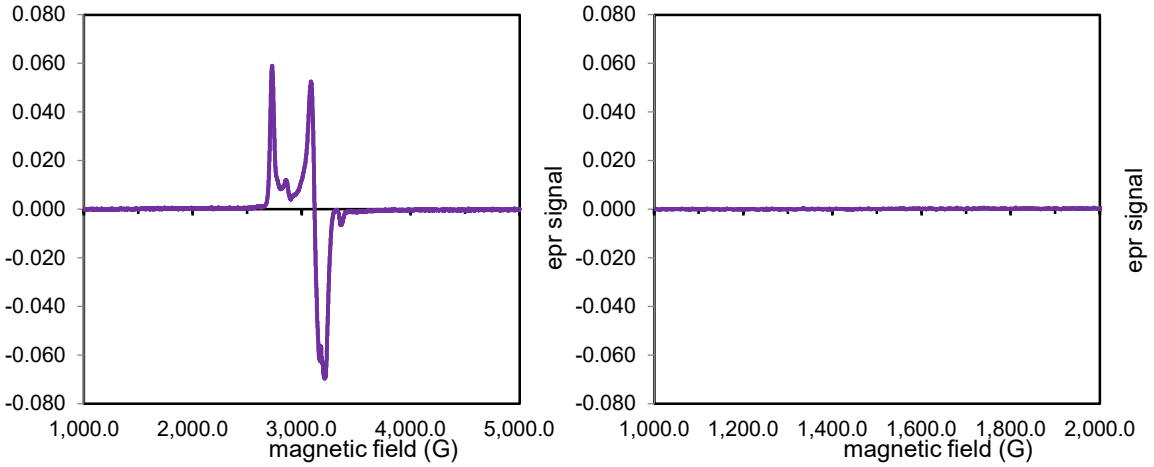

Figure S45. *Expanded scan for the reduced* ***L2****Ni(I) species at 45 minutes. X band (9.39 GHz) EPR spectra were collected at 2 mW microwave power. Left: full scan. Right: spectroscopic region of oligomeric species.*

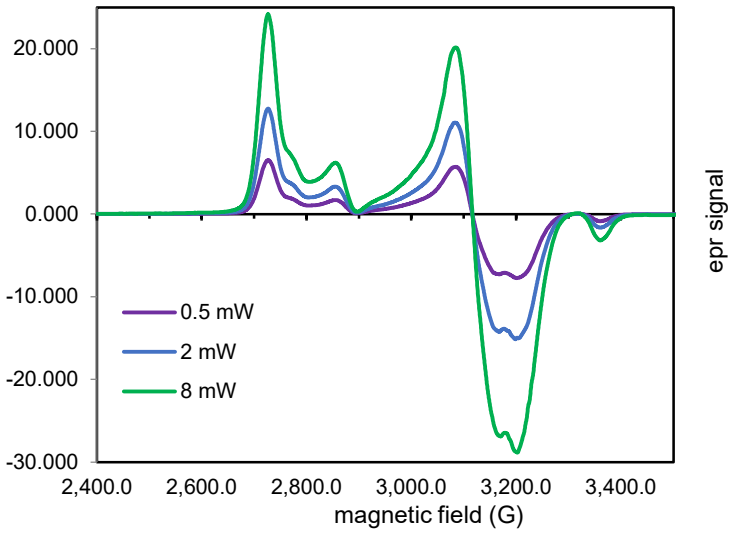

Figure S46. *Power dependency of the X band (9.39 GHz) EPR spectra of the reduced* ***L2****Ni(I) species with 10 equivalents of DMA present at 10 minutes (first trial). The double-integrated intensities were 2.71*10^5, 5.37*10^5, and 1.06*10^6 for spectra collected at 0.5, 2, and 8 mW microwave power, respectively.*

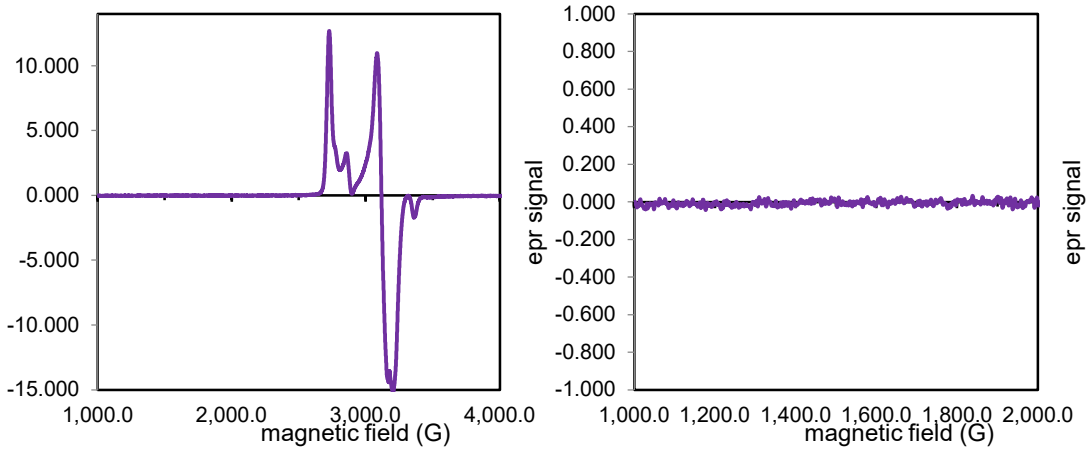

Figure S47. *Expanded scan for the reduced* ***L2****Ni(I) species with 10 equivalents of DMA present at 10 minutes (first trial). X band (9.39 GHz) EPR spectra were collected at 2 mW microwave power. Left: full scan. Right: spectroscopic region of oligomeric species.*

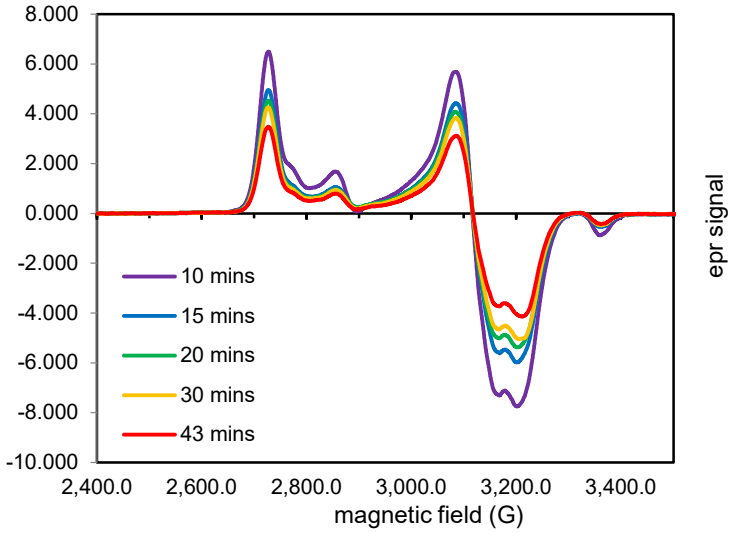

Figure S48. *Decay of* ***L2****Ni(I) species with 10 equivalents of DMA present (first trial). X band (9.39 GHz) EPR spectra were collected at 0.5 mW microwave power. The double-integrated intensities were 2.71*10^5, 1.98*10^5, 1.94*10^5, 1.78*10^5, and 1.52*10^{5}at 10, 15, 20, 25, 30, and 43 minutes, respectively.*

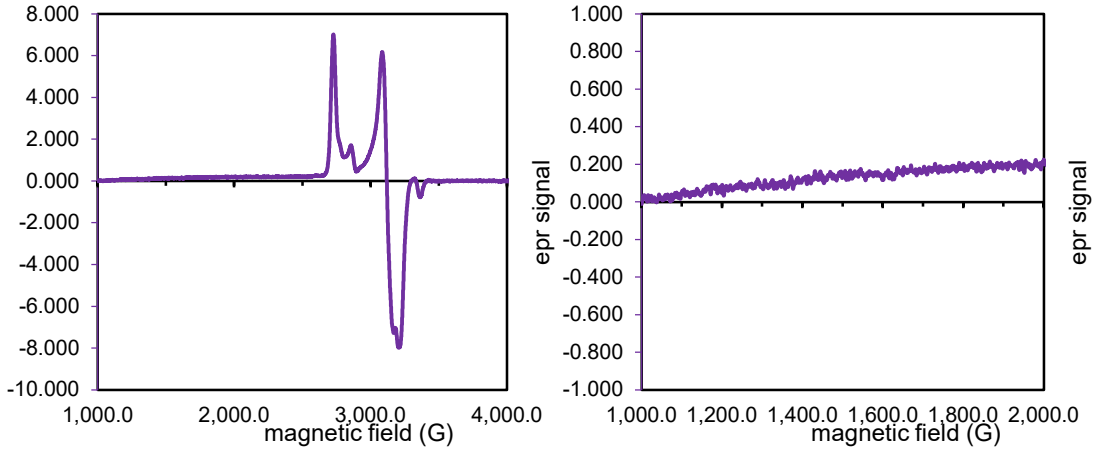

Figure S49. *Expanded scan for the reduced* ***L2****Ni(I) species with 10 equivalents of DMA present at 43 minutes (first trial). X band (9.39 GHz) EPR spectra were collected at 2 mW microwave power. Left: full scan. Right: spectroscopic region of oligomeric species.*

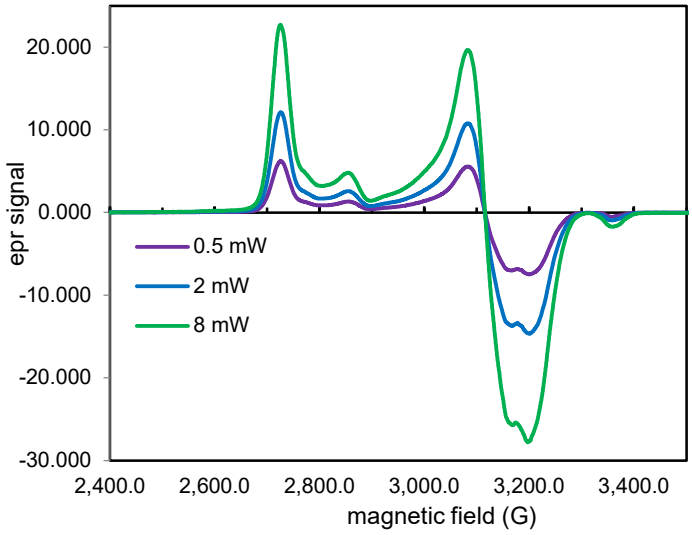

Figure S50. *Power dependency of the X band (9.39 GHz) EPR spectra of the reduced* ***L2****Ni(I) species with 10 equivalents of DMA present at 9 minutes (second trial). The double-integrated intensities were 2.56*10^5, 5.04*10^5, and 9.42*10^5 for spectra collected at 0.5, 2, and 8 mW microwave power, respectively.*

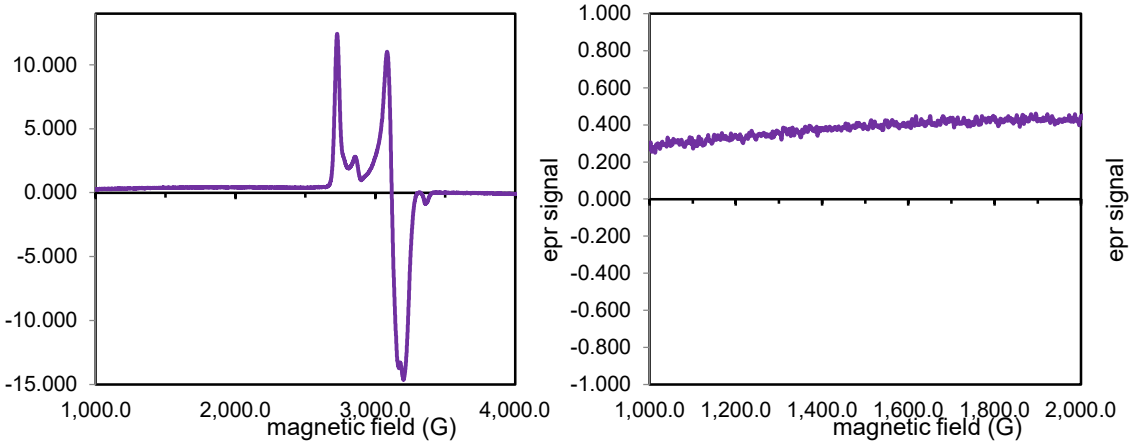

Figure S51. *Expanded scan for the reduced* ***L2****Ni(I) species with 10 equivalents of DMA present at 9 minutes (second trial).X band (9.39 GHz) EPR spectra were collected at 2 mW microwave power. Left: full scan. Right: spectroscopic region of oligomeric species.*

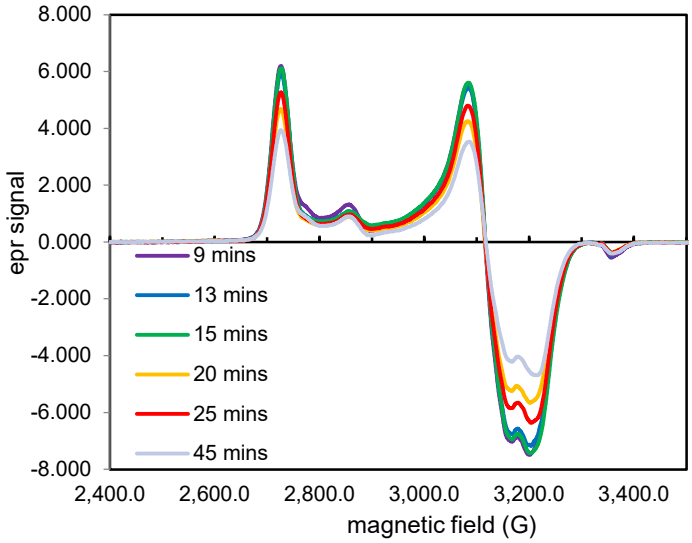

Figure S52. *Decay of* ***L2****Ni(I) species with 10 equivalents of DMA present (second trial). X band (9.39 GHz) EPR spectra were collected at 0.5 mW microwave power. The double-integrated intensities were 2.56*10^5, 2.40*10^5, 2.44*10^5, 1.93*10^5, 2.01*10^5 and 1.50*10^{5}at 9, 13, 15, 20, 25, and 45 minutes, respectively.*

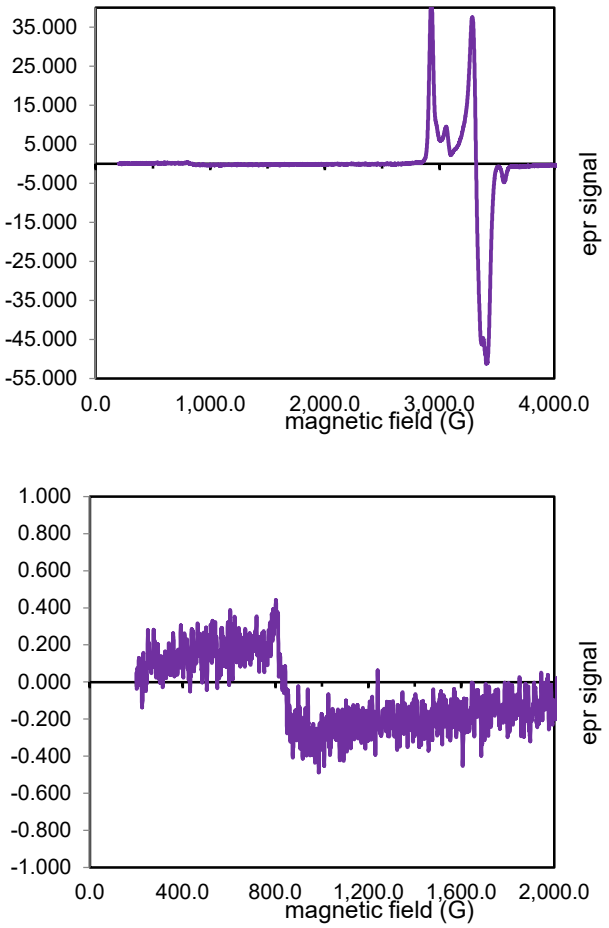

Figure S53. *Expanded scan for the reduced* ***L2****Ni(I) species with 10 equivalents of DMA present at 45 minutes (second trial).X band (9.39 GHz) EPR spectra were collected at 2 mW microwave power. Left: full scan. Right: potential higher-order aggregates.*

Note: To fit the decay of **L2**Ni(I) species with 10 equivalents of DMA present, the two data sets were combined, and the averaged value between the two trials was used for the 15-minute time-point.

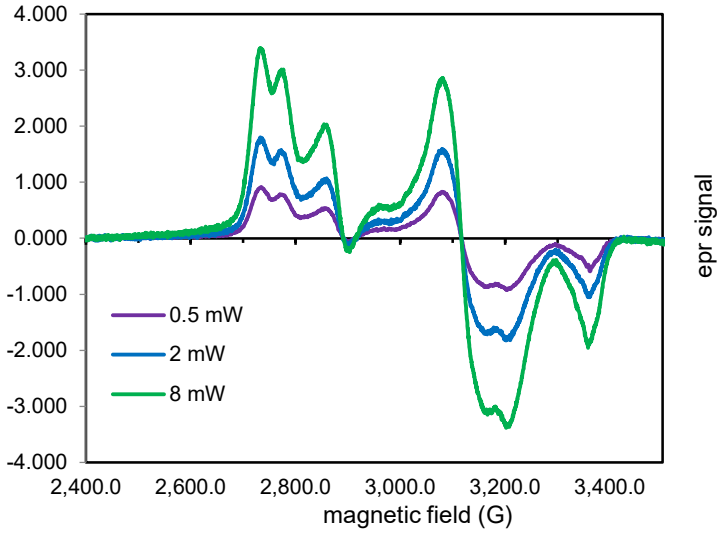

Figure S54. *Power dependency of the X band (9.41 GHz) EPR spectra of the reduced* ***L2****Ni(I) species with 11 equivalent of anhydride present at 19 minutes. The double-integrated intensities were 6.94*10^4, 1.07*10^5, and 2.02*10^5 for spectra collected at 0.5, 2, and 8 mW microwave power, respectively.*

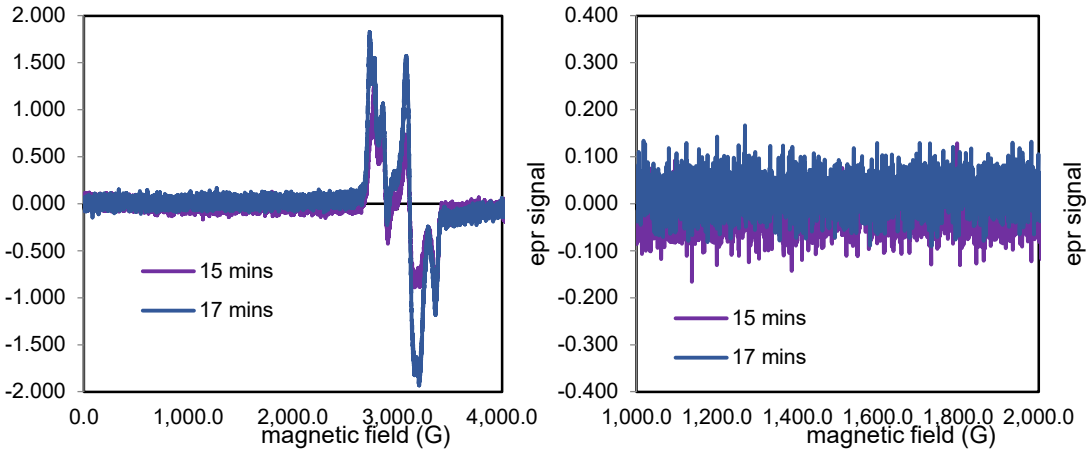

Figure S55. *Expanded scan for the reduced* ***L2****Ni(I) species with 1 equivalent of anhydride present at 15 and 17 minutes. X band (9.41 GHz) EPR spectra were collected at 2 mW microwave power. Left: full scan. Right: spectroscopic region of oligomeric species.*

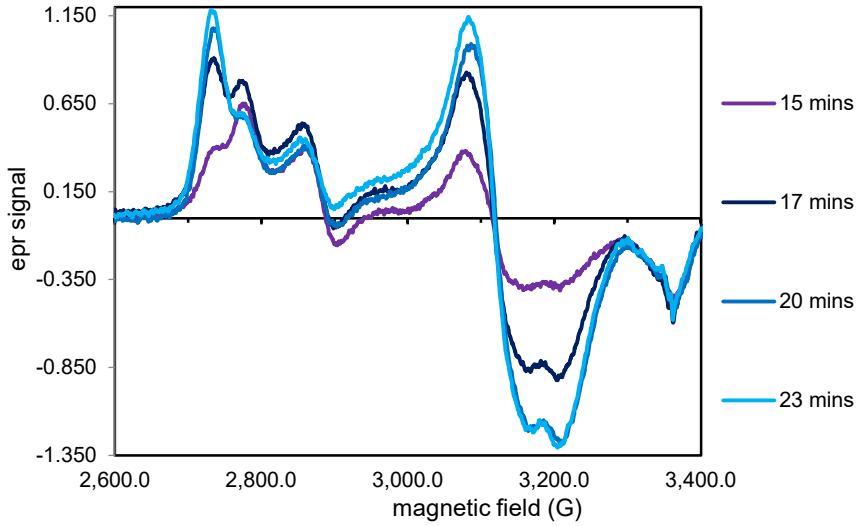

Figure S56. *Initial speciation change for the reduced* ***L2****Ni(I) species with 1 equivalent of anhydride present. X band (9.41 GHz) EPR spectra were collected at 0.5 mW microwave power. The double-integrated intensities were 3.66*10^4, 6.94*10^4, 5.62*10^4, and 6.02*10^4 at 15, 17, 20, and 23 minutes, respectively.*

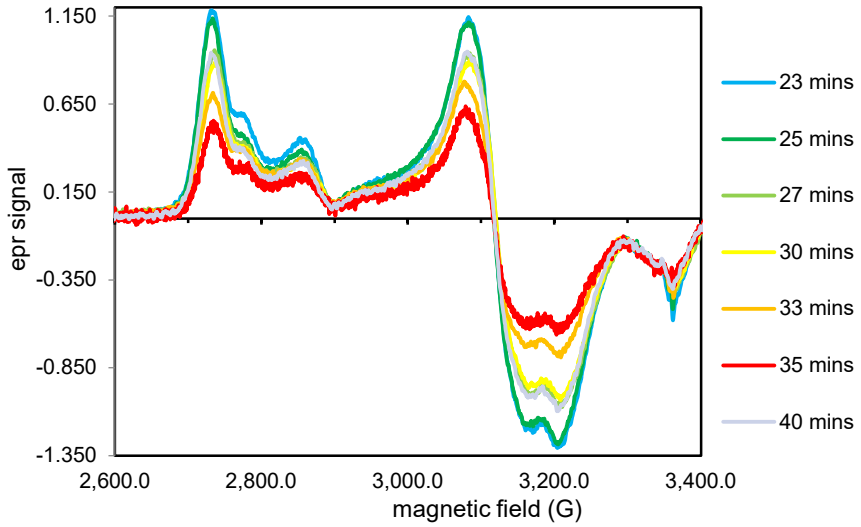

Figure S57. *Decay of* ***L2****Ni(I) species with 1 equivalent of anhydride present. X band (9.41 GHz) EPR spectra were collected at 0.5 mW microwave power. The double-integrated intensities were 6.02*10^4, 5.33*10^4, 5.26*10^4, 4.79*10^4, 4.10*10^4, 3.88*10^4, and 4.66*10^4 at 23, 25, 27, 30, 33, 35, and 40 minutes, respectively.*

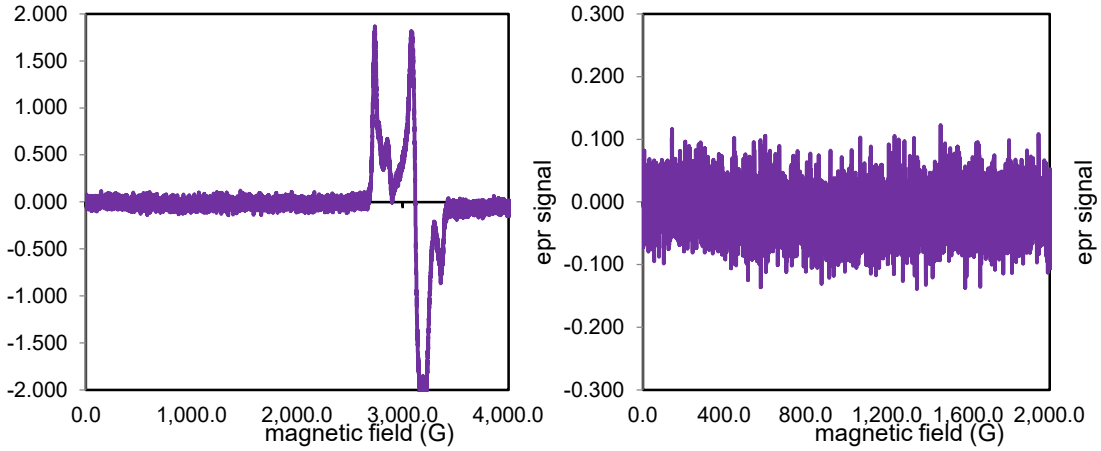

Figure S58. *Expanded scan for the reduced* ***L2****Ni(I) species with 1 equivalent of anhydride present at 40 minutes. X band (9.41 GHz) EPR spectra were collected at 2 mW microwave power. Left: full scan. Right: spectroscopic region of oligomeric species.*

4.8.4 *Supplementary Information to IR Studies*

Experimental Procedure

In situ absorbance IR spectroscopy was collected with a Mettler Toler 702L spectrometer in conjunction with a 305 mm DST Series 9.5 mm AgX Fiberconduit Dicomp probe. This combination permitted detecting absorbance between 800 and 1850 cm^{-1} at a 4 cm^{-1} resolution. All spectra were collected under an inert N_2 environment with the default setting. The spectra were averaged 128 scans for every minute. A background absorbance due to THF had been subtracted from all spectra. Transmittance IR spectroscopy of the putative oxidative addition complex was collected with a Bruker Alpha Platinum ATR spectrometer with OPUS software in an N_2-filled glovebox. The sample was deposited onto the spectrometer as a THF solution; the solution was allowed to evaporate prior to data collection. The reported spectrum was averaged over 32 scans.

The representative sample preparation for *in situ* IR studies is not described: In an N_2-filled glovebox, 30.8 mg (1 equiv., 0.2 mmol) of cis-cyclohexane-1,2-dicarboxylic

anhydride (0.2 mmol) was added to a 1-dram vial and dissolved in 250 μL anhydrous THF. The vial was then sealed with a septum cap and brought outside of the glovebox. Within a ventilated fume hood, a custom-made 3 mL conical vial with a stopcock-controlled 14/20 side-arm was charged with a 1-dram stir bar. This conical vial was then flame-dried and connected to the Schlenk line. Under a continuous flow of N_2, the react IR probe was inserted through a custom-drilled septum cap for the conical vial into the bottom of the conical vial. The spectrometer was then turned on and allowed to stabilize for 20 minutes. At this stage, 250 μL anhydrous THF was added to the reaction vessel, and an IR background of the solvent was collected. The probe was then raised, and under a continuous flow of N_2,154 mg (1 equiv., 0.2 mmol) of the **L2**$NiBr_2$ was added to the bottom of the conical vial as solids. The probe was then lowered, and the conical cap was sealed by tightening the septum cap. After closing the stopcock, the stir plate was turned on, and the stir rate was set to 1000 rpm. The *in situ* IR experiment was set to commence via the software. After a stable IR spectrum of the precatalyst was obtained, the *in situ* IR experiment was paused, and the stopcock was opened to allow a continuous flow of N_2. The septum cap was then untightened to raise the probe. Then, the 250 μL solution of anhydride was injected into the reaction vial, after which the probe was lowered, and the conical vessel was sealed. Upon closing the stopcock, the *in situ* IR experiment was restarted via the software to collect the IR spectra of the precatalyst and anhydride mixture. Repeating the protocol for the addition of anhydride, the *in situ* IR experiment was paused, and the reaction apparatus was opened to allow the injection of 12.3 μL of BF_3•Et_2O (0.5 equiv., 0.1 mmol) under a continuous flow of N_2. The *in situ* IR

experiment was restarted to monitor the IR changes until IR spectra stabilized. Finally, under a similar protocol, 11.0 mg of Mn powder was added under a continuous flow of N_2. The reaction vessel was then sealed, the probe was tightly secured, and the stopcock was closed. At this stage, the *in situ* IR experiment was restarted to monitor the reaction changes over the next 240 minutes. The reported IR intensities of each peak were normalized over the maximum IR intensity of that peak.

Note: It was essential to tightly secure the React IR probe after the addition of the Mn, as the change in the immersion depth of the probe could influence signal intensity.

Additional IR spectra

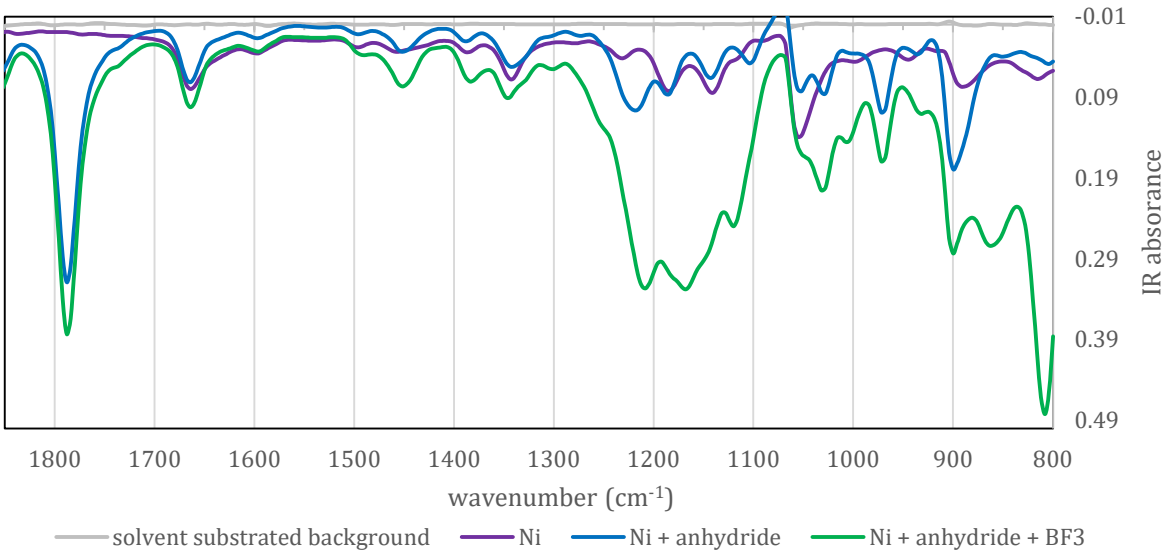

Figure S59. *IR changes between the addition of reaction components during the in situ IR monitoring of anhydride activation by* ***L2****Ni(I) species.*

4.8.5 *Supplementary Information to Electrochemical Studies*

Preparation of Electrochemical Cells

Under an N_2 atmosphere, 1.935 g (5 mmol) of tetrabutylammonium hexafluorophosphate ($TBAPF_6$) was charged to a flame-dried 40 mL vial and was

dissolved in 25 mL of anhydrous THF to generate a 0.2 M electrolyte stock solution. The vial was sealed with a septum-caped vial. The electrochemical cell, the glassy carbon working electrode, and the Pt wire counter electrode were rinsed thrice with the electrolyte solution, wiped clean, and placed onto a clean Chemwipe prior to the assemblage of the electrochemical. Separately, the nonaqueous Ag/Ag^+ electrode was assembled by inserting a PTFE capped Ag wire into a 9.5 mm OD fritted glass tube (Pine Research) that has been filled with a 10 mM MeCN electrolyte solution[1] of $AgNO_3$ (electrochemical grade, Strem). Then, the outside of the glass tube was similarly rinsed with the electrolyte solution. With the electrodes prepared and cleaned, 5 mL of the electrolyte solution was then transferred to an oven-dried electrochemical cell with a 1 mL syringe. The electrodes were inserted into the cell and connected to the Biologic potentiostat. At this stage, impedance spectroscopy was taken to determine the uncompensated resistance of the cell, which typically measured a resistance of 1.0–1.5 k Ω. Then, 85% of the measured resistance was compensated with the manual IR compensation function of the biological program. At this stage, a cyclic voltammogram of the electrolyte solution was collected to assess the presence of impurities. In the absence of impurity and electrical interference, a nonfaradic current of a few nano amperes was typically observed with no distinct redox couples. If large faradic currents indicate redox active impurities were present, the electrochemical cell was dissembled, and the cleaning procedure was repeated.

With the electrochemical cell prepared, 15.2 mg (20 μmol) of the isolated precatalyst (**L2**$NiBr_2$) was measured and added to the electrochemical cell. Upon full solvation of the precatalyst solid, cyclic voltammograms were collected at 100, 225, 400,

625, and 900 mV/s scan rates unless specified otherwise. For electrochemical catalysis of the substrate (BnCl or cis-cyclohexane-1,2-dicarboxylic anhydride), the current responses were collected at the aforementioned scan rates in the presence of 1,5, 6.67, 10,20,50, 100 equivalents of a substrate to represent a catalyst loading of 100, 20, 15, 10, 5, 2, 1 mol% respectively. For BnCl (d = 1.062), this was accomplished by sequentially adding 2.6 μL (20 μmol), 10.4 μL (80 μmol), 4.3 μL (33 μmol), 8.7 μL (67 μmol), 26.0 μL (200 μmol), 78 μl (600 μmol), and 130 μl (1 mmol) with a 10 or 25 μL Hamilton microsyring. For anhydride, this was accomplished by adding 3.1 mg (20 μmol), 12.3 mg (80 μmol), 5.1 mg (33 μmol), 10.3 mg (67 μmol), 30.8 μL (200 μmol), 92.4 mg (600 μmol), and 154 mg (1 mmol) of anhydride as solid. The first scan, which contained kinetic information, was reported for all cases.

All cyclic voltammograms were reported against the Fc/Fc^+ couple as the internal standard. For this reason, at the completion of each set of electrochemical experiments, a trace amount of ferrocene was added to the solution, and the Fc/Fc^+ couple was measured at 100 mV/s. Under the conditions reported herein, a reversible wave near 0.13 V vs Ag/Ag^+ was typically observed with a peak separation of ca. 100 mV.

IR Compensation

Uncompensated resistance was measured with the default setting of the PEIS function of the Biologic program. A Nyquist plot containing a single semicircle at a low real value of the impedance followed by a straight line at a high real value of the impendence should be expected. The uncompensated resistance was quantified with the real value of the impedance at the junction point between the semicircle and the straight line. A resistance of 1.0–1.5 k Ω was typically measured in THF with 0.2 M of $TBAPF_6$

of electrolyte. In comparison, the automatic IR compensation function of the software undervalued the resistance by 600–1000 Ω. For this reason, manual compensation was preferred.

Preparation of $AgNO_3$ Electrolyte Solution

Under an N2 atmosphere, in a 40 mL flamed dried vial, 967.5 g (2.5 mmol) of tetrabutylammonium hexafluorophosphate ($TBAPF_6$) was dissolved in 25 mL of anhydrous MeCN to generate a 0.1 M electrolyte solution. 5 mL of this solution was then transferred to a 2-dram vial to dissolve 8.5 mg $AgNO_3$ (Strem, electrochemical grade). The solution was protected from exposure to light by tapping the vial with electrical tape.

Mathematical Proof that Equation 5 Provides an Upper-bound of k_{obs} for Any Intermediate Catalytic Current Under a Kinetic Control

This proof assumes the unitless catalytic current is a strictly increasing function of the kinetic parameter of the rate-limiting step λ_{lim}. It should be noted from Saveant's work graphs, this condition may be met for $\gamma > 10$.

Proof: Suppose that ψ is a monotonically increasing bijective function of $\log(\lambda)$. Since the log function is also a strictly increasing bijective function, it can be shown that:

$$\psi(\lambda_a) \leq \psi(\lambda_b) \; if \; and \; only \; if \;\; \lambda_a \leq \lambda_b \qquad \text{SI. 1}$$

Under this condition, the catalytic current in the intermediate kinetic region as a function of λ_{RDS} is bounded by the limiting behavior of the peak currents observed at the KS or KT region:

$$0.4463 \leq \sqrt{\gamma \lambda_{KS}} = \psi_{KS} \leq \;\; \psi(\lambda_{RDS}) < \psi_{KT} = 1.365\gamma, for \; a \; given \; \gamma \qquad \text{SI. 2}$$

Experimentally, when an observed catalytic current that fell under the intermediate kinetic regime follows the inequality:

$$(\psi_{obs})^2 \geq \left(\psi_{KS,true}\right)^2 = \gamma\lambda_{obs} \qquad \text{SI. 3}$$

Expressing the second half of the equation with the definition of λ for an EC_{RDS} mechanism yields

$$\lambda_{obs} \equiv \frac{RT}{F}\left(\frac{\overset{\circ}{c_{ox}} * k_{RDS}}{v_{obs}}\right) \qquad \text{SI. 4}$$

$$\left(\frac{v_{obs}F}{\overset{\circ}{c_A}RT}\right)\psi_{obs}{}^2 \geq k_{RDS} \qquad \text{SI. 5}$$

Therefore, Eqn.SI.5 indicates that using the electrochemical current under an intermediate kinetic regime gives an upper estimate of the underlying rate-limiting step.

Qualitative Accuracy of the Electrochemically Determined Rate Constant

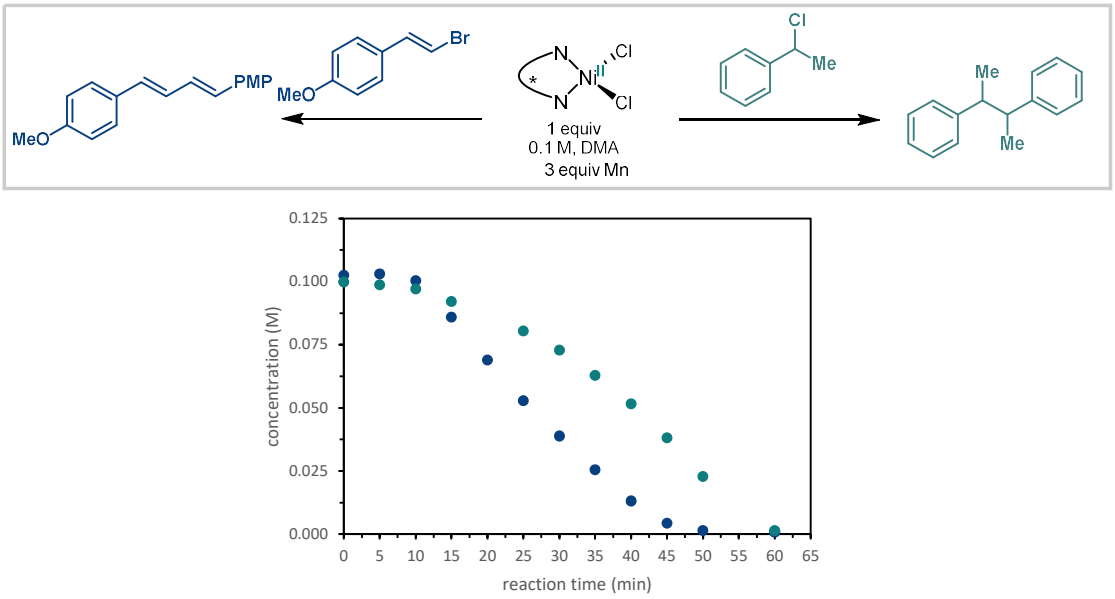

Figure S60. *Relative rate of electrophile activation monitored by GS kinetics.*

The qualitative accuracy of the electrochemical rate extracted from the catalytic peak current was assessed preliminarily with the GC kinetic data of substrate activation by **IndaBox**$NiBCl_2$. In Chapter 3, the relative activation rate of the alkenyl bromides was 4.1

times or 1.3 times greater than benzylic chlorides when comparing the velocity at 15% conversion or the maximal velocity, respectively.

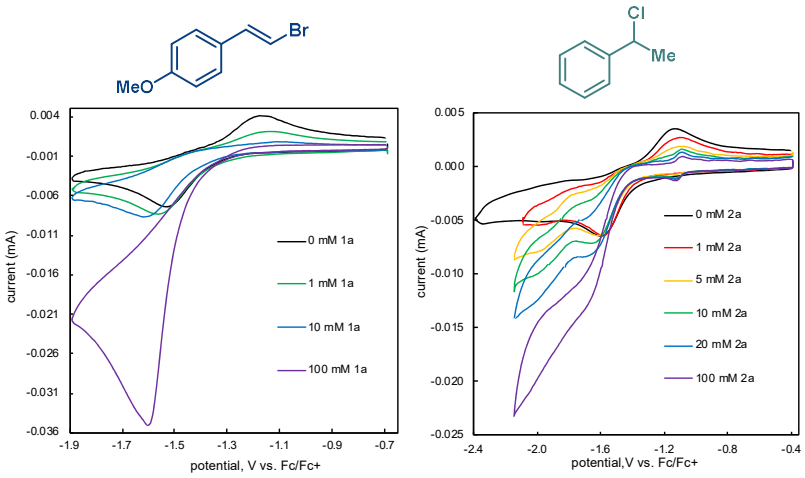

Figure S61. *Electrochemical substrate activation by* ***Indabox****$NiCl_2$.*

For comparison, electrochemical rates were extracted at a substrate excess ratio of 100 at a scan rate of 100 mV/s. For alkenyl bromide, extending the analysis to a two-electron process as described by Saveant[57] estimates the upper limit of alkenyl bromide activation rates from a current ratio i_c/i_p of 4.8 as follows:

$$k_{C(sp\ )} \leq \frac{(4.8 * 0.446)^2 * 0.1}{0.1 * 2}\left(\frac{96485}{8.414 * 298}\right) = 88\ M^{-1}s^{-1}$$

Similarly, for the activation of benzylic chloride, the estimated upper limit was

$$k_{C(sp3)} \leq \frac{(2.04 * 0.446)^2 * 0.1}{0.1}\left(\frac{96485}{8.414 * 298}\right) = 31\ M^{-1}s^{-1}$$

Thus, electrochemical rate extraction reports that the activation of alkenyl bromides is 2.83 times greater than that of the benzylic chlorides, which qualitatively falls in the 1.3–4.1 range provided by GC kinetic analyses. It is worth noting that despite the differences in reaction concentrations and the substrate excess ratios, the GS kinetics and electrochemical

kinetics appeared to be in good agreement with each other.

Additional Cyclic Voltammograms

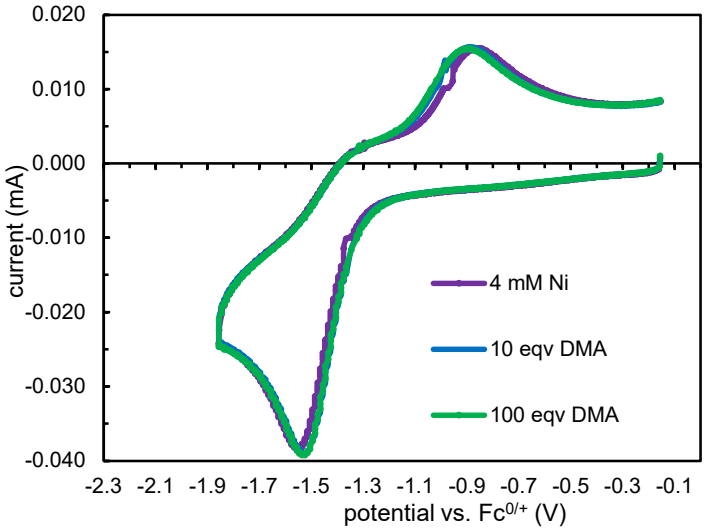

Figure S62. *Current behavior of* ***L2***$NiBr_2$ *with various equivalents of DMA present. The concentration was 0.1 M for* $TBAPF_6$ *electrolyte and 1 mM for* ***L2***$NiBr_2$ *instead. The scan rate was 100 mV/s.*

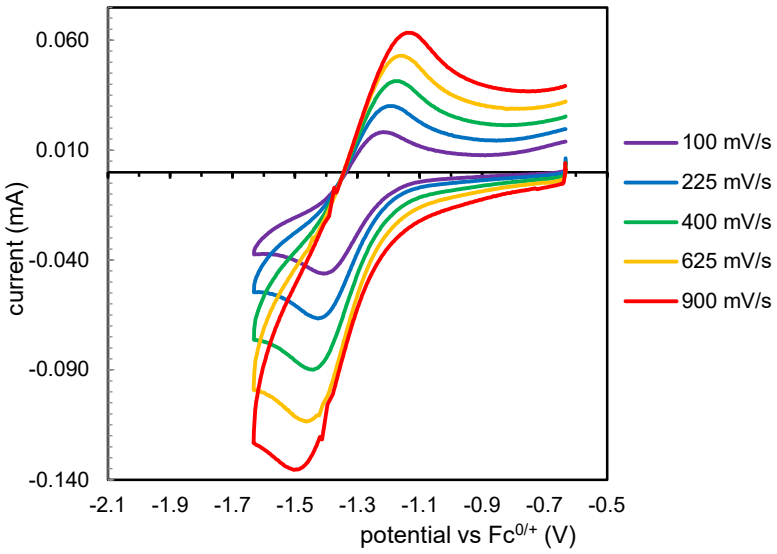

Figure S63. *Scan rate dependency of 4 mM* ***L1***$NiBr_2$.

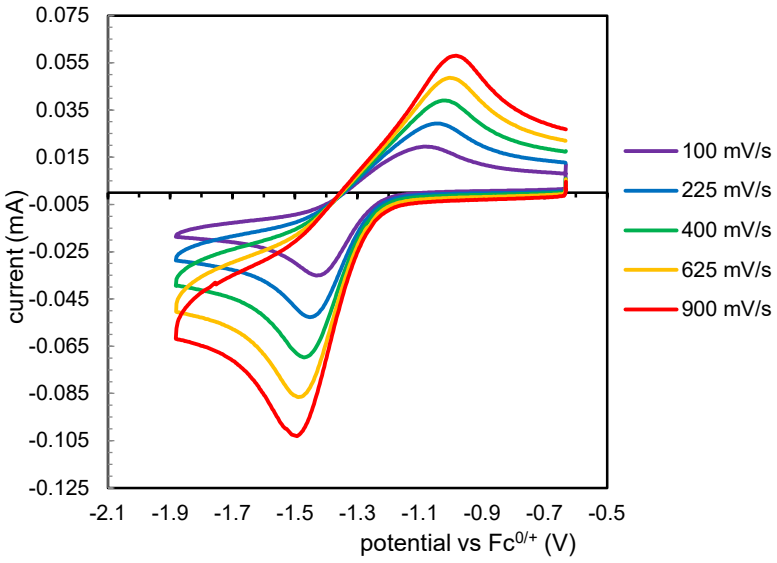

Figure S64. *Scan rate dependency of 4 mM* ***L2****NiBr*$_2$*. Results from this experiment were discussed in the main text and reported in* ***Scheme 16, 24, 26****.*

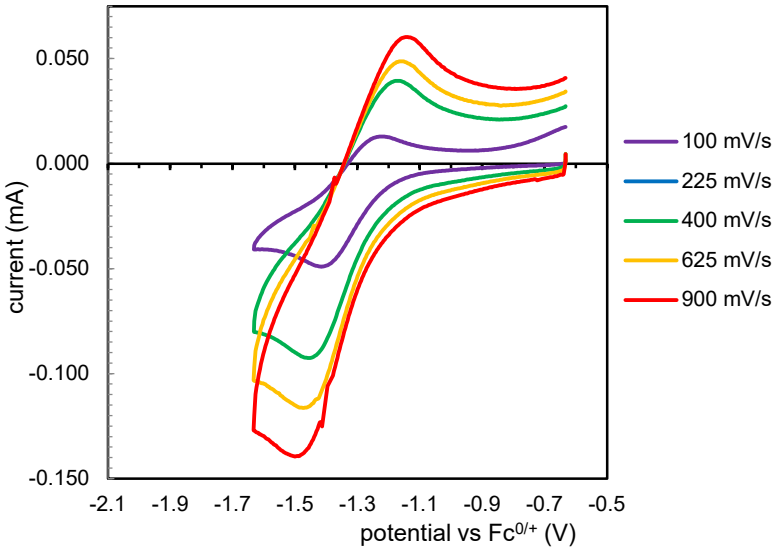

Figure S65. *Scan rate dependency of electrochemical activation of 4 mM benzylic chlorides by 4 mM* ***L1****NiBr*$_2$ *(*$\gamma = 1$*).*

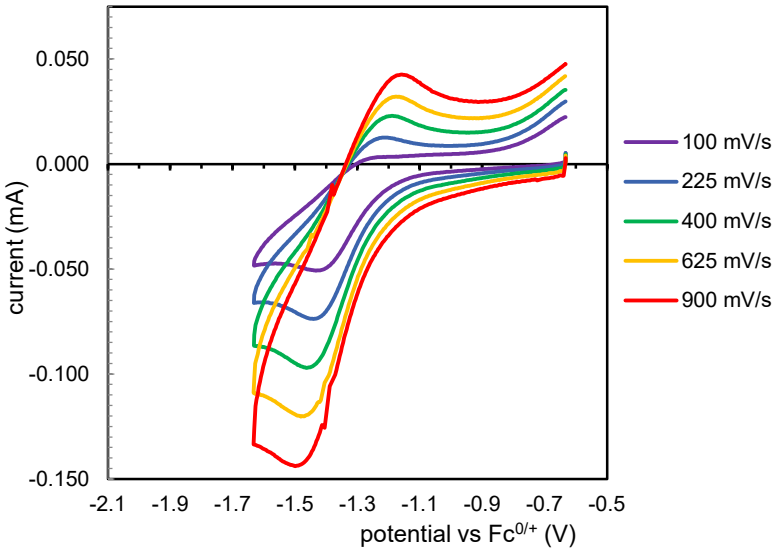

Figure S66. *Scan rate dependency of electrochemical activation of 20 mM benzylic chlorides by 4 mM* ***L1****$NiBr_2$ (γ = 5).*

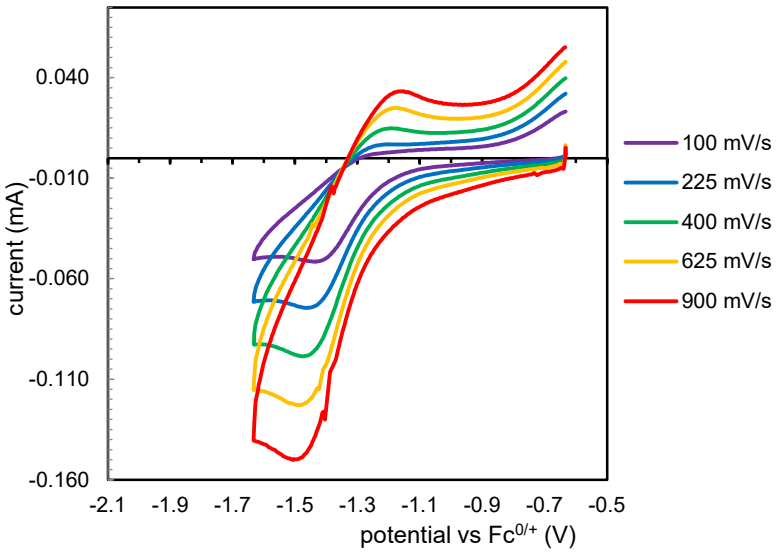

Figure S67. *Scan rate dependency of electrochemical activation of 26.7 mM benzylic chlorides by 4 mM* ***L1****$NiBr_2$ (γ = 6.7).*

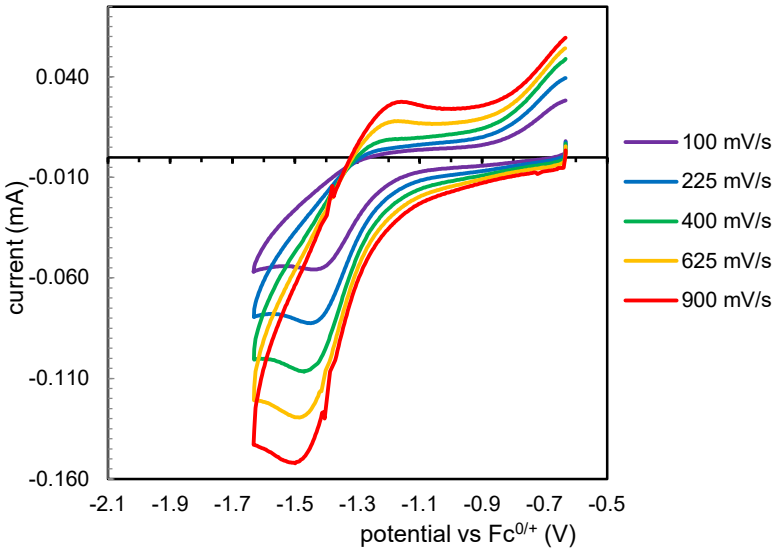

Figure S 68. *Scan rate dependency of electrochemical activation of 40 mM benzylic chlorides by 4 mM* ***L1****$NiBr_2$ (γ = 10).*

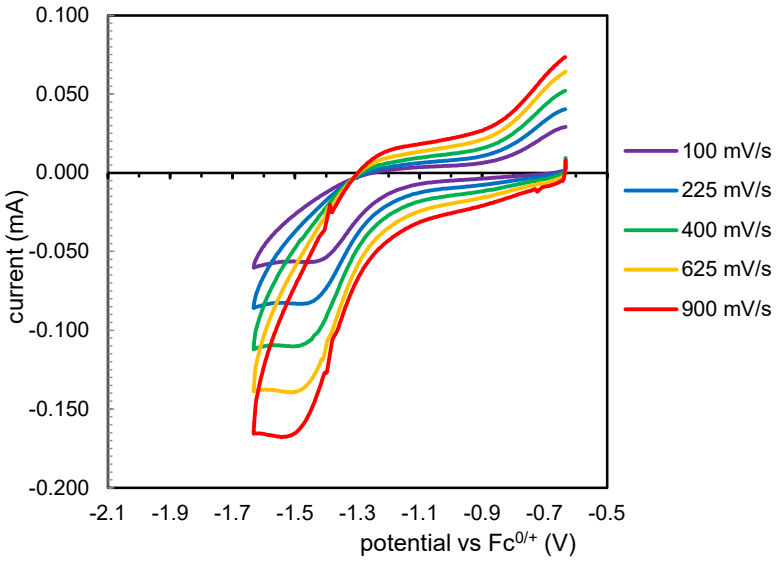

Figure S 69. *Scan rate dependency of electrochemical activation of 80 mM benzylic chlorides by 4 mM* ***L1****$NiBr_2$ (γ = 20).*

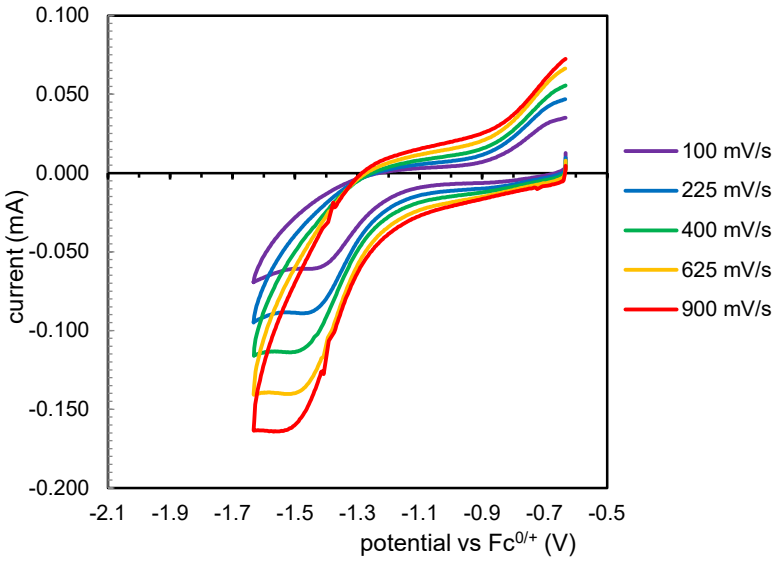

Figure S70. *Scan rate dependency of electrochemical activation of 200 mM benzylic chlorides by 4 mM* ***L1****$NiBr_2$ (γ = 50).*

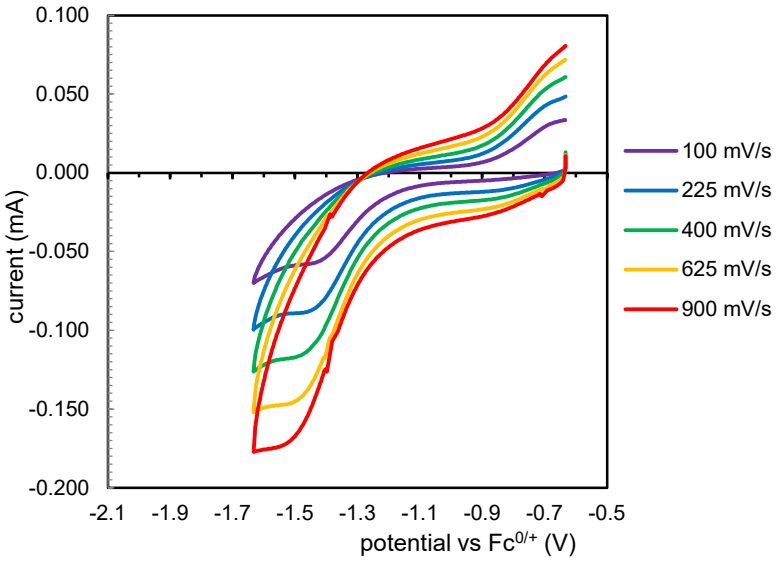

Figure S71. *Scan rate dependency of electrochemical activation of 400 mM benzylic chlorides by 4 mM* ***L1****$NiBr_2$ (γ = 100).*

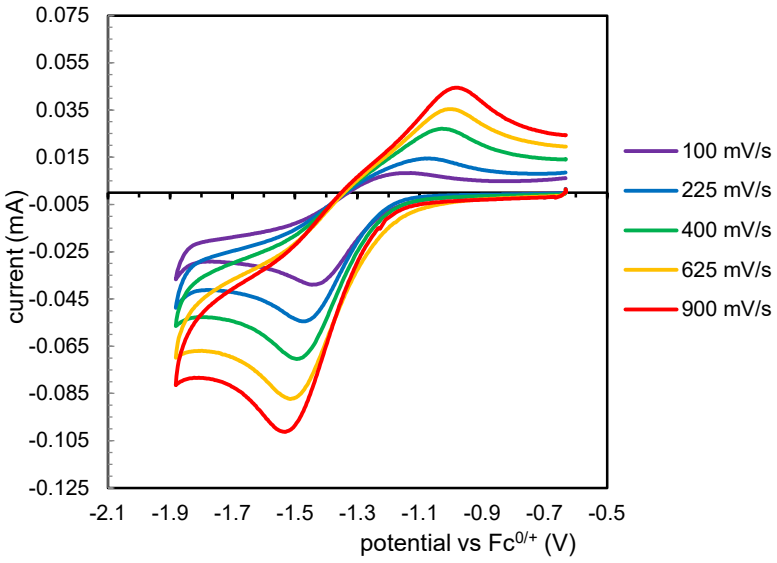

Figure S72. *Scan rate dependency of electrochemical activation of 4 mM benzylic chlorides by 4 mM* ***L2****NiBr₂ (γ = 1).*

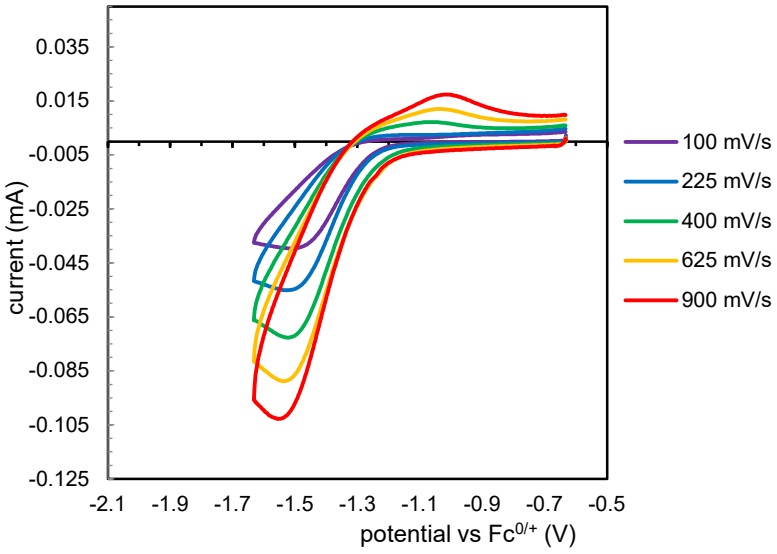

Figure S 73. *Scan rate dependency of electrochemical activation of 20 mM benzylic chlorides by 4 mM* ***L2****NiBr₂ (γ = 5).*

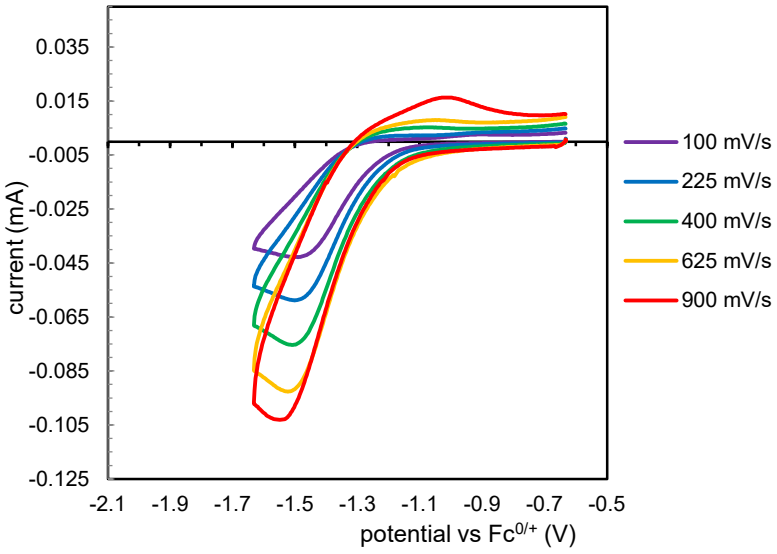

Figure S74. *Scan rate dependency of electrochemical activation of 26.7 mM benzylic chlorides by 4 mM* ***L2****$NiBr_2$ (γ = 6.7).*

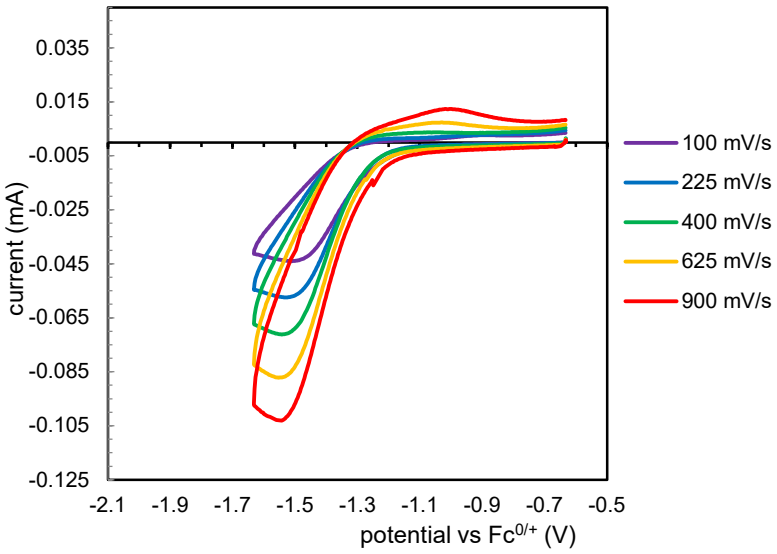

Figure S75. *Scan rate dependency of electrochemical activation of 40 mM benzylic chlorides by 4 mM* ***L2****$NiBr_2$ (γ = 10).*

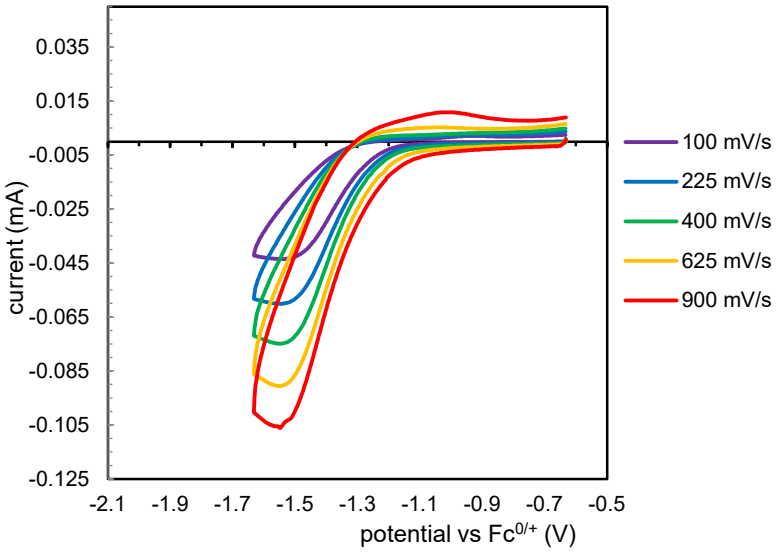

Figure S 76. *Scan rate dependency of electrochemical activation of 80 mM benzylic chlorides by 4 mM* ***L2****$NiBr_2$ (γ = 20).*

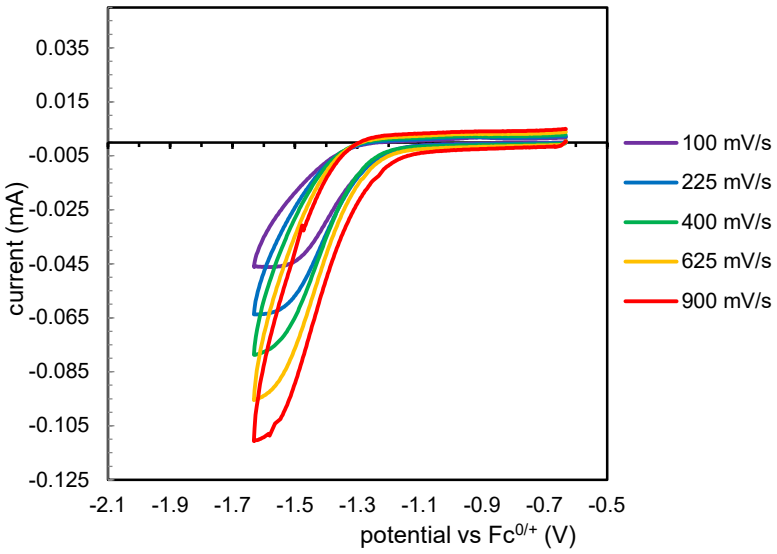

Figure S 77. *Scan rate dependency of electrochemical activation of 200 mM benzylic chlorides by 4 mM* ***L2****$NiBr_2$ (γ = 50).*

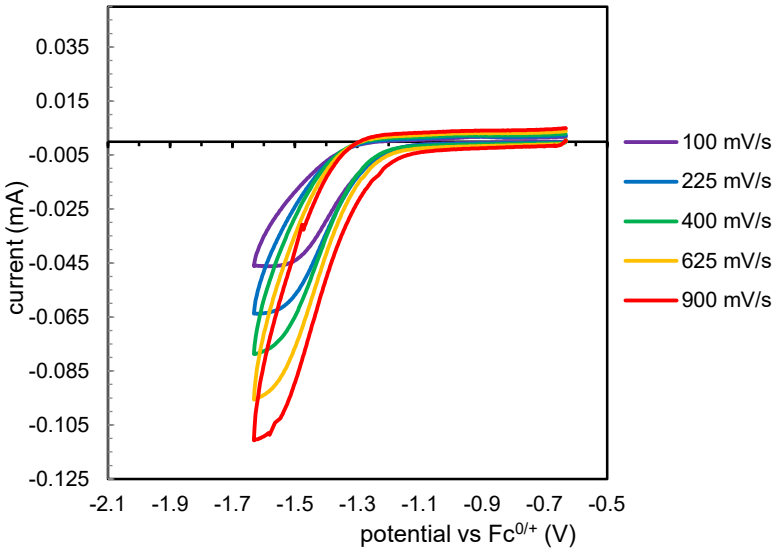

Figure S78. *Scan rate dependency of electrochemical activation of 400 mM benzylic chlorides by 4 mM* ***L2****$NiBr_2$ (γ = 100).*

Note: For electrochemical anhydride activation, we noted that the peak separations were larger due to an anodically shifted anodic peak. Equally, the cathodic peak also appeared to shift cathodically, although to a lesser extent.

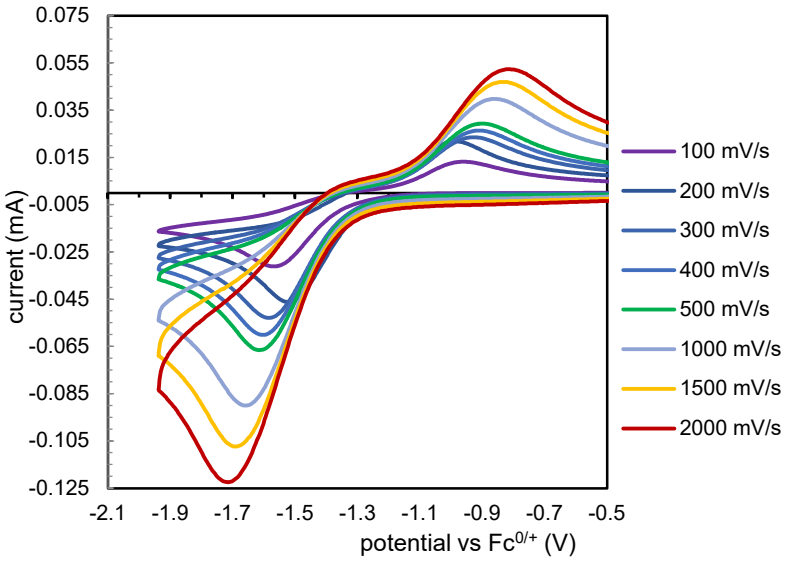

Figure S79. *Scan rate dependency of the cure by 4 mM* ***L2****$NiBr_2$ (γ = 1).*

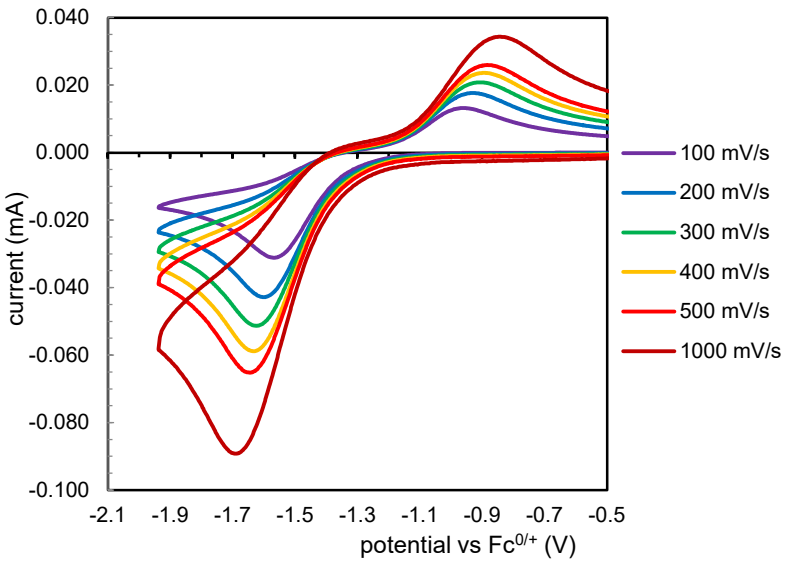

Figure S80. *Scan rate dependency of electrochemical activation of 4 mM anhydrides by 4 mM* ***L2****NiBr₂ (γ = 1).*

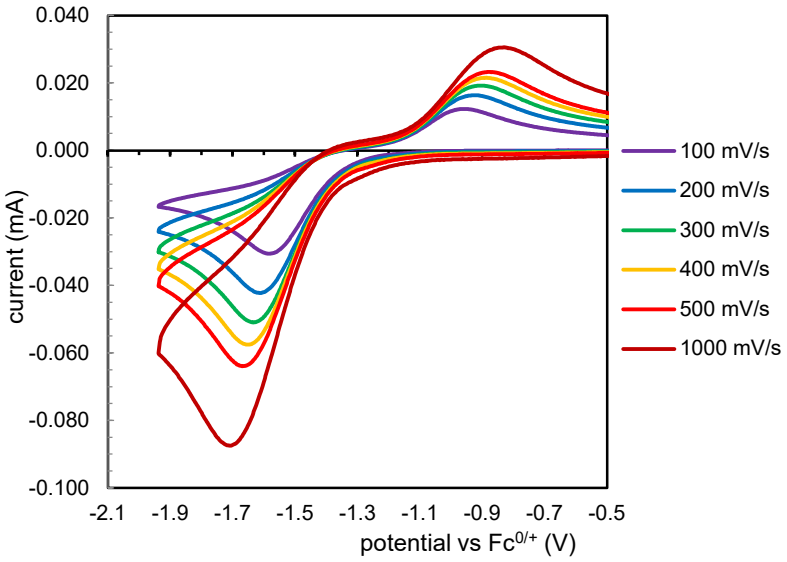

Figure S81. *Scan rate dependency of electrochemical activation of 12 mM anhydrides by 4 mM* ***L2****NiBr₂ (γ = 3).*

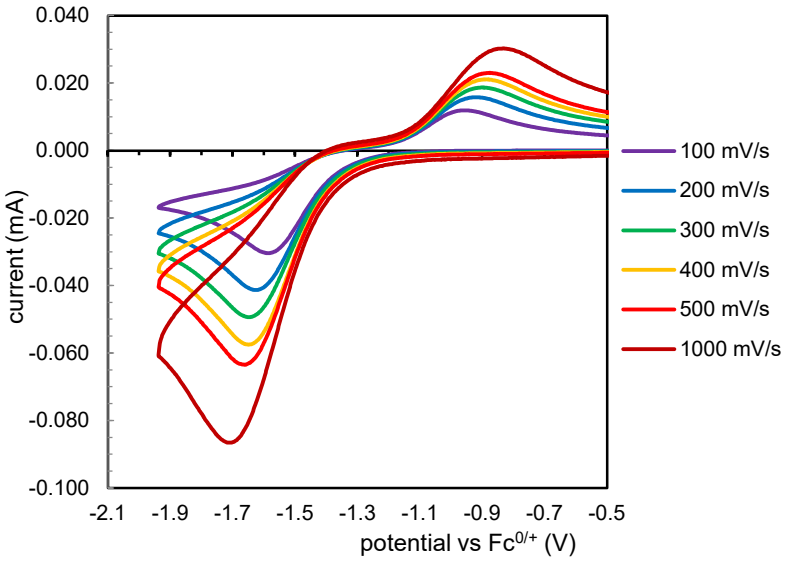

Figure S82. *Scan rate dependency of electrochemical activation of 26.7 mM anhydrides by 4 mM* ***L2****NiBr$_2$ (γ = 6.7).*

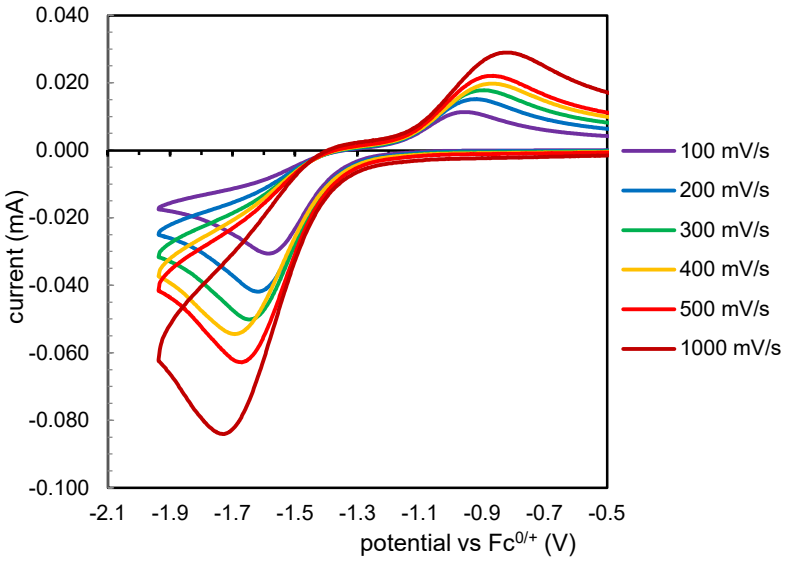

Figure S83. *Scan rate dependency of electrochemical activation of 40 mM anhydrides by 4 mM* ***L2****NiBr$_2$ (γ = 10).*

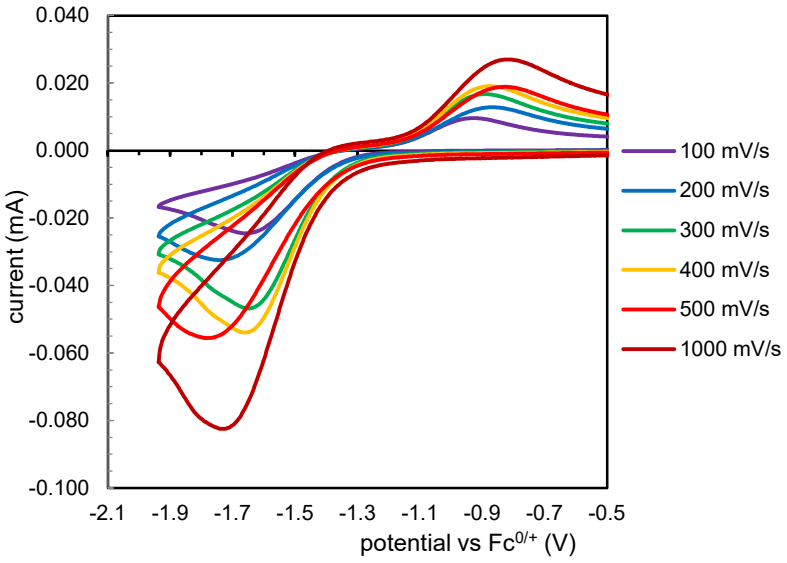

Figure S84. *Scan rate dependency of electrochemical activation of 100 mM anhydrides by 4 mM* ***L2****NiBr$_2$ (γ = 25).*

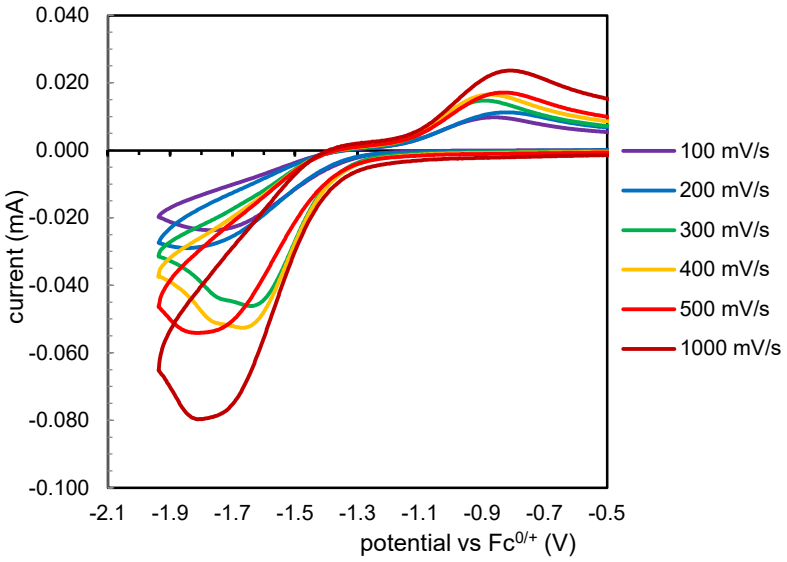

Figure S85. *Scan rate dependency of electrochemical activation of 200 mM anhydrides by 4 mM* ***L2****NiBr$_2$ (γ = 50).*

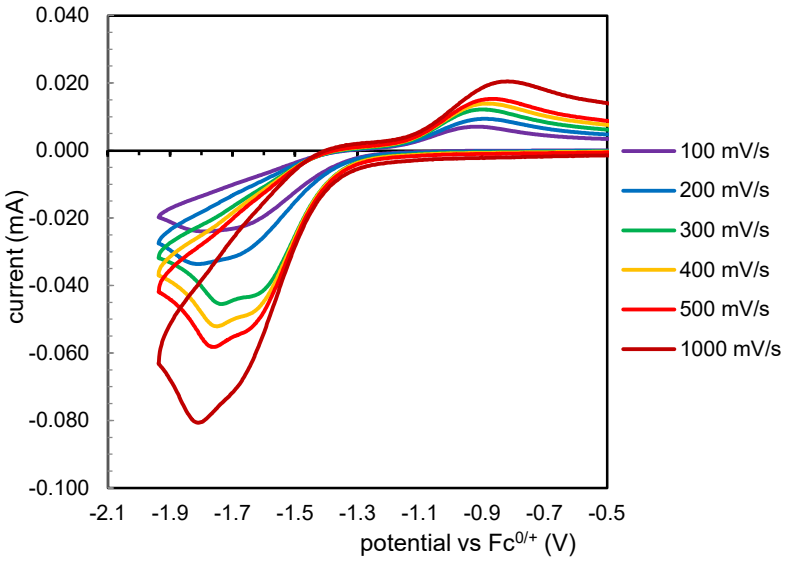

Figure S86. *Scan rate dependency of electrochemical activation of 400 mM anhydrides by 4 mM* ***L2****NiBr$_2$ (γ = 100).*

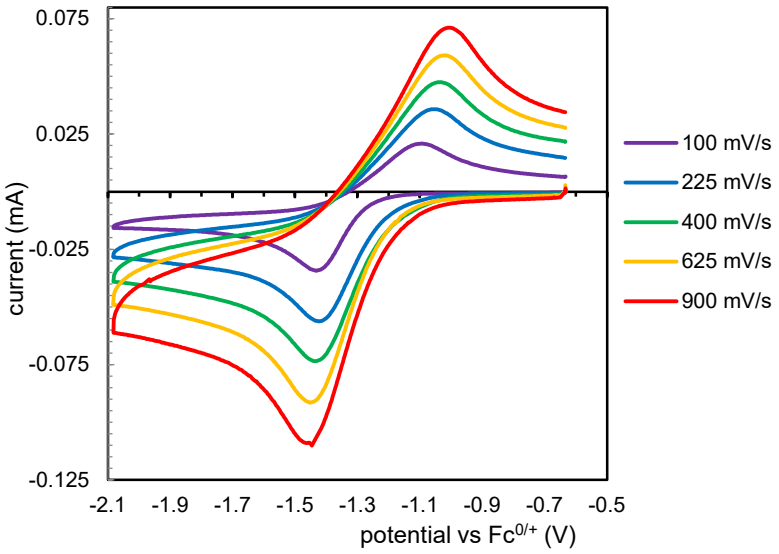

Figure S87. *Scan rate dependency of 4 mM* ***L2****NiBr$_2$ (prior to the addition of 4 mM BF$_3$•Et$_2$O). Results from this experiment were reported in* ***Scheme 27****.*

Note: The cyclic voltammograms observed for Figure S56 and Figure S33 were highly comparable.

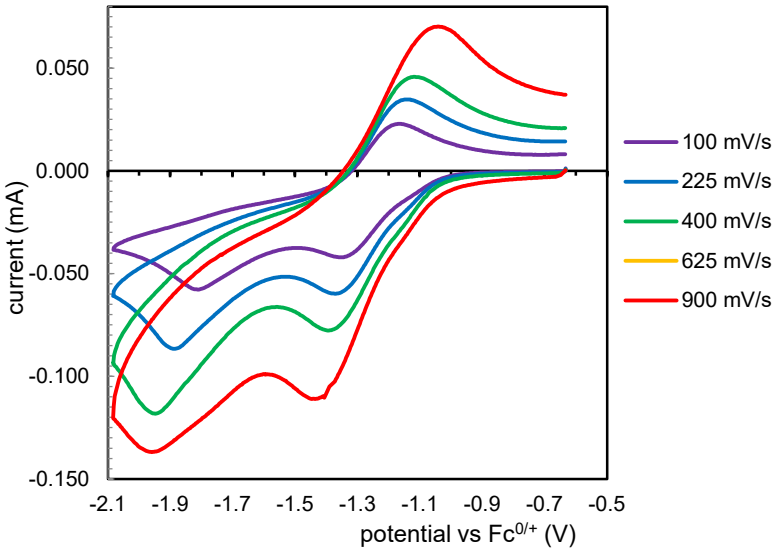

Figure S88. *Scan rate dependency of 4 mM* ***L2****$NiBr_2$ and 4 mM BF_3•Et_2O.*

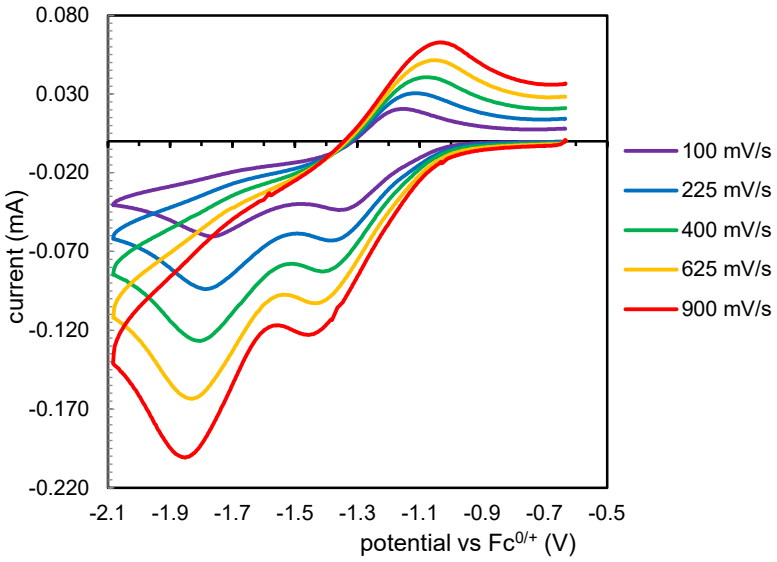

Figure S89. *Scan rate dependency of electrochemical activation of 4 mM anhydrides by 4 mM* ***L2****$NiBr_2$ and 4 mM BF_3•Et_2O. (γ = 1).*

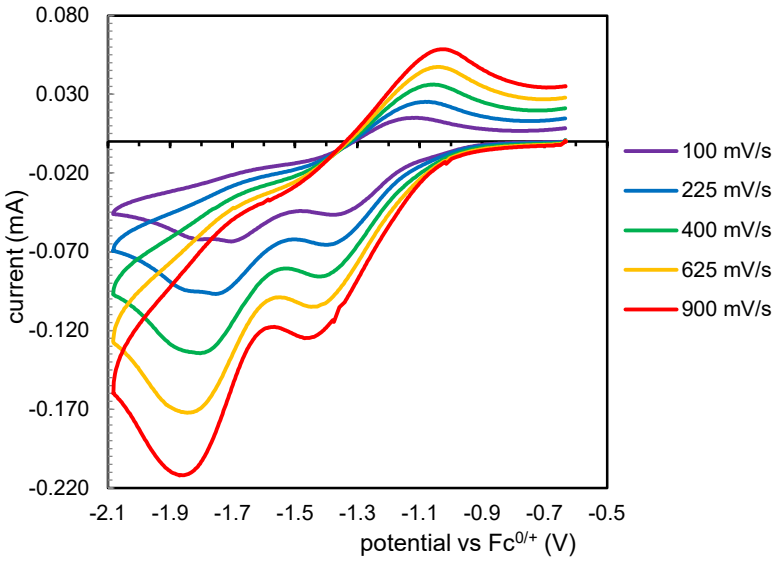

Figure S90. *Scan rate dependency of electrochemical activation of 20 mM anhydrides by 4 mM* ***L2****$NiBr_2$ and 4 mM BF_3•Et_2O. (γ = 5).*

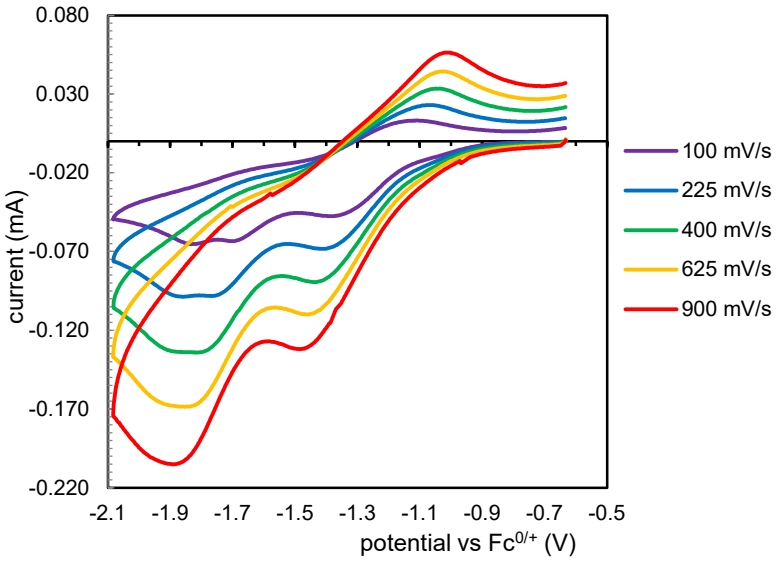

Figure S91. *Scan rate dependency of electrochemical activation of 26.7 mM anhydrides by 4 mM* ***L2****$NiBr_2$ and 4 mM BF_3•Et_2O. (γ = 6.7).*

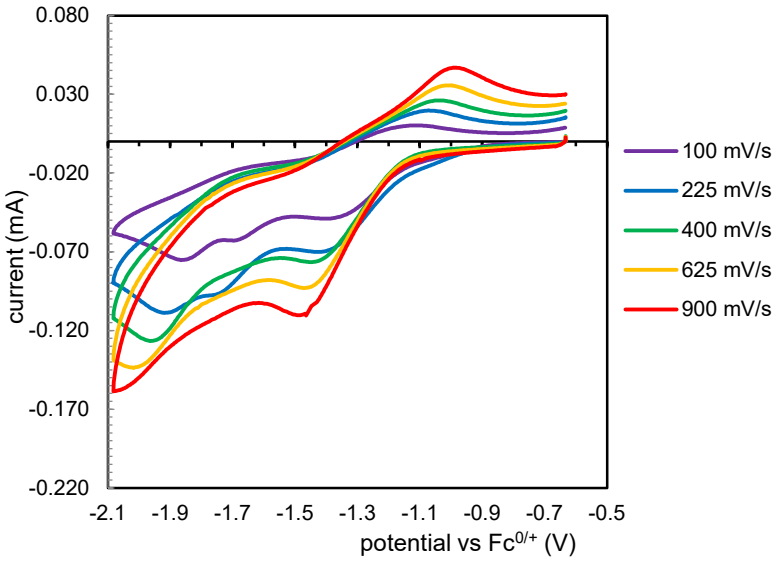

Figure S92. *Scan rate dependency of electrochemical activation of 40 mM anhydrides by 4 mM* ***L2****NiBr$_2$ and 4 mM BF$_3$•Et$_2$O. (γ = 10).*

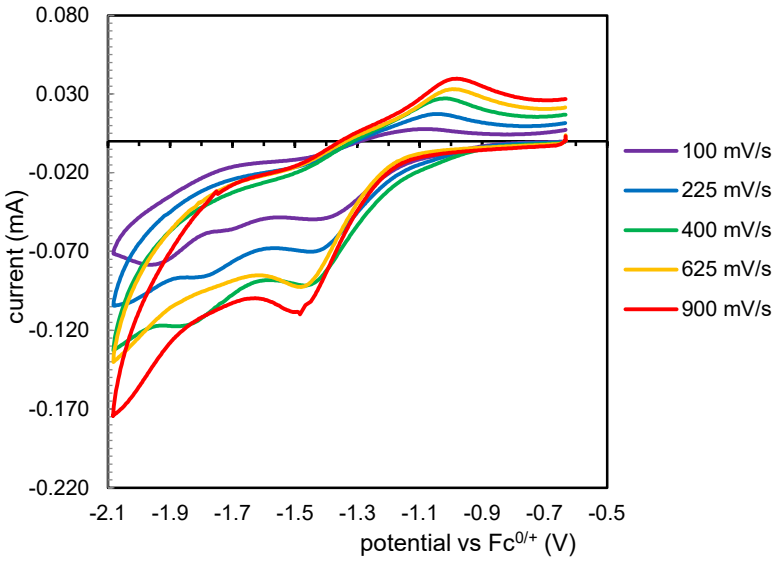

Figure S93. *Scan rate dependency of electrochemical activation of 80 mM anhydrides by 4 mM* ***L2****NiBr$_2$ and 4 mM BF$_3$•Et$_2$O. (γ = 20).*

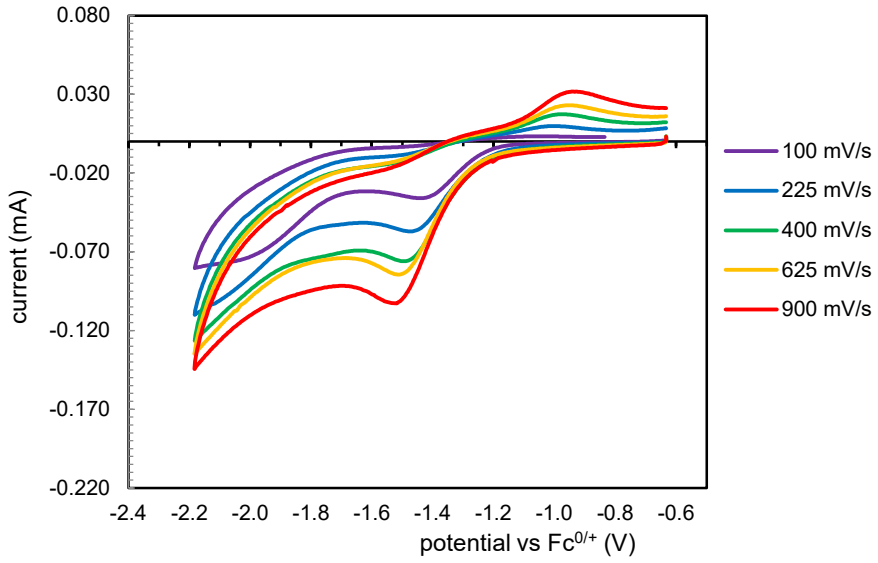

Figure S94. *Scan rate dependency of electrochemical activation of 200 mM anhydrides by 4 mM* ***L2****$NiBr_2$ and 4 mM BF_3•Et_2O. (γ = 50).*

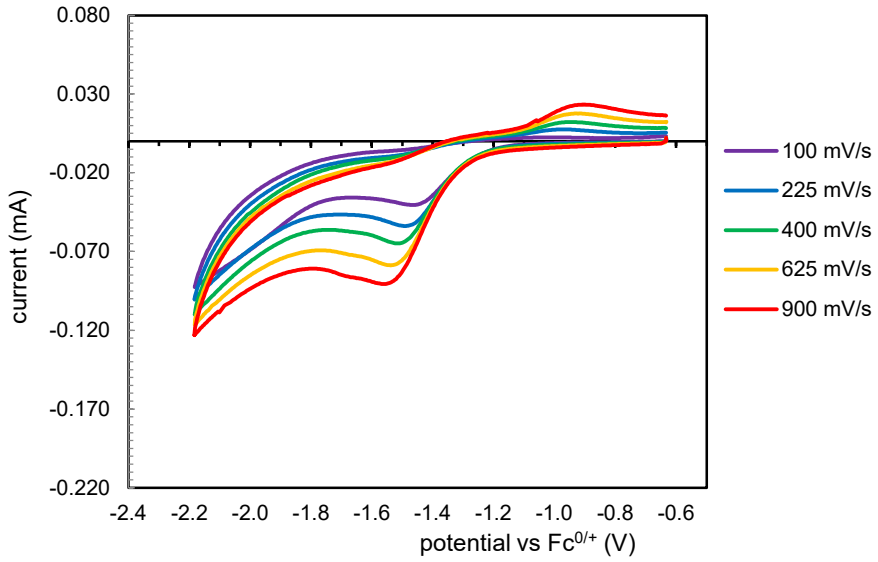

Figure S95. *Scan rate dependency of electrochemical activation of 400 mM anhydrides by 4 mM* ***L2****$NiBr_2$ and 4 mM BF_3•Et_2O. (γ = 100).*

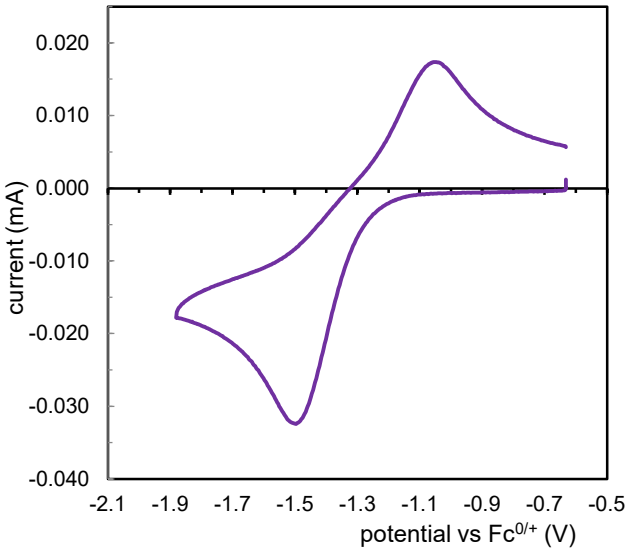

Figure S96. *Cyclic voltammogram of 4 mM* ***L2****NiBr$_2$ (prior to the addition of 20 mM BF$_3$•Et$_2$O.*

Note: The cyclic voltammogram observed for Figure S65 was highly comparable to those observed for S56 and Figure S33.

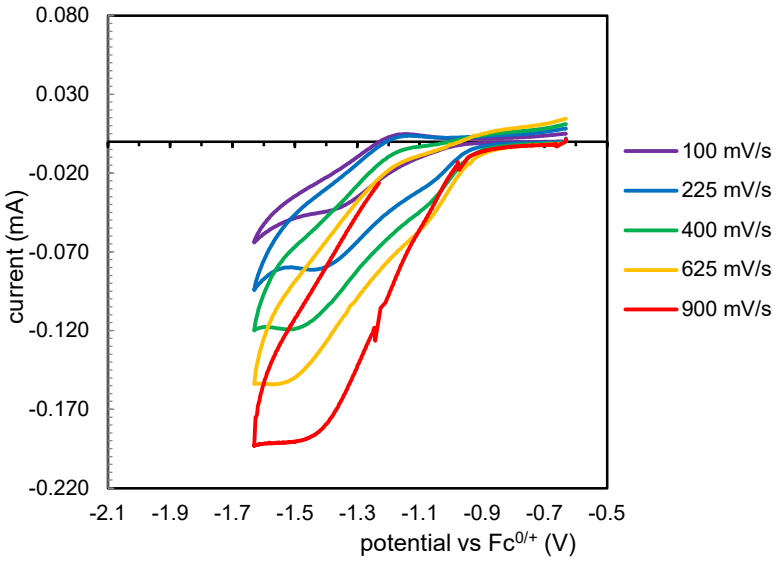

Figure S97. *Scan rate dependency of electrochemical activation of 400 mM anhydrides by 4 mM* ***L2****NiBr$_2$ and 20 mM BF$_3$•Et$_2$O.*

Note: Titration experiments with anhydride were unsuccessful as the pink solution

gradually discolored to colorless over the course of the experiment, suggesting the irreversible bulk consumption of **L2**$NiBr_2$ potentially due to electrolysis or irreversible electrochemical reaction with anhydride.

4.9 Notes and References

(1) Mesganaw, T.; Garg, N. K. Ni- and Fe-Catalyzed Cross-Coupling Reactions of Phenol Derivatives. *Org. Process Res. Dev.* **2013**, *17* (1), 29–39. https://doi.org/10.1021/op300236f.

(2) Yu, D.-G.; Li, B.-J.; Shi, Z.-J. Exploration of New C−O Electrophiles in Cross-Coupling Reactions. *Acc. Chem. Res.* **2010**, *43* (12), 1486–1495. https://doi.org/10.1021/ar100082d.

(3) Amaike, K.; Muto, K.; Yamaguchi, J.; Itami, K. Decarbonylative C–H Coupling of Azoles and Aryl Esters: Unprecedented Nickel Catalysis and Application to the Synthesis of Muscoride A. *J. Am. Chem. Soc.* **2012**, *134* (33), 13573–13576. https://doi.org/10.1021/ja306062c.

(4) Caenepeel, S.; Brown, S. P.; Belmontes, B.; Moody, G.; Keegan, K. S.; Chui, D.; Whittington, D. A.; Huang, X.; Poppe, L.; Cheng, A. C.; Cardozo, M.; Houze, J.; Li, Y.; Lucas, B.; Paras, N. A.; Wang, X.; Taygerly, J. P.; Vimolratana, M.; Zancanella, M.; Zhu, L.; Cajulis, E.; Osgood, T.; Sun, J.; Damon, L.; Egan, R. K.; Greninger, P.; McClanaghan, J. D.; Gong, J.; Moujalled, D.; Pomilio, G.; Beltran, P.; Benes, C. H.; Roberts, A. W.; Huang, D. C.; Wei, A.; Canon, J.; Coxon, A.; Hughes, P. E. AMG 176, a Selective MCL1 Inhibitor, Is Effective in Hematologic Cancer Models Alone and in Combination with Established Therapies. *Cancer Discov.* **2018**, *8* (12), 1582–1597. https://doi.org/10.1158/2159-8290.CD-18-0387.

(5) Cherney, A. H.; Kadunce, N. T.; Reisman, S. E. Catalytic Asymmetric Reductive Acyl Cross-Coupling: Synthesis of Enantioenriched Acyclic α,α-Disubstituted Ketones. *J. Am. Chem. Soc.* **2013**, *135* (20), 7442–7445. https://doi.org/10.1021/ja402922w.

(6) Cherney, A. H.; Reisman, S. E. Nickel-Catalyzed Asymmetric Reductive Cross-Coupling Between Vinyl and Benzyl Electrophiles. *J. Am. Chem. Soc.* **2014**, *136* (41), 14365–14368. https://doi.org/10.1021/ja508067c.

(7) Stache, E. E.; Rovis, T.; Doyle, A. G. Dual Nickel- and Photoredox-Catalyzed Enantioselective Desymmetrization of Cyclic Meso-Anhydrides. *Angew. Chem. Int. Ed.* **2017**, *56* (13), 3679–3683. https://doi.org/10.1002/anie.201700097.

(8) Lin, Q.; Diao, T. Mechanism of Ni-Catalyzed Reductive 1,2-Dicarbofunctionalization of Alkenes. *J. Am. Chem. Soc.* **2019**, *141* (44), 17937–17948. https://doi.org/10.1021/jacs.9b10026.

(9) Cagan, D. A.; Bím, D.; McNicholas, B. J.; Kazmierczak, N. P.; Oyala, P. H.; Hadt, R. G. Photogenerated Ni(I)–Bipyridine Halide Complexes: Structure–Function Relationships for Competitive C(Sp2)–Cl Oxidative Addition and Dimerization Reactivity Pathways. *Inorg. Chem.* **2023**, *62* (24), 9538–9551. https://doi.org/10.1021/acs.inorgchem.3c00917.

(10) Cusumano, A. Q.; Chaffin, B. C.; Doyle, A. G. Mechanism of Ni-Catalyzed Photochemical Halogen Atom-Mediated C(Sp3)–H Arylation. *J. Am. Chem. Soc.* **2024**, *146* (22), 15331–15344. https://doi.org/10.1021/jacs.4c03099.

(11) McManus, B. D.; Hung, L. C.; Taylor, O. R.; Nguyen, P. Q.; Cedeño, A. L.; Arriola, K.; Bradley, R. D.; Saucedo, P. J.; Hannan, R. J.; Luna, Y. A.; Farias, P.; Bahamonde, A. Mechanistic Interrogation of Photochemical Nickel-Catalyzed Tetrahydrofuran Arylation

Leveraging Enantioinduction Data. *J. Am. Chem. Soc.* **2024**, *146* (46), 32135–32146. https://doi.org/10.1021/jacs.4c13485.

(12) St. John, P. C.; Guan, Y.; Kim, Y.; Kim, S.; Paton, R. S. Prediction of Organic Homolytic Bond Dissociation Enthalpies at near Chemical Accuracy with Sub-Second Computational Cost. *Nat. Commun.* **2020**, *11* (1), 2328. https://doi.org/10.1038/s41467-020-16201-z.

(13) Li, Z.; Zhang, S.-L.; Fu, Y.; Guo, Q.-X.; Liu, L. Mechanism of Ni-Catalyzed Selective C−O Bond Activation in Cross-Coupling of Aryl Esters. *J. Am. Chem. Soc.* **2009**, *131* (25), 8815–8823. https://doi.org/10.1021/ja810157e.

(14) Hong, X.; Liang, Y.; Houk, K. N. Mechanisms and Origins of Switchable Chemoselectivity of Ni-Catalyzed C(Aryl)–O and C(Acyl)–O Activation of Aryl Esters with Phosphine Ligands. *J. Am. Chem. Soc.* **2014**, *136* (5), 2017–2025. https://doi.org/10.1021/ja4118413.

(15) McNicholas, B. J.; Tong, Z. J.; Bím, D.; Turro, R. F.; Kazmierczak, N. P.; Chalupský, J.; Reisman, S. E.; Hadt, R. G. Electronic Structures of Nickel(II)-Bis(Indanyloxazoline)-Dihalide Catalysts: Understanding Ligand Field Contributions That Promote C(Sp2)–C(Sp3) Cross-Coupling. *Inorg. Chem.* **2023**, *62* (34), 14010–14027. https://doi.org/10.1021/acs.inorgchem.3c02048.

(16) Turro, R. F.; Wahlman, J. L. H.; Tong, Z. J.; Chen, X.; Yang, M.; Chen, E. P.; Hong, X.; Hadt, R. G.; Houk, K. N.; Yang, Y.-F.; Reisman, S. E. Mechanistic Investigation of Ni-Catalyzed Reductive Cross-Coupling of Alkenyl and Benzyl Electrophiles. *J. Am. Chem. Soc.* **2023**, *145* (27), 14705–14715. https://doi.org/10.1021/jacs.3c02649.

(17) Zhou, Y.-Y.; Wang, L.-J.; Li, J.; Sun, X.-L.; Tang, Y. Side-Arm-Promoted Highly Enantioselective Ring-Opening Reactions and Kinetic Resolution of Donor–Acceptor Cyclopropanes with Amines. *J. Am. Chem. Soc.* **2012**, *134* (22), 9066–9069. https://doi.org/10.1021/ja302691r.

(18) Bour, J. R.; Camasso, N. M.; Sanford, M. S. Oxidation of Ni(II) to Ni(IV) with Aryl Electrophiles Enables Ni-Mediated Aryl–CF3 Coupling. *J. Am. Chem. Soc.* **2015**, *137* (25), 8034–8037. https://doi.org/10.1021/jacs.5b04892.

(19) Mohadjer Beromi, M.; Brudvig, G. W.; Hazari, N.; Lant, H. M. C.; Mercado, B. Q. Synthesis and Reactivity of Paramagnetic Nickel Polypyridyl Complexes Relevant to C(Sp2)–C(Sp3)Coupling Reactions. *Angew. Chem. Int. Ed.* **2019**, *58* (18), 6094–6098. https://doi.org/10.1002/anie.201901866.

(20) Sun, R.; Qin, Y.; Ruccolo, S.; Schnedermann, C.; Costentin, C.; Nocera, D. G. Elucidation of a Redox-Mediated Reaction Cycle for Nickel-Catalyzed Cross Coupling. *J. Am. Chem. Soc.* **2019**, *141* (1), 89–93. https://doi.org/10.1021/jacs.8b11262.

(21) Newman-Stonebraker, S. H.; Raab, T. J.; Roshandel, H.; Doyle, A. G. Synthesis of Nickel(I)–Bromide Complexes via Oxidation and Ligand Displacement: Evaluation of Ligand Effects on Speciation and Reactivity. *J. Am. Chem. Soc.* **2023**, *145* (35), 19368–19377. https://doi.org/10.1021/jacs.3c06233.

(22) Gutierrez, O.; Tellis, J. C.; Primer, D. N.; Molander, G. A.; Kozlowski, M. C. Nickel-Catalyzed Cross-Coupling of Photoredox-Generated Radicals: Uncovering a General Manifold for Stereoconvergence in Nickel-Catalyzed Cross-Couplings. *J. Am. Chem. Soc.* **2015**, *137* (15), 4896–4899. https://doi.org/10.1021/ja513079r.

(23) Yuan, M.; Song, Z.; Badir, S. O.; Molander, G. A.; Gutierrez, O. On the Nature of C(Sp3)–C(Sp2) Bond Formation in Nickel-Catalyzed Tertiary Radical Cross-Couplings: A Case Study of Ni/Photoredox Catalytic Cross-Coupling of Alkyl Radicals and Aryl Halides. *J. Am. Chem. Soc.* **2020**, *142* (15), 7225–7234. https://doi.org/10.1021/jacs.0c02355.

(24) Ananikov, V. P. Nickel: The "Spirited Horse" of Transition Metal Catalysis. *ACS Catal.* **2015**, *5* (3), 1964–1971. https://doi.org/10.1021/acscatal.5b00072.

(25) Claridge, R. F. C.; Fischer, H. Self-Termination and Electronic Spectra of Substituted Benzyl Radicals in Solution. *J. Phys. Chem.* **1983**, *87* (11), 1960–1967. https://doi.org/10.1021/j100234a026.

(26) Mayouff, A. M.; Lemmetyinen, H. Oxidation—Reduction Reaction of Photoinduced Benzyl Radicals in Water: Para Substituent Effect. *J. Photochem. Photobiol. Chem.* **1993**, *73* (3), 205–211. https://doi.org/10.1016/1010-6030(93)90006-7.

(27) Meiggs, T. O.; Grossweiner, L. I.; Miller, S. I. Extinction Coefficient and Recombination Rate of Benzyl Radicals. II. Photolysis of Several Benzyl Phenylacetates in Methanol. *J. Am. Chem. Soc.* **1972**, *94* (23), 7986–7991. https://doi.org/10.1021/ja00778a009.

(28) Griller, D.; Ingold, K. U. Persistent Carbon-Centered Radicals. *Acc. Chem. Res.* **1976**, *9* (1), 13–19. https://doi.org/10.1021/ar50097a003.

(29) Olivella, S.; Ballester, M.; Castañer, J. Perchlorobenzyl, a Stable Carbon Free Radical. *Tetrahedron Lett.* **1974**, *15* (7), 587–590. https://doi.org/10.1016/S0040-4039(01)82278-4.

(30) Schreiner, K.; Berndt, A. ESR Spectrum of a Perpendicular Benzyl Radical. *Angew. Chem. Int. Ed. Engl.* **1974**, *13* (2), 144–145. https://doi.org/10.1002/anie.197401441.

(31) Griller, D.; Ingold, K. U. Free-Radical Clocks. *Acc. Chem. Res.* **1980**, *13* (9), 317–323. https://doi.org/10.1021/ar50153a004.

(32) Newcomb, M. Radical Kinetics and Clocks. In *Encyclopedia of Radicals in Chemistry, Biology and Materials*; John Wiley & Sons, Ltd, 2012. https://doi.org/10.1002/9781119953678.rad007.

(33) Poremba, K. E.; Dibrell, S. E.; Reisman, S. E. Nickel-Catalyzed Enantioselective Reductive Cross-Coupling Reactions. *ACS Catal.* **2020**, *10* (15), 8237–8246. https://doi.org/10.1021/acscatal.0c01842.

(34) Leifert, D.; Studer, A. The Persistent Radical Effect in Organic Synthesis. *Angew. Chem. Int. Ed.* **2020**, *59* (1), 74–108. https://doi.org/10.1002/anie.201903726.

(35) Liu, W.; Lavagnino, M. N.; Gould, C. A.; Alcázar, J.; MacMillan, D. W. C. A Biomimetic SH2 Cross-Coupling Mechanism for Quaternary Sp3-Carbon Formation. *Science* **2021**, *374* (6572), 1258–1263. https://doi.org/10.1126/science.abl4322.

(36) Wang, J. Z.; Mao, E.; Nguyen, J. A.; Lyon, W. L.; MacMillan, D. W. C. Triple Radical Sorting: Aryl-Alkylation of Alkenes. *J. Am. Chem. Soc.* **2024**, *146* (23), 15693–15700. https://doi.org/10.1021/jacs.4c05744.

(37) Hofstra, J. L.; Cherney, A. H.; Ordner, C. M.; Reisman, S. E. Synthesis of Enantioenriched Allylic Silanes via Nickel-Catalyzed Reductive Cross-Coupling. *J. Am. Chem. Soc.* **2018**, *140* (1), 139–142. https://doi.org/10.1021/jacs.7b11707.

(38) Hofstra, J. L. Development and Mechanistic Studies of Ni-Catalyzed Asymmetric Reductive Cross-Coupling Reactions, California Institute of Technology.

(39) Suzuki, N.; Hofstra, J. L.; Poremba, K. E.; Reisman, S. E. Nickel-Catalyzed Enantioselective Cross-Coupling of *N* -Hydroxyphthalimide Esters with Vinyl Bromides. *Org. Lett.* **2017**, *19* (8), 2150–2153. https://doi.org/10.1021/acs.orglett.7b00793.

(40) Yin, H.; Fu, G. C. Mechanistic Investigation of Enantioconvergent Kumada Reactions of Racemic α-Bromoketones Catalyzed by a Nickel/Bis(Oxazoline) Complex. *J. Am. Chem. Soc.* **2019**, *141* (38), 15433–15440. https://doi.org/10.1021/jacs.9b08185.

(41) Mishra, B. K.; Sathyamurthy, N. Π−π Interaction in Pyridine. *J. Phys. Chem. A* **2005**, *109* (1), 6–8. https://doi.org/10.1021/jp045218c.

(42) Frontera, A.; Quiñonero, D.; Deyà, P. M. Cation–π and Anion–π Interactions. *WIREs Comput. Mol. Sci.* **2011**, *1* (3), 440–459. https://doi.org/10.1002/wcms.14.

(43) Ciszewski, J. T.; Mikhaylov, D. Y.; Holin, K. V.; Kadirov, M. K.; Budnikova, Y. H.; Sinyashin, O.; Vicic, D. A. Redox Trends in Terpyridine Nickel Complexes. *Inorg. Chem.* **2011**, *50* (17), 8630–8635. https://doi.org/10.1021/ic201184x.

(44) Mohadjer Beromi, M.; Banerjee, G.; Brudvig, G. W.; Hazari, N.; Mercado, B. Q. Nickel(I) Aryl Species: Synthesis, Properties, and Catalytic Activity. *ACS Catal.* **2018**, *8* (3), 2526–2533. https://doi.org/10.1021/acscatal.8b00546.

(45) Müller, P.; Finkelstein, P.; Trapp, N.; Bismuto, A.; Jeschke, G.; Morandi, B. Nickel(I)–Phenolate Complexes: The Key to Well-Defined Ni(I) Species. *Inorg. Chem.* **2023**, *62* (41), 16661–16668. https://doi.org/10.1021/acs.inorgchem.3c01559.

(46) Tong, X.; Schneck, F.; Fu, G. C. Catalytic Enantioselective α-Alkylation of Amides by Unactivated Alkyl Electrophiles. *J. Am. Chem. Soc.* **2022**, *144* (32), 14856–14863. https://doi.org/10.1021/jacs.2c06154.

(47) Bannwarth, C.; Ehlert, S.; Grimme, S. GFN2-xTB—An Accurate and Broadly Parametrized Self-Consistent Tight-Binding Quantum Chemical Method with Multipole Electrostatics and Density-Dependent Dispersion Contributions. *J. Chem. Theory Comput.* **2019**, *15* (3), 1652–1671. https://doi.org/10.1021/acs.jctc.8b01176.

(48) Newman-Stonebraker, S. H.; Smith, S. R.; Borowski, J. E.; Peters, E.; Gensch, T.; Johnson, H. C.; Sigman, M. S.; Doyle, A. G. Univariate Classification of Phosphine Ligation State and Reactivity in Cross-Coupling Catalysis. *Science* **2021**, *374* (6565), 301–308. https://doi.org/10.1126/science.abj4213.

(49) Connelly, N. G.; Geiger, W. E. Chemical Redox Agents for Organometallic Chemistry. *Chem. Rev.* **1996**, *96* (2), 877–910. https://doi.org/10.1021/cr940053x.

(50) Su, Z.-M.; Deng, R.; Stahl, S. S. Zinc and Manganese Redox Potentials in Organic Solvents and Their Influence on Nickel-Catalysed Cross-Electrophile Coupling. *Nat. Chem.* **2024**, *16* (12), 2036–2043. https://doi.org/10.1038/s41557-024-01627-5.

(51) Metallacyclische Acyl-Carboxylate Des Nickels: Reaktivität Der Acylgruppe Und Synthesepotential Bei Kreuzkopplungsreaktionen Mit Alkylhalogeniden. *J. Organomet. Chem.* **1993**, *447* (1), 131–136. https://doi.org/10.1016/0022-328X(93)80282-G.

(52) Tang, T.; Hazra, A.; Min, D. S.; Williams, W. L.; Jones, E.; Doyle, A. G.; Sigman, M. S. Interrogating the Mechanistic Features of Ni(I)-Mediated Aryl Iodide Oxidative Addition Using Electroanalytical and Statistical Modeling Techniques. *J. Am. Chem. Soc.* **2023**, *145* (15), 8689–8699. https://doi.org/10.1021/jacs.3c01726.

(53) J. Martin, D.; D. McCarthy, B.; S. Rountree, E.; L. Dempsey, J. Qualitative Extension of the EC′ Zone Diagram to a Molecular Catalyst for a Multi-Electron, Multi-

Substrate Electrochemical Reaction. *Dalton Trans.* **2016**, *45* (24), 9970–9976. https://doi.org/10.1039/C6DT00302H.

(54) Savéant, J. M.; Su, K. B. Homogeneous Redox Catalysis of Electrochemical Reaction: Part VI. Zone Diagram Representation of the Kinetic Regimes. *J. Electroanal. Chem. Interfacial Electrochem.* **1984**, *171* (1), 341–349. https://doi.org/10.1016/0022-0728(84)80125-4.

(55) Costentin, C.; Savéant, J.-M. Multielectron, Multistep Molecular Catalysis of Electrochemical Reactions: Benchmarking of Homogeneous Catalysts. *ChemElectroChem* **2014**, *1* (7), 1226–1236. https://doi.org/10.1002/celc.201300263.

(56) Andrieux, C. P.; Blocman, C.; Dumas-Bouchiat, J. M.; M'Halla, F.; Savéant, J. M. Homogeneous Redox Catalysis of Electrochemical Reactions: Part V. Cyclic Voltammetry. *J. Electroanal. Chem. Interfacial Electrochem.* **1980**, *113* (1), 19–40. https://doi.org/10.1016/S0022-0728(80)80508-0.

(57) Andrieux, C. P.; Dumas-Bouchiat, J. M.; Savéant, J. M. Homogeneous Redox Catalysis of Electrochemical Reactions: Part IV. Kinetic Controls in the Homogeneous Process as Characterized by Stationary and Quasi-Stationary Electrochemical Techniques. *J. Electroanal. Chem. Interfacial Electrochem.* **1980**, *113* (1), 1–18. https://doi.org/10.1016/S0022-0728(80)80507-9.

(58) Moulton, R. D.; Bard, A. J.; Feldberg, S. W. Digital Simulations of Cyclic Voltammetry for the CEq and CEqC2 Mechanisms. *J. Electroanal. Chem. Interfacial Electrochem.* **1988**, *256* (2), 291–307. https://doi.org/10.1016/0022-0728(88)87005-0.

(59) Rountree, E. S.; McCarthy, B. D.; Eisenhart, T. T.; Dempsey, J. L. Evaluation of Homogeneous Electrocatalysts by Cyclic Voltammetry. *Inorg. Chem.* **2014**, *53* (19), 9983–10002. https://doi.org/10.1021/ic500658x.

(60) Homogeneous Redox Catalysis of Electrochemical Reaction: Part VI. Zone Diagram Representation of the Kinetic Regimes. *J. Electroanal. Chem. Interfacial Electrochem.* **1984**, *171* (1–2), 341–349. https://doi.org/10.1016/0022-0728(84)80125-4.

(61) Molina, A.; López-Tenés, M.; Laborda, E. Unified Theoretical Treatment of the Eirrev, CE, EC and CEC Mechanisms under Voltammetric Conditions. *Electrochem. Commun.* **2018**, *92*, 48–55. https://doi.org/10.1016/j.elecom.2018.03.011.

(62) Andrieux, C. P.; Le Gorande, A.; Saveant, J. M. Electron Transfer and Bond Breaking. Examples of Passage from a Sequential to a Concerted Mechanism in the Electrochemical Reductive Cleavage of Arylmethyl Halides. *J. Am. Chem. Soc.* **1992**, *114* (17), 6892–6904. https://doi.org/10.1021/ja00043a039.

(63) Pause, L.; Robert, M.; Savéant, J.-M. Stepwise and Concerted Pathways in Photoinduced and Thermal Electron-Transfer/Bond-Breaking Reactions. Experimental Illustration of Similarities and Contrasts. *J. Am. Chem. Soc.* **2001**, *123* (21), 4886–4895. https://doi.org/10.1021/ja004234u.

(64) Pause, L.; Robert, M.; Savéant, J.-M. Stabilities of Ion/Radical Adducts in the Liquid Phase as Derived from the Dependence of Electrochemical Cleavage Reactivities upon Solvent. *J. Am. Chem. Soc.* **2001**, *123* (48), 11908–11916. https://doi.org/10.1021/ja0117985.

(65) Costentin, C.; Robert, M.; Savéant, J.-M. Stepwise and Concerted Electron-Transfer/Bond Breaking Reactions. Solvent Control of the Existence of Unstable π Ion

Radicals and of the Activation Barriers of Their Heterolytic Cleavage. *J. Am. Chem. Soc.* **2004**, *126* (51), 16834–16840. https://doi.org/10.1021/ja045294t.

(66) Costentin, C.; Donati, L.; Robert, M. Passage from Stepwise to Concerted Dissociative Electron Transfer through Modulation of Electronic States Coupling. *Chem. – Eur. J.* **2009**, *15* (3), 785–792. https://doi.org/10.1002/chem.200801240.

(67) Chénard, E.; Sutrisno, A.; Zhu, L.; Assary, R. S.; Kowalski, J. A.; Barton, J. L.; Bertke, J. A.; Gray, D. L.; Brushett, F. R.; Curtiss, L. A.; Moore, J. S. Synthesis of Pyridine– and Pyrazine–BF3 Complexes and Their Characterization in Solution and Solid State. *J. Phys. Chem. C* **2016**, *120* (16), 8461–8471. https://doi.org/10.1021/acs.jpcc.6b00858.

(68) Bauer, J.; Braunschweig, H.; Kraft, K.; Radacki, K. Oxidative Addition of Boron Trifluoride to a Transition Metal. *Angew. Chem. Int. Ed.* **2011**, *50* (44), 10457–10460. https://doi.org/10.1002/anie.201103226.

(69) Saraev, V. V.; Kraikivskii, P. B.; Matveev, D. A.; Zelinskii, S. N.; Lammertsma, K. EPR Study of the Oxidation Reaction of Nickel(0) Phosphine Complexes with Lewis and Brønsted Acids. *Inorganica Chim. Acta* **2006**, *359* (7), 2314–2320. https://doi.org/10.1016/j.ica.2006.01.028.

(70) Zhu, J.; Lin, Z.; Marder, T. B. Trans Influence of Boryl Ligands and Comparison with C, Si, and Sn Ligands. *Inorg. Chem.* **2005**, *44* (25), 9384–9390. https://doi.org/10.1021/ic0513641.

(71) Zhang, P.; Eun, J.; Elkin, M.; Zhao, Y.; Cantrell, R. L.; Newhouse, T. R. A Neural Network Model Informs the Total Synthesis of Clovane Sesquiterpenoids. *Nat. Synth.* **2023**, *2* (6), 527–534. https://doi.org/10.1038/s44160-023-00271-0.

(72) Li, C.; Shenvi, R. Total Synthesis of Twenty-Five Picrotoxanes by Virtual Library Selection. ChemRxiv June 3, 2024. https://doi.org/10.26434/chemrxiv-2024-g8j1r.

(73) Orvig, C. A Simple Method to Perform a Liquid Diffusion Crystallization. *J. Chem. Educ.* **1985**, *62* (1), 84. https://doi.org/10.1021/ed062p84.

(74) Pracht, P.; Grimme, S.; Bannwarth, C.; Bohle, F.; Ehlert, S.; Feldmann, G.; Gorges, J.; Müller, M.; Neudecker, T.; Plett, C.; Spicher, S.; Steinbach, P.; Wesołowski, P. A.; Zeller, F. CREST—A Program for the Exploration of Low-Energy Molecular Chemical Space. *J. Chem. Phys.* **2024**, *160* (11), 114110. https://doi.org/10.1063/5.0197592.

(75) Neese, F. The ORCA Program System. *Wiley Interdiscip. Rev. Comput. Mol. Sci.* **2012**, *2* (1), 73–78. https://doi.org/10.1002/wcms.81.